



U.S. Department
of Transportation
**National Highway
Traffic Safety
Administration**



DOT HS 811 692

December 2012

Investigation of Opportunities for Lightweight Vehicles Using Advanced Plastics and Composites

DISCLAIMER

This publication is distributed by the U.S. Department of Transportation, National Highway Traffic Safety Administration, in the interest of information exchange. The opinions, findings, and conclusions expressed in this publication are those of the authors and not necessarily those of the Department of Transportation or the National Highway Traffic Safety Administration. The United States Government assumes no liability for its contents or use thereof. If trade names, manufacturers' names, or specific products are mentioned, it is because they are considered essential to the object of the publication and should not be construed as an endorsement. The United States Government does not endorse products or manufacturers.

Suggest APA Format Citation:

Park, C-K., Kan, C-D., Hollowell, W., & Hill, S.I. (2012, December). *Investigation of opportunities for lightweight vehicles using advanced plastics and composites*. (Report No. DOT HS 811 692). Washington, DC: National Highway Traffic Safety Administration.

Investigation of Opportunities for Lightweight Vehicles Using Advanced Plastics and Composites

Technical Report Documentation Page

1. Report No. DOT HS 811 692		2. Government Accession No.		3. Recipient's Catalog No.	
4. Title and Subtitle Investigation of Opportunities for Lightweight Vehicles Using Advanced Plastics And Composites				5. Report Date December 2012	
				6. Performing Organization Code	
7. Author(s) Chung-Kyu Park and Cing-Dao (Steve) Kan William Thomas Hollowell Susan I. Hill				8. Performing Organization Report No.	
9. Performing Organization Name and Address National Crash Analysis Center, The George Washington University 45085 University Drive, Suite 301, Ashburn, VA 20147 WTH Consulting LLC 2634 Iveysprings Court, Apex, NC 27539 Structural Integrity Division, University of Dayton Research Institute 300 College Park, Dayton, OH 45469				10. Work Unit No. (TRAIS)	
				11. Contract or Grant No. DTFH61-09-D-0001 (task order 15)	
12. Sponsoring Agency Name and Address National Highway Traffic Safety Administration 1200 New Jersey Avenue SE. Washington, DC 20590				13. Type of Report and Period Covered Final Report	
				14. Sponsoring Agency Code NVS-300	
15. Supplementary Notes					
16. Abstract As part of implementing the Plastics and Composite Intensive Vehicle (PCIV) safety roadmap, the National Crash Analysis Center of the George Washington University undertook this research project to investigate opportunities for light-weight vehicles using advanced plastics and composites. The primary goal of this research project was to identify and evaluate the safety benefits of structural plastics and composites applications in future lighter, more fuel efficient, and environmentally sustainable vehicles. The research objectives of this project were (1) to evaluate the current state of modeling and simulation tools for predicting impact response of composite materials in automotive structures, (2) to investigate weight reduction opportunities in a current vehicle, and (3) to evaluate the impact of weight reduction on crashworthiness. This report includes a comprehensive literature review focused on the characteristics and mechanics of plastics and composites, the applicability of advanced plastics and composites to automotive components, and the capabilities and limitations of simulations to composite analysis. Also, the report describes the development of a light-weight vehicle numerical model (i.e., finite element model) that was used to investigate the weight reduction opportunities in a current vehicle. This involved conducting material tests of carbon fiber braided composites under various conditions, incorporating material substitutions of steel components into the 2007 Chevrolet Silverado FE model to composite components, and simulating frontal New Car Assessment Program tests of the developed light-weight vehicle to evaluate its crashworthiness. In conclusion, the original vehicle weight, 2,307 kg, was reduced to 1,874 kg, which is about a 19-percent decrease. As a result, the light-weight vehicle represented by a FE model contains about 442 kg of plastic and composites, which represents about 23.6 percent of the total weight of the lightweight vehicle.					
17. Key Words Plastics, Composites, Plastics and Composites Intensive Vehicle (PCIV), Light-Weight Vehicle, Material tests, Carbon fiber braided composite, Safety, Crashworthiness, Frontal crash simulations				18. Distribution Statement Document is available to the public from the National Technical Information Service www.ntis.gov	
19. Security Classif. (of this report) Unclassified		20. Security Classif. (of this page) Unclassified		21. No. of Pages 416	
				22. Price	

Form DOT F 1700.7 (8-72) Reproduction of completed page authorized

List of Acronyms

2D3A	2-dimension triaxial
ABS	acryl butadiene styrene
ABS	automatic braking systems
ACC PD	American Chemistry Council Plastics Division
Al	aluminum
APC	American Plastics Council
ASA/AES	acrylonitrile styrene acrylate/acrylonitrile-EPDM-styrene
ASTM	American Society for Testing and Materials
BIW	body-In-white
BMC	bulk molding compound
CAE	computer-aided engineering
CAFÉ	Corporate Average Fuel Economy
CDM	continuum damage mechanics
CFM	continuous fiber mat
CFRT	continuous fiber reinforced thermoplastic
CG	center of gravity
CLT	classical lamination theory
CMC	ceramic matrix composite
CNG	compressed natural gas
CSM	chopped strand mat
EP	epoxy
EPDM	ethylene propylene diene monomer
F-D	force-displacement
FE	finite element
FHWA	Federal Highway Administration
FRP	fiber-reinforced polymer
GMT	glass mat thermoplastic
GVWR	gross vehicle weight rating
GWU	George Washington University
HD-SRIM	high-density structural reaction injection molding
HSS	high-strength steel
IAA	Inter-Agency Agreement
IP	instrumental panel
LED	light emitting diode
LFT	long-fiber thermoplastic
LST	laminated shell theory
MF	melamine formaldehyde
MLT	Matzenmiller, Lubliner, and Taylor
MMC	metal matrix composite
NCAC	National Crash Analysis Center
NCAP	New Car Assessment Program
NHTSA	National Highway Traffic Safety Administration
NVH	noise, vibration, and harshness
PA	olyamide

PBT	polybutylene terephthalate
PC	polycarbonate
PCIV	plastics and composite intensive vehicle
PE	polyethylene
PEEK	polyetherether ketone
PEI	polyetherimide
PEK	polyetherketone
PEKK	polyetherketonetone
PES	polyether sulfone
PET	polyether terephthalate
PF	phenolics
PFM	progressive failure model
PI	polyimide
PMC	polymer matrix composite
PMMA	polymethylmethacrylate
POM	polyoxymethylene
PP	polypropylene
PPE	polyphenylene ether
PPS	polyphenylene sulfide
PS	polystyrene
PSF	polysulfone
PU	polyurethane
PVC	polyvinyl chloride
RMI	Rocky Mountain Institute
RIM	reaction injection molding
RRIM	reinforced reaction injection molding
RTM	resin transfer molding
RVE	representative volume element
S-S	strain-stress
SAP	sintered aluminum powder
SEA	specific energy absorption
SFT	short-fiber thermoplastic
SMA	styrene maleic anhydride)
SMC	sheet molding compound
SRIM	structural reaction injection molding
SUV	sport utility vehicle
TD	thoria-dispersed
TPE	thermoplastic elastomer
TPO	thermoplastic olefin
UDRI	University of Dayton Research Institute
UF	urea formaldehyde
UPE	unsaturated polyester
USDOE	U.S. Department of Energy
USDOT	U.S. Department of Transportation
VE	vinyl ester

Executive Summary

In 2009 an Inter-Agency Agreement provided funding to George Washington University to give technical support to the National Highway Traffic Safety Administration's research on the potential safety benefits of plastics and composite-intensive vehicles. As part of implementing the PCIV safety roadmap, the National Crash Analysis Center of the GWU undertook this research project to investigate opportunities for lightweight vehicles using advanced plastics and composites.

The primary goal of this research project was to identify and evaluate the safety benefits of structural plastics and composites applications in future lighter, more fuel efficient, and environmentally sustainable vehicles. The research objectives of this project were (1) to evaluate the current state of modeling and simulation tools for predicting impact response of composite materials in automotive structures, (2) to investigate weight reduction opportunities in a current vehicle, and (3) to evaluate the impact of such weight reduction on crashworthiness.

The methodology of the research consisted of:

- A comprehensive literature review focused on the:
 - Characteristics and mechanics of plastics and composites,
 - Applicability of advanced plastics and composites to automotive components, and
 - Capabilities and limitations of simulations to composite analysis.
- Development of a lightweight vehicle numerical model (i.e., finite element [FE] model) to investigate the weight reduction opportunities in a current vehicle. This involved:
 - Using as a baseline FE model of a 2007 Chevrolet Silverado, which is a body-on-frame pickup truck.
 - Lighter weight components of the Silverado based on the literature review and with help from the American Chemistry Council Plastics Division's member companies, Saudi Basic Industries Corp. (SABIC), BASF Corp., and Bayer MaterialScience AG.
 - Reducing the weight of the Silverado's ladder frame with a carbon fiber-thermoset matrix braided composite whose material properties were obtained from various physical material tests.
- Frontal New Car Assessment Program test simulations of the developed lightweight vehicles to evaluate the impact of weight reduction on crashworthiness.

In conclusion, the original vehicle weight, 2,307 kg, was reduced to 1,874 kg, which is about a 19-percent decrease. As a result, the lightweight vehicle represented by a FE model contains about 442 kg of plastic and composites, which represents about 23.6 percent of the total weight of the lightweight vehicle. To reach or exceed a 30-percent content of plastics and composites in the development of a PCIV, additional applications of plastics and composites to the vehicle structural components, especially occupant compartment and closures, would be required.

Based on the frontal NCAP simulations of five lightweighted vehicles, structural performance of lightweighted vehicles can be summarized as:

- It was observed that the vehicle mass reduction contributes to a decrease in the vehicle frontal intrusion when the baseline and lightweighted vehicles have similar frontal structure stiffness characteristics.
- The deceleration of a vehicle was more likely to be dependent on the vehicle stiffness and crash mechanisms, rather than vehicle mass reduction.
- Overall, the light-weighted vehicles using advanced plastics and composites provide equivalent structural performance (intrusion and crash pulse) to the baseline vehicle in the full frontal impact condition.

Preface and Acknowledgements

This research was sponsored by the National Highway Traffic Safety Administration under a contract with the Federal Highway Administration of the U.S. Department of Transportation.

The primary authors of this report are Dr. Chung-Kyu Park, research scientist, and Dr. Cing-Dao (Steve) Kan, director, of the National Crash Analysis Center of The George Washington University, and Dr. William Thomas Hollowell, president of WTH Consulting LLC. Susan I. Hill of University of Dayton Research Institute is the author of the material test report which is Appendix A of this report. Other NCAC/GWU staffs and graduate students who contributed to this study include Dr. Pradeep Mohan (currently at the Channabasaveshwara Institute of Technology, India), Richard M. Morgan, Daniel Brown, Alexander Zoellner, Alexander Weller, and Martin Werz. Paul A. Du Bois (CAE Consultants) provided his expertise in numerical material modeling and crash simulations.

The American Chemistry Council Plastics Division industry partners voluntarily participated in this research and provided information and new models of plastics and composite components. Special appreciation is due to James Kolb of ACC PD, Matthew D. Marks and Dhanendra Nagwanshi of SABIC Innovative Plastics, Scott C. Schlicker and Jeffrey Plott of BASF Corporation, and Don Schomer of Bayer MaterialScience LLC.

Table of Contents

List of Acronyms	ii
Executive Summary	iv
Preface and Acknowledgements	vi
List of Figures	viii
List of Tables	xi
1. Introduction	1
2. Plastics and Composites	4
2.1. Lightweight vehicles	4
2.2. Plastics and composites	8
2.3. Fiber-reinforced polymer composites	14
2.4. Automotive applications of plastics and composites	25
3. Basic Composite Mechanics	33
3.1. Stress-strain relationship	33
3.2. Effective moduli of a continuous fiber-reinforced lamina	33
3.3. Analysis of laminates	42
3.4. Composite failure theory	45
4. Numerical Analysis of Composites Using LS-DYNA	51
4.1. Basic keywords for composite analysis	51
4.2. Composite material model	52
4.3. Composite modeling approach	64
5. Development of a Lightweight Vehicle	66
5.1. 2007 Chevrolet Silverado	66
5.2. Candidate components for weight reduction	73
6. Composite Ladder Frame	77
6.1. Physical material test	77
6.2. Numerical analysis	87
6.3. Composite ladder frame	96
7. Lightweight Components	108
7.1. Occupant compartment structure	108
7.2. Interiors	110
7.3. Closures	110
7.4. Truck bed structure	112
7.5. Power-train related	114
7.6. Suspension-related	119
7.7. Ladder frame structure	122
7.8. Summary	158
8. Frontal NCAP Simulations	129
8.1. Lightweight vehicle configurations	129
8.2. Frontal NCAP simulations	130
8.3. Summary	158
9. Conclusions	161
References	165
Appendix A. Material Test Report by University of Dayton Research Institute	A-1

List of Figures

Figure 2.1. Average material consumption for a domestic light vehicle, model years 1995, 2000, and 2009	8
Figure 2.2. Classification of structural materials	9
Figure 2.3. Classification of polymers	10
Figure 2.4. Classification of composites	13
Figure 2.5. Classification of composites	13
Figure 2.6. Classification of fibers	15
Figure 2.7. Specific strength versus specific stiffness of some fibers	15
Figure 2.8. Fabric forms	17
Figure 2.9. Two-dimensional fiber architectures	17
Figure 2.10. Typical values of specific energy absorption for some materials	23
Figure 2.11. Tubular crash test	23
Figure 2.12. Unstable modes of failure showing	24
Figure 2.13. Crush failure modes	25
Figure 3.1. General three-dimensional state of stress	34
Figure 3.2. Orthotropic lamina with principal coordinate and non-principal coordinate	36
Figure 3.3. Representative volume element	39
Figure 3.4. Laminated plates	42
Figure 4.1. Description of invariant node numbering option in *CONTROL_ACCURACY	49
Figure 4.2. Usage of *PART_COMPOSITE	50
Figure 4.3. Options for defining principle material axes	51
Figure 5.1. 2007 Chevrolet Silverado	67
Figure 5.2. Deformation of the original FE model of 2007 Chevrolet Silverado in frontal NCAP test	68
Figure 5.3. Frontal NCAP test (test # 5877)	68
Figure 5.4. Deformation modes of ladder frame of Silverado in frontal NCAP test	69
Figure 5.5. Frontal NCAP test (test # 5907)	70
Figure 5.6. Frontal NCAP test (test # 7121)	70
Figure 5.7. Original ladder frame	71
Figure 5.8. Original ladder frame (modified)	71
Figure 5.9. Deformation of the original FE model (modified) of 2007 Chevrolet Silverado in frontal NCAP test	72
Figure 5.10. Deformation of ladder frame	72
Figure 5.11. Absorbed energy distribution	73
Figure 5.12. Responses (at rear floor) of the vehicle in frontal NCAP test	73
Figure 5.13. Assembly of the FE model of Silverado	74
Figure 6.1. 2D3A braided composite	78
Figure 6.2. Cross-section of panel	78
Figure 6.3. Cross-section of tube	79
Figure 6.4. Specimens of ASTM D3039 tension test	80
Figure 6.5. Bowtie specimens	80
Figure 6.6. Specimens of compression test	86
Figure 6.7. Stress-strain curves for modified ASTM D3039 tension tests	83
Figure 6.8. Stress-strain curves for bowtie tension tests (axial)	83
Figure 6.9. Stress-strain curves for bowtie tension tests (transverse)	84
Figure 6.10. Stress-strain curves for compression tests (axial)	84
Figure 6.11. Stress-strain curves for compression tests (transverse)	84

Figure 6.12. Stress-strain curves for shear tests (axial)	85
Figure 6.13. Stress-strain curves for shear tests (transverse)	85
Figure 6.14. Load-displacement curves of tube compression tests	86
Figure 6.15. Tube failure	89
Figure 6.16. FE models (coarse) of specimens for coupon test	89
Figure 6.17. FE models (fine) of specimens for coupon test	89
Figure 6.18. FE model of tube for compression test	89
Figure 6.19. F-D curves of bowtie axial tension tests	91
Figure 6.20. F-D curves of bowtie transverse tension tests	91
Figure 6.21. F-D curves of axial compression tests	91
Figure 6.22. F-D curves of transverse compression tests	92
Figure 6.23. F-D curves of axial shear tests	92
Figure 6.24. F-D curves of transverse shear tests	94
Figure 6.25. Strain-stress curves of bowtie tension simulations	95
Figure 6.26. Strain-stress curves of ASTM tension simulations	99
Figure 6.27. Strain-stress curves of compression simulations	95
Figure 6.28. Strain-stress curves of shear simulations	95
Figure 6.29. Strain-stress curves of shear simulations (with straight-sided specimen)	95
Figure 6.30. Force and absorbed energy curves of tube compression simulations	102
Figure 6.31. Tube deformation in tube compression simulation	102
Figure 6.32. Ladder frame of Silverado	103
Figure 6.33. Stiffness tests of Silverado ladder frame	104
Figure 6.34. Stiffness of ladder frame	105
Figure 6.35. Rigid wall impact test of Silverado ladder frame	106
Figure 6.36. Close-up view of front area of ladder frame (undeformed)	106
Figure 6.37. Deformation of original steel ladder frame	102
Figure 6.38. Deformation of new composite ladder frame (normalized thickness=1.0)	103
Figure 6.39. Deformation of new composite ladder frame (normalized thickness=2.0)	104
Figure 6.40. Deformation of new composite ladder frame (normalized thickness=3.0)	105
Figure 6.41. X-velocity profiles of ladder frames	106
Figure 6.42. Wall forces of ladder frames	106
Figure 6.43. Maximum displacement of ladder frame	109
Figure 7.1. Roof	109
Figure 7.2. Pillar reinforcements	109
Figure 7.3. Roof tests	109
Figure 7.4. B-pillar punch tests	110
Figure 7.5. Front fenders	111
Figure 7.6. Rear window	111
Figure 7.7. Door beams	112
Figure 7.8. Truck bed	113
Figure 7.9. Tailgate assembly	113
Figure 7.10. Rear fenders	114
Figure 7.11. Silverado engines	115
Figure 7.12. Silverado body styles	115
Figure 7.13. Front-end module assembly	116
Figure 7.14. Engine and transmission oil pans	116

Figure 7.15. Drive shaft and yokes	118
Figure 7.16. Rear differential carrier	118
Figure 7.17. Fuel tank	118
Figure 7.18. Wheels	119
Figure 7.19. Front brake disks	126
Figure 7.20. Tires	126
Figure 7.21. Spare tire and its carrier	127
Figure 7.22. Leaf springs	127
Figure 7.23. Steering stabilizer links	128
Figure 7.24. Transmission crossbeam assembly	124
Figure 7.25. Rear bumper assembly	130
Figure 7.26. Front bumper assembly	131
Figure 7.27. Rigid wall tests	131
Figure 7.28. Pole tests	132
Figure 8.1. Acceleration history of vehicles	137
Figure 8.2. Crumple zone of the baseline vehicle	138
Figure 8.3. Velocity history of vehicles	139
Figure 8.4. Force history for rigid wall	134
Figure 8.5. Measurement points of vehicle intrusion	136
Figure 8.6. Vehicle intrusions of the New1 vehicle configuration	137
Figure 8.7. Vehicle intrusions of the New2 and New3 vehicle configuration	138
Figure 8.8. Vehicle intrusions of the New4 and New5 vehicle configuration	139
Figure 8.9. Deformation of baseline vehicle	140
Figure 8.10. Deformation of baseline vehicle (frontal area)	141
Figure 8.11. Deformation of steel ladder frame of baseline vehicle	142
Figure 8.12. Deformation of New1 vehicle configuration	143
Figure 8.13. Deformation of New1 vehicle configuration (frontal area)	144
Figure 8.14. Deformation of the steel ladder frame of the New1 vehicle configuration	145
Figure 8.15. Deformation of the New2 vehicle configuration	146
Figure 8.16. Deformation of the New2 vehicle configuration (frontal area)	147
Figure 8.17. Deformation of the composite ladder frame (2×t) of the New2 vehicle configuration	148
Figure 8.18. Deformation of the New3 vehicle configuration	149
Figure 8.19. Deformation of the New3 vehicle configuration (frontal area)	150
Figure 8.20. Deformation of the composite ladder frame (3×t) of the New3 vehicle configuration	151
Figure 8.21. Deformation of the New4 vehicle configuration	152
Figure 8.22. Deformation of the New4 vehicle configuration (frontal area)	153
Figure 8.23. Deformation of the composite ladder (2×t) frame of the New4 vehicle configuration	154
Figure 8.24. Deformation of the New5 vehicle configuration	155
Figure 8.25. Deformation of the New5 vehicle configuration (frontal area)	156
Figure 8.26. Deformation of the composite ladder frame (3×t) of the New5 vehicle configuration	157

List of Tables

Table 2.1. Automotive materials with corresponding mass reduction and relative cost	5
Table 2.2. Summary of vehicle mass-reduction studies	5
Table 2.3. Summary of lightweight automotive safety studies	7
Table 2.4. Typical properties of thermoset resins	11
Table 2.5. Typical properties of thermoplastic resins	12
Table 2.6. Typical properties of fibers	15
Table 2.7. Comparison of the most commonly used composite molding processes	19
Table 2.8. Description of internal failure types of FRP composites	21
Table 2.9. Summary of failure modes of FRP composites	24
Table 2.10. Component weight-reduction potential from technologies on production vehicles	34
Table 4.1. Composite material models in LS-DYNA	52
Table 4.2. Variables of MAT22	52
Table 4.3. Variables of MAT54 and MAT55	53
Table 4.4. Variables of MAT58	54
Table 4.5. Variables of MAT158	57
Table 4.6. Variables of MAT116	58
Table 4.7. Variables of MAT117	58
Table 4.8. Variables of MAT118	58
Table 4.9. Variables of MAT158	59
Table 4.10. Variables of MAT161	60
Table 5.1. Specification of the FE model of 2007 Chevrolet Silverado	67
Table 5.2. Mass distribution of the FE model of Silverado	75
Table 5.3. Candidate components for weight reduction	76
Table 6.1. Mechanical properties of carbon fiber and resin	78
Table 6.2. Coupon test matrix	79
Table 6.3. Tube compression test matrix	79
Table 6.4. Bowtie tension nominal specimen dimensions	81
Table 6.5. Shear nominal specimen dimensions	81
Table 6.6. Data summary for coupon tests	82
Table 6.7. Data summary of tube compression tests	86
Table 6.8. Material properties of MAT58	88
Table 6.9. Comparison of material properties of braided composite and simple laminated composite.....	90
Table 6.10. Thickness and weight of ladder frame	98
Table 7.1. Specifications of Silverado	114
Table 7.2. Summary of weight savings	127
Table 8.1. Description of lightweight vehicle configurations	129
Table 8.2. Weight of the various vehicle configurations	130
Table 8.3. CG point movement from original location	130
Table 8.4. Summary of vehicle responses	135

1. Introduction

In fiscal year 2006, Congress directed the National Highway Traffic Safety Administration of the Department of Transportation to begin the development of a program to examine the possible safety benefits of lightweight Plastics- and Composite-Intensive Vehicles (PCIVs) and to develop a foundation for cooperation with the U.S. Department of Energy, industry and other automotive safety stakeholders (Senate Report No. 109-293). NHTSA tasked the Volpe National Transportation Systems Center to conduct focused research, in cooperation with industry partners from the American Plastics Council, now the American Chemistry Council Plastics Division.

NHTSA concentrated on the safety-related research issues affecting the deployment of PCIVs in 2020. In 2007, the Volpe Center developed a safety roadmap for future PCIVs and described the approach, activities, and results of an evaluation of potential safety benefits of PCIVs (Brecher, 2007, 2009). In the 2008 PCIV safety workshop conducted by the Volpe Center, attendees indicated that a minimum of 30 percent to 40 percent (by weight) of plastics and composite content in one or more subsystems beyond interior trim could be considered to qualify a vehicle as a PCIV (Volpe Center, 2008). Barnes et al. identified outstanding safety issues and research needs for PCIVs to facilitate their safety deployment by 2020, and recommended three topics pertinent to crashworthiness of PCIVs: (1) material database, (2) crashworthiness test method development, and (3) crash modelling (Barnes, 2010).

In 2001, the APC (now the ACC PD) outlined a Vision and Technology Roadmap for the automotive and plastics industries (Fisher, 2002). In the technology integration workshop in 2005, the ACC PD provided an expansive safety road mapping effort examining PCIVs (Fisher, 2007). In 2009, the ACC PD updated the vision and technology roadmap to outline the industry's action priorities for achieving the technology and manufacturing innovations required to realize PCIVs (ACC PD, 2009b). Also, the ACC PD recommended three research activities: (1) improve the understanding of composite component response in vehicle crashes, (2) development a database of relevant parameters for composite materials, and (3) enhance predictive models to avoid costly overdesign (ACC PD, 2009a).

There is an increasing need to investigate opportunities for weight reduction the vehicle fleet to improve fuel economy and compatibility of the vehicle fleet. However, this should be achieved without sacrificing the current self-protection levels in the vehicle fleet. Innovative plastics and fiber reinforced composite materials offer a means to lightweight vehicle structures. The main advantages of composites over the more conventional isotropic materials are the lower density, very high specific strength, and specific stiffness that can be achieved.

Previous studies have shown that composite structures deform in a manner different than similar structural components made of conventional materials like steel and aluminum. The micro-failure modes, such as matrix cracking, delamination, fiber breakage, etc., constitute the main failure modes of composite structures. These complex fracture mechanisms make it difficult to analytically and numerically model the collapse behavior of fiber reinforced composite

structures. This has limited the application of composites materials for mass production in the automotive industry.

In 2009, an Inter-Agency Agreement provided funding to The George Washington University to give technical support to the NHTSA research on the potential safety benefits of PCIVs. As part of implementing the PCIV safety roadmap, the National Crash Analysis Center at GWU initiated this research project to investigate opportunities for lightweight vehicles using advanced plastics and composites.

The primary goal of this multi-year research project was to identify and evaluate the safety benefits of structural plastics and composites applications in future lighter, more fuel efficient, and environmentally sustainable vehicles. This PCIV safety research also supports national and global efforts to design and deploy vehicles with improved fuel efficiency and emissions, without compromising their crash safety. The research objectives of this project were (1) to evaluate the current state of modeling and simulation tools for predicting impact response of composite materials in automotive structures, (2) to investigate weight reduction opportunities in a current vehicle, and (3) to evaluate the impact of weight reduction on crashworthiness.

A research approach was formulated to advance the simulation capabilities to effectively model and predict the behavior of composite structures in automotive applications. At first, a comprehensive literature review was undertaken to understand the existing research works, the composite characteristics and mechanics, the applicability of advanced plastics and composites to automotive components, and the capability and limitation of simulations to composite analysis.

In order to investigate the weight reduction opportunities in a current vehicle, a lightweight vehicle was developed numerically (i.e., a finite element model was developed). An FE model of a 2007 Chevrolet Silverado, which is a body-on-frame pickup truck, was selected as the candidate vehicle for weight reduction. Plastics and composites were considered as the primary substitute materials in this study. Based on the literature review and with help from the ACC PD's member companies, candidate steel vehicle components in the Silverado were selected and weight was reduced by substituting plastics and composites for the heavier steel components.

Furthermore, the steel ladder frame, which is the primary structural member of the Silverado, was selected and weight-reduced with a composite material in order to evaluate the crashworthiness of a structural composite member in the vehicle structure. A carbon fiber-thermoset matrix braided composite was considered as the substitute material for the ladder frame. To identify the mechanical properties of the carbon braided composite, material tests were conducted using various test configurations.

Last, the frontal New Car Assessment Program tests of the developed lightweight vehicles were simulated to investigate the weight reduction effect on vehicle crashworthiness, to evaluate the crash performance of the composite structural component (ladder frame), and to look into the opportunities of using plastics and composites for weight reduction in a current vehicle.

In this study, costs were not considered. In particular, a cost increase is one of the critical barriers to using plastics and composites in automobiles. However, in order to investigate opportunities

for weight-reduced vehicles using plastics and composite and identifying the potential safety benefits of plastics and composites applications in future lighter, this study mainly focused on identifying currently available plastics and composite materials and their applicability to current vehicle components, and did not consider cost variations. Also, the manufacturability for vehicle components using plastics and composites is another critical issue. Instead, the existing vehicle design, which has optimal structures for steel material and steel manufacturing technologies, was used to develop the lightweight vehicle having plastics and composite as material substitutes in this study. So, the design changes of original vehicle structures and components were limited to replacing components, and therefore are considered to be a minimal approach that could be taken for reducing the weight in the weight reduction process. A more optimal approach would have been a comprehensive, clean-sheet design from the ground up to achieve a maximized weight reduction for the Silverado. However, such an approach was beyond the scope and available funding for this project.

This report consists of nine chapters including the introduction and conclusions. Chapters 2 to 4 contain summarized information from the literature reviews. Chapter 2 provides a description of the plastics and composites. Chapter 3 describes the basic composite mechanics. Chapter 4 describes the composite material models available in the FE code LS-DYNA used for the crash simulations. Chapters 5 to 7 provide details for developing a lightweight vehicle. Chapter 5 describes the candidate vehicle and components for weight reduction. Chapter 6 describes the development procedure of the composite ladder frame. Chapter 7 describes the light-weighted components. Chapter 8 shows the results from the frontal NCAP simulations of lightweight vehicles. In addition, the material test report by University of Dayton Research Institute is added as Appendix A.

2. Plastics and Composites

2.1. Lightweight vehicles

According to the USDOE, the United States currently uses nearly 20 million barrels of oil a day. The transportation sector accounted for almost 30 percent of total U.S. energy use in 2010, two-thirds of the nation's petroleum consumption, and a third of the nation's carbon emissions. Nearly, 28 percent of U.S. greenhouse gas emissions are generated from transportation, the second-largest source after power generation.

There are quite a number of barriers to weight reduction in automobiles:

- (1) historically low prices of fuel in the United States;
- (2) higher costs of advanced, lightweight materials;
- (3) lack of familiarity with lightweight materials;
- (4) extensive capital investment in metal-forming technologies;
- (5) lack of large automotive composites and magnesium industries;
- (6) preferences for large vehicles;
- (7) perceptions of safety;
- (8) recycling issues of plastics and composites;
- (9) increased emphasis on alternative fuels such as non-conventional petroleum, biofuels, and electricity;
- (10) alternative propulsion systems such as hybrids and fuel cells; and
- (11) the automotive industry's lack of long-term pricing strategies and stable long-term partners (Carpenter, 2008; Vaidya, 2011).

The CAFÉ standard had remained mostly unchanged for past three and a half decades since 1975, however, until a new rule was issued in 2010. New passenger cars and light trucks, including SUVs, pickups, and minivans, are now required on average to achieve at least 34.1 miles per gallon by year 2016 (Light-Duty Vehicle and CAFÉ Standards, , 2010). Recent changes to the CAFÉ standard were driving automakers to seek more aggressive methods for fuel consumption deductions. Weight reduction of vehicles will be a factor in meeting these requirements due to the inherent relationship between mass and fuel consumption.

It was estimated that 75 percent of fuel consumption directly relates to vehicle weight (McWilliams, 2011). With everything else remaining the same and considering mass compounding, a 6- to 8-percent increase in fuel economy can be realized for every 10-percent reduction in weight (Carpenter, 2008; Cheah, 2010). Table 2.1 provides a comprehensive overview of the weight saving and cost for automotive lightweight materials, including composites and metals.

Vehicle weight reduction is a known strategy to improve fuel economy in vehicles. However, Cheah addressed that the opportunity to reduce energy use by vehicle weight reduction is not as straightforward as it seems on three different fronts (Cheah, 2010). First, the average new U.S. vehicle weight has increased steadily over the past two decades. Second, the topic of vehicle weight reduction should be studied with a life-cycle perspective, considering energy-intensive production and recycling of lightweight materials. Third, while the effectiveness of weight

reduction in lowering fuel use at a vehicle level is reasonably well understood, the effectiveness at a vehicle fleet level is less so.

Table 2.1. Automotive materials with corresponding mass reduction and relative cost (Powers, 2000)

Lightweight material	Material replaced	Mass reduction (%)	Relative cost* (per part, assuming HSS=1)
High strength steel	Mild steel	10 - 25	1
Aluminum	Steel, cast iron	40 - 60	1.3 - 2
Magnesium	Steel or cast iron	60 - 75	1.5 - 2.5
Magnesium	Aluminum	25 - 35	1 - 1.5
Glass FRP composites	Steel	25 - 35	1 - 1.5
Carbon FRP composites	Steel	50 - 60	2 - 10+
Al matrix composites	Steel or cast iron	50 - 65	1.5 - 3+
Titanium	Alloy steel	40 - 55	1.5 - 10+
Stainless steel	Carbon steel	20 - 45	1.2 - 1.7

* include both materials and manufacturing

Table 2.2. Summary of vehicle mass-reduction studies (Lutsey, 2010)

Project	Mass reduction ^a	Cost impact findings ^a
IMPACT Ford F150	<ul style="list-style-type: none"> Body: 20% Vehicle: 25% 	<ul style="list-style-type: none"> Most mass reduction actions came with cost savings from baseline A 19% overall vehicle mass reduction comes at net zero cost A 25% mass reduction comes at a \$500 increase in the total variable vehicle manufacturing cost of the vehicle Mass-reduction features are currently entering Ford's new vehicle fleet
Porsche Engineering ULSAB-AVC	<ul style="list-style-type: none"> Body: 17% Vehicle: 19-32% 	<ul style="list-style-type: none"> The total estimated manufactured cost of the mass-optimized vehicles is found to be about \$9,200 to \$10,200 per vehicle. Mass-optimized vehicle designs using high-strength steels are affordable with minimal additional manufacturing costs
ThyssenKrupp New Steel Body	<ul style="list-style-type: none"> Body: 24% 	<ul style="list-style-type: none"> Material, assembly, tool/die costs decrease; production costs increase Overall: 24% body mass reduction has a 2% manufacturing cost increase
IBIS aluminum-intensive design	<ul style="list-style-type: none"> Body: 48% Vehicle: 17% 	<ul style="list-style-type: none"> Aluminum body has a \$500-600 cost increase from steel (22% increase) Aluminum vehicle overall has an approximate \$100 additional cost (1% increase) over conventional baseline vehicle retail price
EDAG steel-intensive Future Steel Vehicle	<ul style="list-style-type: none"> Body: 16-30% Vehicle: 17% 	<ul style="list-style-type: none"> Found mass-optimization allows hybrids and plug-ins can have improved total ownership cost from conventional 2020 vehicles (i.e., reductions in fuel consumption and other benefits offset mass-reduction and powertrain costs).
US AMP concept magnesium-intensive body	<ul style="list-style-type: none"> Body: 49% 	<ul style="list-style-type: none"> Reduced part count (-78%) along with reduced mass (-161 kg) Increased variable cost (3%), decreased investment cost (-46%)
Volkswagen-led Super Light Car	<ul style="list-style-type: none"> Body: 14-39% 	<ul style="list-style-type: none"> Steel-intensive (-14%, 40 kg): less than 2.5 €/kg Multi-material, economic (-22%, 62 kg): less than 5.0 €/kg Multi-material, advanced (-39%, 114 kg): less than 10 €/kg "Multi-material concepts promise cost effective light weight solutions"
Lotus Engineering Low Development	<ul style="list-style-type: none"> Body: 16% Vehicle: 20% 	<ul style="list-style-type: none"> Body-in-white cost decreases by 18%, or about \$60/vehicle The vehicle cost is decreased by 2%, or about \$300/vehicle
Lotus Engineering High Development	<ul style="list-style-type: none"> Body: 42% Vehicle: 33% 	<ul style="list-style-type: none"> Body-in-white cost increases by 35%, or about \$1000/vehicle The vehicle cost is increases by 3%, or about \$500/vehicle
RMI Revolution	<ul style="list-style-type: none"> Body: 57% Vehicle: 52% 	<ul style="list-style-type: none"> Sticker price of \$35,000, designed for cost comparability with luxury sport utility vehicles (e.g., Lexus RX, Mercedes ML). Cost-competitiveness due to parts consolidation and reduction and the reduction in use of materials offsetting price of high-cost composites

^a This table's findings are based on a variety of sources from the various projects (See Lutsey, 2010, for further details and sources)

Reductions in vehicle weight can be achieved by a combination of (1) vehicle downsizing, (2) vehicle redesign and contents reduction, and (3) material substitution (Cheah, 2010; Center for Automotive Research, 2011). Actually, there are a number of major research projects that have sought to determine the mass-reduction technology and materials potential for future

vehicles. Lutsey (2010) reviewed 17 vehicle mass-reduction studies and summarized achieved mass-reductions and cost impacting findings in Table 2.2. In these studies, the new manufacturing technologies and the lightweight materials, such as high strength steel, aluminum, magnesium, plastics, and composites, are used to reduce the vehicle weight. Table 2.2 shows that a range of mass reduction is 16 to 57 percent in body and 19 to 52 percent in vehicle with the average of these vehicle designs achieving about 30-percent mass reduction.

Schewel (2008) identified that lightweight vehicle could be a potent solution to triple safety (safety of climate, drivers, and other road users) simultaneously, without compromise. Lightweight vehicles enhance the environment (climate) safety through their higher fuel efficiency. However, the safety (self- and partner-protection) of lightweight vehicles is not clearly identified yet. There have been many debates about the relationship about between safety and vehicle weight and size. Rocky Mountain Institute (Chan-Lizardo, 2011) reviewed the lightweight automotive safety studies and summarized conclusions of these studies in Table 2.3 . The conclusions of lightweight safety studies have not provided clearly the safety implications of lightweight vehicles to vehicle weight and size. These lightweight safety concerns are still lively studied by many researchers.

NHTSA (2011) hosted a workshop on the effects of light-duty vehicle mass and size on vehicle safety on February 25, 2011. The purpose was to bring together experts in the field to discuss and try to reach consensus on some of the overarching questions that NHTSA must grapple with in its upcoming CAFE rulemaking. In the workshop, Summers (2011) described three on-going projects to study about feasible, lightweight vehicle design and safety evaluations of lightweight vehicles.

In 2006, Congress directed NHTSA (S. Rep. 109-293) to begin development of a program to examine the possible safety benefits of lightweight PCIVs and to develop a foundation for cooperation with USDOE, industry and other automotive safety stakeholders. In NHTSA's 2008 PCIV safety workshop, attendees indicated that a minimum of 30 percent to 40 percent (by weight) plastics and composite content in one or more subsystems beyond interior trim could qualify a vehicle as a PCIV (Volpe Center, 2008).

The ACC PD (2009a) addressed the advantages that PCIVs have:

- (1) sourced from strong U.S. chemical manufacturing industry;
- (2) improved global competitiveness of U.S. automakers (technology and jobs);
- (3) reduced dependency on foreign oil;
- (4) lower carbon and other emissions;
- (5) increased sustainability through renewable materials; end-of-life recovery and recycling options;
- (6) leapfrog fuel efficiency requirements;
- (7) lower vehicle weight while maintaining size; and
- (8) enhanced crash safety.

Table 2.3. Summary of lightweight automotive safety studies (Chan-Lizardo, 2011)

Year	Author	Description	Conclusion
1989	Crandall and Graham	Used regression model to predict traffic fatalities based on vehicle weight.	Increased weight leads to fewer fatalities, CAFE would increase fatalities 14–28%.
1992 1994 2004	Evans	Focused on momentum of collision partners and safety risk.	Fatality likelihood increases as mass ratio (ratio of collision partner's weight) increases.
1997 2003 2004	Kahane	NHTSA ^a study, regression analysis of fatalities per billion miles. Included vehicle type and mass, driver age and gender, and crash location and type. Ignored coupes and certain vehicle dimensions, ie. assumed mass and size were equivalent.	Fatality rates increase with weight decrease (100 lb. reduction in vehicles leads to over 1100 more fatalities in 1999, from 258 to 1555).
2001 2002	Wenzel and Ross	Separated collision data by driver, make, and model; analyzed size and weight independently. Ignored driver behavior and crash location.	Found similar safety for drivers in all vehicle classes, but increased danger to others by SUVs. Pickups are least safe. Determined that mass alone does not explain variations in safety/risk.
2002 2003 2004 2005	Van Auken and Zellner	Commissioned by Honda, reanalyzed Kahane's six types of crashes plus many configurations/orientations of vehicles using statistical analysis of NASS data. Accounted for track width and wheelbase.	Found that a weight reduction would have no statistically significant effect on fatalities in 1999 (different trends in different sizes/weights of vehicles). Size, not weight, connected to safety.
2004	Kebschull, Kelly, Van Auken, and Zellner	Modeled a Ford Explorer, a lightweight (aluminum-intensive) Explorer, and lengthened (increased crush space) Explorer in NASS ^b crashes.	Found 15% Equivalent Life Unit (ELU) reduction in the lightweight Explorer, 26% reduction in the long Explorer.
2006	Robertson	Investigated NHTSA's Fatality Analysis Reporting System for relationships between collision fatality and vehicle size, stability, and weight.	Vehicles with the same wheelbase vary widely in weights and safety ratings. If all vehicles were the lightest in their wheelbase class, fatalities would decrease 28% (16% less fuel consumption).

^a National Highway Traffic Safety Administration^b National Automotive Sampling System

As shown in Figure 2.1, the average U.S. light vehicle contains about 384 pounds (174 kg) of plastics and composites in 2009 – about 10 percent of total vehicle weight but more than 50 percent of vehicle volume (ACC PD, 2009a). Sehanobish (2009) reported that the use of 100 pounds of plastics could replace approximately 200 to 300 pounds of mass from the use of traditional materials. Advantages of composites compared to steels for automotive and transportation are:

- (1) weight reduction of 20-40 percent,
- (2) styling flexibility in terms of deep drawn panels, which is limited in metal stampings,
- (3) 40-60 percent savings in tooling cost,
- (4) reduced assembly costs and time in part consolidation,
- (5) resistance to corrosion, scratches and dents, and improvement in damping and NVH (noise, vibration and harshness),

(6) materials and process innovations capable of adding value while providing cost saving, and (7) safer structure due to the composite material's higher specific energy absorption (SEA) (Carpenter, 2008; Vaidya, 2011).

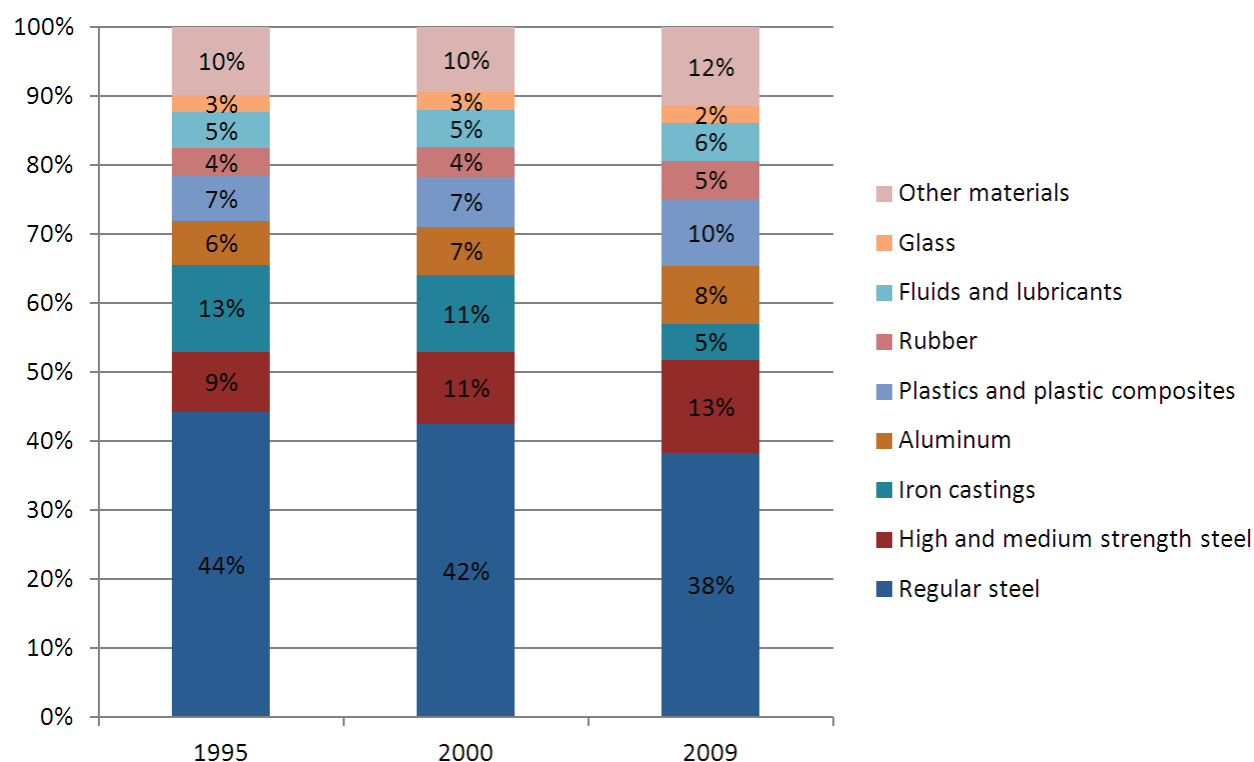


Figure 2.1. Average material consumption for a domestic light vehicle, model years 1995, 2000, and 2009 (Source: Ward's Communications, Ward's Motor Vehicle Facts and Figures, 2010, Detroit, MI, 2010, pp. 65).

The following reviews are about the plastics and composites, and are referred from several references (Mamalis, 1998; Tucker, 2002; Lu, 2003; Sehanobish, 2009; Lukkassen, 2008; Mallick, 2010; Courteau, 2011; and Vaidya, 2011).

2.2. Plastics and composites

Structural materials can be divided into four basic categories: metals, plastics, composites, and ceramics, as shown in Figure 2.2. Metals include all kinds of steels (iron steel, HSS, stainless steel, etc.) and non-ferrous metals (aluminum, magnesium, etc.). Ceramic materials are inorganic, non-metallic, often crystalline oxide, nitride or carbide materials. Plastics are polymers composed of long covalent-bonded molecules. Composites consist of two or more separate materials combined in a macroscopic structural unit. Specifically, plastics and composites are the focus of this study.

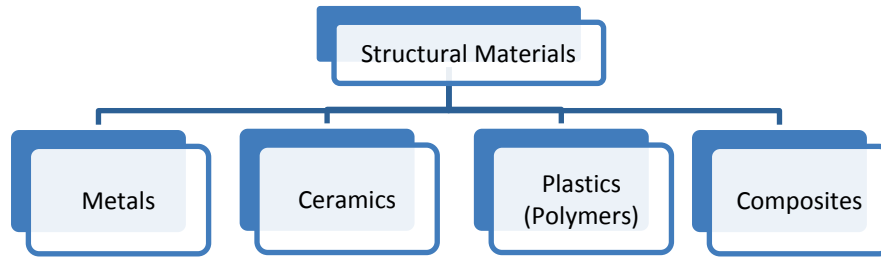


Figure 2.2. Classification of structural materials.

Plastics (polymers)

Polymers have quite different material characteristics as compared to steel. General benefits of polymers are:

- (1) light weight,
- (2) corrosion resistance,
- (3) electric resistance,
- (4) low thermal conductivity,
- (5) variety of optical properties,
- (6) formability,
- (7) surface finish,
- (8) comparatively low cost, and
- (9) low energy content.

While polymers have many advantages over metals, they behave differently from metals when subjected to mechanical loads or exposed to thermal or chemical environments. Some of the differences between polymers and metals are:

- (1) they have much lower modulus and strength,
- (2) their mechanical properties are influenced by temperature and strain-rate, and for some polymers by humidity,
- (3) they exhibit creep and stress relaxation,
- (4) they do not exhibit an endurance limit when subjected to fatigue loading,
- (5) they have a significantly higher coefficient of thermal expansion than metals,
- (6) their ductility and impact resistance is influenced by temperature,
- (7) their notch sensitivity are various and affects impact behaviors, and
- (8) their long-term use should take into account the possibility of creep and stress relaxation and the effect of aging on their properties.

Polymers can be classified into three categories: thermosets, thermoplastics, and rubber, as shown in Figure 2.3. This distinction is somewhat artificial, as a given polymer can often be processed to produce a thermoset, a thermoplastic, or a rubber end product.

Thermosets, also known as thermosetting plastics, are not fully polymerized in their raw state. They are usually in a solid or resinous liquid state prior to use. Most thermosets require the use of an extra component to achieve cure, this often termed a catalyst or curing agent. An

application of heat and pressure will cause the polymer to first go through a softening stage during which it will flow easily. Then, a following chemical reaction completes the polymerization, which is the curing (vulcanizing) process. Curing is an irreversible chemical reaction in which permanent connections (known as crosslinks) are made between the material's molecular chains. These crosslinks give the cured polymer a three-dimensional structure, as well as a higher degree of rigidity than it possessed prior to curing. Most thermoset polymers have a highly crosslinked structure when cured and therefore can no longer be made to flow. At this point in the process, a re-application of heat only degrades the resin. Compared to thermoplastics, thermosets have much lower viscosity, and a higher thermal and chemical resistance. The material properties of typical thermosets are listed in Table 2.4.

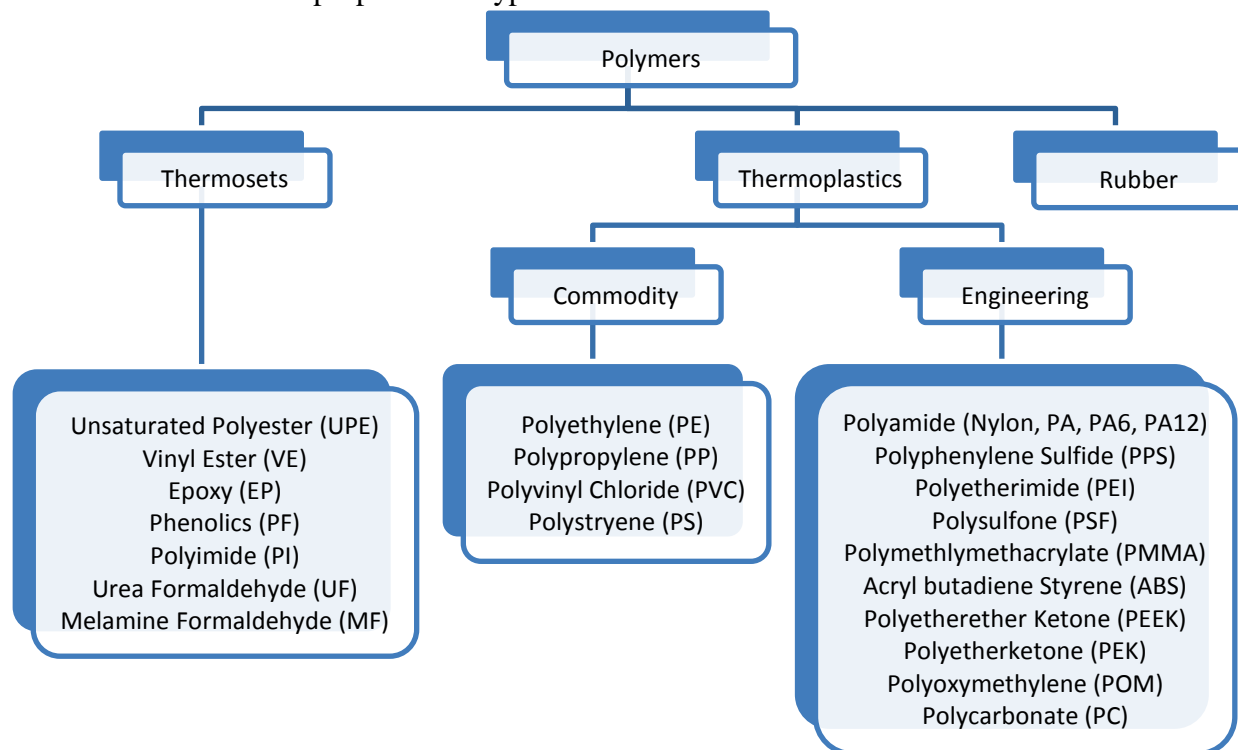


Figure 2.3. Classification of polymers.

Table 2.4. Typical properties of thermoset resins (Vaidya, 2011)

Material (thermosets)	Specific gravity	Tensile strength (MPa)	Tensile modulus (GPa)	Elongation (%)	Heat Deflection temperature (°C)	Glass Transition temperature (°C)	Cure shrinkage (%)
Unsaturated Polyester (UPE)	1.1-1.4	35-105	2.0-3.5	1-5	60-205	-	5-12
Vinyl Ester (VE)	1.1-1.32	73-81	3-3.5	3.5-5.5	93-135	-	5-10
Epoxy (EP)	1.2-1.3	55-130	2.75-4	1-3	70-80	180-260	1-5
Phenolics (PF)	1.35-1.41	6-9	2-3.5	1-3	95-105	-	3-5
Polyimide (PI)	1.28-1.34	38-85	3.9-4.1	1.5	-	220-320	1-2

Thermoplastics, also known as thermosoftening plastics, are fully polymerized in their raw state. There is essentially no chemical reaction involved in the processing. The use of thermoplastics involves a physical processing step (melting). Application of heat will result in softening or melting, at which time the material will flow and can be formed or molded into the desired shape. Cooling of the material returns it to its former solid state, locking in any dimensional or shape changes. No cross-links are formed as with a thermoset material. The changes seen in the thermoplastic are purely physical. With the reapplication of heat, the cycle is wholly reversible and can be repeated many times, or until the cumulative effects from the thermal cycling and high shear during processing start to degrade the polymer. Injection molding is the principal processing method for the vast majority of thermoplastics automotive parts. It is capable of being used for producing parts of complex shapes and geometry at high production rates, with good dimensional accuracy and excellent surface finish. However, the cooling time in the mold has a major effect on the injection molding cycle time.

Thermoplastic composites offer attractive advantages in terms of cost, recycling, and performance and are the highest growing material for use in automotive plastics and/or composites. Compared to thermosets, the benefits of thermoplastic composites include:

- (1) enhanced ductility, fracture toughness, low notch sensitivity and superior impact resistance;
- (2) ability to be economically recycled and reused;
- (3) enhanced environmental, moisture and corrosion resistance;
- (4) unlimited shelf life of raw material;
- (5) tailored product forms and processes to meet the needs of the application;
- (6) elimination of exothermic reactions, toxic or solvent emissions, thereby making them environmentally benign;
- (7) adaptability to manufacturing for low as well as high volume;
- (8) low tooling costs and rapid cycle times; and
- (9) improved assembly and joining methods.

The material properties of typical thermoplastics are listed in Table 2.5.

Table 2.5. Typical properties of thermoplastic resins (Vaidya, 2011)

Material (thermoplastics)	Tensile modulus (GPa)	Tensile strength (yield) (MPa)	Melt flow (g/10 min)	Melting point (°C)	Density (g/cm ³)
Polypropylene	1.5-1.75	28-39	0.47-350	134-165	0.89-0.91
Polyethylene	0.15	10-18	0.25-2.6	104-113	0.918-0.919
Polyurethane	0.028-0.72	5-28	4-49	220-230	1.15-1.25
Polyamide	0.7-3.3	40-86	15-75	211-265	1.03-1.16
Polyphenylene sulfide	3.4-4.3	28-93	75	280-282	1.35-1.43
Polybutylene Terephthalate	1.75-2.5	40-55	10	230	1.24-1.31
Polyetherketonetone	4.4	110	30	360	1.31
Polyetheretherketone	3.1-8.3	90-11	4-49.5	340-344	1.3-1.44
Polyether imide	2.7-6.4	100-105	2.4-16.5	220	1.26-1.7
Polyether sulfone	2.4-8.62	83-126	1.36-1.58	220	1.36-1.58
Polyether Terephthalate	2.47-3	50-57	30-35	243-250	1.3-1.33

Natural rubber is an elastomer (an elastic hydrocarbon polymer) and a thermoplastic. However, once the rubber is vulcanized, it will have turned into a thermoset. Most rubber in everyday use is vulcanized. Thermoplastic elastomers, referred to as thermoplastic rubbers, are copolymers (derived from a physical mix of polymers) which consist of materials with both thermoplastic and elastomeric properties.

Composites

Composites are materials that combine two or more materials that have quite different properties. When combined, composites offer properties which are more desirable than the properties of the individual materials. The different materials work together to give the composite unique properties, but they do not dissolve or blend into each other.

Composites can be categorized by the processing routes and the overall processing technologies as shown in Figure 2.4. Most of the structural elements found in nature are composites, such as wood, horn, and shells. Bio-composites include natural materials such as wood, but also include artificial composites made with synthetic resins and reinforcing fibers such as jute, banana fiber, coconut fiber, and bamboo fiber, etc. Carbon-carbon composites are made from carbon fibers embedded in a carbon or graphite matrix. Ceramics, metals, and polymers are all used as matrix materials in composites, depending on the particular requirements. The matrix materials are reinforced by fillers in the form of single-crystal whiskers, platelets, long fibers, short fibers, small particles, or precipitates (or a combination of any of these). Whereas metals and polymers

are reinforced for increased strength and modulus, ceramics are reinforced to increase their toughness and damage tolerance. Polymers are unquestionably the most widely used matrix materials in modern composites. Although plastics have a poor strength-to-density ratio by themselves, polymer matrix composites -- PMCs -- have advanced as structural materials while offering many advantages over metal. PMCs amount to 75 percent of the world composite market by value or by tonnage.

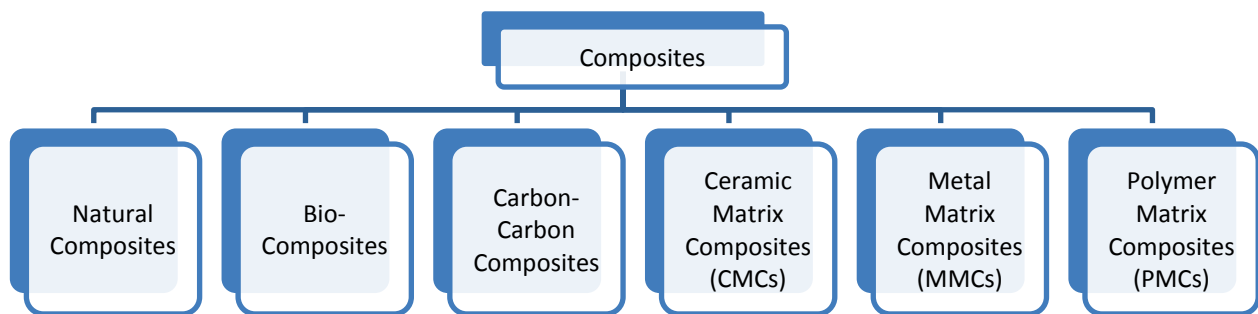


Figure 2.4. Classification of composites (by processing routes).

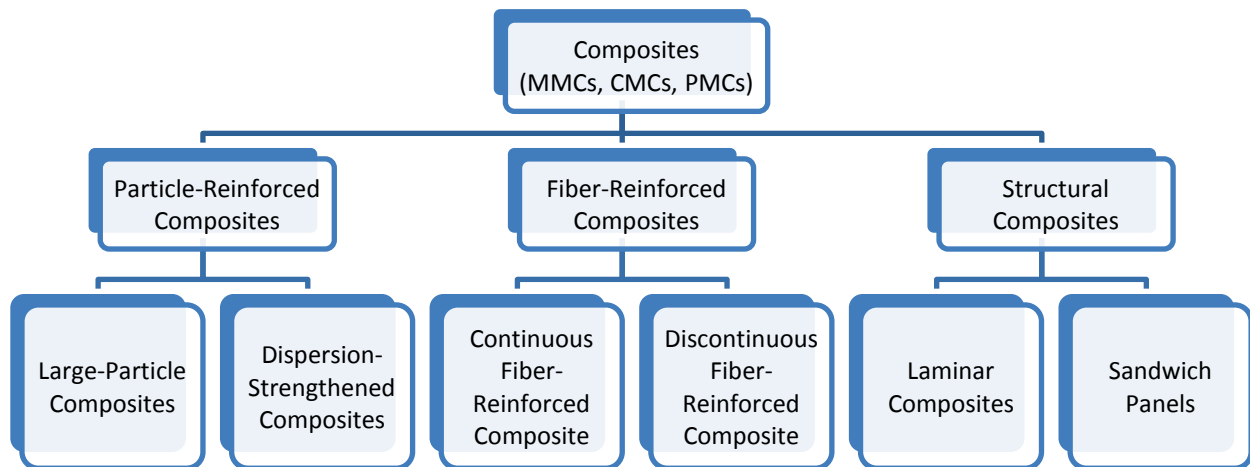


Figure 2.5. Classification of composites by filler types.

Furthermore, composites can be categorized by filler types as shown in Figure 2.5. The matrix materials are reinforced by fillers in the form of single-crystal whiskers, platelets, long fibers, short fibers, small particles, or precipitates (or a combination of any of these). Particle-reinforced composites are the cheapest and most widely used. They fall in two categories depending on the size of the particles: large-particle composites (cermet, tire, concrete, etc.) and dispersion-strengthened composites (thoria-dispersed nickel, sintered aluminum powder, etc.). Fiber-reinforced composites are divided into two categories depending on the fiber length. These fibers may be short or long, and they may be aligned in the directions where loading will be greatest, or randomly oriented to give it equal strength in all directions. The properties of structural composites depend on the properties of the constituents and the geometric arrangement of these

materials. There are two types of structural composites, laminar composites and sandwich panels. The fiber-reinforced polymer composites are the main interest in this review.

2.3. Fiber-reinforced polymer composites

FRP composites consist of a polymer resin matrix and fiber reinforcements. The fiber reinforcement is the primary load bearing constituent of a composite. The stiffness and strength characteristics of composites are dependent on the type and form of the fiber reinforcement used. As a common characteristic, all reinforcing fibers exhibit high specific modulus (modulus of weight ratio) and specific strength (strength to weight ratio). The matrix holds the fibers together in a structural unit and protects them from external damage, transfers and distributes the applied loads to the fibers, and in many cases contributes some needed property such as ductility, toughness, or electrical insulation.

Fibers

Fibers are the principal load-carrying members in FRP composites. Fibrous reinforcement is so effective because many materials such as glass and graphite are much stronger and stiffer in fiber form than they are in bulk form. For very small diameters, the fiber strength approaches the theoretical cohesive strength between adjacent layers of atoms; whereas for large diameters, the fiber strength drops to nearly the strength of bulk glass. Fibers can be categorized in some groups as shown in Figure 2.6.

Glass and carbon fibers are categorized into mineral fibers. E-glass is the most common reinforcing fiber used today, which layman commonly and often mistakenly call “fiberglass,” as in a “fiberglass boat Or “fiberglass insulation.” The principal advantages of E-glass fibers are their low cost, high tensile strength, high chemical resistance, and excellent insulation properties. However, they have higher density, low static fatigue resistance, low tensile modulus, and lower fatigue strength than carbon fibers. Another drawback of E-glass is its high sensitivity to moisture absorption and abrasion. The advantages of carbon fibers are their high modulus-to-density ratio and strength-to-density ratio, very low coefficient of thermal expansion, high fatigue strength, and high thermal conductivity. But the disadvantages are their low strain-to-failure, low impact strength, and high electric conductivity. Typical polymer fibers are aramid fibers, which are commonly known as Kevlar, a name trademarked by DuPont. Aramid fibers have the lowest density and highest tensile strength-to-density ratio of currently available reinforcing fibers. But their limitations are high cost, high moisture absorption, and low compressive strength. The mechanical properties of typical fibers are listed in Table 2.6. Also, Figure 2.7 shows the specific strength versus specific stiffness of some fibers.

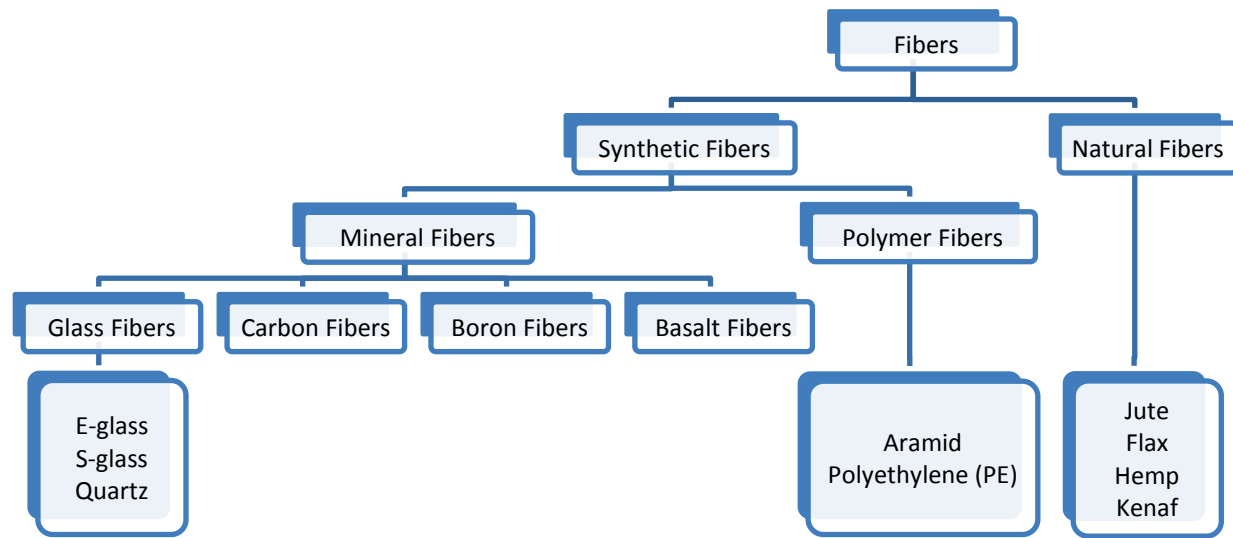


Figure 2.6. Classification of fibers.

Table 2.6. Typical properties of fibers (Mallick, 2010, Vaidya, 2011)

Material (fibers)	Tensile modulus (GPa)	Tensile strength (yield) (GPa)	Tensile Strain (%)	Coefficient of thermal expansion ($10^{-6}/^{\circ}\text{C}$)	Density (g/cm^3)
E-glass fiber	72.4	3.5	4.8	5	2.54
S-glass fiber	86.9	4.3	5.0	2.9	2.49
Pan-based carbon fiber	210-400	3.5-5.2	1.5-1.8		1.8
Pitch-based carbon fiber	370	1.9	0.5		2.0
Boron fiber	385	2.8			2.63
Basalt fiber	93-110	3.0-4.8	3.1-6.0		
Kevlar 49 (aramid fiber)	131	3.62	2.8		1.45

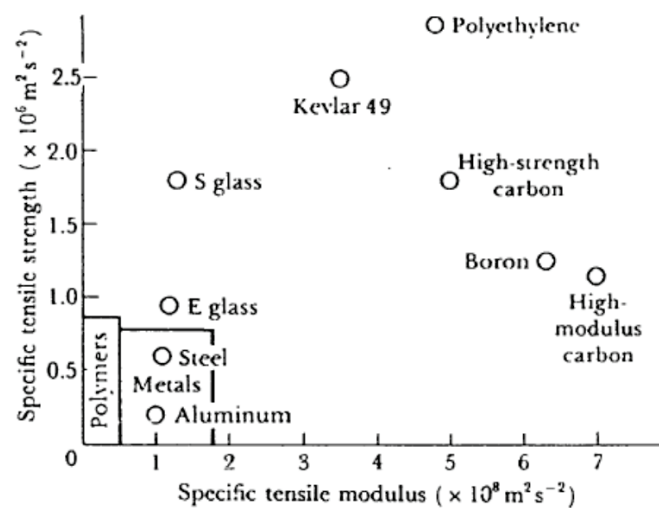


Figure 2.7. Specific strength versus specific stiffness of some fibers (Lukkassen, 2008).

Fibers are produced as very small diameter continuous filaments, with the filament diameter typically ranging between 2 to 20 μm . Since filaments are very fragile and difficult to handle, fibers are treated as bundles of filaments. Untwisted bundles of filaments are called rovings in the glass fiber industry and tows in the carbon fiber industry. Twisted bundles are called yarns. A dry fiber preform is an assembly of dry fiber layers that have been pre-shaped to the form of the desired product and bonded together using a binder resin.

Fiber reinforcements are available in a wide range of size and forms. The fiber aspect ratio (l/d) is defined as the ratio of fiber length (l) to fiber diameter (d). There are discontinuous and continuous fibers. Discontinuous fibers are limited to the fiber aspect ratio of 2000. Short discontinuous fibers have about 1-3 mm length, and long discontinuous fibers have 2-25 mm length. Generally, for a fiber aspect ratio approaching 2000, the strength and stiffness of the composite approach 80- to 90 percent those of continuous fiber-reinforced composites. The forms of discontinuous fibers have short and long fibers, and aligned and random chopped strand mats. Continuous fibers have unidirectional and multi-axial orientations. The forms for continuous fibers are unidirectional or multi-axial laminates, woven, knitted, and braided fabrics. continuous fiber mats have random swirl patterns. Figure 2.8 shows the classification of fabric forms and Figure 2.9 shows the architecture of fabrics.

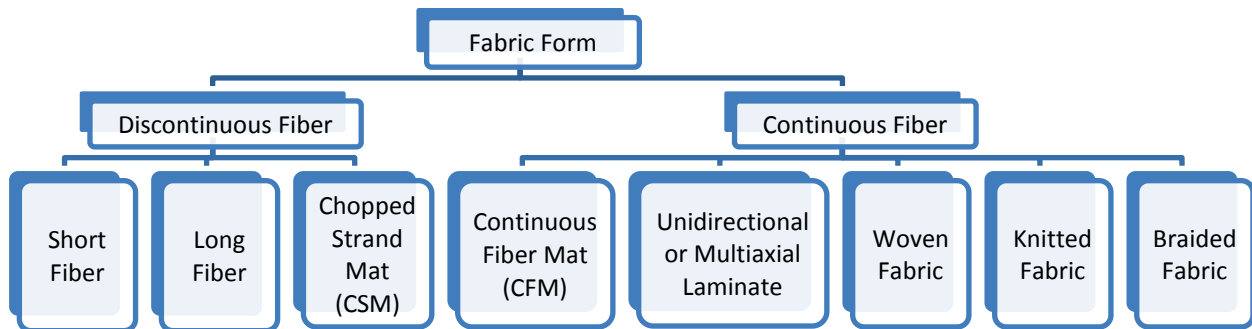


Figure 2.8. Fabric forms.

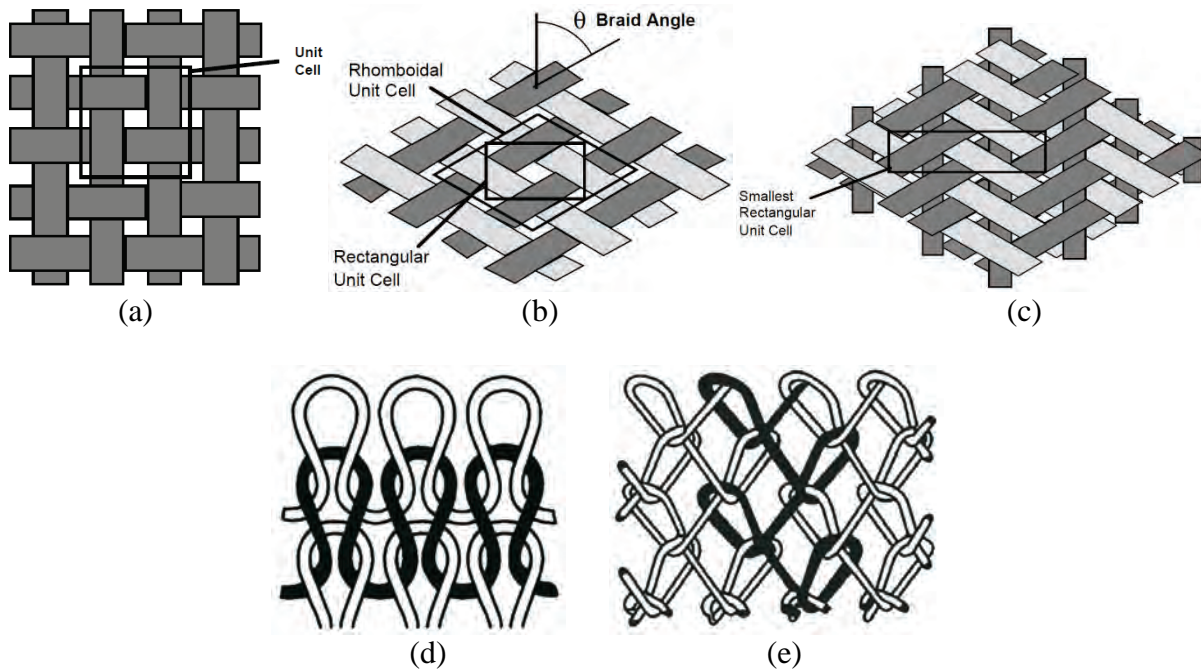


Figure 2.9. Two-dimensional fiber architectures (Cox, 1997; Mallick, 2010): (a) bi-directional plain weave, (b) bias braid (c) triaxial braid, (d) weft-knit, and (e) warp-knit.

Chopped fiber composites are used extensively in high-volume applications due to their low manufacturing cost, but their mechanical properties are considerably poorer than those of continuous fiber composites. Continuous fibers have unidirectional and multi-axial orientations. They are used in highly loaded structural panels such as roof modules, hoods, rear carriers, underbody parts, trailer liners, and CNG tanks. Although the continuous fiber laminate is used extensively, the potential for delamination, or separation of the laminae, is still a major problem because the interlaminar strength is matrix-dominated. Woven fiber composites do not have distinct laminae and are not susceptible to delamination, but strength and stiffness are sacrificed due to the fact that the fibers are not straight as in the continuous fiber laminate.

Woven fabric yarns accumulate stresses due to fiber waviness (undulation). As a result, their in-plane properties, such as tensile strength, are lower than non-crimped (without undulation) fibers.

Non-crimped stitch bonded fabrics offer greater flexibility compared to woven fabrics, especially multiaxial (three plies or more) fibers, and are widely used in automotive parts. The reinforcements in the form of biaxial, triaxial, and multiaxial fabrics exhibit up to 30-percent higher tensile strength than woven fabrics. Multiaxial reinforcements can be engineered to meet specific requirements and perform multiple tasks such as providing good surface finish, impact and abrasion resistance, and structural integrity. Compared to 2D textile laminates, 3D weave composites have superior through-thickness properties.

Manufacturing processes

All composites manufacturing processes involve mixing the matrix material with the reinforcing material. The choice of a specific fabrication method depends on the costs and on the technical requirements of components to be produced. In order to guarantee economic production, methods which provide a high throughput are absolutely necessary. High throughput can be achieved by means of low clock times or by means of highly integrative parts. Table 2.7 compares the most commonly used composite fabrication processes available today, and addresses their advantages, disadvantages, and cycle time.

One of the key aspects of processing thermoset and thermoplastic composites is the fiber length scale. The fiber length determines whether discontinuous or continuous fiber processes apply to the part under consideration. For short fibers (typically < 3 mm in length), processes such as injection molding may be suitable; for long fibers (3-25 mm in length), extrusion-compression or sheet extrusion processes may be appropriate; while for continuous fibers or woven fabrics, processing methods such as pultrusion, thermostamping, or compression molding would apply. Some of the processing methods for thermosets and thermoplastics are reviewed below.

Thermoplastic-matrix composites currently used in the automotive industry are mostly reinforced with E-glass fibers due to their low cost. Glass fibers are incorporated in the thermoplastic-matrix in a variety of forms, but randomly oriented short glass fibers are very common because they can be processed by the traditional injection molding techniques. However, they are used in semi-structural parts and functional parts. The use of continuous fiber reinforced thermoplastic-matrix composites lags behind that of thermoset-matrix composites due to the high viscosity of the liquid thermoplastics. The advantages of thermoplastic-matrix composites are their lower processing time, weldability, higher damage resistance, and recyclability.

Short fiber thermoplastics (SFTs) contain fibers that are typically less than 1.0 mm long. Adding short fibers to a polymer increases its modulus and heat deflection temperature, decreases its coefficient of thermal expansion and mold shrinkage, and reduces the creep strain. SFTs are processed by injection molding. Practically, the maximum weight fraction in injection molded SFTs is limited to about 40 percent.

Table 2.7. Comparison of the most commonly used composite molding processes (Das, 2001)

Molding Process	Advantages	Disadvantages	Cycle Time
Prepreg	Better resin/fiber control	Labor intensive for large complex parts	5-10 hrs.
Preforming	Good moldability with complicated shapes and the elimination of trimming operation	Cost-effective only for large complicated shape parts and large scrap generated when fiber mats used	45-75 secs. (Compform Process) 4-5 mins (Vacuum forming)
RTM	Inside and outside finish possible with thickness control, more complex parts possible with vacuum assisted	Low viscosity resin necessary and the possibility of voids formation without vacuum assisted	8-10 mins for large parts; 3-4 mins for vacuum assisted
Liquid Compression Molding	Favored method for mass production with high fiber volumes	Expensive set up cost for low production	1-2 mins.
SMC	Cost effective for production volume 10K-80K/year.	Minimum weight savings potential	50-100 secs
RIM	Low cost tooling where prototypes can be made with soft tools	Difficult to control the process	1-2 mins
BMC	Low cost base material	Low fiber content, randomly oriented, low structural quality, poor surface finish	30-60 secs.
Extrusion Compression Molding	Fully automated, variety of polymers and fibers can be used with fiber volumes up to 60% by weight	Not for surface finish parts without paint film or similar process	3-6 mins
Structural Reaction Injection Molding	Low tooling cost with the good surface finish capability	Difficult to control the process particularly with low viscosity resin and longer cure cycle time.	4 mins

Long fiber thermoplastics (LFTs) contain randomly oriented fibers ranging in length from 5 to 25 mm. LFTs exhibit higher tensile modulus, tensile strength and impact strength than SFTs. LFTs can be molded by injection molding, compression molding, or injection-compression molding with using pre-compounded pellets, or by directly compounding the fibers.

Glass mat thermoplastics (GMTs) are available in sheet form. Polypropylene is the most commonly used thermoplastic for GMTs. The fiber mat usually contains either randomly oriented chopped glass fibers or randomly oriented continuous glass fibers. Also, oriented fiber mats can be used. Compression molding is the common manufacturing process used for making GMTs.

Glass fabric thermoplastics are commingled rovings of continuous glass filaments and thermoplastics filaments that are woven into a two-dimensional fabric. Upon heating in the mold, the thermoplastic filaments in the fabric melt and form liquid pools around the glass fibers.

Laminated thermoplastic composites are made by stacking several layers of either unidirectional continuous fiber “prepregs” or bi-directional fabric prepregs, heating the stack, and then thermostamping the heated stack in a press. A prepreg is a fiber layer pre-impregnated with a polymer.

Thermoplastic and thermoplastic-matrix composite parts can be joined together by mechanical joining, adhesive and welding or fusion bonding. While mechanical joining and adhesive bonding are the only options for joining thermoplastics or thermoplastics-matrix composite parts to metal parts, welding can be used for joining one thermoplastic or thermoplastic-matrix composite part to another. Mechanical joining includes bolted joints, threaded joints, screw and snap fits.

Manufacturing of thermoset-matrix composites involves curing of the uncured or partially cured thermoset resin. High cure temperatures are required to initiate and sustain the chemical reaction. The time required to properly cure a part is called the cure cycle.

Compression molding is currently the most commonly used manufacturing process for producing thermoset-matrix composite parts in automotive industry, because of its high production rate and its ability to produce large size parts with complex shapes and automation. The compression molding process uses sheet molding compounds (SMCs) as the starting material. SMC is a thin ready-to-mold continuous sheet containing fibers dispersed in a thermosetting resin. Common resins for SMCs are polyesters and vinyl esters. SMCs contain randomly oriented discontinuous fibers, typically 25 mm long.

Resin transfer molding (RTM) is a liquid injection molding process that uses liquid resin injection under pressure through either a stack of dry fiber layers or a dry fiber preform placed in a closed mold cavity. Compared to the compression molding process, RTM has a very low tooling cost and simple mold clamping requirements.

Reaction injection molding (RIM) is similar to injection molding except thermosets are used, which requires a curing reaction to occur within the mold. First, two highly chemically reactive, low-viscosity liquid chemicals are mixed together. The mixture is then injected into the mold under high pressure using an impinging mixer. The mixture is allowed to sit in the mold long enough for it to expand and cure. If reinforcing agents are added to the mixture, the process is then known as reinforced reaction injection molding (RRIM). Common reinforcing agents are glass fibers. This process is usually used to produce rigid foam automotive panels. A subset of RRIM is structural reaction injection molding (SRIM), which uses a dry fiber stack or a preform. The fiber stack is first arranged in the mold and then the polymer mixture is injection molded over it. The most common RIM processable materials are polyurethane and polyurea.

Crash performance

The energy-absorption behavior of composites and their structural components is affected by a number of factors. These factors may be broadly classified into composite materials and properties, fabrication conditions, geometry and dimensions of the structural components, and

test conditions. FRP composites are governed by the fiber materials, matrix materials, fiber/matrix interface, and fiber content. Along with the fiber stacking sequence, fiber orientation and fiber form are important factors. Geometry includes both the cross-sectional shape of a tube (circular, square, or rectangular) and lengthwise shape (tapered or constant). Geometry may also involve a triggering system, such as chamfering of a tube end, to initiate collapse. Testing conditions specify the loading direction with respect to the components (axial or transverse) and loading rate (static or dynamic). Most properties are highly temperature-dependent, and thus temperature is also an important factor.

In the case of composite materials, internal material failure generally is initiated long before any change in its macroscopic appearance or behavior is observed. The internal material failure may be observed in many forms, separately or jointly, such as (1) braking of the fibers, (2) microcracking of the matrix, (3) separation of fibers from the matrix form of debonding or/and pull-out, and (4) separation of laminae from each other in a laminated composite (called delamination), which are described in Table 2.8. The effect of internal damage on macroscopic material response is observed only when the frequency of internal damage is sufficiently high.

Composite crush testing can be divided into three categories: coupon, element, and structure testing. Coupons are small, inexpensive, and easily fabricated shapes; and coupon tests reveal the mechanical properties of the composites. Elements are larger self-supporting specimens including tubes, angles, and channels that incorporate realistic geometries used in many vehicle structures; and element tests can evaluate the energy absorption capability and crashworthiness of the composite elements. Structures are full-sized assemblies of elements that make up the entire energy absorbing system of a vehicle.

Table 2.8. Description of internal failure types of FRP composites (Mamalis, 1998)

Failure type	Description
Fiber breakage	Whenever a crack has to propagate in the direction normal to the fibers, fiber breakage will eventually occur for complete separation of the laminate. Fibers will fracture when their fracture strain is reached. Its contribution to the total energy absorption is very small.
Matrix deformation and cracking	The matrix material surrounding the fibers has to fracture to complete the fracture of the composite. Thermosetting resins are brittle materials and can undergo only a limited deformation prior to fracture. Their contribution to the total energy absorption is relatively insignificant.
Fiber debonding	During the fracture process the fibers may separate from the matrix material by cracks running parallel to the fibers (debonding cracks). In this process, the chemical or secondary bonds between the fibers and the matrix material are broken. This type of cracking occurs when fibers are strong and the interface is weak. Extensive debonding may contribute to the increase of energy absorption.
Fiber pull-out	Fiber pull-outs occur when brittle or discontinuous fibers are embedded in a tough matrix. The fracture may be proceed by broken fibers, being pulled-out of matrix, rather than fibers fracturing again at the plane of composite fracture. The fiber pull-outs are usually accompanied by extensive matrix deformation.
Delamination	A crack propagating through a ply in a laminate may be arrested as the crack tip reaches the fibers in the adjacent ply. Due to high shear stresses in the matrix adjacent to the crack tip, the crack may be bifurcated and start running at the interface parallel to the plane of the plies. These cracks are called delamination cracks. They absorb a significant amount of fracture energy.

Most members of the vehicle BIW (body-in-white) structure are thin-walled steel columns because thin-walled columns have high-energy absorption capability in compression and impact loading conditions. Composites are known as high SEA (specific energy absorption) materials. Figure 2.10 shows the typical SEA values for some materials. It indicates that carbon FRP composites have 3-10 times higher SEA than steel materials. The compression capability and impact crashworthiness of FRP composite tubes are reviewed here.

Figure 2.11 shows the compression test of a tubular composite. An axial cross section of a typical tubular specimen is shown in Figure 2.11(a). It has a 45° bevel at the top of the specimen for triggering the stable crush mode. Figure 2.11(b) shows the stable crush behavior of the specimen. It depicts the crushed displacement (δ) and the sustained damage zone (d). The load versus displacement curve of the test is shown in Figure 2.11(c). The SEA is defined as the energy absorption per unit mass of structural member. The total energy absorption (W) is expressed as

$$W = \int_0^{\delta} P dx .$$

Then, the SEA can be obtained by

$$E_s = \frac{W}{A\rho\delta}$$

where A is the section area, ρ is the density, and δ is the aforementioned crush displacement.

The crush behavior of composite specimen can be generally classified as either stable or unstable. Unstable crushing is characterized by an initial load peak followed by a sudden catastrophic failure. In contrast, stable crushing is characterized by an increase in load until an initial failure occurs. Ideal energy absorbing materials and structures should exhibit a constant load versus crush displacement as shown in Figure 2.11(c). Unstable failure modes include buckling, interpenetration, and barreling as shown in Figure 2.12.

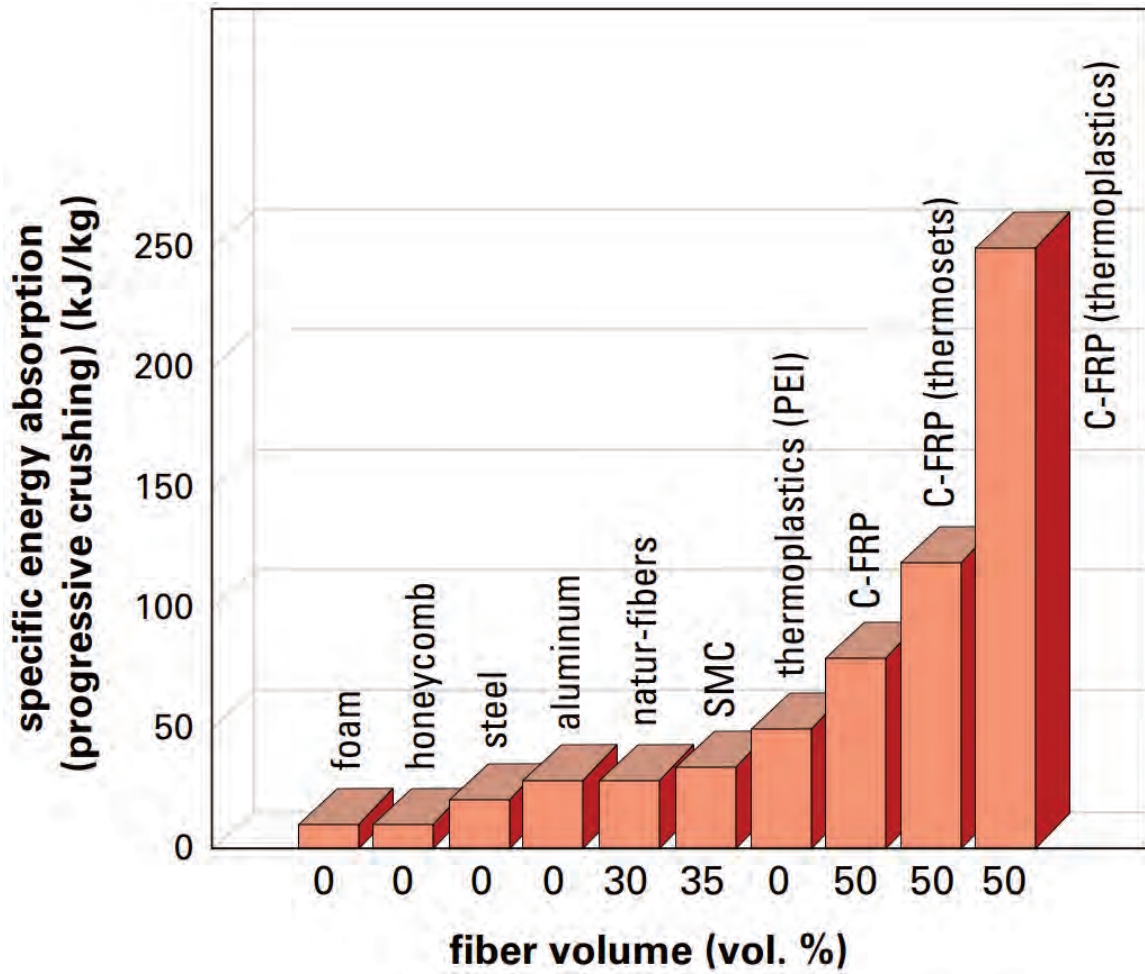


Figure 2.10. Typical values of SEA for some materials (Herrman, 2002).

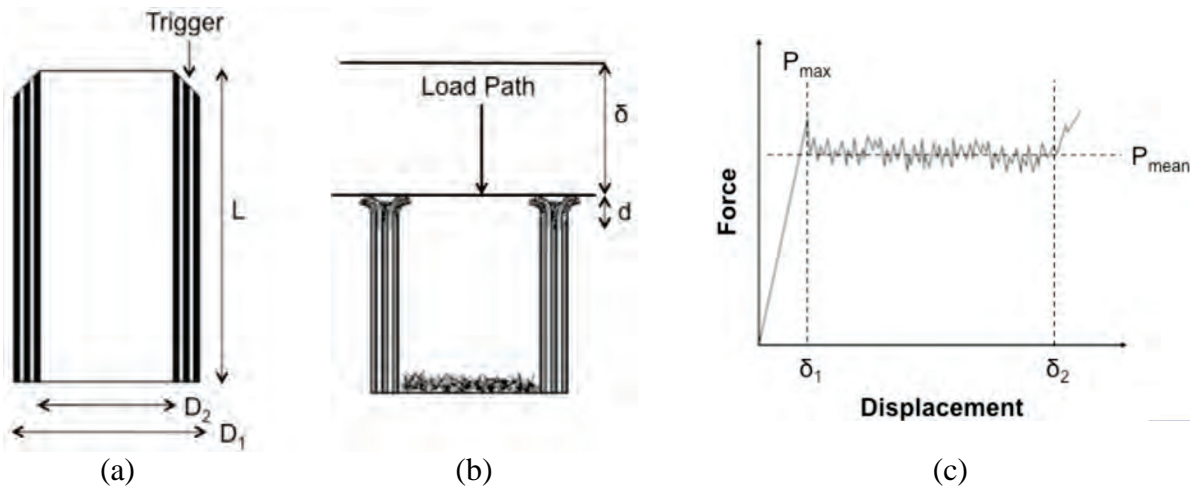


Figure 2.11. Tubular crash test (Courteau, 2011): (a) pre-specimen, (b) post-specimen, and (c) load versus displacement curve of the test.

Numerous failure modes can be observed to take place in a FRP composite structure during stable crush. These failure modes are generally classified into four broad modes: (1) fiber splaying and lamina bending, (2) fragmentation, (3) brittle fracture, and (4) folding. Figure 2.13(a) shows a typical cross-section of a tube wall that has failed by fiber splaying. The key characteristic of the fiber splaying mode is long (greater than laminate thickness) interlaminar, intralaminar, and axial cracks that separate the fibers into bundles, referred to as fronds. These fronds are divided and bent either to the inside or outside of the tube wall. Figure 2.13(b) shows the fragmentation mode of a composite cross-section. The key characteristic of fragmentation mode is the formation of short (less than laminate thickness) interlaminar, intralaminar, and axial cracks. Figure 2.13(c) shows the brittle fracture mode of a composite cross-section. This failure mode is essentially a combination of the fiber splaying and fragmentation modes and has characteristics common in both. Figure 2.13(d) shows the folding modes of a composite tube. The folding mode is analogous to the failure mode experienced by metal tubes when in axial compression. Table 2.9 summarizes the failure modes of FRP composites.

Table 2.9. Summary of failure modes of FRP composites (Courteau, 2011)

	Fiber splaying	Fragmentation	Brittle fracture	Folding
Characteristics	Long axial cracks. Fronds are developed but do not fracture. Small debris wedge may be present.	Short axial cracks. Sections of structure wall are sheared off. No debris wedge present.	Intermediate length axial cracks. Fronds develop and fracture. Large debris wedge present.	Plastic hinges are formed locally. Inter-/intra-laminar cracking occurs near hinges.
Failure mechanisms	Mode I and II fracture.	Fiber and matrix fracture.	Mode I and II fracture. Fiber and matrix fracture.	Buckling and plastic deformation. Some fiber and matrix fracture.
Energy absorption mechanisms	Friction, crack growth, frond bending.	Fiber and matrix fracture.	Friction, fiber and matrix fracture, crack growth.	Deformation, fiber and matrix fracture.

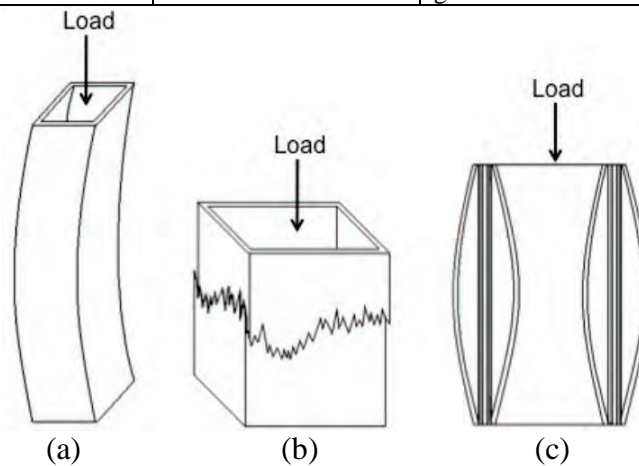


Figure 2.12. Unstable modes of failure showing (Courteau, 2011): (a) buckling, (b) interpenetration, and (c) barreling.

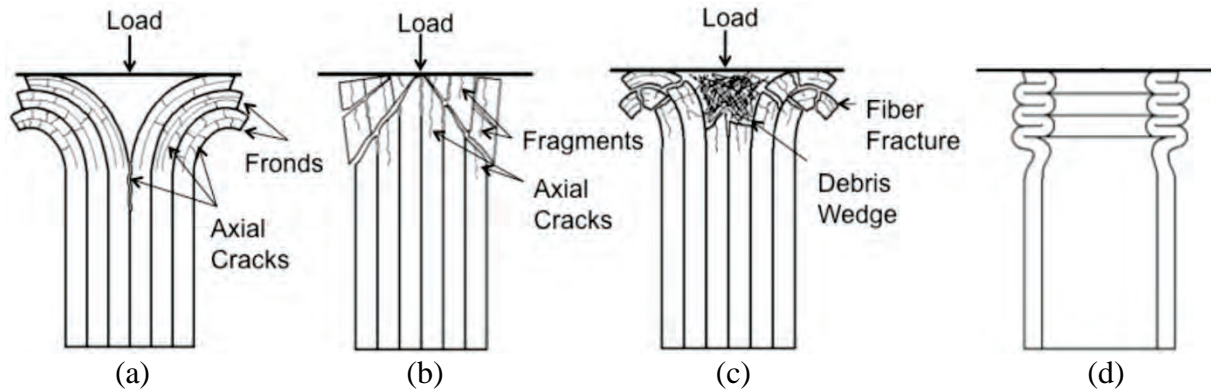


Figure 2.13. Crush failure modes (Courteau, 2011): (a) fiber splaying, (b) fragmentation, (c) brittle fracture, and (d) folding.

2.4. Automotive applications of plastics and composites

Plastic car bumpers and fascia systems

Front and rear bumpers became standard equipment on all cars in 1925. What were then simple metal beams attached to the front and rear of a car have evolved into complex, engineered components that are integral to the protection of the vehicle in low-speed collisions. Today's plastic auto bumpers and fascia systems are aesthetically pleasing, while offering advantages to both designers and drivers.

The majority of modern plastic car bumper system fascias are made of thermoplastic olefins (TPOs), polycarbonates, polyesters, polypropylene, polyurethanes, polyamides, or blends of these with, for instance, glass fibers, for strength and structural rigidity.

The use of plastic in auto bumpers and fascias gives designers a tremendous amount of freedom when it comes to styling a prototype vehicle, or improving an existing model. Plastic can be styled for both aesthetic and functional reasons in many ways without greatly affecting the cost of production. Plastic bumpers contain reinforcements that allow them to be as impact-resistant as metals while being less expensive to replace than their metal equivalents. Plastic car bumpers generally expand at the same rate as metal bumpers under normal driving temperatures and do not usually require special fixtures to keep them in place.

Some of the plastic products used in making auto bumpers and fascias can be recycled. This enables the manufacturer to reuse scrap material in a cost-effective manner. A new recycling program uses painted TPO scrap to produce new bumper fascias through an innovative and major recycling breakthrough process that removes paint from salvage yard plastic. Tests reveal post-industrial recycled TPO performs exactly like virgin material, thereby allowing the conversion of hundreds of thousands of pounds of material destined for landfills into workable grade-A material, and as a result reducing material costs for manufacturers.

Car lighting systems

Plastics are rapidly updating car lighting systems. Glass headlight lenses have been virtually replaced by transparent polycarbonate plastics. These plastics are designed to resist high levels of heat, are shatter-resistant, and can be molded into almost any shape. With such design the risk of igniting gas and other fumes during a collision is reduced. Additionally, this gives car designers and engineers far more flexibility in the styling and placement of headlights. Plastics' versatility also allows auto headlights to incorporate high-tech focusing designs in the lenses, providing the benefit of increased highway safety.

Tail lights, turn signals, cornering lamps, back-up lights, and fog lights are all made of polycarbonate plastics or, in some cases, acrylic plastics. These lenses have similar design and engineering advantages as auto headlight lenses, and incorporate reflective optical surfaces too. Major changes in the future of both head and tail light systems are imminent, with the incorporation of plastic-based LED brake-light systems and "lightbox" systems, whereby an easily accessible, single light source is used to provide exterior lighting for the car via acrylic fiber-optic wires. The incorporation of "light box" LED car lighting technology will eliminate the need for high-heat resistant plastics in auto lighting systems, allowing substitution for even lighter plastic lenses that retain the ability to resist impacts.

Auto trim

Trim is an important operative and aesthetic component of car exteriors. Auto trim comprises everything from mirror housings to door handles, side trim, wheel covers, and radiator grilles. Today, auto trim parts depend largely on plastic to add functionality and decoration to a vehicle's exterior. A variety of plastics are used in manufacturing exterior trim. Nylons, polystyrene, polycarbonates, weatherable ASA/AES, PVC, polypropylene, polyesters, and urethanes are the most commonly used plastics in these applications.

A number of important innovations have allowed manufacturers to save both time and money when building exterior car trim parts. Mirror housings can now be in-mold painted, thanks to weatherable ASA-AES plastics systems, which allow car manufacturers to save on painting costs and eliminate the need for timing the cure of mirror housings with their painting on the production line. Another noteworthy innovation is in plastic wheel covers. By using plastic instead of metal to manufacture wheel covers, and then plating the plastic with a metallic finish, manufacturers spend a fraction of the cost while making the plastic look like a metal alloy. Engineers and consumers also enjoy the added benefits of weight reduction that go hand-in-hand with a switch to plastics. Plastic has also led to innovations in pickup trucks as well. In addition to the familiar truck bed liners, the entire pickup truck bed can be blow-molded from high-density polyethylene.

Recent innovations and buying trends demonstrate a bright future for plastic in exterior automobile applications because it is an excellent, cost-saving alternative to traditional materials. Plastic's ability to reduce weight and improve efficiency provides environmental benefits while maintaining safety. With high-mileage performance becoming an increasingly important issue to

consumers and car manufacturers, plastics have an added advantage of making strong future environmental achievements possible.

Auto upholstery

Urethane foams are the most common plastics used in auto upholstery cushioning. Recyclability, combined with their ability to fulfill design and economic demands set forth by a manufacturer, make them an ideal choice for car upholstery materials.

Recent innovations in cushioning technology now allow a manufacturer to save on the quantity of urethane foam used in cushioning by injecting the foam with carbon dioxide to increase its volume without sacrificing comfort levels; noise, vibration, and harshness (NVH) levels; or flexibility on the assembly line. Arm rests, head rests, headliners and cushioned instrument panels are all made with urethane foams. Thanks to efficient and cost-effective processes, urethane foams can be recycled to make carpeting for cars, homes, and offices.

The carpet padding typically used in automobiles consists of a needled vinyl-based fiber that lies between the floor panels and the carpet itself. Insulating carpet padding is especially important in helping reduce NVH. A new process now allows for the use of polyurethane foam padding between the carpet and the floor panel, which promises even greater reductions in NVH, a more comfortable surface, and an improved fit and finish. Most importantly, however, is that it is a cost-effective process easily adaptable to existing assembly lines and changes in model specification.

Instrument panels

Traditionally, instrument panels were made from several separate components that needed to be painted and that were all held together by a steel supporting beam that lay behind the panel. Today, thanks to modern plastics technology, instrument panels are made of ABS, ABS/PC alloys, polycarbonates, polypropylene, modified polyphenylene ether and styrene maleic anhydride resins. These plastics allow for complex designs in items such as airbag housings; center stacks for instrument panels; and large, integrated instrument panel pieces. They are also used in manufacturing the rest of the automobile's interior trim. These plastics are also capable of eliminating the need for a steel support beam, allowing manufacturers to save dramatically on the cost of the instrument panel while substantially reducing its weight.

Wholly integrated single-piece units can be manufactured from all-urethane and all-polypropylene resins. This results in a seamless instrument panel with greatly reduced NVH levels, molded-in color and with significant cost savings for the manufacturer. Cost effective post-consumer and in-plant recycling is also achievable.

Steering wheels

Steering wheels are made from either molded, pigmented vinyl resins or from RIM pigmented urethane when a ductile material is required. Plastic has helped make possible modern interior steering columns made from a variety of in-mold thermoplastic and metal components. The use

of coils and magnets in modern steering columns requires an injected material that seals off magnetic areas off all together, while ensuring limited interference with the magnetic fields. For example, in the case of acetyl, its low friction, high strength, and naturally smooth finish make it an ideal material to use in a steering column's switches, levers, and bearings. Similar metal products can be made but are generally heavier and require extensive polishing to ensure the low friction surface necessary for their smooth operation.

Air ducts

Heating and air conditioning ducts and consoles now provide temperature regulation to rear as well as front passenger seats. The consoles themselves are typically manufactured from ABS resins, as well as polypropylene and SMA resins. Both blow-molded and injection molded polypropylene is used to manufacture the air ducts that feed the console outlets. The air ducts themselves are complex and odd-shaped, yet at the same time lightweight and durable. They would be difficult to reproduce using any other family of materials.

Other interior components

Other interior applications for plastic include seat bases, headliners, and load floors of GMT composite (polypropylene/fiber glass); door trim panels of ABS or GMT composite; and rear package shelves of PC/ABS or GMT composite materials.

Plastic has revolutionized the interior of a car. It has proven to be an ideal material for creating comfortable, durable, and aesthetically pleasing interior components, while reducing NVH levels from the interior of the car. Plastic's design flexibility helps manufacturers create innovative, integral single-piece light weight components, while cutting costs, saving time, and helping lessen the problems associated with vehicle redesign.

Structure

The world's second all-plastic vehicle, the Baja, has a plastic composite chassis. The vehicle is ideal for off-road tropical environments where its composite body and chassis resist sand and seawater. Its combined thermoplastic and thermoset skin and frame take advantage of plastic's strength to manage energy, enabling it to pass both the United States' and the more stringent European computerized crash tests. The chassis' light weight is a tremendous advantage to manufacturers, since weight savings makes parts easier to transport. It also provides consumers better fuel economy, and with the fuel savings that light weight brings, helps preserve resources and protect the environment.

Since plastic and plastic composites have only recently been considered for use in frames, there is not yet a track record as to what types may be best suited to these applications. Experiments with plastic in frames may lead to future innovations enabling plastic to replace metal on a broader scale.

Crash-absorbing foam is a well-tested application. Door panels are filled with rigid, energy-absorbing polystyrene or urethane-based foam that acts as side impact absorbers, and help

maintain a car's structural rigidity. These lightweight foams provide excellent energy management capability during a crash.

A drive shaft helps transmit power from the engine of a car to an axle. Thanks to plastic's excellent energy-management characteristics, a single-piece plastic-based drive shaft can help reduce levels of NVH. Since a drive shaft runs the length of the underbody of a car, it also behaves as a structural beam, helping to absorb energy in case of a collision.

Support

The development of integrated plastic-steel applications has led to making radiator support from injection molded nylon that consists of a part with complex nylon contours, filled with a simple central steel piece. Any extra strength and rigidity needed in non-steel embodied extremities of the part is achieved by adding "ribs." Ribbing a flat surface can give that surface a tremendous amount of strength. Thanks to plastics' design flexibility, many different types of ribbing can be designed for a single piece, all with different important structural advantages.

A vehicle's chassis, as a term, also encompasses working parts exclusive of the body of a car. This includes suspension systems and brakes.

Suspension

Suspension tubing and links connecting the suspension system to support structures use plastics' strength and smooth surface with no need for machining or polishing. Additionally, plastics' lightweight successfully helps complete a suspension system that is strong and rigid, yet light in weight and fully functional. Injection molded acetyl, nylon, and polypropylene are among the plastics used to make these components.

Brakes

The braking system is one of the most important systems in a car. In certain situations, accident prevention can be virtually impossible without fully functioning brakes. Modern braking systems put thousands of pounds of pressure on each of the four brakes. Plastic helps make today's braking systems possible. ABS housings are molded from plastic; and the electronic circuit boards controlling the brakes are made of an efficient, flexible plastic. Plastic-based brake pads are oftentimes made from a tough aramid fiber, employing the same material used to make bullet-proof vests.

The chassis is fundamental to the proper functioning and safety of a car. Plastic is helping make the chassis lighter, stronger, and more crashworthy, while reducing manufacturing costs, integrating multiple components into single units, and substantially reducing NVH levels.

Transmission

Phenolic resins with glass fiber reinforcement have been used successfully to manufacture stationary transmission parts with attached revolving rotors in revolutionary one-piece designs.

The single-piece design replaces several separate metal components that would otherwise be needed, resulting in a substantial reduction in assembly time and underscoring the outstanding design efficiency attainable when using plastic.

Plastic can also be used to manufacture transmission oil screens and other components requiring exposure to hot transmission oil. As with fuel tanks, plastic helps free designers from the space constraints that arise with the use of sheet metals. The ability to design a transmission with few design limitations allows design engineers to place transmission components in tight-fitting spaces. This is especially important in front-wheel drive vehicles where several components compete for a limited amount of space. The use of plastics in front-wheel drive transmissions also helps lessen the weight in the front of the vehicle, improving vehicle handling.

Polyetherimide resins are used extensively in transmission sensors and valve solenoid applications because of their resistance to high temperatures and creeping.

Plastic has found remarkable acceptance as a substitute for metal in transmission components. Plastics offer engineers a variety of materials featuring an excellent combination of physical properties, including heat and chemical resistance, high strength, impact strength and molding ease. These performance characteristics can be tailored by materials suppliers to meet particular needs. The use of additives, fillers, and reinforcements will vary the properties of a plastic to meet specific customer requirements. Polyetherimide, for instance, is used extensively in transmissions for its superior dimensional, heat, and creep performance, while a single piece of nylon can replace several steel washers.

Plastics' light weight, durability, design flexibility, and uniform surface make them an ideal family of materials to use in a power train. From reducing costs and weight, to dampening noise and vibrations, plastics have been used to make single-piece clutch cylinders, shift control cables, air intake manifolds, engine covers, accelerator and parking brake pedals, fuel system and cooling system components, and gear-lever housing.

From housing and covers protecting gears and bearings, to the bearings themselves, specifying plastic adds value by reducing weight and lowering assembly costs, while providing an economical material capable of durable operation under the most strenuous of conditions.

A key factor behind the strong and steady growth of many of these plastics is recyclability. The use of the large quantities of the same or similar materials greatly improves the economics of recycling. As more plastics are used in automobiles, we are likely to see a trend towards the increasing recycling of these plastics.

Drive shaft

The drive shaft connects a transmission to the differential. Thanks to plastic's excellent energy-management characteristics, a single-piece plastic-based drive shaft can lead to a reduction in NVH. Not only does this allow for a more pleasant driving experience, but by putting less stress on connecting components it can help increase the life span of these components. Additionally, this can help enhance passenger protection, by helping to manage energy in a collision.

Fuel tank

For car fuel system components, plastic has several advantages that enable it to outperform metals. Plastic frees engineers from the design constraints that metal imposes. The environment benefits from plastic's light weight, which makes cars more fuel-efficient, and from innovative techniques that minimize vapor emissions. And from a safety standpoint, rupture-resistant plastics with high impact strength help in keeping a cars' fuel delivery systems leak-proof and reliable.

Powertrain

Many of today's car engine components are plastic. From air-intake systems to cooling systems to actual engine parts, plastic helps make engine systems both easier to design, easier to assemble, and lighter in weight. Plastics' versatility has revolutionized car engine component design.

There have been a lot of efforts to reduce the weight of automotive components using all kinds of lightweight materials and new techniques. Table 2.10 summarizes vehicle components that have seen mass-reduction innovations in material use or design in automotive applications. As shown, there is a large array of different measures, big and small, being used to reduce component mass within vehicles. The mass reductions are taken from many different sources, many of them being automaker press release materials for the vehicle models that are distributed for automobile shows and reviews. As enumerated in the table, there are many potential mass reduction opportunities throughout the vehicles' various components and systems that have been used in production vehicles. However, there are countless other measures that are less publicized and more subtle than those that are documented here. Some of the innovations (e.g., high-strength steel in all body parts; aluminum engine and wheels) are relatively widespread, whereas others are in lower volume production, are just emerging, or are relatively rare.

Table 2.10. Component weight-reduction potential from technologies on production vehicles (Lutsey, 2010)

Vehicle system	Subcomponent	New material or technique ^a	Weight reduction (lb) ^b	Example automaker (models) ^c	Source(s)
Power-train	Block	Aluminum block	100	Ford (Mustang); most vehicles	Tyell, 2010; Ford, 2010
	Engine, housing, etc	Alum-Mg-composite	112	BMW (R6)	Kulekci, 2008
	Engine	Smaller optimized molds (Al)	55	Toyota (Camry)	Simpson, 2007
	Valvetrain	Titanium intake valves	0.74	GM (Z06)	Gerard, 2008
	Connecting rod (8)	Titanium	3.5	GM (Z06); Honda (NSX)	Gerard, 2008
	Driveshaft	Composite	7	Nissan; Mazda; Mitsubishi	ACC, 2006
	Cradle system	Aluminum	22	GM (Impala)	Taub et al, 2007
	Engine cradle	Magnesium	11-12	GM (Z06)	Gerard, 2008; US AMP, 200x
	Intake manifold	Magnesium	10	GM (V8); Chrysler	Kulekci, 2008; US AMP
	Camshaft case	Magnesium	2	Porsche (911)	Kulekci, 2008; US AMP
	Auxiliaries	Magnesium	11	Audi (A8)	Kulekci, 2008
	Oil pan	Modular composite	2	Mercedes (C class)	Stewart, 2009
	Trans. housing	Aluminum	8	BMW (730d); GM (Z06)	Gerard, 2008
	Trans. housing	Magnesium	9-10	Volvo; Porsche (911); Mercedes; VW (Passat); Audi (A4, A8)	Kulekci, 2008; US AMP
Body and closures	Unibody design	Vs. truck body-on-frame	150-300	Honda (Ridgeline); Ford; Kia; most SUV models	Honda, 2010; Motor Trend, 2009
	Frame	Aluminum-intensive body	200-350	Audi (TT, A2, A8); Jaguar (XJ); Lotus; Honda (NSX, Insight)	Brooke and Evans, 2009; Autointel, 1999; EAA, 2007; Audi, 2010
	Frame	Aluminum spaceframe	122	GM (Z06)	Taub et al, 2007
	Panel	Thinner, aluminum alloy	14	Audi (A8)	Audi, 2010
	Panel	Composite	42	BMW	Diem et al, 2002
	Doors (4)	Aluminum-intensive	5-50	Nissan (370z); BMW (7); Jaguar (XJ)	Keith, 2010; BMW, 2008; Birch, 2010
	Doors (4)	New production process	86	Porsche (Cayenne)	Stahl, 2010
	Door inner (4)	Magnesium	24-47		Kulekci, 2008; US AMP
	Hood	Aluminum	15	Honda (MDX); Nissan (370z)	Monaghan, 2007; Keith, 2010
	Roof	Aluminum	15	BWW (7 series)	BMW, 2008
Suspension and chassis	Lift gate	Magnesium	5-10		Kulekci, 2008; US AMP
	Chassis	Aluminum	145	Porsche (Cayenne)	Carney, 2010
	Chassis	Hydroformed steel structure, tubular design	100	Ford (F150)	FordF150.net, 2010
	Steering wheel	Magnesium	1.1	Ford (Thunderbird, Taurus); Chrysler (Plymouth); Toyota (LS430); BMW (Mini); GM (Z06)	Kulekci, 2008; Gerard, 2008
	Steering column	Magnesium	1-2	GM (Z06)	Kulekci, 2008; Gerard, 2008; US AMP
	Wheels (4)	Magnesium	26	Toyota (Supra); Porsche (911); Alfa Romeo	Kulekci, 2008; US AMP
	Wheels (4)	Lighterweight alloy, design	13	Mercedes (C-class)	Tan, 2008
	Brake system	Heat dissipation, stainless steel pins, aluminum caps	30	Audi (A8)	Audi, 2010
	Tires	Design (low RR)	4	Mercedes (C-class)	Tan, 2008
Interior	Suspension	Control arms (2)	6	Dodge (Ram)	SSAB, 2009
	Seat frame (4)	Magnesium	28	Toyota (LS430); Mercedes (Roadster)	Kulekci, 2008; US AMP
	Instrument panel	Magnesium	7-13	Chrysler (Jeep); GM; Ford (Explorer, F150); Audi (A8); Toyota (Century); GM	Kulekci, 2008; US AMP; Taub et al, 2007
	Dashboard	Fiber-reinforced thermoplastic	18	VW (Golf)	Stewart, 2009
	Console and shifter	Injection molded glass reinforced polypropylene	5	Ford (Flex)	Stewart, 2009
Misc.	Windows	Design, material thickness	3	Mercedes (C-class)	Tan, 2008
	Running board	Glass-reinforced polypropylene	9	Ford (Escape)	Stewart, 2009

^a These technologies can include a change in design, a reduction in parts, a reduction in material amount, and use of various metallic alloys; note that weight (lb) and mass (kg) variables are used in this report. 1 kg = 2.205 lb.

^b Weight reduction estimates are approximate, based on media sources and technical reports

^c A number of these models are not available in the U.S.; some model names have changed in recent product changes

3. Basic Composite Mechanics

Basic composite mechanics are described in this chapter. This review refers to three particular references (Gibson, 1994; Staab, 1999; Ugural, 1999). Some of the equations found in this chapter are used in Chapter 6 to compare the composite test results with theoretical values. Later in this chapter, some of the composite failure theories used in the LS-DYNA composite material models are reviewed.

3.1. Stress-strain relationship

A general three-dimensional state of stress at a point in a material can be described by nine stress components σ_{ij} (where $i,j=1,2,3$), as shown in Figure 3.1. Corresponding to each of the stress components, there is a strain component ε_{ij} describing the deformation at the point. In prescribing the most general stress-strain relationship at a point in an elastic material, each stress component is related to each of the nine components by an equation of the form

$$\sigma_{ij}=f_{ij}(\varepsilon_{11}, \varepsilon_{12}, \varepsilon_{13}, \varepsilon_{21}, \varepsilon_{22}, \varepsilon_{23}, \varepsilon_{31}, \varepsilon_{32}, \varepsilon_{33}) \quad (3.1)$$

where the functions f_{ij} may be nonlinear. For the linear elastic material, the most general linear stress-strain relationship at a point in the material is given by the equations of the form

$$\begin{Bmatrix} \sigma_{11} \\ \sigma_{22} \\ \sigma_{33} \\ \sigma_{23} \\ \sigma_{32} \\ \sigma_{13} \\ \sigma_{31} \\ \sigma_{12} \\ \sigma_{21} \end{Bmatrix} = \begin{bmatrix} C_{1111} & C_{1122} & C_{1133} & C_{1123} & C_{1132} & C_{1113} & C_{1131} & C_{1112} & C_{1121} \\ C_{2211} & C_{2222} & C_{2233} & C_{2223} & C_{2232} & C_{2213} & C_{2231} & C_{2212} & C_{2221} \\ C_{3311} & C_{3322} & C_{3333} & C_{3323} & C_{3332} & C_{3313} & C_{3331} & C_{3312} & C_{3321} \\ C_{2311} & C_{2322} & C_{2333} & C_{2323} & C_{2332} & C_{2313} & C_{2331} & C_{2312} & C_{2321} \\ \dots & \dots & \dots & \dots & \dots & \dots & \dots & \dots & \dots \\ \dots & \dots & \dots & \dots & \dots & \dots & \dots & \dots & \dots \\ \dots & \dots & \dots & \dots & \dots & \dots & \dots & \dots & \dots \\ \dots & \dots & \dots & \dots & \dots & \dots & \dots & \dots & \dots \\ C_{2111} & C_{2122} & C_{2133} & C_{2123} & C_{2132} & C_{2113} & C_{2131} & C_{2112} & C_{2121} \end{bmatrix} \begin{Bmatrix} \varepsilon_{11} \\ \varepsilon_{22} \\ \varepsilon_{33} \\ \varepsilon_{23} \\ \varepsilon_{32} \\ \varepsilon_{13} \\ \varepsilon_{31} \\ \varepsilon_{12} \\ \varepsilon_{21} \end{Bmatrix} \quad (3.2)$$

where $[C]$ is a fully populated 9×9 matrix of stiffness or elastic constants having 81 components. If no further restrictions are placed on the elastic constants, the material is called anisotropic and Eq. (3.2) is referred to as the generalized Hooke's law for anisotropic materials.

Both stresses and strains are symmetric (i.e., $\sigma_{ij} = \sigma_{ji}$ and $\varepsilon_{ij} = \varepsilon_{ji}$), so that there are only six independent stress components and six independent strain components. This means that the elastic constants must be symmetric (i.e., $C_{ijkl} = C_{jikl}$ and $C_{ijkl} = C_{ijlk}$ where $i,j,k,l=1,2,3$), and that the number of non-zero elastic constants is now reduced to 36. These simplifications lead to a contracted notation:

$$\begin{array}{ll} \sigma_{11}=\sigma_1 & \varepsilon_{11}=\varepsilon_1 \\ \sigma_{22}=\sigma_2 & \varepsilon_{22}=\varepsilon_2 \\ \sigma_{33}=\sigma_3 & \varepsilon_{33}=\varepsilon_3 \end{array} \quad (3.3)$$

$$\begin{aligned}\sigma_{23} &= \sigma_{32} = \sigma_4 \\ \sigma_{13} &= \sigma_{31} = \sigma_5 \\ \sigma_{12} &= \sigma_{21} = \sigma_6\end{aligned}$$

$$\begin{aligned}2\varepsilon_{23} &= 2\varepsilon_{32} = \gamma_{23} = \gamma_{32} = \varepsilon_4 \\ 2\varepsilon_{13} &= 2\varepsilon_{31} = \gamma_{13} = \gamma_{31} = \varepsilon_5 \\ 2\varepsilon_{12} &= 2\varepsilon_{21} = \gamma_{12} = \gamma_{21} = \varepsilon_6.\end{aligned}$$

With this contracted notation the generalized Hooke's law can now be written as

$$\sigma_i = C_{ij} \varepsilon_j, \quad i, j = 1, 2, \dots, 6 \quad (3.4)$$

and the repeated subscript j implies summation on that subscript. Alternatively, in the generalized Hooke's law can be written in matrix form as

$$\{\sigma\} = [C]\{\varepsilon\} \quad (3.5)$$

where the elastic constant matrix or stiffness matrix $[C]$ is now 6×6 with 36 components and the stresses $\{\sigma\}$ and strains $\{\varepsilon\}$ are column vectors, each having six elements. Alternatively, the generalized Hooke's law relating strains to stresses can be written as

$$\varepsilon_i = S_{ij} \sigma_j, \quad i, j = 1, 2, \dots, 6 \quad (3.6)$$

or in matrix form as

$$\{\varepsilon\} = [S]\{\sigma\} \quad (3.7)$$

where $[S]$ is the compliance matrix, which is the inverse of the stiffness matrix ($[S] = [C]^{-1}$).

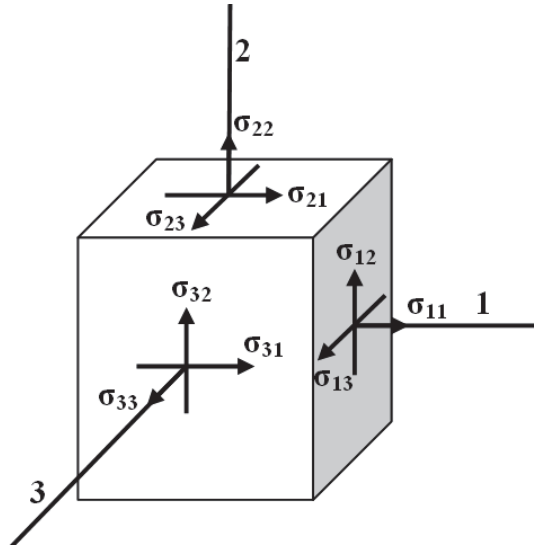


Figure 3.1. General three-dimensional state of stress.

The strain energy density function, W , is defined as

$$W = 1/2 C_{ij} \varepsilon_i \varepsilon_j \quad (3.8)$$

which satisfies the equation

$$\sigma_i = \partial W / \partial \varepsilon_i = C_{ij} \varepsilon_j. \quad (3.9)$$

By taking a second derivative of W, we find that

$$\partial^2 W / \partial \varepsilon_i \partial \varepsilon_j = C_{ij} \quad (3.10)$$

and by reversing the order of differentiation, we find that

$$\partial^2 W / \partial \varepsilon_j \partial \varepsilon_i = C_{ji}. \quad (3.11)$$

Since the result must be the same regardless of the order of the differentiation, $C_{ij} = C_{ji}$ and the stiffness matrix is symmetric. Similarly, the compliance matrix is symmetric. Due to this symmetric condition, only 21 of the 36 anisotropic elastic moduli or compliances are independent in the form

$$C_{ij} = \begin{bmatrix} C_{11} & C_{12} & C_{13} & C_{14} & C_{15} & C_{16} \\ & C_{22} & C_{23} & C_{24} & C_{25} & C_{26} \\ & & C_{33} & C_{34} & C_{35} & C_{36} \\ & & & C_{44} & C_{45} & C_{46} \\ & \text{SYM} & & & C_{55} & C_{56} \\ & & & & & C_{66} \end{bmatrix}. \quad (3.12)$$

As shown in Figure 3.2, unidirectional composite lamina has three mutually orthogonal planes of material property symmetry (i.e., the 12, 23, and 13 planes) and is called an orthotropic material. Unlike the anisotropic stiffness matrix, the form of the stiffness matrix for the orthotropic material depends on the coordinate system used. The 123 coordinate axes in Figure 3.2 are referred to as the principal material coordinate since they are associated with the reinforcement directions, The stiffness matrix for a so-called specially orthotropic material associated with the principal material coordinate is of the form

$$C_{ij} = \begin{bmatrix} C_{11} & C_{12} & C_{13} & 0 & 0 & 0 \\ & C_{22} & C_{23} & 0 & 0 & 0 \\ & & C_{33} & 0 & 0 & 0 \\ & & & C_{44} & 0 & 0 \\ & \text{SYM} & & & C_{55} & 0 \\ & & & & & C_{66} \end{bmatrix} \quad (3.13)$$

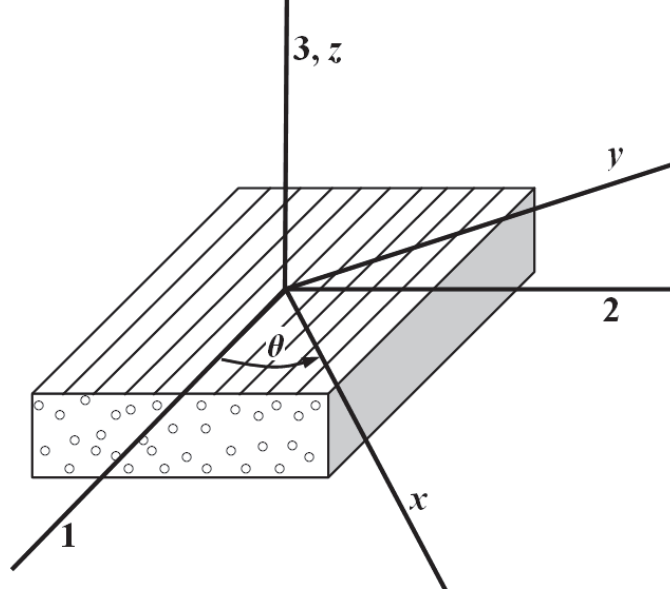


Figure 3.2. Orthotropic lamina with principal coordinate and non-principal coordinate.

which has only 12 nonzero elastic constants and 9 independent elastic constants. When the material is in non-principal coordinate system, the stiffness matrix is of the same form as that of the anisotropic material and is called generally orthotropic material.

It is convenient to relate the components of stiffness matrix to engineering moduli, such as the Young moduli (E_1, E_2, E_3), Poisson's ratios ($\nu_{12}, \nu_{13}, \nu_{23}$) and shear moduli (G_{12}, G_{13}, G_{23}). The correspondences are

$$\begin{aligned}
 C_{11} &= E_1(1 - (E_3/E_2) \nu_{23}^2)D \\
 C_{12} &= (E_2 \nu_{12} + E_3 \nu_{13} \nu_{23})D \\
 C_{13} &= E_3(\nu_{12} \nu_{23} + \nu_{13})D \\
 C_{22} &= E_2(1 - (E_3/E_1) \nu_{13}^2)D \\
 C_{23} &= (E_3/E_1)(E_1 \nu_{23} + E_2 \nu_{12} \nu_{13})D \\
 C_{33} &= E_3(1 - (E_2/E_1) \nu_{12}^2)D \\
 C_{44} &= G_{23} \\
 C_{55} &= G_{13} \\
 C_{66} &= G_{12}
 \end{aligned} \tag{3.14}$$

with $D^{-1} = 1 - 2(E_3/E_1) \nu_{12} \nu_{23} \nu_{13} - \nu_{13}^2(E_3/E_2) - \nu_{23}^2(E_3/E_2) - \nu_{12}^2(E_2/E_1)$. The compliance matrix can be expressed in terms of the engineering moduli:

$$S_{ij} = \begin{bmatrix} \frac{1}{E_1} & -\frac{\nu_{21}}{E_2} & -\frac{\nu_{31}}{E_3} & 0 & 0 & 0 \\ -\frac{\nu_{12}}{E_1} & \frac{1}{E_2} & -\frac{\nu_{32}}{E_3} & 0 & 0 & 0 \\ -\frac{\nu_{13}}{E_1} & -\frac{\nu_{23}}{E_2} & \frac{1}{E_3} & 0 & 0 & 0 \\ 0 & 0 & 0 & \frac{1}{G_{23}} & 0 & 0 \\ 0 & 0 & 0 & 0 & \frac{1}{G_{13}} & 0 \\ 0 & 0 & 0 & 0 & 0 & \frac{1}{G_{12}} \end{bmatrix} \quad (3.15)$$

with $\nu_{ij}/E_i = \nu_{ji}/E_j$ by the symmetry condition of the compliance matrix.

In most composites the fiber-packing arrangement is statistically random in nature, so that the properties are assumed to be nearly the same in any direction perpendicular to the fibers (i.e., the properties along the 2 direction are the same as those along the 3 direction), and the material is transversely isotropic. For such a material, we would expect that $C_{22}=C_{33}$, $C_{12}=C_{13}$, $C_{55}=C_{66}$, and that C_{44} would not be independent from the other stiffness. The stiffness matrix for a specially orthotropic, transversely isotropic material is of the form

$$C_{ij} = \begin{bmatrix} C_{11} & C_{12} & C_{12} & 0 & 0 & 0 \\ & C_{22} & C_{23} & 0 & 0 & 0 \\ & & C_{22} & 0 & 0 & 0 \\ & & & (C_{22} - C_{23})/2 & 0 & 0 \\ & \text{SYM} & & & C_{66} & 0 \\ & & & & & C_{66} \end{bmatrix} \quad (3.16)$$

which has 12 nonzero elastic constants and only 5 independent elastic constants. For the engineering moduli in Eq. (3.15), we have $G_{13}=G_{12}$, $E_2=E_3$, $\nu_{12}=\nu_{13}$ and $\nu_{23}=\nu_{32}$. In addition, we have the relationship:

$$G_{23}=E_2/2(1+\nu_{32}) \quad (3.17)$$

When the material is isotropic and every coordinate axis is an axis of symmetry, then the stiffness matrix is of the form

$$C_{ij} = \begin{bmatrix} C_{11} & C_{12} & C_{12} & 0 & 0 & 0 \\ & C_{11} & C_{12} & 0 & 0 & 0 \\ & & C_{11} & 0 & 0 & 0 \\ & & & (C_{11} - C_{12})/2 & 0 & 0 \\ & \text{SYM} & & & (C_{11} - C_{12})/2 & 0 \\ & & & & & (C_{11} - C_{12})/2 \end{bmatrix} \quad (3.18)$$

which has 12 nonzero elastic constants and only 2 independent elastic constants.

The lamina is often assumed to be in a simple two-dimensional state of stress (or plane stress). In this case the specially orthotropic stress-strain relationships with Eq. (3.15) can be simplified by letting $\sigma_3 = \sigma_4 = \sigma_5 = 0$, so that

$$\begin{Bmatrix} \varepsilon_1 \\ \varepsilon_2 \\ \gamma_{12} \end{Bmatrix} = \begin{bmatrix} S_{11} & S_{12} & 0 \\ S_{21} & S_{22} & 0 \\ 0 & 0 & S_{66} \end{bmatrix} \begin{Bmatrix} \sigma_1 \\ \sigma_2 \\ \tau_{12} \end{Bmatrix} \quad (3.19)$$

where the compliance S_{ij} and the engineering constants are related by the equations

$$\begin{aligned} S_{11} &= 1/E_1 \\ S_{22} &= 1/E_2 \\ S_{12} &= S_{21} = -\nu_{21}/E_2 = -\nu_{12}/E_1 \\ S_{66} &= 1/G_{12}. \end{aligned} \quad (3.20)$$

Thus there are five nonzero compliance and only four independent compliances for the specially orthotropic lamina. The lamina stresses in terms of tensor strain are given by

$$\begin{Bmatrix} \sigma_1 \\ \sigma_2 \\ \tau_{12} \end{Bmatrix} = \begin{bmatrix} Q_{11} & Q_{12} & 0 \\ Q_{21} & Q_{22} & 0 \\ 0 & 0 & Q_{66} \end{bmatrix} \begin{Bmatrix} \varepsilon_1 \\ \varepsilon_2 \\ \gamma_{12} \end{Bmatrix} \quad (3.21)$$

where the Q_{ij} are the components of the lamina stiffness matrix, which are related to the compliances and the engineering constants by

$$\begin{aligned} Q_{11} &= S_{22}/(S_{11}S_{22}-S_{12}^2) = E_1/(1-\nu_{12}\nu_{21}) \\ Q_{12} &= -S_{12}/(S_{11}S_{22}-S_{12}^2) = \nu_{12}E_2/(1-\nu_{12}\nu_{21}) = Q_{21} \\ Q_{22} &= S_{11}/(S_{11}S_{22}-S_{12}^2) = E_2/(1-\nu_{12}\nu_{21}) \\ Q_{66} &= 1/S_{66} = G_{12} \end{aligned} \quad (3.22)$$

The stress-strain relationship in the generally orthotropic lamina in non-principal coordinates is

$$\begin{Bmatrix} \sigma_x \\ \sigma_y \\ \tau_{xy} \end{Bmatrix} = \begin{bmatrix} \bar{Q}_{11} & \bar{Q}_{12} & \bar{Q}_{16} \\ \bar{Q}_{21} & \bar{Q}_{22} & \bar{Q}_{26} \\ \bar{Q}_{61} & \bar{Q}_{62} & \bar{Q}_{66} \end{bmatrix} \begin{Bmatrix} \varepsilon_x \\ \varepsilon_y \\ \gamma_{xy} \end{Bmatrix} \quad (3.23)$$

with

$$\begin{aligned} \bar{Q}_{11} &= Q_{11}\cos^4\theta + Q_{22}\sin^4\theta + 2(Q_{12} + 2Q_{66})\sin^2\theta\cos^2\theta \\ \bar{Q}_{12} &= (Q_{11} + Q_{22} - 4Q_{66})\sin^2\theta\cos^2\theta + Q_{12}(\sin^4\theta + \cos^4\theta) \\ \bar{Q}_{22} &= Q_{11}\sin^4\theta + Q_{22}\cos^4\theta + 2(Q_{12} + 2Q_{66})\sin^2\theta\cos^2\theta \\ \bar{Q}_{16} &= (Q_{11} - Q_{12} - 2Q_{66})\sin\theta\cos^3\theta - (Q_{22} - Q_{12} - 2Q_{66})\sin^3\theta\cos\theta \\ \bar{Q}_{26} &= (Q_{11} - Q_{12} - 2Q_{66})\sin^3\theta\cos\theta - (Q_{22} - Q_{12} - 2Q_{66})\sin\theta\cos^3\theta \\ \bar{Q}_{66} &= (Q_{11} + Q_{22} - 2Q_{12} - 2Q_{66})\sin^2\theta\cos^2\theta + Q_{66}(\sin^4\theta + \cos^4\theta) \end{aligned} \quad (3.24)$$

where θ is the angle between off-axis coordinate and fiber orientation in Figure 3.2.

$$\rho_c = \sum_{i=1}^n \rho_i v_i = \rho_f v_f + \rho_m v_m \quad (3.27)$$

or

$$\rho_c = \frac{1}{\sum_{i=1}^n (w_i / \rho_i)} = \frac{1}{(w_f / \rho_f) + (w_m / \rho_m)} \quad (3.28)$$

where ρ_i , ρ_f , ρ_m , and ρ_c are the densities of the i th constituent, fiber, matrix, and composite, respectively.

Under assumptions about either stress or strains in the RVE which has been subjected to a simple state of stress, volume-averaged stress, strain and displacement are obtained as

$$\bar{\sigma} = \frac{1}{V} \int \sigma dV = \frac{1}{A} \int \sigma dA \quad (3.29)$$

$$\bar{\varepsilon} = \frac{1}{V} \int \varepsilon dV = \frac{1}{A} \int \varepsilon dA \quad (3.30)$$

$$\bar{\delta} = \frac{1}{V} \int \delta dV = \frac{1}{A} \int \delta dA \quad (3.31)$$

where σ = stress, ε = strain, δ = displacement, V = volume, and A = area associated with the face on which loading is applied. Combining the static equilibrium condition in longitudinal direction with Eq. (3.29), we get

$$\bar{\sigma}_{c1} A_1 = \bar{\sigma}_{f1} A_f + \bar{\sigma}_{m1} A_m \quad (3.32)$$

Since the area fractions are equal to the corresponding volume fractions, Eq. (3.32) becomes

$$\bar{\sigma}_{c1} = \bar{\sigma}_{f1} v_f + \bar{\sigma}_{m1} v_m \quad (3.33)$$

The one-dimensional Hooke's law is

$$\bar{\sigma}_{c1} = E_1 \bar{\varepsilon}_{c1}, \quad \bar{\sigma}_{f1} = E_f \bar{\varepsilon}_{f1}, \quad \bar{\sigma}_{m1} = E_m \bar{\varepsilon}_{m1} \quad (3.34)$$

and Eq. (3.33) becomes

$$E_1 \bar{\varepsilon}_{c1} = E_f \bar{\varepsilon}_{f1} v_f + E_m \bar{\varepsilon}_{m1} v_m. \quad (3.35)$$

It is assumed that the average strains in the composite, fiber, and matrix along the longitudinal direction are equal:

$$\bar{\varepsilon}_{c1} = \bar{\varepsilon}_{f1} = \bar{\varepsilon}_{m1}. \quad (3.36)$$

Substituting of Eq. (3.36) in Eq. (3.35) yields the equation for the longitudinal modulus

$$E_1 = E_f v_f + E_m v_m.$$

Geometric compatibility requires that the total transverse composite displacement must equal the sum of the corresponding transverse displacements in the fiber and the matrix:

$$\bar{\delta}_{c2} = \bar{\delta}_{f2} = \bar{\delta}_{m2}. \quad (3.38)$$

The definition of normal strain is expressed as

$$\bar{\delta}_{c2} = \bar{\varepsilon}_{c2} L_2, \quad \bar{\delta}_{f2} = \bar{\varepsilon}_{f2} L_f, \quad \bar{\delta}_{m2} = \bar{\varepsilon}_{m2} L_m \quad (3.39)$$

where L_2 , L_f , and L_m are the transverse length of composite, fiber, and matrix, respectively. Then Eq. (3.38) becomes

$$\bar{\varepsilon}_{c2} L_2 = \bar{\varepsilon}_{f2} L_f + \bar{\varepsilon}_{m2} L_m. \quad (3.40)$$

Since the length fraction must be equal to the volume fractions, Eq. (3.40) becomes

$$\bar{\varepsilon}_{c2} = \bar{\varepsilon}_{f2} v_f + \bar{\varepsilon}_{m2} v_m. \quad (3.41)$$

The one-dimensional Hooke's law for the transverse direction is

$$\bar{\sigma}_{c2} = E_2 \bar{\varepsilon}_{c2}, \quad \bar{\sigma}_{f2} = E_f \bar{\varepsilon}_{f2}, \quad \bar{\sigma}_{m2} = E_m \bar{\varepsilon}_{m2}. \quad (3.42)$$

Combining Eqs. (3.41) and (3.42), we get

$$\frac{\bar{\sigma}_{c2}}{E_2} = \frac{\bar{\sigma}_{f2}}{E_f} v_f + \frac{\bar{\sigma}_{m2}}{E_m} v_m. \quad (3.43)$$

If we assume that the stresses in the composite, fiber, and matrix are all equal, Eq. (3.43) reduces to the inverse equation for the transverse modulus:

$$\frac{1}{E_2} = \frac{v_f}{E_f} + \frac{v_m}{E_m}. \quad (3.44)$$

The Poisson's ration is defined as

$$\nu_{12} = \frac{\bar{\epsilon}_{c2}}{\bar{\epsilon}_{c1}}.$$

Using Eqs. (3.36) and (3.41), Eq. (3.45) becomes

$$\nu_{12} = \nu_{f2}\nu_f + \nu_{m2}\nu_m. \quad (3.46)$$

The shear modulus is defined as

$$G_{12} = \frac{\bar{\sigma}_{c12}}{\bar{\gamma}_{c12}}. \quad (3.47)$$

Using the approach similar to that which was used for the transverse modulus, Eq. (3.47) becomes to the inverse equation of shear modulus:

$$\frac{1}{G_{12}} = \frac{\nu_f}{G_{f12}} + \frac{\nu_m}{G_m}. \quad (3.48)$$

3.3. Analysis of laminates

Classical lamination theory (CLT) is used to analyze laminated plates. Figure 3.4(a) shows the stress resultants and layer profile of laminated plates. Also Figure 3.4(a) defines the coordinate system for the CLT.

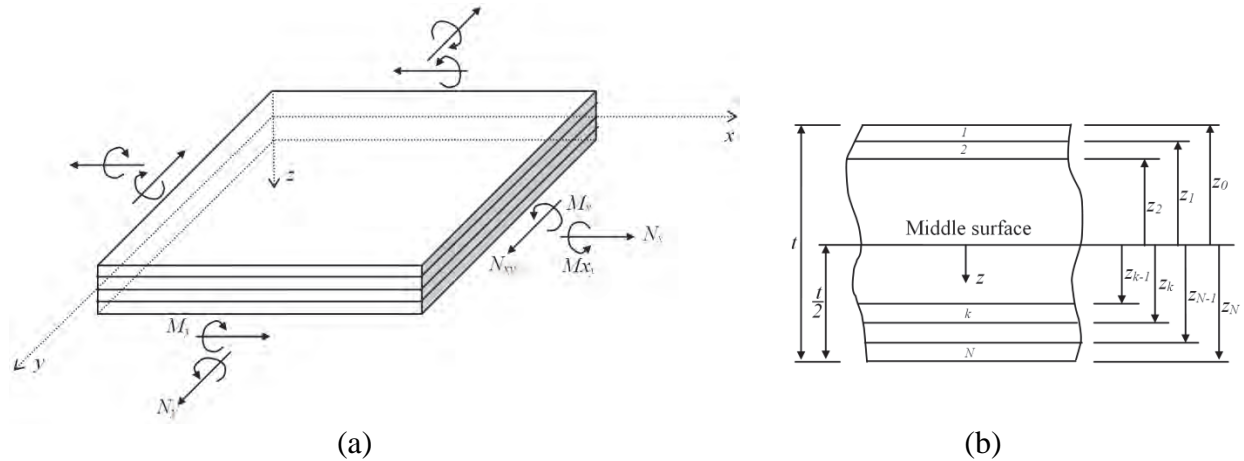


Figure 3.4. Laminated plates: (a) stress resultants, (b) layer profile.

Assuming the state of plane stress in each ply and Kirchhoff deformation hypothesis that normals to the middle surface straight and normal during deformation, the displacements can be expressed as

$$\begin{aligned} u &= u^0(x, y) + z \frac{\partial w}{\partial x} \\ v &= v^0(x, y) + z \frac{\partial w}{\partial y} \\ w &= w(x, y) \end{aligned} \quad (3.49)$$

where u , v and w are the displacements in the x , y and z directions, respectively, and u^0 and v^0 are the tangential displacements of the middle surface along the x and y directions, respectively. The strain-displacement relations for the in-plane strains are

$$\begin{aligned} \varepsilon_x &= \frac{\partial u}{\partial x} = \varepsilon_x^0 + z\kappa_x \\ \varepsilon_y &= \frac{\partial v}{\partial y} = \varepsilon_y^0 + z\kappa_y \\ \gamma_{xy} &= \frac{\partial u}{\partial y} + \frac{\partial v}{\partial x} = \gamma_{xy}^0 + z\kappa_{xy} \end{aligned} \quad (3.50)$$

where the strains on the middle surface are

$$\varepsilon_x^0 = \frac{\partial u^0}{\partial x}, \quad \varepsilon_y^0 = \frac{\partial v^0}{\partial y}, \quad \gamma_{xy}^0 = \frac{\partial u^0}{\partial y} + \frac{\partial v^0}{\partial x}, \quad (3.51)$$

and the curvatures of the middle surface are

$$\kappa_x = -\frac{\partial^2 w}{\partial x^2}, \quad \kappa_y = -\frac{\partial^2 w}{\partial y^2}, \quad \kappa_{xy} = -2\frac{\partial^2 w}{\partial x \partial y}. \quad (3.52)$$

Since Eqs. (3.50) give the strains at any distance z from the middle surface, the stresses along arbitrary xy axes in the k^{th} lamina of a laminate may be found by substituting Eqs. (3.50) into Eq. (3.23) as follows:

$$\begin{Bmatrix} \sigma_x \\ \sigma_y \\ \tau_{xy} \end{Bmatrix}_k = \begin{bmatrix} \bar{Q}_{11} & \bar{Q}_{12} & \bar{Q}_{16} \\ \bar{Q}_{21} & \bar{Q}_{22} & \bar{Q}_{26} \\ \bar{Q}_{61} & \bar{Q}_{62} & \bar{Q}_{66} \end{bmatrix}_k \begin{Bmatrix} \varepsilon_x^0 + z\kappa_x \\ \varepsilon_y^0 + z\kappa_y \\ \gamma_{xy}^0 + z\kappa_{xy} \end{Bmatrix} \quad (3.53)$$

where the subscript k refers the k^{th} lamina shown in Figure 4.3(b). Using the static equilibrium relationship, the stress resultants shown in Figure 3.4(a) can be obtained. The force per unit length and the moment per unit length are given by

$$N_x = \int_{-t/2}^{t/2} \sigma_x dz = \sum_{k=1}^N \left\{ \int_{z_{k-1}}^{z_k} (\sigma_x)_k dz \right\} \quad (3.54)$$

$$M_x = \int_{-t/2}^{t/2} \sigma_x z dz = \sum_{k=1}^N \left\{ \int_{z_{k-1}}^{z_k} (\sigma_x)_k z dz \right\} \quad (3.55)$$

where t = laminate thickness, $(\sigma_x)_k$ = stress in the k^{th} lamina, and z_k = corresponding distance from middle surface to outer surface of the k^{th} lamina, as shown in Figure 3.4(b). Substituting Eq. (5.53) into Eqs. (3.54) and (3.55) and combining terms, we get

$$N_x = A_{11}\varepsilon_x^0 + A_{12}\varepsilon_y^0 + A_{16}\gamma_{xy}^0 + B_{11}\kappa_x + B_{12}\kappa_y + B_{16}\kappa_{xy} \quad (3.56)$$

$$M_x = B_{11}\varepsilon_x^0 + B_{12}\varepsilon_y^0 + B_{16}\gamma_{xy}^0 + D_{11}\kappa_x + D_{12}\kappa_y + D_{16}\kappa_{xy} \quad (3.57)$$

where the extensional stiffness is expressed as

$$A_{ij} = \int_{-t/2}^{t/2} (\bar{Q}_{ij})_k dz = \sum_{k=1}^N (\bar{Q}_{ij})_k (z_k - z_{k-1}), \quad (3.58)$$

the extension-bending coupling stiffness is

$$B_{ij} = \int_{-t/2}^{t/2} (\bar{Q}_{ij})_k z dz = \frac{1}{2} \sum_{k=1}^N (\bar{Q}_{ij})_k (z_k^2 - z_{k-1}^2), \quad (3.59)$$

and the bending stiffness is

$$D_{ij} = \int_{-t/2}^{t/2} (\bar{Q}_{ij})_k z^2 dz = \frac{1}{3} \sum_{k=1}^N (\bar{Q}_{ij})_k (z_k^3 - z_{k-1}^3).$$

The complete set of the force-displacement equations can be expressed in matrix form as

$$\begin{Bmatrix} N_x \\ N_y \\ N_{xy} \\ \dots \\ M_x \\ M_y \\ M_{xy} \end{Bmatrix} = \begin{bmatrix} A_{11} & A_{12} & A_{16} & \vdots & B_{11} & B_{12} & B_{16} \\ A_{12} & A_{22} & A_{26} & \vdots & B_{12} & B_{22} & B_{26} \\ A_{16} & A_{26} & A_{66} & \vdots & B_{16} & B_{26} & B_{66} \\ \dots & \dots & \dots & \dots & \dots & \dots & \dots \\ B_{11} & B_{12} & B_{16} & \vdots & D_{11} & D_{12} & D_{16} \\ B_{12} & B_{22} & B_{26} & \vdots & D_{12} & D_{22} & D_{26} \\ B_{16} & B_{26} & B_{66} & \vdots & D_{16} & D_{26} & D_{66} \end{bmatrix} \begin{Bmatrix} \varepsilon_x^0 \\ \varepsilon_y^0 \\ \gamma_{xy}^0 \\ \dots \\ \kappa_x \\ \kappa_y \\ \kappa_{xy} \end{Bmatrix}. \quad (3.61)$$

Considering a symmetric laminate under in-plane loads only, Eq. (3.61) can be reduced to

$$\begin{Bmatrix} N_x \\ N_y \\ N_{xy} \end{Bmatrix} = \begin{bmatrix} A_{11} & A_{12} & A_{16} \\ A_{12} & A_{22} & A_{26} \\ A_{16} & A_{26} & A_{66} \end{bmatrix} \begin{Bmatrix} \varepsilon_x^0 \\ \varepsilon_y^0 \\ \gamma_{xy}^0 \end{Bmatrix} \quad (3.62)$$

a and the corresponding inverted force-displacement relationships are

$$\begin{Bmatrix} \varepsilon_x^0 \\ \varepsilon_y^0 \\ \gamma_{xy}^0 \end{Bmatrix} = \begin{bmatrix} A_{11} & A_{12} & A_{16} \\ A_{12} & A_{22} & A_{26} \\ A_{16} & A_{26} & A_{66} \end{bmatrix}^{-1} \begin{Bmatrix} N_x \\ N_y \\ N_{xy} \end{Bmatrix} = \begin{bmatrix} A'_{11} & A'_{12} & A'_{16} \\ A'_{12} & A'_{22} & A'_{26} \\ A'_{16} & A'_{26} & A'_{66} \end{bmatrix} \begin{Bmatrix} N_x \\ N_y \\ N_{xy} \end{Bmatrix}. \quad (3.63)$$

The effective longitudinal Young's modulus of the laminate governs the response of the laminate under the single axial load per unit length N_x with $N_y=N_{xy}=0$ and is defined as

$$E_x = \frac{\sigma_x}{\varepsilon_x^0} = \frac{N_x/t}{A'_{11}N_x} = \frac{1}{tA'_{11}}. \quad (3.64)$$

Similarly, the effective transverse Young's modulus, the effective in-plane shear modulus, and the effective laminate longitudinal Poisson's ratio are

$$E_y = \frac{\sigma_y}{\varepsilon_y^0} = \frac{N_y/t}{A'_{22}N_y} = \frac{1}{tA'_{22}}, \quad (3.65)$$

$$G_{xy} = \frac{\tau_{xy}}{\gamma_{xy}^0} = \frac{N_{xy}/t}{A'_{66}N_{xy}} = \frac{1}{tA'_{66}}, \quad (3.66)$$

$$\nu_{xy} = -\frac{A'_{12}}{A'_{11}}, \quad (3.67)$$

respectively.

3.4. Composite failure theory

Four composite failure theories, which are implemented in LS-DYNA material models, are described. X_t , X_c , Y_t , Y_c and S are longitudinal tensile strength, longitudinal compressive strength, transverse tensile strength, transverse compressive strength, and shear strength, respectively, which are obtained from material strength measurement.

Tsai-Wu failure criterion

The Tsai-Wu (Tsai & Wu, 1971) theory is an interactive criterion because it predicts the failure load by using a single quadratic polynomial equation involving all stress components. Tsai-Wu failure criteria is expressed as

$$F_{11}\sigma_1^2 + 2F_{12}\sigma_1\sigma_2 + F_{22}\sigma_2^2 + F_{66}\tau_{12}^2 + F_1\sigma_1 + F_2\sigma_2 = 1 \quad (3.68)$$

where

$$F_1 = \frac{1}{X_t} - \frac{1}{X_c}, \quad F_2 = \frac{1}{Y_t} - \frac{1}{Y_c}, \quad F_{11} = \frac{1}{X_t X_c}, \quad F_{22} = \frac{1}{Y_t Y_c}, \quad F_{66} = \frac{1}{S^2}, \quad (3.69)$$

and F_{12} = experimentally determined .

Hashin failure criterion

The Hashin (1980) theory is a separate mode criterion because it separates the matrix failure criterion from the fiber failure criterion. The Hashin failure criterion in plane stress condition is expressed as

- Tension fiber mode ($\sigma_1 > 0$):

$$\left(\frac{\sigma_1}{X_t}\right)^2 + \left(\frac{\tau_{12}}{S}\right)^2 = 1, \quad (3.70)$$

- Compression fiber mode ($\sigma_1 < 0$):

$$\frac{\sigma_1}{X_c} = 1, \quad (3.71)$$

- T Tension matrix mode ($\sigma_2 > 0$):

$$\left(\frac{\sigma_2}{Y_t}\right)^2 + \left(\frac{\tau_{12}}{S}\right)^2 = 1, \quad (3.72)$$

- Compression matrix mode ($\sigma_2 < 0$):

$$\left(\frac{\sigma_2}{2S}\right)^2 + \left[\left(\frac{Y_c}{2S}\right)^2 - 1\right] \frac{\sigma_2}{Y_c} + \left(\frac{\tau_{12}}{S}\right)^2 = 1. \quad (3.73)$$

Chang-Chang failure criterion

The Chang-Chang theory (Chang, 1987a, 1987b) is also a separate mode criterion. In plane stress, the nonlinear shear strain is given in terms of the stress as

$$\gamma_{12} = \frac{1}{G_{12}} \tau_{12} + \alpha \tau_{12}^3 \quad (3.74)$$

and the fiber matrix shearing term augments is defined as

$$\bar{\tau} = \frac{\int_0^{\gamma_{12}} \sigma_{12} d\gamma_{12}}{\int_0^{\gamma_{12}^u} \sigma_{12} d\gamma_{12}} = \frac{\frac{\tau_{12}^2}{2G_{12}} + \frac{3}{4} \alpha \tau_{12}^4}{\frac{S^2}{2G_{12}} + \frac{3}{4} \alpha S^4} \quad (3.75)$$

where γ_{12}^u is the ultimate shear strain and α is the nonlinear shear stress parameter. If $\alpha=1$, then Eq. (3.75) becomes

$$\bar{\tau} = \left(\frac{\tau_{12}}{S}\right)^2. \quad (3.76)$$

Then the Chang-Chang failure criterion is expressed as

- Matrix cracking failure (tension):

$$\left(\frac{\sigma_2}{Y_t}\right)^2 + \bar{\tau} = 1, \quad (3.77)$$

- Fiber-matrix shearing and fiber breakage (tension):

$$\left(\frac{\sigma_1}{X_t}\right)^2 + \bar{\tau} = 1, \quad (3.78)$$

Compressive failure was predicted by the Hashin failure criterion, which has the form

- Compression matrix failure:

$$\left(\frac{\sigma_2}{2S}\right)^2 + \left[\left(\frac{Y_c}{2S}\right)^2 - 1\right] \frac{\sigma_2}{Y_c} + \bar{\tau} = 1. \quad (3.79)$$

MLT (Matzenmiller, Lubliner, and Taylor) failure criterion

This theory (Matzenmiller, Lubliner, & Taylor, 1995) is also a separate mode criterion. Based on physical reasoning and due to limited material data, the contribution of distinct invariants to the various failure criteria is considered as insignificant (Matzenmiller, & Schweizerhof, 1991). So, the Hashin failure criterion in plane stress condition is reduced to the following simple forms:

- Tension fiber mode ($\sigma_1 > 0$):

$$\left(\frac{\sigma_1}{X_t}\right)^2 = 1, \quad (3.80)$$

- Compression fiber mode ($\sigma_1 < 0$):

$$\left(\frac{\sigma_1}{X_c}\right)^2 = 1, \quad (3.81)$$

- Tension matrix mode ($\sigma_2 > 0$):

$$\left(\frac{\sigma_2}{Y_t}\right)^2 + \left(\frac{\tau_{12}}{S}\right)^2 = 1, \quad (3.82)$$

- Compression matrix mode ($\sigma_2 < 0$):

$$\left(\frac{\sigma_2}{Y_c}\right)^2 + \left(\frac{\tau_{12}}{S}\right)^2 = 1. \quad (3.83)$$

4. Numerical Analysis of Composites Using LS-DYNA

The LS-DYNA hydrocode is a well-known computer-aided engineering program and provides many features to analyze composite materials. In this chapter, the basic keywords and composite material models of LS-DYNA for composite analysis are described as based on the references (Hallquist, 2006, 2009). Later, the FE modeling approaches of composites are described.

4.1. Basic keywords for composite analysis

*CONTROL_ACCURACY

As the solution progresses and the elements rotate and deform, the material coordinate system is automatically updated. The orientation change of the material coordinate system can be very sensitive to in-plane shearing deformation and hourglass deformation of orthotropic elements. In that sense, the node numbering order in elements can affect the material coordinate system as illustrated in Figure 4.1. In order to minimize this sensitivity, the INN option needs to be invoked for composite material models.

- INN: Invariant node numbering for shell and solid elements (1 = off, 2 = on for shell elements only, 3 = on for solid elements only, 4 = on for both shell and solid elements)
-

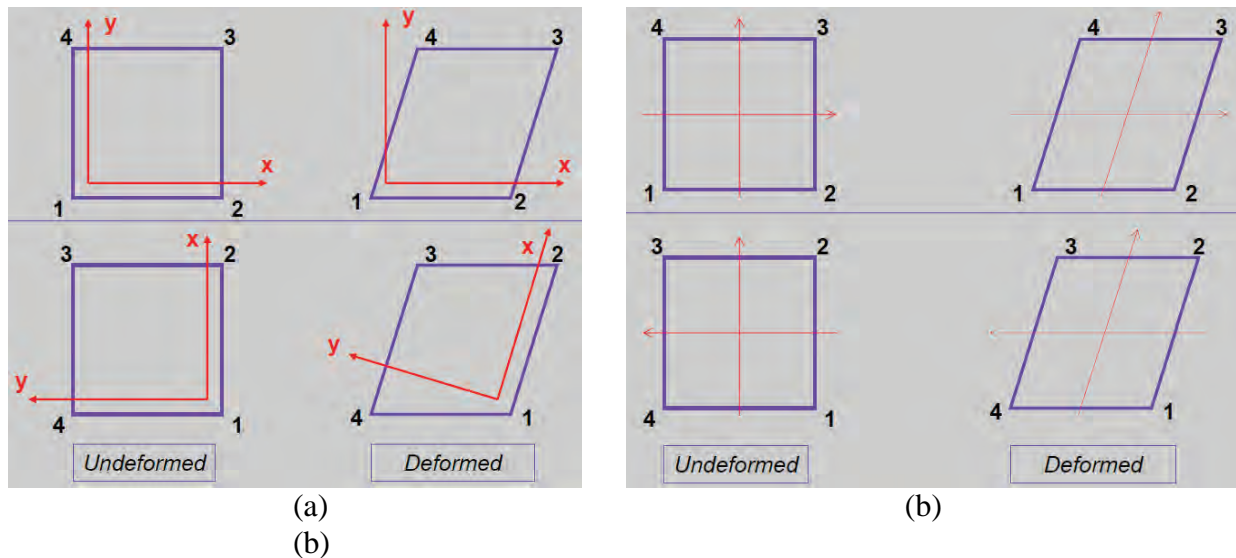


Figure 4.1. Description of invariant node numbering (INN) option in *CONTROL_ACCURACY (Livermore Software Technology Corporation, 2012): (a) without INN, (b) with INN.

*CONTROL_SHELL

The use of the laminated shell theory (LST) is important if a composite shell has layers. In order to invoke LST for material models 22, 54, 55, and 76, the LAMSHT option needs to be set to on.

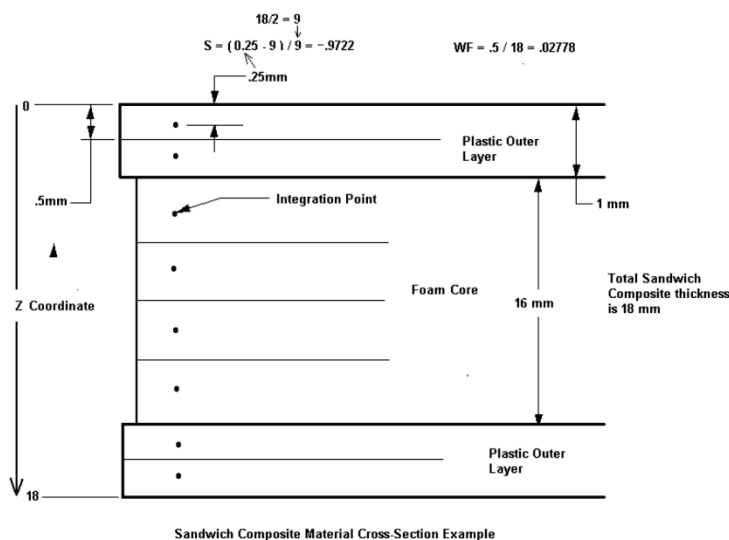
- LAMSHT: Laminated shell theory option (0 = off, 1 = on)

*PART_COMPOSITE

This keyword is to define the user-defined integration points in the through-thickness direction. For composites, this keyword is used to define the composite layers, their thickness and offset angle (BETA). Basically, *PART_COMPOSITE replaces *INTEGRATION_SHELL in version 970. An example of using this keyword is shown in Figure 4.2.

4.2. Composite material models

LS-DYNA provides several composite material models as listed in Table 4.1. Each material model is limited by element type, degradation law, and so on. The degradation law of continuum mechanics can be divided into two categories; progressive failure model (PFM) and continuum damage mechanics (CDM) model. PFM use a ply discount method to degrade elastic properties of the ply from its undamaged state to a fully damaged state. CDM describes the gradual deterioration of the elastic properties of a material.



(a)

```
*PART_COMPOSITE
$ pid, elform
1, 2
$ mid, thick, beta, mid, thick, beta
11, 0.5,,, 11, 0.5
12, 4.0,,, 12, 4.0
12, 4.0,,, 12, 4.0
11, 0.5,,, 11, 0.5
*mat_layered_linear_plasticity
11, 2.7e-6, 73.4, 0.32, 1e9
$ NOTE: foam core could use a different
$ material model (971)
*mat_layered_linear_plasticity
12, 6.3e-7, 0.286, 0.3, 1e9

*ELEMENT_SHELL
1 1 1 2 33
2 1 2 3 34
```

(b)

Figure 4.2. Usage of *PART_COMPOSITE (LSTC, 2012): (a) layer profile, (b) example.

Defining principle material axes

In general, composite materials are anisotropic. So, it is crucial to determine the material directions in the numerical model appropriately. Defining principle material directions is illustrated in Figure 4.3. The **a-b-c** coordinate system is referred to as the material directions. There are five material axes options (AOPT). Two options (AOPT=1.0 and 4.0) are only available for solid elements. After the **a-b-c** system is defined by the AOPT options, it can be offset by an offset angle (BETA) about the **c**-axis. This option is available in material model keywords.

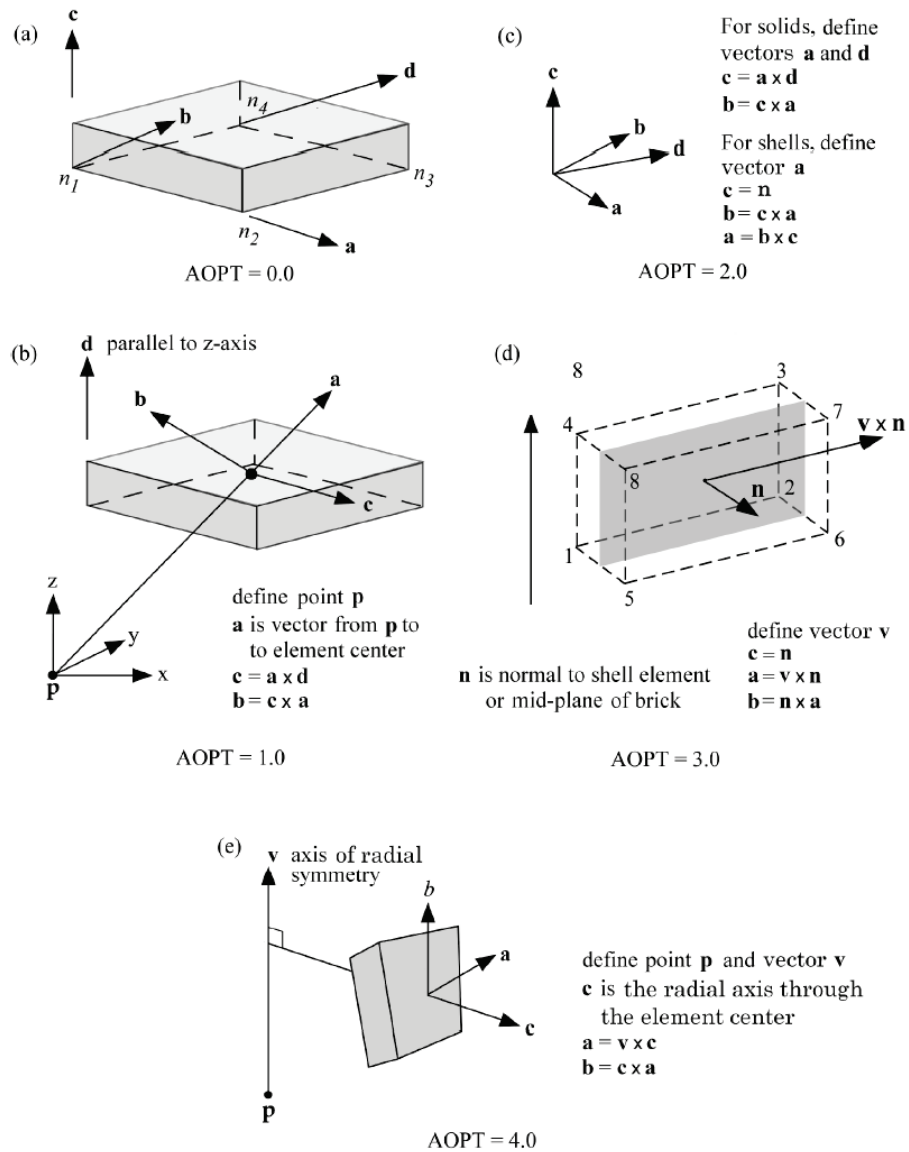


Figure 4.3. Options for defining principle material axes: (a) AOPT=0.0, (b) AOPT=1.0 for solid elements, (c) AOPT=2.0, (d) AOPT=3.0, (e) AOPT=4.0 for solid elements (Hallquist, 2009).

Table 4.1. Composite material models in LS-DYNA

MAT	title	solid	thin shell	thick shell	degradation law
22	*MAT_COMPOSITE_DAMAGE	o	o	o	progressive failure
54/55	*MAT_ENHANCED_COMPOSITE_DAMAGE		o		progressive failure
58	*MAT_LAMINATED_COMPOSITE_FABRIC		o	o	damage mechanics
59	*MAT_COMPOSITE_FAILURE_option_MODEL	o	o		progressive failure
116	*MAT_COMPOSITE_LAYUP		o		no failure
117	*MAT_COMPOSITE_MATRIX		o		no failure
118	*MAT_COMPOSITE_DIRECT		o		no failure
158	*MAT_RATE_SENSITIVE_COMPOSITE_FABRIC		o	o	damage mechanics
161	*MAT_COMPOSITE_MSC	o			damage mechanics
162	*MAT_COMPOSITE_MSC_DMG	o	o		damage mechanics

***MAT_COMPOSITE_DAMAGE (MAT22)**

MAT22 is an orthotropic material with optional brittle failure for composites. Chang-Chang failure criterion, which is described in Chapter 3.4, is implemented for brittle failure. Laminated shell theory can be activated to properly model the transverse shear deformation by turning on LAMSHT in *CONTROL_SHELL. MAT22 can be used with both solid and shell elements. The variables of MAT22 are listed in Table 4.2. Typically, MAT22 is used to model thick composite structures with solid elements (Sevkat, 2008; Zhang, 2008; Chatiri, 2009).

Table 4.2. Variables of MAT22

	1	2	3	4	5	6	7	8
Card1	MID	RO	EA	EB	EC	PRBA	PRCA	PRCB
Card2	GAB	GBC	GCA	KFAIL	AOPT	MACF		
Card3	XP	YP	ZP	A1	A2	A3		
Card4	V1	V2	V3	D1	D2	D3	BETA	
Card5	SC	XT	YT	YC	ALPH	SN	SYZ	SZX

MID: material identification
RO: mass density
EA, EB, EC: E_a , E_b , E_c , Young's modulus in **a**-, **b**-, **c**-direction
PRBA, PRCA, PRCB: ν_{ab} , ν_{ca} , ν_{cb} , Poisson ratios
GAB, GBC, GCA: G_{ab} , G_{dc} , G_{ca} , shear modulus
KFAIL: bulk modulus of failed material (solid elements only)
AOPT: material axes options
MACF: material axes change flag for brick elements
XP, YP, ZP: coordinate of point **p** for AOPT=1
A1, A2, A3: coordinate of point **a** for AOPT=2
V1, V2, V3: coordinate of point **v** for AOPT=3
D1, D2, D3: coordinate of point **d** for AOPT=2
BETA: material angle in degrees for AOPT=3
SC: shear strength
XT: longitudinal tensile strength
YT: transverse tensile strength
YC: transverse compressive strength
ALPH: nonlinear shear stress parameter
SN: normal tensile strength (solid elements only)
SYZ, SZX: transverse shear strength (solid elements only)

***MAT_ENHANCED_COMPOSITE_DAMAGE (MAT54 and MAT55)**

MAT54 and MAT55 are enhanced versions of MAT22. Laminated shell theory can be activated by turning on LAMSHT in *CONTROL_SHELL. MAT54 adopts the Chang-Chang failure criterion, in which the matrix failure criteria are the same as Eqs. (3.77) and (3.79), but the fiber failure criteria are modified as

- Fiber tensile mode:

$$\left(\frac{\sigma_1}{X_t}\right)^2 + \beta \bar{\tau} = 1,$$

- Fiber compressive mode:

$$\left(\frac{\sigma_1}{X_t}\right)^2 = 1.$$

If $\alpha = 1$ and $\beta = 1$, the Chang-Chang failure criterion becomes the Hashin failure criterion, which is described in Chapter 3.4. In MAT55, the tensile and compressive fiber modes are treated as in Chang-Chang failure criterion shown above. The failure criterion for the tensile and compressive matrix modes is given as

$$\frac{\sigma_2^2}{Y_c Y_t} + \left(\frac{\tau_{12}}{S}\right)^2 + \left(\frac{1}{Y_t} - \frac{1}{Y_c}\right)\sigma_2 = 1.$$

which is the Tsai-Wu failure criterion described in Chapter 3.4. Only shell elements can be used with these material models. The variables of MAT54 and MAT55 are listed in Table 4.3. MAT54 was used in the numerical analysis of textile composites in crush tests (Bisagni, 2005; Han, 2007; Zarei, 2008; Huang, 2009; Deleo, 2010; El-Hage, 2010) and local impact tests (Cheng, 2008; Heimbs, 2009; Li, 2009). MAT55 was also used to simulate crush tests of fiber-reinforced composites (Mamalis, 2005).

Elements in MAT54 can fail in several ways: due to time step criterion (TFAIL), due to effective strain (EFS), or all integration points having failed by the way of reaching any of strain values (DFAILM, DFAILS, DFAILT, DFAILC). If DFAIL values are specified, a layer (an integration point) is elasto-plastic after the stress reaches the strength until failure occurs (stress drops to zero) at the DFAIL value of strain. If DFAILT is given, DFAILC should be given. Otherwise DFAILC will be taken as zero and the integration point will be failed immediately if fibers get any non-zero compressive strain. If DFAIL is zero, the behavior is elasto-brittle (stresses drop to zero) in fiber tension whereby integration points fail when the stress reaches the stress-based failure criterion. For other modes, the behavior is elasto-plastic. The crash-front algorithm (SOFT) is invoked only if TFAIL > 0.

Table 4.3. Variables of MAT54 and MAT55

	1	2	3	4	5	6	7	8
Card1	MID	RO	EA	EB		PRBA		
Card2	GAB	GBC	GCA		AOPT			
Card3				A1	A2	A3	MANGLE	
Card4	V1	V2	V3	D1	D2	D3	DFAILM	DFAILS
Card5	TFAIL	ALPH	SOFT	FBRT	YCFAC	DFAILT	DFAILC	EFS
Card6	XC	XT	YC	YT	SC	CRIT	BETA	
MANGLE: material angle in degrees for AOPT=3 DFAILM: maximum strain for matrix straining in tension or compression (only for MAT54) DFAILS: maximum shear strain (only for MAT54) TFAIL: time step size criteria for element deletion SOFT: softening reduction factor for material strength in crash-front elements FBRT: softening for fiber tensile strength YCFAC: reduction factor for compressive fiber strength after matrix compressive failure (only for MAT54) DFAILT, DFAILC: maximum strain for fiber tension, compression (only for MAT54) EFS: effective failure strain (only for MAT54)								

XC: longitudinal compressive strength
CRIT: failure criteria (54=Chang-Chang failure criterion, 55=Tsai-Wu criterion for matrix failure)
BETA: weight factor for shear term in tensile fiber mode (only for MAT54)

***MAT_LAMINATED_COMPOSITE_FABRIC (MAT58)**

MAT58 is a so-called elastic damage model. The main difference of MAT58 to MAT54 lies in the smooth increase of damage. The constitutive matrix is a function of damage parameters (Matzenmiller, Lubliner, & Taylor 1995; Schweizerhof, Weimar, Münz, & Rottner, 1998). The MLT failure criterion described in the chapter 3.4 is used. Only shell elements can be used with MAT58. The variables of MAT58 are listed in Table 4.4. MAT58 was used in the numerical analysis of textile composites in crush tests (Xiao, 2009, Xiao, McGregor, Vaziri, & Poursartip, 2009; Xiao, Botkin, & Johnson, 2009) and local impact tests (Littell, Binienda, Roberts, & Goldberg 2008; Littell, Binienda, Arnold, Roberts, & Goldberg, 2009; Roberts, Goldberg, Binienda, Arnold, Littell, & Kohlman, 2009; Goldberg, Blinzler, & Binienda, 2010).

ERODS, maximum effective strain, controls the failure of an element layer. The layer in the element is completely removed after the maximum effective strain is reached. SLIM**, stress limits, are factors to limit the stress in the softening part to a given value,

$$\sigma = \text{SLIM}^{**} \times \text{strength} .$$

When SLIM** is 1.0, the stress remains at a maximum value identical to the strength (XC,XT, YC,YT,SC), which is similar to ideal elasto-plastic behavior. With small values, it is similar to elasto-brittle behavior. The shear strain values (GAMMA1, GMS) are engineering shear strains, i.e., twice the tensorial shear strain. The crash-front algorithm (SOFT) is invoked only if TSIZE > 0.

Table 4.4. Variables of MAT58

	1	2	3	4	5	6	7	8
Card1	MID	RO	EA	EB		PRBA	TAU1	GAMMA1
Card2	GAB	GBC	GCA	SLIMT1	SLIMC1	SLIMT2	SLIMC2	SLIMS
Card3	AOPT	TSIZE	ERODS	SOFT	FS			
Card4	XP	YP	ZP	A1	A2	A3		
Card5	V1	V2	V3	D1	D2	D3	BETA	
Card6	E11C	E11T	E22C	E22T	GMS			
Card7	XC	XT	YC	YT	SC			

TAU1: τ_1 , stress limit of the first slightly nonlinear part of the shear stress versus shear strain curve
GAMMA1: γ_1 , strain limit of the first slight nonlinear part of the shear stress versus shear strain curve
SLIMT1: factor to determine the minimum stress limit after stress maximum (fiber tension)
SLIMC1: factor to determine the minimum stress limit after stress maximum (fiber compression)
SLIMT2: factor to determine the minimum stress limit after stress maximum (matrix tension)
SLIMC2: factor to determine the minimum stress limit after stress maximum (matrix compression)
SLIMS: factor to determine the minimum stress limit after stress maximum (shear)
TSIZE: time step for automatic element deletion
ERODS: maximum effective strain for element layer failure
FS: failure surface type
BETA: material angle in degrees for AOPT=3

E11C, E11T: strain at longitudinal compressive, tensile strength, **a**-axis
E22C, E22T: strain at transverse compressive, tensile strength, **b**-axis
GMS: strain at shear strength

MAT58 with FS=0 is appropriate for unidirectional layered composites only. Loading surfaces are defined as

$$f_{longitudinal} = \frac{\sigma_1^2}{(1-\varpi_{1c,t})^2 X_{c,t}^2} - r_{c,t}^{longitudinal} = 0$$

$$f_{transverse} = \frac{\sigma_2^2}{(1-\varpi_{2c,t})^2 Y_{c,t}^2} + \frac{\tau^2}{(1-\varpi_{12})^2 S^2} - r_{c,t}^{transverse} = 0$$

where subscripts c and t are compression and tension, ϖ_1 , ϖ_2 , and ϖ_{12} is the damage parameters, and $r^{longitudinal}$ and $r^{transverse}$ are damage thresholds. The damage thresholds take an initial value of 1 when the material is undamaged, and they increase with damage.

MAT58 with FS=1 or FS=-1 is favorable for complete laminates and fabrics, as all directions are treated in a similar fashion. When FS=1, Eq. (4.5) is changed to

$$f_{longitudinal} = \frac{\sigma_1^2}{(1-\varpi_{1c,t})^2 X_{c,t}^2} + \frac{\tau^2}{(1-\varpi_{12})^2 S^2} - r_{c,t}^{longitudinal} = 0.$$

When FS=-1, Eq. (4.5) is same but Eq (4.6) is changed to

$$f_{transverse} = \frac{\sigma_2^2}{(1-\varpi_{2c,t})^2 Y_{c,t}^2} - r_{c,t}^{transverse} = 0$$

and a loading surface in shear mode is added as

$$f_{shear} = \frac{\tau^2}{(1-\varpi_{12})^2 S^2} - r^{shear} = 0.$$

With FS=-1, TAU1 and GAMMA1 are used to describe a nonlinear shear stress-strain curve.

***MAT_COMPOSITE_FAILURE_option_MODEL (MAT59)**

MAT59 can be used with both solid and shell elements. The option in the keyword is the choice of element types; SHELL or SOLID. The failure criterion of MAT59 for shell elements is

$$\frac{4[\sigma_1 - (X_t - X_c)/2]^2}{(X_t + X_c)^2} + \frac{4[\sigma_2 - (Y_t - Y_c)/2]^2}{(Y_t + Y_c)^2} + \left(\frac{\sigma_{12}}{S}\right)^2 + \left(\frac{\sigma_{13}}{S}\right)^2 + \left(\frac{\sigma_{23}}{S}\right)^2 = 1 \quad (4.10)$$

which is similar but not identical with the Tsai-Wu failure criterion. Particularly, it does not contain a coupling term between the orthotropic directions (Schweizerhof, Weimar, Münz, & Rottner, 1998). The failure criterion of MAT59 for solid elements has 8 modes:

- Longitudinal tension mode:

$$\left(\frac{\sigma_1}{X_t}\right)^2 + \left(\frac{\sigma_4}{S_{ba}}\right)^2 + \left(\frac{\sigma_6}{S_{ca}}\right)^2 = 1$$

- Transverse tension mode:

$$\left(\frac{\sigma_2}{Y_t}\right)^2 + \left(\frac{\sigma_4}{S_{ba}}\right)^2 + \left(\frac{\sigma_5}{S_{cb}}\right)^2 = 1$$

- Through-thickness shear mode (longitudinal):

$$\left(\frac{\sigma_1}{X_t}\right)^2 + \left(\frac{\sigma_6}{S_{ca}}\right)^2 = 1$$

- Through-thickness shear mode (transverse):

$$\left(\frac{\sigma_2}{Y_t}\right)^2 + \left(\frac{\sigma_5}{S_{cb}}\right)^2 = 1$$

- Delamination mode (through-thickness tension):

$$\left(\frac{\sigma_3}{Z_t}\right)^2 + \left(\frac{\sigma_5}{S_{cb}}\right)^2 + \left(\frac{\sigma_6}{S_{ca}}\right)^2 = 1$$

- Longitudinal compression mode:

$$\left(\frac{\sigma_1}{X_c}\right)^2 = 1$$

- Transverse compression mode:

$$\left(\frac{\sigma_2}{S_{ba} + S_{cb}}\right)^2 + \left[\left(\frac{Y_c}{S_{ba} + S_{cb}}\right)^2 - 1\right] \frac{\sigma_2}{|Y_c|} + \left(\frac{\sigma_4}{S_{ba}}\right)^2 + \left(\frac{\sigma_5}{S_{cb}}\right)^2 = 1$$

- Through-thickness compression mode:

$$\left(\frac{\sigma_3}{S_{ca} + S_{cb}}\right)^2 + \left[\left(\frac{Z_c}{S_{ca} + S_{cb}}\right)^2 - 1\right] \frac{\sigma_3}{|Z_c|} + \left(\frac{\sigma_6}{S_{ca}}\right)^2 + \left(\frac{\sigma_5}{S_{cb}}\right)^2 = 1.$$

The variables of MAT59 are listed in Table 4.5. MAT59 was used to conduct impact tests of thick composite structures with solid elements (Fawaz, Zheng, & Behdinan, 2004; Menna, Asprone, Caprino, Lopresto, & Prota, 2011) and to simulate a crush test of a braided composite (Zeng, Fang, & Lu, 2005).

The tensile stresses in the softening part are given as

$$\sigma_{1t} = (1-SF) \times X_t$$

$$\sigma_{2t} = (1-SF) \times Y_t.$$

If the softening factor (SF) = 0, this results in a fully elasto-plastic behavior with the initial strength values. When SF = 1, all tensile strengths drop to zero after failure, and then only compressive loads and shear can be carried after the corresponding failure. The reduction factor (SR) reduces the strength values.

Table 4.5. Variables of MAT59

	1	2	3	4	5	6	7	8
Card1	MID	RO	EA	EB	EC	PRBA	PRCA	PRCB
Card2	GAB	GBC	GCA	KF	AOPT	MACF		
Card3	XP	YP	ZP	A1	A2	A3		
Card4	V1	V2	V3	D1	D2	D3	BETA	
for shell option								
Card5	TSIZE	ALP	SOFT	FBRT	SR	SF		
Card6	XC	XT	YC	YT	SC			
for solid option								
Card5	SBA	SCA	SCB	XXC	YYC	ZZC		
Card6	XXT	YYT	ZZT					
ALP: nonlinear shear stress parameter SR: s _r , reduction factor SF: s _f , softening factor SBA: in plane shear strength SCA, SCB: transverse shear strength XXC, XXT: longitudinal compressive, tensile strength a -axis YYC, YYT: transverse compressive, tensile strength b -axis ZZC, ZZT: normal compressive, tensile strength c -axis								

***MAT_COMPOSITE_LAYUP (MAT116)**

This material is for modeling the elastic responses of composite layups. A pre-integration is used to compute the extensional, bending, and coupling stiffness for use with the Belytschko-Tsay resultant shell formulation. It is very efficient for large number of layers. Only shell elements can be used with MAT116. The variables of MAT116 are listed in Table 4.6.

Table 4.6. Variables of MAT116

	1	2	3	4	5	6	7	8
Card1	MID	RO	EA	EB	EC	PRBA	PRCA	PRCB
Card2	GAB	GBC	GCA	AOPT				
Card3	XP	TP	ZP	A1	A2	A3		
Card4	V1	V2	V3	D1	D2	D3	BETA	

***MAT_COMPOSITE_MATRIX (MAT117)**

This material is used for the elastic responses of composites where a pre-integration is used to compute the extensional, bending, and coupling stiffness coefficients for use with the Belytschko-Tsay resultant shell formulation. 21 coefficients of symmetric stiffness matrix, which are in material (global) coordinate system, are input directly. Uniform thickness of a part is required because the shell thickness is inherent in the stiffness matrix. Only shell elements can be used with MAT117. The variables of MAT117 are listed in Table 4.7.

Table 4.7. Variables of MAT117

	1	2	3	4	5	6	7	8
Card1	MID	RO						
Card2	C11	C12	C22	C13	C23	C33	C14	C24
Card3	C34	C44	C15	C25	C35	C45	C55	C16
Card4	C26	C36	C46	C56	C66	AOPT		
Card5	XP	TP	ZP	A1	A2	A3		
Card6	V1	V2	V3	D1	D2	D3	BETA	
CIJ: C _{ij} , coefficients of stiffness matrix								

***MAT_COMPOSITE_DIRECT (MAT118)**

This material is the same as MAT117 except that 21 coefficients of the symmetric stiffness matrix are in the element (local) coordinate system. Thus, MAT118 needs less storage than MAT117. The variables of MAT118 are listed in Table 4.8.

Table 4.8. Variables of MAT118

	1	2	3	4	5	6	7	8
Card1	MID	RO						
Card2	C11	C12	C22	C13	C23	C33	C14	C24
Card3	C34	C44	C15	C25	C35	C45	C55	C16
Card4	C26	C36	C46	C56	C66			
CIJ: C _{ij} , coefficients of stiffness matrix								

*MAT_RATE_SENSITIVE_COMPOSITE_FABRIC (MAT158)

MAT158 is similar to MAT58, but includes strain-rate effects. Rate effects are taken into account through a Maxwell model using linear visco-elasticity by a convolution integral of the form:

$$\sigma_{ij} = \int_0^t g_{ijkl}(t-\tau) \frac{\partial \varepsilon_{kl}}{\partial \tau} d\tau$$

where $g_{ijkl}(t-\tau)$ is the relaxation functions for the different stress measures. This stress is added to the stress tensor determined from the strain energy functional. The relaxation function is represented by six terms from the Prony series:

$$g(t) = \sum_{m=1}^N G_m e^{-\beta_m t}, \quad N \leq 6$$

where G_m is shear relaxation moduli (GI) and β_m is decay constants (BETAI). Only shell elements can be used with MAT158. MAT158 was used in the high speed impact test (Anghileri, Castelletti, Invernizzi, & Mascheroni, 2005; Heimbs, Middendorf, & Maier, 2006; Carney, Goldberg, & Pereira, 2008). The variables of MAT158 are listed in Table 4.9.

Table 4.9. Variables of MAT158

	1	2	3	4	5	6	7	8
Card1	MID	RO	EA	EB		PRBA	TAU1	GAMMA1
Card2	GAB	GBC	GCA	SLIMT1	SLIMC1	SLIMT2	SLIMC2	SLIMS
Card3	AOPT	TSIZE	ERODS	SOFT	FS			
Card4	XP	YP	ZP	A1	A2	A3		
Card5	V1	V2	V3	D1	D2	D3	BETA	
Card6	E11C	E11T	E22C	E22T	GMS			
Card7	XC	XT	YC	YT	SC			
Card8	K							
Optional card for viscoelastic constants (up to 6 cards)								
Card9	GI	BETAI						
K: optional bulk modulus for the viscoelastic material GI: optional shear relaxation modulus for the i th term BETAI: optional shear decay constant for the i th term								

*MAT_COMPOSITE_MSC_option (MAT161 and MAT162)

The material models are developed by Material Sciences Corporation. The option of this keyword is blank (MAT161) and _DMG (MAT162). In MAT161, the progressive layer failure criteria have been established by adopting the methodology developed by Hashin (Hashin, 1980) with a generalization to include the effect of highly constrained pressure on composite failure. MAT162 is a generalization of the layer failure model of MAT161 by adopting the MLT damage mechanics approach for characterizing the softening behavior after damage initiation. These material models are for solid elements. The variables of MAT161 and MAT162 are listed in Table 4.10. MAT161 and MAT162 are used to simulate the local deformation of thick textile

composites in impact tests (Chan, Fawaz, Behdinan, & Amid, 2007; Xiao, Gama, & Gillespie, 2007; Hufenbach, Marques Ibraim, Langkamp, Böhm, & Hornig, 2008; Deka, Bartus, & Vaidya, 2009; Wu, Yan, & Shen, 2010).

Unidirectional lamina model (AMODEL=1)

Three failure criteria are used for fiber failure. They are chosen in terms of quadratic stress forms as follows:

- Tensile/shear fiber mode:

$$\left(\frac{\langle \sigma_a \rangle}{S_{aT}} \right)^2 + \left(\frac{\tau_{ab}^2 + \tau_{ca}^2}{S_{FS}^2} \right) = 1$$

- Compression fiber mode:

$$\left(\frac{\langle \sigma'_a \rangle}{S_{aC}} \right)^2 = 1, \sigma'_a = -\sigma_a + \left\langle -\frac{\sigma_b + \sigma_c}{2} \right\rangle$$

Table 4.10. Variables of MAT161

	1	2	3	4	5	6	7	8
Card1	MID	RO	EA	EB	EC	PRBA	PRCA	PRCB
Card2	GAB	GBC	GCA	AOPT	MACF			
Card3	XP	TP	ZP	A1	A2	A3		
Card4	V1	V2	V3	D1	D2	D3	BETA	
Card5	SAT	SAC	SBT	SBC	SCT	SFC	SFS	SAB
Card6	SBC	SCA	SFFC	AMODEL	PHIC	E_LIMIT	S_DELM	
Card7	OMGMX	ECRSH	EEXPAN	CERATE1	AM1			
for DMG option								
Card8	AM2	AM3	AM4	CERATE2	CERATE3	CERATE4		
SAT, SAC: longitudinal tensile, compressive strengths SBT, SBC: transverse tensile, compressive strengths SCT: through thickness tensile strength SFC: crush strength SFS: fiber mode shear strength SAB, SBC, SCA: matrix mode shear strengths, ab -, bc -, ca - plane SFFC: scale factor for residual compressive strength AMODEL: material models (1=unidirectional layer model, 2= fabric layer model) PHIC: coulomb friction angle for matrix and delamination failure E_LIMIT: element eroding axial strain S_DELM: scale factor for delamination criterion OMGMX: limit damage parameter for elastic modulus reduction ECRSH, EEXPAN: limit compressive, tensile volume strains for element eroding CERATE1: coefficient for strain rate depending strength properties CERATE2: coefficient for strain rate depending axial moduli CERATE3: coefficient for strain rate depending shear moduli CERATE4: coefficient for strain rate depending transverse moduli AM1: coefficient for strain rate softening property for fiber damage in a direction AM2: coefficient for strain rate softening property for fiber damage in b direction AM3: coefficient for strain rate softening property for fiber crush and punch shear damage AM4: coefficient for strain rate softening property for fiber matrix and delamination damage								

- Crush mode:

$$\left(\frac{\langle p \rangle}{S_{FC}} \right)^2 = 1, p = -\frac{\sigma_a + \sigma_b + \sigma_c}{3}$$

where $\langle \rangle$ is the Macaulay brackets, S_{aT} and S_{aC} are the tensile and compressive strengths in the fiber direction, and S_{FS} and S_{FC} are the layer strengths associated with the fiber shear and crush failure, respectively. For compressive fiber failure, the layer is assumed to carry a residual axial load ($S_{FC} \times S_{aC}$), while the transverse load carrying capacity is reduced to zero.

Matrix failure must occur without fiber failure, and then it will be on planes parallel to fibers. Two failure planes are considered. Their failure modes have the forms:

- Perpendicular matrix mode:

$$\left(\frac{\langle \sigma_b \rangle}{S_{bT}} \right)^2 + \left(\frac{\tau_{bc}}{S'_{bc}} \right)^2 + \left(\frac{\tau_{ab}}{S_{ab}} \right)^2 = 1$$

- Parallel matrix mode (Delamination):

$$S^2 \left\{ \left(\frac{\langle \sigma_c \rangle}{S_{cT}} \right)^2 + \left(\frac{\tau_{bc}}{S''_{bc}} \right)^2 + \left(\frac{\tau_{ca}}{S_{ca}} \right)^2 \right\} = 1$$

where S_{bT} is the transverse tensile strength. Based on the Coulomb-Mohr theory, the shear strengths for transverse shear failure and two axial shear failure modes are assumed to be the forms:

$$S_{ab} = S_{ab}^{(0)} + \tan(\varphi) \langle -\sigma_b \rangle$$

$$S'_{bc} = S_{bc}^{(0)} + \tan(\varphi) \langle -\sigma_b \rangle$$

$$S_{ca} = S_{ca}^{(0)} + \tan(\varphi) \langle -\sigma_c \rangle$$

$$S''_{bc} = S_{bc}^{(0)} + \tan(\varphi) \langle -\sigma_c \rangle$$

where φ is a material constant as $\tan(\varphi)$ is similar to the coefficient of friction, $S_{ab}^{(0)}$, $S_{ca}^{(0)}$, and $S_{bc}^{(0)}$ are the shear strength values of the corresponding tensile modes, and S is the scale factor (S_{DELM}) to provide better correlation of delamination area with experiments.

Fabric lamina model (AMODEL=2)

The fiber failure criteria of Hashin for a unidirectional layer are generalized to characterize the fiber damage in terms of strain components for a plain weave layer. So, the fiber failure modes become as

- Tensile/shear fiber mode:

$$\left(\frac{\langle \sigma_a \rangle}{S_{aT}} \right)^2 + \left(\frac{\tau_{ab}^2 + \tau_{ca}^2}{S_{aFS}^2} \right) = 1$$

$$\left(\frac{\langle \sigma_b \rangle}{S_{bT}} \right)^2 + \left(\frac{\tau_{ab}^2 + \tau_{bc}^2}{S_{bFS}^2} \right) = 1$$

- Compression fiber mode:

$$\left(\frac{\langle \sigma'_a \rangle}{S_{aC}} \right)^2 = 1,$$

$$\sigma'_a = -\sigma_a + \langle -\sigma_c \rangle$$

$$\left(\frac{\langle \sigma'_b \rangle}{S_{bC}} \right)^2 = 1,$$

$$\sigma'_a = -\sigma_a + \langle -\sigma_c \rangle$$

where S_{aFS} and S_{bFS} are the layer shear strengths due to fiber shear failure in the fill and warp directions. It is assumed $S_{aFS} = SFS$ and $S_{bFS} = SFS \times S_{bT} / S_{aT}$. Crush mode is the same as Eq. (4.25). For compressive fiber failure, residual axial loads become $SFFC \times S_{aC}$ and $SFFC \times S_{bC}$.

A plain weave layer can fail under in-plane shear stress without occurrence of fiber breakage. This in-plane matrix mode is given by

$$\left(\frac{\tau_{ab}}{S_{ab}} \right)^2 = 1.$$

Another failure mode, which is due to the quadratic integration between the thickness stresses, is expected to be mainly a matrix failure. This through-thickness matrix mode is

$$S^2 \left\{ \left(\frac{\langle \sigma_c \rangle}{S_{cT}} \right)^2 + \left(\frac{\tau_{bc}}{S_{bc}} \right)^2 + \left(\frac{\tau_{ca}}{S_{ca}} \right)^2 \right\} = 1$$

where the shear strengths are assumed to be

$$S_{ca} = S_{ca}^{(0)} + \tan(\varphi) \langle -\sigma_c \rangle,$$

$$S_{bc} = S_{bc}^{(0)} + \tan(\varphi) \langle -\sigma_c \rangle.$$

The effect of strain-rate on the layer strength values of the fiber failure modes is modeled by the strain-rate dependent functions for the strength values $\{S_{RT}\}$ as

$$\{S_{RT}\} = \{S_0\} \left(1 + C_{rate1} \ln \frac{\{\dot{\epsilon}\}}{\dot{\epsilon}_0} \right)$$

where

$$\{S_{RT}\} = \begin{Bmatrix} S_{aT} \\ S_{aC} \\ S_{bT} \\ S_{bC} \\ S_{FC} \\ S_{FS} \end{Bmatrix}, \quad \{\dot{\epsilon}\} = \begin{Bmatrix} |\dot{\epsilon}_a| \\ |\dot{\epsilon}_a| \\ |\dot{\epsilon}_b| \\ |\dot{\epsilon}_b| \\ |\dot{\epsilon}_c| \\ \left(\dot{\epsilon}_{ca}^2 + \dot{\epsilon}_{bc}^2 \right)^{1/2} \end{Bmatrix},$$

and C_{rate} is the strain-rate constant (CRATE1). $\{S_0\}$ are the strength values of $\{S_{RT}\}$ at the reference strain-rate $\dot{\epsilon}_0$.

Damage model

The damage model is a generalization of the layer failure model of MAT161 by adopting the MLT damage mechanics approach for characterizing the softening behavior after damage initiation. The damage parameters are defined as

$$\varpi_i = 1 - e^{\frac{1}{m}(1-r_j^m)}, \quad r_j \geq 1.$$

The effect of strain-rate on the nonlinear stress-strain response of a composite layer is modeled by the strain-rate dependent functions for the elastic moduli $\{E_{RT}\}$ as

$$\{E_{RT}\} = \{E_0\} \left(1 + \{C_{rate}\} \ln \frac{\{\dot{\epsilon}\}}{\dot{\epsilon}_0} \right)$$

where

$$\{E_{RT}\} = \begin{Bmatrix} E_a \\ E_b \\ E_c \\ G_{ab} \\ G_{bc} \\ G_{ca} \end{Bmatrix}, \quad \{\dot{\varepsilon}\} = \begin{Bmatrix} \dot{\varepsilon}_a \\ \dot{\varepsilon}_b \\ \dot{\varepsilon}_c \\ \dot{\varepsilon}_{ab} \\ \dot{\varepsilon}_{bc} \\ \dot{\varepsilon}_{ca} \end{Bmatrix}, \quad \{C_{rate}\} = \begin{Bmatrix} C_{rate2} \\ C_{rate2} \\ C_{rate4} \\ C_{rate3} \\ C_{rate3} \\ C_{rate3} \end{Bmatrix},$$

and $\{C_{rate}\}$ are the strain-rate constants. $\{E_0\}$ are the strength values of $\{E_{RT}\}$ at the reference strain-rate $\dot{\varepsilon}_0$.

A failed element is eroded in any of three different ways: if the tensile strain is greater than E_LIMT, if the compressive relative volume is smaller than ECRSH, or if the tensile relative volume is greater than EEXPV.

4.3. Composite modeling approach

In general, textile composites show a various failure modes depending on textile forms, composite structures, and loading conditions. Common failure modes of textile composites are matrix cracking, fiber breakage, delamination, splaying, fragmentation, progressive folding, and so on. Some of failure modes can be treated by composite material models, but some other fracture modes are required to be treated by composite material models as well as by appropriate FE modeling techniques because those failure modes are induced by the post-failure behavior of composites. Three modeling approach are described below.

Single-layer approach

Single-layer modeling approach is the simplest one. In this approach, the composite FE model has only one layer of laminated elements and laminated elements have effective material properties of a composite. This approach was used to simulate the crush test of textile composites with MAT54 (Deleo, Wade, Feraboli, & Rassaian, 2010; Bisagni, Pietro, Frasnini, & Terletti, 2005). The deficiency of this approach is the inability to simulate delamination and splaying of textile composites and to capture the local damage deformation of composites.

Multilayers approach

Multi-layers modeling approach is developed to simulate the delamination and splaying of textile composites effectively. In this approach, the laminated composite is modeled by multi-layers of elements and the layers are connected by the tie-break contacts to simulate layer delamination. The multi-layer approach was used to simulate crush tests of textile composites with MAT54 (Zarei, Kroger, & Albertsen, 2008; Huang, 2009) and with MAT58 (Xiao, 2009a, 2009b, 2009c). The influence of single- and multi-layers approaches is studied also (Zarei, 2008, Heimbs, 2009).

Unit cell approach

Binienda *et al.* developed unit cell approach to capture the local damage shape of 2D triaxial braided composites during impact. The unit cell is defined as a smallest unit of repeated fiber architecture. This unit cell is divided into several sub-cells, with each sub-cell consisting of fiber tows with varying size, fiber orientation, and ply layup based on the actual geometrical shape and location. Each sub-cell is modeled with layer composites using one shell element with several through the thickness integration points. The unit cell approach was used to capture local damage of braided composite plates in impact tests with MAT54 (Cheng, 2008, Li, 2009) and with MAT58 (Littell, 2008, 2009b, Roberts, 2009, Goldberg, 2010).

5. Development of a Lightweight Vehicle

As part of NHTSA's program to examine the possible safety benefits of lightweight PCIVs, a lightweight vehicle was developed numerically by using plastics and composites. For this purpose, a candidate vehicle and candidate components for weight reduction were selected. In this chapter, the candidate vehicle and components are described.

5.1. 2007 Chevrolet Silverado

A pickup truck was selected as the candidate vehicle for weight reduction. Since the pickup truck is relatively heavy and aggressive compared to cars, it was projected that there would be more opportunities for reducing its vehicle weight. Due to its size, it was felt that equivalent safety could be achieved, and furthermore improved safety could be realized in collisions of the redesigned vehicle with the lighter passenger cars. Additionally, it was felt that weight reduction a vehicle of this type provides the potential in achieving substantial fuel savings in future fleets due to their popularity and accompanying high new vehicle sales. For this study, the Chevrolet Silverado was selected. The Silverado was selected with the knowledge that a FE model of the 2007 Chevrolet Silverado was available in the FE model database of NCAC/GWU (NCAC, 2009a).

A 2007 Chevrolet Silverado is shown in Figure 5.1(a) and an FE model of this vehicle is shown in Figure 5.1(b). The FE vehicle model was created by NCAC/GWU (NCAC, 2009b). The specifications of the FE model of 2007 Chevrolet Silverado are summarized in Table 5.1. The vehicle is a 4 door crew pickup truck with a body-on-frame platform and its weight is 2307 kg. The FE vehicle model consists of about a million elements and 680 parts.

The FE vehicle model was validated with test results from a frontal NCAP test (NCAC, 2009b) and from suspension tests (Mohan, 2009a, 2009b). In the full frontal rigid barrier NCAP test, a vehicle with two dummies in the front seats collides with the rigid barrier in the full overlap configuration at the impact speed of 56 km/h. In the full frontal NCAP simulation, dummies were considered as added masses. The deformations of the Silverado in the frontal NCAP simulation are shown in Figure 5.2. The actual deformation of the Silverado in the NCAP test #5877 (Patel & Richardson, 2006) is shown in Figure 5.3. It can be observed that buckling deformation, caused by bending moments, occurs at the ladder frame, which is indicated by the red oval in Figures 5.2(b) and 5.3(b).



(a)



(b)

Figure 5.1. 2007 Chevrolet Silverado (crew pickup body style): (a) actual vehicle, (b) FE model.

Table 5.1. Specification of the FE model of 2007 Chevrolet Silverado

Vehicle weight	2,307 kg
Vehicle size	5,846 mm (L) \times 2,029 mm (W) \times 1,917 mm (H)
Distance between front and rear axles	3,645 mm
Center of gravity (CG)	1,661 mm, 2 mm, and 732 mm (from front axle, horizontal center, and ground)
Body style	crew pickup (4 doors)
Engine type	4.8L V8 SFI
Number of elements	929,131
Number of nodes	942,677
Number of parts	679

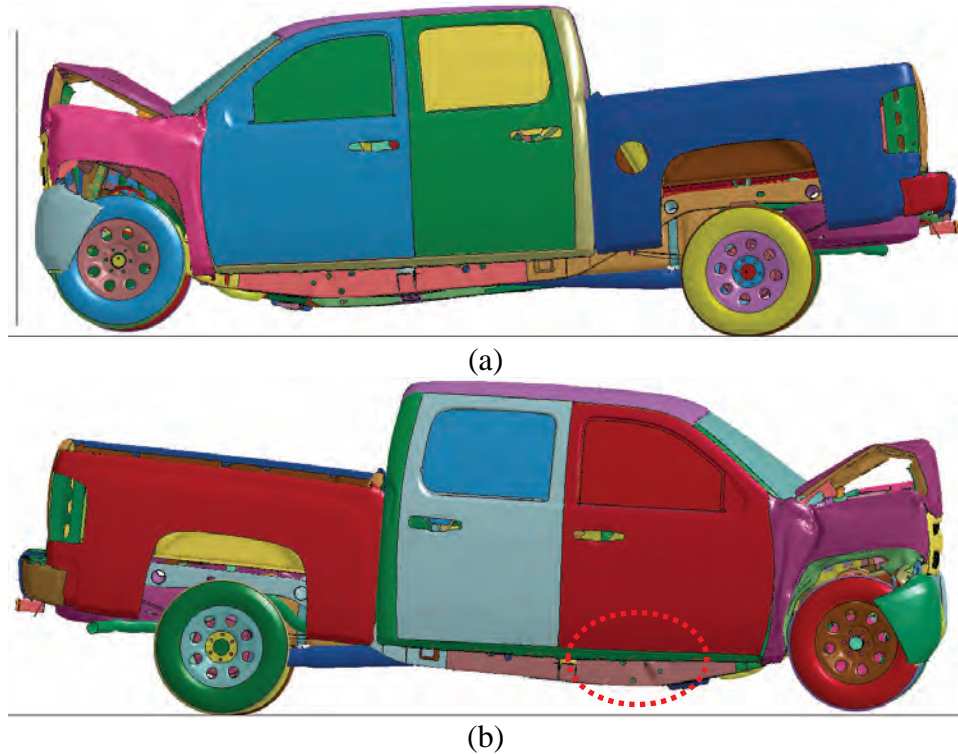


Figure 5.2. Deformation of the original FE model of 2007 Chevrolet Silverado in frontal NCAP test: (a) left side view, (b) right side view.

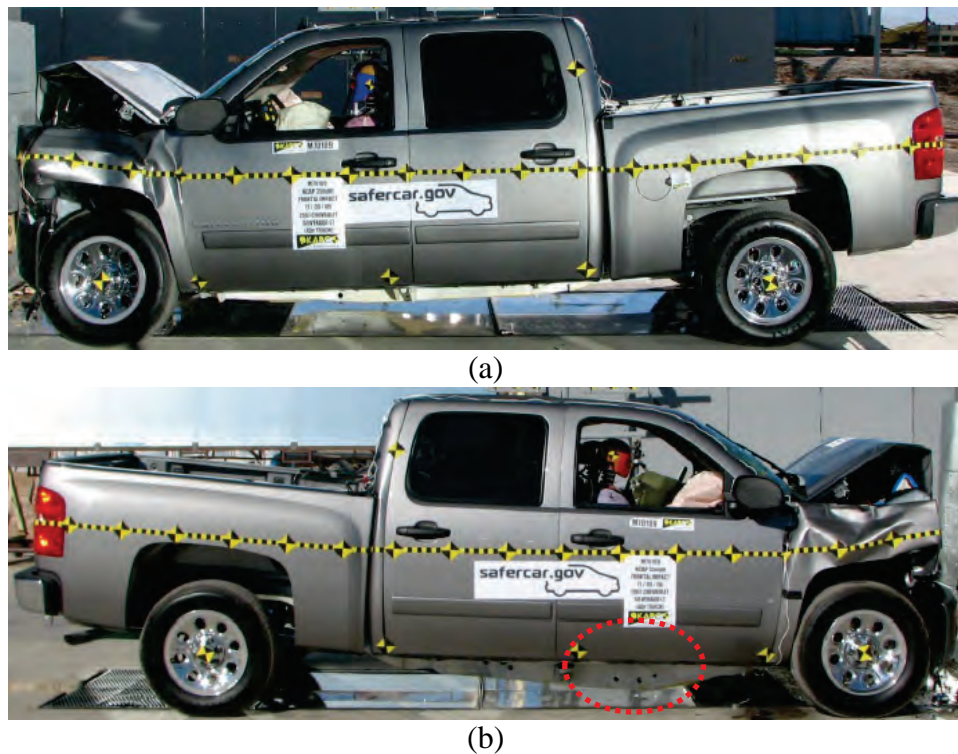


Figure 5.3. Frontal NCAP test (test # 5877) (Patel & Richardson, 2006): (a) left side view, (b) right side view.

The ladder frame has three deformation modes in the NCAP test. Figure 5.4 shows these deformation modes. The deformation modes occur at three locations as indicated by the arrows in Figure 5.4(a). The first deformation of the ladder frame occurs between the front bumper and the front-end module mount points as shown in Figure 5.4(b). The second deformation of the ladder frame occurs between the front-end module mount points and the engine mount points as shown in Figure 5.4(c). The third deformation of the ladder frame occurs behind the transmission crossbeam mount points as shown in Figure 5.4(d). The first and second deformation modes are characterized as being a progressive folding mode and the third deformation mode is characterized as being a bending mode.

The deformations of the FE vehicle in Figure 5.2 are compared with the deformations of Silverado in other NCAP tests as shown in Figures 5.5 and 5.6. It can observe that no bending deformation occurs at the ladder frame in the other NCAP tests shown in Figures 5.5(b) and 5.6(b). Basically, the bending deformation is not the desired deformation mode of the ladder frame for absorbing the impact energy optimally.

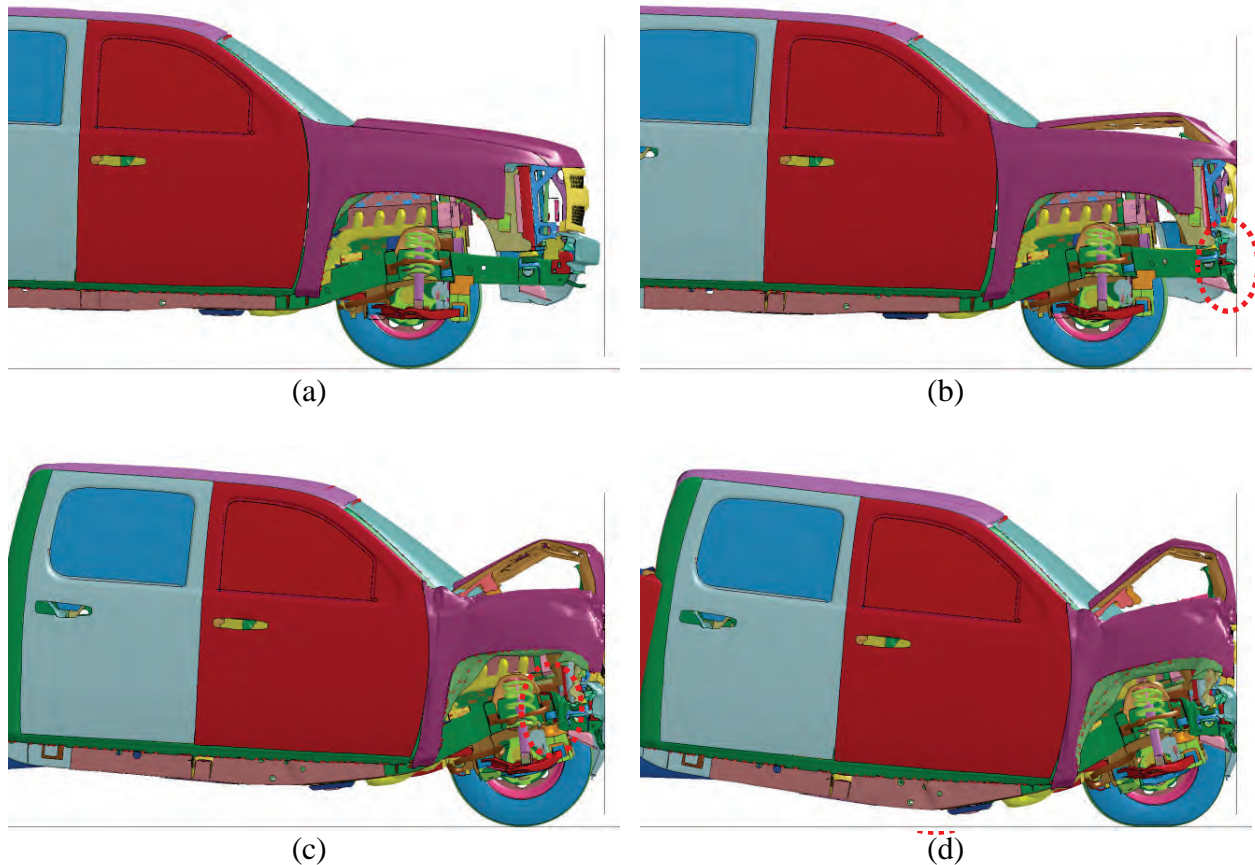


Figure 5.4. Deformation modes of ladder frame of Silverado in frontal NCAP test (wheel hidden): (a) before impact, (b) the first mode, (c) the second mode, (d) the third mode.



(a)



(b)

Figure 5.5. Frontal NCAP test (test # 5907) (Fischer, 2007): (a) left side view, (b) right side view.



(a)



(b)

Figure 5.6. Frontal NCAP test (test # 7121) (Travale & Paolini, 2010): (a) left side view, (b) right side view.

The original ladder frame in the NCAP test simulation is shown in Figure 5.7. It can be seen that the bending deformation occurs at the edge of the plate shown in red color in Figure 5.7(b). Thus the original model in Figure 5.7(a) was modified by adding a small reinforcement as shown in Figure 5.8(a). As a result, the bending deformation was effectively prevented as shown in Figure 5.8(b). Since the modification is minimal and small, there was almost no mass increase. Figure 5.9 shows the deformation of the FE vehicle with the reinforced ladder frame. The bending deformation of the ladder frame does not occur anymore in the frontal NCAP simulation. Actually, the location of the third deformation mode moved to a location behind the engine mount points as shown in Figure 5.10(b).

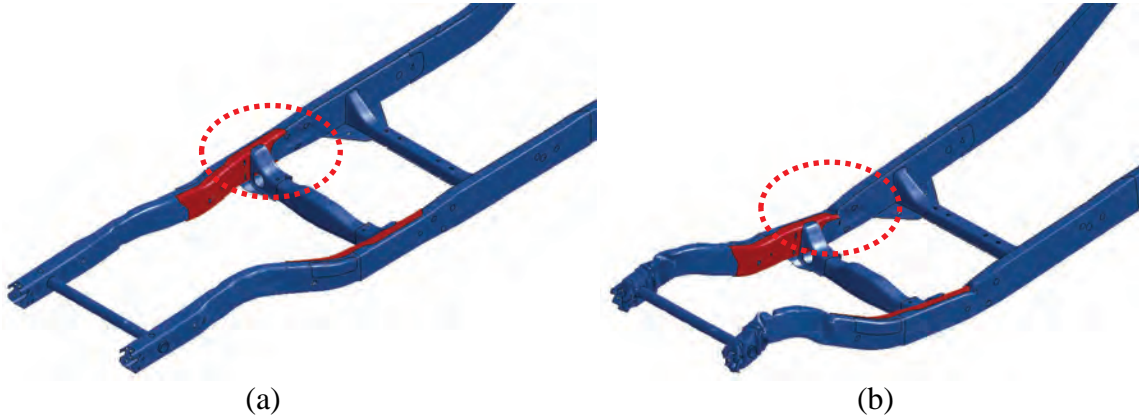


Figure 5.7. Original ladder frame: (a) before test, (b) after test.

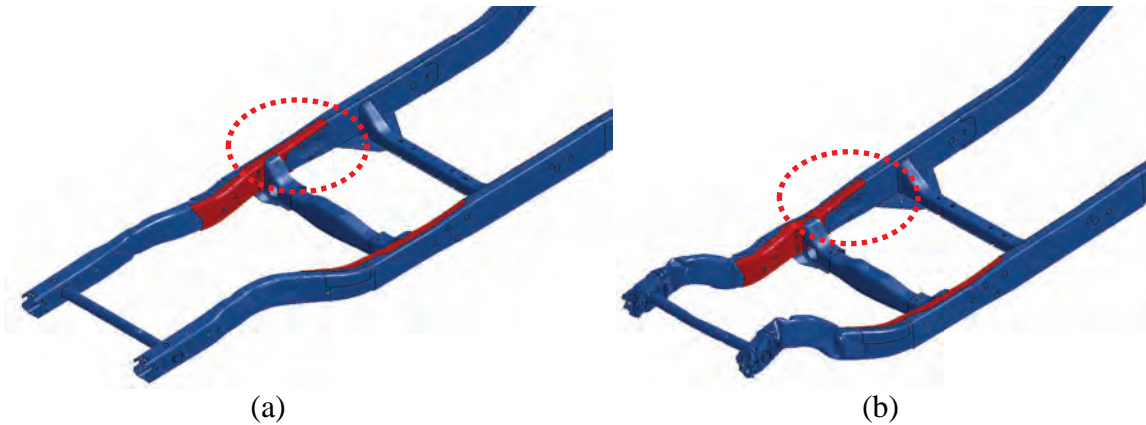


Figure 5.8. Original ladder frame (modified): (a) before test, (b) after test.

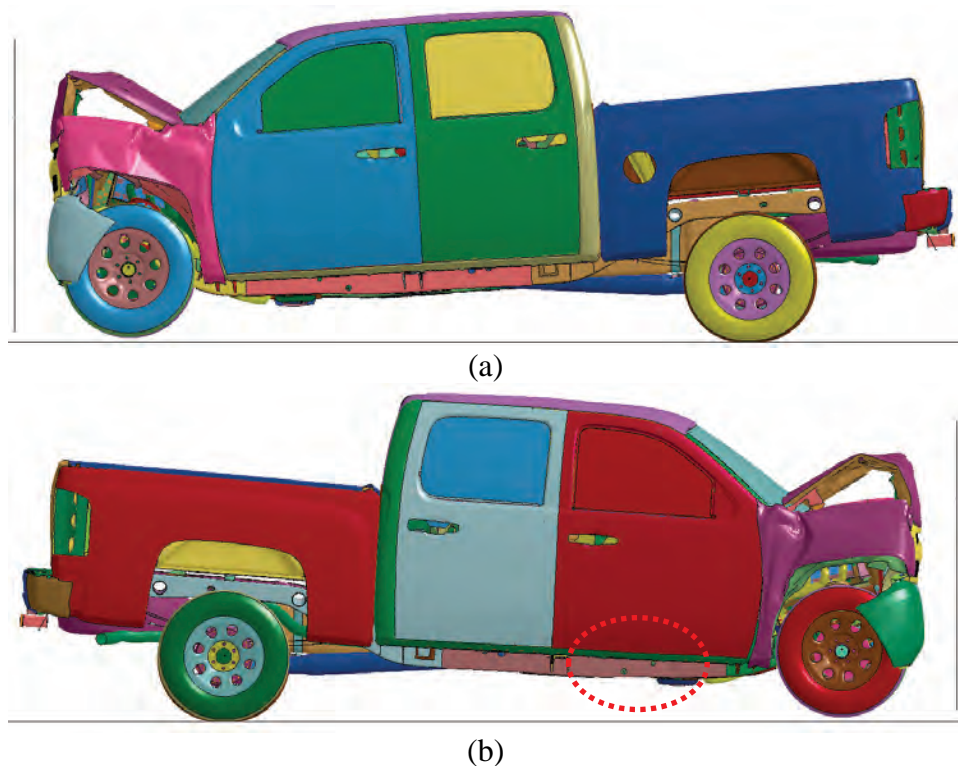


Figure 5.9. Deformation of the original FE model (modified) of 2007 Chevrolet Silverado in frontal NCAP test: (a) left side view, (b) right side view.



Figure 5.10. Deformation of ladder frame (wheel hidden): (a) original, (b) original (modified).

Figure 5.11 shows the absorbed energy distribution of vehicle components in the frontal NCAP test simulation. The term ‘sub-total’ in Figure 5.11 means the summation of six components. Six components account for absorbing 90 percent of the total impact energy. Especially important was the ladder frame which absorbs 70 percent of impact energy. In other words, the ladder frame is the primary structural member of body-on-frame vehicles subjected to a frontal NCAP test. Figure 5.12 shows the vehicle responses in the frontal NCAP simulations and test. The simulation results are comparable with the test results. The responses between the original and

reinforced original vehicles are relatively close as well. Basically, the FE model is a validated representation of the real vehicle.

5.2. Candidate components for weight reduction

The FE vehicle model is divided into seven assemblies as shown in Figure 5.13: closures, occupant compartments structure, interiors, truck bed structure, ladder frame structure, power train related, and suspension related components. Their mass distributions are summarized in Table 5.2. It shows that the weight of the power-train related and suspension related components accounts for almost 50 percent of the vehicle weight. The weight of the ladder frame structure is about 13 percent of the vehicle weight.

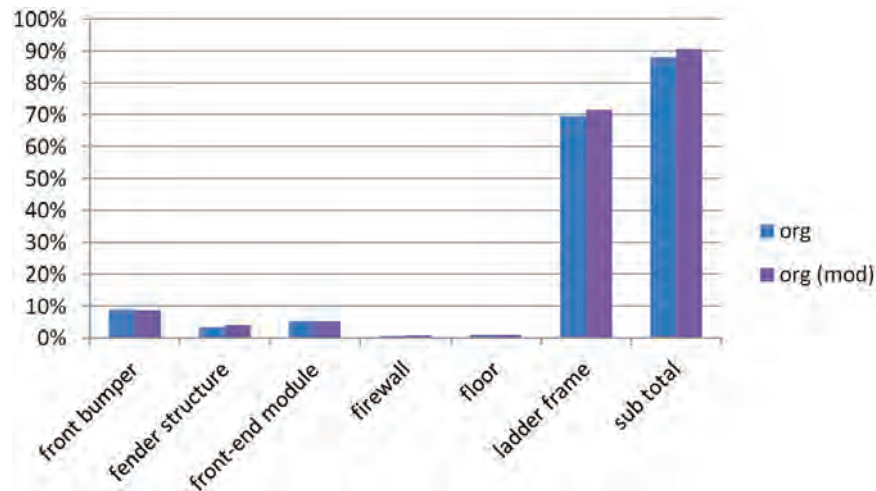


Figure 5.11. Absorbed energy distribution.

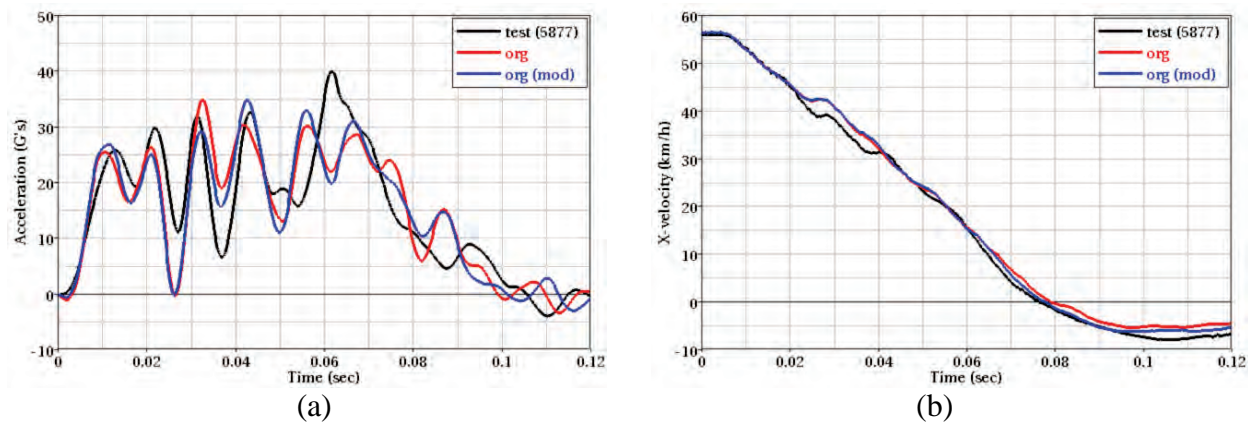


Figure 5.12. Responses (at rear floor) of the vehicle in Frontal NCAP test: (a) acceleration, (b) velocity.

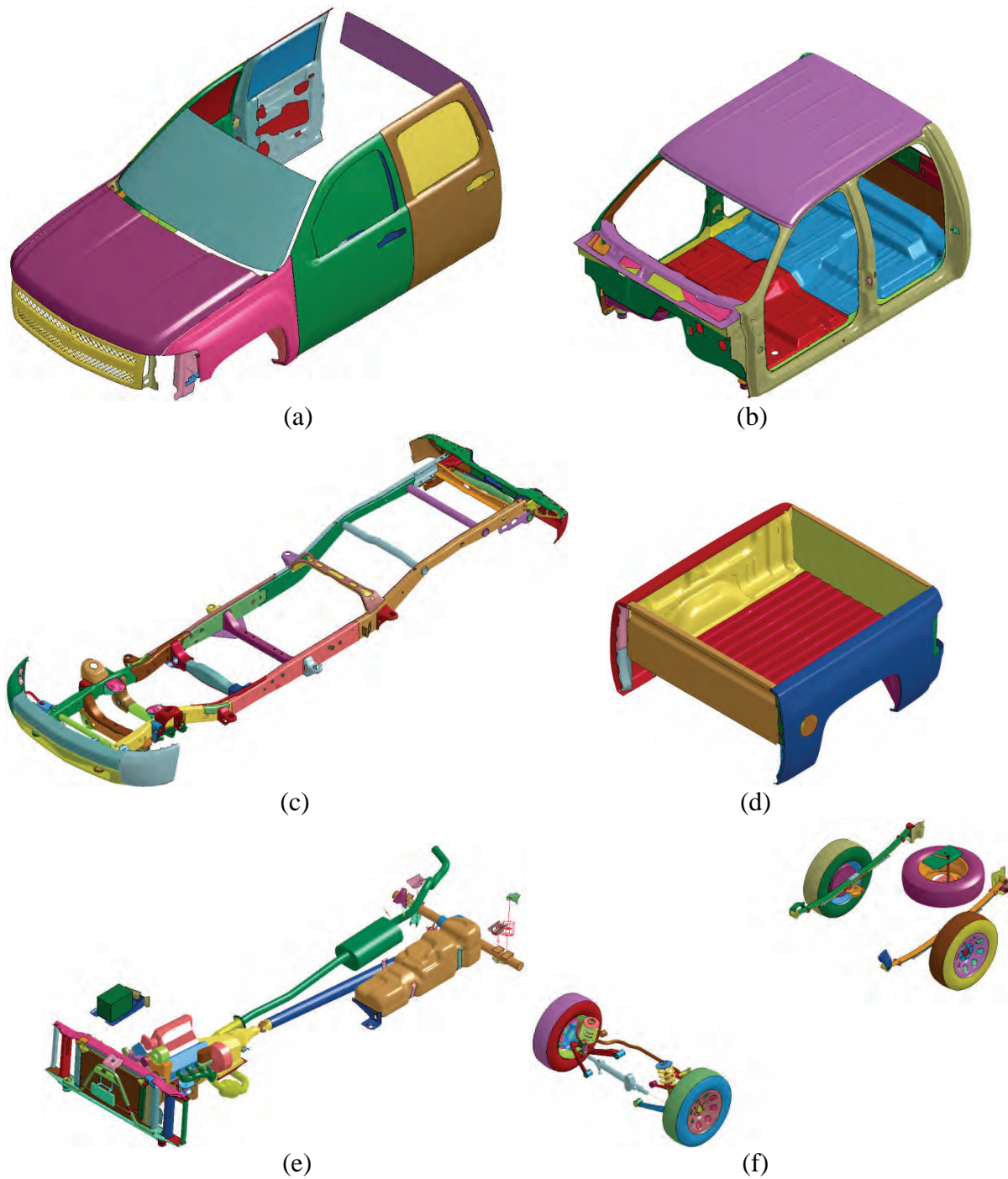


Figure 5.13. Assembly of the FE model of Silverado: (a) closures, (b) occupant compartment structure, (c) ladder frame structure, (d) truck bed structure, (e) power-train related, (f) suspension related.

Table 5.2. Mass distribution of the FE model of Silverado

Assembly	Mass (kg) [%]	Items
Closures	240 [10.4]	doors, glasses, hood, front grille, front fenders
Occupant compartment structure	290 [12.6]	roof, floor, firewall, toepan, pillars, cowl
Ladder frame structure	290 [12.6]	ladder frame, front and rear bumpers, tow packages
Truck bed structure	160 [6.9]	bed, tailgate, rear fenders
Power-train related	680 [29.4]	engine, transmission, battery, fuel tank, driveshaft, rear axle, exhaust pipe, front-end module
Suspension related	447 [19.4]	front and rear suspensions, wheels, tires, spare tire and carrier, steering
Interiors	200 [8.7]	seats, dash, trim
Total	2,307	

The Silverado pickup truck was used to develop a lightweight vehicle numerically. In order to reduce the vehicle weight, three methods were considered. The first method was to substitute lighter weight materials, especially plastics and composites, for the steel material in the current vehicle. The second method was to change the current components to lighter weight ones. The last was to remove any component which was not related to the vehicle's operation.

Material substitution

In order to reduce the vehicle weight, the steel material in the vehicle structure was replaced with other lighter weight materials. In particular, plastics and composites were used as a substitute for the steel material since these materials were primarily the main focus in this study. Plastics and composites have quite different material characteristics than steel. Steel material is isotropic and ductile, while plastics and composites are anisotropic and brittle mostly. So, the ACC PD and some of its member chemical companies (SABIC, BASF, and Bayer) voluntarily participated in this project to provide information about available components for plastics and composites. In addition, other resources, such as journals, magazines, internet websites, etc., were used to gather information about the applications of lightweight materials.

When the steel material in the Silverado was replaced by plastics or composites, the components were re-designed by ACC PD's chemical companies if a design change was deemed necessary. Note that, in this study, only the frontal NCAP test of the light-weighted vehicle was considered for investigating the effect of weight reduction on the vehicle's crashworthiness. So, if any component was not engaged in the frontal NCAP test, the material substitution was realized by adjusting the weight of the particular component numerically without changing the component design.

When it was determined that there were no plastics or composites available for a given component but other lightweight materials were available, the original material was replaced with the other lighter weight materials without undertaking a design change. For example, the steel material of the wheels and rear differential carrier were changed to aluminum and magnesium alloys, respectively.

Component change

In the vehicle, there are many finished components, such as the engine, transmission, battery, and so on. It was decided that those existing components could be changed to lightweight ones to reduce the vehicle weight if it was determined that the new components could provide equivalent performance. Since the current vehicle weight was to be reduced, a smaller engine and transmission also could be adopted. Additionally, a lighter weight battery could be adopted.

Component removal

It was decided that any component which is not directly related to the vehicle operation could be removed to reduce the vehicle weight. Thus, for example, the spare tire and its carrier in the current vehicle could be removed.

Based on the above lightweight strategies with the information from ACC PD's chemical companies and references, candidate components for weight reduction of the current FE model of the Silverado were selected and are summarized in Table 5.3.

Table 5.3. Candidate components for weight reduction

Assembly	Items	
Occupant compartment structure	• Roof	• A- & B-pillars
Interiors	• Seats	• IP carrier
Closures	• Front fenders • Rear windows	• Door beam • Door modules
Truck bed structure	• Bed • Tailgate	• Rear fenders
Power-train related	• Engine & transmission • Oil pans • Drive shaft	• Rear differential carrier • Front-end module • Battery
Suspension related	• Wheels • Front brake disks • Tires	• Spare tire & carrier • Leaf spring • Steering stabilizer links
Ladder frame structure	• Front bumper • Rear bumper	• Transmission crossbeam • Ladder frame

The ladder frame was selected as a candidate component for weight reduction in this study. The ladder frame is a large steel structural member and also is the primary energy absorber in frontal NCAP test. The weight of the ladder frame accounts for about 10 percent of the vehicle weight. Composite materials, especially carbon FRP, are well known as high SEA materials. SEA is defined as the energy absorption per unit mass of structural member. In other words, if the steel ladder frame could be changed to a composite ladder frame without compromising its stiffness and crashworthiness, some of the vehicle weight could be reduced efficiently. For this purpose, physical material tests were conducted to identify the material properties of a composite material.

The material substitution procedures and mass savings of the components are described in Chapters 6 and 7. The results of the frontal NCAP simulation of a lightweight vehicle are shown in Chapter 8.

6. Composite Ladder Frame

The ladder frame of the Silverado pickup truck is a large steel structure and also is the primary energy absorber in the frontal NCAP test. The weight of the ladder frame accounts for about 10 percent of the vehicle weight. In this study, the original steel ladder frame is changed to a composite ladder frame to reduce the vehicle weight. Furthermore, by adopting the composite material as a replacement for the main structural member in the vehicle structure, the impact performance of structural composite in the vehicle structure can be investigated, and its applicability and feasibility can be evaluated.

The overall consensus from technical experts in the aerospace and automotive community was to use a braided carbon-thermoset composite since both mechanical and impact properties were important in the potential application of the ladder frame.

Triaxial braided composites can offer an isotropic design by using axial and angled fiber bundles in a single plan. Braided composites also offer better damage resistance, torsional stability, and bending strength compared to unidirectional or weaved composites. Triaxial braided composites have been used in the commercial aerospace and automotive industry for over 20 years. It is well-suited for components that are of simple geometry and need to provide off-axis as well as unidirectional strength. In addition, various studies using braided composites have been conducted and published. Naik calculated the mechanical properties of woven and braided composites by analytical methods (Naik, 1995). In order to analyze the damage and fracture mechanism of braided composites, tension tests (Ivanov, 2009, Littell, 2009a), bending tests (Quek, 2006, Fujihara, 2007, Dauda, 2009), and compressive crushing tests (Chiu, 1997, 1998, Hamada, 2001, Inai, 2003, Okano, 2005, Gui, 2009) have been conducted. Also, to develop modeling techniques of braided composites, many numerical studies have been performed by simulating material tests (Littell, 2008, Li, 2011), bending tests (Huang, 2002, Janapala, 2008), crushing tests (Zeng, 2005, Han, 2007, Xiao, 2009a, 2009b, 2009c, McGregor, 2010), and impact tests (Littell, 2009b, Roberts, 2009, Goldberg, 2010).

Therefore, a braided carbon-fiber thermoset composite was selected as the substitute for steel in the ladder frame. In order to identify the mechanical properties of the braided composite, material tests and numerical simulations were conducted. The results from these tests and numerical studies have been used to develop the material characteristics for the composite ladder frame.

6.1. Physical material test

Physical material tests were conducted by the UDRI. The test report is found in Appendix A. A brief summary of this report is found below.

Test material

A braided carbon-thermoset composite was selected for the material tests. The carbon fiber was Torayca T700S C 12000, manufactured by Toray Carbon Fibers America, Inc. The braid architecture is $0^\circ/\pm 60^\circ$ 2D triaxial (2D3A), shown in Figure 6.1. The axial fiber tows contained

24K fibers. The bias tows contained 12K fibers. The resin was Epon 862 epoxy with an Epikure W curing agent, both manufactured by Momentive. The mechanical properties of carbon fiber and resin are summarized in Table 6.1 (Morgan, 2005, Tack, 2006). The unit cell size of the specimen of braided composite used in the physical material tests is about $17.9 \text{ mm} \times 5.2 \text{ mm}$.

Table 6.1. Mechanical properties of carbon fiber and resin

	Density (g/cm ³)	Young's Modulus (GPa)		Shear Modulus (GPa)	Poisson's Ratio
		Axial	Transverse		
Torayca T700S carbon fiber	1.8	230	28	27	0.28
Epon 862 epoxy resin	1.2	2.6		1.0*	0.35

* calculated by Eq. (3.17)

The cross-sections of panel and tube are shown in Figure 6.2 and 6.3. All test materials have three layers of braided composite and the average unit cell size is $17.9 \text{ mm} \pm 0.53 \text{ mm} \times 5.2 \text{ mm} \pm 0.22 \text{ mm}$. For the panel, the average thickness is 1.7 mm and the average fiber content in volume is 57 percent. For the tube, the average thickness is 1.9 mm and the average fiber content in volume is 44 percent.

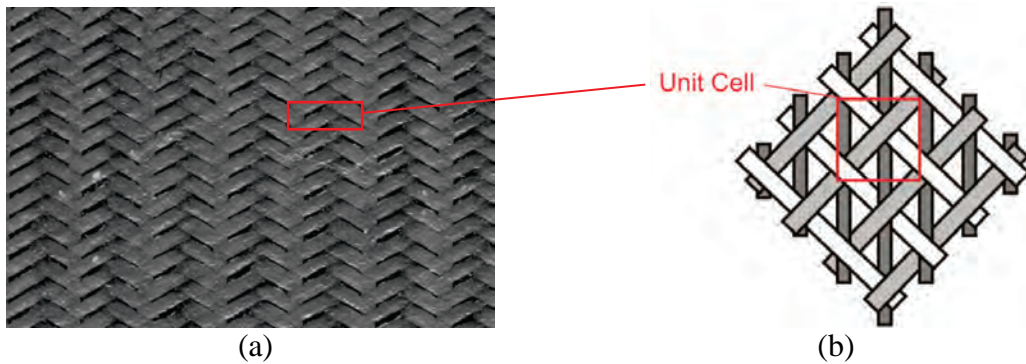


Figure 6.1. 2D3A braided composite: (a) panel, (b) unit cell.

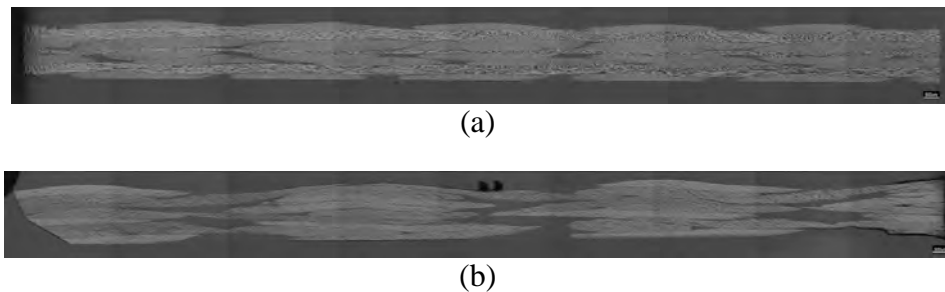


Figure 6.2. Cross-section of panel: (a) axial, (b) transverse.

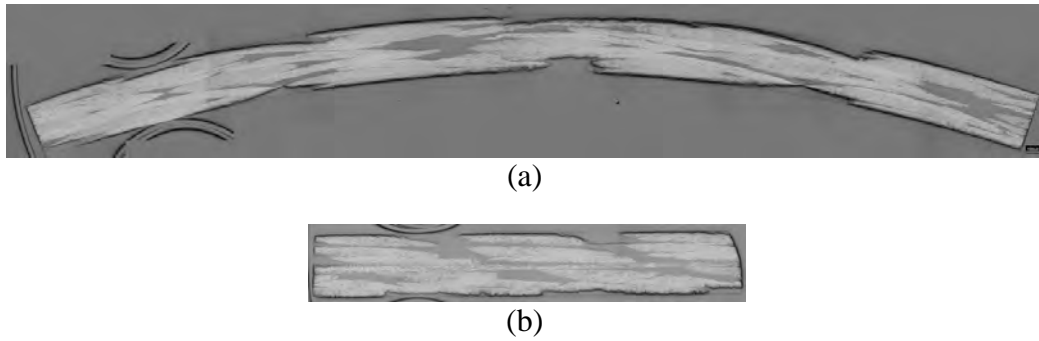


Figure 6.3. Cross-section of tube: (a) axial, transverse.

Test matrix

Tension, compression and shear coupon tests were performed with two different directions (axial and transverse) and four different rates. The tension test used two different types of specimen; standard specimen and bowtie specimen. The total number of tests was 72 and these tests are summarized in Table 6.2. Tube compression tests were performed with three different rates. The total number of tests was 17 and these tests are summarized in Table 6.3.

Table 6.2. Coupon test matrix

		Machine Rate [m/min]			
		0.00127	0.5	4.5-5.0	38-49
Tension (ASTM D3039)	Axial	3	-	-	-
	Transverse	3	-	-	-
Tension (Bowtie)	Axial	3	3	3	3
	Transverse	3	3	3	3
Compression	Axial	3	3	3	-
	Transverse	3	3	3	-
Shear	Axial	3	3	3	3
	Transverse	3	3	3	3
Total		24	18	18	12
Grand total		72			

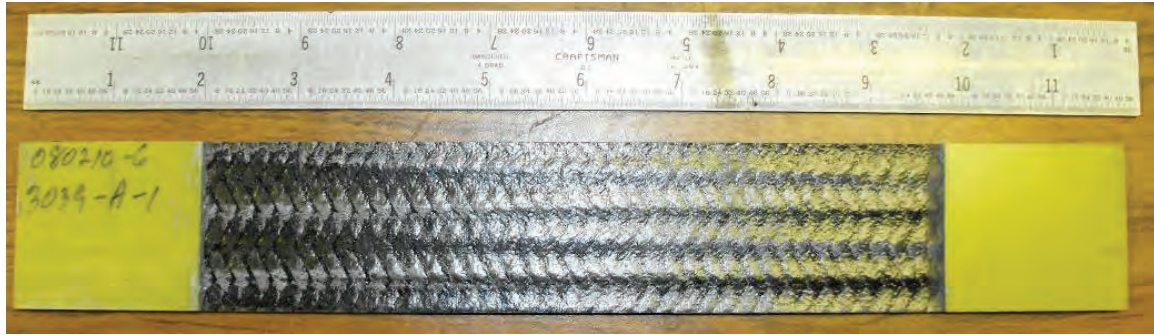
Table 6.3. Tube compression test matrix

	Machine Rate [m/min]		
	1.5	140	440
Straight End	1	-	-
Single bevel	3	7	6
Total	4	7	6
Grand total	17		

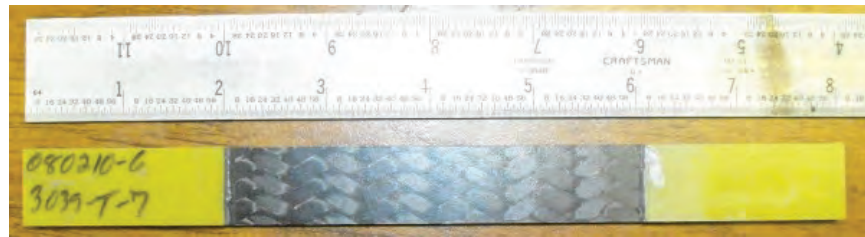
Configuration of specimen

Figure 6.4 shows the modified specimens used for the ASTM D3039 tension test. The specimen width is at least 2.5 times the unit cell to ensure that at least two full unit cells are located in the

gage section. The modified size of axial specimen is 286 mm \times 44.2 mm with 185 mm between the tabs. The transverse specimen is 203 mm \times 19 mm with 102 mm between the tabs. Figure 6.5 shows the bowtie specimens for tension and shear tests and Table 6.4 and 6.5 list the dimensions of specimens. In the tension test shown in Figure 6.5(a), the grips are extended down past the end of tab to ensure full engagement of the bias tows.



(a)



(b)

Figure 6.4. Specimens of ASTM D3039 tension test: (a) axial, (b) transverse.

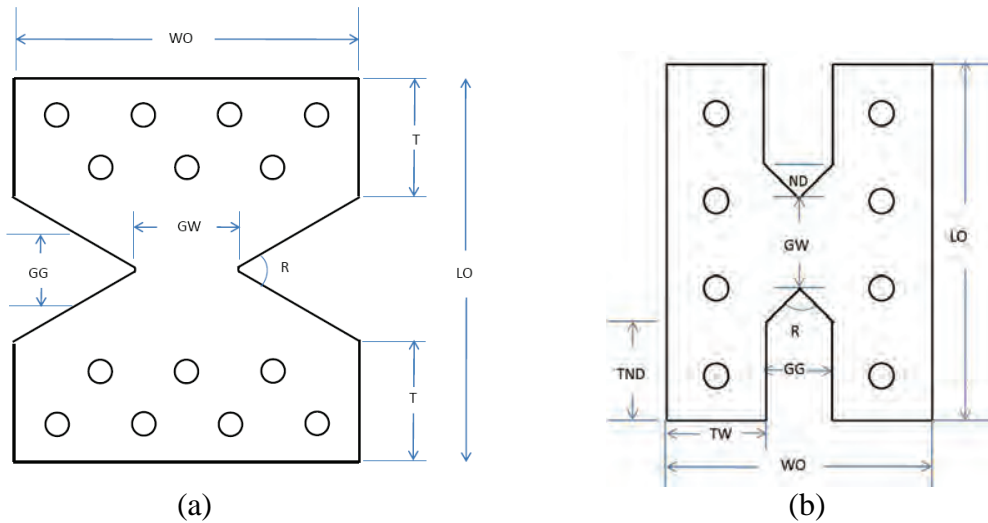


Figure 6.5. Bowtie specimens: (a) tension, (b) shear.

Table 6.4. Bowtie tension nominal specimen dimensions

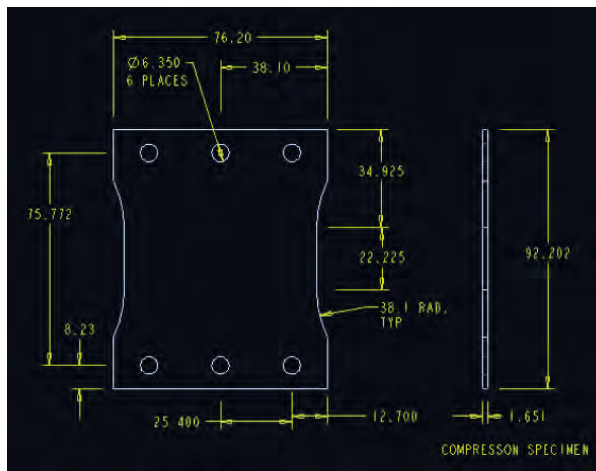
Specimen Orientation	LO Length overall [mm]	WO Width Overall [mm]	GW Gage Width [mm]	GG Grip-to-grip Distance [mm]	R Notch Radius [degrees]	T Tab length [mm]
0°/+60°/-60° Axial	162.8	147.8	45.7	29.6	60	50.8
0°/+60°/-60° Transverse	172.7	58.42	17.8	46.8	120	50.8

Table 6.5. Shear nominal specimen dimensions

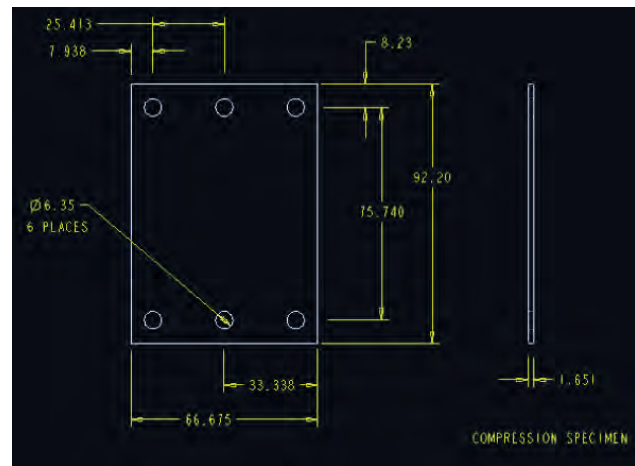
Specimen Orientation	LO Length overall [mm]	WO Width Overall [mm]	GW Gage Width [mm]	GG Grip-to-grip Distance [mm]	R Notch Radius [degrees]	TND Tab Notch Depth [mm]	TW Tab Width [mm]	ND Notch Depth [mm]
0°/+60°/-60° Axial	162.8	137.2	47.9	35.8	90	50.8	50.8	17.9
0°/+60°/-60° Transverse	104	86.4	12.7	10.2	90	39.9	50.8	5.1

Figure 6.6 shows the specimens used for the compression test. The initial configuration was a tapered dog bone style geometry shown in Figure 6.6(a) but cracking was initiated at the radius/tab transition of the dog bone. So, the specimen was modified to a straight-sided rectangle as shown in Figure 6.6(b). As shown in Figure 6.6(c), anti-bucking support was provided with a backing plate that covers the entire back surface of specimen. The front plate covered most of the surface and included a window for strain measurement.

The tube specimen is 254 mm long and has a nominal inner diameter of 102 mm. The length to diameter ratio is 2.5. Since the flat end tube exceeds the actuator capacity, a single 45° bevel is machined into one end of tubes to act as a crack initiator.



(a)



(b)

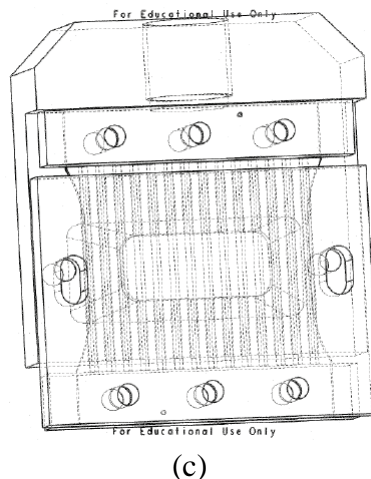


Figure 6.6. Specimens of compression test: (a) dog bone (axial), (b) straight-side (both directions), (c) fixture.

Coupon test result

Table 6.6 summarizes the results of coupon tests. Figure 6.7 through Figure 6.13 show their stress-strain curves. In the axial tension tests, the bowtie tests shows higher elastic modulus and failure strain than the ASTM D3039 tests, but the failure stress of both tests is similar. In the transverse tension tests, the bowtie tests shows higher elastic modulus, failure strain, and failure stress than the ASTM D3039 tests.

The carbon fiber is relatively rate independent (Zhou, 2001, Das, 2007) and the epoxy resin is rate sensitive (Gilat, 2005). The test results do not show consistent rate dependency of the carbon-thermoset braided composite material.

Table 6.6. Data summary for coupon tests

test	direction	rate (m/min)	engineering breaking stress [MPa]	normalized peak stress to 56 vol % fiber [MPa]	engineering breaking strain [%]	elastic modulus [GPa]	Poisson's ratio
ASTM D3039 tension	axial	0.00127	857		1.95	43.3	0.31
	transverse		337		1.44	34.7	0.32
bowtie tension	axial	0.00127	798	775	1.31	67.0	0.25
		0.5	865	815	1.44	66.4	0.36
		5	803	782	1.27	80.6	0.38
		50	783	744	1.33	85.4	0.40
		avg.	812	779	1.34	74.9	
	transverse	0.00127	965	942	2.07	66.4	0.01 - 0.36
		0.5	1017	992	1.72	116.0	0.25 - 0.60
		5	1046	1026	2.02	81.9	0.03 - 0.47
		50	918	950	2.34	57.9	0.03 - 0.06
		avg.	987	978	2.04	80.6	
compression	axial	0.00127	283	282	0.64	51.7	
		0.05	252	237	0.73	34.5	
		0.5	284	271	0.71	40.7	

		5	280	269	0.76	37.7	
		avg.	275	265	0.71	41.2	
	transverse	0.00127	226	221			
		0.05	265	249	0.72	39.3	
		0.5	288	271	0.75	40.1	
		5	305	288	0.74	45.0	
		avg.	271	257	0.74	41.5	
	axial	0.00127	180	177	0.75	32.9	
		0.5	190	188	0.83	28.5	
		5	177	174	0.72	25.5	
		50	201	199	0.84	26.0	
shear	axial	avg.	187	185	0.79	28.2	
		0.00127	200	195	0.75	29.2	
		0.5	218	212	0.86	28.5	
		5	239	233	0.86	32.9	
	transverse	50	226	216	0.86	33.4	
		avg.	221	214	0.83	31.0	

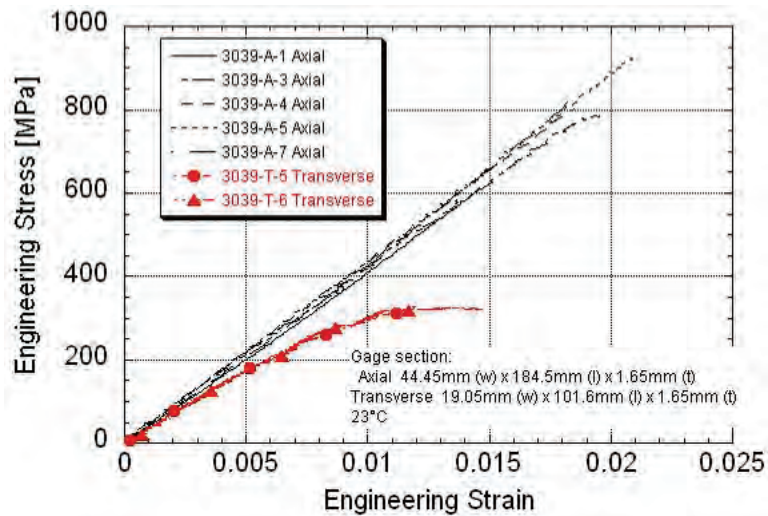


Figure 6.7. Stress-strain curves for modified ASTM D3039 tension tests.

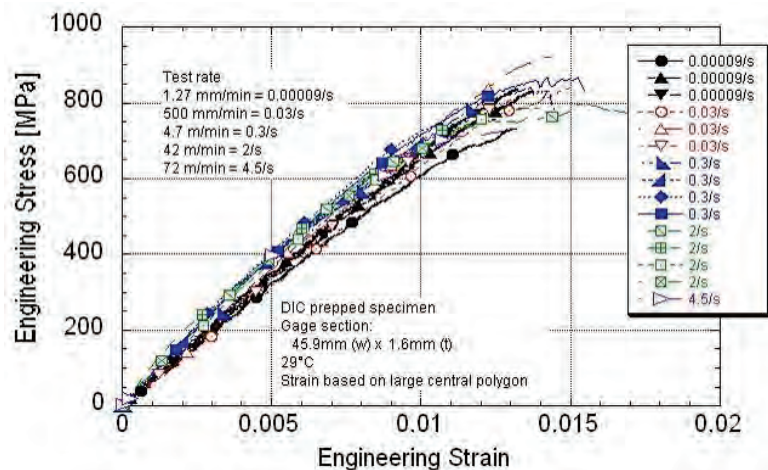


Figure 6.8. Stress-strain curves for bowtie tension tests (axial).

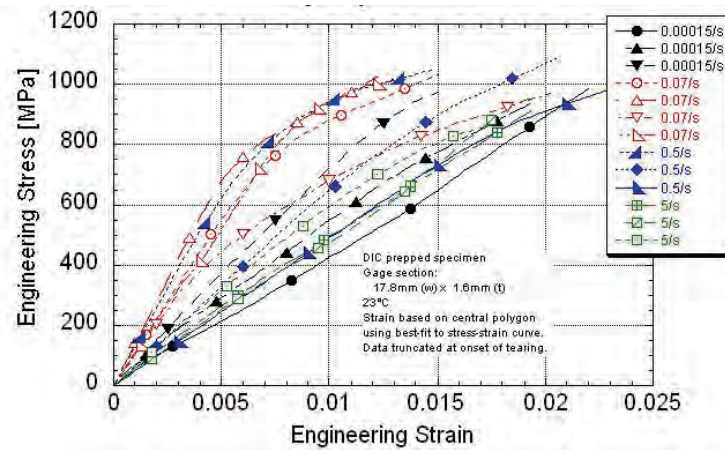


Figure 6.9. Stress-strain curves for bowtie tension tests (transverse).

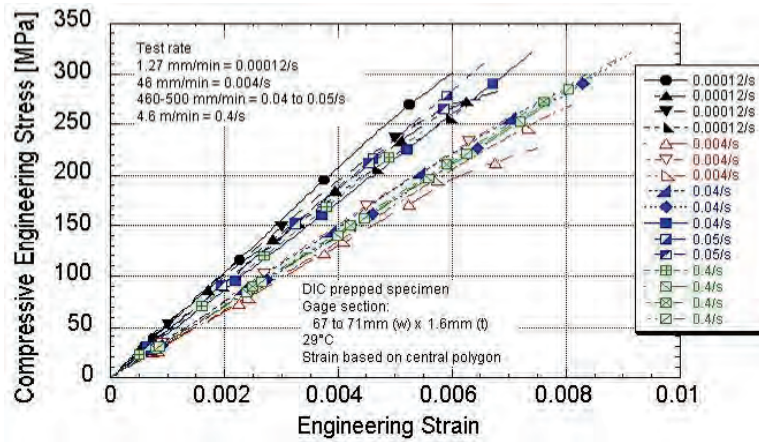


Figure 6.10. Stress-strain curves for compression tests (axial).

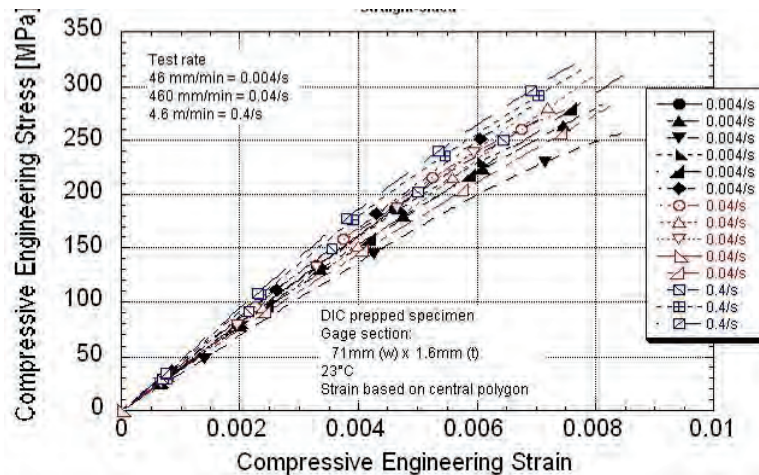


Figure 6.11. Stress-strain curves for compression tests (transverse).

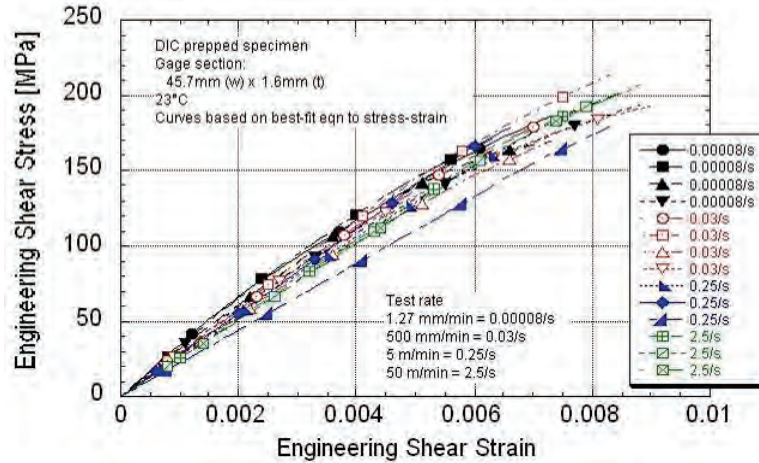


Figure 6.12. Stress-strain curves for shear tests (axial).

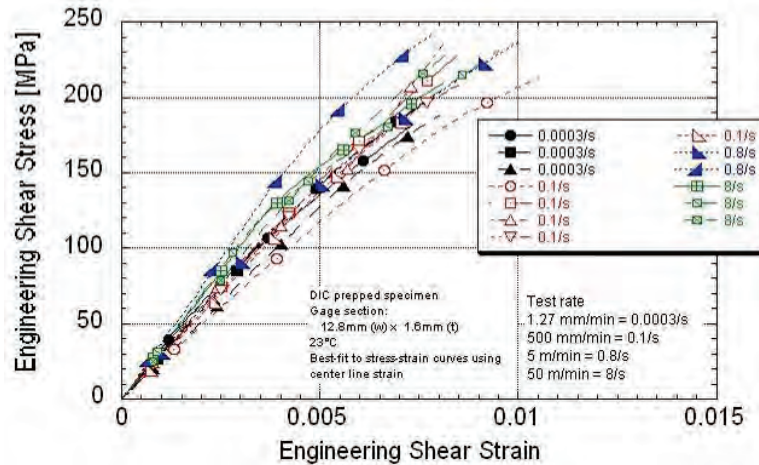


Figure 6.13. Stress-strain curves for shear tests (transverse).

Tube compression test result

Table 6.7 summarizes the tube compression test result and Figure 6.14 shows the load-displacement curves. Figure 6.15 shows the failure of tubes. There are two different tube failure modes: folding failure mode in low rate and fracture failure mode in high rate. However, the load-displacement curves are similar regardless of the tube failure mode as shown in Figure 6.14.

Table 6.7. Data summary of tube compression tests

		Median Crush Load* [kN]	Median Crush Stress* [MPa]	Median Stress Normalized to 56% Fiber Volume [MPa]	Specific Sustained Crushing Stress [SSCS] [MPa]	Crush Compression Ratio**	Specific Energy Absorption ⁽¹⁾ with folding mode failure [SEA-FM] [kJ/kg]	Specific Energy Absorption ⁽²⁾ [SEA] [kJ/kg]	Specific Energy Absorption ⁽³⁾ [SEA] [kJ/kg ²]	Range of Peak Temperatures During Crush [°C]
1.5 m/min 0.0254 m/s	Average	47.0	74.9	95.8	51.5	0.35	43.3	53.3	19.9	-
	Std.Dev.	3.66	5.79	9.61	4.29	0.04	2.96	4.56	2.00	-
	Coeff. of Var. [%]	7.78	7.74	10.0	8.32	10.0	6.84	8.56	10.0	-
140 m/min 2.4 m/s	Average	47.8	77.1	97.4	53.2	0.36	-	52.5	20.9	173-362
	Std.Dev.	2.14	3.44	4.55	2.01	0.02	-	2.30	0.81	
	Coeff. of Var. [%]	4.48	4.46	4.67	3.77	4.67	-	4.37	3.89	
440 m/min 7.4 m/s	Average	43.3	69.2	85.8	47.8	0.32	-	48.9	19.0	254-308
	Std.Dev.	2.35	3.24	3.77	1.95	0.01	-	1.95	0.94	
	Coeff. of Var. [%]	5.43	4.69	4.39	4.08	4.39	-	3.98	4.96	

1) SEA calculated using $E_s = \text{Work}/(\text{area} \cdot \text{density}) \cdot [\text{actuator displacement} + \text{displacement of folded length}]$

2) SEA calculated using $E_s = \text{Work}/(\text{area} \cdot \text{density}) \cdot \text{total actuator displacement}$

3) SEA for design purposes $E_s = \text{Work}(\text{displacement at peak} - \text{displacement at end})/(\text{mass of tube} \cdot \text{displacement at end})$

The peak temperatures exceeded the calibration curve maximum of 200°C for all but one of the specimens.

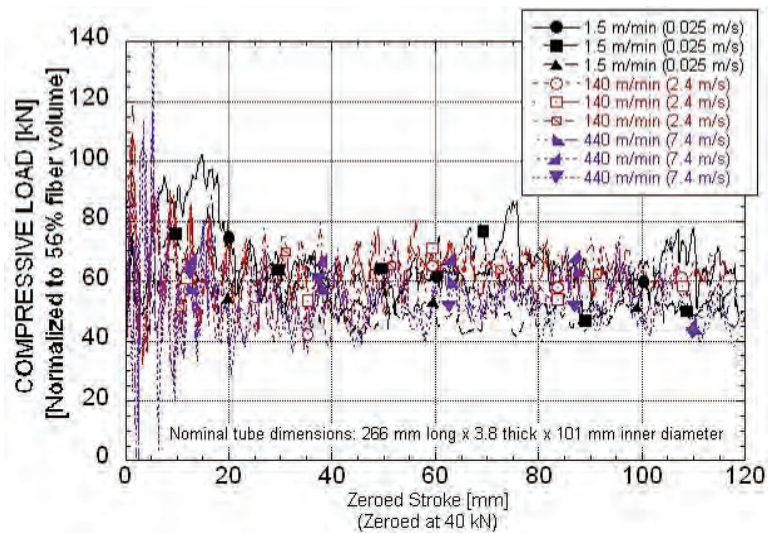


Figure 6.14. Load-displacement curves of tube compression tests.

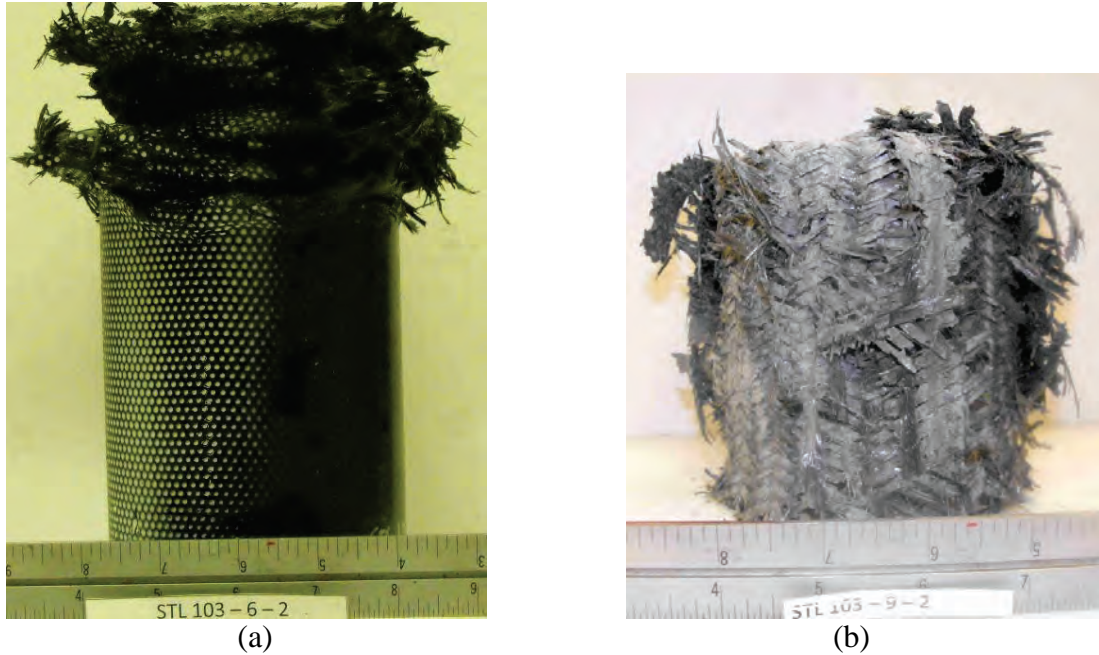


Figure 6.15. Tube failure: (a) low rate, (b) high rate.

6.2. Numerical analysis

LS-DYNA hydrocode was used for the numerical analysis of material tests. In all simulations in this study, the base unit system of the FE model was mm (length), sec (time), and ton (mass). Accordingly, units of other physical quantities were N (force), MPa (stress), and so on.

Finite element model

In this study, a concern was to develop a practical FE model of the braided composite which could be used in full-scale vehicle crash simulation. In general, a 1.0 micro-second time-step size was widely used for full-scale vehicle crash analysis, and 5.0 mm to 15.0 mm range of element size was correspondingly selected for generating the FE vehicle models.

In this study, the single-layer approach was adopted for modeling the braided composite. Two different element sizes were considered to observe mesh size effects. The coarse mesh was built by using approximately 10.0 mm elements and the fine mesh was built by using approximately 5.0 mm elements. Figure 6.16 shows the FE models of specimens for the coupon tests using a coarse mesh, and Figure 6.17 shows the FE models using fine mesh. The green colored area in Figures 6.16 and 6.17 indicates the grip, and the red colored area shows the deformable area of the composite. The straight-sided specimens for the shear test shown in Figures 6.16(f) and 6.17(f) were considered in the numerical analysis for comparing with the test specimen which has a notch. The deformable area of the straight-sided specimen is 50.0 mm × 50.0 mm. The FE models of the tube for compression tests are shown in Figure 6.18. There are two FE models: a coarse mesh model with 10.0 mm elements and a fine mesh model with 5.0 mm elements.

In the physical tests, different machine rates were conducted to investigate whether any strain rate effects exist in the composite material. However, the test results did not show a consistent rate dependency. So, a rate parameter was not considered in the numerical analysis, and the numerical results did not include any rate effects accordingly.

Material properties

In this study, the MAT58 in the material database of LS-DYNA was used for the braided composite. The material properties of MAT58 for the braided composite can be obtained directly from coupon test results in Table 6.6. Table 6.8 shows the values of the material variables of MAT58. Mostly, average values from coupon tests were taken for moduli, failure stresses, failure strains and Poisson's ratio. It has been known that the ASTM specimens shown in Figure 6.4 are not the optimum specimens for tension tests because the straight-sided specimen has a number of bias cut-fibers. However, bias fibers in the bowtie specimen shown in Figure 6.5 remain intact. So, instead, the elastic moduli are taken from the bowtie test results.

Table 6.8. Material properties of MAT58

Card1	MID	RO	EA	EB		PRBA	TAU1	GAMMA1
		1.5e-9	80000	80000		0.35	0.0	0.0
Card2	GAB	GBC	GCA	SLIMT1	SLIMC1	SLIMT2	SLIMC2	SLIMS
	30000	30000	30000	0.3	1.0	0.1	1.0	0.4
Card3	AOPT	TSIZE	ERODS	SOFT	FS			
			0.5		1.0			
Card4	XP	YP	ZP	A1	A2	A3		
Card5	V1	V2	V3	D1	D2	D3	BETA	
Card6	E11C	E11T	E22C	E22T	GMS			
	0.01	0.015	0.01	0.02	0.01			
Card7	XC	XT	YC	YT	SC			
	300	850	300	1000	200			

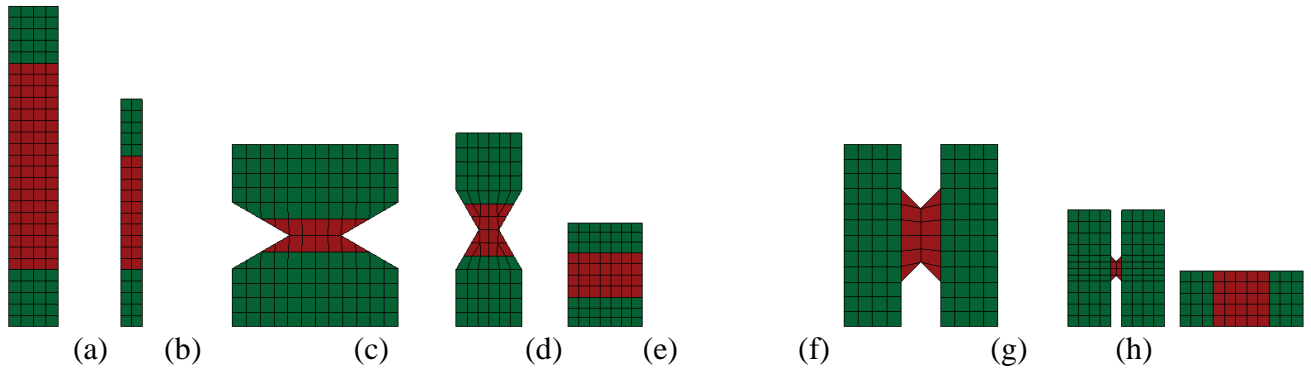


Figure 6.16. FE models (coarse) of specimens for coupon test: (a) ASTM D3039 axial tension, (b) ASTM D3039 transverse tension, (c) bowtie axial tension, (d) bowtie transverse tension, (e) compression, (f) axial shear, (g) transverse shear, (h) shear (straight-sided).

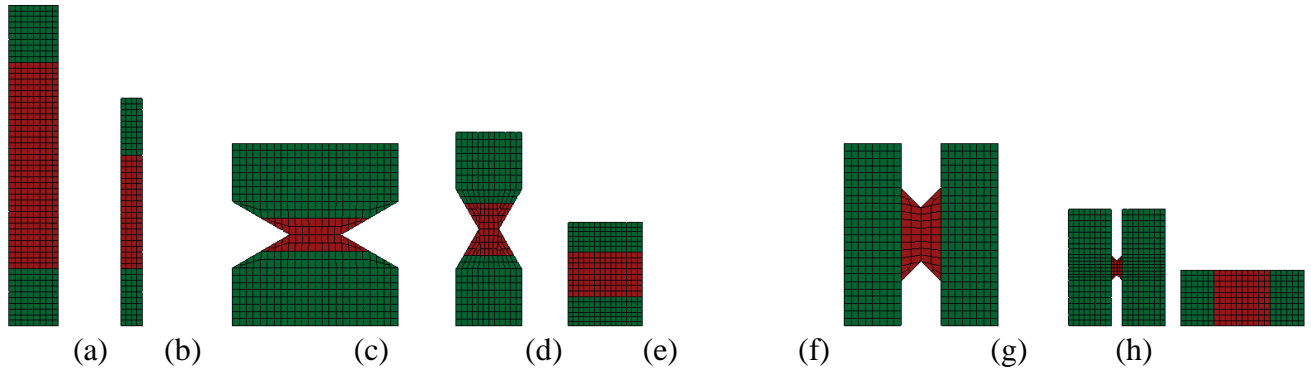
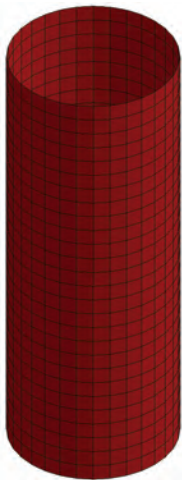


Figure 6.17. FE models (fine) of specimens for coupon test: (a) ASTM D3039 axial tension, (b) ASTM D3039 transverse tension, (c) bowtie axial tension, (d) bowtie transverse tension, (e) compression, (f) axial shear, (g) transverse shear, (h) shear (straight-sided).



(a)

(b)

Figure 6.18. FE model of tube for compression test: (a) coarse mesh, (b) fine mesh. Even though the braided composite shown in Figure 6.1 was different from the simple laminated composite, it is worthwhile to compare the material properties of two composites to understand

their mechanical capabilities. The material properties of a simple laminated composite can be calculated by using the CLT described in Chapter 3. The architecture of the braided composite was $[0/\pm 60]$. In order to make an equivalent and symmetric laminate, the layer profile was assumed as $[60/0/-60/0/0/-60/0/60]$. With the mechanical properties of fiber and resin in Table 6.1, the longitudinal, transverse, and shear moduli and Poisson's ratio of lamina were obtained by using Eqs. (3.37), (3.44), (3.48), and (3.46), respectively. Then, the force-displacement equation, Eq. (3.62), was obtained by Eq. (3.24) and (3.58). Finally, the material properties of the simple laminated composite were estimated by using Eqs. (3.64), (3.65), (3.66) and (3.67). The density was calculated by Eq. (3.27). Table 6.9 compares the material properties of braided composite and simple laminated composite. The axial Young's modules, Poisson's ratio, and density of two composites are close, but the transverse Young's modulus and shear modulus of braided composite are about twice those of a simple laminated composite. This is reasonable since the triaxial braided composite can offer isotropic characteristics.

Table 6.9. Comparison of material properties of braided composite and simple laminated composite

	Young's modulus (GPa)		Shear modulus (GPa)	Poisson's ratio	Density (g/cm ³)
	Axial	Transverse			
Braided composite	80.0	80.0	30.0	0.35	1.5
Simple laminated composite (estimated by CLT)	74.3	41.9	15.0	0.32	1.536

The carbon-thermoset braided composite is a brittle material, which means that the material can fail without plastic hardening. However, after the material has failed in the coupon tests, it can be seen that there is still some resistant force in the force-displacement (F-D) curves as shown in Figure 6.19 to Figure 6.24. Actually, the post-failure behavior of a composite material is very important in structural crash analysis because considerable crash energy of composite structure is absorbed during this post-failure stage. So, the values of the post-failure parameters of MAT58 (slimit1, slimit2, slimic1, slimic2, and slims) in Table 6.8 were chosen based on the F-D curves.

Figure 6.19 and Figure 6.20 show the F-D curves of bowtie axial and transverse tension tests. It can be seen that some resistant force remains in the axial tension tests but is small in the transverse tension tests. Probably, this is because the bias fibers keep resisting some force after axial fibers have failed in the axial tension tests, but there is little resistance after bias fibers have failed in the transverse tension test. Figure 6.21 and Figure 6.22 show the F-D curves of axial and transverse compression tests. It can be seen that great resistant force close to the failure force remains for a while in both the axial and transverse compression tests. The amount of absorbed energy of composite after composite failure is considerable. Figure 6.23 and Figure 6.24 show the F-D curves of the axial and transverse shear tests. It can be seen that a considerable resistant force remains for a while in both the axial and transverse shear tests.

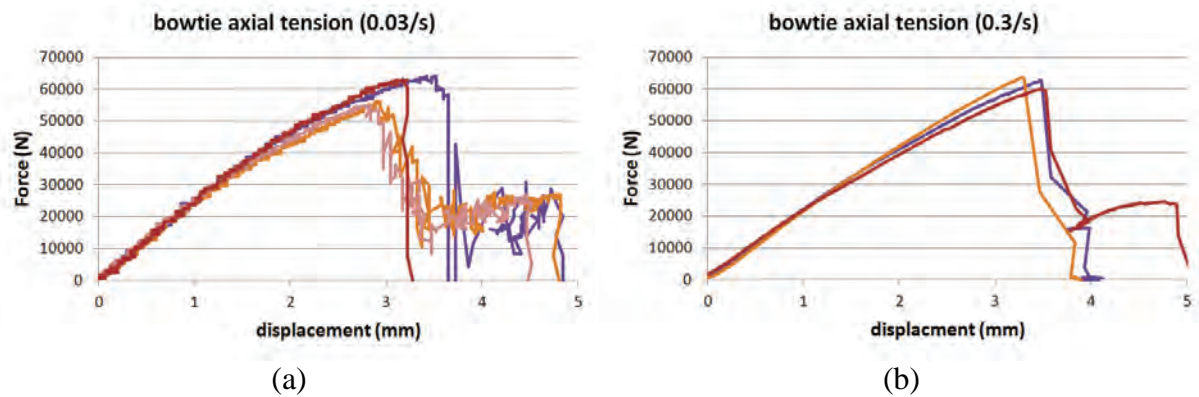


Figure 6.19. F-D curves of bowtie axial tension tests: (a) rate=0.03/s, (b) rate=0.3/s.

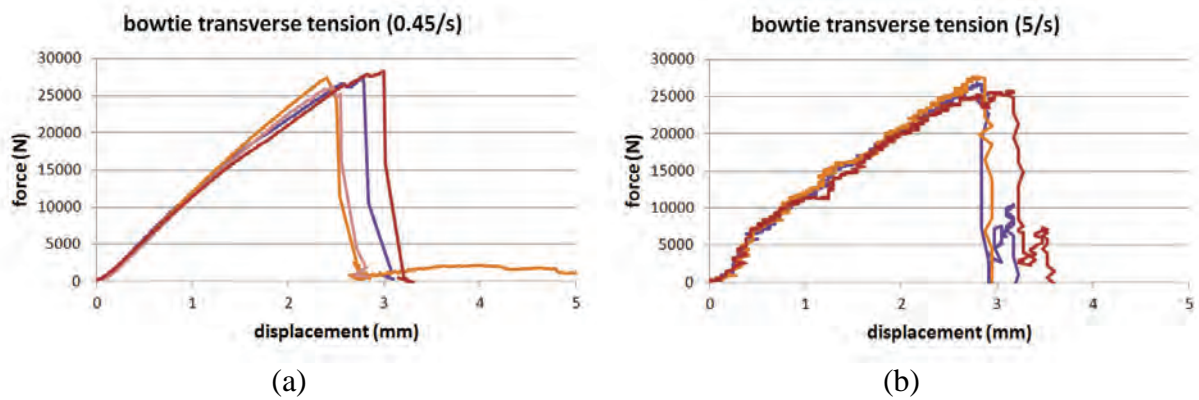


Figure 6.20. F-D curves of bowtie transverse tension tests: (a) rate=0.45/s, (b) rate=5/s.

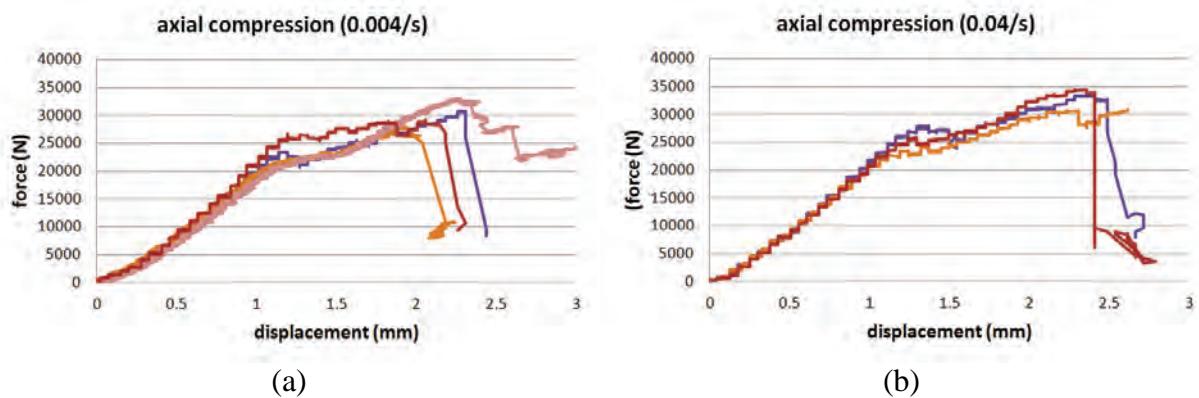


Figure 6.21. F-D curves of axial compression tests: (a) rate=0.004/s, (b) rate=0.04/s.

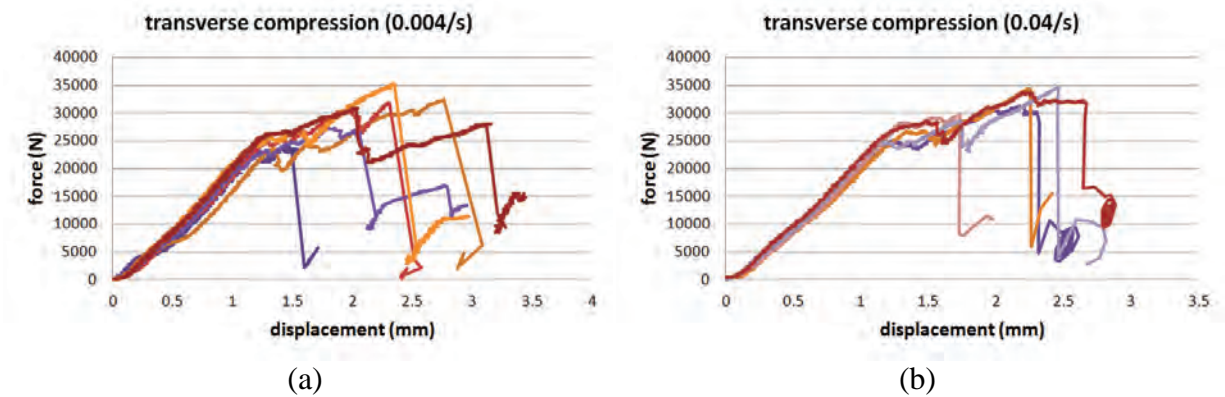


Figure 6.22. F-D curves of transverse compression tests: (a) rate=0.004/s, (b) rate=0.04/s.

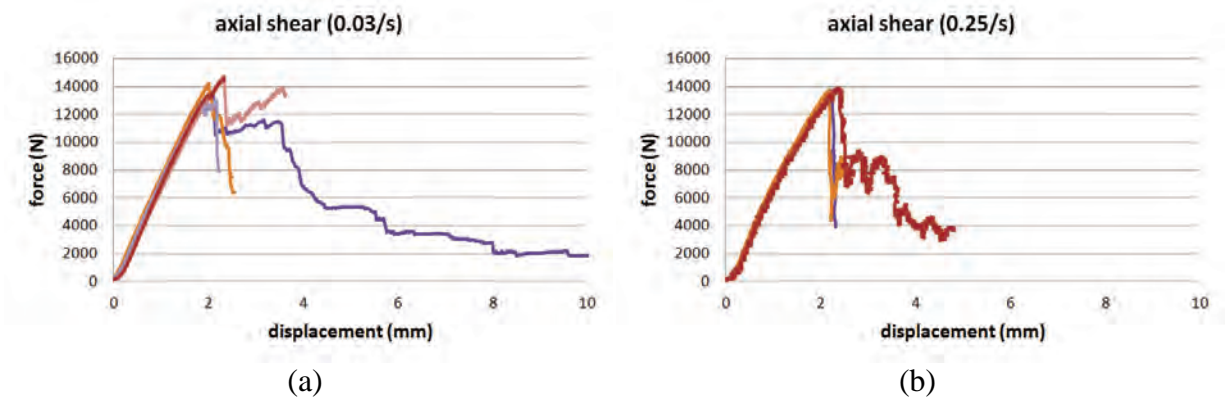


Figure 6.23. F-D curves of axial shear tests: (a) rate=0.03/s, (b) rate=0.25/s.

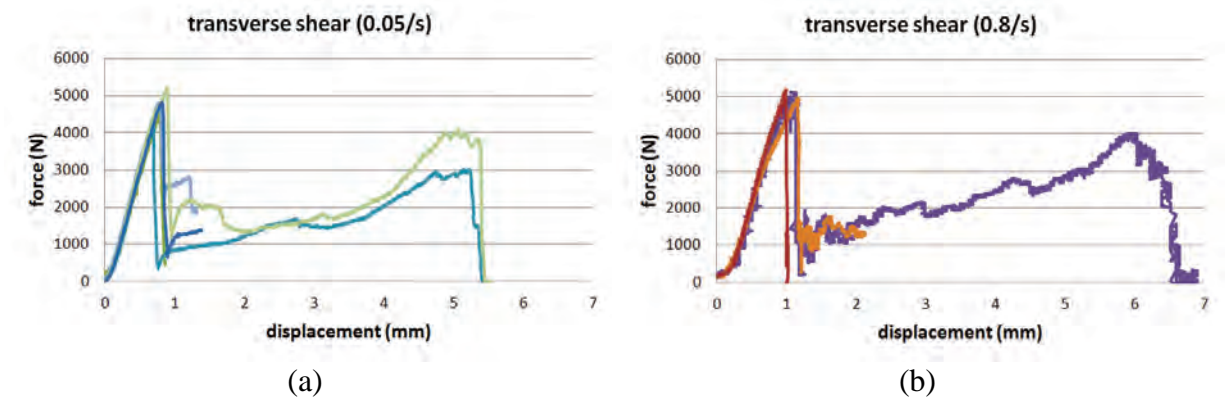


Figure 6.24. F-D curves of transverse shear tests: (a) rate=0.05/s, (b) rate=0.8/s.

Coupon test

By using the FE models shown in Figures 6.16 and 6.17 and the material properties found in Table 6.8, the coupon tests were simulated. Figure 6.25 to Figure 6.29 show the strain-stress (S-S) curves of the simulated coupon tests. In the simulation, the global response of a specimen is of interest rather than the local response at any element. Therefore, the force is divided by the average coupon section area to get the engineering stress of the simulated coupon tests and the displacement is divided by the length between the grips to get the engineering strain of simulated coupon tests.

Figure 6.25 shows the S-S curves of the bowtie tension simulations. The coupon test results are overlaid for the purpose of comparison. The test specimen number is in parentheses. The initial slopes of S-S curves of bowtie tension simulations and tests are close, but the failure stress in the simulation is much lower than that in the tests. Basically, the bowtie specimen shown in Figure 6.5(a) has wedge-shaped sides like a notch. In the simulation, the bowtie FE model has a single layer in the thickness direction with effective material properties of braided composite. During the tension test simulation, the stress concentration occurred at the wedge tips of the bowtie FE model, which made the failure occur earlier. In the actual tests, the stress concentration was small since the side angle of the bowtie specimen followed the bias fiber angle. So, the bowtie specimen FE model is not suitable for the coupon test simulation with the single-layer approach. In this study, the ASTM specimen FE model, which had straight sides, was used for the tension simulations and their results are compared with the bowtie test results. Figure 6.26 shows the ASTM tension simulations. The S-S curves of ASTM tension simulation are well matched with those of bowtie tension tests. The S-S curves of ASTM tension tests show much lower initial slope and failure stress in Figure 6.26. The tension simulations with fine mesh show the same initial slope, but a bit lower failure stress.

Figure 6.27 shows the S-S curves of compression simulations. The specimen FE model is shown in Figures 6.16(e) and 6.17(e). The initial slopes between the simulation and tests are fairly close. Also, there is no difference between the coarse and fine meshes.

Figure 6.28 shows the S-S curves of shear tests. It shows good agreement of the initial slope and failure stress of the S-S curves between the simulations and tests. The specimen for the shear tests is shown in Figure 6.5(b), and the FE models are in Figures 6.16(f), 6.16(g), 6.17(f), and 6.17(g). For comparison, the straight-sided specimen shown in Figures 6.16(h) and 6.17(h) was used for shear simulation. The initial slope and failure stress of shear simulations with the straight-sided specimen are lower than those with wedge-shaped specimen.

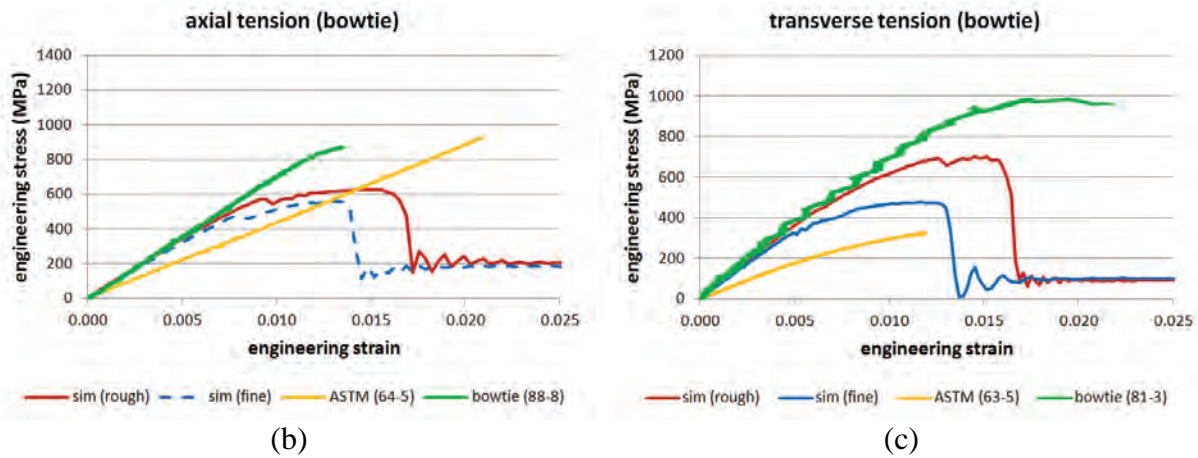


Figure 6.25. Strain-stress curves of bowtie tension simulations: (a) axial, (b) transverse.

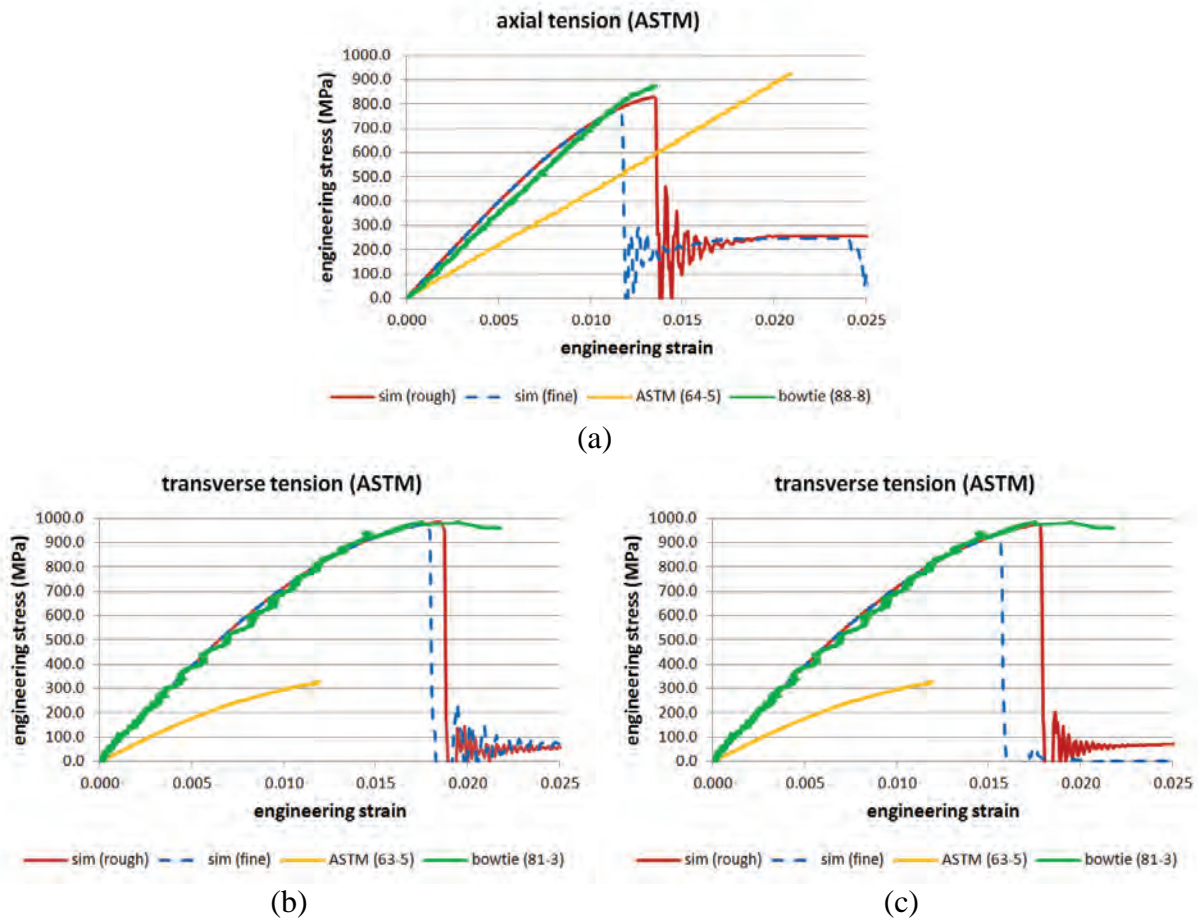


Figure 6.26. Strain-stress curves of ASTM tension simulations: (a) axial, (b) transverse, (c) transverse (using axial ASTM specimen).

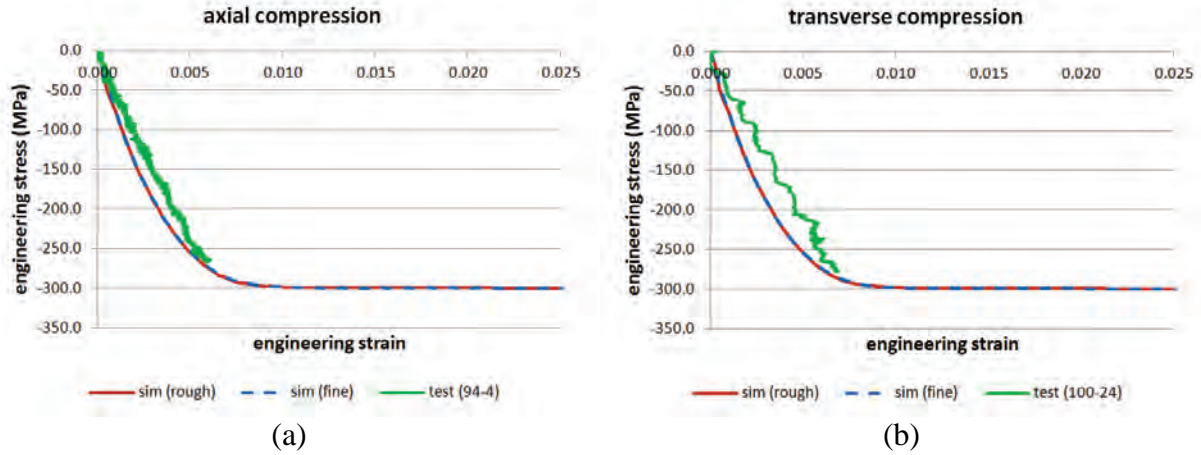


Figure 6.27. Strain-stress curves of compression simulations: (a) axial, (b) transverse.

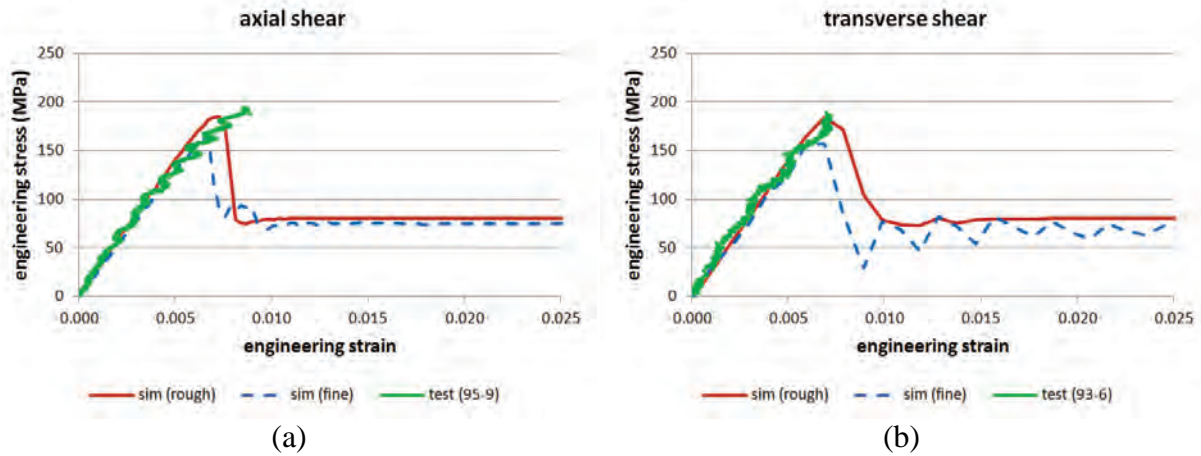


Figure 6.28. Strain-stress curves of shear simulations: (a) axial, (b) transverse.

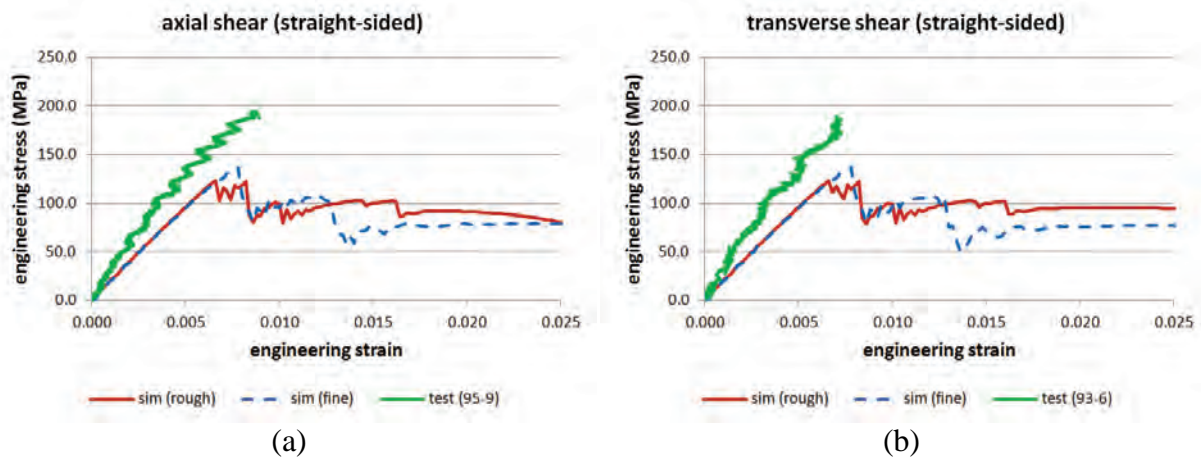


Figure 6.29. Strain-stress curves of shear simulations (with straight-sided specimen): (a) axial, (b) transverse.

Tube test

By using the tube FE model shown in Figure 6.18 and the material properties found in Table 6.8, tube compression tests were simulated. Figure 6.30(a) shows the F-D curves of the tube compression simulations. It shows that the average force level between the tests and simulation are close. In the simulation, the oscillation was much larger than that in the tests, which was probably caused by the relatively large element size. Especially, the initial peak force in the simulations was much higher than that in the test. In the test, the tube specimen had a single 45° bevel to act as a crack initiator. In the simulation, the punch had the crack initiator instead, but it was inefficient to initiate the crack and reduce the magnitude of initial peak force in the F-D curve. Figure 6.30(b) compares the absorbed energy of tubes in compression tests. It shows that fine mesh FE model absorbs more energy than the coarse mesh FE model. The energy curve of the test is between the energy curves of the two simulations. The deformed shapes of tubes are shown in Figure 6.31. The post-test tubes are shown in Figure 6.15. The failure mode of the tube in the compression simulation is similar to that shown in Figure 6.15(b) of the compression test.

6.3. Composite ladder frame

Traditionally, the ladder frame is made of steel because of excellent energy absorbing performance and relatively simple manufacturing. The carbon fiber composite material is known as an excellent SEA material. In other words, the substitution of steel to composite in ladder frame provides an opportunity to reduce the weight of ladder frame without compromising its stiffness and crash performance.

Based on the material properties of MAT58 and the FE model of the braided composite developed above, the original steel ladder frame is changed to the composite ladder frame. Since the composite material has different characteristics than steel, the applicability of composite material to ladder frame was tested by stiffness and impact tests. Both tests would evaluate if the composite ladder frame can provide equivalent performance to the steel ladder frame.

In this study, cost increases in the manufacturing process of composite products with current or near future technology were not considered. Also, no geometric design changes induced by material changes were considered.

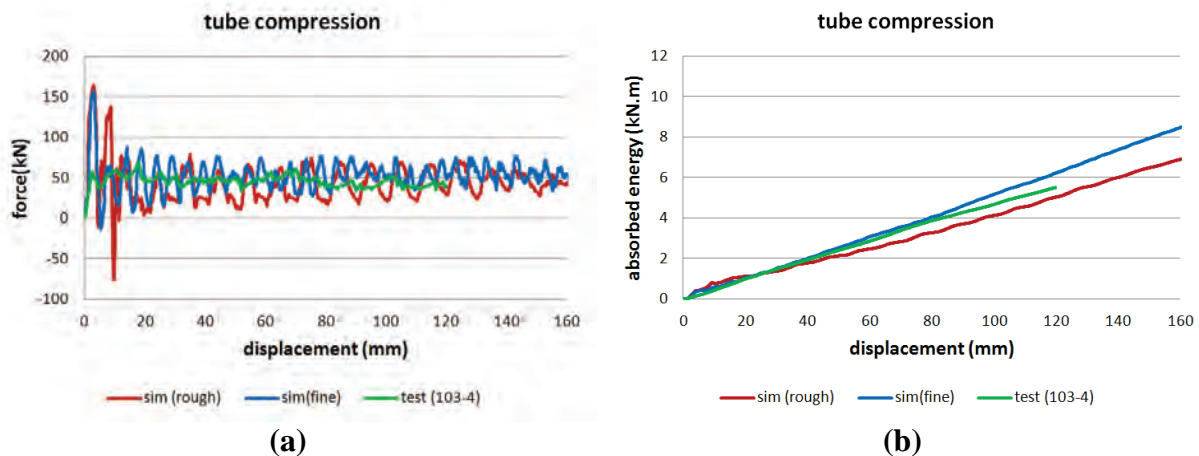


Figure 6.30. Force and absorbed energy curves of tube compression simulations: (a) force, (b) absorbed energy.

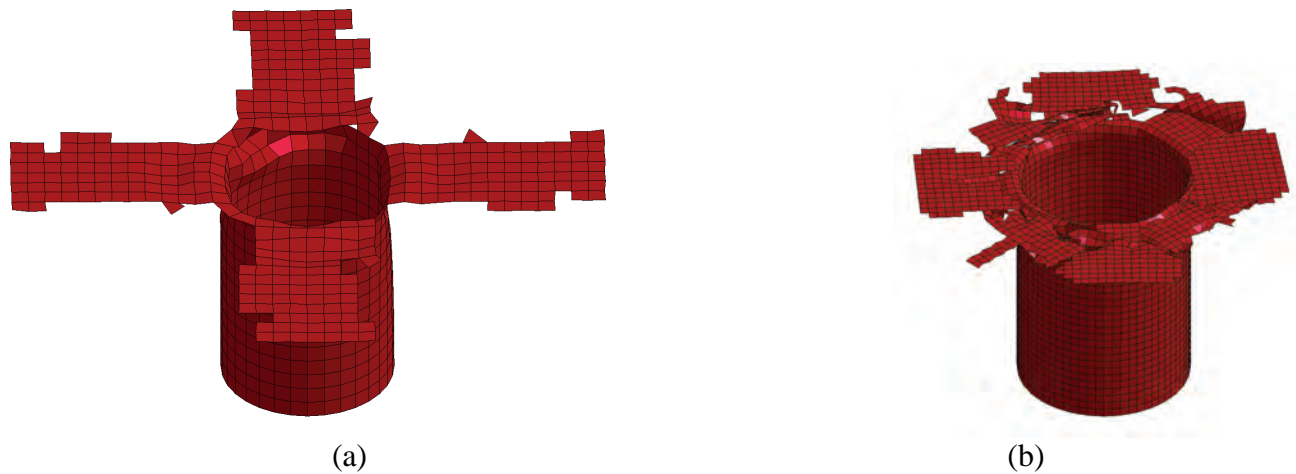


Figure 6.31. Tube deformation in tube compression simulation: (a) rough mesh, (b) fine mesh.

Material substitution

The steel ladder frame of the Silverado is shown in Figure 6.32. The weight of the ladder frame is 232 kg. The ladder frame consists of three sub-components; side rails, crossbeams, and mount supporters. The side rails shown in red color in Figure 6.32 are the main energy absorbing structure in frontal impact. The geometry of the side rails is a simple rectangular box shape. The crossbeams, shown in green and brown in Figure 6.32, hold the side rails together and prevent localized bending and twisting of the side rails. Also some of crossbeam supports the engine and transmission. The mount supporters, shown in blue color in Figure 6.32, support the truck bodies and suspensions. So, the mount supporters require high stiffness, durability, and hardness. The weights of the side rails, crossbeams, and mount supporters are 125 kg, 47 kg, and 60 kg, respectively. The carbon-thermoset braided composite was selected as the substitution material for steel. The braided composite material was adapted only to the side rails. The design of the ladder frame remained unchanged. The principle axes of the composite were oriented in the vehicle longitudinal direction.

In order to evaluate the stiffness and crashworthiness of the ladder frame, component tests were simulated. The thickness of side rails was adjusted to determine the equivalent stiffness and strength of the composite ladder frame to the steel ladder frame. Three different thicknesses of side rails were considered. The thickness and the corresponding weight of ladder frame are listed in Table 6.10. The thickness is normalized by the original thickness. The weight of the ladder frame was reduced up to 43.1 percent when the steel material of the side rails was changed to composite material without a change to the thickness. When the thickness was increased to twice and three times, the weight reduction was 32.3 percent and 21.6 percent, respectively.

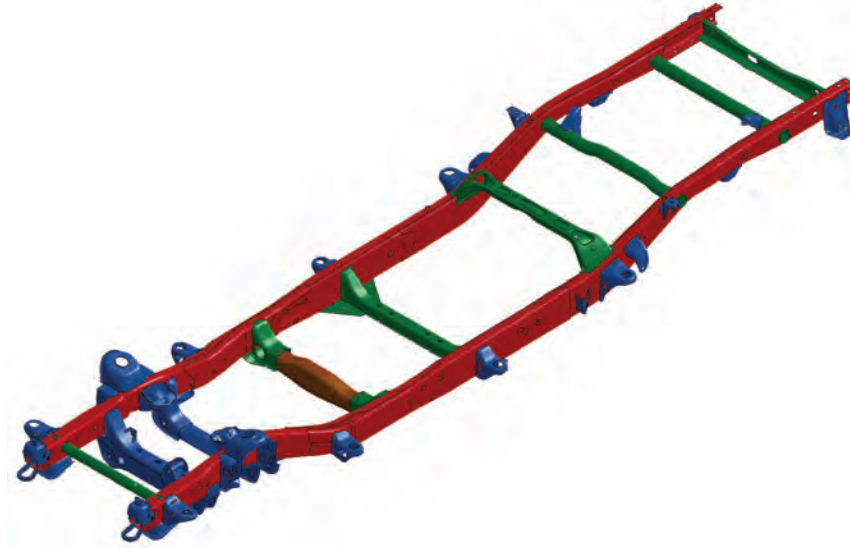


Figure 6.32. Ladder frame of Silverado.

Table 6.10. Thickness and weight of ladder frame

	normalized thickness	weight [box frame only] (kg)	weight difference (kg)	weight reduction ratio (box frame only) (%)
original	1.0	231.6 [125.1]		
new	1.0	131.8 [25.3]	99.8	43.1 [79.8]
	2.0	156.8 [50.3]	74.9	32.3 [59.8]
	3.0	181.7 [75.2]	49.9	21.6 [39.9]

Stiffness tests

Stiffness tests of the ladder frame were conducted to compare the bending and torsional stiffness of the original and new ladder frame. The boundary conditions of stiffness tests are shown in Figure 6.33. In the bending test, forces were applied to points at the middle of ladder frame and the wheel location points of the ladder frame were constrained as shown in Figure 6.33(a). In the torsion test, the rear wheel location points were constrained and forces were applied to the points at the front wheel locations as shown in Figure 6.33(b).

Figure 6.34 shows the results of the stiffness tests. The stiffness of the composite ladder frame is normalized by the stiffness of the original steel ladder frame. The composite ladder frame with the original thickness of the steel ladder frame shows softer response than the steel one, but the three times thicker composite ladder frame shows a stiffer response than the steel ladder frame. The twice thicker composite ladder frame shows almost equivalent stiffness to the steel ladder frame. It is observed that the stiffness of the composite ladder frame increased linearly when the thickness was increased.

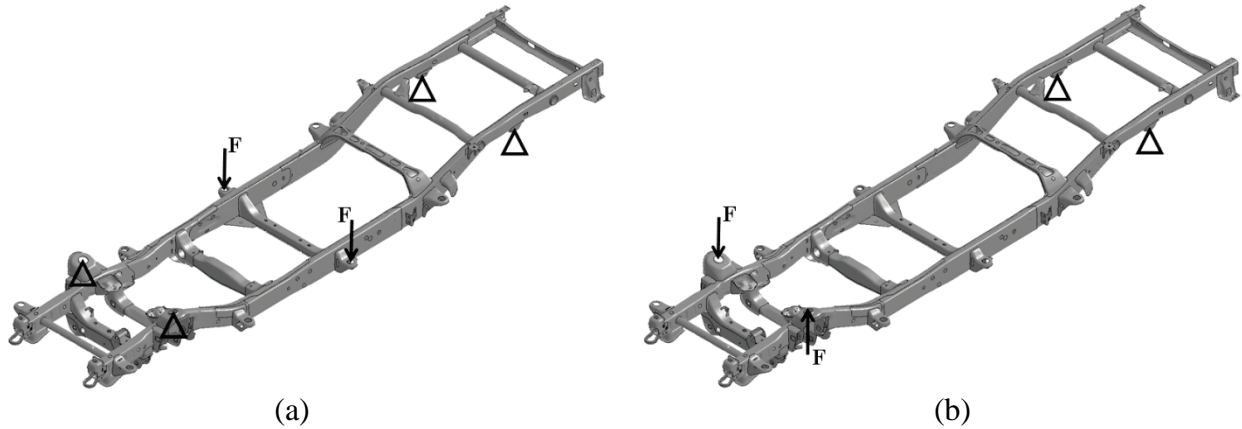


Figure 6.33. Stiffness tests of Silverado ladder frame: (a) bending, (b) torsion.

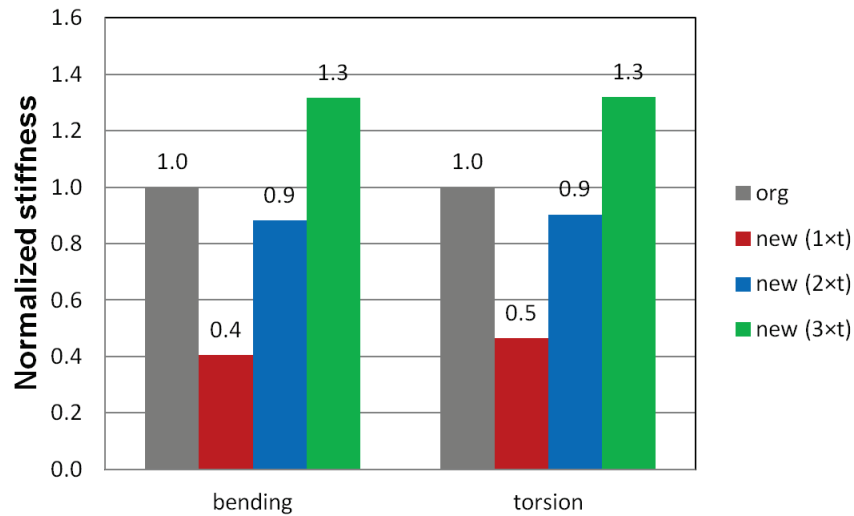


Figure 6.34. Stiffness of ladder frame.

Rigid wall impact tests

Rigid wall impact tests were performed to evaluate the crash performance of the composite ladder frame. The test setup is shown in Figure 6.35. The front bumper was attached to simulate the actual frontal impact test of a vehicle. The impact speed was 56 km/h (35 mph). Additional mass was added at the mounting points to make the total weight of the ladder frame structure becomes around 1000 kg.

Figure 6.36 shows a close-up view of the front area of the ladder frame. Figures 6.37 to 6.40 show the deformation of the ladder frame that occurred in the impact test. The original steel ladder frame shown in Figure 6.37 demonstrated a folding deformation mode. The deformation of the side rails reaches the suspension mount points as indicated by green arrows in Figure 6.37. Figures 6.38 to 6.40 show the deformation of the composite ladder frame. The composite ladder

frame demonstrated a fracture deformation mode. The composite ladder frame with the original thickness of the steel ladder frame shows that the side rails are crushed just beyond the suspension mount points as shown in Figure 6.38. The side rails with the twice the thickness are crushed just beyond the front-end module mount points as shown in Figure 6.39. The side rails with the three times the thickness are crushed just around the front bumper mount area as shown in Figure 6.40.

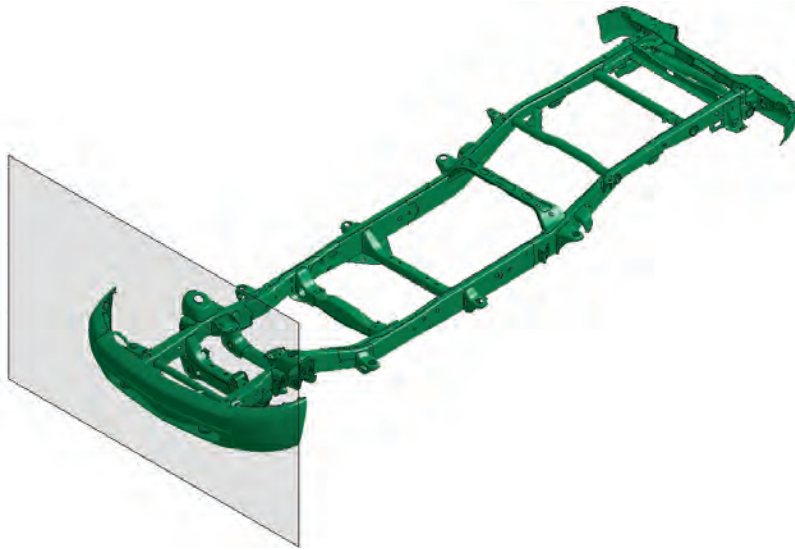


Figure 6.35. Rigid wall impact test of Silverado ladder frame.

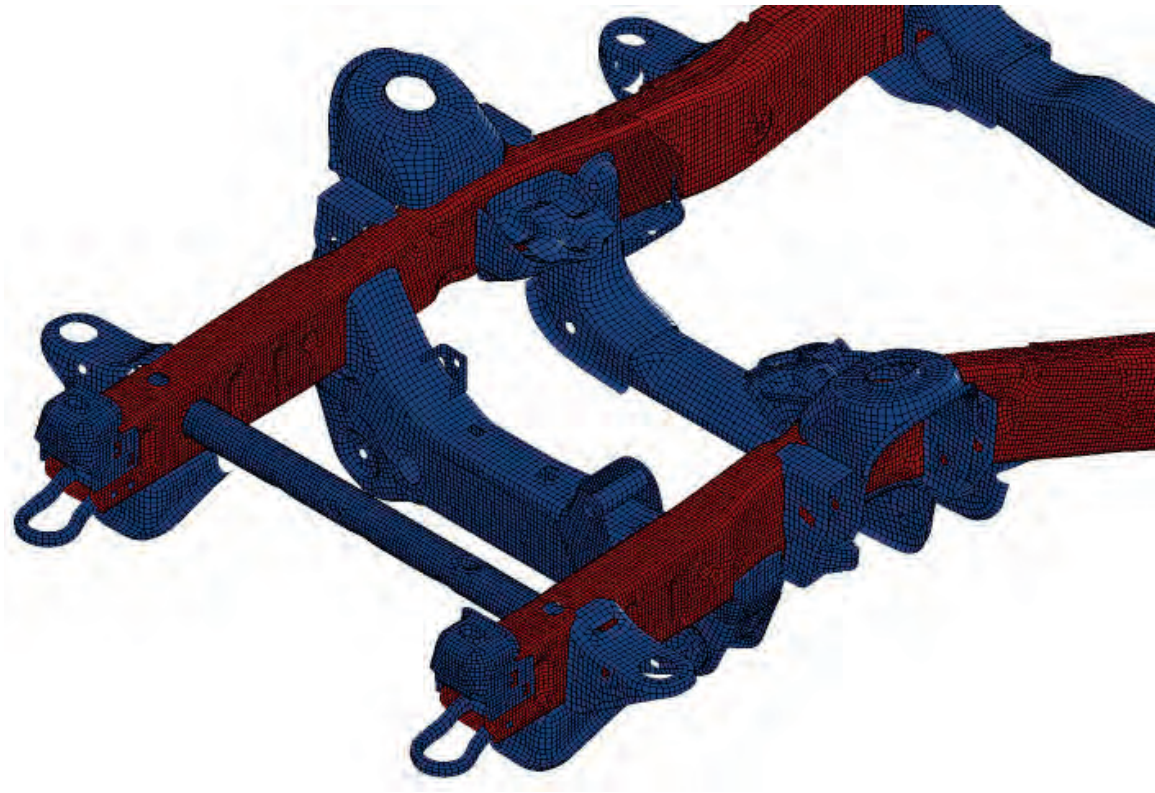
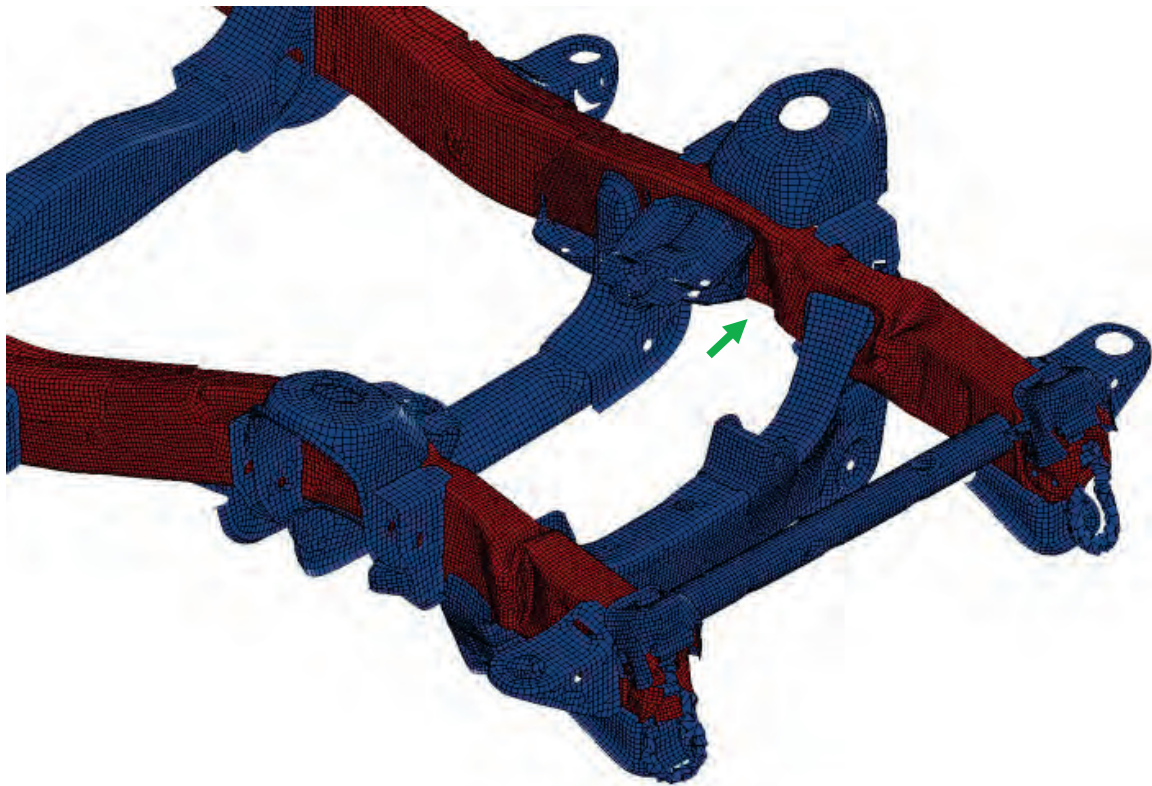
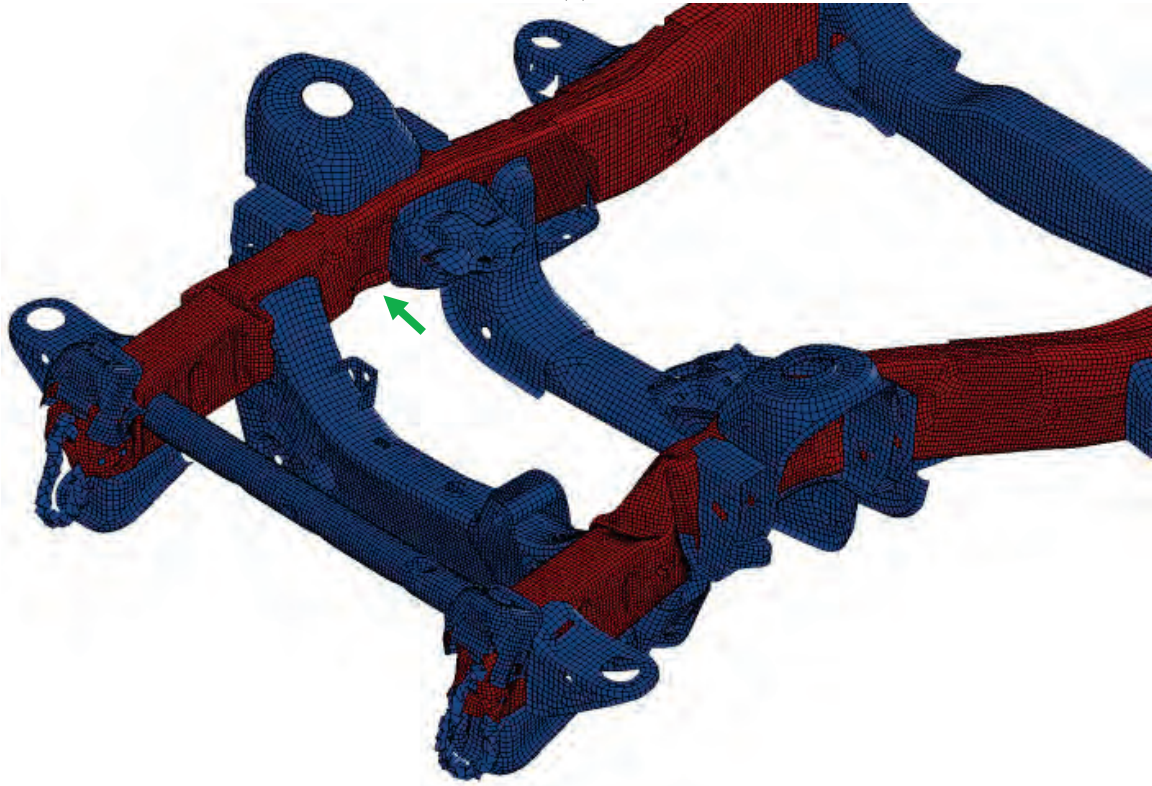


Figure 6.36. Close-up view of front area of ladder frame (undeformed).

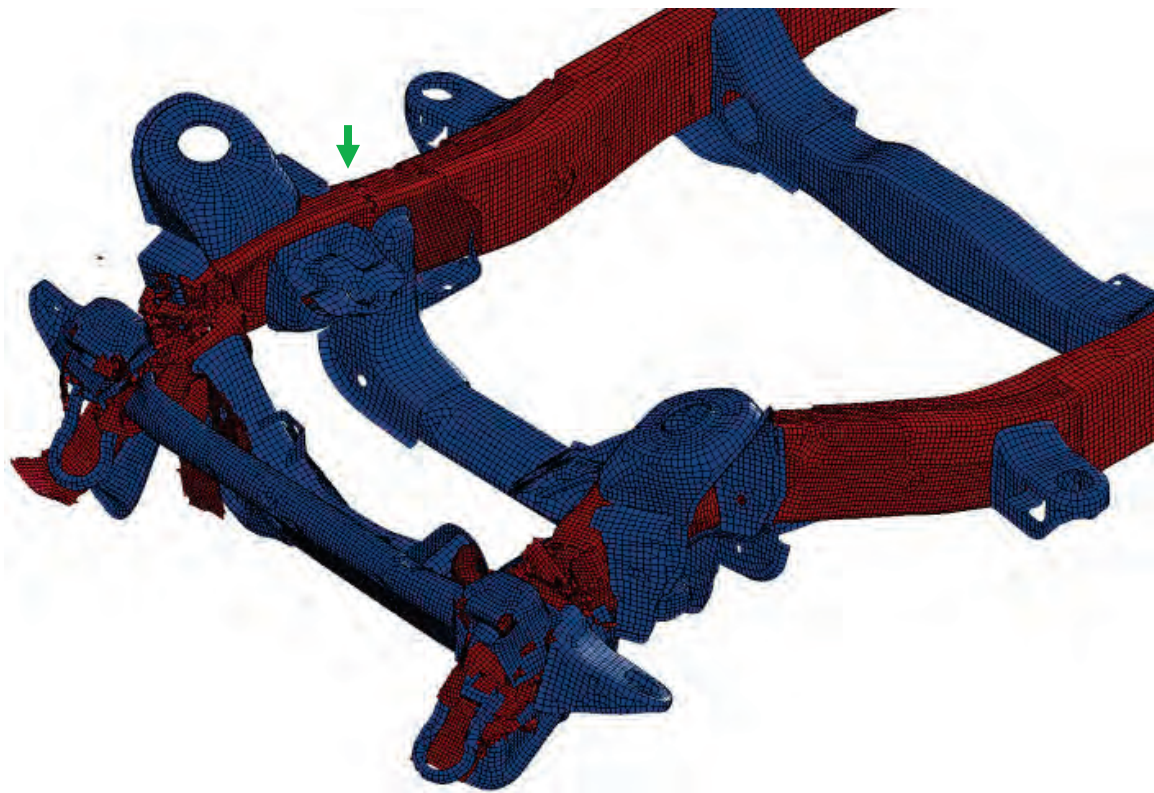


(a)

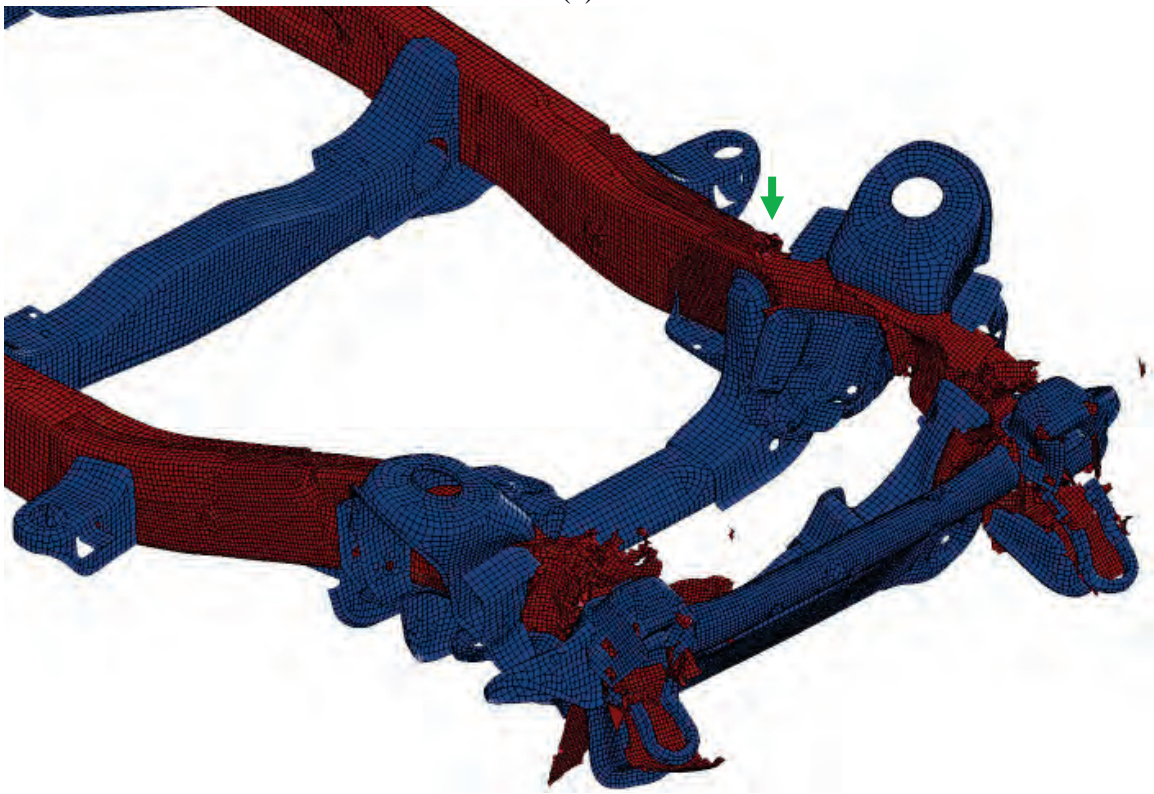


(b)

Figure 6.37. Deformation of original steel ladder frame.

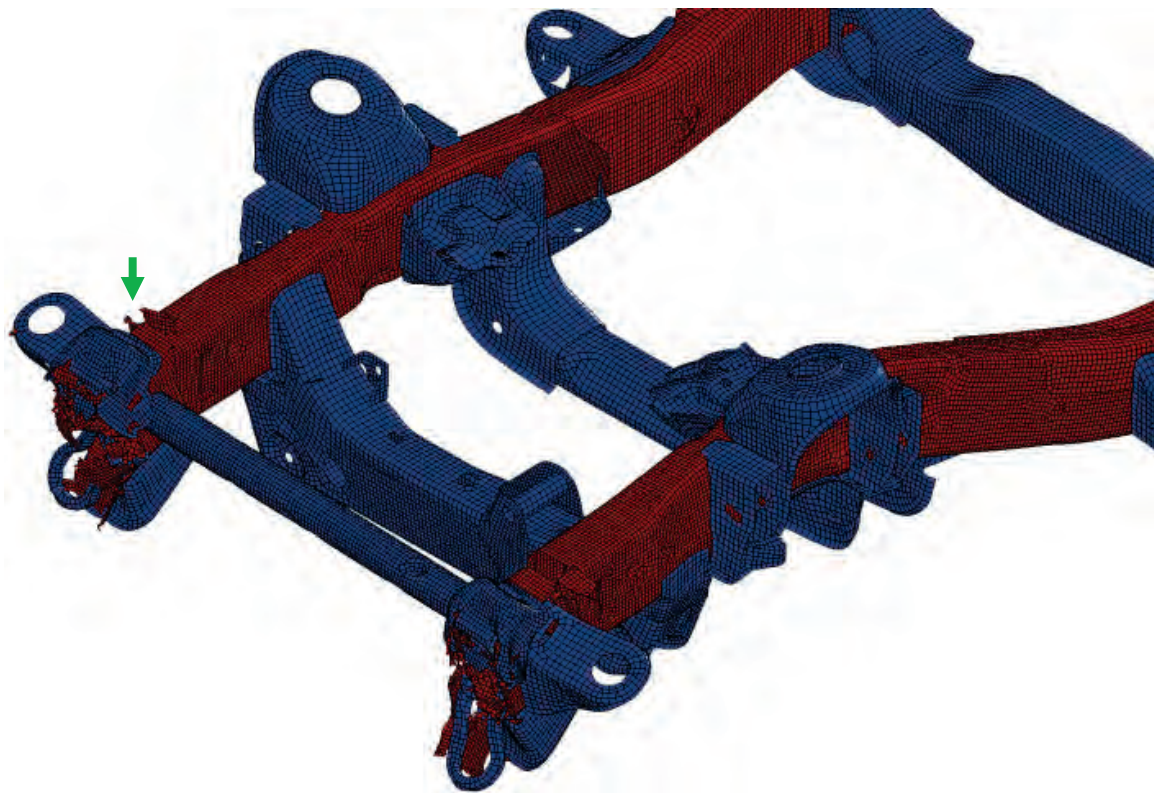


(a)

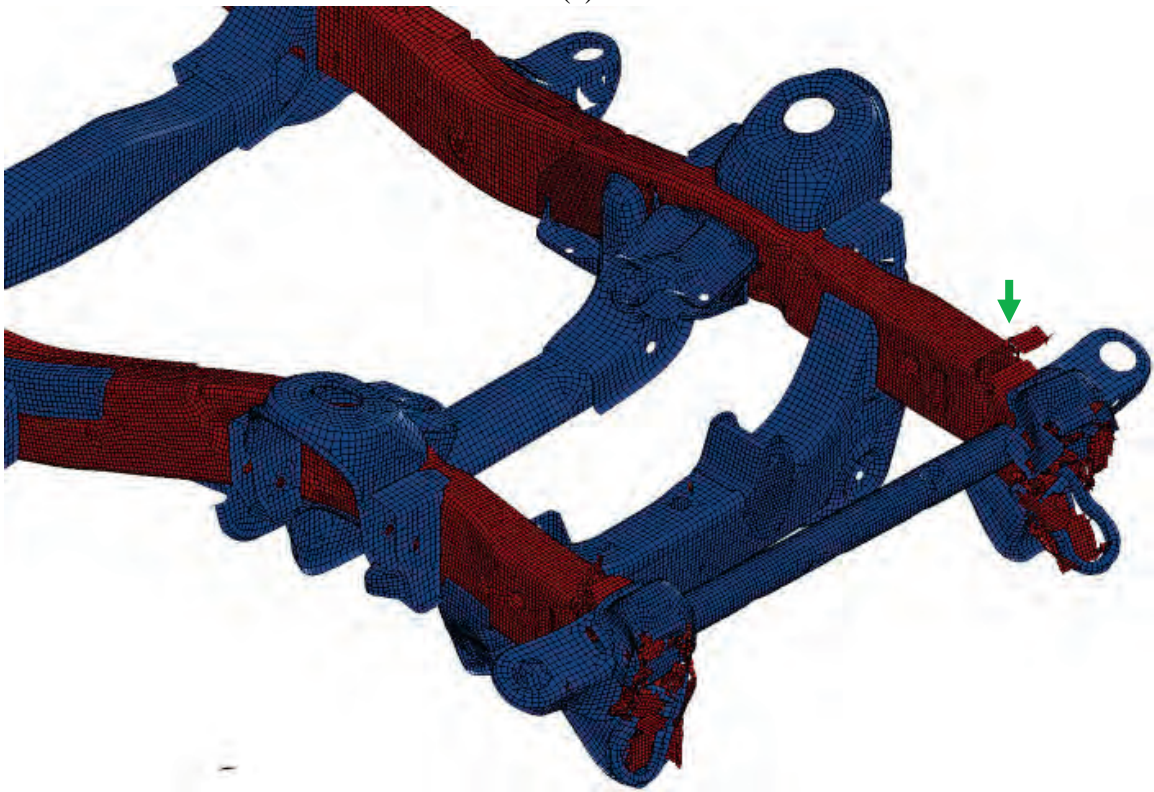


(b)

Figure 6.38. Deformation of new composite ladder frame (normalized thickness=1.0).

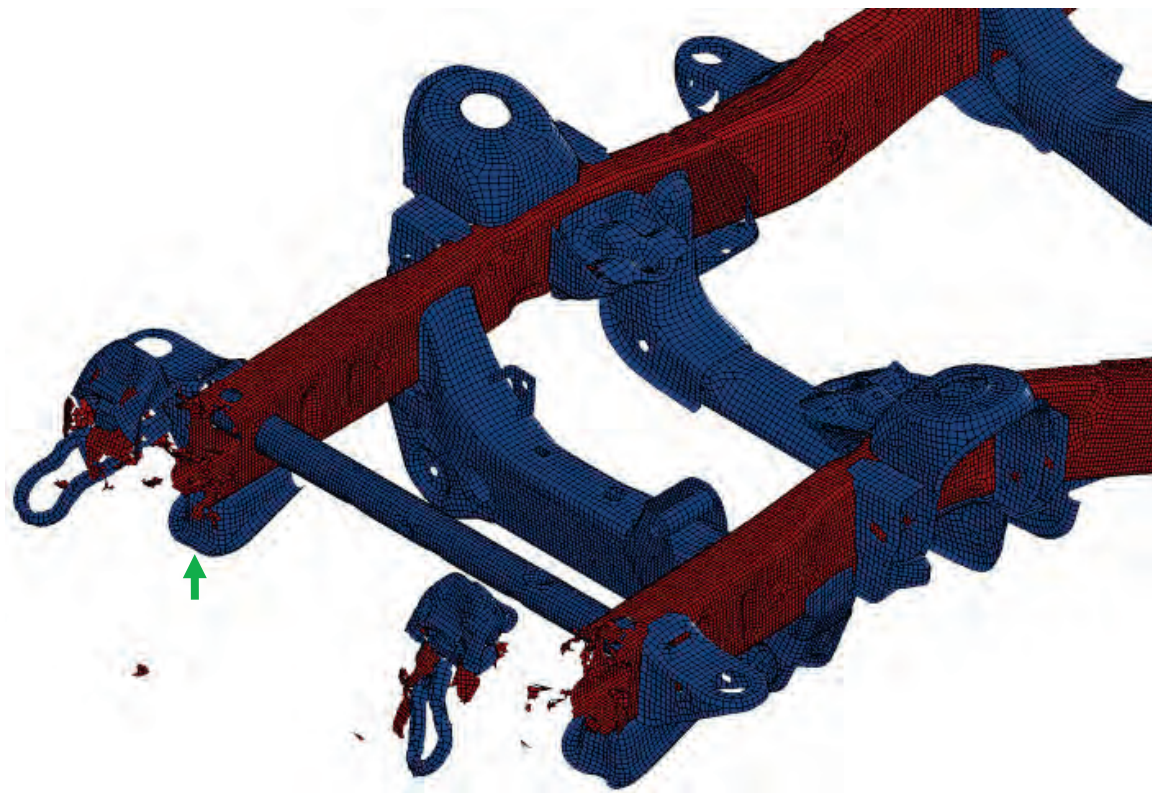


(a)

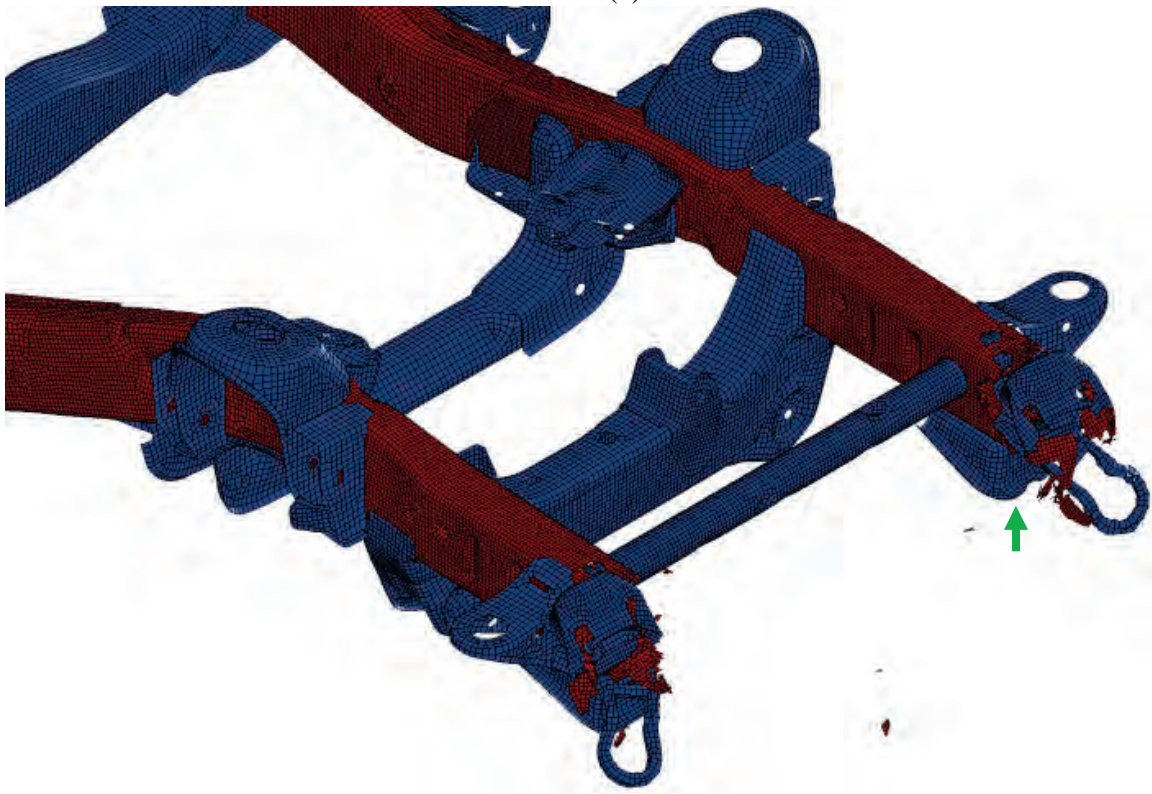


(b)

Figure 6.39. Deformation of new composite ladder frame (normalized thickness=2.0).



(a)



(b)

Figure 6.40. Deformation of new composite ladder frame (normalized thickness=3.0).

Figures 6.41 and 6.42 show the velocity and wall force time histories, respectively. In Figure 6.42, the wall force curve of the original ladder frame had two big peaks, which means that the side rails were effectively designed to absorb impact energy by progressive folding. The wall force curves of the composite ladder frame with twice or three times the thickness have one big peak. The steel and composite ladder frames have different fracture modes. The original geometric design of the steel ladder frame may not be efficient for the composite ladder frame. The progressive fracture of composite side rails gets discontinued by the crossbeams and mount supporters. The ladder frame had local buckling initiators as shown in Figure 6.36, but there was no fracture initiator. So, when the initial fracture of the composite side rails stopped, initiating the next fracture would require a higher force. In other words, the composite ladder frame has a discontinuous fracture mode.

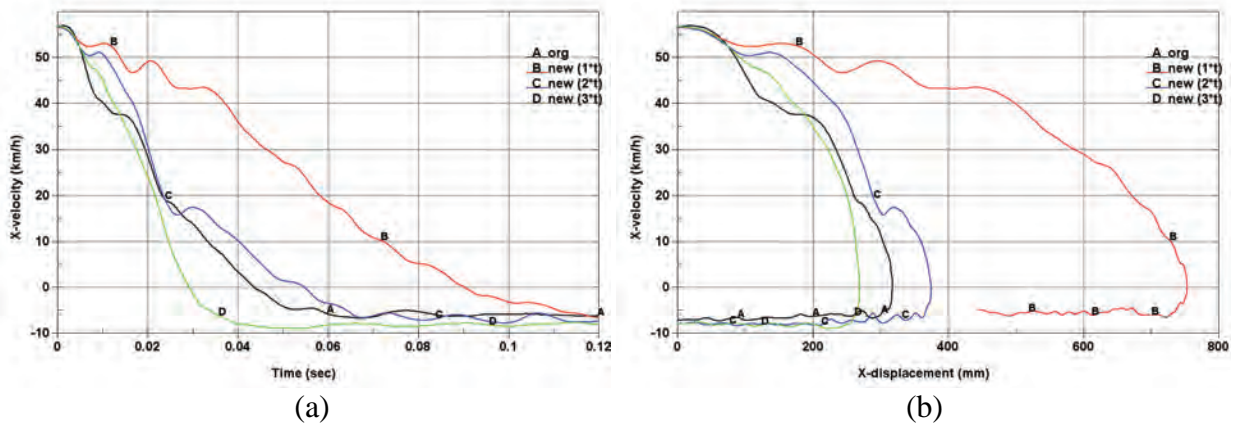


Figure 6.41. X-velocity profiles of ladder frames: (a) in time, (b) in displacement.

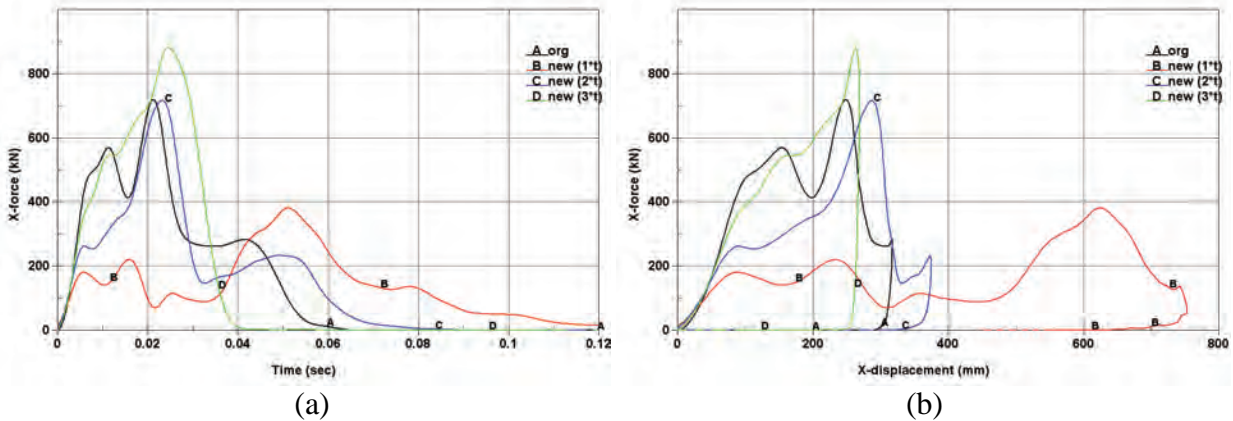


Figure 6.42. Wall forces of ladder frames: (a) in time, (b) in displacement.

Figure 6.43 shows the maximum crush of the ladder frame. The maximum crush of the composite ladder frame is normalized by the maximum crush of the original ladder frame. It shows that the original thickness composite ladder frame was quite soft. The twice the thickness composite ladder frames was a little softer but the three times the thickness composite ladder

frame was a little stronger. Unlike the stiffness test results, the impact test results are not linearly increasing. This might have been induced by the discontinuous fracture mode of the composite ladder frame.

Based on the stiffness and rigid wall impact tests, even if the twice the thickness composite ladder frame was a little softer than the original steel ladder frame, it was determined that the twice the thickness composite ladder frame provided equivalent stiffness and crash performance because the new vehicle was light-weighted. Therefore, the weight of the ladder frame was reduced to 156.8 kg, and thereby had a weight saving of 74.8 kg, which is a 32 percent decrease. If the composite material had been applied to the cross members and mount supporters, the weight of ladder frame could have been reduced more.

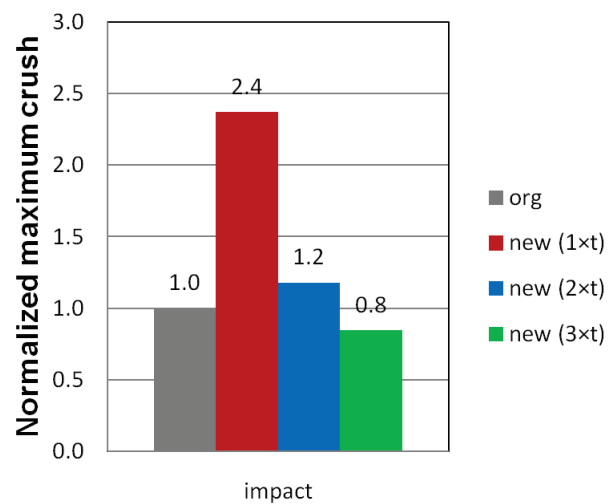


Figure 6.43. Maximum displacement of ladder frame.

7. Lightweight Components

Chapter 5 discusses the development of a lightweight vehicle. The Chevrolet Silverado was selected as the candidate vehicle. The components listed in Table 5.3 were light-weighted to develop the lightweight Silverado. Since part of the objective of this project was to examine the possible safety benefits of lightweight PCIVs, component test simulations were conducted to evaluate if the new lightweight components that are energy absorbing members provided equivalent performance to their original steel component counterparts. This chapter provides a description of the lightweight components and the results of their performance evaluations.

7.1. Occupant compartment structure

Roof

The roof panel is shown in Figure 7.1. The same structure was used as in the original, but reinforcements were added around the roof boundary and B-pillar cross. The steel material was switched to a polycarbonate plastic (SABIC, 2011a) and the reinforcement was a blend of semi-crystalline polyester and polycarbonate (i.e., a PBT(or PET)/PC blend) (SABIC, 2011c). The weight of the rear window was reduced from 20.54 kg to 11.72 kg, and thereby had a weight saving of 8.82 kg, which is a 43 percent decrease.

A- and B-pillar reinforcements

In order to save some weight in the A- and B-pillars, composite inserts were applied to the A- and B-pillar as shown in Figure 7.2 and the thickness of steel pillars was reduced. BASF designed the composite inserts by using a 35 percent glass reinforced polyamide (PA6) (BASF, 2011). Both pillars were gauged down 20 percent. The total weight saving is about 1.5 kg.

Component tests

To evaluate the crashworthiness performance of the A- and B-pillars with composite inserts, two component tests were conducted; a roof test as shown in Figure 7.3(a) and a B-pillar punch test as shown in Figure 7.4(a). Figures 7.3(b) and 7.4(b) show that the modified A- and B-pillars provide comparable crash performance to the original model.

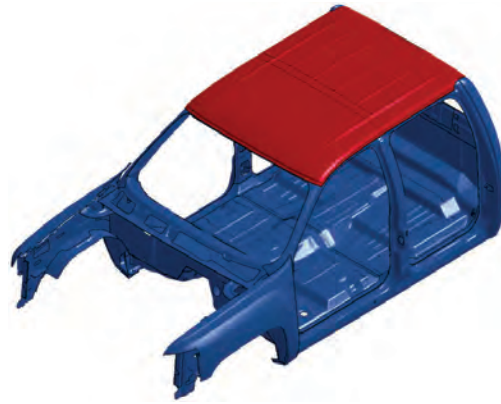


Figure 7.1. Roof (denoted by the red color).



Figure 7.2. Pillar reinforcements: (a) A-pillar, (b) B-pillar.

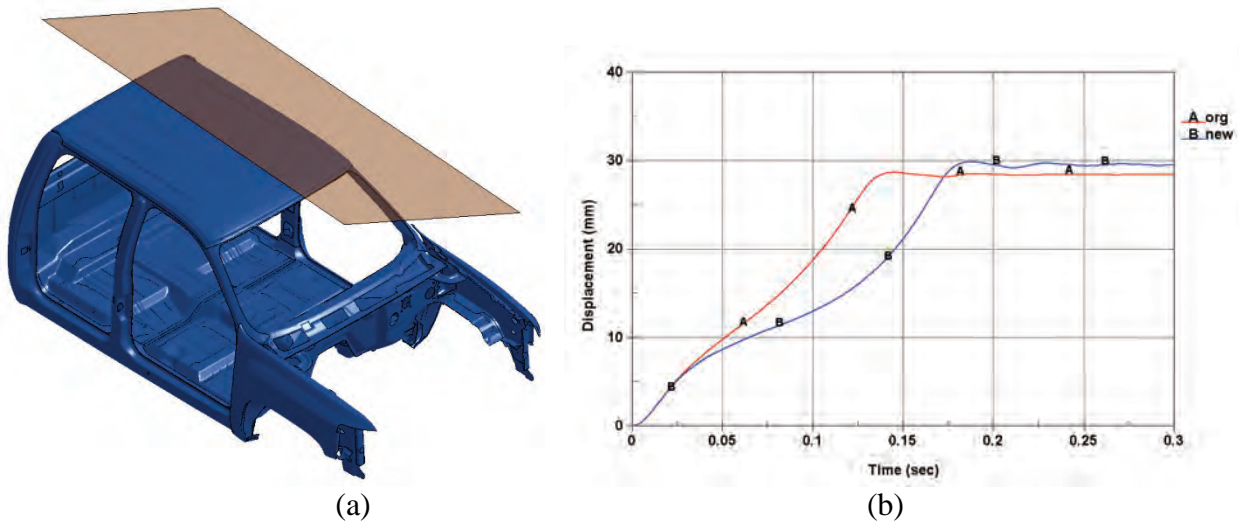


Figure 7.3. Roof tests: (a) test configuration, (b) comparison.

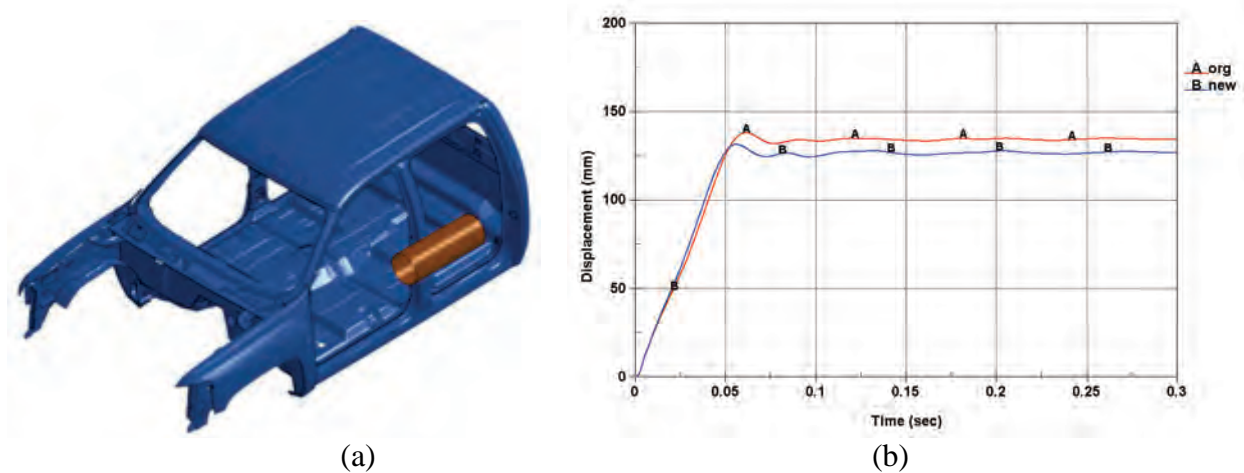


Figure 7.4. B-pillar punch tests: (a) test configuration, (b) comparison.

7.2. Interiors

Seats

Chemical companies estimated that the weight of a rear seat could be reduced in the range of 20 percent to 40 percent by using lightweight plastics (Hojnacki, 2011, Naughton, 2009). LOTUS estimated that the weight of the automotive seats could be reduced up to 50 percent (LOTUS, 2010). In the Silverado FE model, the seats were not modeled. Instead, the weight of seats was distributed into the model as point masses. The original weights of the front seats and rear seat were 50.5 kg and 44.56 kg, respectively. Based on the references and the discussion with BASF (Plott, 2011), it was assumed that the weight of seats could be reduced 20 percent in this study. Thus, the new weight of the front seats and rear seat was adjusted to 40.5 kg and 35.66 kg, respectively. The total weight saving is 18.9 kg.

Instrument panel carrier

There are new lightweight materials and designs for replacing the traditional instrument panel carrier (Bayer 2011, Slik, 2002, Jahn, 2005, Marks, 2008, Melzig, 2006). The details of the instrument panel assemblies were not modeled in the FE vehicle model since they were not structural components. Instead, they were added in as a distributed mass. In this study, it was assumed that the weight of the instrument panel carrier was reduced around 4.0 kg and then the added masses were adjusted accordingly.

7.3. Closures

Front fenders

The front fenders are shown in Figure 7.5. The steel material was changed to a modified polyphenylene ether/polyamide resin (PPE/PA) blend (SABIC, 2011b). The original design was

not changed. Instead the thickness was adjusted from 0.76 mm to 2.8 mm, which is a 360 percent increase. However, the weight of the front fenders was reduced from 7.92 kg to 4.38 kg, and thereby had a weight saving of 3.54 kg, which is a 45 percent decrease.



Figure 7.5. Front fenders (denoted by the red color).

Rear window

The rear window is shown in Figure 7.6. The same structure was used as the original, but reinforcements were added around the boundary. The glass material was switched to a polycarbonate plastic (SABIC, 2011a) and the reinforcement was a PBT(or PET)/PC blend (SABIC, 2011c). The weight of the rear window was reduced from 6.5 kg to 3.77 kg, and thereby had a weight saving of 2.73 kg, which is a 42 percent decrease.

Door beams

The original door beams are shown in Figure 7.7(a). BASF redesigned the door beams by changing the original steel material to a 35 percent glass reinforced polyamide (PA6) (BASF, 2011) as shown in Figure 7.7(b). The weight of the door beams was reduced from 8.97 kg to 4.04 kg, and thereby had a weight saving of 4.92 kg, which is a 55 percent decrease.

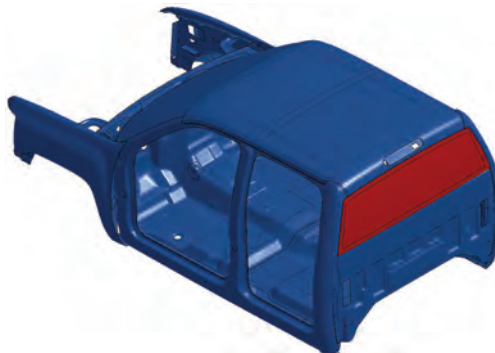


Figure 7.6. Rear window (denoted by the red color).

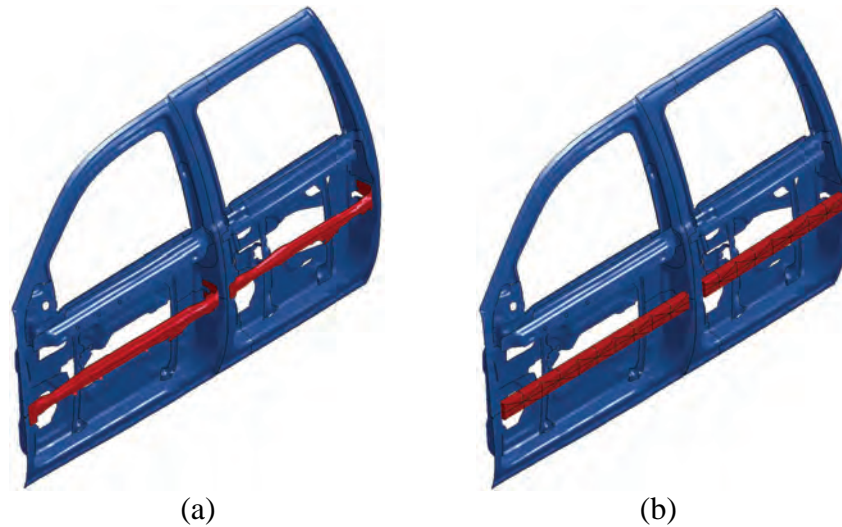


Figure 7.7. Door beams (denoted by the red color): (a) original, (b) new.

Door modules

SABIC suggested that the use of a long glass fiber reinforced polypropylene in door modules applications could reduce some weight (SABIC, 2010). The detail structures of door modules were not modeled in the FE vehicle model. Instead, their weight was added in the model as a point mass. Since the redesigning work of door modules using composite material was extensive, the original added mass was modified. SABIC recommended that, by using a long glass fiber reinforced polypropylene, approximately 0.5 kg per door could be saved (Marks, 2011). The total weight saving is about 2.0 kg.

7.4. Truck bed structure

Bed

The truck bed is shown in Figure 7.8. Actually, Bayer replaced the steel material to a high density structural reaction injection molding (HD-SRIM) for about a 30-percent weight saving (Seagrave, 2003, USDOE, 2001). In this study, the design of truck bed was not changed but its material density was adjusted because the truck bed is not one of the involved structural components in a frontal impact. The weight of the truck bed was reduced from 66.2 kg to 45.74 kg, and thereby had a weight saving of 20.46 kg, which is a 31-percent decrease.

Tailgate

The original tailgate is shown in Figure 7.9(a). SABIC redesigned the tailgate as shown in Figure 7.9(b). The steel material was changed to a long glass fiber reinforced polypropylene (SABIC, 2010), which is used for the middle structure, and a PBT (or PET)/PC blend (SABIC, 2011c), which is used for both cover sheets. The weight of the tailgate was reduced from

19.62 kg to 10.96 kg, and thereby had a weight saving of 8.66 kg, which is a 44-percent decrease.



Figure 7.8. Truck bed (denoted by the red color).

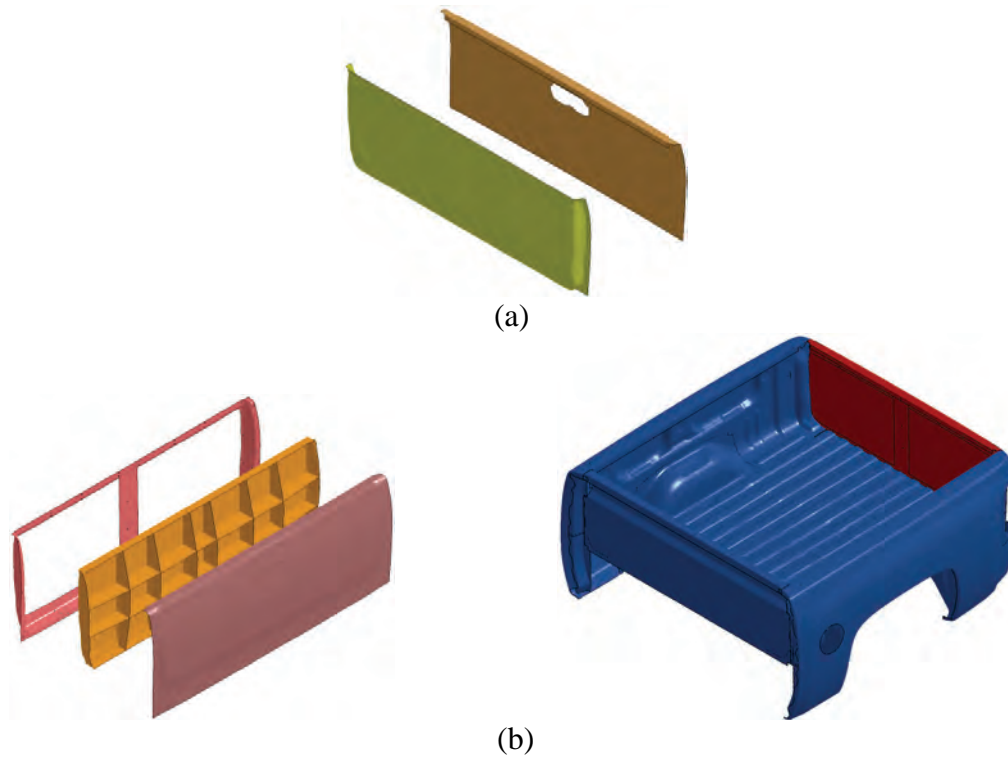


Figure 7.9. Tailgate assembly: (a) original, (b) new.

Rear fenders (truck bed outer panels)

The rear fenders (truck bed outer panels) are shown in Figure 7.10. The steel material was changed to a modified PPE/PA blend (SABIC, 2011b). The original design was not changed. Instead, the thickness was adjusted from 0.94 mm to 3.38 mm, which is the same increment used in the front fenders. Actually, at this time it is difficult for a modified PPE/PA blend to be

adapted for manufacturing wide rear fenders because of material shrinkage or expansion issues during extremes of cold and heat (SABIC, 2006). In this study, however, it is assumed that manufacturing processes could be improved and that the material could be made to meet dimensional specification requirements in the near future. The weight of the rear fenders was reduced from 23.93 kg to 13.09 kg, and thereby had a weight saving of 10.84 kg, which is a 45-percent decrease.



Figure 7.10. Rear fenders (denoted by the red color).

7.5. Power train related

Engine and transmission

Table 7.1 shows the specifications of Silverado. The Silverado has two kinds of engines: the V6 and V8 engines as shown in Figure 7.11. Also, the Silverado has two body styles: the extended cab and crew pickups as shown in Figure 7.12. The FE vehicle model is for the crew pickup with the V8 engine. The vehicle size of all three vehicles listed in Table 7.1 is similar, but there is a weight difference. In the extended cab pickup, there is 84 kg weight difference depending on which engine is adopted. Basically, this weight difference comes from the change of engine, transmission, and connecting assemblies.

In addition, the difference of the gross vehicle weight rating (GVWR) is 182 kg depending on which engine is adopted. This means it would be reasonable to assume that, if the vehicle weight is reduced below 183 kg, the V8 engine can be replaced by the V6 engine.

Table 7.1. Specifications of Silverado

NCAP Test No.	Model	Year	Body Style	Engine Type	GVWR (kg)	Vehicle Weight (kg)	Wheel Base (mm)	Vehicle Length (mm)
6171	SILVERADO	2007	EXTENDED CAB PICKUP	4.3L V6 MPI	2903	2210	3654	5821
6174	SILVERADO	2007	EXTENDED CAB PICKUP	4.8L V8 SFI	3085	2294	3658	5824
6168	SILVERADO	2007	CREW PICKUP	4.8L V8 SFI	3085	2307	3660	5830

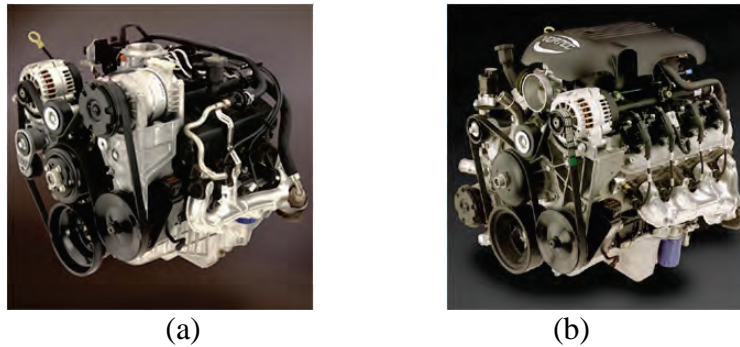


Figure 7.11. Silverado engines: (a) 4.3L V6 MPI, (b) 4.8L V8 SFI.



Figure 7.12. Silverado body styles: (a) extended cab pickup, (b) crew pickup.

In this study, the original V8 engine was replaced by the V6 engine and as a result the total vehicle weight was lighter by over 15 percent of original vehicle weight, which is a decrease of over 350 kg. It was assumed that the engine, transmission, and their assemblies were not changed; but instead the material density was adjusted, although the actual size of V6 and V8 engines are different. Also, it was assumed that even the weight of the V6 engine could be made lighter by using newer technologies and lighter materials, such as aluminum and magnesium. With these assumptions, the substitutions led to a 100kg weight saving in the engine and transmission.

Front-end module

The original front-end module is shown in Figure 7.13(a). SABIC redesigned the front-end module shown in Figure 7.13(b). The original parts of the front bumper assembly were reduced from nine parts to one part. The steel material was changed to a long glass fiber reinforced polypropylene (SABIC, 2010). The weight of the rear bumper was reduced from 13.43 kg to 5.65 kg, and thereby had a weight saving of 7.77 kg, which is a 58-percent decrease.

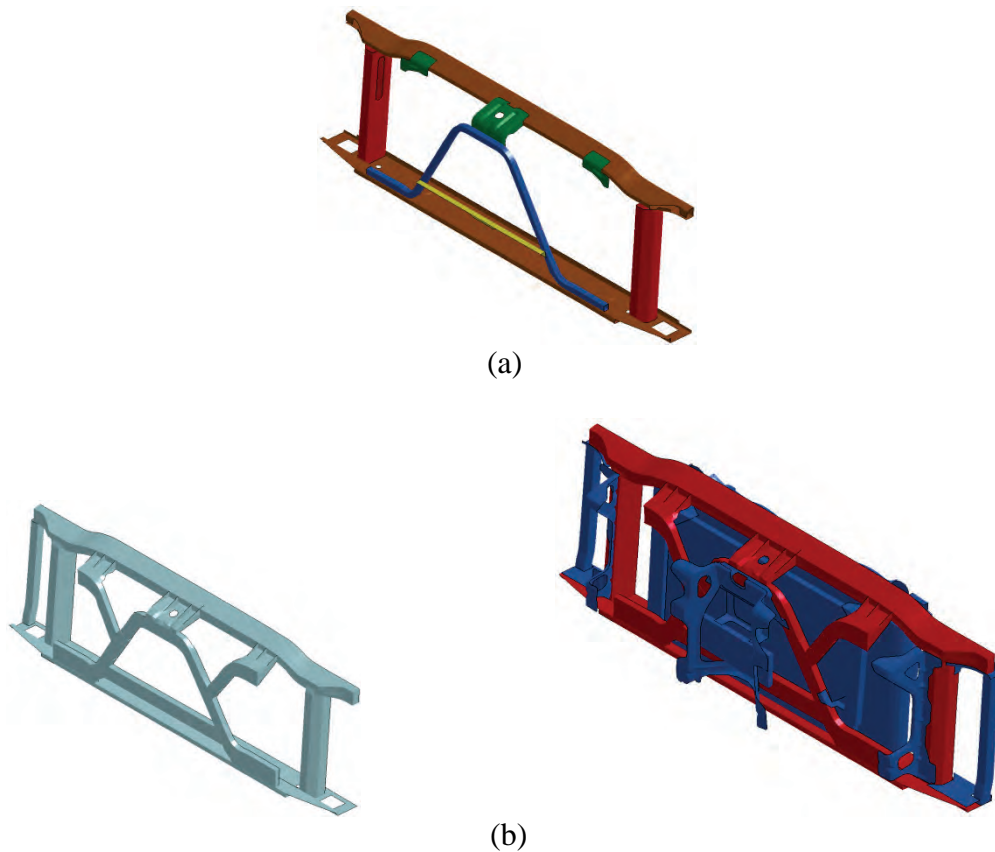


Figure 7.13. Front-end module assembly: (a) original, (b) new.

Battery

In general, the lithium-ion battery is about 65-percent smaller and lighter than a lead-acid battery (Energy Efficiency & Technology, 2011, Lithiummoto, 2011, Motor Sports Newswire, 2011, Porsche, 2009). The weight of the lead-acid battery in the Silverado is 17.39 kg. In this study, it was assumed that the original lead-acid battery could be changed to a lithium-ion battery without changing the design or size. Thus the new weight becomes 7.17 kg, and thereby had a weight saving of 10.76 kg, which is 60-percent decrease.

Oil pans

The engine and transmission oil pans are shown in Figure 7.14. Plastic oil pans have been developed by chemical companies to reduce some weight (Smock, 2009). In this study, the steel oil pans were changed to a 35-percent glass reinforced polyamide (PA6) (BASF, 2011). The total weight of both the engine and transmission oil pans was reduced from 10.46 kg to 5.24 kg, and thereby had a weight saving of 5.22 kg, which is a 50-percent decrease.

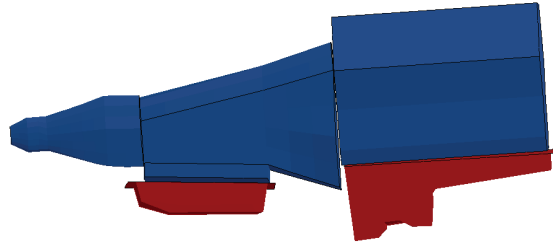


Figure 7.14. Engine and transmission oil pans (denoted by the red color).

Drive shaft and yokes

The drive shaft and yokes are shown in Figure 7.15. Composite materials are used for replacing the steel material to increase performance and to reduce the weight about 40 percent - 60 percent (ACC, 2011a, BAC, 2011, Ogando, 2003, Strongwell, 2011). In this study, the steel material was changed to composite material and the density is adjusted numerically. The total weight of drive shaft and yokes was reduced from 6.37 kg to 2.69 kg, and thereby had a weight saving of 3.69 kg, which is a 58-percent decrease.

Rear differential carrier

The rear differential carrier is shown in Figure 7.16. Magnesium alloys are used for replacing steel components to reduce the weight about 20 percent - 30 percent (Kulekci, 2008, Magnesium, 2011). In this study, it was assumed that the steel material could be changed to a magnesium material, and the density was adjusted numerically. The weight of the rear differential carrier was reduced from 35.19 kg to 26.39 kg, and thereby had a weight saving of 8.8 kg, which is a 25-percent decrease.

Fuel tank

The fuel tank is shown in Figure 7.17. In general, replacing the steel fuel tank to plastic tank can achieve about a 35-percent weight saving (ACC, 2011b). The original material of the fuel tank of Silverado is plastic already. So, no material change was applied.

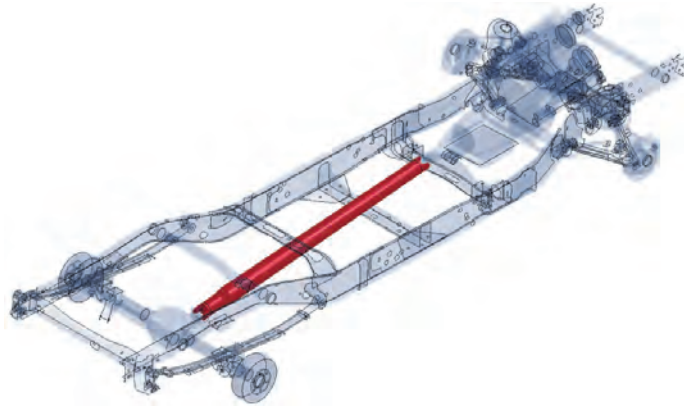


Figure 7.15. Drive shaft and yokes (red color).

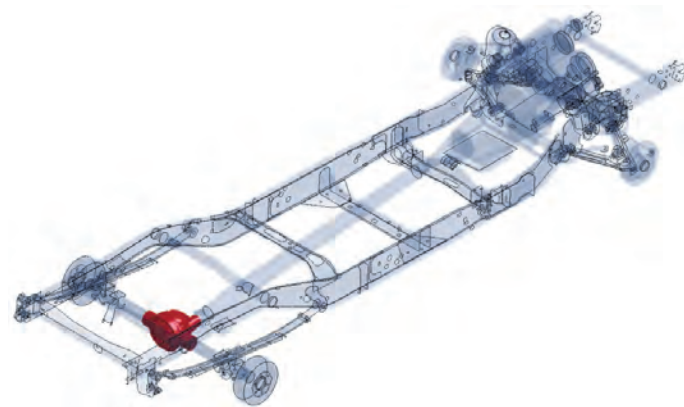


Figure 7.16. Rear differential carrier (denoted by the red color).

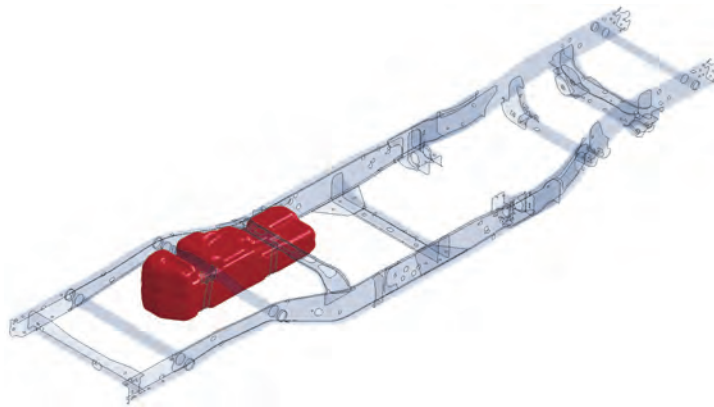


Figure 7.17. Fuel tank (denoted by the red color).

7.6. Suspension related

Wheels

The wheels are shown in Figure 7.18. Steel wheels were used in the original Silverado. In general, the aluminum alloy wheels are about 40-percent lighter than the steel wheels (Langsdorf, 2011). In this study, the steel wheels were changed to aluminum alloy wheels. Since the wheels are basically rigid in a frontal impact, the original wheel design was not changed and only the density of the steel wheel was adjusted numerically. The total weight of all four wheels was reduced from 50.16 kg to 30.09 kg, and thereby had a weight saving of 20.06 kg.

Front brake disks

The front brake disks are shown in Figure 7.19. A carbon-ceramic brake disk is around 50-percent lighter than a standard cast iron brake disk (SGL, 2011). In this study, it was assumed that the weight of brake disks could be reduced 50 percent. The total weight of two frontal brake disks was reduced from 28.77 kg to 14.39 kg, and thereby had a weight saving of 14.39 kg.

Tires

The tires are shown in Figure 7.20. Chemical companies are developing lightweight tires and a 5 percent - 20-percent weight reduction is achieved (DuPont, 2009, ExxonMobil, 2011). In this study, it was assumed that the weight of the tires could be reduced 10 percent. The total weight of all four tires was reduced from 87.49 kg to 78.74 kg, and thereby had a weight saving of 8.75 kg.

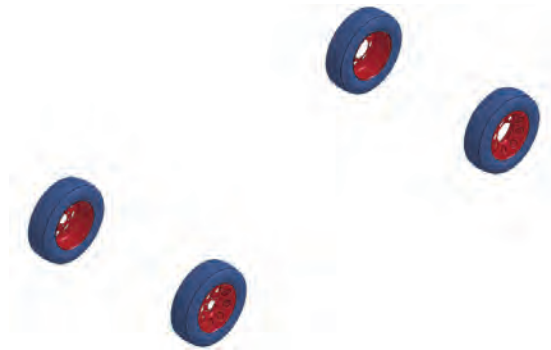


Figure 7.18. Wheels (denoted by the red color).

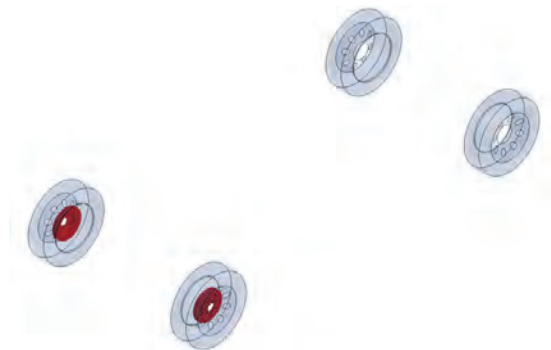


Figure 7.19. Front brake disks (denoted by the red color).

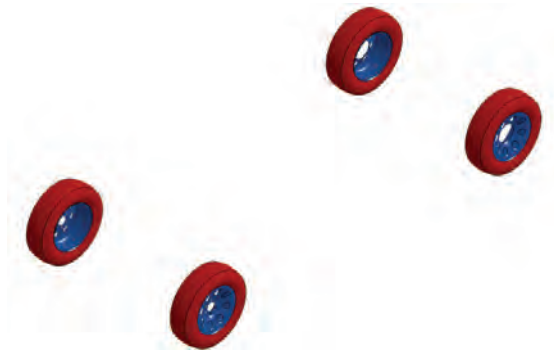


Figure 7.20. Tires (denoted by the red color).

Spare tire and its carrier

The spare tire and its carrier are shown in Figure 7.21. Some automakers replace the spare tire with inflator kits to reduce the vehicle weight (AAA, 2011, Williams, 2011). In this study, the spare tire and its carrier were removed, and thereby had a weight saving of 38.79 kg.

Leaf springs

The leaf springs are shown in Figure 7.22. The weight of a composite leaf spring is 50-percent - 80-percent lighter than the steel leaf spring (Hexcel, 2006, HYPERCO, 2011, Siddaramanna, 2006). Because the rear leaf springs are non-structural components in a frontal impact, it was assumed that the original steel leaf spring could be changed to a composite without changing the design. The material density of the leaf springs was adjusted numerically to save 70 percent of its weight. The total weight of two leaf springs was reduced from 49.62 kg to 14.88 kg, and thereby had a weight saving of 34.73 kg.



Figure 7.21. Spare tire and its carrier (denoted by the red color).

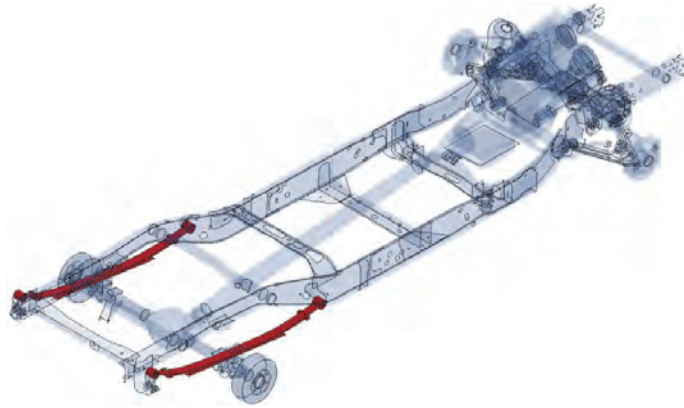


Figure 7.22. Leaf springs (denoted by the red color).

Steering stabilizer links

The steering stabilizer link is shown in Figure 7.23. It is modeled as a beam element. Its steel material was changed to a 35-percent glass reinforced polyamide (PA6) (BASF, 2011). The total weight of the two steering stabilizer links was reduced from 0.36 kg to 0.22 kg, and thereby had a weight saving of 0.14 kg, which is a 40-percent decrease.



Figure 7.23. Steering stabilizer links: (a) actual model, (b) FE model (denoted by the red color).

7.7. Ladder frame structure

Ladder frame

The ladder frame is shown in Figure 6.32. Its original weight was 231.6 kg. Based on the result of material tests and simulations, the steel in side rails was changed to the carbon fiber-thermoset braided composite. The detail material substitution of the ladder frame is described in Chapter 6. The design of the ladder frame was not changed but the thickness of side rails was increased to twice the thickness of the original design in order to have equivalent stiffness and impact performance to the original steel ladder frame. Therefore, the weight of the ladder frame was reduced to 156.8 kg, and thereby had a weight saving of 74.8 kg, which is a 32-percent decrease. If the composite material is applied to cross members and mount supporters and optimal design is adopted, the weight of ladder frame could be reduced more.

Transmission crossbeam

The original transmission crossbeam is shown in Figure 7.24(a). BASF redesigned the transmission crossbeam as shown in Figure 7.24(b). The steel material was changed to a 35-percent glass reinforced polyamide (PA6) (BASF, 2011), which is for the inner structure, and a carbon continuous fiber reinforced thermoplastic (CFRT), which is for the outer covers. The weight of the transmission crossbeam was reduced from 7.9 kg to 3.5 kg, and thereby had a weight saving of 4.4 kg, which is a 56-percent decrease.

Rear bumper

The original rear bumper is shown in Figure 7.25(a). SABIC redesigned the rear bumper as shown in Figure 7.25(b). The original parts of the rear bumper assembly were reduced from six parts to three parts. The steel material was changed to a PBT(or PET)/PC blend (SABIC, 2011c), which is used for the middle structure, and a polypropylene plastic (SABIC, 2011a), which is used for the bumper cover. The insert support is made of steel. The weight of the rear bumper was reduced from 16.07 kg to 9.75 kg, and thereby had a weight saving of 6.32 kg, which is a 39-percent decrease.

Front bumper

The original front bumper is shown in Figure 7.26(a). SABIC redesigned the front bumper as shown in Figure 7.26(b). The original parts of the front bumper assembly were reduced from nine parts to five parts. The steel material was changed to a PBT(or PET)/PC blend (SABIC, 2011c), which is for the deformable crash box, and a polypropylene plastic (SABIC, 2011a), which is for the cover sheet. The insert support is made of steel. The weight of the rear bumper was reduced from 16.31 kg to 8.70 kg, and thereby had a weight saving of 7.61 kg, which is a 47-percent decrease.

Component tests

The front bumper absorbs about 9 percent of impact energy in the frontal NCAP simulation as shown in Figure 5.11. So, it is important to evaluate if the new front bumper can provide the

equivalent crash performance to the original one. Therefore, component tests were conducted to compare their crash performance. Two components tests were performed: a rigid wall test and a pole test. The original front bumper was impacted into the rigid wall and into the pole with a speed of 35 mph. For the new front bumper, the speed was adjusted to 30 mph to take into consideration the lesser crash energy absorption requirements resulting from the vehicle mass reduction. Figure 7.27 shows the rigid wall impact tests and Figure 7.28 shows the pole impact tests. The new front bumper exhibits comparable crash performance in both tests as shown in Figure 7.27(c) and Figure 7.28(c).

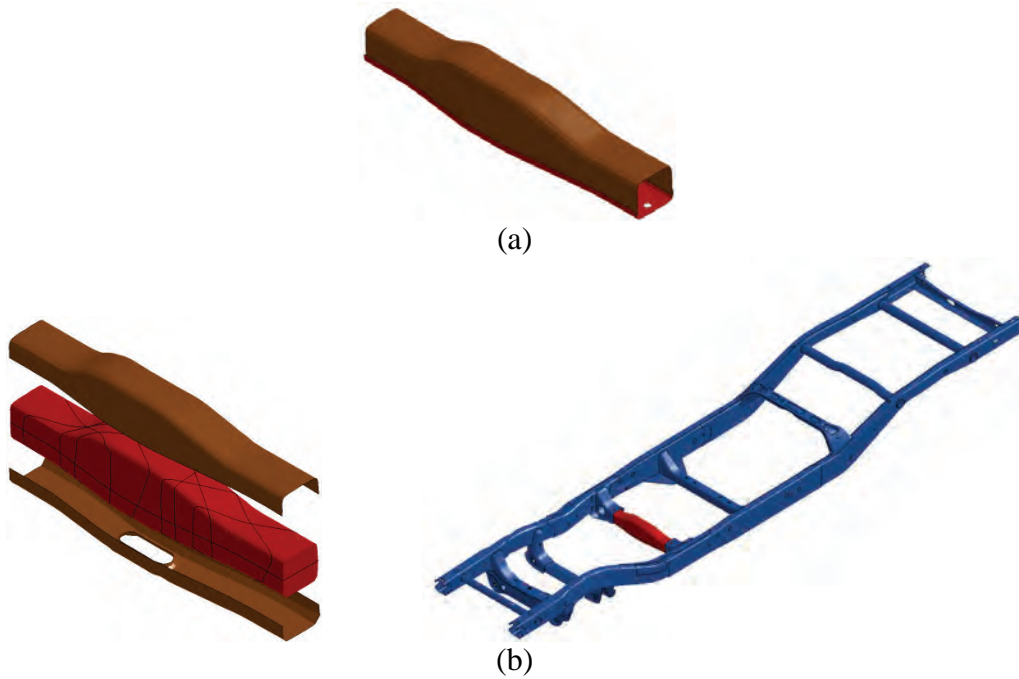
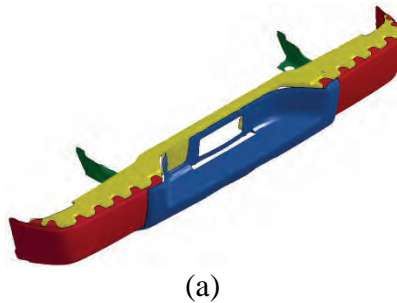


Figure 7.24. Transmission crossbeam assembly: (a) original, (b) new.



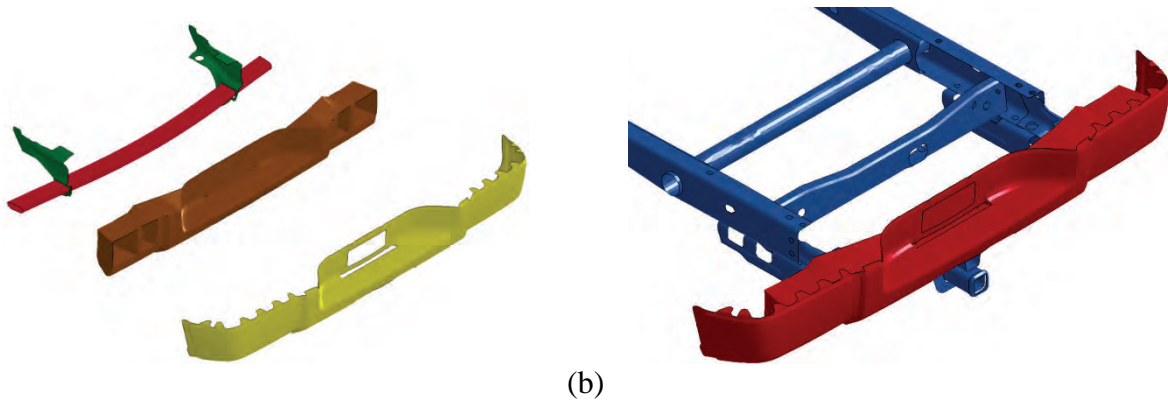


Figure 7.25. Rear bumper assembly: (a) original, (b) new.

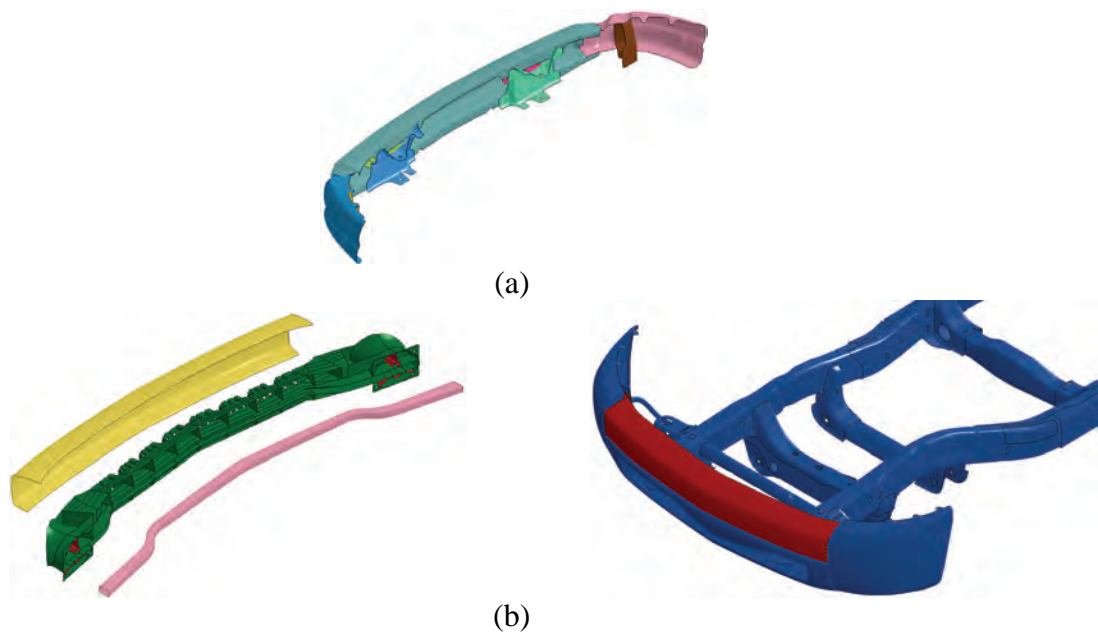
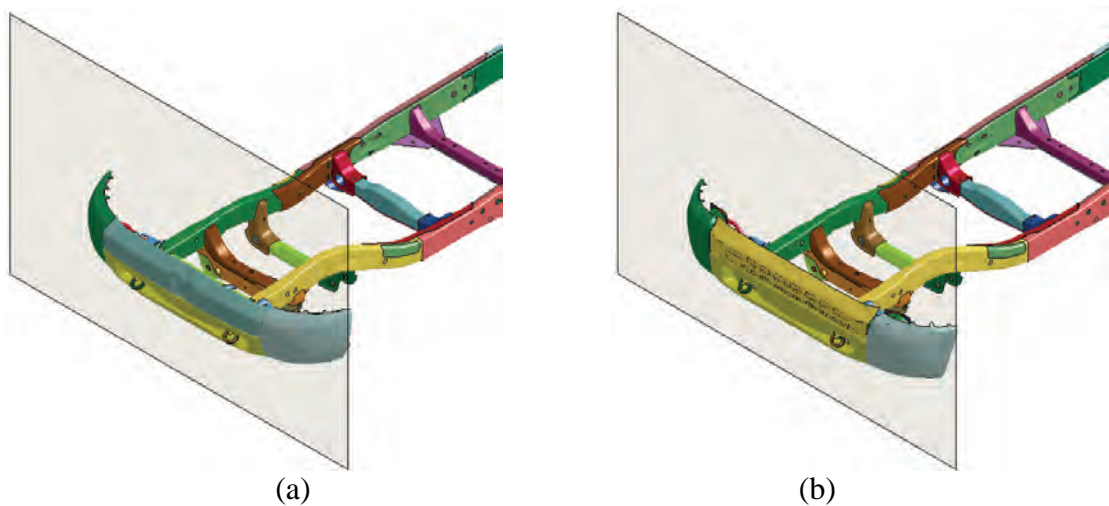
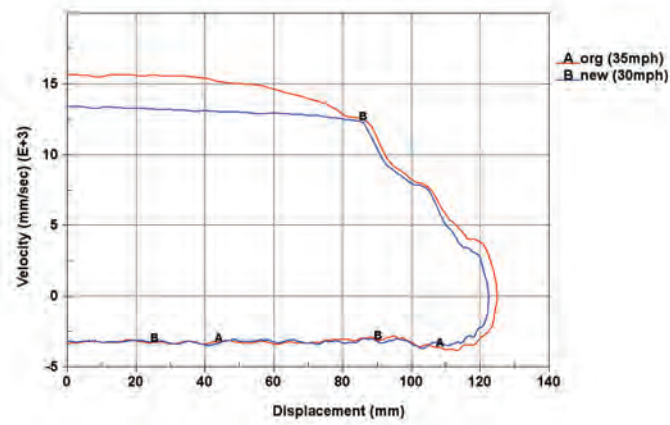


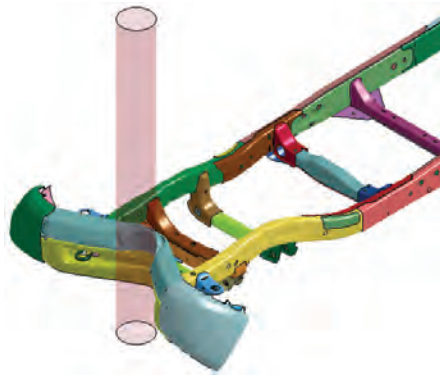
Figure 7.26. Front bumper assembly: (a) original, (b) new.



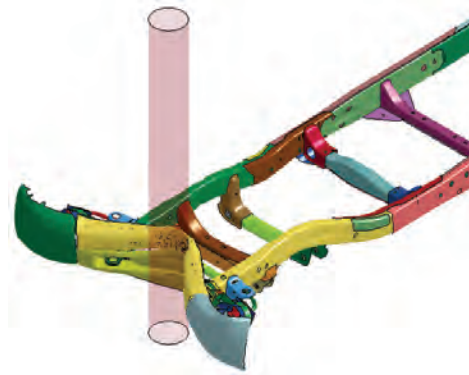


(c)

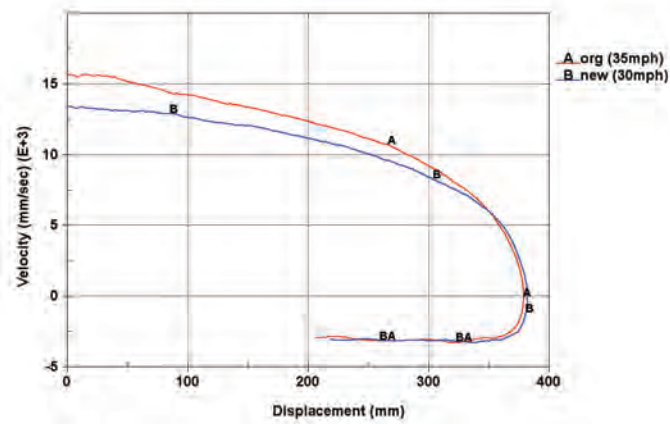
Figure 7.27. Rigid wall tests: (a) original, (b) new, (c) comparison.



(a)



(b)



(c)

Figure 7.28. Pole tests: (a) original, (b) new, (c) comparison.

7.8. Summary

Table 7.2 summarizes all the weight savings described above. The total saving is 432.76 kg which is about 19 percent of the original vehicle weight. Thus, the weight of the lightweight vehicle becomes 1,874.24 kg.

Figure 2.1 shows that today's average U.S. light vehicle contains plastics and composites that account for about 10 percent of the total vehicle weight. Based on this fact, it can be assumed that the weight portion of plastics and composites in the original Silverado is about 10 percent (i.e., about 187.4 kg). Using this assumption, the total weight of plastics and composites in the lightweight vehicle can be obtained by summing up the weight of existing plastics and composites (187.4 kg) and the weight of newly added plastics and composites (254.35 kg). In other words, the lightweight vehicle contains about 441.75 kg of plastics and composites, which is about 23.6 percent of the total lightweight vehicle weight.

Table 7.2. Summary of weight savings

items	old weight (kg)	new weight (kg)	weight saving (%)	saving weight (kg)		
				(using plastics & composites)	(using other materials)	(changing or removing components)
Occupant compartment structure						
roof	20.54	11.72	43%	8.82		
A-pillar				0.20		
B-pillar				1.32		
Interiors						
front seat	50.50	40.50	20%	10.00		
rear seat	44.56	35.66	20%	8.90		
IP retainer				4.10		
Closures						
front fenders	7.92	4.38	45%	3.53		
rear window	6.50	3.77	42%	2.73		
door beams	8.97	4.04	55%	4.92		
door modules				2.00		
Truck bed structure						
bed	66.20	45.74	31%	20.46		
tailgate	19.62	10.96	44%	8.66		
rear fenders	23.93	13.09	45%	10.84		
Power train related						
engine & transmission						100.00
engine oil pan	7.54	3.72	51%	3.82		
transmission oil pan	2.92	1.52	49%	1.43		
drive shaft & yokes	6.37	2.69	58%	3.69		
rear differential carrier	35.19	26.39	25%		8.80	
front-end module	13.43	5.65	58%	7.77		
battery	17.93	7.17	60%			10.76
Suspension related						
wheels (4)	50.16	30.09	40%		20.06	
front brake disks (2)	28.77	14.39	50%	14.39		
tires (4)	87.49	78.74	10%	8.75		
spare tire & carrier	38.79	0.00	100%			38.79
leaf springs (2)	49.62	14.88	70%	34.73		
stabilizer links	0.36	0.22	40%	0.14		
Ladder frame structure						
front bumper	16.31	8.70	47%	7.61		
rear bumper	16.07	9.75	39%	6.32		
transmission crossbeam	7.90	3.50	56%	4.40		
ladder frame	231.60	156.80	32%	74.80		
Vehicle	2307.00	1874.24	19%			
	sub-total saving			254.35	28.86	149.55
	total saving			432.76		

(BLANK)

8. Frontal NCAP Crash Simulations

8.1. Lightweight vehicle configurations

The light-weighted Chevrolet Silverado described in the previous chapter was developed by substituting the original material with lightweight materials, such as plastics and composites. Among all the substituted components in the Silverado, the ladder frame was found to be the primary structural member due to its crash energy absorption role, and therefore its crash safety performance was determined to be of great interest. In order to evaluate the crashworthiness performance of the composite ladder frame, five different light-weight vehicle configurations were investigated as described in Table 8.1.

The first lightweight vehicle configuration, which is referred to as New1, has the new lightweight components with the exception that the original steel ladder frame of the baseline vehicle was retained. The second and third lightweight vehicle configurations, referred to as New2 and New3, have all the new lightweight components including the newly developed lightweight composite ladder frame. The fourth and fifth lightweight vehicle configurations, referred to as New4 and New5, have the original Silverado components, but include the lightweight composite ladder frame. The New2 and New4 configurations use the composite ladder frame but with the frame's wall section thickness doubled; while the New3 and New5 configurations use the composite ladder frame with the frame's wall section thickness tripled. The weight differences for the various vehicle configurations are summarized in Table 8.2. The New2 is the lightest vehicle configuration and its weight is 1,874 kg, which constitutes an 18.8 - percent weight reduction from the baseline vehicle. The movement of the CG from the original location of the baseline vehicle is summarized in Table 8.3. The CG of the New2 configuration moved 20.0 mm toward the front of the vehicle and 11.0 mm in the upward direction.

Table 8.1. Description of lightweight vehicle configurations

Light-weighted vehicles	Description
Baseline (original)	original components + original steel ladder frame
New1	new components + original steel ladder frame
New2	new components + new composite ladder frame (2×t)
New3	new components + new composite ladder frame (3×t)
New4	original components + new composite ladder frame (2×t)
New5	original components + new composite ladder frame (3×t)

Table 8.2. Weight of the various vehicle configurations

	Baseline	New1	New2	New3	New4	New5
Vehicle weight (kg)	2,307	1,949	1,874	1,899	2,232	2,257
Weight reduction (kg)	-	358	433	408	75	50
Weight reduction ratio (%)	-	15.5	18.8	17.7	3.2	2.2

Table 8.3. CG point movement from original location (units: mm)

	New1	New2	New3	New4	New5	Note
Longitudinal direction (x)	22	20	20	-2	-2	Positive movement is toward vehicle front
Horizontal direction (y)	5	5	5	0	0	Positive movement is toward left side of vehicle
Vertical direction (z)	3	11	8	7	4	Positive movement is upward

8.2. Frontal NCAP crash simulations

Frontal NCAP crash simulations of the five lightweight vehicle configurations were performed. The responses and deformations of the lightweight vehicle configurations are compared with those of the baseline vehicle. Figure 8.1 shows the acceleration curves of each of the lightweight vehicle configurations along with that of the baseline vehicle. The notable point in the acceleration curves of the baseline vehicle is a big drop at 27 msec as highlighted in red circle. The baseline vehicle has a large crumple zone which is depicted in the red circle shown in Figure 8.2. During the frontal impact, the steel side rails in the crumple zone are crumpled to absorb impact energy, which results in the big drop in the acceleration curve. In Figure 8.1, the New1 acceleration is close to that of the baseline vehicle. New2 and New4, which have the double wall thickness of the composite side rails, also result in accelerations that are close to the baseline vehicle except they show a higher peak at a later time (after 60 msec) during the crash event. All acceleration curves of the New1, New2, and New4 configurations show the drop at around 27 msec. However, New3 and New5, which have the triple wall thickness of the composite side rails, show a higher peak at around 27 msec.

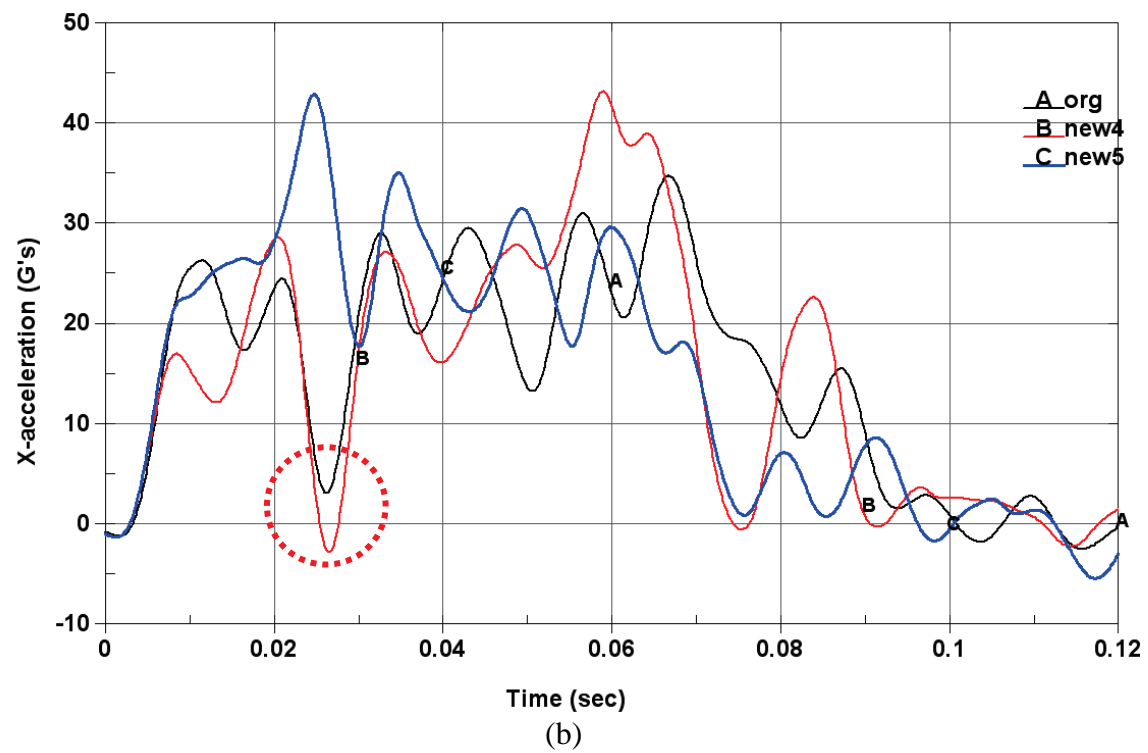
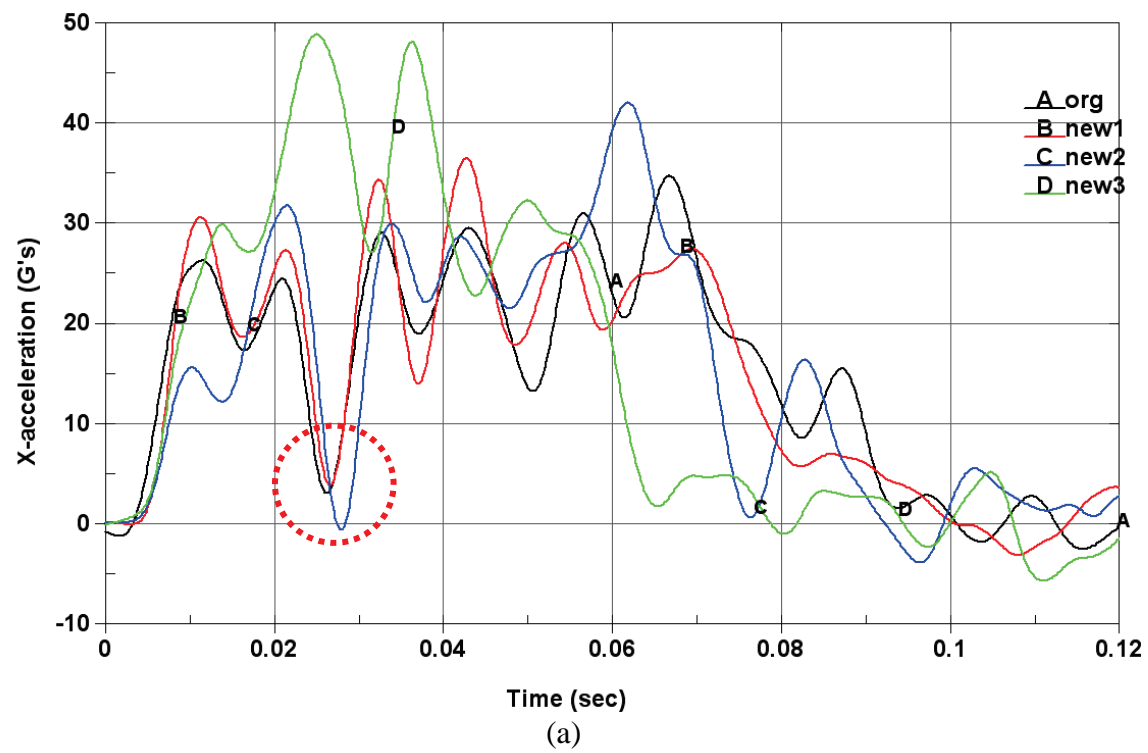


Figure 8.1. Acceleration history of vehicles: (a) New1, New2 and New3, (b) New4 and New5.

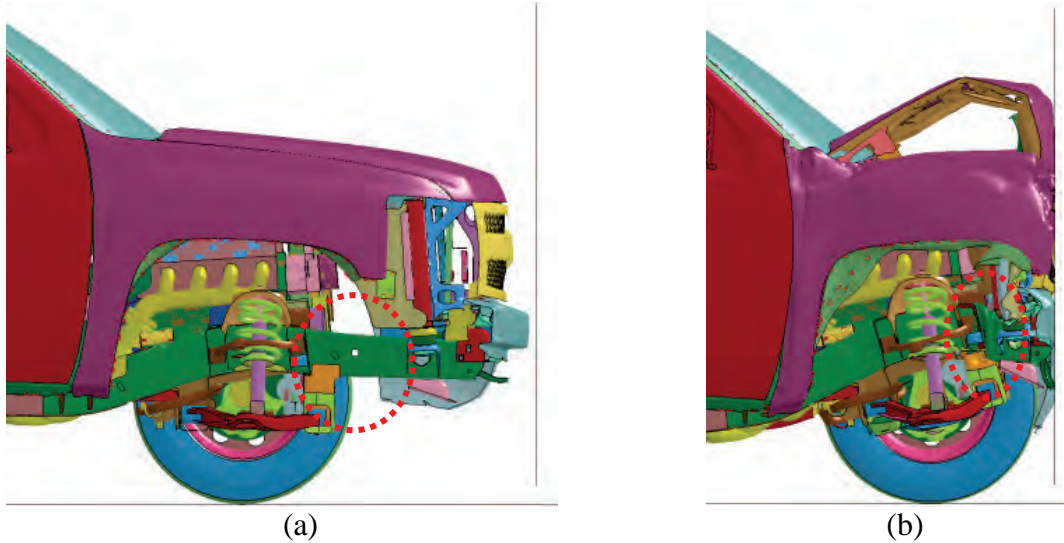


Figure 8.2. Crumple zone of the baseline vehicle (wheel hidden): (a) undeformed, (b) deformed.

Figure 8.3 shows the velocity curves for the various vehicle configurations. The initial speed of the vehicles specified for the crash simulation was 56 km/h (35 mph), which is the specified NCAP speed. All vehicles exhibited a similar rebounding speed, in the range of 4 to 7 km/h. The red circle in Figure 8.3 highlights the vehicle responses that occurred during the crumple zone deformation. The New1, New2 and New4 vehicle configurations show the similar slopes of the velocity curves in Figure 8.3(a). The New3 and New5 configurations show somewhat steeper slopes. Figure 8.3(b) show the velocity curves versus displacement. New2 shows a similar velocity-crush response as the baseline vehicle. The New1 configuration exhibited a little less crush while the New4 configuration has a little more crush than the baseline vehicle. The New3 and New5 configurations exhibited much less crush than the baseline vehicle.

Figure 8.4 shows the wall force curves. It can be seen that the force curve of the baseline vehicle has five peaks within a certain force range. This less variable force profile is desirable because it is indicative of a controlled and gradual absorption of impact energy by the vehicle structure, especially by the ladder frame. New1 shows a similar force curve and most of the peaks are smaller than those for the baseline vehicle. This is explained by the facts that the vehicle mass is reduced and the steel ladder frame is used. New2 has two peaks in the force curve and those peak values are not much different. New4 also has two peaks but the second peak is very high relative to the other. In general, this excessive high peak force before rebounding is indicative that the energy absorbing capability of the frontal structure, especially the composite ladder frame, bottomed out and resulted in an impact of the engine to the firewall. This was probably due to the fact that the composite ladder frame was not re-designed optimally to absorb the impact energy gradually. Nevertheless, the twice thickness of the composite ladder frame in New2, which is the lightest vehicle configuration, relatively well-managed the impact energy without any high peak. New3 and New5, which have the triple wall thickness of the composite ladder frame, show one high peak in wall force curve at an early time (25 msec). That is, the triple wall thickness of the composite ladder frame might be too stiff to provide a gradual absorption of the impact energy.

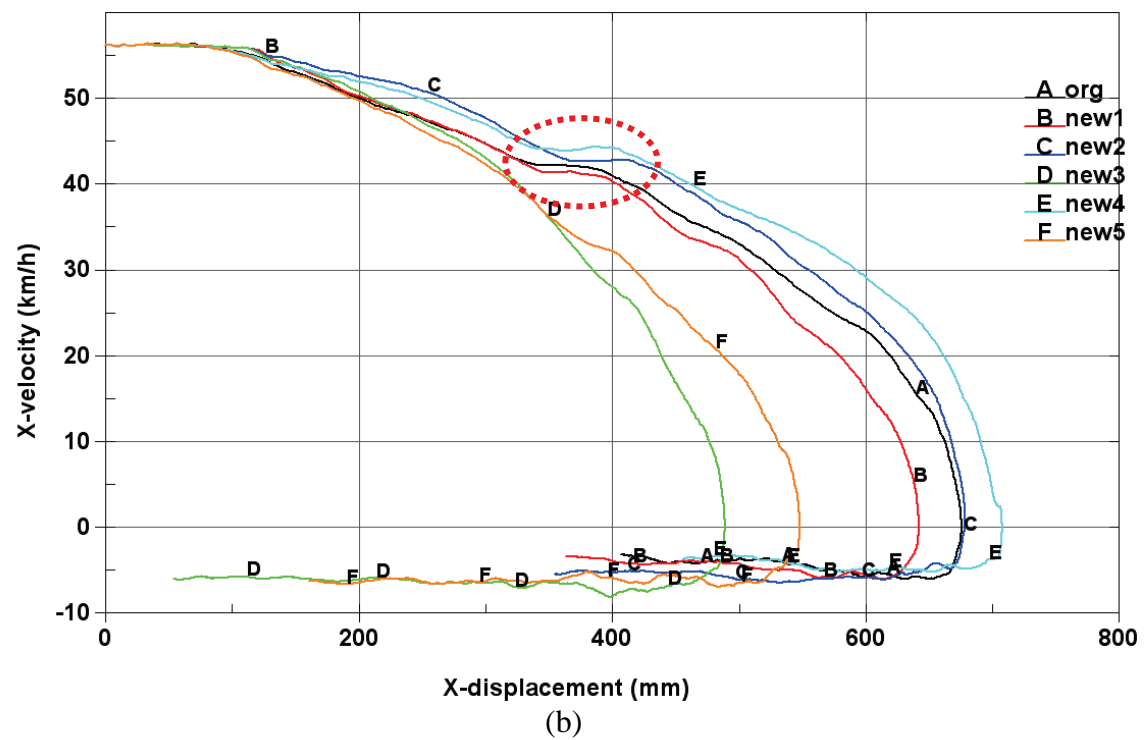
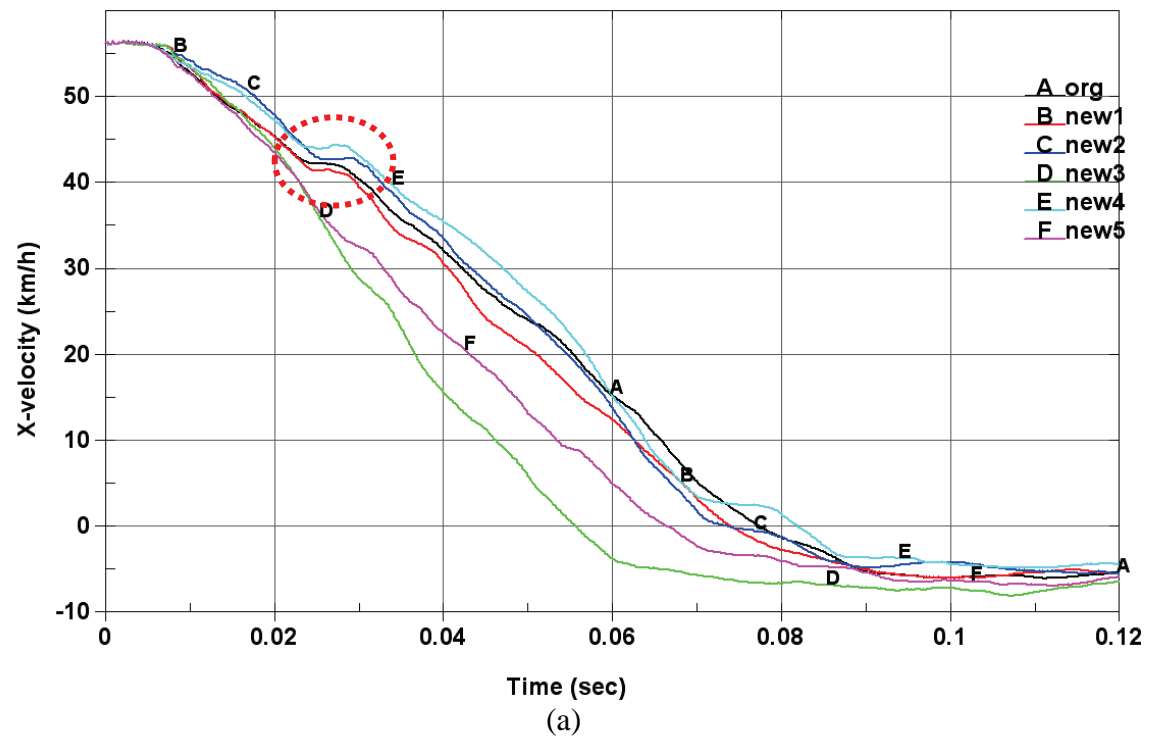


Figure 8.3. Velocity history of vehicles: (a) versus time, (b) versus displacement.

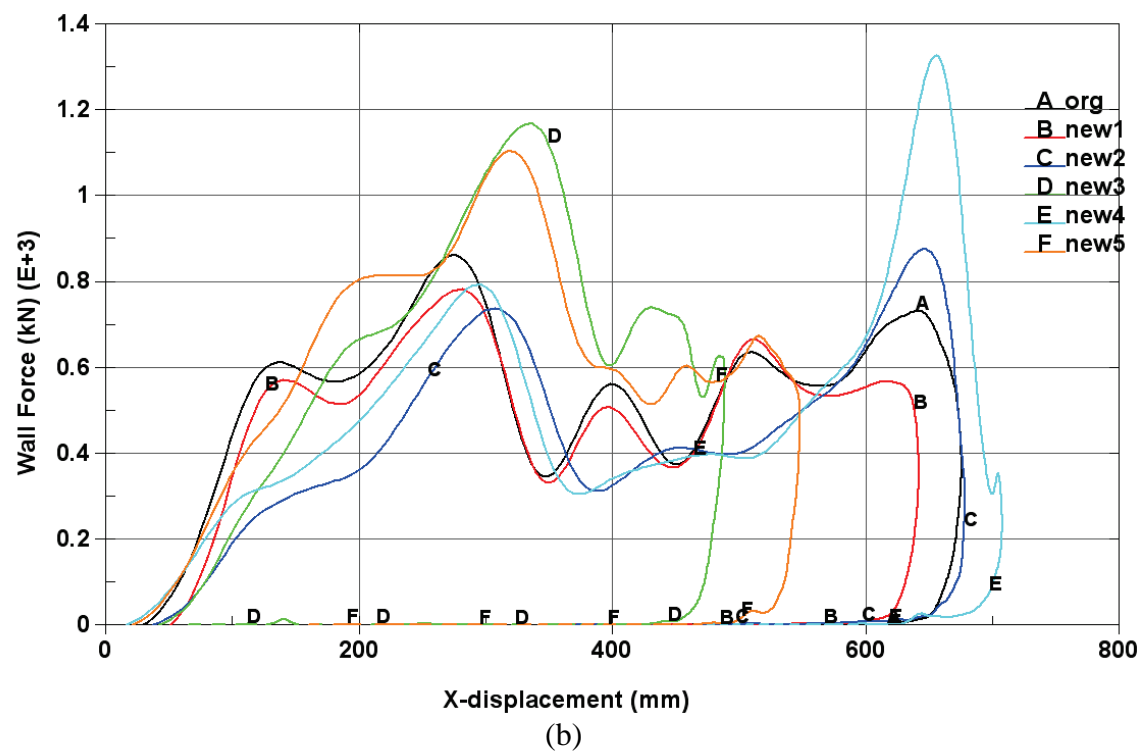
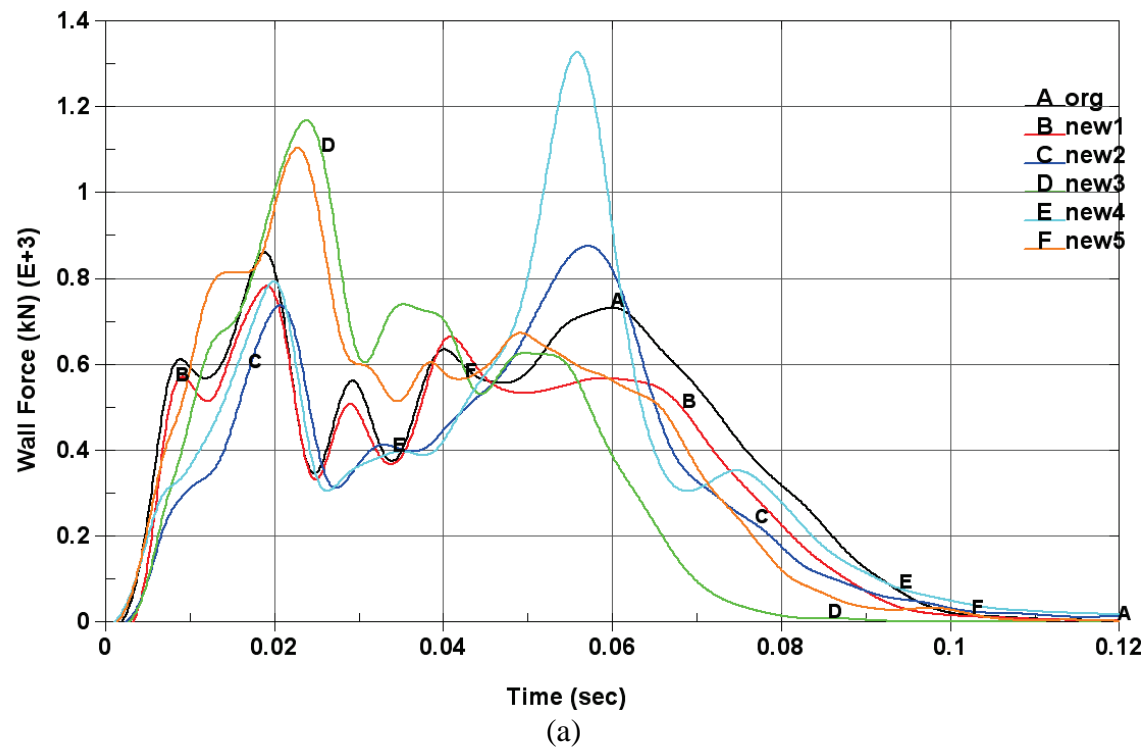


Figure 8.4. Force history for rigid wall: (a) versus time, (b) versus displacement. Table 8.4 summarizes the single response values of various vehicle configurations. In terms of the maximum crush, the New1 vehicle configuration has less maximum crush than the baseline vehicle and the New2 configuration demonstrated similar maximum crush as the baseline

vehicle. The New3 and New5 vehicle configurations exhibited quite small maximum crush values. Especially, the New4 configuration has the largest level. In terms of the maximum acceleration, the New1 vehicle configuration exhibited a similar peak as the baseline vehicle, and the New3 vehicle achieved the overall highest peak. The New2, New4, and New5 vehicle configurations exhibited similar maximum accelerations that were higher than the baseline vehicle's maximum acceleration.

The vehicle stiffnesses, i.e., the crush-work stiffness (K_{W400}) (Mohan, 2007) and the global energy-equivalent stiffness (K_E) (Nusholtz, 2005), were calculated using the wall force curves as shown in Figure 8.4(b). The New1, New2, and New4 vehicle configurations are softer than the baseline vehicle. Above all, the New2 vehicle configuration is the softest. On the other hand, the New3 and New5 vehicle configurations are stiffer than the original. The New4 configuration is the stiffest with respect to K_E and the New5 configurations is the stiffest with respect to K_{W400} .

Table 8.4. Summary of vehicle responses

Vehicle	Org	New1	New2	New3	New4	New5
Maximum X-crush (mm)	675.8	642.1	678.7	489.0	707.9	548.2
Maximum X-acceleration (G's)	36.5	36.7	42.2	49.2	43.5	43
K_{W400} (MPa)	2413.4	2180.8	1768.2	2869.8	1993.2	3043.0
K_E (MPa)	1530.8	1453.2	1255.8	2404.6	1368.6	2189.5

As shown in Figure 8.5, the intrusions at the fifteen cross-points of five Y-lines and three Z-lines were measured at the end of the simulation time. Only the driver-side intrusion was investigated. Z1 was located 100 mm above the vehicle floor. The horizontal and vertical intrusion profiles are shown in Figures 8.6 through 8.8.

Figure 8.6 shows that the X-intrusions of the New1 vehicle configuration is smaller than those of the baseline, but the Z-intrusions of the New1 configuration are close to those of the baseline vehicle. Figure 8.7 shows the intrusions of the New2 and New3 vehicle configurations. The New2 configuration has smaller intrusions in both the X- and Z-directions. The New3 configuration has similar X-intrusions, but larger Z-intrusions. The New3 configuration shows the smallest maximum crush, which means the composite ladder frame did not absorb enough of the kinetic energy of the vehicle to reduce the inertia force on the front body (i.e., occupant compartment structure and closures). So, the remaining inertia force induces the forward-down movement of the front body. In addition, the crashed composite front-end module does not provide enough support of the shotgun structures to prevent the rotational motion of the front body. These movements led to the large Z-intrusion. The crash of the composite front-end module led to the large Z-intrusions of the New1 configuration as well.

Figure 8.8 shows the intrusions of the New4 and New5 vehicle configurations. The New4 configuration shows similar X-intrusions and smaller Z-intrusions as the baseline vehicle. The New5 configuration shows very small intrusions. Even though the New3 and New5 vehicle configurations show similarly small levels of maximum crush, the New5 configuration has the

original steel front-end module which deformed but did not fail during impact test and thereby kept supporting the shotgun structure and prevented the rotational motion of the front body.

Figures 8.9 through 8.26 show the deformations of the baseline vehicle and the various vehicle configurations. The deformation of the baseline vehicle is shown in Figures 8.9 to 8.11. The folding mode of the steel ladder frame is observed. The deformation of the steel ladder frame reaches a level that is behind the engine. The deformation of New1 vehicle configuration is shown in Figures 8.12 to 8.14. The deformation of the New1 configuration, which has the original steel ladder frame, is very similar to that of the baseline vehicle.

The deformation of the New2 vehicle configuration is shown in Figures 8.15 to 8.17. The fracture mode of the composite ladder frame can be observed. The bending fracture of the composite side rails occurs at around the transmission crossbeam. The deformation of the New4 vehicle configuration shown in Figures 8.21 to 8.23 is very close to that of the New2 configuration. The deformation of New3 vehicle configuration is shown in Figures 8.18 to 8.20. Recall that the New3 configuration has the composite ladder frame with the triple wall thickness. The fracture of the composite ladder frame of the New3 configuration reaches to a location in the area around the front-end module mounts. The deformation of the New5 vehicle configuration shown in Figures 8.24 to 8.26 is also very close to that of the New3 configuration.

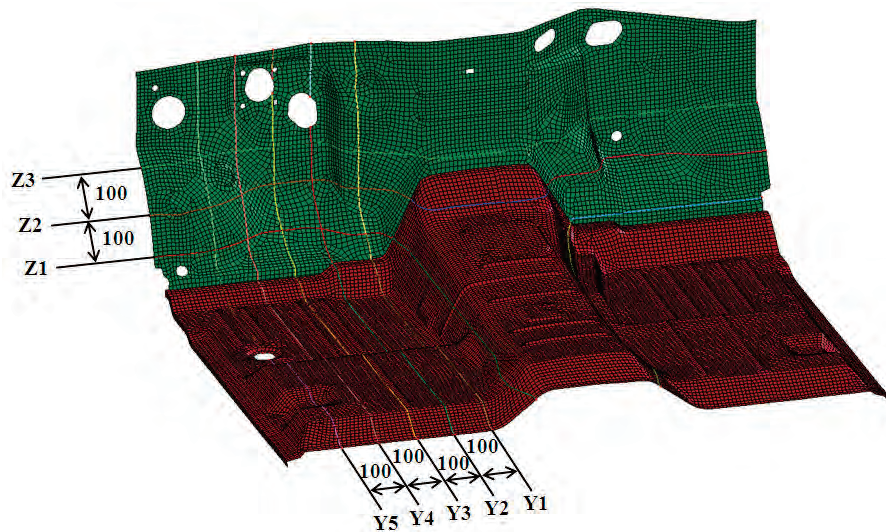


Figure 8.5. Measurement points of vehicle intrusion (unit: mm).

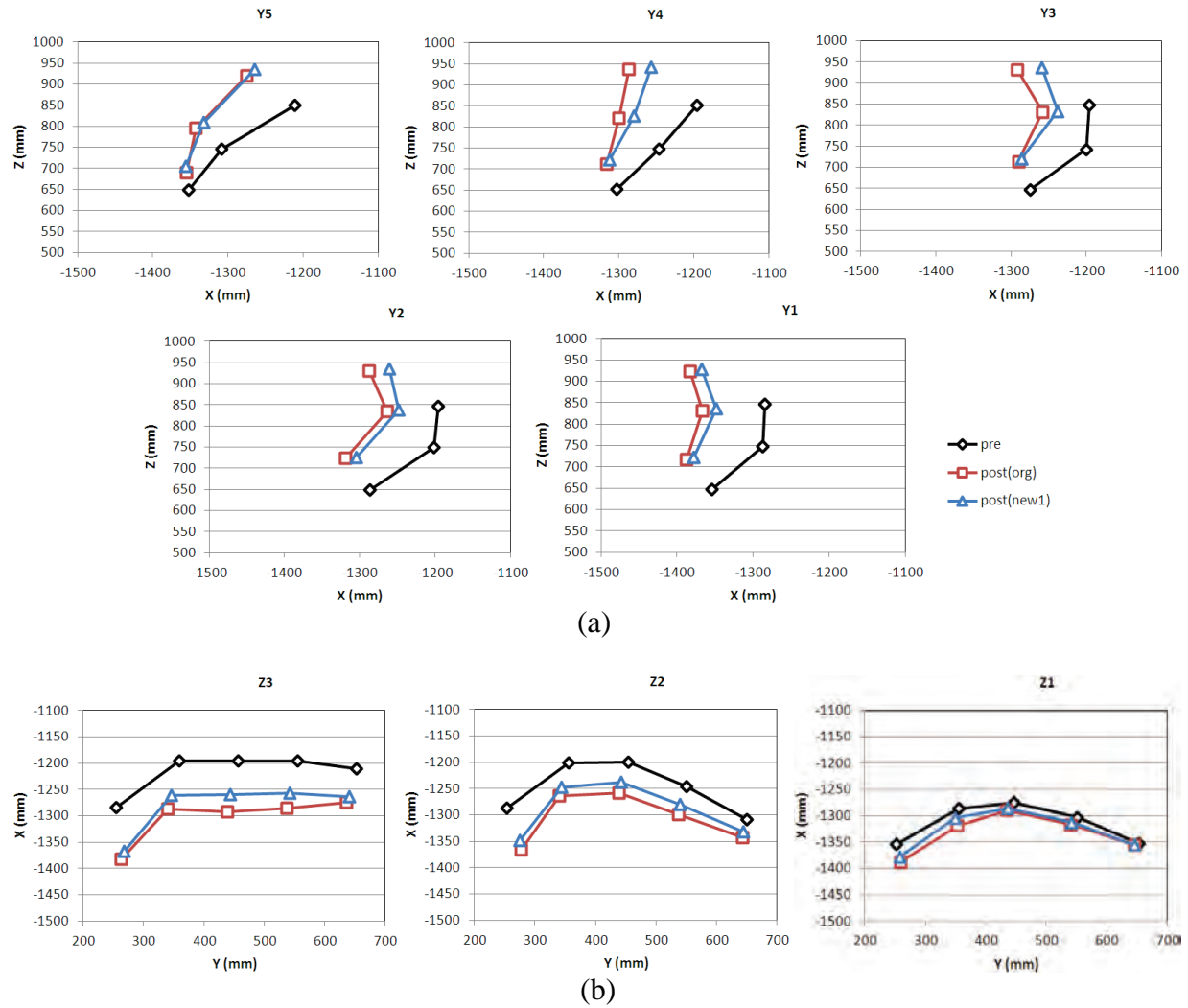


Figure 8.6. Vehicle intrusions of the New1 vehicle configuration: (a) vertical profile, (b) horizontal profile.

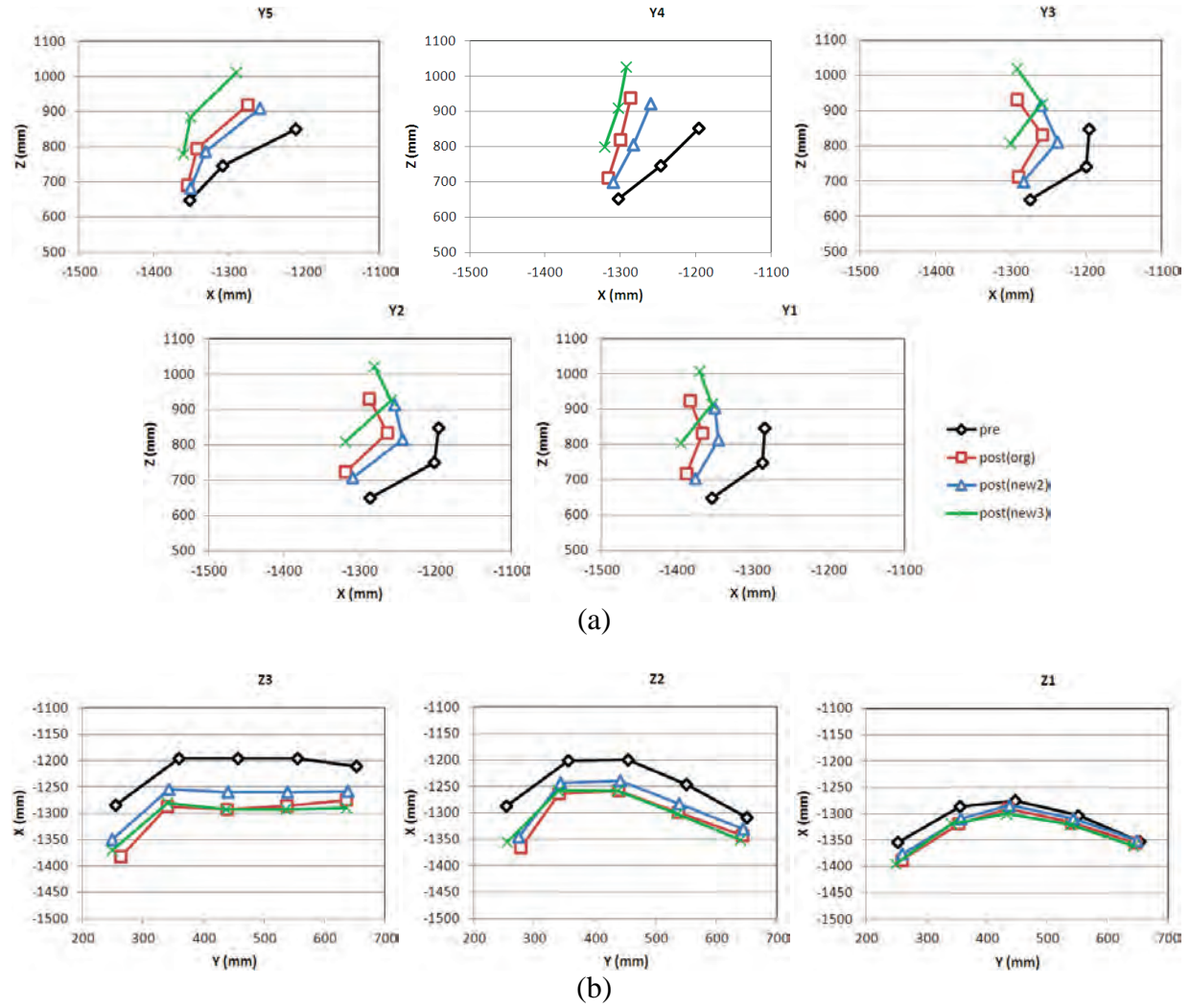
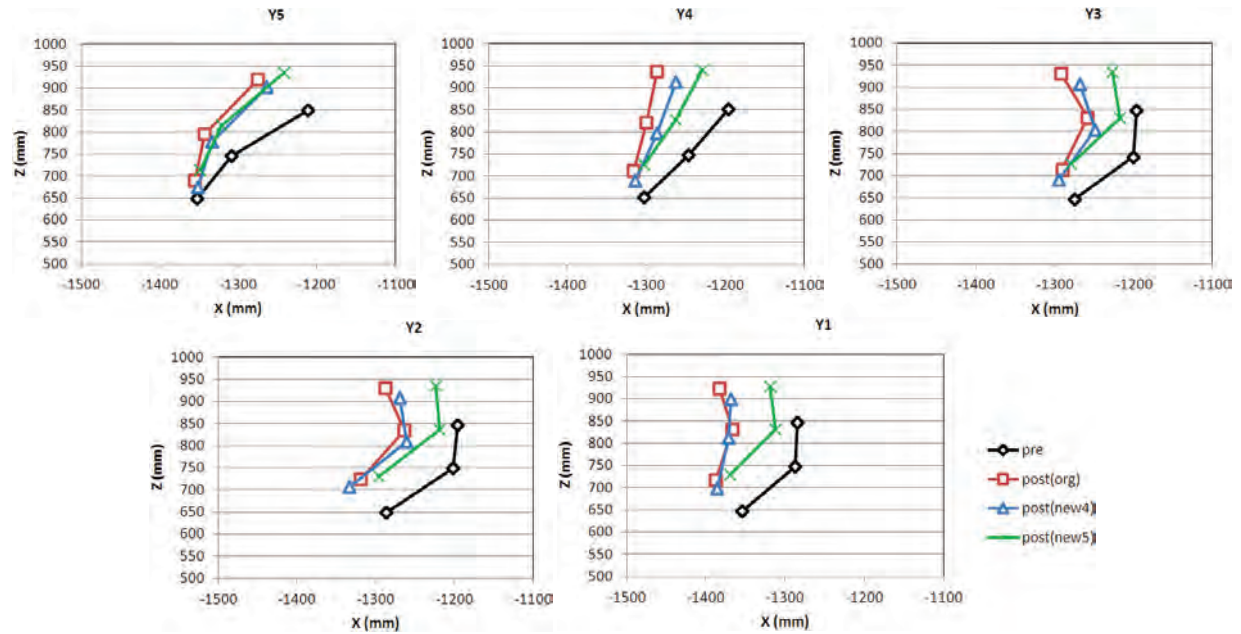
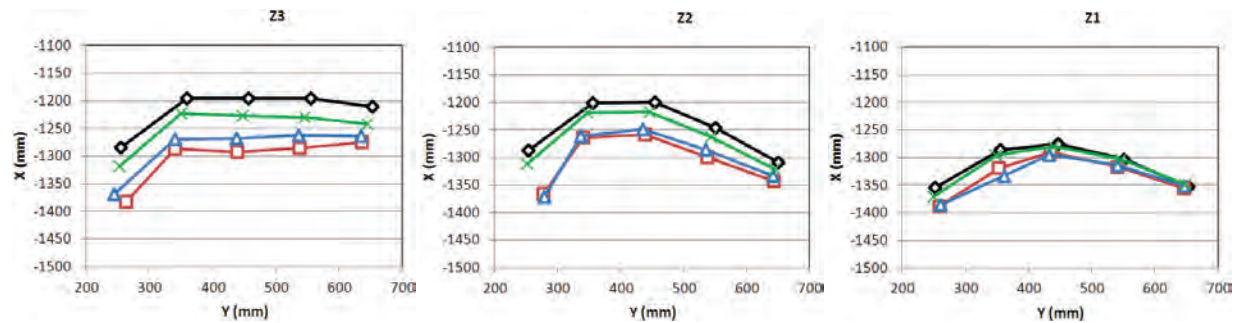


Figure 8.7. Vehicle intrusions of the New2 and New3 vehicle configuration: (a) vertical profile, (b) horizontal profile.



(a)



(b)

Figure 8.8. Vehicle intrusions of the New4 and New5 vehicle configuration: (a) vertical profile, (b) horizontal profile.

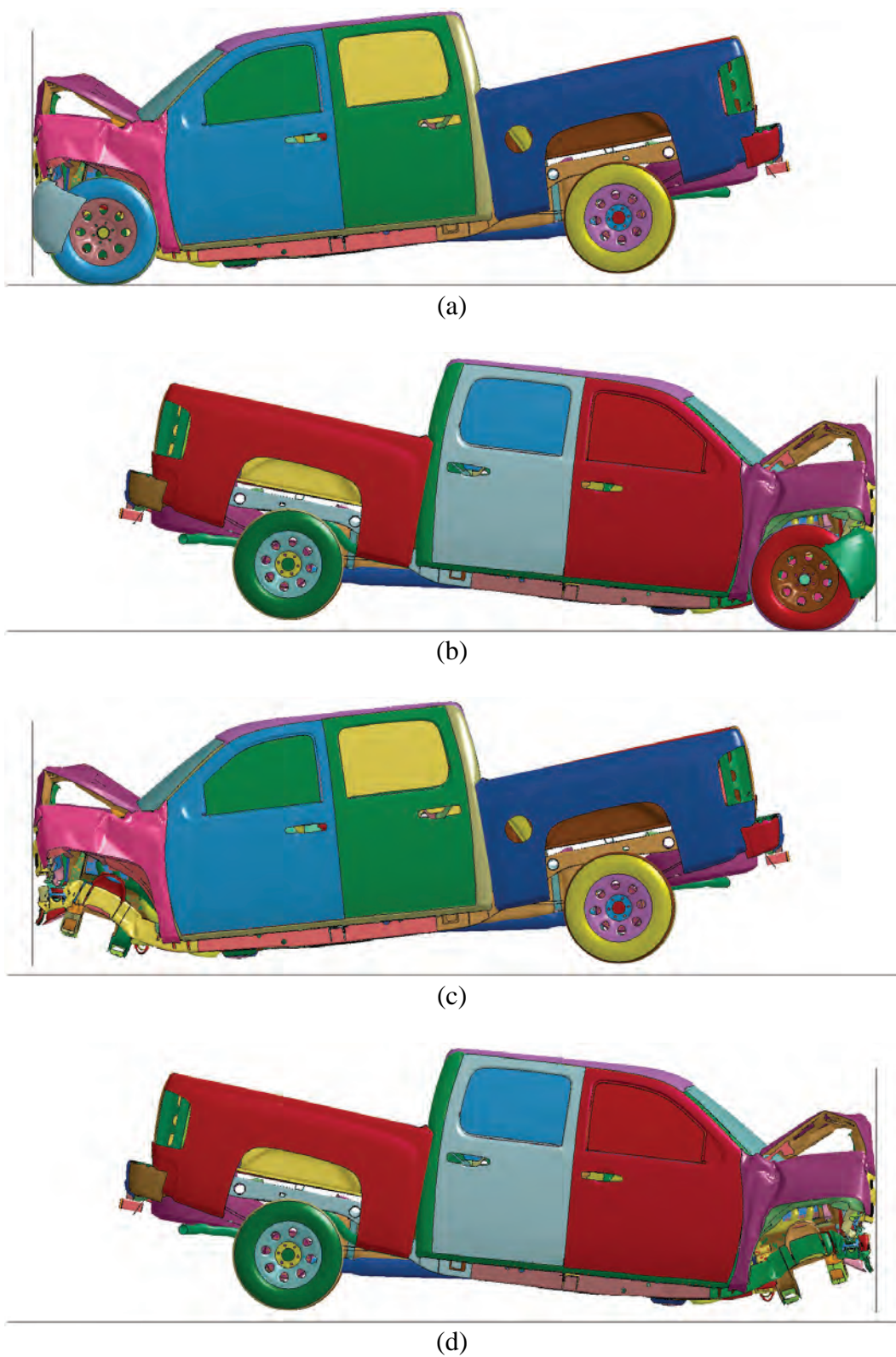
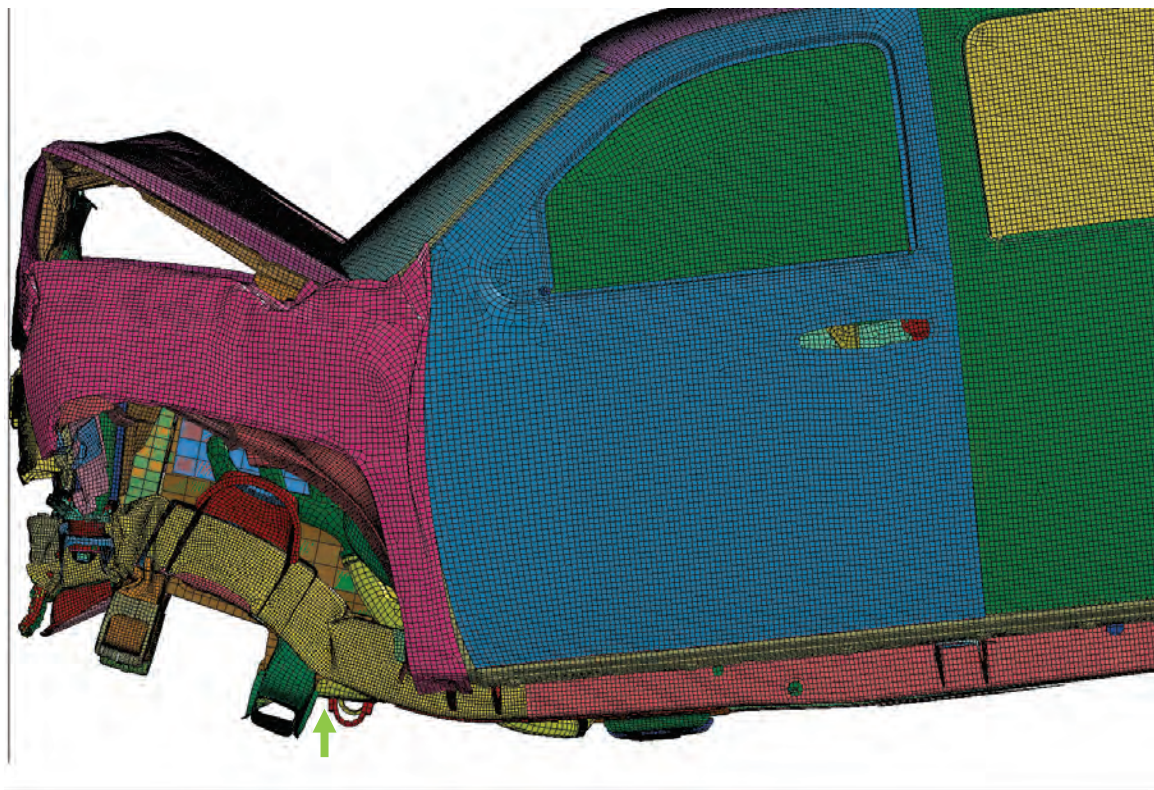
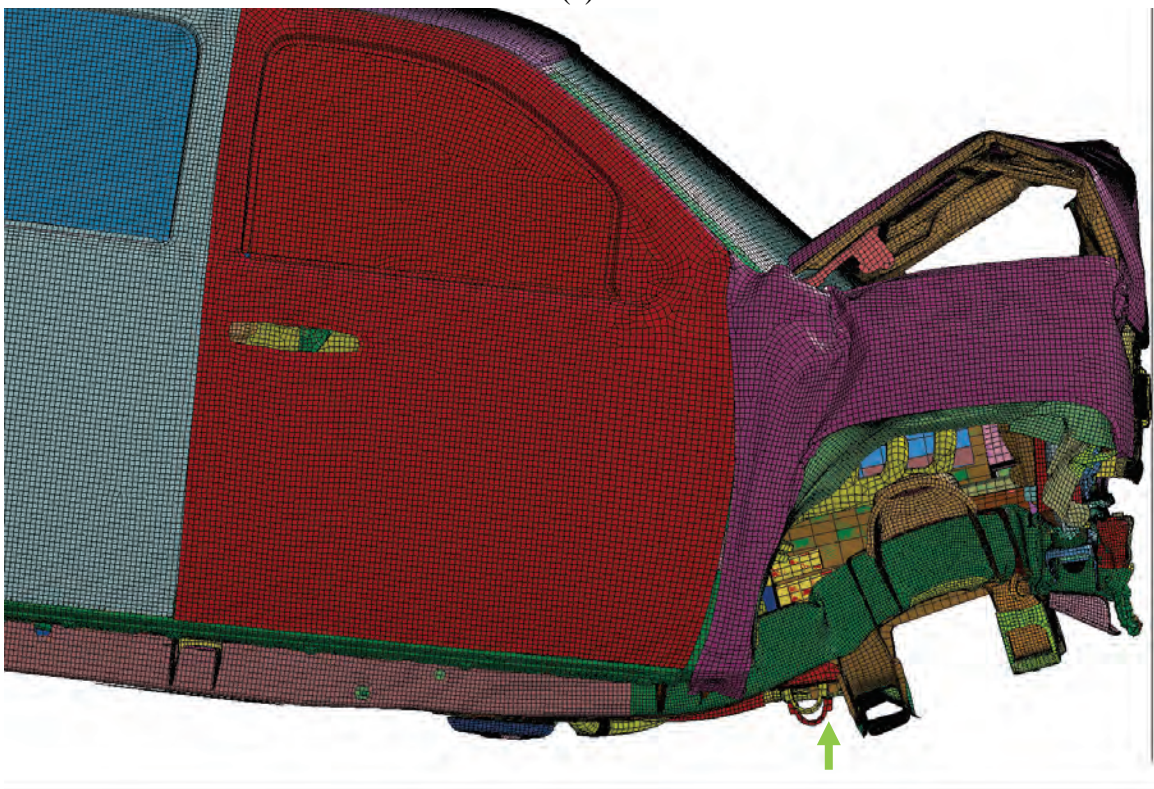


Figure 8.9. Deformation of baseline vehicle.

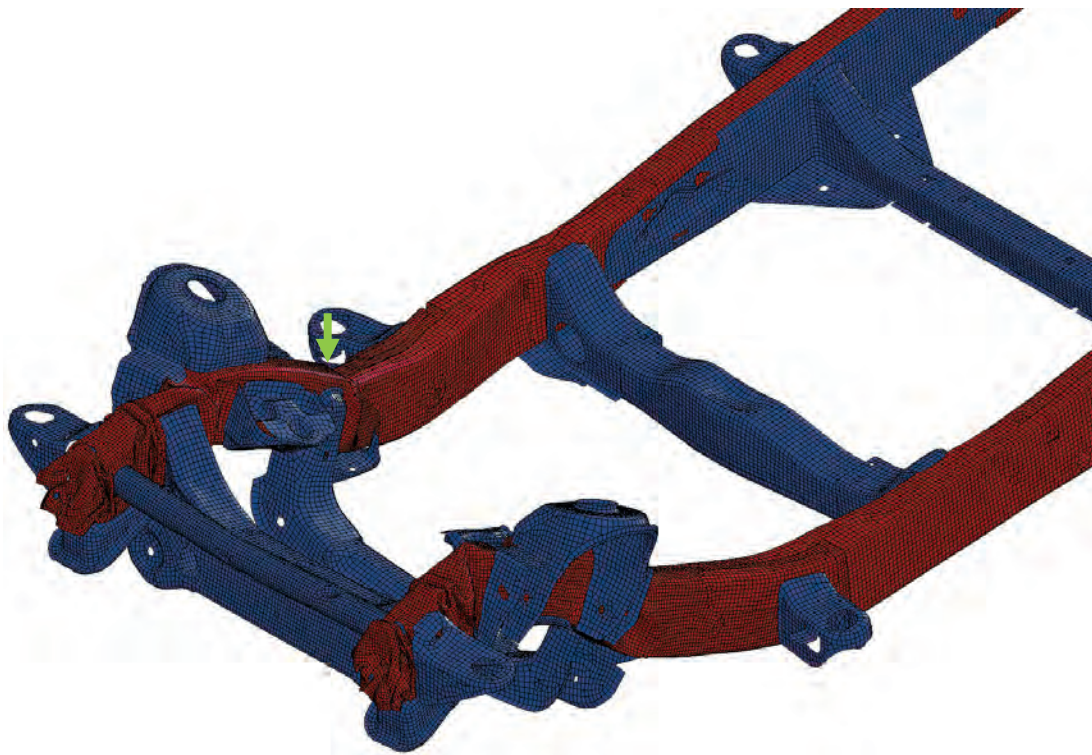


(a)

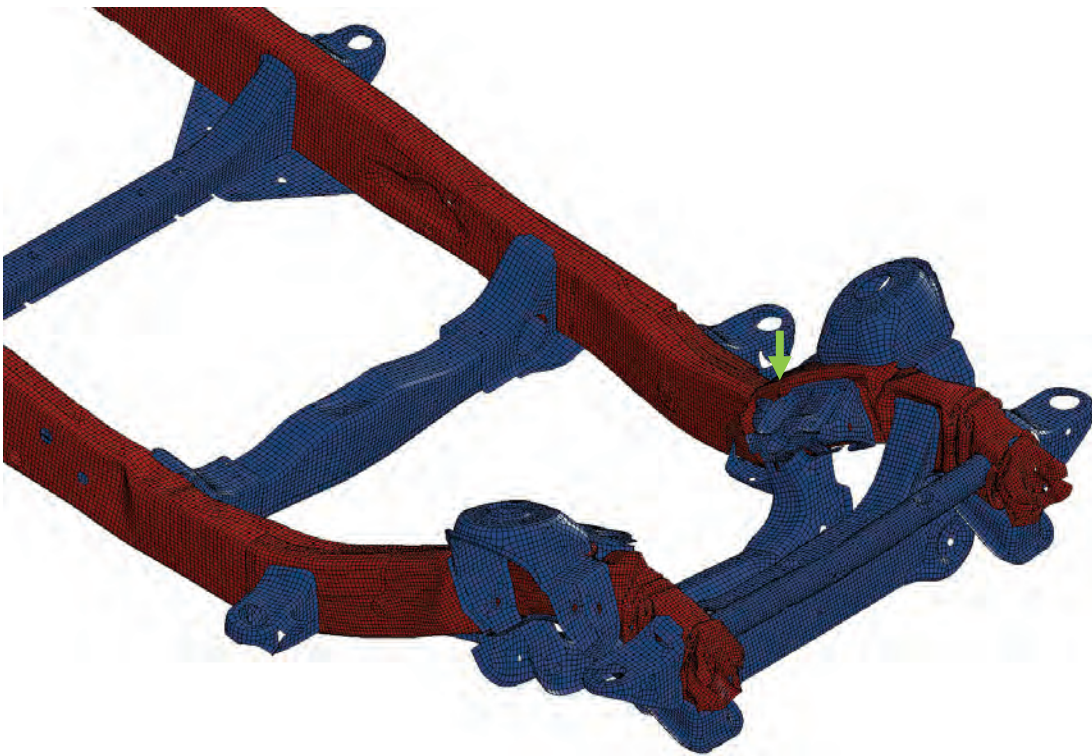


(b)

Figure 8.10. Deformation of baseline vehicle (frontal area, wheel hidden).



(a)



(b)

Figure 8.11. Deformation of steel ladder frame of baseline vehicle.

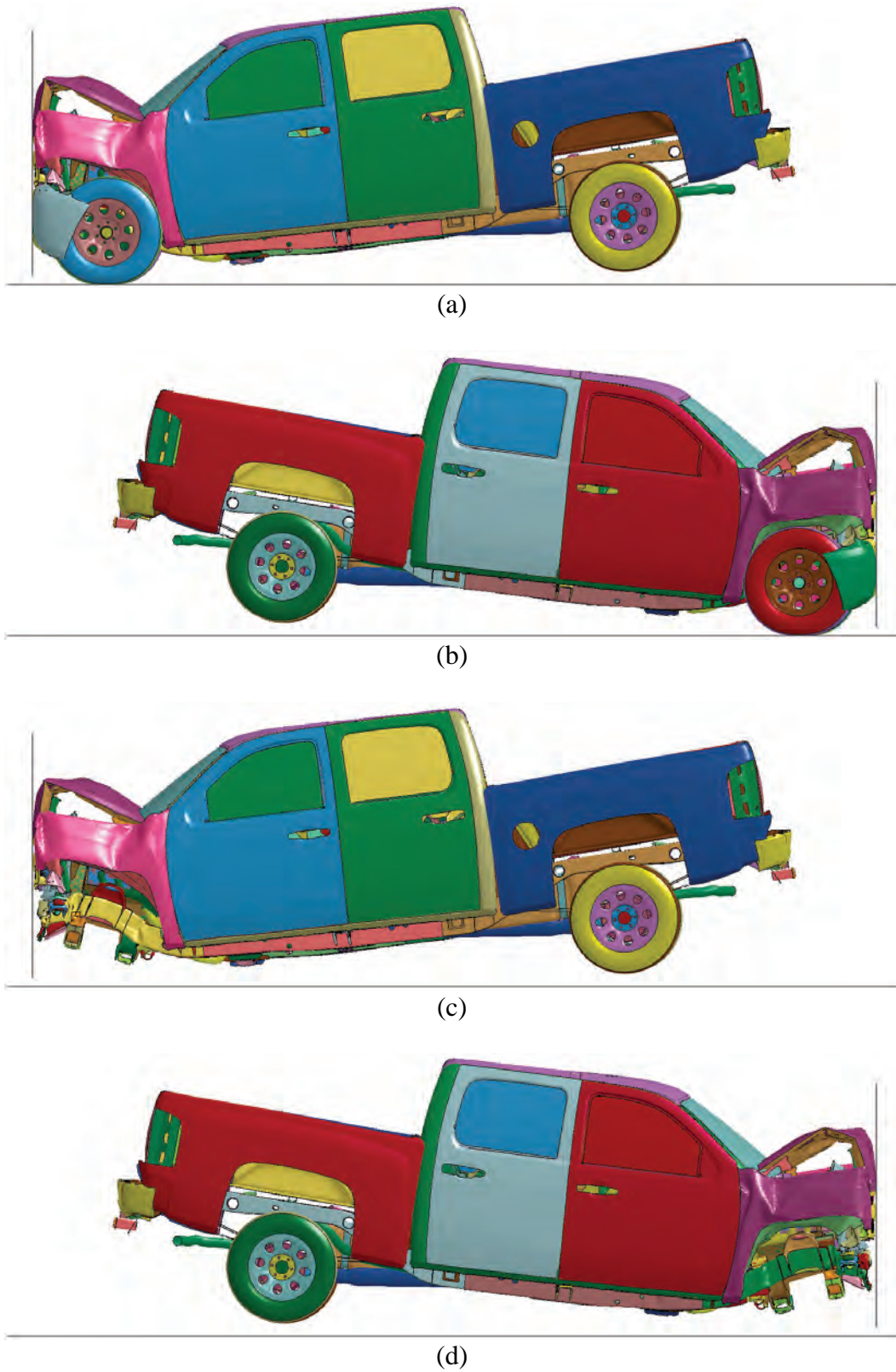
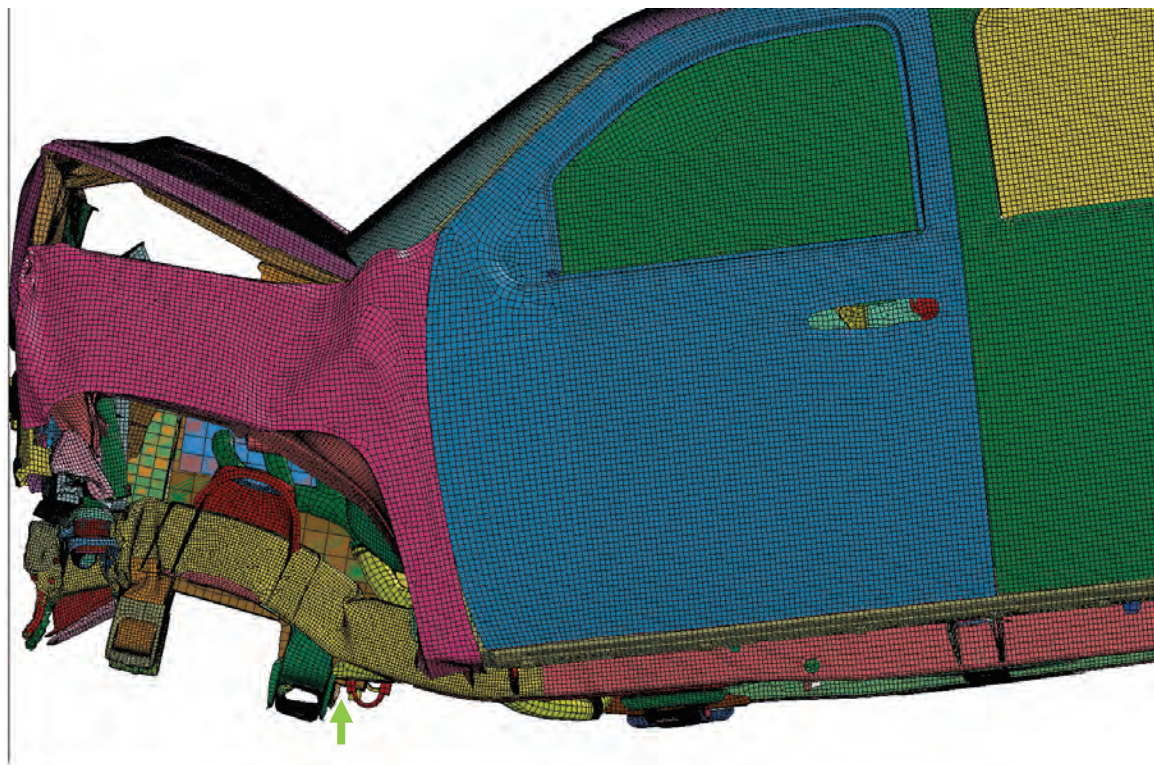
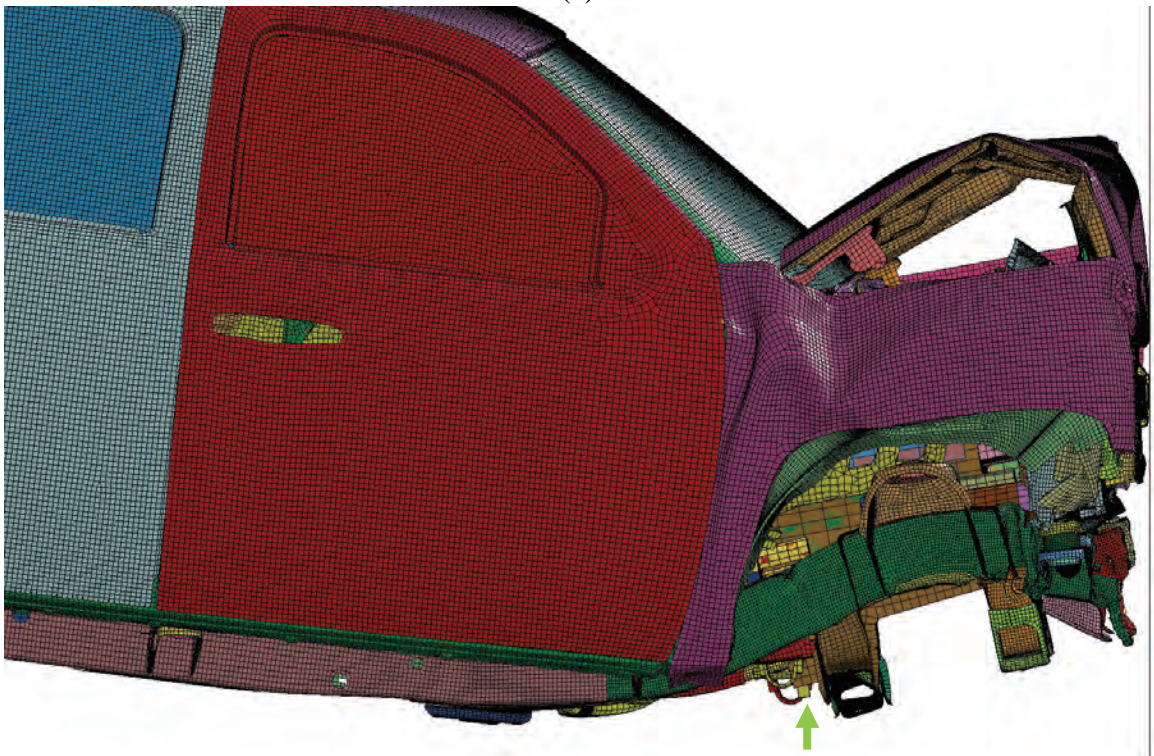


Figure 8.12. Deformation of New1 vehicle configuration.

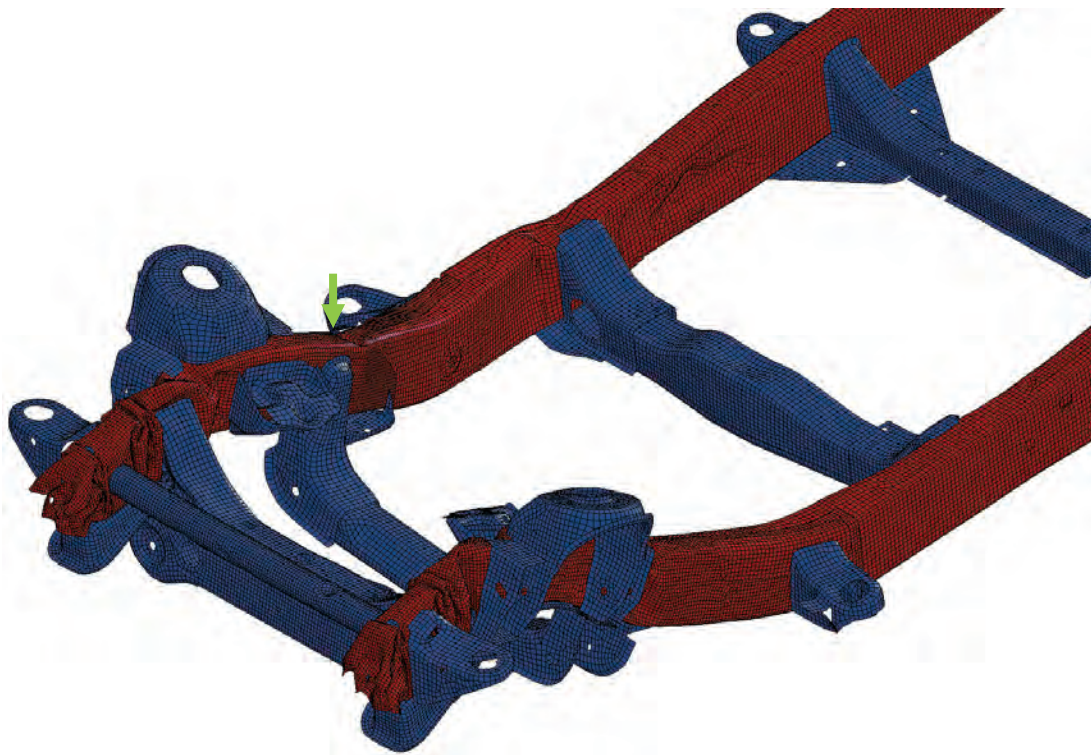


(a)

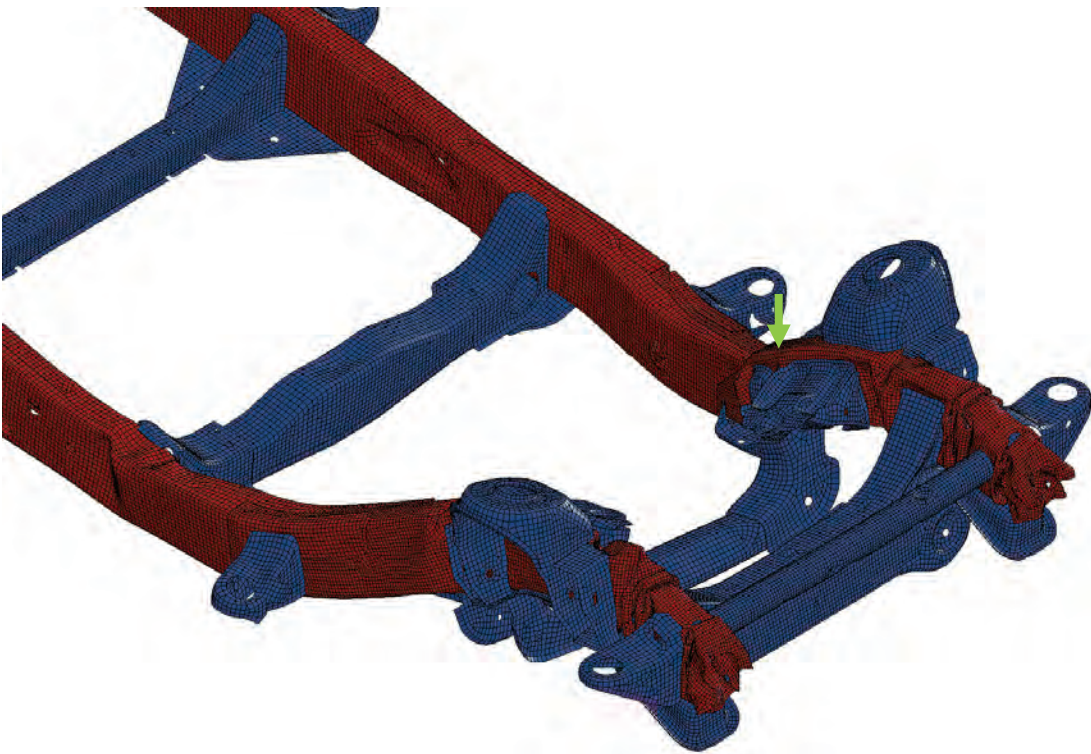


(b)

Figure 8.13. Deformation of New1 vehicle configuration (frontal area, wheel hidden).



(a)



(b)

Figure 8.14. Deformation of the steel ladder frame of the New1 vehicle configuration.

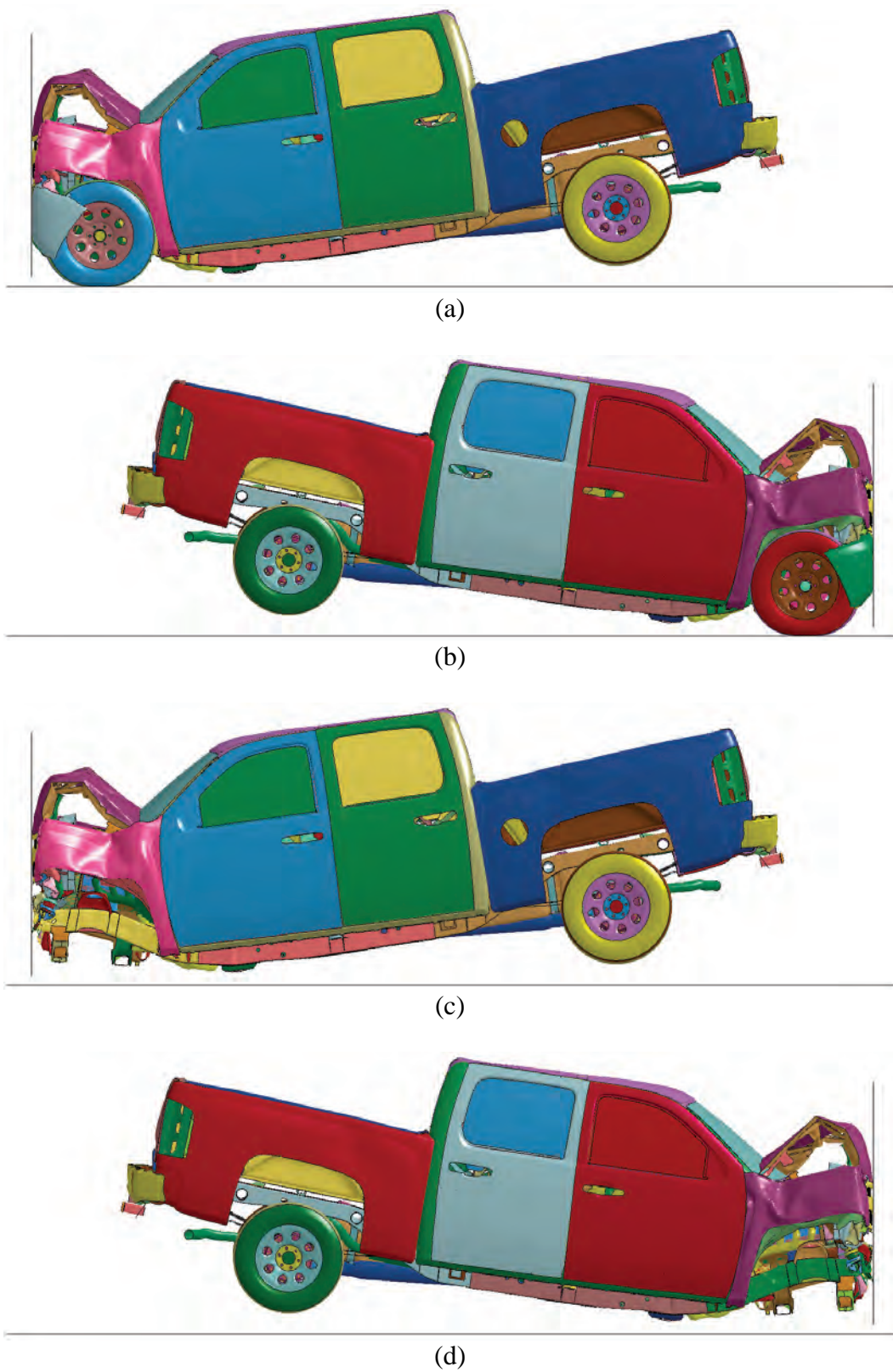
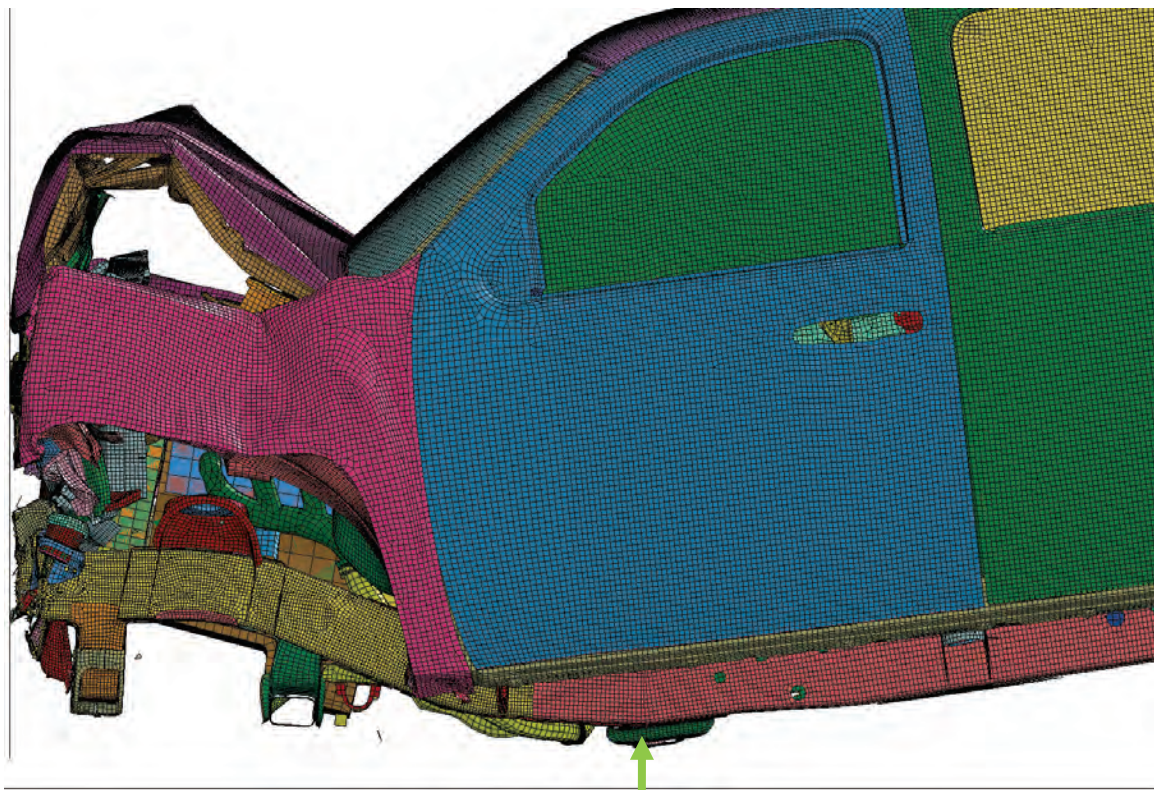
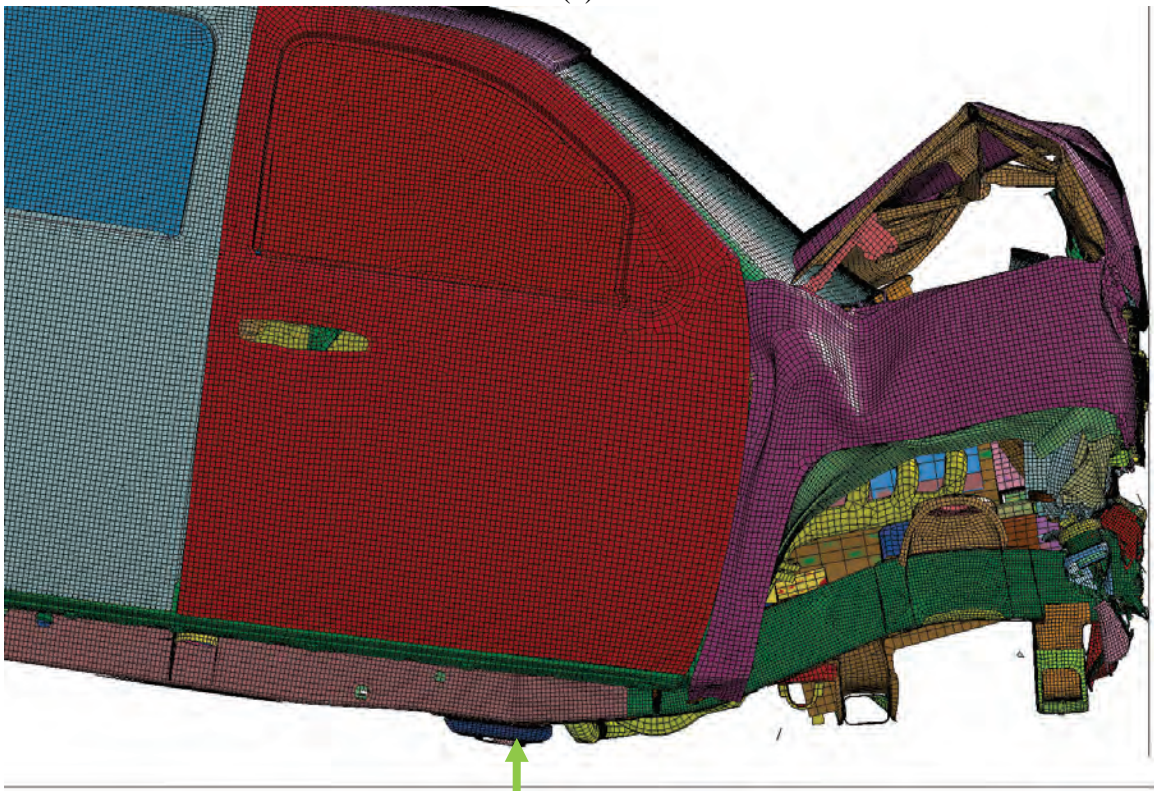


Figure 8.15. Deformation of the New2 vehicle configuration.

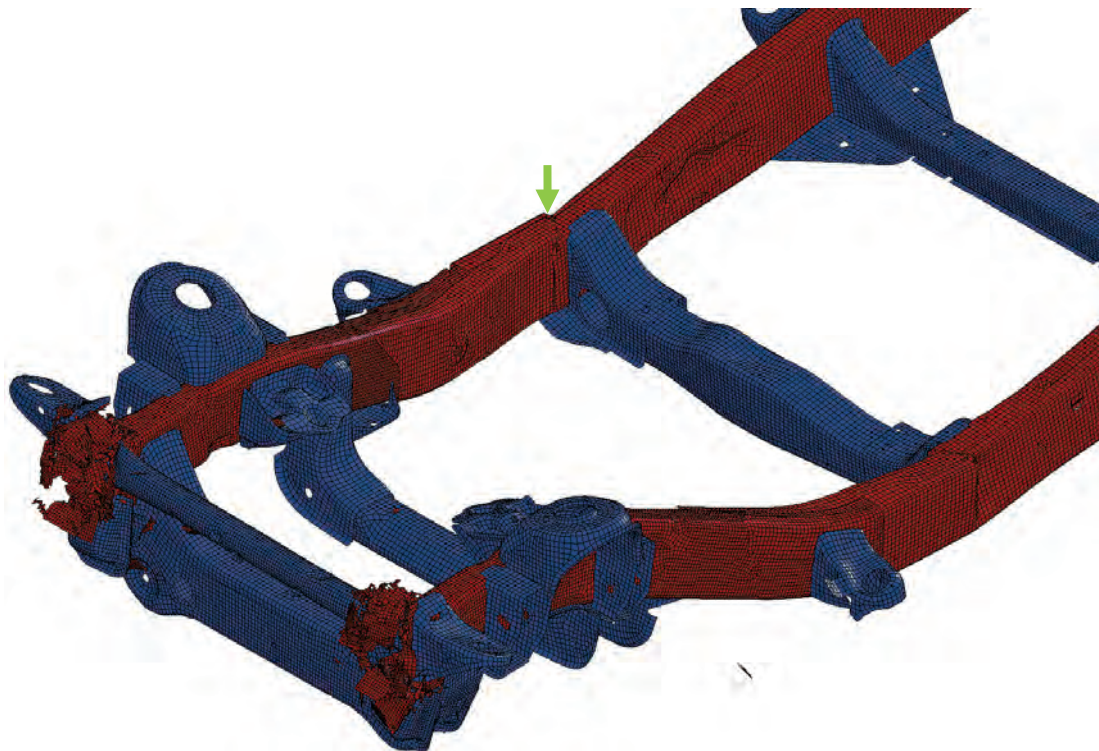


(a)

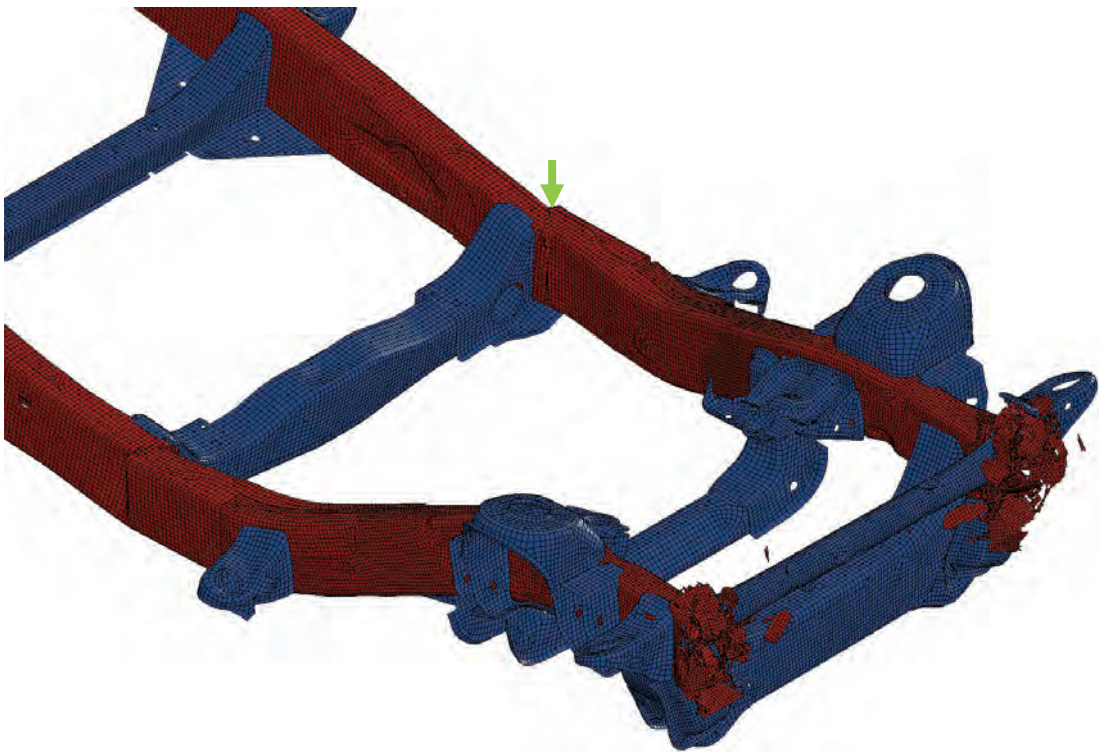


(b)

Figure 8.16. Deformation of the New2 vehicle configuration (frontal area, wheel hidden).



(a)



(b)

Figure 8.17. Deformation of the composite ladder frame (2×t) of the New2 vehicle configuration.

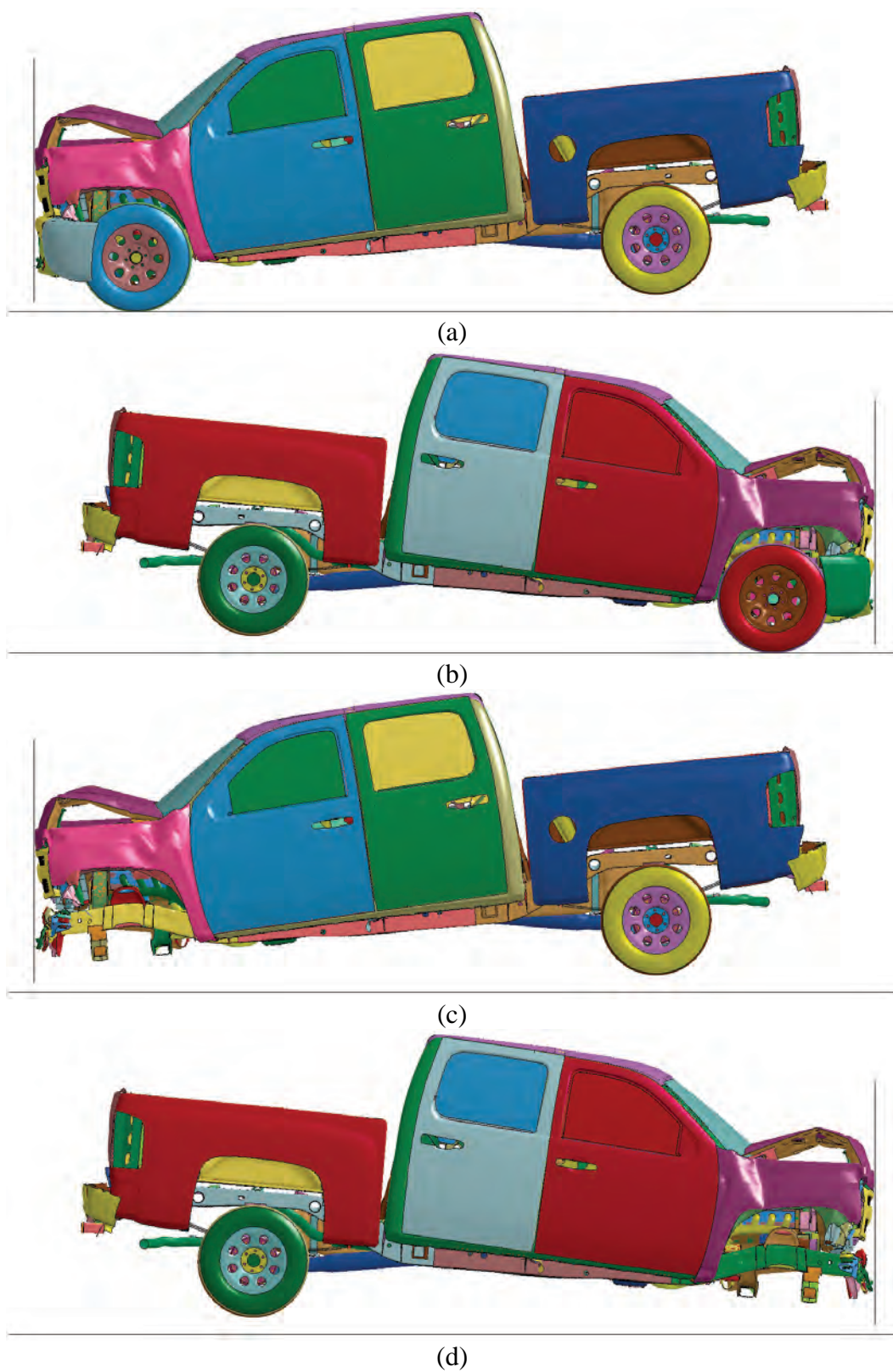
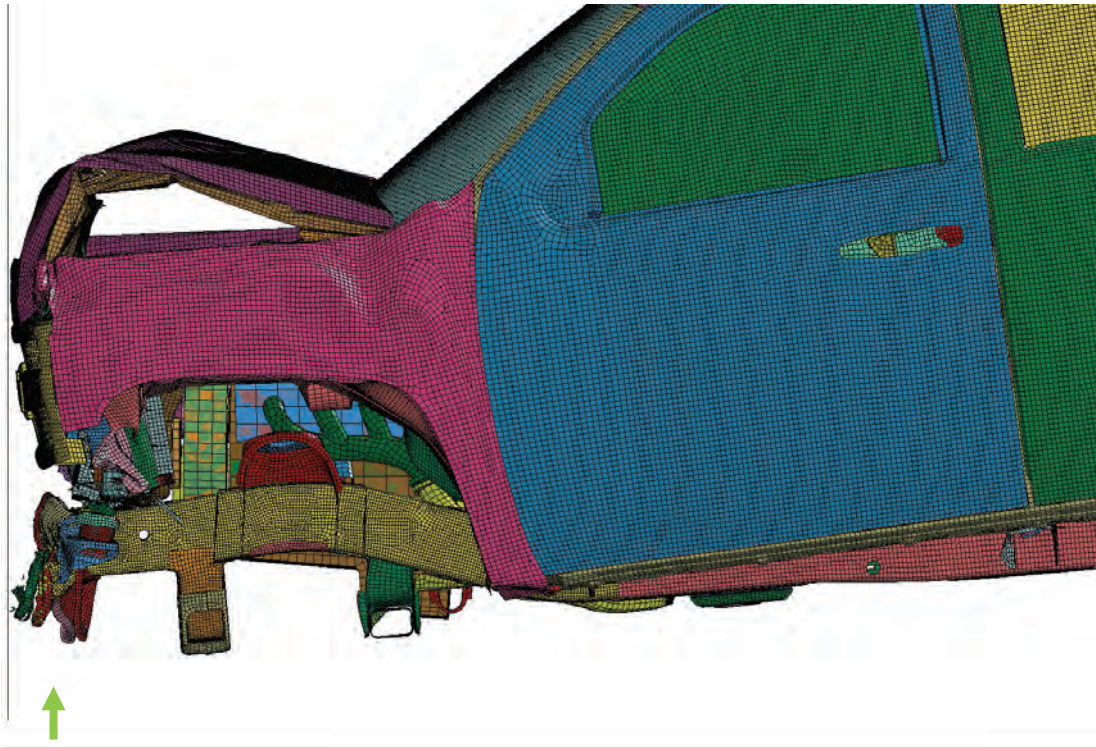
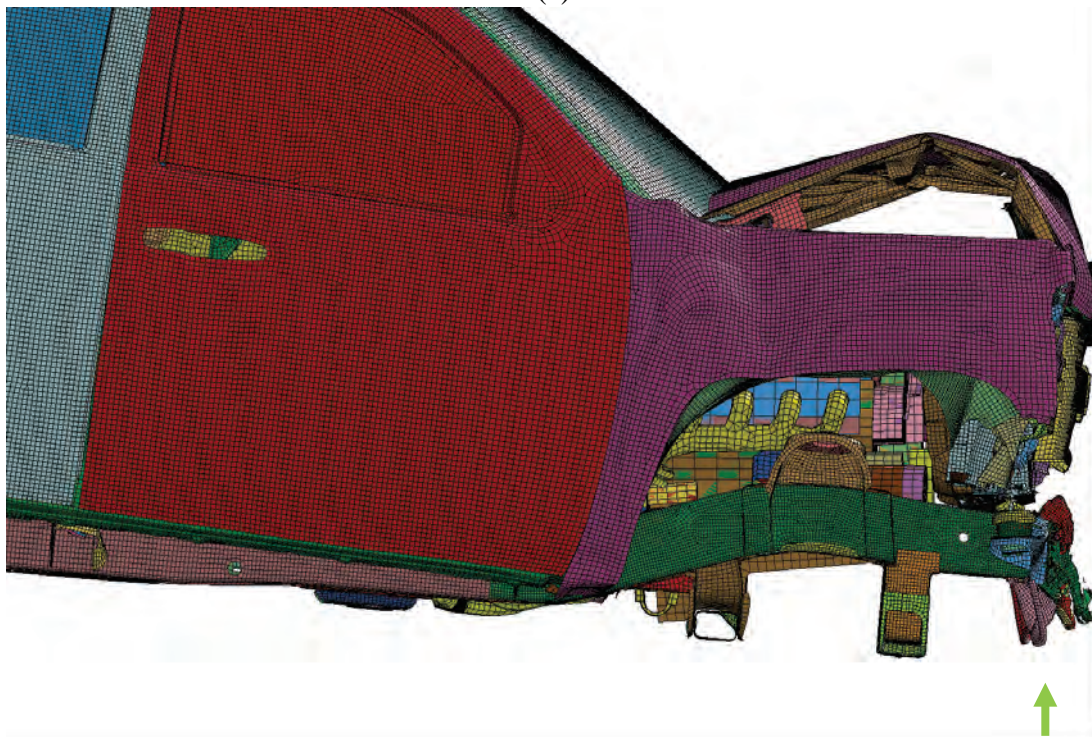


Figure 8.18. Deformation of the New3 vehicle configuration.



(a)

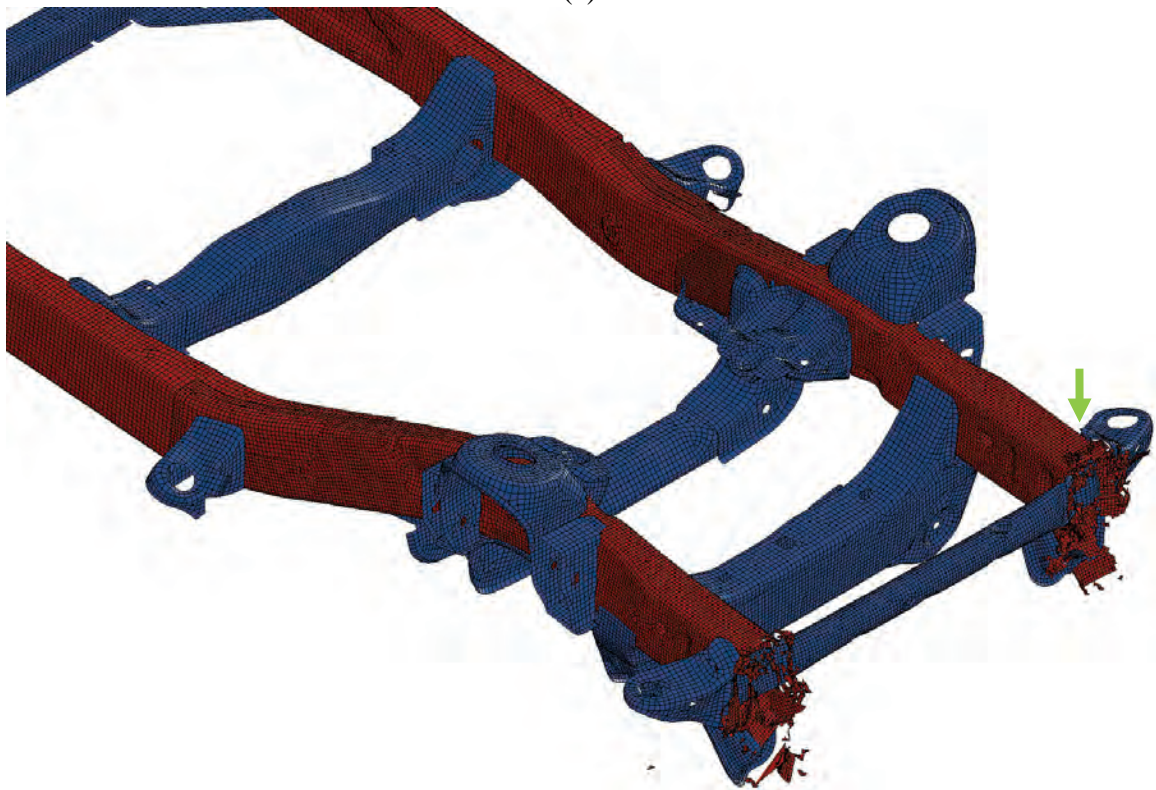


(b)

Figure 8.19. Deformation of the New3 vehicle configuration (frontal area, wheel hidden).



(a)



(b)

Figure 8.20. Deformation of the composite ladder frame (3×t) of the New3 vehicle configuration.

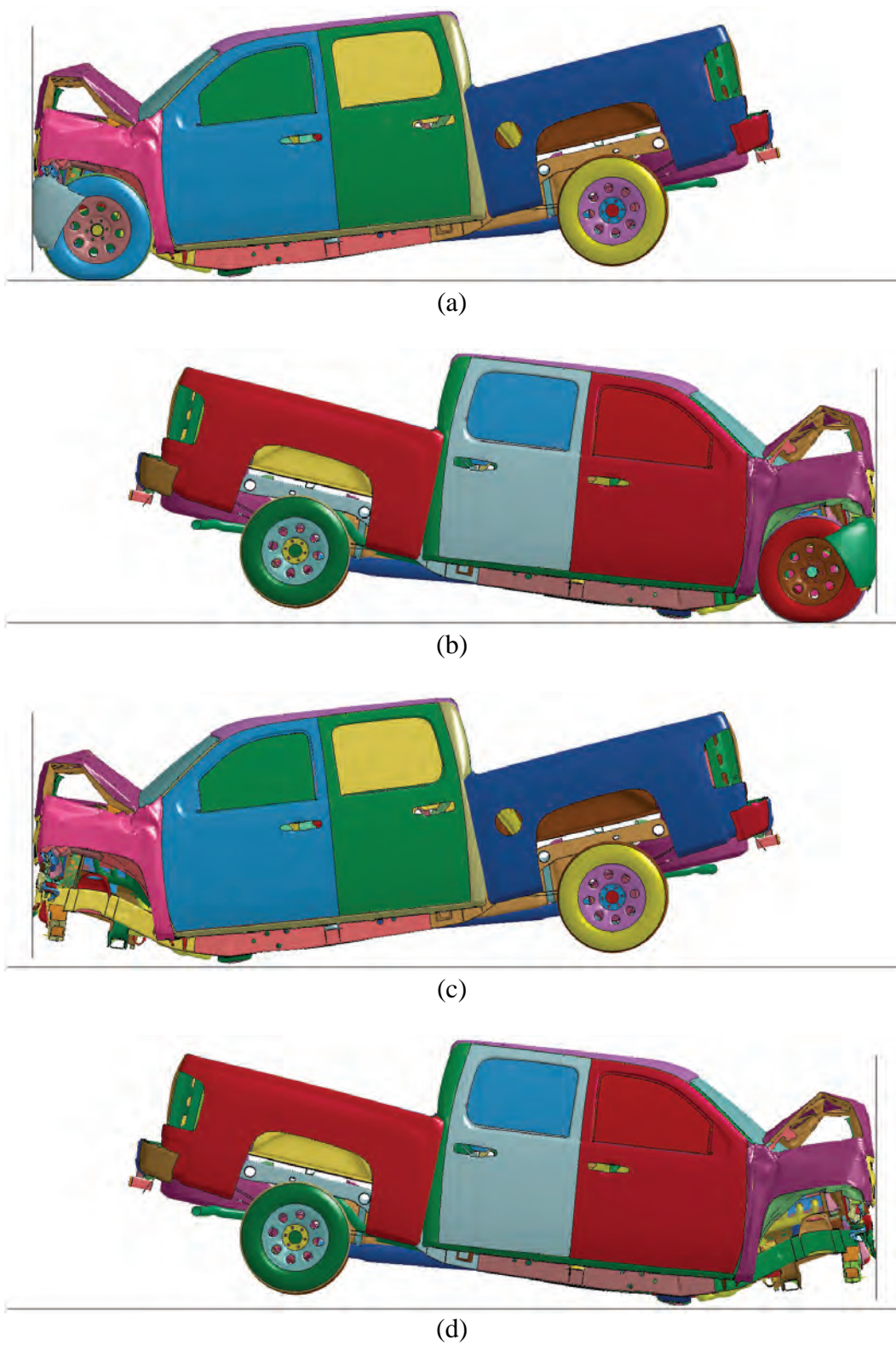


Figure 8.21. Deformation of the New4 vehicle configuration.

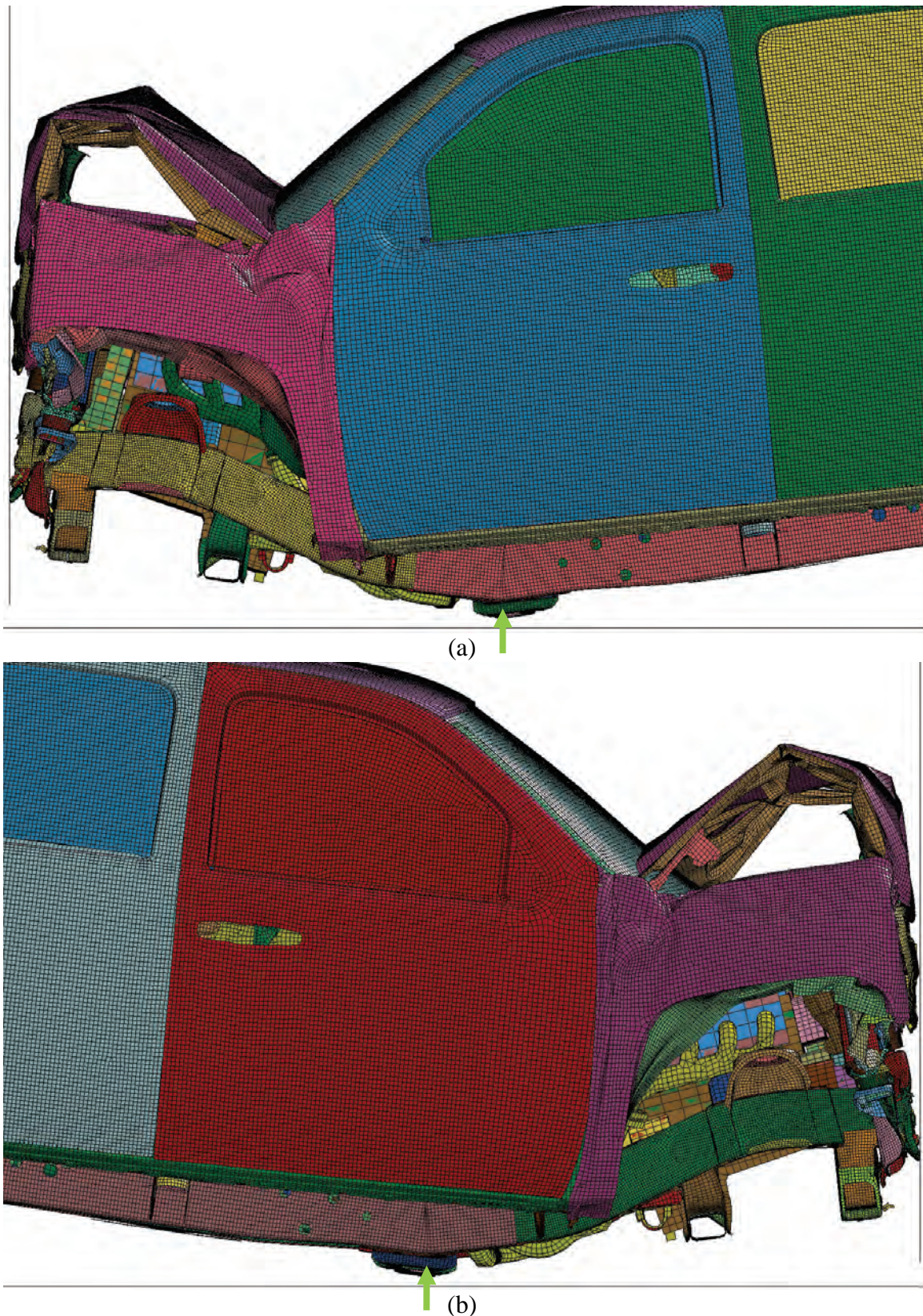
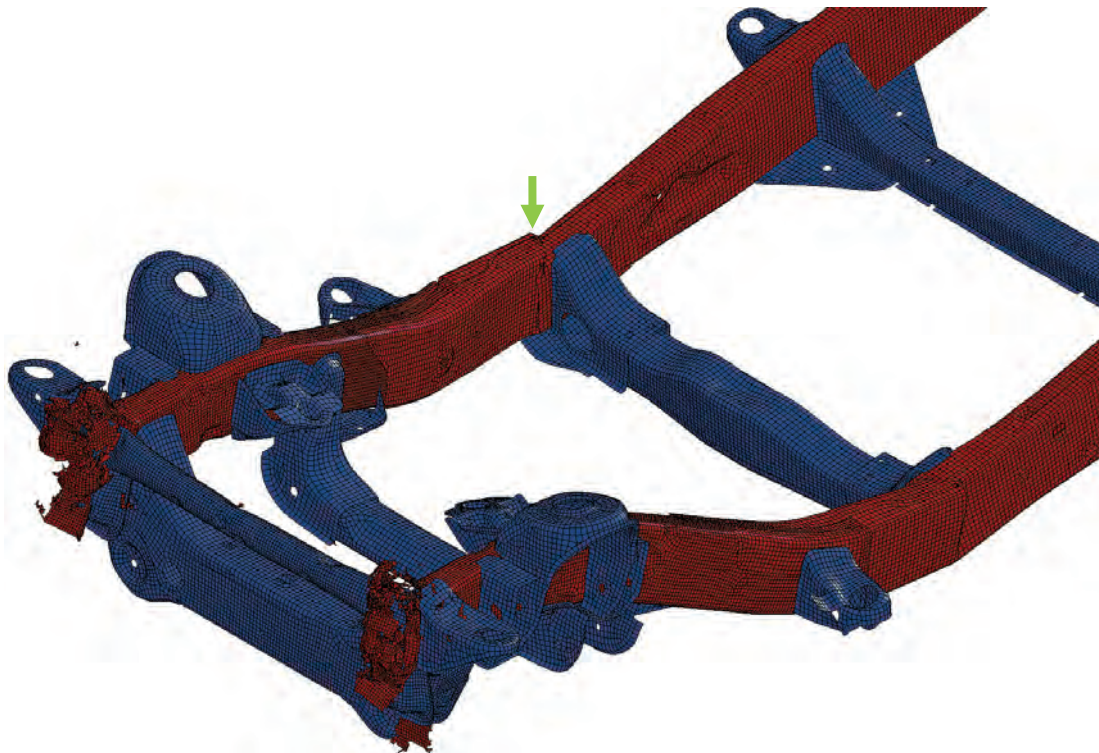
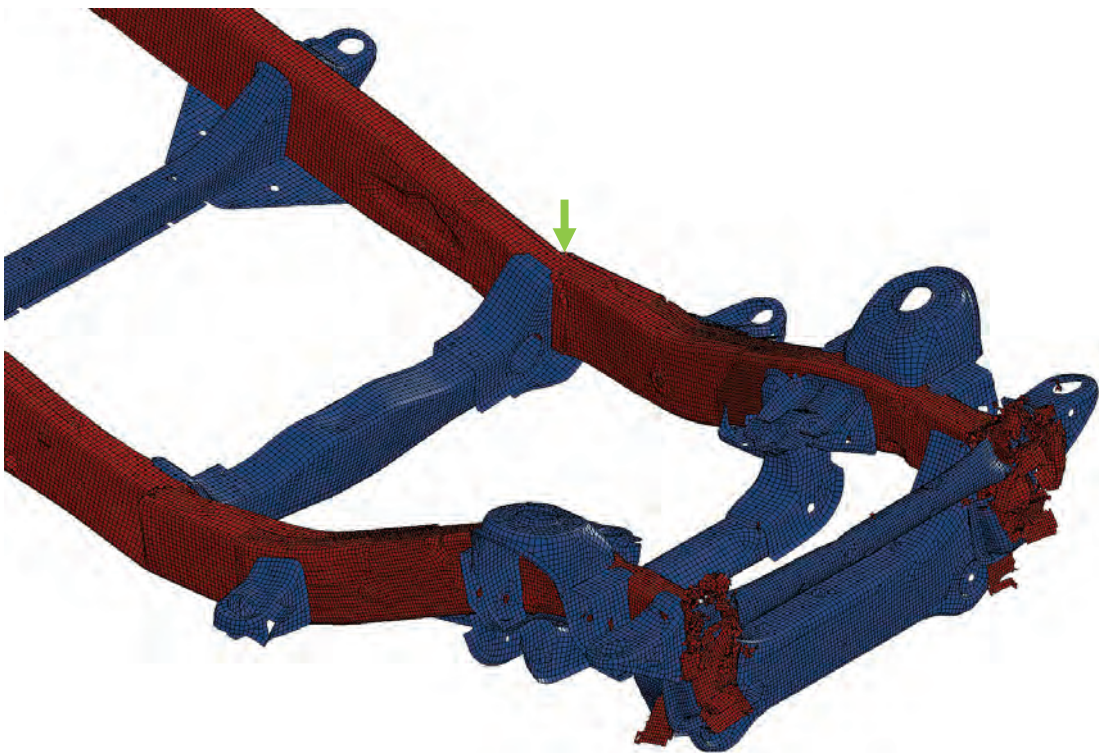


Figure 8.22. Deformation of the New4 vehicle configuration (frontal area, wheel hidden).

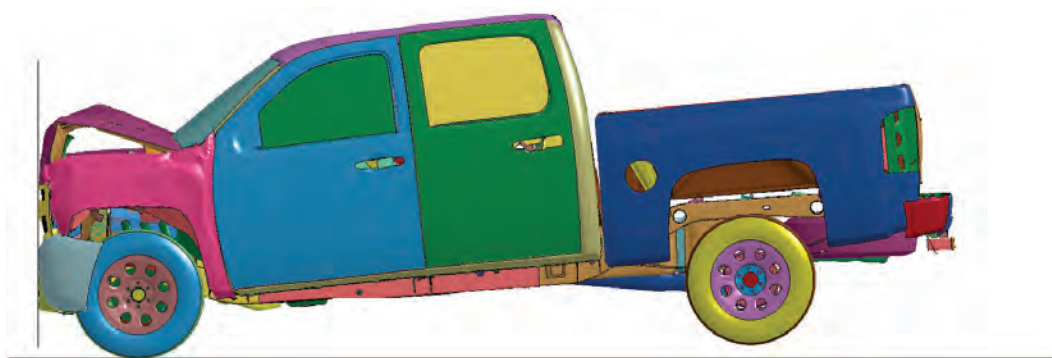


(a)

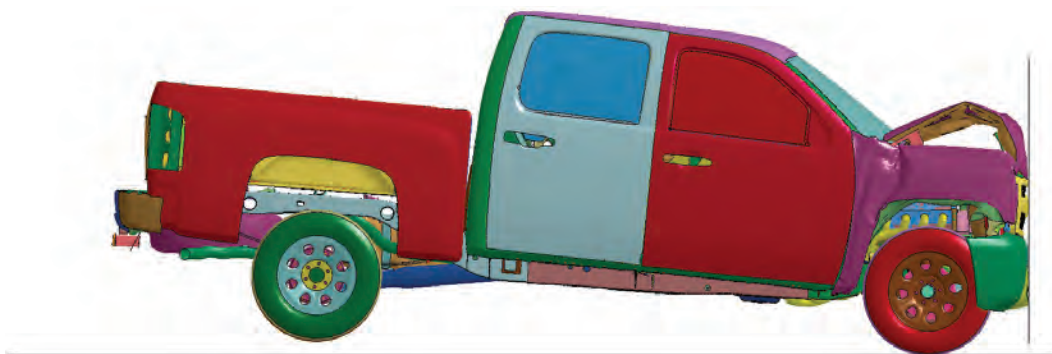


(b)

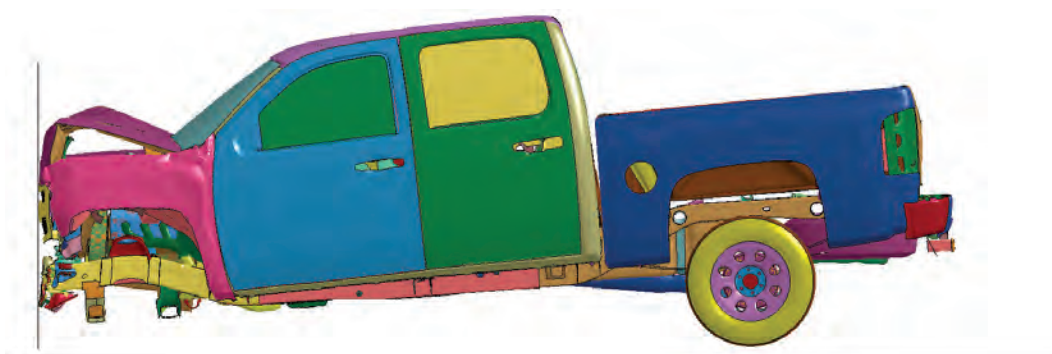
Figure 8.23. Deformation of the composite ladder (2×t) frame of the New4 vehicle configuration.



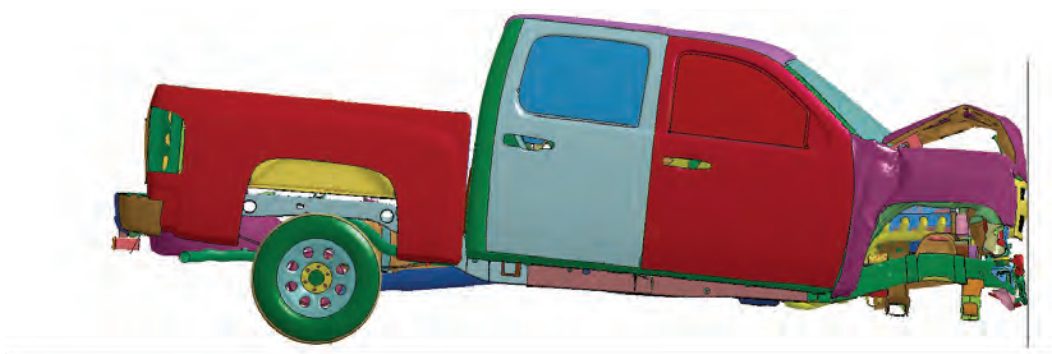
(a)



(b)

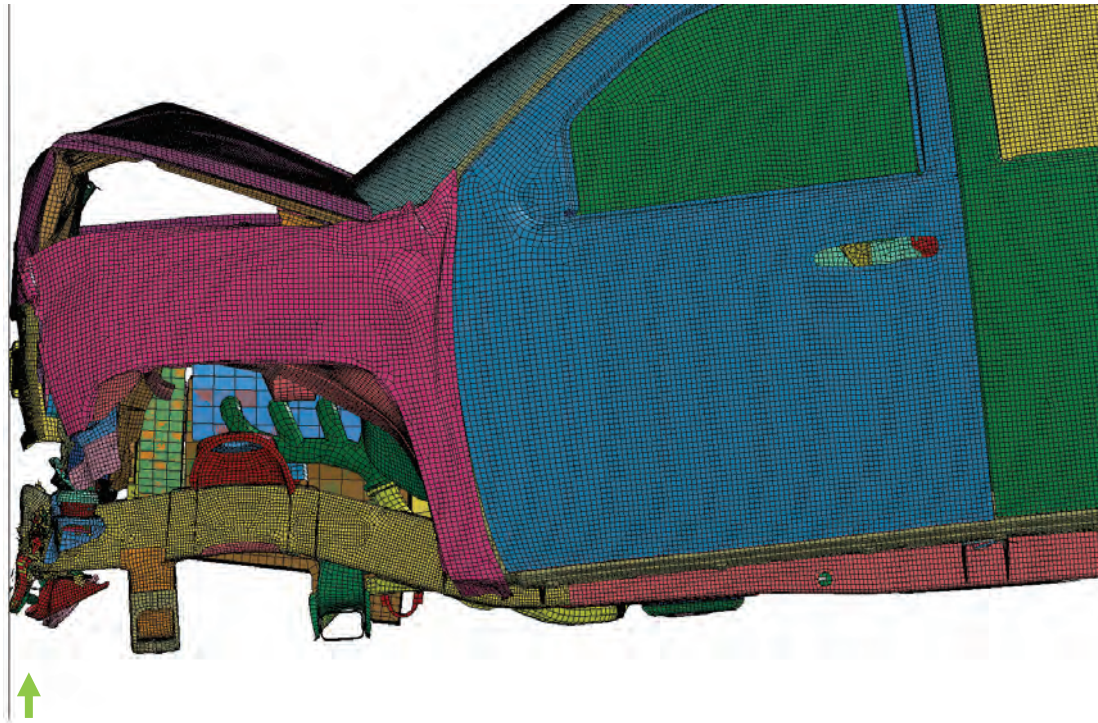


(c)

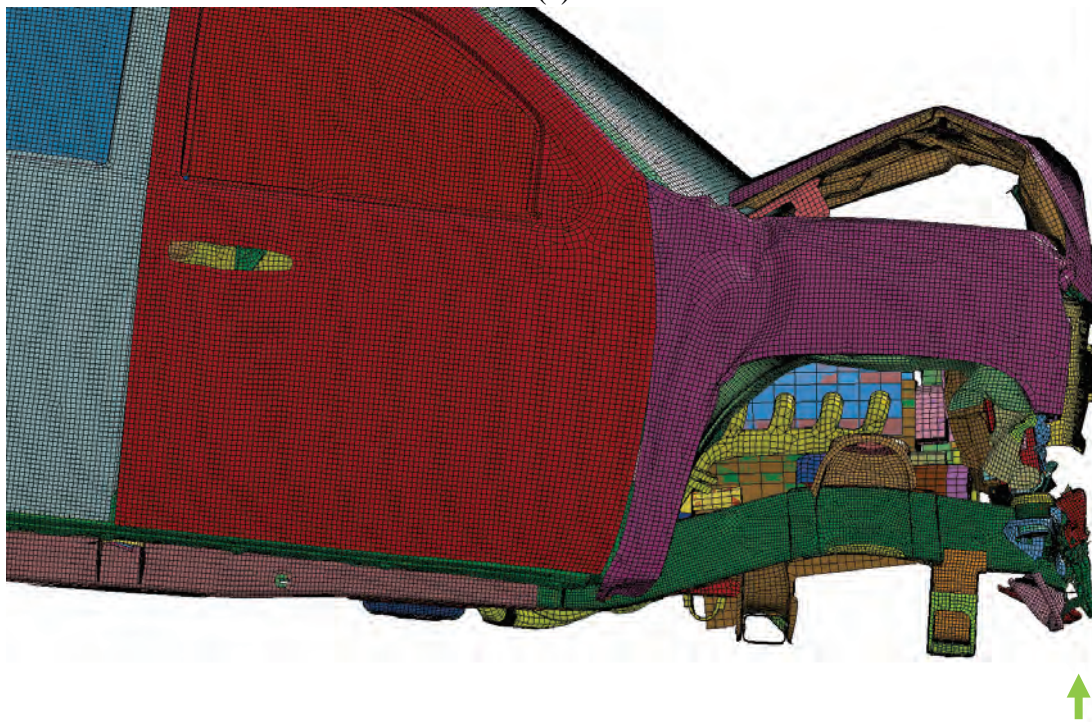


(d)

Figure 8.24. Deformation of the New5 vehicle configuration.

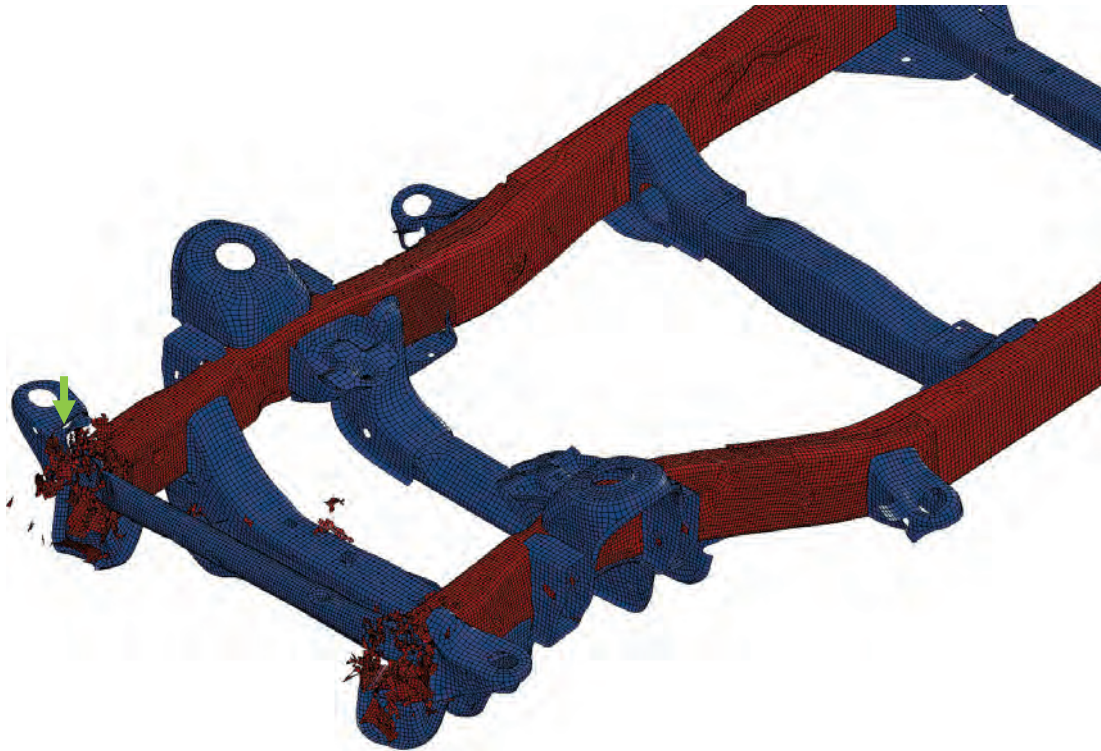


(a)

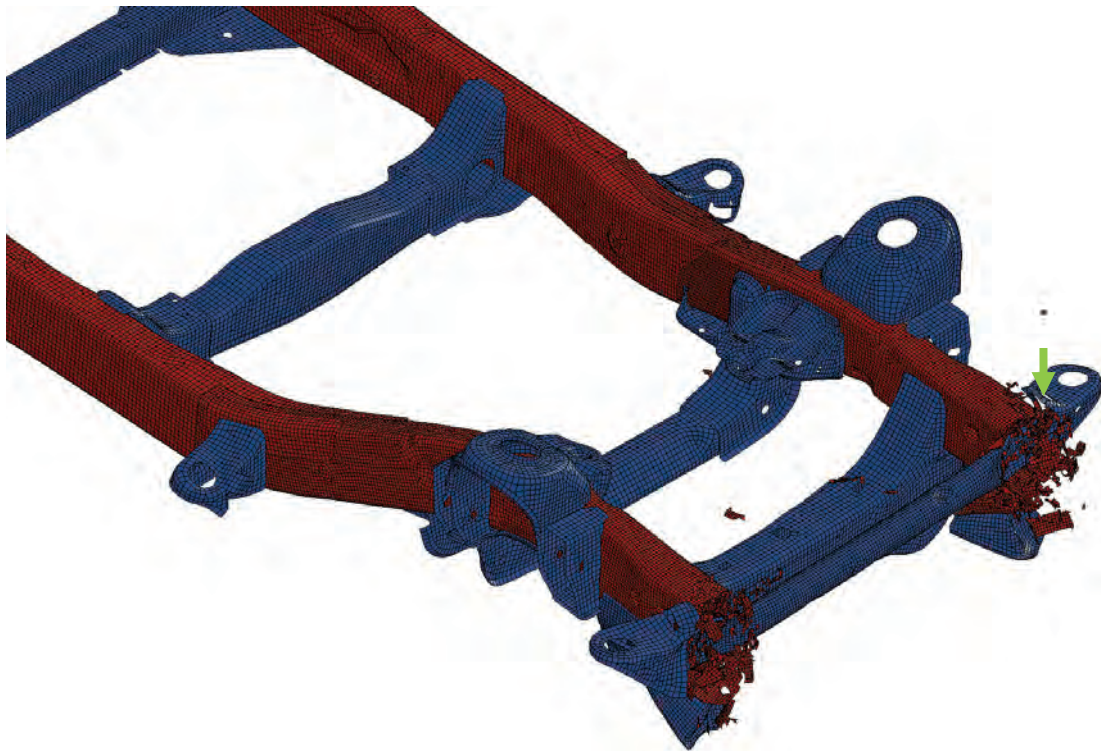


(b)

Figure 8.25. Deformation of the New5 vehicle configuration (frontal area, wheel hidden).



(a)



(b)

Figure 8.26. Deformation of the composite ladder frame (3×t) of the New5 vehicle configuration.

8.3. Summary

The crashworthiness of the lightweighted vehicle is investigated using frontal NCAP crash simulations. The five lightweighted vehicle configurations listed in Table 8.1 were developed to evaluate the crash performance of the composite ladder frame. The responses of five vehicles in the frontal NCAP simulations are analyzed above. Because the ladder frame of the Silverado is the primary energy absorbing member during a frontal crash, it can be observed that the material replacement in the ladder frame substantially affects the change in vehicle responses in frontal NCAP simulation.

The New1 substantially has all new components listed in Table 7.2 except for the composite ladder frame. The weight of the New1 configuration is 1,949kg, which is a 15.5-percent decrease from the baseline vehicle. Since the New1 configuration has the original steel ladder frame, the vehicle response curves and deformations in the frontal NCAP test are not much changed from the baseline vehicle. However, it can be seen that the New1 substantially has smaller intrusions than the baseline vehicle, which resulted from the effect of the weight reduction of the vehicle. Actually, it is observed that the vehicle intrusion becomes smaller when the vehicle weight gets lighter through reducing the mass in the non-structural components (Tahan, 2012).

Since all other vehicles except the New1 configuration have the composite ladder frame, their responses and deformations changed from those of the baseline vehicle. The steel ladder side rails demonstrated a folding deformation mode, while the composite side rails exhibited a fracture mode. It is noted that the fracture mechanism of the composite ladder frame may not have absorbed the impact energy in an optimally efficient way because the ladder frame had not been redesigned accordingly.

The New2 vehicle configuration has all new components including the composite ladder frame where the thickness of side rails is the twice that of the baseline vehicle. The weight of the New2 configuration is 1,874 kg, which is an 18.8-percent decrease from that of the baseline vehicle. The New2 configuration has a little higher acceleration peak at a later time during the crash event, but the intrusions are smaller than the baseline vehicles. The New4 vehicle configuration has the composite ladder frame but the other components are the same as the baseline vehicle. The weight savings is just 3.2 percent. The New4 vehicle configuration has a little higher acceleration peak at a later time during the crash event, but the intrusions are a bit smaller than those of the baseline vehicle. The New3 and New5 vehicle configurations have the composite ladder frame with triple wall thickness of the side rails. The simulation results show that the triple thickness of the composite side rails were strong and stiff and did not deformed much. That is, the New3 and New5 vehicle configurations became more aggressive.

Consequently, the structural performance of lightweighted vehicles can be summarized as

- It was observed that the vehicle mass reduction contributes to decrease the vehicle frontal intrusion when vehicles have similar front structures.
- The deceleration of a vehicle was more likely to be dependent on the vehicle stiffness and crash mechanisms, rather than vehicle mass reduction. A composite ladder frame optimally

designed for efficient energy absorption may improve the deceleration of light-weighted vehicles.

- Overall, the light-weighted vehicles using advanced plastics and composites provide equivalent structural performance (intrusion and crash pulse) to the baseline vehicle in the frontal impact condition.
- In order to evaluate the comprehensive crashworthiness performance of the light-weighted vehicles, it is required to investigate occupant responses and structural performance using other impact conditions (e.g., frontal offset, vehicle-to-vehicle and vehicle-to-pole side, and rear impacts).

(BLANK)

9. Conclusions

The primary goal of this multi-year research project was to identify and evaluate the safety benefits of structural plastics and composites applications in future lighter, more fuel-efficient, and environmentally sustainable vehicles. The research objectives of this project were (1) to evaluate the current state of modeling and simulation tools for predicting impact response of composite materials in automotive structures, (2) to investigate weight reduction opportunities in a current vehicle, and (3) to evaluate the impact of light weighting on crashworthiness.

In order to investigate the weight reduction opportunities in a current vehicle, a lightweight vehicle was developed numerically from the original FE model of a 2007 Chevrolet Silverado, which is a body-on-frame pickup truck. Based on the literature review and with help from the ACC PD's member companies (particularly, SABIC, BASF, and Bayer MaterialScience), candidate steel vehicle components in the Silverado were selected and light-weighted. These components included:

- Occupant compartment structure: roof, A- and B-pillars;
- Interior: seats, IP carrier;
- Closures: front fenders, rear windows, door beam, door modules;
- Truck bed structure: bed, tailgate, rear fenders;
- Power-train related: engine and transmission, oil pans, drive shaft, rear differential carrier, front-end module, battery;
- Suspension related: wheels, front brake disks, tires, spare tire and carrier, leaf spring, steering stabilizer links; and the
- Ladder frame structure: front bumper, rear bumper, transmission crossbeam, and ladder frame.

Plastics and composites were considered as the primary substitute materials in this study. However, some components were changed to other lightweight materials (aluminum or magnesium), replaced to lightweight components, or removed. The original vehicle weight, 2,307 kg, was reduced to 1,874 kg, which is about a 19-percent decrease. As a result, the lightweight vehicle contains about 442 kg of plastic and composites, which represents about 23.6 percent of the total weight of the lightweight vehicle.

Among the various components, the steel ladder frame (which is the primary structural member of the Silverado) was also light-weighted with a carbon fiber-thermoset matrix braided composite which material properties were obtained from various physical material tests. The component simulation results of the composite ladder frame shows that the composite ladder frame with side rails with double wall thickness could provide an equivalent stiffness and impact performance to the original steel ladder frame.

In order to evaluate the impact of light weighting on crashworthiness, the frontal NCAP test of the developed lightweight vehicles was simulated. Six vehicles configurations were considered:

- Baseline (original) vehicle: original components and original steel ladder frame,

- Light-weighted vehicle 1 (New1): new components and original steel ladder frame,
- Light-weighted vehicle 2 (New2): new components and new composite ladder frame (double wall thickness of side rails),
- Light-weighted vehicle 3 (New3): new components and new composite ladder frame (triple wall thickness of side rails),
- Light-weighted vehicle 4 (New4): original components and new composite ladder frame (double wall thickness of side rails), and
- Light-weighted vehicle 5 (New5): original components and new composite ladder frame (triple wall thickness of side rails).

The accelerations, velocities, and intrusions of the vehicles; wall forces; and deformation behaviors of the various vehicle configurations and ladder frames were analyzed. The responses and deformations of the vehicles with the composite ladder frame were changed from those of the Baseline vehicle, which has the steel ladder frame. The steel ladder side rails deformed in a folding deformation mode; while the composite side rails exhibited a fracture mode.

The results of the frontal NCAP simulations can be summarized as:

- Compared to the baseline vehicle, the intrusion of the light-weighted vehicles was smaller. It was observed that the vehicle mass reduction contributes to decrease the vehicle frontal intrusion when the baseline and light-weighted vehicles have similar frontal structure stiffness characteristics.
- Compared to the baseline vehicle, the maximum acceleration of light-weighted vehicles was increased. The deceleration of a vehicle was more likely to be dependent on the vehicle stiffness and crash mechanisms, rather than vehicle mass reduction. A composite ladder frame optimally designed for efficient energy absorption may improve the deceleration of light-weighted vehicles.
- Overall, the light-weighted vehicles using advanced plastics and composites provide equivalent structural performance to the baseline vehicle in the full frontal impact condition.
- In order to evaluate the comprehensive crashworthiness performance of the light-weighted vehicles, it is required to investigate occupant responses and structural performance using other impact conditions (e.g., frontal offset, vehicle-to-vehicle and vehicle-to-pole side, and rear impacts).

In conclusion, this study demonstrates that:

- Using plastics and composites can reduce the vehicle weight efficiently,
- Automotive structural member of carbon FRP composites can provide equivalent crash performance in the frontal impact condition, and
- The light-weighted Silverado using advanced plastics and composites provides equivalent structural performance in the frontal impact condition.

Also, this study recommends further research, such as:

- Undertaking a clean sheet design from the ground up (rather than the less optimal component redesign approach) to provide an maximal approach for weight reduction,
- The investigation of the lightweight opportunities of other types of vehicles (passenger car, van, sports utility vehicle),
- The evaluation of the crashworthiness of light-weighted vehicles in other crash configurations (side and rear impacts and roof crush, etc.),
- The study of cost analysis, and vehicle repair and maintenance issues of plastics and composites components
- The enrichment of material database of plastics and composite, and
- The improvement of crash analysis methods of plastic and composites.

(BLANK)

References

- AAA. (2011). Vehicles without a spare tire. Retrieved from www.aaa.com/AAA/corpcomm/socialmedia/No_Spare-Tires.pdf
- American Chemistry Council. (2011a). Composite drive shafts can increase torque and can help prevent injuries. Retrieved from www.plastics-car.com/driveshafts
- ACC. (2011b). Plastic fuel tanks can decrease vehicle weight and incidence of corrosion Retrieved from www.plastics-car.com/plasticfueltanks
- ACC Plastics Division. (2009a). Plastic and composite intensive vehicles: an innovation platform for achieving national priorities. Retrieved from www.plastics-car.com/pcivs
- ACC Plastics Division. (2009b). Retrieved from Plastic in automotive markets technology roadmap – a new vision for the road ahead. Retrieved from www.plastics-car.com/roadmap_fullversion
- Anghileri, M., Castelletti, L. L., Invernizzi, F., & Mascheroni, M. (2005). Birdstrike onto the composite intake of a turbofan engine, 5th European LS-DYNA Users Conference, Milano, Italy.
- BAC Technology LTD.. (2011). Carbon fiber driveshafts. Retrieved from www.bactechnologies.com/shafts.htm
- Barnes, G., Coles, I., Roberts, R., Adams, S. O., & Garner, D. M. (2010). Crash safety assurance strategies for future plastic and composite intensive vehicles (PCIVs). (Report No. DOT-VNTSC-NHTSA-10-01). Cambridge, MA: Volpe National Transportation Systems Center.
- BASF Corp.. (2011). Ultramid B3ZG7 OSI PA6 (Optimized for Stone Impact) PA^ (Polyamide 6). Wyandotte, MI: Author. Retrieved from www2.basf.us/PLASTICSWEB/displayanyfile?id=0901a5e1801631d8
- Bayer MaterialScience. (2011). Bayblend T88 GF-10 and T88 GF-2. Leverkusen, Germany: Author. Retrieved from http://plastics.bayer.com/plastics/emea/en/library/newpublications/docId-2903947/PCS-3018_en_Bayblend_T88_GF-10_and_T88_GF-20.pdf
- Bisagni, C., Pietro, G. D., Fraschni, L., & Terletti, D. (2005). Progressive crushing of fiber-reinforced composite structural components of a formula one racing car, *Composite Structures*, 68, 491-503.
- Brecher, A. (2007, November). A safety roadmap for future plastics and composites intensive vehicles. (Report No. DOT HS 810 863). Washington, DC: National Highway Traffic Safety Administration.

- Brecher, A., Brewer, J., Summers, S., & Patel S. (2009). Characterizing and enhancing the safety of future plastic and composite intensive vehicles. 21st International Conference on the Enhanced Safety of Vehicles, Stuttgart, Germany.
- Center for Automotive Research. (2011). Automotive technology: greener products, changing skills – lightweight materials & forming report. Washington, DC: Employment and Training Administration. Available at <http://drivingworkforcechange.org/reports/lightweightMaterials.pdf>
- Carney, K. S., Goldberg, R. K., & Pereira, J. M. (2008). A heterogeneous constitutive model for reinforced carbon-carbon using LS-DYNA, 10th International LS-DYNA Users Conference, Dearborn, MI.
- Carpenter, J. A.,. (2008). Overview of freedomCAR and its composites crash-energy management work. Safety Characterization of Future Plastics and Composite-Intensive Vehicles Workshop, Cambridge, MA.
- Chan, S., Fawaz, Z., Behdinin, K., & Amid, R. (2007). Ballistic limit prediction using a numerical model with progressive damage capability *Composite Structures*, 77(4):466–474.
- Chan-Lizardo, K., Lovins, AB., Schewel, L., & Simpson, M. (2011). Ultralight vehicles – non-linear correlations between weight and safety. International Crashworthiness Conference, Leesburg, VA.
- Chang, F. K., & Chang, K. Y. (1987a). A progressive damage model for laminated composites containing stress concentrations. *Journal of Composite Materials*, 21:834-855.
- Chang, F. K., & Chang, K. Y. (1987b). Post-failure analysis of bolted composite joints in tension or shear-out mode failure. *Journal of Composite Materials*, 21:809-833.
- Chatiri, M., Gull, T., & Matzenmiller A. (2009). An assessment of the new LS-DYNA layered solid element: basics, patch simulation and its potential for think composite structural analysis. 7th European LS-DYNA Conference, Salzburg, Austria.
- Cheah, L. W. (2010). *Cars on a diet: the material and energy impacts of passenger vehicle weight reduction in the U.S.* (Doctoral dissertation). Massachusetts Institute of Technology, Cambridge, MA. Available at http://web.mit.edu/sloan-auto-lab/research/beforeh2/files/LCheah_PhD_thesis_2010.pdf
- Cheng, J., & Binienda, W. K. (2008). Simplified braiding through integration points model for triaxially braided composites. *Journal of Aerospace Engineering*, 21(3):152-161.
- Chiu, C. H., Lu, C. K., & Wu, CM., (1997). Crushing characteristics of 3-D braided composite square tubes. *Journal of Composite Materials*, 31:2309-2327.

- Chiu, C. H., Tsai, K.H., & Huang, W. J., (1998). Effects of braiding parameters on energy absorption capability of triaxially braided composite tubes. *Journal of Composite Materials*, 32:1964-1983.
- Courteau, M. A., & Adams, D. O. (2011). Composite tube testing for crashworthiness applications: a review. *Journal of Advanced Materials*, 43(2):13-34.
- Cox, B. N., & Flanagan, G., (1997) Handbook of analytical methods for textile composites. (NASA C R 4750). Hampton, VA: Langley Research Center, National Aeronautics and Space Administration. Available at http://ntrs.nasa.gov/archive/nasa/casi.ntrs.nasa.gov/19970017583_1997024417.pdf
- Das, B., Sahu, SK., & Ray, B. C. (2007). Effects of loading speed on the failure behavior of FRP composites. *Aircraft Engineering and Aerospace Technology: An International Journal*, 79(1):45-52.
- Das, S. (2001, January). The cost of automotive polymer composites: a review and assessment of DOE's lightweight materials composites research. (Report No. ORNL/TM-2000/283). Washington, DC: Office of Advanced Automotive Technology & Office of Transportation Technologies. Available at http://cta.ornl.gov/cta/Publications/Reports/ORNL_TM_2000_283.pdf
- Dauda, B., Oyadiji, S. O., & Potluri, P. (2009). Characterising mechanical properties of braided and woven textile composite beams. *Applied Composite Materials*, 16:15-31.
- Deka, L. J., Bartus, S. J., & Vaidya, U. K. (2009). Multi-site impact response of S2-glass/epoxy composite laminates. *Composites Science and Technology*, 69:725-735.
- Deleo, F., Wade, B., Feraboli, P., & Rassaian, M. (2010). Crashworthiness of composite structures: experiment and simulation. FAA Joint Advanced Materials and Structures (JAMS) Technical Review Meeting, Seattle, WA.
- DuPont. (2009). 20% less weight: Revolutionary ultra-lightweight concept tire from Dunlop with DuPont.
- El-Hage, H., Mallick, P. K., & Zamani, N. (2010). Numerical modeling of quasi-static axial crush of square aluminum-composite hybrid tubes. *International Journal of Crashworthiness*, 9(6):653-664.
- Energy Efficiency & Technology. (2011). Lithium technology comes to car batteries. http://eetweb.com/power-supplies/lithium_batteries_3411/
- Light-Duty Vehicle Greenhouse Gas Emission Standards and Corporate Average Fuel Economy Standards; Final Rule. 40 CFR Parts 85, 86, & 600; 49 CFR Parts 531, 533, 536, et al. (May 7, 2010). Available at www.nhtsa.gov/staticfiles/rulemaking/pdf/cafe/CAFE-GHG_MY_2012-2016_Final_Rule_FR.pdf

- Exxon Mobil Corp. (2011). Exxcure DVA resin. www.exxonmobilchemical.com/Chem-English/brands/butyl-rubber-exxcure-dva-resin.aspx?ln=productsservices
- Fawaz, Z., Zheng, W., & Behdinan, K. (2004). Numerical simulation of normal and oblique ballistic impact on ceramic composite armours. *Composite Structures*, 63:387-395.
- Fischer, B. (2007). New car assessment program frontal barrier impact test: 2007 Chevrolet Silverado ext cab 1500. NHTSA number, M70110, Test number: 5907.(Report No. NCAP-MGA-2007-011). (NHTSA number, M70110, Test number: 5907. Washington, DC: National Highway Traffic Safety Administration.
- Fisher, M., & Cundiff, B. (2002). APC Vision and Technology Roadmap for the Automotive Market-Defining Priority Research for Plastics in 21st Century Vehicles. (SAE Technical Paper 2002-01-1890). Warrendale, PA: Society of Automotive Engineers.
- Fisher, M., Kolb, J., & Cole, S. (2007). Enhancing Future Automotive Safety with Plastics. (Paper Number 07-0451). 20th International Conference on the Enhanced Safety of Vehicles, Lyon, France.
- Fujihara, K., Yoshida, E., Nakai, A., Ramakrishna, S., & Hamada, H. (2007). Influence of macro-structure on bending properties of braided laminated composites. *Composites Science and Technology*, 67:2191-2198.
- Gibson, R. F. (2011). *Principles of composite material mechanics*. 2nd edition. Boca Raton, FL: CRC Press.
- Gilat, A., Goldberg, R.K., & Roberts, G. D. (2005, March). Strain rate sensitivity of epoxy resin in tensile and shear loading. (Report No. NASA/TM-2005-213595). Washington, DC: National Aeronautics and Space Administration.
- Goldberg, R. K., Blinzler, B. J., & Binienda, W. K. (2010). Modification of a macromechanical finite-element based model for impact analysis of triaxially-braided composites. (Report No. NASA/TM-2010-216922). Washington, DC: National Aeronautics and Space Administration.
- Gui, L. J., Zhang, P., & Fan, Z.J., (2009). Energy absorption properties of braided glass/epoxy tubes subjected to quasi-static axial crushing. *International Journal of Crashworthiness*, 14(1):17-23.
- Hadavinia, H., & Ghasemnejad, H. (2009). Effects of mode-I and mode-II interlaminar fracture toughness on the energy absorption of CFRP twill/weave composite box sections. *Composite Structures*, 89:303-314.
- Hallquist, J. O. (2006). LS-DYNA theory manual. Livermore, CA: Livermore Software Technology Corporation,

- Hallquist, J. O. (2006) LS-DYNA keyword user's manual. Livermore, CA: Livermore Software Technology Corporation.
- Hamada, H. (2001), Crushing behavior of braided composites. Proceedings of ASME International Mechanical Engineering Congress and Exposition, New York, NY.
- Han, H., Taheri, F., Pegg, N., & Lu, Y. (2007). A numerical study on the axial crushing response of hybrid pultruded and $\pm 45^\circ$ braided tubes. *Composite Structures*, 80:253-264.
- Hashin, Z., 1980, Failure criteria for unidirectional fiber composites. *Journal of Applied Mechanics*, 47:329-334.
- Heimbs, S., Heller, S., Middendorf, P., Hahnel, F., & Weibe, J. (2009). Low velocity impact on CFRP plates with compressive preload: test and modeling. *International Journal of Impact Engineering*, 36:1182-1193.
- Heimbs, S., Middendorf, P., & Maier, M. (2006). Honeycomb sandwich material modeling for dynamic simulations of aircraft interior components. 9th International LS-DYNA Users Conference, Dearborn, MI.
- Herrmann, H. G., Mohrdieck, C., & Bjekovic, R. (2002). Materials for the automotive lightweight design. Euromotor: New Advances in Body Engineering: Lightweight material applications, Passive safe. Aachen, Germany: Institut für Kraftfahrzeuge.
- Hexcel Corp. (2006). New cost optimized axle module for composite leaf springs - from Magna Steyr, composite trends. www.hexcel.com/news/newsletters/letter-20060401.pdf
- Hojnacki, H. E., & Taka, G. (2011). Lightweight automotive seating system. (SAE Paper Number: 2011-01-0424). Warrendale, PA: Society of Automotive Engineers.
- Huang, J., & Wang, X. (2009). Numerical and experimental investigations on the axial crushing response of composite tubes. *Composite Structures*, 91:222-228.
- Huang, Z. M. (2002). Modeling and characterization of bending strength of braided fabric reinforced laminates. *Journal of Composite Materials*, 36:2537-2566.
- Hufenbach, W., Marques Ibraim, F., Langkamp, A., Böhm, R., & Hornig, A. (2008). Charpy impact tests on composite structures – An experimental and numerical investigation. *Composites Science and Technology*, 68(12):2391–2400.
- HYPERCO. (2011). Composite leaf springs. www.hypercoils.com/products/hyperco-composite-leaf-springs.aspx
- Inai, R., Chirwa, E. C., Saito, H., Uozumi, T., Nakai, A., & Hamada, H. (2003). Experimental investigation on the crushing properties of carbon fiber braided composite tubes. *International Journal of Crashworthiness*, 8(5):513-521.

- Ivanov, D. S., Baudry, F., Van Den Broucke, B., Lomov, S. V., Xie, H., & Verpoest, I. (2009). Failure analysis of triaxial braided composite. *Composites Science and Technology*, 69:1372-1380.
- Jahn, T., Baudouin, I., Vatel, P., Karnik, S., Perez, O., Cue, JM., Benichou, H. P., Dittmar, H., Sengbusch, J., & Kurcz M. (2005). Development of Lightweight, Hybrid Steel / GMT Composite IP Carrier to Meet World Crash Requirements on Passenger Vehicles. The 5th Annual SPE Automotive Composites Conference, Troy MI. www.speautomotive.com/SPEA_CD/SPEA2005/pdf/1/11.pdf
- Janapala, N., Wu, Z., Chang, F. K., & Goldberg, R. K. (2008). Lateral crashing of tri-axially braided composite tubes. Proceedings of the 11th International Conference on Engineering, Science, Construction, and Operations in Challenging Environments (Earth and Space 2008), Long Beach, CA.
- Kulekci, M. K. (2008). Magnesium and its alloys applications in automotive industry. *The International Journal of Advanced Manufacturing Technology*, 39(9-10): 851-865, DOI: 10.1007/s00170-007-1279-2
- Langsdorf, J. (2011). Weight savings: steel vs. aluminum wheels. www.ehow.com/about_5664238_weight-steel-vs_-aluminum-wheels.html
- Li, X., Binienda, W. K., & Goldberg, R. K. (2011). Finite-element model for failure study of two-dimensional triaxially braided composite. *Journal of Aerospace Engineering*, 24(2):170-181.
- Li, X., Binienda, W. K., & Littell, J. D. (2009). Methodology for impact modeling of triaxial braided composites using shell elements. *Journal of Aerospace Engineering*, 22(3):310-317.
- Lithiummoto. (2011). Lithium high performance replacement batteries. www.lithiummoto.com/index.html
- Littell, J. D., Binienda, W. K., Roberts, G. D., & Goldberg, R. K. (2008). A modeling technique and representation of failure in the analysis of triaxial braided carbon fiber composites. NASA/TM-2008-215245.
- Littell, J. D., Binienda, W. K., Roberts, G. D., & Goldberg, R. K. (2009a, Characterization of damage in triaxial braided composites under tensile loading. *Journal of Aerospace Engineering*, 22(3):270-279.
- Littell, J. D., Binienda, W. K., Arnold, W. A., Roberts, G. D., & Goldberg, R. K. (2009b, Effect of microscopic damage events on static and ballistic impact strength of triaxial braid composites. *Composites: Part A*, 40:1846-1862.

- LOTUS engineering. (2010). Vehicle mass reduction opportunities. www.epa.gov/air/caaac/mstrs/oct2010/5_peterson.pdf
- Lu, G. & Yu, T. (2003). Energy absorption of structures and materials. CRC Press, Boca Raton, FL.
- Lukkassen, D. & Meidell, A. (2008). Advanced materials and structures and their fabrication processes. Narvik University College, Narvik, Norway.
- Lutsey, N. P. (2010, May). Review of technical literature and trends related to automobile mass-reduction technology. (Research Report No. UCD-ITS-RR-10-10). Sacramento, CA: California Air resources Board. Available at http://www.arb.ca.gov/msprog/levprog/leviii/meetings/051810/2010_ucd-its-rr-10-10.pdf
- Livermore Software Technology Corporation. (2012, Modeling of composites in LS-DYNA. (PowerPoint presentation). Retrieved from <http://awg.lstc.com/tiki/tiki-index.php?page=LSTC%20Tutorials%20and%20Topic%20Presentations>
- Magnesium Elektron. (2011). Magnesium in automotive. Retrieved from www.magnesium-elektron.com/markets-applications.asp?ID=7
- Mallick, P. K. (2010). Materials, design and manufacturing for lightweight vehicles. Boca Raton, FL: CRC Press.
- Mamalis, A. G., Manolakos, D. E., Demosthenous, G. A., & Ioannidis, M. B., (1998) Crashworthiness of composite thin-walled structural components. Boca Raton, FL: CRC Press.
- Mamalis, A. G., Manolakos, D. E., Ioannidis, M. B., & Papapostolou, D. P. (2005). Finite element modeling of the crushing response of square carbon FRP tubes subjected to static and dynamic axial compression. *WIT Transaction on Engineering Sciences*, 49:373-386.
- Marks, M. (2008, September). Long glass fiber-polypropylene light weight instrument panel retainers & door modules. SPE Automotive Composites Conference & Exhibition, Troy MI. Available at www.speautomotive.com/SPEA_CD/SPEA2008/pdf/a/TP-08c.pdf
- Marks, M. D. (2011, July.). Personal communication, SABIC.
- Matzenmiller, A., & Schweizerhof K., 1991, Crashworthiness simulations of composite structures – a first step with explicit time integration. in Nonlinear Computational Mechanics State of Art. In P. Wriggers & W. Wagner, eds., Springer-Verlag, Berlin, pp. 642-670.
- Matzenmiller, A., Lubliner, J., & Taylor, R. L., 1995, A constitutive model for anisotropic damage in fiber-composites. *Mechanics of Materials*, 20:125-152.

- McGregor, C., Vaziri, R., & Xiao, X. (2010). Finite element modeling of the progressive crushing of braided composite tubes under axial impact. *International Journal of Impact Engineering*, 37:662-672.
- McWilliams, A. . (2011, February). Lightweight materials in transportation, (Report Code AVM056B). Wellesley, MA: BBC Research.
- Melzig, J., & Lehner, M. (2006). Lightweight construction due to thermoplastic foams as exemplified in an instrument-panel support. (SAE Paper Number: 2006-01-1404).
- Menna, C., Asprone, D., Caprino, G., Lopresto, V., & Prota, A. (2011). Numerical simulation of impact tests on GFRP composite laminates. *International Journal of Impact Engineering*, 38,677-685.
- Mohan, P., Marzougui, D., Arispe, E., & Story, C. (2009a, Component and full-scale tests of the 2007 Chevrolet Silverado suspension system. (Report No. NCAC 2009-W-004). Washington, DC: Federal Highway Administration. Available at www.ncac.gwu.edu/research/pubs/NCAC-2009-R-004.pdf
- Mohan, P., Ritter, M., Marzougui, D., Brown D., Kan, C. D., & Opiela, K. (2009b, Modeling, testing, and validation of the 2007 Chevy Silverado finite element model. (Report No. NCAC 2009-W-005). Washington, DC: Federal Highway Administration. Available at www.ncac.gwu.edu/research/pubs/NCAC-2009-W-005.pdf
- Mohan, P., & Smith, DL. (2007). Finite element analysis of compatibility metrics in frontal collisions. Proceedings of the 20th International Technical Conference on the Enhanced Safety of Vehicles Conference, Lyon, France, June 18-21.
- Morgan, P. (2005). Carbon fibers and their composites. Boca Raton, FL: CRC Press.
- Motor Sports Newswire. (2011). Racing batteries USA sparks agreements with the California superbike school & zipty racing. Retrieved from <http://motorsportsnewswire.wordpress.com/tag/lightweight-batteries/>
- Naik, R. A., 1995, Failure analysis of woven and braided fabric reinforced composites. *Journal of Composite Materials*, 29:2334-2363.
- Naughton, P., Shembekar, P., Lokhande, A., Kauffman, K., Rathod, S., & Malunekar, G. (2009). Eco-friendly automotive plastic seat design. (SAE Paper Number: 2009-26-0087).
- National Crash Analysis Center. (2009a, Finite element model archive: 2007 Chevy Silverado, detailed model (929,131 elements). Ashburn, VA: Author,. Available at www.ncac.gwu.edu/vml/models.html

- National Crash Analysis Center. (2009b, Finite element model of element model of Chevy Silverado. Ashburn, VA: Author,. Available at www.ncac.gwu.edu/vml/archive/ncac/vehicle/silverado-v2.pdf
- National Highway Traffic Safety Administration. (2011). NHTSA workshop on vehicle mass-size-safety. Washington, DC: Author. Available at www.nhtsa.gov/Laws+&+Regulations/CAFE+-+Fuel+Economy/NHTSA+Workshop+on+Vehicle+Mass-Size-Safety
- Nusholtz, G. S., Xu, L., Shi, Y., & Domenico, L. D. (2005). Vehicle mass, stiffness and their relationship. Proceedings of The 19th International Technical Conference on the Enhanced Safety of Vehicles Conference, Washington, DC, June 6-9.
- Ogando, J. (2003). Carbon-fiber drives shaft systems. Design News. Retrieved from www.designnews.com/document.asp?doc_id=222235
- Okano, M., Nakai, A., & Hamda, H. (2005). Axial crushing performance of braided composite tubes. *International Journal of Crashworthiness*, 10(3):287-294.
- Patel, R. B. & Richardson, F. (2006, November). New car assessment program frontal barrier impact test: 2007 Chevrolet Silverado LT1 4-door truck. NHTSA Number M70109, Test Number: 5877. (Report No. TR-P27001-04-NC). Washington, DC: National Highway Traffic Safety Administration.
- Plott, J. (2011, June). Personal communication, BASF.
- Porsche. (2009). New lightweight battery option for the Porsche 911 GT3, 911 GT3 RS and Boxster Spyder. Retrieved from <http://press.porsche.com/news/release.php?id=510>
- Powers, W. F. (2000, Automotive materials in the 21st century. *Advanced Materials & Processes*, 157(5):38-41.
- Quek, S. C., Waas, A. M., Shashwan, K. W., & Agaram, V. (2006). Failure mechanics of triaxially braided carbon composites under combined bending-compression loading. *Composites Science and Technology*, 66:2548-2556.
- Roberts, G. D., Goldberg, R. K., Binienda, W. K., Arnold, W. A., Littell, J. D., & Kohlman, L. W. (2009, September). Characterization of triaxial braided composite material properties for impact simulation. (Report No. NASA/TM-2009-215660). Washington, DC: National Aeronautics and Space Administration. Available at http://ntrs.nasa.gov/archive/nasa/casi.ntrs.nasa.gov/20090034480_2009034927.pdf
- SABIC. (2006). SABIC innovative plastics helps GM create first thermoplastic fenders in a North American truck platform with 2006 HUMMER. Retrieved from http://kbam.geampod.com/KBAM/Reflection/Assets/9816_5.pdf

- SABIC. (2010, November). SABIC innovative plastics' SABIC STAMAX long glass fiber PP helps Hyundai Sonata's plastic door module win 2010 SPE innovation award. Retrieved from www.sabic-ip.com/gep/en/NewsRoom/PressReleaseDetail/november_10_2010_sabicinnovativeplasticssabic.html
- SABIC. (2011a) Lexan resin. Retrieved from www.sabic-ip.com/gep/Plastics/en/ProductsAndServices/ProductLine/lexan.html
- SABIC. (2011b) Noryl GTX resin. Retrieved from www.sabic-ip.com/gep/Plastics/en/ProductsAndServices/ProductLine/norylgtx.html
- SABIC. (2011c, Xenoy resin. www.sabic-ip.com/gep/Plastics/en/ProductsAndServices/ProductLine/xenoy.html
- Schewel, L. (2008). Triple safety: lightweighting automobiles to improve occupant, highway, and global safety. (SAE Technical Paper 2008-01-1282). Warrendale, PA: Society of Automotive Engineers.
- Schweizerhof, K., Weimar, K., Münz, T., & Rottner, T., 1998, Crashworthiness analysis with enhanced composite material models in LS-DYNA – merits and limits. The 5th International LS-DYNA User's Conference, Detroit, MI.
- Seagrave, T. D. (2003). Structural RIM choices for today's automotive design. The 3rd Annual SPE Automotive Composites Conference, Troy MI. Available at www.speautomotive.com/SPEA_CD/SPEA2003/pdf/i01.pdf
- Sehanobish, K. (2009, April). Engineering plastics and plastic composites in automotive applications. Warrendale, PA: Society of Automotive Engineers.
- Sevkat, E., Liaw, B. M., Delale, F., & Raju, B. B. (2008). Drop-weight impact responses of woven hybrid glass-graphite/toughened epoxy composites. Proceeding of ASME International Mechanical Engineering Congress and Exposition (IMECE), Boston, MA.
- SGL Group. (2011). Carbon-ceramic brake disks. Retrieved from www.sglgroup.com/cms/international/products/product-groups/bd/carbon-ceramic-brake-disks/index.html?_locale=en
- Siddaramanna, G., Shankar, S., & Vijayarangan, S. (2006). Mono composite leaf spring for light weight vehicle – design , end joint analysis and testing. *Materials Science*, 12(3):220-225.
- Slik, G. (2002). Evolution of structural instrumental panels. (SAE Paper Number: 2002-01-1270). Warrendale, PA: Society of Automotive Engineers.
- Smock, D. (2009). Plastic oil pans present major integration opportunity. Design News. Retrieved from www.designnews.com/document.asp?doc_id=228511.

- Staab, G. H., 1999, Laminar composites. First edition. Woburn, MA: Butterworth-Heinemann.
- Strongwell. (2011). Composite driveshafts. Retrieved from www.strongwell.com/selected_markets/comp_driveshaft/
- Summers, S. (2011, February). Finite element modeling in fleet safety studies. (PowerPoint presentation). NHTSA Vehicle Mass-Size-Safety Symposium. Available at www.nhtsa.gov/staticfiles/rulemaking/pdf/MSS/MSSworkshop_Summers.pdf
- Tack, J. L. (2006). Thermodynamic and mechanical properties of EPON 862 with coupling agent Detda by molecular simulation. (Master's thesis). College Station, TX: Texas A&M University.
- Tahan, F., Park, CK., Morgan, RM., Cui, C., & Kan, C. D. (2012, Crashworthiness effects of reduced vehicle mass. Asburn, VA: National Crash Analysis Center.
- Travale, D. J., & Paolini, V. M. (2010, November). New car assessment program frontal barrier impact test: 2011 Chevrolet Silverado 1500 crew cab 4WD pickup. NHTSA number, MB0114, Test number: 7121. (Report No. NCAP-CAL-11-016). Washington, DC: National Highway Traffic Safety Administration.
- Tsai, S. W, & Wu, E. M., 1971, A general theory of strength for anisotropic materials. *Journal of Composite Materials*, 5:58-79.
- Tucker, N & Linsey, K. (2002). An introduction to automotive composites. Shropshire, UK: Smithers Rapra Press.
- Ugural, A. C., 1999, Stresses in plates and shells. 2nd edition. New York: McGraw-Hill.
- U.S. Department of Energy. (2001, Composite materials production methods developed. Vehicle Technologies Program. Washington, DC: Author. Retrieved from www1.eere.energy.gov/vehiclesandfuels/pdfs/success/composite_mtls_mar_2001_2.pdf
- Vaidya, U. (2011). Composites for automotive, truck and mass transit. Lancaster, PA: DEStech Publications, Inc. Volpe National Transportation Systems Center. (2008). A summary of proceedings for the safety characterization of future plastic and composite intensive vehicles (PCIVs). Cambridge, MA: Author. Available at http://ntl.bts.gov/lib/32000/32200/32205/summary_pciv_workshop.pdf.
- Williams, D. (2011). GM offering tire inflator kits instead of spare tires on some models Retrieved from www.everycarlisted.com/blog/2011/05/gm-offering-tire-inflator-kits-instead-of-spare-tires-on-some-models/

- Wu, C. D., Yan, X. Q., & Shen, L. M. (2010). A numerical study on dynamic failure of nanomaterial enhanced laminated glass under impact. Proceedings of WCCM/APCOM 2010, Sydney, Australia; Material Science and Engineering, Vol. 10.
- Xiao, J. R., Gama, B. A., & Gillespie, Jr., J. W. (2007). Progressive damage and delamination in plain weave S-2 glass/SC-15 composites under quasi-static punch-shear loading. *Composite Structures*, 78(2), 182–196.
- Xiao, X. (2009) Modeling energy absorption with a damage mechanics based composite material model. *Journal of Composite Materials*, 43, 427-444.
- Xiao, X., McGregor, C., Vaziri, R., & Poursartip, A. (2009) Progress in braided composite tube crush simulation. *International Journal of Impact Engineering*, 36, 711-719.
- Xiao, X., Botkin, M. E., & Johnson, N. (2009) Axial crush simulation of braided carbon tubes using MAT58 in LS-DYNA. *Thin-Walled Structures*, 47, 740-749.
- Zarei, H., Kroger, M., & Albertsen, H. (2008). An experimental and numerical crashworthiness investigation of thermoplastic composite crash boxes. *Composite Structures*, 85, 245-257.
- Zeng, T., Fang, D., & Lu, T. (2005). Dynamic crashing and impact energy absorption of 3D braided composite tubes. *Materials Letters*, 59, 1491-1496.
- Zhang, G. M., Batra, R. C., & Zheng, J. (2008). Effect of frame size, frame type, and clamping pressure on the ballistic performance of soft body armor. *Composites: Part B*, 39, 476-489.
- Zhou, Y., Jiang, D., & Xia, Y. (2001). Tensile mechanical behavior of T300 and M40J fiber bundles at different strain rate. *Journal of Materials Sciences*, 36, 919-922.

Appendix A.
Material Test Report
by
University of Dayton Research Institute
(UDRI)



UDR-TR-2011-78

**INVESTIGATE OPPORTUNITIES
FOR LIGHTWEIGHTING
VEHICLES USING ADVANCED
PLASTICS AND COMPOSITES -
HIGHER RATE TESTING OF TWO
DIMENSION TRIAXIAL BRAID
CARBON COMPOSITE**

Prepared for:

Dr. Cing-Dao (Steve) Kan
Director of FHWA/NHTSA National Crash Analysis
Center
The George Washington University, Virginia Campus
20101 Academic Way
Ashburn, VA 20147

FINAL REPORT

Purchase Order Number 1000142132

Prepared by:

Susan I. Hill
Structural Integrity Division
University of Dayton Research Institute
300 College Park
Dayton, OH 45469-0123

JUNE 2011

INDUSTRY PROPRIETARY
Distribution limited to those
with Sponsor approval

TABLE OF CONTENTS

LIST OF APPENDICES.....	vii
1.0 INTRODUCTION	1
2.0 INITIAL TEST MATRIX.....	1
3.0 MATERIAL.....	2
3.1 General Background	2
3.2 Composite Architecture and Resin	3
3.3 Final Material Selection.....	4
3.4 2D3A Specifications	5
3.5 Panel Fabrication and Properties	6
3.6 Tube Fabrication and Properties	8
3.7 Unit Cell Size and Orientation.....	9
4.0 SPECIMEN DESIGN	12
4.1 Standards.....	12
4.2 General Background on High Rate Testing.....	12
4.3 Gage Width for Testing the 2D3A.....	14
4.4 Tensile Specimen Configuration for Quasi-static Tests per ASTM D 3039	14
4.5 Bowtie Tensile for Higher Rates.....	15
4.5.1 Background.....	15
4.5.2 High Rate Tensile Specimen Configuration	17
4.6 Compression Specimen for Higher Rates	18
4.6.1 Background.....	18
4.6.2 High Rate Compression Specimen Configuration.....	18
4.7 Shear Specimen for Higher Rates	19
4.7.1 Background.....	19
4.7.2 High Rate Shear Specimen Configuration.....	20
4.8 Braided Tubes	21
5.0 FINAL TEST MATRICES	21
6.0 TEST PROCEDURES – SME AT UDRI.....	22
6.1 SME Servo-hydraulic Equipment.....	22
6.2 Oak Ridge National Laboratory (ORNL) Equipment.....	26
6.3 Strain Measurement with Digital Image Correlation System (DIC) with ISTRASoftware	26
6.3.1 General.....	26
6.3.2 Specimen Preparation	27
6.3.3 DIC Measured Region	28
6.4 Strain Measurement with Strain Gages.....	29
7.0 DATA ANALYSES.....	29
7.1 General.....	29
7.2 DIC Strain Analysis	30
7.3 DIC Strain	32
7.4 Tube Crush Analysis.....	32
8.0 RESULTS AND DISCUSSION	33
8.1 Fixture Design – General	33

8.2 Rate Effect on 2D3A Strength	34
8.3. Tensile.....	36
8.3.1 Modified ASTM D 3039 Tensile	36
8.3.2 Bowtie Axial Tensile	39
8.3.3 Bowtie Transverse Tensile.....	40
8.3.4 Comparison of Bowtie Axial and Transverse Tensile Mechanical Properties	44
8.3.3 Comparison of Modified D 3039 and Bowtie Axial and Transverse	44
8.4 Compression	48
8.4.1 Axial Compression.....	48
8.4.2 Transverse Compression.....	52
8.4.3 Comparison of Axial and Transverse Compression	56
8.5 Shear	58
8.5.1 Comparison to Published Data.....	58
8.5.2 Axial Shear (Shearing Across 0° Fiber Bundles)	58
8.5.2 Transverse Shear (Shearing Along 0° Fiber bundles)	63
8.5.3 Comparison of Axial and Transverse Shear	66
8.6 Compression Tube Tests.....	68
8.6.1 Tube Compression Strength.....	71
8.6.2 Tube Compression Strain.....	73
8.6.3 Tube Temperatures	74
9.0 OVERALL SUMMARY	75
9.1 Material Selection and High Rate Specimen Designs	75
9.2 Comparison of Tensile Data Using the ASTM D 3039 and Bowtie Configuration	75
9.3 High Rate Coupon Mechanical Properties.....	76
9.3.1 Tensile.....	76
9.3.2 Compression	76
9.3.3 Shear	76
9.4 Tube Compression	77
10.0 RECOMMENDATIONS	77
11.0 REFERENCES	78

LIST OF FIGURES

Figure 1. Axial Cross-Section of Panel 073010-1 at 25X	7
Figure 2. Axial Cross-Section of Panel 080210-6 at 25X	7
Figure 3. Transverse Cross-Section of Panel 073010-1 at 25X.....	7
Figure 4. Transverse Cross-Section of Panel 080210-6 at 25X.....	7
Figure 5. Axial Cross-Section of Tube STL103-1 at 25X	9
Figure 6. Transverse Cross-Section of Tube STL103-1 at 25X	9
Figure 7. Smallest Unit Cells for a 2-D Braid and 2-D Triaxial Braid	10
Figure 8. Unit Cell Size	10
Figure 9. Test Orientation for Panels.....	11
Figure 10. Difference in the Measured Response for Test Systems with Different Natural Resonant Frequencies	14
Figure 11. Modified ASTM D 3039 Axial Tensile.....	15
Figure 12. Modified ASTM D 3039 Transverse Tensile.....	15
Figure 13. NASA Bowtie Tensile Specimens [Reference 11].....	16
Figure 14. Relative Amounts of Bias and Axial Tows Gripped in Modified ASTM D 3039 and Bowtie Specimen Configurations	16
Figure 15. Bowtie Tensile Nominal Specimen Dimensions	17
Figure 16. Shear Specimen Nominal Dimensions	20
Figure 17. Low Rate Setup for Axial Tensile Testing	23
Figure 18. High Rate Setup for Axial Tensile Testing	23
Figure 19. Transverse Tensile in Fixture	24
Figure 20. Edge View of Compression Setup showing Unsupported Region.....	24
Figure 21. Front View of Compression Setup Used with Strain Measurement.....	25
Figure 22. Axial Shear Setup	25
Figure 23. Transverse Shear Setup	25
Figure 24. TMAC Equipment at ORNL	26
Figure 25. DIC Pattern on Axial Shear Specimen	27
Figure 26. Grid Mesh and Measured Regions for a Slow Rate Axial Tension Test.....	28
Figure 27. Possible Features for DIC Analysis.....	28
Figure 28. Grid Mesh (a) and Measured Regions (b) for an Axial Compression Test.....	29
Figure 29. DIC Strain Output for Different Regions (a) and DIC Image (b) for an Axial Shear Test [Specimen STL095-1]	31
Figure 30. Stress Response at Low (a) and Fast Test Rate (b) for an Axial Shear Test.....	32
Figure 31. Peak Axial Strength of 2D3A at All Rates – Normalized to 56% Fiber Content	35
Figure 32. Peak Transverse Strength of 2D3A at All Rates Rates – Normalized to 56% Fiber Content.....	36
Figure 33. Tensile Stress-strain Curves for Modified ASTM D 3039 2D3A.....	37
Figure 34. Strain Gage Location for Axial Modified ASTM D 3039 2D3A.....	38
Figure 35. Comparison of Stress-strain Curves using Strain Gage and DIC Data	38
Figure 36. Typical Failure Locations for Axial (a) and Tensile (b) Modified D 3039 Specimens	38
Figure 37. Representative Stress-strain Curves for 2D3A Bowtie Axial Specimens at All Rates.....	40
Figure 38. Typical Failure of Axial Bowtie Tensile Specimen	40

Figure 39. Representative Stress-strain Curves for 2D3A Bowtie Transverse Specimens at All Rates.....	42
Figure 40. Schematic of Fiber Tow Location in Center Gage for Axial (a) and Transverse (b) Tensile Bowtie Specimen	43
Figure 41. Measured Peak Tensile Stress of Axial and Transverse 2D3A Normalized to 56 vol% Fiber	44
Figure 42. Measured Modulus of Axial and Transverse 2D3A.....	45
Figure 43. Failure Strain of Axial and Transverse 2D3A.....	45
Figure 44. Comparison of Axial Tensile Stress-strain Response at 1.27 mm/min.....	47
Figure 45. Comparison of Transverse Tensile Stress-strain Response at 0.6 to 1.27 mm/min for Modified ASTM D 3039 and Bowtie Specimens	47
Figure 46. Axial Compressive Stress-strain Response at All Rates Using Straight-sided Specimens	50
Figure 47. Axial Compressive Stress-strain Response at All Rates Using Dogbone and Straight-sided Specimens.....	50
Figure 48. 2D3A Axial Compressive Strength as a Function of Strain Rate	51
Figure 49. 2D3A Axial Compressive Modulus as a Function of Strain Rate.....	51
Figure 50. 2D3A Axial Compressive Failure Strain as a Function of Strain Rate	52
Figure 51. Failure Location for Dogbone and Straight-sided Axial Compressive Specimens	52
Figure 52. Transverse Compressive Stress-strain of 2D3A at All Rates.....	54
Figure 53. 2D3A Transverse Compressive Strength as a Function of Strain Rate.....	54
Figure 54. 2D3A Transverse Compressive Modulus as a Function of Strain Rate	55
Figure 55. 2D3A Transverse Compressive Failure Strain as a Function of Strain Rate	55
Figure 56. Typical Failure Location for Transverse Compressive Specimens.....	56
Figure 57. 2D3A Compressive Strength as a Function of Strain Rate	56
Figure 58. 2D3A Compressive Modulus as a Function of Strain Rate.....	57
Figure 59. 2D3A Compressive Modulus as a Function of Strain Rate Using Straight-sided Specimens	57
Figure 60. 2D3A Compressive Failure Strain as a Function of Strain Rate	58
Figure 62. Axial Shear Stress-Strain Response of 2D3A Across Tested Rates.....	60
Figure 62. Axial Shear Strength of 2D3A Across Tested Rates	60
Figure 63. Axial Shear Modulus of 2D3A Across Tested Rates	61
Figure 64. Axial Shear Failure Strain of 2D3A Across Tested Rates	61
Figure 65. Typical Axial Shear Failure Locations.....	62
Figure 66. Unsmoothed Axial Shear Stress-Strain Response at 0.25/s	62
Figure 67. Transverse Shear Stress-Strain Response of 2D3A Across Tested Rates	64
Figure 68. Transverse Shear Strength of 2D3A Across Tested Rates	64
Figure 69. Transverse Shear Modulus of 2D3A Across Tested Rates	65
Figure 70. Transverse Shear Failure Strain of 2D3A Across Tested Rates.....	65
Figure 71. Typical Transverse Shear Failure Locations	66
Figure 72. 2D3A Shear Strength as a Function of Strain Rate	66
Figure 73. 2D3A Shear Modulus as a Function of Strain Rate	67
Figure 74. 2D3A Shear Failure Strain as a Function of Strain Rate.....	67
Figure 75. Typical Tube Crush Load-Displacement Curves at a Slow and Fast Rate.....	68
Figure 76. Low Rate Tube Failure.....	69
Figure 77. High Rate Tube Failure	69

Figure 78. Polygon Regions Tracked by the DIC and Comparison of the Measured Displacements to the Actuator Displacement	70
Figure 79. Load-Displacement Curves Across the Tested Rates.....	71
Figure 80. SEA Across Tested Rates	72
Figure 81. Tube Compressive Stress-Strain at 1.5 m/min	73
Figure 82. Comparison of Tube and Coupon Compressive Stress-Strain	73
Figure 83. Composite Tube Temperatures During Crush.....	74

LIST OF TABLES

Table 1. Initial Coupon-Level Test Matrix	2
Table 2. Initial Tube Compression Matrix.....	2
Table 3. Carbon and Glass Fiber Strength and Stiffness	3
Table 4. 2D3A Tow Description.....	5
Table 5. Laminate Physical Properties.....	7
Table 6. Tube Physical Properties	9
Table 7. Unit Cell Sizes for Panels	11
Table 8. Final Coupon-Level Test Matrix	21
Table 9. Final Tube Compression Matrix	22
Table 10. Comparison of UDRI and Published Data for 2D3A with Epon 862W at Quasi-static Rates.....	37
Table 11. Bowtie Axial Tensile Data Summary for 2D3A.....	39
Table 12. Bowtie Transverse Tensile Data Summary for 2D3A	41
Table 13. Comparison of Bowtie and Modified ASTM D 3039 Tensile Properties at 1.27 mm/min	46
Table 14. Comparison of Axial Compression UDRI and Published Data [13]	49
Table 15. Axial Compression Data Summary for 2D3A	49
Table 16. Comparison of Transverse Compression UDRI and Published Data [13]	53
Table 17. Transverse Compression Data Summary for 2D3A	53
Table 18. Comparison of UDRI Shear Data and Published Data [13]	59
Table 19. Axial Shear Data Summary for 2D3A	59
Table 20. Transverse Shear Summary Table of 2D3A	63
Table 21. Compression Tube Strength and Peak Temperatures	72

LIST OF APPENDICES

APPENDIX A	
MATERIAL PRODUCT SHEETS.....	A-1
APPENDIX B	
LAMINATE AND TUBE PHYSICAL PROPERTIES	B-1
APPENDIX C	
SELECTED PANEL LAYOUTS	C-1
APPENDIX D	
SAMPLE PHOTOMICROGRAPHS OF PANEL CROSS-SECTIONS AT 50X	
PHOTOMICROGRAPHS OF TUBE CROSS-SECTIONS AT 25X	D-1
APPENDIX E	
UNIT CELL MEASUREMENTS AND LOCATIONS	E-1
APPENDIX F	
BOWTIE TENSILE SPECIMENS AND FIXTURE DRAWINGS.....	F-1
APPENDIX G	
COMPRESSION SPECIMEN AND FIXTURE DRAWINGS.....	G-1
APPENDIX H	
SHEAR SPECIMEN AND FIXTURE DRAWINGS	H-1
APPENDIX I	
SME EQUIPMENT LIST AND CALIBRATIONS.....	I-1
APPENDIX J	
MODIFIED ASTM D3039 TENSILE DATA PACKAGE.....	J-1
APPENDIX K	
BOWTIE AXIAL TENSILE DATA PACKAGE	K-1
APPENDIX L	
BOWTIE TRANSVERSE TENSILE DATA PACKAGE.....	L-1
APPENDIX M	
AXIAL COMPRESSION DATA PACKAGE	M-1
APPENDIX N	
TRANSVERSE COMPRESSION DATA PACKAGE.....	N-1

APPENDIX O	
AXIAL SHEAR DATA PACKAGE	O-1
APPENDIX P	
TRANSVERSE SHEAR DATA PACKAGE.....	P-1
APPENDIX Q	
TUBE COMPRESSION DATA PACKAGE	Q-1

1.0 INTRODUCTION

The Plastic and Composite Intensive Vehicle (PCIV) safety research programs, sponsored by the Department of Energy, are focused on increasing fuel efficiency and reducing vehicle weight without compromising crash safety. Some of the materials currently under investigation are long fiber-filled polymers and composites. It is critical to understand the change in the material response and energy absorption of these materials under impact conditions if they are to be considered in the design of automotive components and structures.

The behavior and deformation of composites under impact conditions is different from the typical metals used in structural components. The failure modes (delamination, matrix debonding, fiber breakage, etc.) have to be modeled on both a micro and macroscopic scale to capture the correct response. Material property data at rates above quasi-static (typically above 0.0001/s) are needed to validate and optimize the models.

The small specimen length needed to achieve the high rates is usually in direct conflict with the size needed to represent bulk material properties, especially for composites. The gage length and cross-sectional area of current high rate specimens are relatively small (approximately 3 to 10 mm) and approach the magnitude of the unit “cell” of many fabric weaves, braids, or hybrid sandwich materials. Increasing the specimen width in order to test a larger volume of material often runs into the roadblock of equipment capacity.

Composite testing at quasi-static rates poses a unique set of concerns, such as specimen-to-specimen variability, failures within the gage section, and non-homogeneous regions. High rate testing introduces several others, such as specimen configuration, resonant ringing, strain measurement to failure, and actuator capacity. The goal of generating representative bulk material properties may be difficult to achieve over a wide strain rate regime depending on the type of composite and equipment capacities.

The goal of the effort at the Structures and Materials Evaluation (SME) Group of the University of Dayton Research Institute (UDRI) was to identify a composite that would be suitable to use for automotive structural components and to generate material property data on a coupon and component level at rates above quasi-static. The program involved material selection, specimen and fixture design, specimen and fixture fabrication, coupon testing (tensile, compression, and shear), and tube testing.

2.0 INITIAL TEST MATRIX

The original scope of the test program is outlined in Tables 1 and 2. The maximum test rates were not known at the start. The results from the lower rate tests and the final specimen designs were to dictate the upper rate for each test. However, some assumptions had to be made regarding the scope of the test program to serve as the basis for the composite panel requirements. The final test matrices are summarized in Section 4.0.

Table 1. Initial Coupon-Level Test Matrix

		Machine Rate [m/min]		
		0.0006	0.6	12-24
		Estimated Nominal Strain Rate [1/s]		
		0.0004	0.04-0.08	4-8
Tension-per ASTM D 3039	Axial	3	0	0
	Transverse	0	0	0
Higher Rate Tension	Axial	3	3	3
	Transverse	3	3	3
Compression	Axial	3	3	3
	Transverse	3	3	3
Higher Rate Shear	Axial	3	3	3
	Transverse	3	3	3
Total		21	18	18
Grand total		57		

Table 2. Initial Tube Compression Matrix

	Machine Rate [m/min]		
	1.5	~60	~480
Straight End	3	0	0
Single bevel	3	3	3
Total	6	3	3
Grand total	12		

3.0 MATERIAL

3.1 General Background

Composite materials are available in a large variety of fiber types, resin systems, and architectures. Current automotive applications are mainly non-structural, such as instrument panels, interior trim, leaf springs, fuel tanks, hoods, fenders and other exterior panels.

Composites are attractive because of the high strength to weight ratio, design versatility, corrosion resistance, and potential for parts consolidation. Some of the disadvantages are low ductility, recyclability, energy absorption, high material costs, and low production volume [1,2]. They are generally made with either glass or carbon fibers and a matrix of a thermoset or thermoplastic polymer. Composite recyclability has increased the interest in the use of natural fibers, such as bamboo, flax, jute, sisal, and banana, as a replacement for glass fiber. [3,4,5]

The focus of this study was to identify a composite architecture that would provide high strength, stiffness, and energy absorption. The potential application was for a F150 truck body rail, which was being modeled by George Washington University (GWU). The DOE specifically tasked UDRI and GWU to not consider the overall cost of the material nor part production¹ in the material selection. The DOE wanted to identify what scale of improvement could be achieved using composites and to use this as a target benchmark. GWU and DOE were also interested in selecting a material for which there was some published quasi-static material properties for comparison to the high rate data. A secondary goal was to provide the general engineering community with a data set of material properties which would be used for model validation.

3.2 Composite Architecture and Resin

The high strength and stiffness of carbon fiber makes it an ideal candidate for an automotive structural application. As shown in Table 3, its strength and stiffness is two to three times that of the typical E-glass. Its modulus is also at least twice that of either E or S-glass. Since the carbon fiber density is also low, the overall performance to weight ratio of a carbon composite is higher than a glass composite. This is an advantage in the design of integrated parts for lightweighting vehicles.

Table 3. Carbon and Glass Fiber Strength and Stiffness

Material	Tensile Strength [MPa]	Elastic Modulus [GPa]	Density [gm/ml]
Carbon Fiber T700S ⁽⁶⁾	4900	230	2.0
E Glass ⁽⁷⁾	1900-2600	73	2.5
S-glass ⁽²⁾	4380-4590	88-91	2.48
Natural fibers ⁽⁸⁾	400-1500		

Thermoset polymers are preferred for high performance applications since the polymer matrix will not soften at the expected maximum service temperatures (e.g. 80°C). Epoxy resins are often used with carbon fibers since epoxies offer high strength, low shrinkage, electrical insulation, and chemical and solvent resistance with low cost [2]. They wet the material easily and the composite can be processed using a variety of methods. Phenolic resins are slightly more expensive and tend to be used for those applications which have stringent fire and smoke requirements.

The polymeric resin serves to bind the fiber architecture and to transfer the applied loads. The composite mechanical properties are mainly defined by the fiber architecture. The optimum design for maximum strength and stiffness is a unidirectional layup of carbon fibers which are located parallel to the loading axis [2]. A single directional fiber lay-up is only practical if the loading direction is well-defined.

¹ Kick-off meeting at the National Crash Analysis Center GWU 19 November 2009

Multi-directional loading requires a series of layers or plies of unidirectional fibers which can be oriented at various angles to coincide with the expected loading directions. The composite can also be designed to represent an isotropic material, usually by using alternating layers of $\pm 45^\circ$ and 0° unidirectional plies. The mechanical properties are dependent on the angles of the layers and the symmetry. The properties will approach, but not equal, those of a unidirectional laminate along a given axis [8].

Some alternative methods use chopped fibers, fabric weaves, or fiber braid as a way to handle the issue of off-axis or multi-directional loads. Chopped fibers can be incorporated in several ways. Two common methods are to use a mat which consists of randomly oriented fibers of a given length or to injection mold the precut fibers along with the resin into the final part. The mechanical attrition of the fiber varies with the processing parameters. Injection molding tends to cause the most damage to the fiber, often reducing the starting length by a factor of 10 or more [9,10].

Fabric weaves provide bundles of fibers in the 0° and 90° directions. The mechanical properties are affected by the number of fiber bundles, or tows, the number of fibers per tow, and the weave pattern. A loose weave, such as an 8 harness satin, allows the fabric to drape and match mold contours. However, the looser weave pattern is a result of fewer bundles per inch of fabric, and the mechanical properties are less than for a tighter weave.

Triaxial braided composites can offer an isotropic design by utilizing axial and angled fiber bundles in a single plane. These are called two-dimensional triaxial braid (2D braid). Typical angles are 0° axial tows with $\pm 60^\circ$ or $\pm 45^\circ$ tows. Through-the-thickness fibers result in a three-dimensional triaxial braid (3D braid). Braided composites also offer better damage resistance, torsional stability, and bearing strength compared to unidirectional or weaved composites [1,2]

Triaxial braid has been used in the commercial aerospace and automotive industry for over 20 years. It has been the focus of the Automotive Composites Consortium (ACC) of US Car and NASA for several years and many articles have been published. [11-14]. It is well-suited for components which are of simple geometry, such as a vehicle shaft, and can provide off-axis as well as unidirectional strength.

3.3 Final Material Selection

Input was solicited from technical members in the aerospace and automotive community regarding the best suited composite material and architecture for the proposed application. Some of the technical points of contact were: Dr. Khaled Shahwan (Chair-ACC100, Energy Management Committee Automotive Composites Consortium, Chrysler Group), Dr. Gary Roberts (Material Engineer, National Aeronautics and Space Administration Glenn Research Center [NASA]), Dr. Ming Xie (Senior Engineer, GE Aviation), Mike Schneider (Chief Consulting Engineer, Composite Applications, GE Aviation), Todd Bullions (Staff Engineer, Composite Material Behavior, GE Aviation), Dan Houston (Chair ACC Materials Committee, Technical Specialist, Manufacturing and Processes Department, Ford Motor Co.), Dr. Steve

Mitchell (Group Leader, Composites Manufacturing and Technology Transition, UDRI), Alan Fatz (Director, National Composites Center), Dr. Anthony Waas (Professor, Aerospace Engineering, University of Michigan) and Dr. Mike Braley (Vice-President Application Engineering, A&P Technology).

The overall consensus from the technical experts was to use a braided carbon-thermoset composite since both mechanical and impact properties were important in the potential application of a shaft. Various studies by NASA had published articles using $0^\circ/\pm 60^\circ$ 2D triaxial braid and quasi-static tensile, compression, and shear data were available [11-14]. The literature and survey results were discussed with GWU and it was decided to proceed using a $0^\circ/\pm 60^\circ$ 2D triaxial braid, hereafter referred to as 2D3A. Although the 60° braid angle may not be the one selected for a final shaft component, results from the program could be used to validate finite element models.

3.4 2D3A Specifications

The carbon fiber was Torayca® T700S C 12000, manufactured by Toray Carbon Fibers America, Inc. The braid architecture is given in Table 4. The axial fiber tows contained 24K fibers. The bias tows contained 12K fibers. The spacing of the axial and bias tows were such to provide the same volume of fiber bundles in all directions so that the properties were in-plane isotropic. The resin was Epon 862 epoxy with Epikure W curing agent, both manufactured by Momentive. The resin and agent were selected because it was the same combination used in the published literature for the 2D3A [11-14]. The material properties are in Appendix A.

Table 4. 2D3A Tow Description

Triaxial Broadgood Design Form (Double Slit)				
Product Code:		AP6699		
INPUTS	Fiber orientation	Bias	Axial	Total
	Fiber type	T700SC 12K	T700SC 12K	
	Total Sleeve Perimeter (in)	47.89		
	Slit Broadgood Width (in)	23.94		
	Diameter (in)	15.243	15.243	
	Angle °	60.0	0.0	
	Number of Carriers	272	136	
	Ends/Carrier	1	2	
	Raw Fiber Yield (yd/lb)	621	621	
	Fiber Density (lb/in ³)	0.064	0.064	
	Yarn Bulk Factor	1.10	1.10	
	Yarn Aspect Ratio	0.056	0.056	
	Part Fiber Volume	57%	57%	
OUTPUTS	Layer Thickness (in)	0.0139	0.0070	0.0209
	Material Content (% by volume)	66.7%	33.3%	100.0%
	Material Content (% by weight)	66.7%	33.3%	100.0%
	Percent Coverage	100.0%	57.9%	
	Areal Weight (oz/yd ²)	10.5	5.3	15.8
	Areal Weight (gsm)	357.3	178.6	535.9
	Yield of full Sleeve (ft/lb)	3.42	6.85	2.28
	Yield of double slit B/G (ft/lb)			4.57
	PPI	4.9		4.9
	EPI	5.7	2.8	
	Bundle Width	0.175	0.247	
	Bias Yarn CL Spacing (in)	0.176		
	Bias Yarn Edge Spacing (in)	0.001		

3.5 Panel Fabrication and Properties

The required number of panels was selected based on initial specimen configuration concepts, discussed in detail in Section 4. A large panel was used to accommodate the expected specimen lengths and to minimize the scrap. The panel thickness was dictated by expected tensile coupon size and UDRI equipment capacity. A maximum of three layers could be accommodated, based on published quasi-static mechanical properties [11-14].

The 2D3A was received as a braided sock. The sock was split along the longitudinal axis and cut to length. Three layers were used for each panel to minimize out-of-plane strains and warpage². The appropriate amount of resin film was added to achieve the desired thickness and target fiber content of 56%. Each panel was assembled, bagged for the autoclave, and then cured by the following cycle: The temperature was ramped up at 1.7°C/min (3°F/min) to 121°C (250°F). The pressure was held at 0.68 MPa (100 psi) for two hours. The temperature was ramped up to 176°C (350°F) at 1.7°C/min and held for two hours. The autoclave was then cooled to room temperature and the pressure released.

Six panels were cured in each cycle. The final panel dimensions were 610 mm x 610 mm x 1.7 mm (24"x24"x0.68"). A total of 18 panels were fabricated. There was some settling of each fiber layer during processing and the 0° axial fiber tows did not necessarily align through the thickness. Regions in a panel where it did occur had wide variations in thickness with noticeable peaks and valleys on the free surface, i.e. the surface not against the tooling. For example, the thickness variation of a relatively flat panel was 0.12 mm compared to 0.47 mm for a panel with noticeable peaks and valleys. The specimen measurement sheets, located on the program CD, illustrate the overall range in thickness.

At least two samples were selected for fiber content analysis. The specific gravity and fiber content of the tested panels are summarized in Table 5. The average specific gravity was 1.522 ± 0.028 and the average fiber content was $57.16\% \pm 5.86\%$. Four of the panels (073010-3, 073010-4, 073010-5, and 080210-6) had standard deviations in the fiber content in excess of 4 percentage points. The rest had standard deviations less than 2 percentage points. The data in Table 5 reflect the input from all of the samples for each panel. The detailed panel physical properties are in Appendix B.

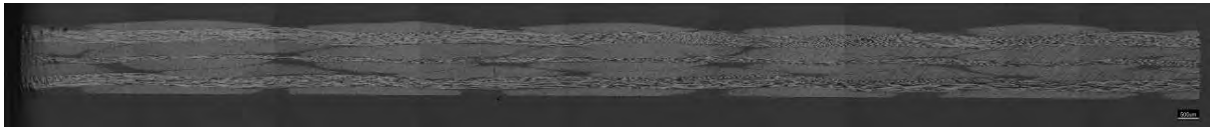
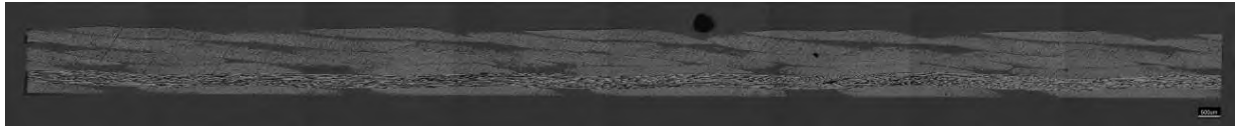
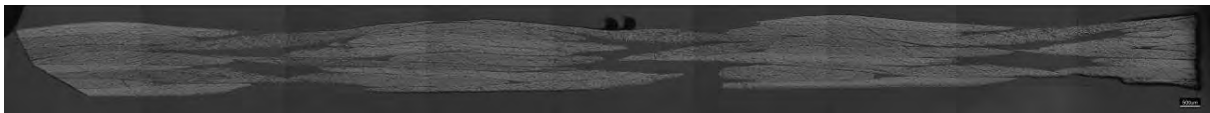
Axial and transverse cross-sections were taken from two regions to check on the fiber distribution. Appendix C contains photographs of select panels and shows the sample locations used for fiber content analyses and the cross-sections. It also shows the specimen locations.

Figures 1 and 2 show the typical axial cross-sections for two panels. The grey regions are the 0° fibers. The two panels vary by 0.24 mm in peak thickness, illustrating the variation mentioned earlier. The 0° fibers are the lighter regions in the transverse cross-section of Figures 3 and 4. A higher amount of resin is noticeable in the tow cross-over regions in both orientations. Sample photomicrographs taken at 50X are in Appendix D. Additional photomicrographs are on the program CD.

² Warpage has been noted using single and double layers, as discussed in phone conversations with Mike Braley on 10 April 2010 (A&P Technology) and Todd Bullions (GE Aviation).

Table 5. Laminate Physical Properties

Panel Identification	Specific Gravity (standard deviation)	Fiber content % (standard deviation)
072910-1	1.528 (0.005)	56.75 (0.91)
072910-2	1.538 (0.006)	59.45 (0.44)
073010-1	1.505	54.11
073010-2	1.516 (0.028)	56.99 (1.90)
073010-3	1.524 (0.006)	59.45 (5.18)
073010-4	1.536 (0.003)	51.71 (6.69)
073010-5	1.529 (0.14)	61.35 (10.8)
073010-6	1.527 (0.007)	57.35 (0.17)
080210-6	1.481 (0.076)	55.30 (3.96)
Overall	1.522 (0.028)	57.16 (5.86)

**Figure 1. Axial Cross-Section of Panel 073010-1 at 25X****Figure 2. Axial Cross-Section of Panel 080210-6 at 25X****Figure 3. Transverse Cross-Section of Panel 073010-1 at 25X****Figure 4. Transverse Cross-Section of Panel 080210-6 at 25X**

3.6 Tube Fabrication and Properties

Part of the test program included testing of a structure, such as a box or tube. Several papers are available detailing the results of crush tests of rectangular boxes, open sided boxes, and tubes [15-17]. A cylindrical tube was chosen because of its simplicity for modeling and ease of fabrication.

The bulk fiber volume of a braided tube is different from a flat panel. The initial layer goes over a mandrel that has been machined to the desired diameter. The first layer will have the tightest braid. Each subsequent layer is a little looser in comparison as the carbon is braided over an increasingly larger diameter. The tows have more freedom to move and settle compared to a flat plaque. Wrinkling can also occur as the number of layers increases. Differences in tube fiber content can be adjusted by normalizing to a given fiber level, given the assumption that the resin contribution is negligible. While this is sufficient for uni-axial compression, it is not accurate for off-axis crush tests.

The bulk volume can be increased by adding a tackifier to the resin. The overbraided mandrel is debulked between layers to remove entrapped air. This method was not chosen for two reasons: 1) the flat panels did not contain a tackifier, and 2) the additional cost was not within the program budget.

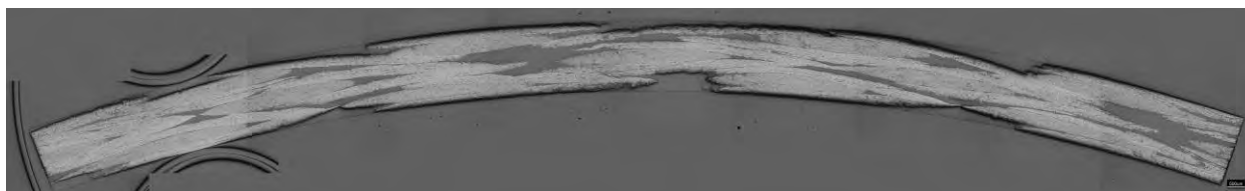
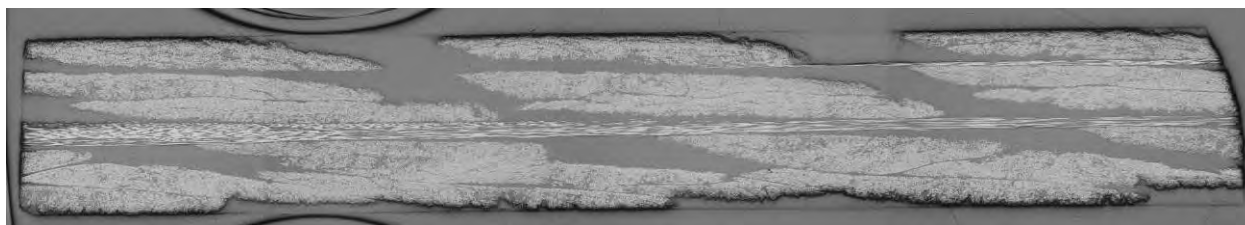
Ten mandrels were machined by the composite molder, AAR Precision, to the desired diameter of 101 mm (4.0"). The mandrels were shipped to A&P Technologies for overbraiding with three layers of $0^\circ/\pm 60^\circ$ T700 carbon fiber. The braided tubes were then shipped back to AAR for molding using Epon 862W resin. One of the tube preforms was damaged during fabrication and was not molded.

The final tube length was 610 mm with a wall thickness of approximately 3.8 mm. Each tube was cut into two pieces, approximately 266 mm long. Samples were taken for fiber content analysis from each end of the original tube and the center. The tube physical properties are in Table 6. The average specific gravity was 1.448 ± 0.019 and the average fiber content was $44.44\% \pm 2.77$. Appendix B contains the detailed physical properties. Both the specific gravity and fiber content was lower than the flat panels. The fiber content was lower by 17 percentage points.

The axial and transverse cross-sections of a tube are shown Figures 5 and 6. The grey areas in Figure 5 are the 0° fibers. The vertical alignment has not been maintained through the thickness. The pockets of resin at the tow intersections are higher than that seen in the panels (Figures 1 to 4). Additional photomicrographs are in Appendix D.

Table 6. Tube Physical Properties

Tube Identification	Specific Gravity (standard deviation)	Fiber content % (standard deviation)
103-1	1.470 (0.022)	46.58 (4.14)
103-2	1.446 (0.014)	43.17 (1.64)
103-3	1.446 (0.005)	42.59 (1.03)
103-4	1.446 (0.012)	42.90 (1.91)
103-5	1.470 (0.020)	46.89 (3.31)
103-6	1.441 (0.010)	43.89 (2.97)
103-7	1.425 (0.026)	42.55 (4.11)
103-8	1.442 (0.005)	45.27 (0.34)
103-9	1.441 (0.008)	44.78 (1.84)
Overall	1.448 (0.019)	44.44 (2.77)

**Figure 5. Axial Cross-Section of Tube STL103-1 at 25X****Figure 6. Transverse Cross-Section of Tube STL103-1 at 25X**

3.7 Unit Cell Size and Orientation

ASTM D 6856-03 Standard Guide for Testing Fabric-Reinforced “Textile” Composite Materials [18] defines the smallest repeating geometric pattern as the unit cell. Figure 7 illustrates the features defining the unit cell for 2D braid. The unit cell of a 2x2, 2D triaxial braid contains two full axial braids and three full widths of both bias tows. This is the definition used for a unit cell in this program.

Figure 8 shows the outline of a unit cell for one of the laminates. The unit cell size varied with each panel and location within the panel. The variations are probably from the relative amount of settling and compaction of the braid layers during processing.

Table 7 summarizes the average unit cell sizes for each panel. The individual cell size measurements and their locations are in Appendix E. The average unit cell size was $17.9 \text{ mm} \pm 0.53 \text{ mm} \times 5.2 \text{ mm} \pm 0.22 \text{ mm}$ ($0.71'' \times 0.20''$).

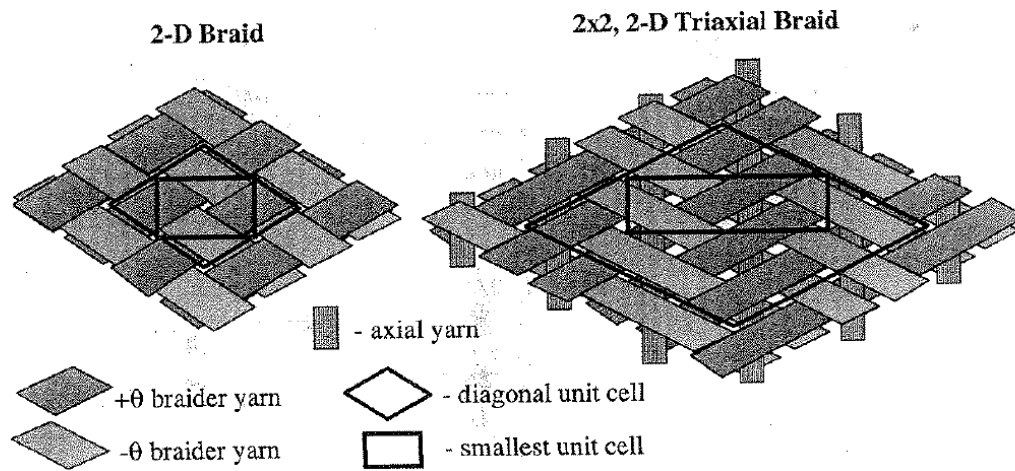


Figure 7. Smallest Unit Cells for a 2-D Braid and 2-D Triaxial Braid
(Reference Figure 2 of ASTM D 6856)

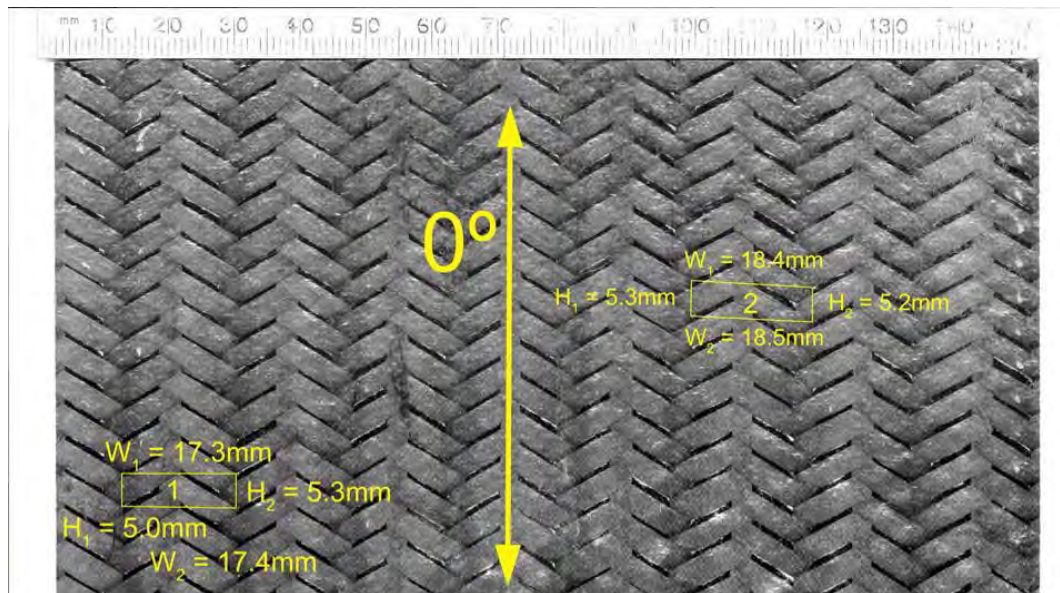
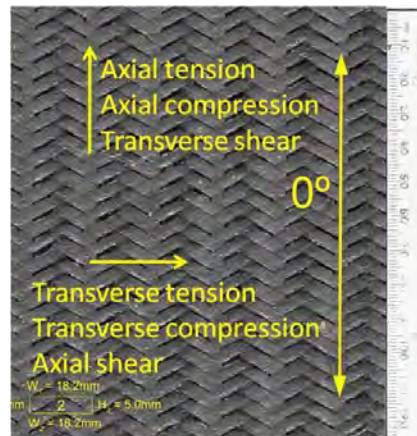


Figure 8. Unit Cell Size

Table 7. Unit Cell Sizes for Panels

Panel		Cell width [mm]	Cell height [mm]
072910-1	Average	18.3	5.3
	Std Dev	0.3	0.2
073010-1	Average	17.6	5.2
	Std Dev	0.7	0.2
073010-2	Average	17.9	5.2
	Std Dev	0.5	0.3
073010-3	Average	18.0	5.4
	Std Dev	0.4	0.3
073010-4	Average	17.8	5.2
	Std Dev	0.4	0.2
073010-5	Average	18.2	5.2
	Std Dev	0.5	0.2
073010-6	Average	17.8	5.4
	Std Dev	0.6	0.1
080210-6	Average	18.1	5.1
	Std Dev	0.3	0.2
OVERALL	Average	17.9	5.2
	Std Dev	0.53	0.22

The testing orientation is shown in Figure 9. The 0° fiber tows are parallel to the short side of the unit cell. This was designated as the axial direction for the tensile and compression specimens as the fibers were parallel to the loading direction. The “axial” shear specimens had the loading parallel to the long side of the unit cell, i.e., it was shearing across the 0° fibers. The transverse shear specimens were 90° from the axial orientation.

**Figure 9. Test Orientation for Panels**

4.0 SPECIMEN DESIGN

4.1 Standards

There are several standards referenced by ASTM D 6856 regarding tensile, compression, and shear testing of textile composites, specifically ASTM D 3039 *Test Method for Tensile Properties of Polymer Matrix Composite Materials*, ASTM D 3410 *Test Method for Compressive Properties of Polymer Matrix Composite Materials with Unsupported Gage Section by Shear Loading*, ASTM D 6641 *Test Method for Determining the Compressive Properties of Polymer Matrix Composite Laminates Using a Combined Loading Compression Test Fixture*, ASTM D 4255, *Test Method for In-Plane Shear Properties of Polymer Matrix Composite Materials by the Rail Shear Method*, ASTM D 5379 *Test Method for Shear Properties of Composite Materials by the V-Notched Beam Method*, and ASTM³ D 7078 *Standard Test Method for Shear Properties of Composite Materials by V-Notched Rail Shear Method*.

All of these standards refer to test procedures under quasi-static conditions, i.e., test speeds below 51 mm/min (2 in/min). These standards have been refined over time through the collaborative efforts of a consortium of members which include academia, research laboratories, industry, and government representatives.

Standardized test procedures are mostly lacking for high rate tests. Several guidelines or recommended procedures have been issued related to tensile testing of polymers and steels, such as SAE J2749 *High Strain Rate Tensile Testing of Polymers* [19] and SEP 1230 *The Determination of the Mechanical Properties of Sheet Metal at High Strain Rates in High-Speed Tensile Tests* [20]. No high rate standards are available for compression or shear testing.

High rate test equipment and procedures tend to be specific to a given laboratory, type of equipment, and material. As a result, high rate data are being generated using a variety of test procedures and specimen sizes. While quasi-static procedures serve as a guideline and basis for many of the high rate methods, the high rate methods will be different.

SAE J2749 provides some additional details regarding the generation of useable data at upper rates. Recommendations related to using a small specimen, minimizing the length of the load train, and raising the natural resonant frequency of the test system were important considerations in the design of the specimen geometries of the 2A3D.

4.2 General Background on High Rate Testing

The main purpose or goal of quasi-static test methods is to create a relatively large homogeneous stress and strain field. This is usually accomplished by having as large a specimen gage section as possible. Four implicit assumptions are made when reducing the data from these tests: 1) the load is equal in any cross section of the load train, 2) the strain is equal in the gage

³ All ASTM standards are available through ASTM International, 100 Bar Harbor Drive, West Conshohocken, PA

section of the specimen, 3) the strain and stress fields are in equilibrium, and, 4) the inertial forces are negligible.

The above assumptions must be scrutinized when measuring material properties at high strain rates. Normally, a constitutive equation is thought of as a function relating stresses to the strains at a point (i.e., an infinitesimal volume of material). A quasi-static test assumes that the stress and strain fields are homogeneous in the gage section. The constitutive equation is simply derived from the average response of the tested volume of material.

The wave propagation speed must be considered in a high rate test. The stress wave propagates along the specimen and is reflected and transmitted at each interface along the line of travel. These interfaces include the transition from grip to specimen, specimen to grip, grip to load washer, etc. As a result, stress waves of varying amplitudes are present in the gage section and a homogeneous stress state does not exist.

The goal in high strain rate tests becomes one of “shocking up” the gage area; i.e., introducing enough stress waves in the gage area so that one can assume that an average stress is present. At best, there is an approximate equilibrium. Since the interest is to find any strain rate dependency in the material properties, it is not necessary to determine the “true” material behavior. Instead, a comparison can be made between the behavior at static rate conditions and the material behavior at higher rates.

High rate tests dictate the use of a small specimen in order to maximize the number of reflected stress waves along the gage length. If one assumes that specimen geometry will bias the results equally over the range of strain rates used, then one can determine information on the strain rate dependency of the material.

An example of the importance of the natural test frequency is described below. SAE J2749 states that at least 10 to 15 reflected stress waves should be present in the elastic region to generate acceptable yield data. A general equation relating the speed of a stress wave through the test system is given by Eq. A 13 of SAE J2749 as:

$$t_{\text{wave}} = 2 \left[\frac{L_{\text{fixt}}}{v_{\text{fixt}}} + \frac{L_{\text{dbg}}}{v_m} \right] \quad (1)$$

where, t_{wave} is the travel time for one stress wave, L_{fixt} is the length of the fixturing, L_{dbg} is the distance between the grips, v_{fixt} is the wave propagation speed through the fixturing and v_m is the wave propagation speed through the material.

The goal is to minimize t_{wave} so that a high number of waves can propagate through the material and fixturing. At some test speed the time scale for t_{wave} will approach that of the time required to achieve the 10 to 15 waves in the elastic region. Discrete stress waves will be observed on the material response.

The v_m is fixed for a given test. The v_{fixt} is dependent on the fixturing material. Test fixtures for composites are made of metal since most composites are high strength materials. The

wave propagation speed of most metals is 4000 to 5000 m/s and altering the fixture metal offers relatively little improvement. The terms which can be easily modified thorough fixture and specimen design are L_{fixt} and L_{dbg} . Minimizing the specimen length, and hence the fixture length and weight, is a key component for a successful high rate test system. Figure 10 illustrates the difference in output one can expect by simply from changing the fixture length and weight and, thus, the natural resonant frequency.

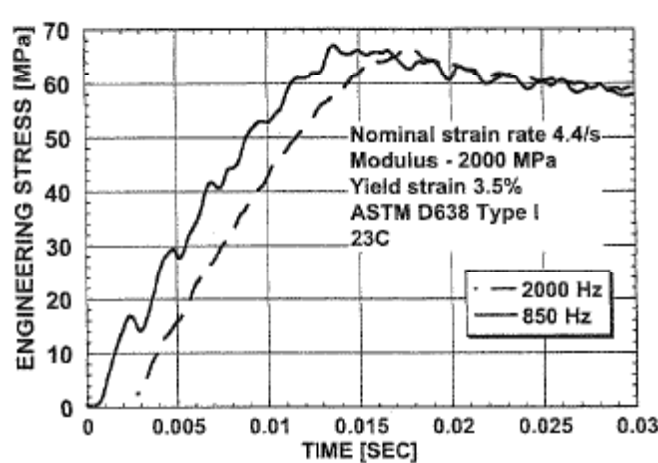


Figure 10. Difference in the Measured Response for Test Systems with Different Natural Resonant Frequencies

Curves shifted along the time axis for ease of comparison. Reference Figure A3 of SAE J2749

4.3 Gage Width for Testing the 2D3A

The ASTM D 6856 recommendation of using at least two unit cells in the gage section was followed for all tests. The final selected widths used at least 2.5 times the unit cell to ensure that at least two full unit cells were located in the gage section. In addition, technical experts who had used this configuration indicated that cracks initiated at the edges were usually blunted within half of one unit cell⁴ from the notch. A gage width of 2.5 unit cells would allow for at least a full unit cell remaining if edge cracking was initiated.

4.4 Tensile Specimen Configuration for Quasi-static Tests per ASTM D 3039

A gage width of 2.5 unit cells was selected for the quasi-static tensile specimens based on the ASTM D 3039 and ASTM D 6825. The specimen length was based on the minimum recommended length using the sum of the gripping, two times the width, and a gage length. The final size for the modified D 3039 axial tensile was 286 mm (l) x 44.2 mm (w) [11.265" x 1.74"], with 185 mm (7.265") between the tabs. The modified D 3039 transverse tensile specimen was 203 mm (l) x 19 mm (w) [8.0" x 0.75"], with 102 mm (4.0") between the tabs. The specimens are shown in Figures 11 and 12.

⁴ Conversations with Dr. Lee Coleman and Dr. Gary Roberts (NASA) on 24 April 2010, Dr. Mike Braley (A&P Technologies) on 10 April 2010, Todd Bullions (GE Aviation)

Several trial runs with tabbed specimens and bolt-loaded specimens were also run in order to determine the load-carrying capability of the 2D3A. The bearing strength data were used to calculate the size and number of bolt holes for the bowtie specimen fixturing.



Figure 11. Modified ASTM D 3039 Axial Tensile



Figure 12. Modified ASTM D 3039 Transverse Tensile

4.5 Bowtie Tensile for Higher Rates

4.5.1 Background

A new high rate tensile specimen was designed based on the need for a short specimen length, lightweight grips, low fixture weight, and a shorter load train. All of these factors combined would serve to shorten the load train length, reduce inertial effects, and raise the natural resonant frequency of the test system. This would enable the generation of useable data with minimal resonant stress waves at the higher test speeds.

A review of published literature did not locate any specimen configuration which would have been suitable for high rate testing of the 2A3D. The reported widths ranged from 3 mm to 15 mm [21-26], which were smaller than one unit cell.

A bowtie-shaped specimen had been used by A&P Technologies, a carbon braid supplier, for their aerospace customers. The axial unit cell defined by A&P is half the size of the unit cell used in this program. The A&P transverse unit cell is equivalent. Data from this type of specimen had also been reported by NASA[11]. The NASA configuration was slightly different, as shown in Figure 13. Both of the bowtie configurations modified the angle of the notch to

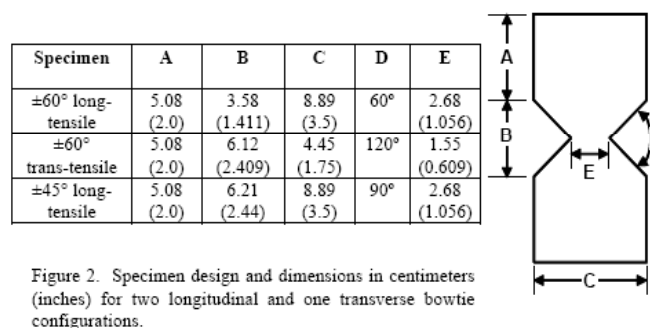


Figure 13. NASA Bowtie Tensile Specimens [Reference 11]

account for the bias tow angle in a given orientation, e.g. 60° for the axial and 120° for the transverse.

The bowtie configuration has the advantage of a shorter length for the axial orientation than the modified ASTM D 3039. This shape has 100% of the axial and bias fibers in the gage section gripped and fully loaded and should be a better measure of the tensile strength of the 2D3A.

The straight-sided ASTM D 3039 specimen has most of the bias fibers in the gage section cut and not gripped, thus minimizing their contribution to the measured strength. In addition, the cut bias fibers can act as crack initiation sites and cause early failure. In contrast to the bowtie configuration, the modified ASTM D 3039 axial specimen grips 100% of the axial and approximately 28% of the bias tows. The transverse tensile grips a few of the axial tows, and only about 70% of the bias tows. The schematic in Figure 14 illustrates the point using the axial tensile specimen configurations.

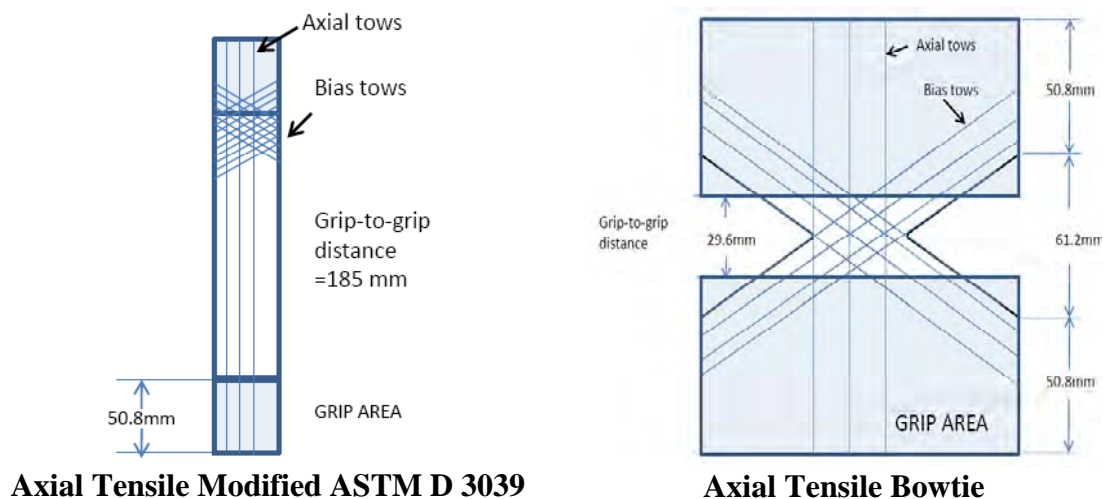
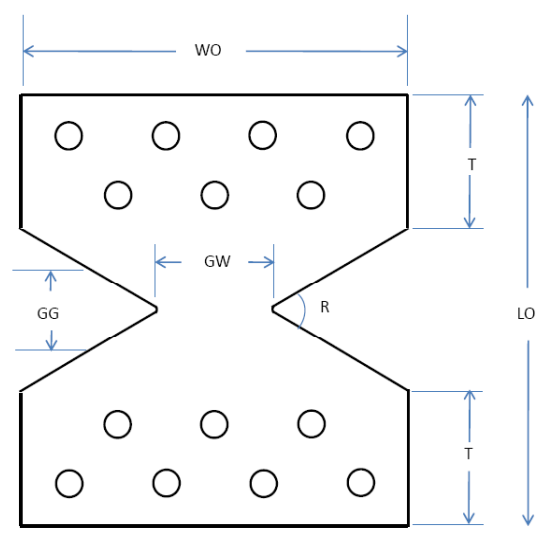


Figure 14. Relative Amounts of Bias and Axial Tows Gripped in Modified ASTM D 3039 and Bowtie Specimen Configurations

4.5.2 High Rate Tensile Specimen Configuration

The final axial and transverse bowtie specimens were designed using the A&P Technologies and NASA configurations as a guideline. The final specimens had 2.5 unit cells in the gage section. The grips were serrated and extended down past the end of tab (as shown in Figure 14) to ensure full engagement of the bias tows. Figure 15 summarizes the tensile specimen dimensions. The specimens were shear and bolt loaded. Appendix F contains the specimen and fixture drawings for both orientations.

Preliminary tensile tests were performed at 1.27 mm/min using tabbed and bolt-loaded specimens to determine the load-carrying capability of the 2D3A for the final specimen design. The final size and number of bolt holes were a result of these tests.



Specimen Orientation	LO Length overall [mm]	WO Width Overall [mm]	GW Gage Width [mm]	GG Grip-to-grip Distance [mm]	R Notch Radius [degrees]	T Tab length [mm]	Fixture Weight [kg]
0°/+60°/-60° Axial	162.8	147.8	45.7	29.6	60	50.8	3.81
0°/+60°/-60° Transverse	172.7	58.42	17.8	46.8	120	50.8	1.48

Figure 15. Bowtie Tensile Nominal Specimen Dimensions

4.6 Compression Specimen for Higher Rates

4.6.1 Background

ASTM D 6856 recommends ASTM D 3410 (shear loading) or ASTM D 6641 (shear and end loading) for quasi-static compression testing of textile composites. The goal is to force failure into an unsupported section. The preferred failure modes include angled, brooming, though the thickness cracking, and longitudinal splitting. Unacceptable modes include delamination and cracking in the tab region [Reference D 6641]. Strain measurement is usually with strain gages, when applicable.

The high rate specimen configuration had to consider the added width due to multiple unit cells and a region for strain measurement. The standard sizes for ASTM D 3410 (140 mm x 25 mm) [5.5" x 1.0"] and ASTM D 6641 (140 mm x 12 mm) [5.5" x 0.5"] are smaller than the desired 2.5 unit cell width of 44.5 mm (1.75"). Mike Booker, Laboratory Manager of Cincinnati Testing Laboratories, has tested various braided composites and uses a modified version of ASTM D 6641. The specimen has a 25 mm (1.0") width with a proportionally longer straight section. The grips are also heavier because of the additional loading from the wider specimen. While the larger specimen accommodated at least one unit cell, the heavy grip weight and long length of the specimen and fixturing were at odds with the requirements for higher rate testing mentioned in Sections 3.1 and 3.2. For these reasons, a simple modification of the standard quasi-static specimen was not considered for the higher rate tests.

Edge compression of a sandwich construction was investigated because of the potentially small specimen size and minimal fixture length and weight. Kim and Crasto [27,28] developed a specimen similar to that used in ASTM D 3410 using a sandwich of composite with a core of the neat resin used in the composite. The panels were cured as a unit and the specimen tabbed and machined to size. The reported compression strength was much higher than using conventional specimens because buckling was avoided. This method was not considered because of the issues mentioned in the previous paragraph and the added specimen fabrication cost.

A combination of the NASA short block method [29] was also considered. It would have used a composite sandwich with foam or honeycomb as the core and clamped ends. However, the NASA report indicated issues with end-loading of sandwich columns because of core:face separation. The reported strengths were significantly lower than those from other compression techniques. This specimen configuration type was also abandoned.

4.6.2 High Rate Compression Specimen Configuration

The initial high rate compression configuration used a tapered dogbone style, using the ASTM D 695 *Standard Test Method for Compressive Properties of Rigid Plastics* specimen as a guideline. The specimen gage section was designed to be at least 3.5 unit cells wide by at least 3 unit cells tall. However, cracking was initiated at the radius/tab transition of the dogbone during the trial runs. The specimen was modified to a straight-sided rectangle. The widths ranged from 66.7 mm [2.62"] to 71.1 mm [2.80"] wide and 92.2 mm [3.63"] long. This allowed for at least

3.75 and 13 unit cells along the loading direction for the axial and transverse orientations, respectively. The unsupported section was 3 mm (0.125") long.

Anti-buckling support was provided with a backing plate that covered the entire back surface. The front plate covered most of the surface and included a window for strain measurement. The window size for the axial orientation was 2.75 unit cells x 3.75 unit cells (high) for the axial and 3.75 unit cells x 2.5 unit cells (high) for the transverse. Appendix G contains the specimen and fixture drawings.

4.7 Shear Specimen for Higher Rates

4.7.1 Background

The shear standards referenced by ASTM D 6856 for textile composites are ASTM D 4255, ASTM D 5379, ASTM D 7079. ASTM D 4255 uses an un-notched specimen that is bolt and tab loaded. The D 5379 specimen is a V-notched specimen loaded on the edges. The ASTM D 7079 specimen is a V-notched specimen that is loaded through the tabs.

ASTM D 7079 is suitable for braid composites; ASTM 4255 and D 5379 are suitable for uni-directional fiber layups or fabric. Technical experts in braid composite testing⁵ and recent literature [11-14] have tried variations on ASTM D 7079 in order to try to drive the crack through the center. Some variations included tabbing, an extended tab length to add stiffness and limit twisting during loading, fixture modifications to limit the spread of the fixturing during loading, increased notched depths, and various notch angles ranging from 45° to 110° [30].

The literature mentioned failures in the center and towards the edges. Cracks would initiate at the notch tip, propagate down along the center, and then often travel along the braid bias angle and into the grip region. In an email dated 5 October 2010, Dr. Dan Adams wrote regarding determining a “good” failure:

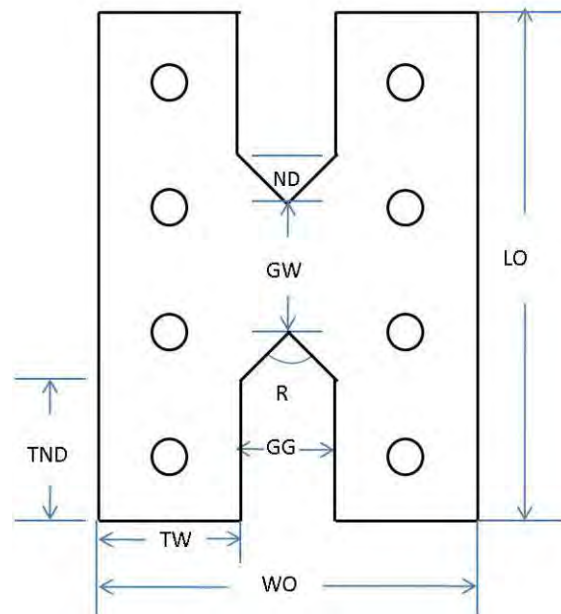
From what I can tell from your emails, you prefer the deeper notch and “sharper” 60 degree notch angle because you can get a crack to form between the notches. I can see why you’d like this to happen... However I feel it’s important to keep in mind that you are testing a 0/+60 laminate(braid) under shear loading, and who’s to say how the “laminate” will fail in shear? That is, a Tau-xy shear stress applied to such a laminate will, in general, produce multiaxial stresses in the plies (in their material coordinate system), and thus at the ply level, the failure may not be through shear... but might be transverse tensile. When we test 0/+45/90 quasi laminates as well as +-45 laminates, the failure is not a crack occurring between the notches, and yet I believe that is how these laminates fail under shear loading.

⁵ Conversations and email correspondence with Mike Booker (Cincinnati Testing Laboratories), Dr. Mike Braley (A&P Technologies), and Todd Bullions (GE Aviation), Dr. Dan Adams (Professor, Mechanical Engineering, University of Utah), Dr. Suresh (Raju) Keshavanarayana (Assoc Professor, Aerospace Engineering, Wichita State University)

Dr. Adams' comments reiterated that there was no clear consensus regarding the specimen configuration or acceptable modes of failure for braid composites. Research programs are currently on-going at NASA and the University of Utah trying variations on the D 7078 test specimen. The results were not available in time for this program. The experts' opinions and comments were incorporated as much as possible into a modified specimen that would be suitable for high rate testing.

4.7.2 High Rate Shear Specimen Configuration

The modified high rate specimen included bolt loading in the tab and an extended tab length in order to maximize load transfer and minimize twisting of the specimen during loading. The ASTM D 7078 notch angle was followed. The specimen details are in Figure 16. The "axial" shear specimen had the 0° fibers located perpendicular to the loading direction; i. e. shearing was across the 0° fibers. Conversely, the transverse specimen had the 0° fibers parallel to the loading direction and shearing was across the bias fibers. Appendix H contains the specimen and fixture drawings.



Specimen Orientation	LO Length overall [mm]	WO Width Overall [mm]	GW Gage Width [mm]	GG Grip-to-grip Distance [mm]	R Notch Radius [degrees]	TND Tab Notch Depth [mm]	Tab Width [mm]	Notch Depth [mm]	Fixture Weight [kg]
$0^\circ/+60^\circ/-60^\circ$ Axial	162.8	137.2	47.9	35.8	90	50.8	50.8	17.9	1.44
$0^\circ/+60^\circ/-60^\circ$ Transverse	104	86.4	12.7	10.2	90	39.9	50.8	5.1	0.582

Figure 16. Shear Specimen Nominal Dimensions

4.8 Braided Tubes

The 610 mm long tubes were cut into two specimens for a total of 18 specimens. Each specimen was 254 mm long [10.0"] and had a nominal inner diameter of 102 mm [4.0"] and a wall thickness of 3.8 mm [0.15"]. The length to diameter ratio was 2.5. A single 45° bevel was machined into one end of a select number of tubes to act as a crack initiator.

5.0 FINAL TEST MATRICES

The original test matrices in Tables 1 and 2 were modified, based on test results at the lower levels. The revised test matrices are in Tables 8 and 9. The numbers in the table indicate the minimum number of tests at each rate.

Quasi-static transverse tensile tests were added for comparison to published literature. Higher test rates were achieved with the new high rate coupon configurations than originally planned; however, discrete stress waves were noticed in some of the responses at the upper rate.

The straight-ended tube exceeded the actuator capacity and so this part of the tube test matrix was dropped. The balance of the tests used tubes which had a single bevel on the end for crack initiation. The tests above 1.5 m/min were performed at Oak Ridge National Laboratories (ORNL) Test Machine for Automotive Crashworthiness facility (TMAC).

Table 8. Final Coupon-Level Test Matrix

		Machine Rate [m/min]			
		0.00127	0.5	4.5-5.0	38-49
Tension-per ASTM D 3039	Axial	3	-	-	-
	Transverse	3	-	-	-
Higher Rate Tension	Axial	3	3	3	3
	Transverse	3	3	3	3
Compression	Axial	3	3	3	-
	Transverse	3	3	3	-
Higher Rate Shear	Axial	3	3	3	3
	Transverse	3	3	3	3
Total		24	18	18	12
Grand total		72			

Table 9. Final Tube Compression Matrix

	Machine Rate [m/min]		
	1.5	140	440
Straight End	1	-	-
Single bevel	3	7	6
Total	4	7	6
Grand total	17		

6.0 TEST PROCEDURES – SME AT UDRI

The test procedures and guidelines of SAE J2749 and SEP1230 were followed, where applicable. The SME equipment list and calibration records are in Appendix I.

6.1 SME Servo-hydraulic Equipment

Tests were performed at room temperature ambient conditions on MTS servo-hydraulic stations equipped with a 97.8 kN (22,000 lb_f) actuator. Actuator displacement was measured with a linear variable differential transformer (LVDT). The tensile and shear tests used a slack adapter to allow the actuator to attain test speed before applying load to the specimen. While this was not necessarily needed at rates below 500 mm/min, it was included for consistency in the load train across the tested rates.

Load at 1.27 mm/min and 500 mm/min was measured using a load cell calibrated up to 90 kN (20,000 lb_f). The LVDT full scale was 1270 mm. Load at rates above 500 mm/min were measured using a piezoelectric load washer dynamically calibrated at 5Hz up to 90 kN (20,000 lb_f). The data acquisition computer used a high speed National Instruments PCI 6110E data acquisition card.

The axial tensile test setups are in Figures 17, 18 and 19. The compression setups are shown in Figures 20 and 21. The shear setups are in Figures 22 and 23.

The composite tubes were tested at both SME and ORNL. Both systems used MTS servo-hydraulic equipment. Tube tests at 1.5 m/min were performed at SME. Tests were filmed using the two high speed Phantom cameras (described in the following section) and displacement and strain data were captured. The filming rate was 250 frames per second (fps).

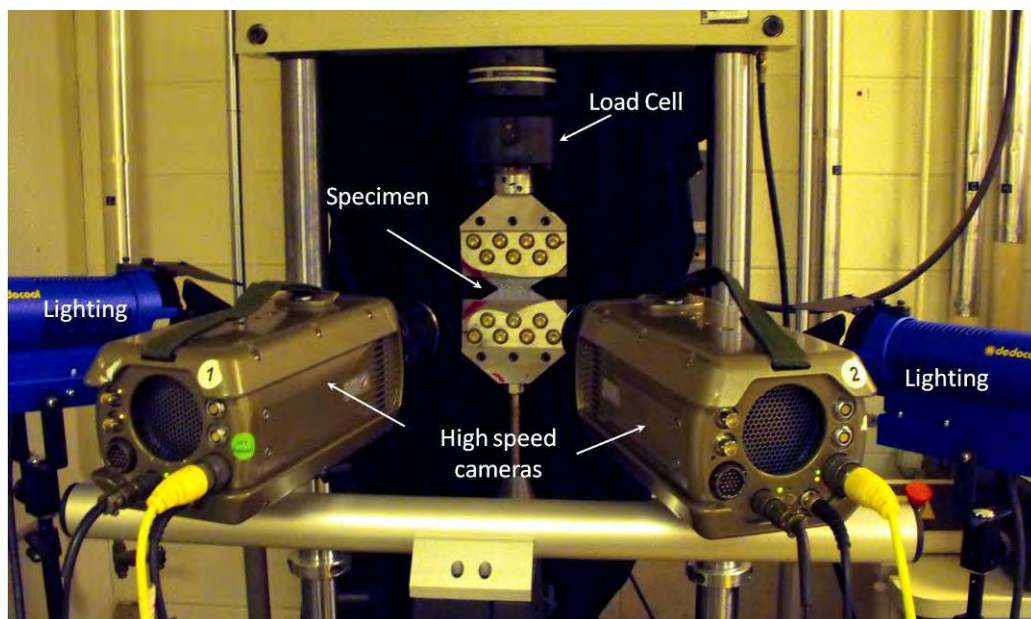


Figure 17. Low Rate Setup for Axial Tensile Testing

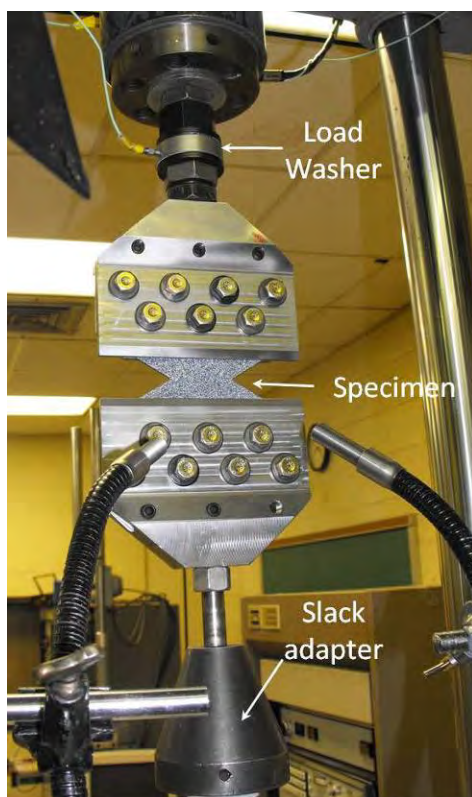


Figure 18. High Rate Setup for Axial Tensile Testing

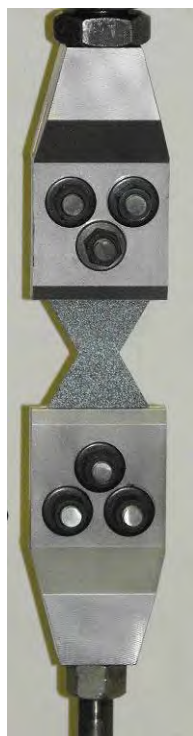


Figure 19. Transverse Tensile in Fixture

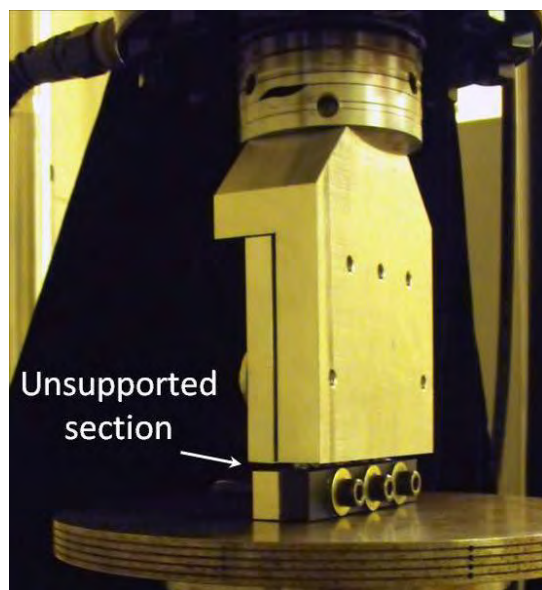


Figure 20. Edge View of Compression Setup showing Unsupported Region

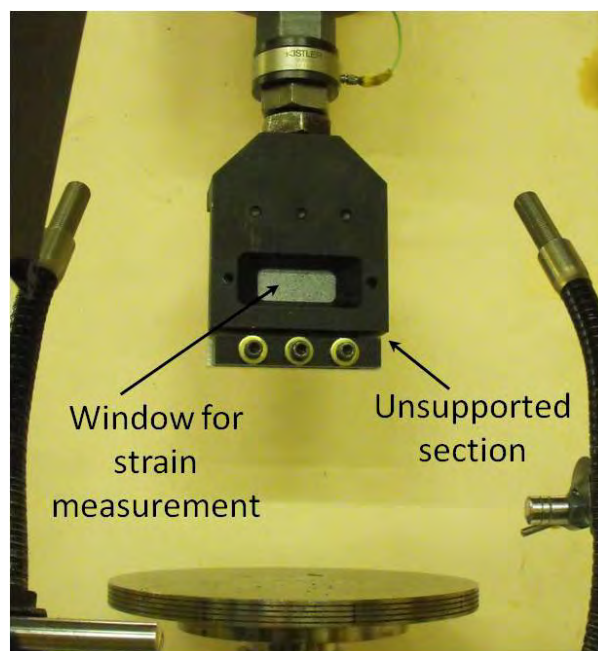


Figure 21. Front View of Compression Setup Used with Strain Measurement

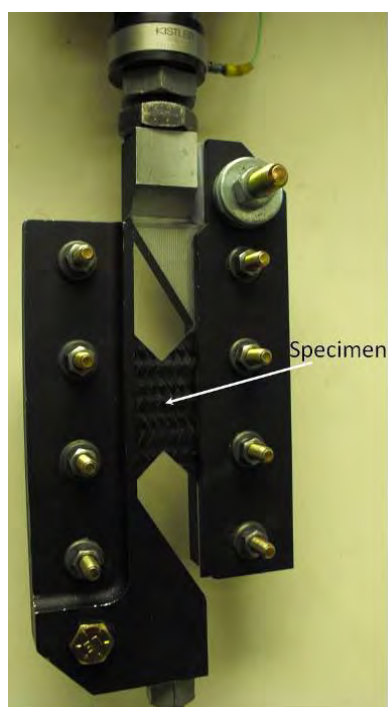


Figure 22. Axial Shear Setup



Figure 23. Transverse Shear Setup

6.2 Oak Ridge National Laboratory (ORNL) Equipment

Tests at 140 m/min and 440 m/min were performed at the TMAC (Test machine for Automotive Crashworthiness) facility of ORNL. The technical point of contact was Dr. Don Erdman. The MTS test station was equipped 1600 gallon per minute servo-valve system and had a load capacity of up to 250 kN at 480 m/min⁶. The tests were filmed with a single Photron high speed camera. The filming rate was 10K fps. Correlated Solutions Vic 2-D image analysis software was used to estimate displacements. The resolution was too coarse to yield strain data.

The thermal response during the crush was captured with an infrared camera [Phoenix Mid-Wave IR Camera, 320 x 256 pixels, 3-5 micron spectral response). Its capture rate was 800 fps. One of the composite tubes was used to generate a correlation curve relating the IR image to temperature. The TMAC is shown in Figure 24.

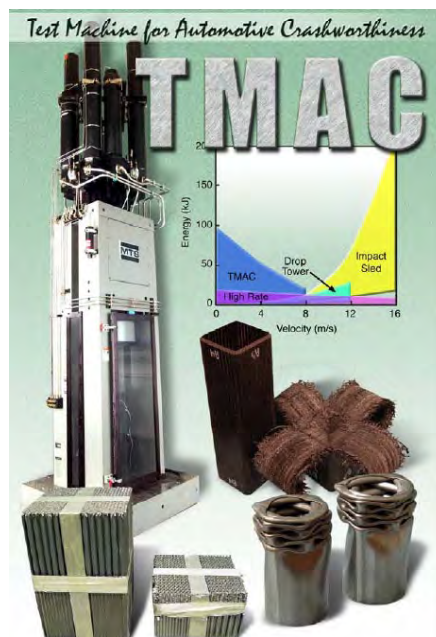


Figure 24. TMAC Equipment at ORNL

6.3 Strain Measurement with Digital Image Correlation System (DIC) with ISTRa Software

6.3.1 General

Full-field 3D deformation was measured using either two high resolution, low-speed Q400 cameras or two Phantom V710 high speed cameras and Dantec Dynamic ISTRa digital image correlation (DIC) software. The general setup is shown in Figure 17.

The ISTRa software tracked the motion of a random pattern on the specimen through the test. Three-dimensional analysis of the pattern movement was used to calculate the net

⁶ <http://www.volpe.dot.gov/safety/pciv/docs/warren.pdf>

displacements and strains of the features of the pattern. The DIC allowed the user to review the strain response throughout the entire test and then extract strain data for various regions of interest, such as the global strain across the entire straight section or at failure. Several sources are available for additional information regarding DIC measurements [31-34].

The user can select the mesh size for the DIC calculations. A typical grid size is 12 pixels and the facet size is 17 pixels. The grid point is located at the center point of each facet. A facet size larger than the grid size allows for some overlap between calculation points. The deformation data are referenced back to the areas defined by the facets.

High speed DIC measurement is limited by the resolution of the images, not the software. The Phantom high speed cameras are capable of framing rates above 600k frames per sec (fps). However, the available region of interest (ROI) is limited to 256x16 pixels at this speed. This in turn limits the number of data points that can be used in the DIC calculations.

The image size varied with the camera type, filming rate, and the specimen size. Typical framing rates were 25 fps at a test rate of 1.27 mm/min and 50k fps at 46 m/min. The corresponding ROI was approximately 1280 x 456 pixels down to 336 x 332 pixels, respectively. The actual number of pixels across the specimen was less. The test run sheets, located on the program CD, indicate the number of pixels for the ROI for the various runs.

6.3.2 Specimen Preparation

The measured regions were spray painted with black paint to remove any surface reflections. They were then oversprayed with white to generate the random pattern. The size of the paint drops varied depending on the camera parameters. An example is shown in Figure 25.

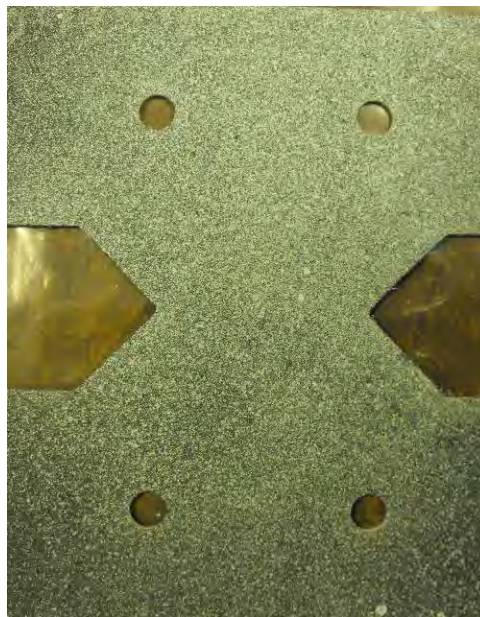


Figure 25. DIC Pattern on Axial Shear Specimen

6.3.3 DIC Measured Region

As mentioned in Section 6.3.1, The DIC software creates a grid over the measured surface. The user can define a point, line or shape over which the displacement and strain data can be extracted. An example is shown in Figure 26, illustrating the grid mesh and the measured regions. The red regions in the V-notch in Figure 26a indicate areas of higher strain and cracking. One can also see differences in the strain carried along the bias tows by the differences in the color (the lighter color blue representing higher strain).

Strain was taken from local regions showing a high or low strain during the test for a select number of specimens. An example is shown in Figure 27. The image shows a high strain point, a low strain point, a line at the center of the V-notch, a small polygon, and a large polygon. The polygon strain data represent a global strain value since the data are averaged across a larger number of grid points than the line and point. The point strain data represented a local strain.

The regions selected for the DIC data extraction varied depending on the specimen shape. In the case of the shear and tensile tests, strain was measured along a line and/or polygon located at the center of the V-notch, as shown in Figures 26 and 27. A larger polygon was used for the compression tests (Figure 28). In contrast to what was seen in the tension and shear tests (Figure 26b), the uniform shading of the center section of the compression tests indicated a relatively uniform strain state.

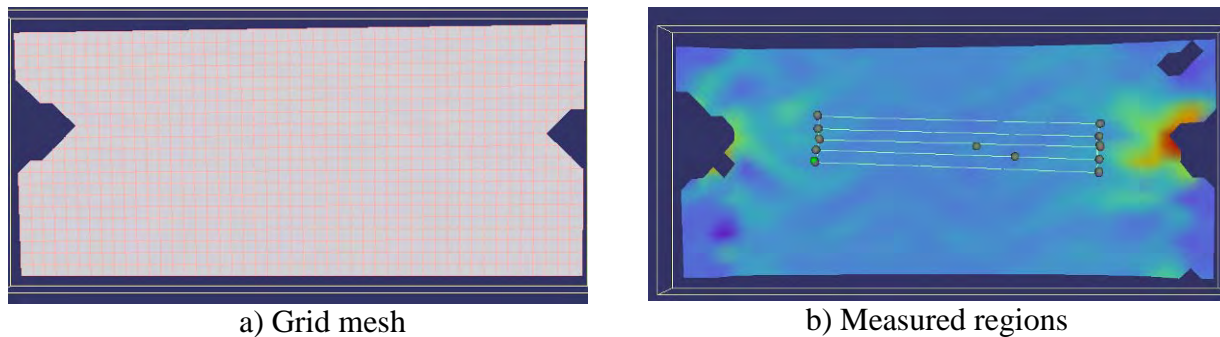


Figure 26. Grid Mesh and Measured Regions for a Slow Rate Axial Tension Test

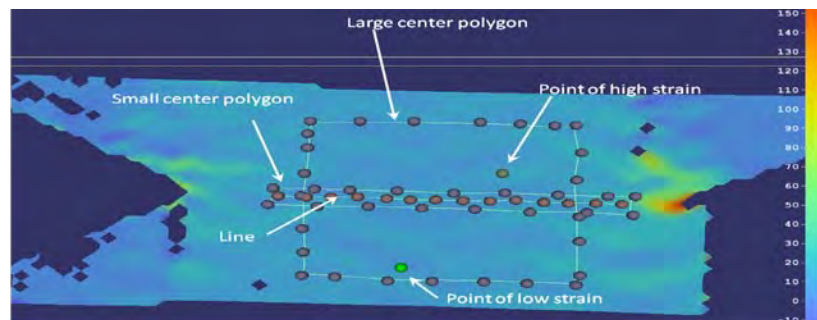


Figure 27. Possible Features for DIC Analysis

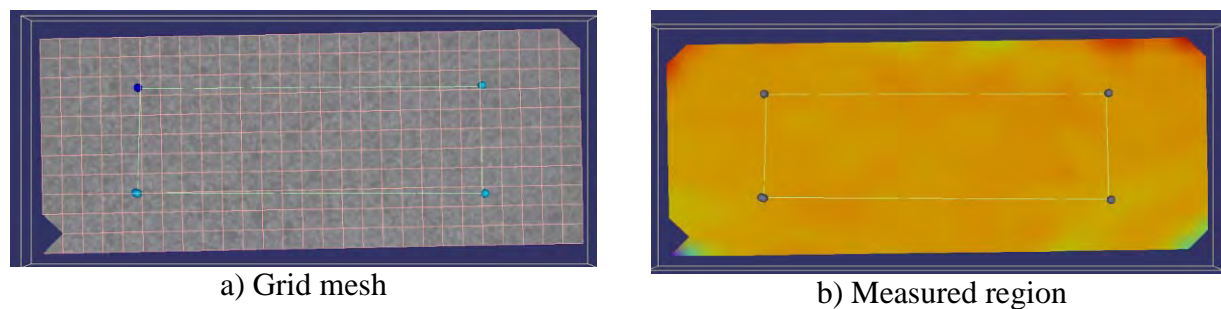


Figure 28. Grid Mesh (a) and Measured Regions (b) for an Axial Compression Test

6.4 Strain Measurement with Strain Gages

Stock strain gages with the grid size needed to cover an entire unit cell were not found. One of the modified ASTM D 3039 axial tensile specimens was strain gaged with a single axis general purpose Vishay Micro Measurements CEA-06-500UW-350 gage. The grid size was 4.57 mm wide (0.19”) x 12.7 mm long (0.50”). It was aligned with the long axis parallel to the 0° fibers. The gage grid covered one-third of a unit cell (horizontally) and 2.5 unit cells (longitudinally).

7.0 DATA ANALYSES

7.1 General

The panel thickness varied depending on whether one measured the “peak” or valley of the surface. The maximum peak was noted where the three layers aligned through the thickness. Two measurements were taken at a peak and two at a valley and averaged for the stress calculations. The specimens measurement sheets, located on the program CD, contain the individual specimen information.

The peak stress was taken as the maximum value before a sudden drop in strength, typically over 25%. Some of the specimens exhibited tearing before failure. The summary tables indicate both peak and failure stress, if applicable. The failure strain was taken at a point of a large drop in load or minimal increase in strain upon continued loading.

The data summary tables include stress data normalized to a fiber content of 56 volume %. This allowed for comparison amongst panels and between the coupon and tube data.

The modulus was determined from the initial slope of the linear best-fit equation to the stress strain curve. The moduli are for informational purposes only and may not represent the bulk material properties. The test procedures did not meet all of the requirements for modulus measurements per ASTM E 111, such as: a longer specimen (and, hence, a larger volume), a Class B-1 or better extensometer, precise alignment, and a slow test speed in order to avoid adiabatic heating.

The strain rate was determined from the slope of the strain versus time curve over a region before failure. This was generally over a strain range of 0.4 to 1.0% strain. The specific range is listed in the data summary tables.

The physical set-up of the test system results in a time lag between the collection of load and the strain data. The load is measured at one end of the specimen while the strain is measured at the middle of the gage section. It is necessary to transform the load data to the same point in time as that of the strain data via a translation of the strain data in the time domain. The validity of this practice relies on a constant wave propagation velocity in the tested material.

The test speed at which the synchronization is required depends on the data collection frequency and the propagation speed of the stress wave through the fixture and specimen. The time shift was in the order of 40 microseconds for most of the tests in this program.

7.2 DIC Strain Analysis

The Dantec Dynamics ISTR software allows one to select a region of interest for analysis. One can choose to track a point, a line, or a shape (*e.g.*, a polygon). The data can be exported as maximum, minimum, and average values for the chosen shape. The polygon data can also be exported as data for the values around the border or across the surface. The data for this program used the average strain for a line and the average strain across the polygon surface.

The default setting of the software is for unfiltered data. Several levels of filtering are available in order to smooth out the calculations between each displacement. The majority of the program data were filtered using the internal local regression program with a 5x5 level of smoothing.

Some oscillations are present in the strain output. The oscillations have several contributing factors:

1. Strain variations in the braid upon loading
2. Artifact of the DIC analysis technique.
3. Resonant ringing in the system.

Strain variations along the fiber were noted, as seen in Figures 26 and 27. Data were extracted from regions which showed a high and low amount of strain for a select number of specimens. The summary tables list a local strain value for those specimens which had a large difference between the local and global strain.

The magnitude of the oscillations is also affected by the resolution of the grid mesh and the number of grids over which the strain data are calculated. Displacement data for each grid point are used for the strain calculations. Strain data for a point are interpolated from the four grid points closest to it. Strain data for a line uses data interpolated using the four grid points defining each grid block intersected by the line. Strain data for a polygon uses data from each grid point defining the grid blocks intersected by the outline of the polygon. Therefore, the localized fluctuations are reflected in point and line data to a greater extent than a polygon. Local

fluctuations are minimized further if a finer grid mesh is used as long as sufficient tracked features remain in the measurement facet.

Figure 29a shows the type of data variations one can have depending on the relative size of the measured area (Figure 29b). The curves are shifted in time to allow for comparison. Note the large oscillations in the data for individual points of high and low strain. The large polygon data are relatively smooth, reflecting the global strain response.

Not all of the oscillations were an artifact of the DIC software. Most of the larger amplitude oscillations occurred after the specimen was loaded. Therefore, a part of the fluctuations are from the transfer of load along the carbon tows.

The strain fluctuations were translated into the stress-strain curve. The stress-strain curve was smoothed using a piecewise polynomial fit of varying orders. The data set for each specimen included both the original and best-fit data for the stress-strain curve. The summary graphs for each data set includes both the as-is and best-fit summary curves. The plots included in the body of the report use the best-fit curves for ease of comparison.

DIC image for the specimen (Figure 29b) shows the strain before failure. The holes in the DIC image are regions where the surface was reflective or the paint was missing. Cracking or flaking of the paint occurred as the specimen started to fail either on or below the surface.

Resonant ringing was not an issue until the top test rate. Figure 30 shows the stress response at the slowest and fastest test rates. The curve at 0.00127 m/min exhibits no resonant waves. A best-fit to the stress curve is the simplest method to filter the response of the small amplitude waves at the 50 m/min rate.

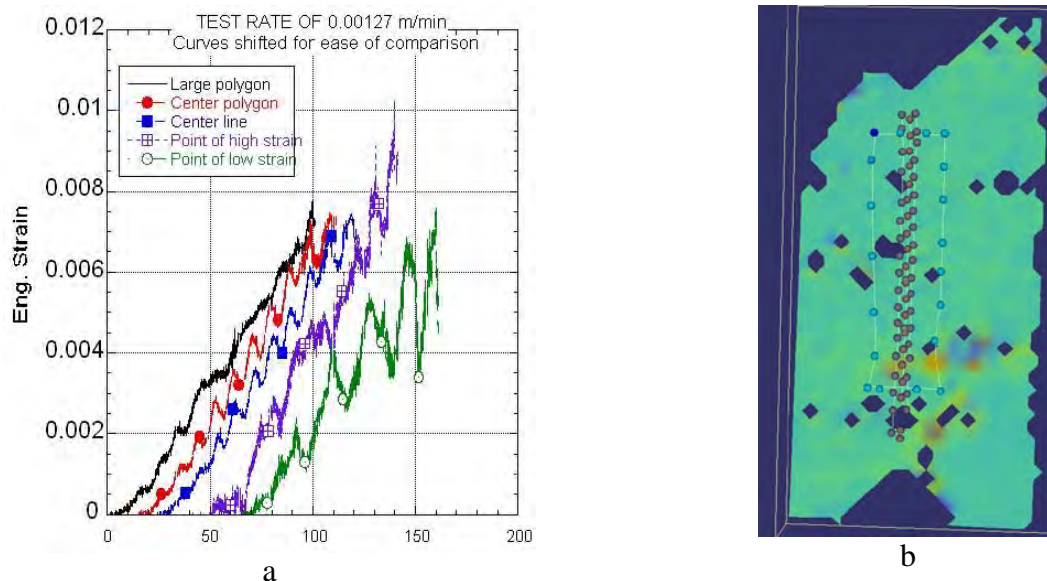


Figure 29. DIC Strain Output for Different Regions (a) and DIC Image (b) for an Axial Shear Test [Specimen STL095-1]

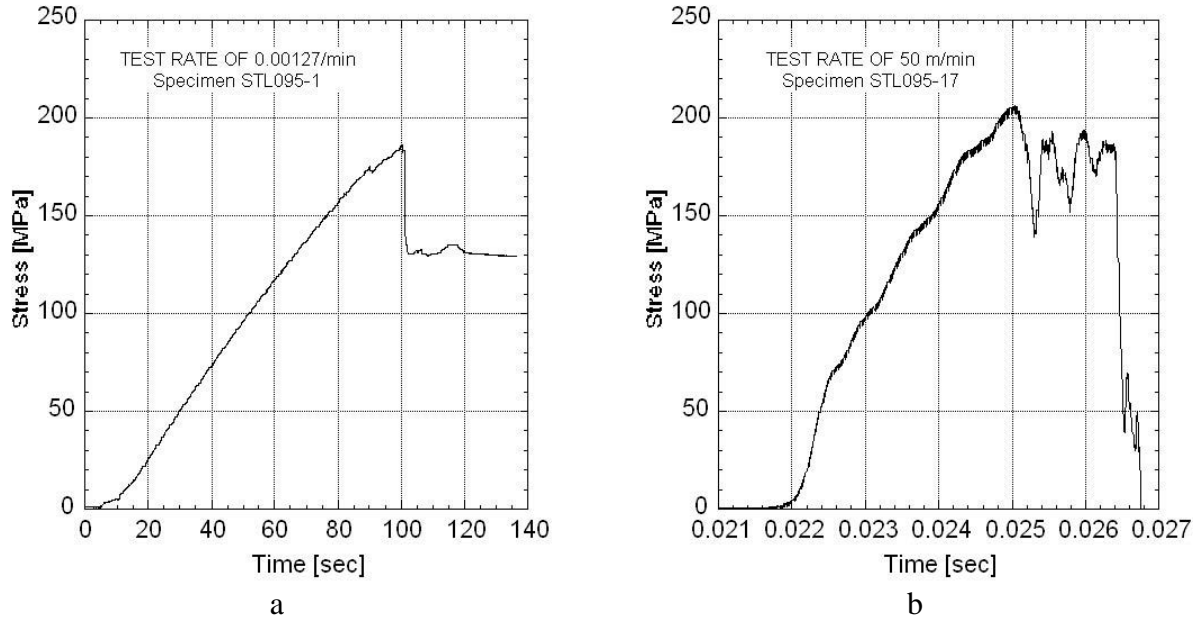


Figure 30. Stress Response at Low (a) and Fast Test Rate (b) for an Axial Shear Test

7.3 DIC Strain

The DIC strain data are given as Lagrangian strain (LS). A MATLAB script was used to compute engineering strain (ES) and true strain, via Eqs. (2) and (3):

$$\begin{bmatrix} T_{11} & T_{12} \\ T_{12} & T_{22} \end{bmatrix} = \frac{1}{2} * \ln \left(2 * \begin{bmatrix} L_{11} & L_{12} \\ L_{12} & L_{22} \end{bmatrix} + \begin{bmatrix} 1 & 0 \\ 0 & 1 \end{bmatrix} \right) \quad (2)$$

$$\begin{bmatrix} E_{11} & E_{12} \\ E_{12} & E_{22} \end{bmatrix} = \sqrt{\left(2 * \begin{bmatrix} L_{11} & L_{12} \\ L_{12} & L_{22} \end{bmatrix} + \begin{bmatrix} 1 & 0 \\ 0 & 1 \end{bmatrix} \right)} - \begin{bmatrix} 1 & 0 \\ 0 & 1 \end{bmatrix} \quad (3)$$

where,

L = Lagrangian Strain	11 = Transverse Strain
T = True Strain	22 = Longitudinal Strain
E = Engineering Strain	12 = Shear Strain

7.4 Tube Crush Analysis

Various methods can be used for the data analysis [35], such as the energy absorption (EA), the specific energy absorption (SEA), the specific sustained crushing stress (SSCS), and the crush compression ratio (CCR). The various equations are:

$$\text{EA} \quad W = \int_0^{\delta} p d\lambda \quad (4)$$

$$\text{SEA} \quad E_s = \frac{W}{A\rho\delta} \quad (5a)$$

$$\text{Fold failure} \quad \text{SEA} \quad E_s = \frac{W}{A\rho(\delta + d)} \quad (5b)$$

$$\text{For design purposes} \quad \text{SEA} \quad E_s = \frac{W(\delta_2 - \delta_1)}{m\delta_2} \quad (5c)$$

$$\text{SSCS} \quad \overline{\sigma}_s = \frac{\overline{\sigma}}{\rho} \quad (6)$$

$$\text{CCR} \quad CCR = \frac{\overline{\sigma}}{\sigma_{ult}} \quad (7)$$

P = load, δ = crushed length of tube/displacement, ρ = density, $\overline{\sigma}$ = average crush stress, σ_{ult} = ultimate compressive stress of the braid, d= crush/fan fold length, and m= mass of the entire tube. The value for δ is used for the total crush length if the value for d is small in comparison to the total crush length.

The data for this program were compared using the SEA, the SSCS, and the CCR. The W was calculated using an embedded macro within Kalediagraph® graphing software⁷.out to a zeroed displacement of 115 mm. The specific starting and endpoints used for δ_1 and δ_2 were selected after analysis of the crush behavior across all rates. Further details are given in Section 8.6.

8.0 RESULTS AND DISCUSSION

The program CD contains electronic copies of the individual specimen data files, specimen measurements, test data, summary graphs in JPEG and Kalediagraph® format, test setup photographs, calibration records, panel information, photomicrographs of the cross-section, photographs of the failed specimens, and other relevant documents.

8.1 Fixture Design – General

The fiber architecture of the braid was the primary concern in the fixture design for the various tests. Incorporation of at least 2.5 unit cells in the test section defined the specimen length, failure loads, fixture length, and fixture mass.

⁷ The area is found by calculating the sum of the trapezoids formed by the data points selected.

The various fixture designs were able to transfer the load into the specimens. Grip marks were evident in the tab region which was indicative of load transfer through shear. The specific amount of load transferred through the bolts was not determined. No deformation was noted in the bolt holes.

A maximum test rate of 12 to 24 m/min was thought to be a practical limit for the various tests. Clean, useable tension and shear data were generated at rates of 5 m/min. Data at 49 m/min had system resonant waves superimposed onto the material response. Approximately five to 10 waves of varying amplitudes were present before specimen failure, depending on the exact test type and fixture. The compression curves showed resonant waves at a lower test rate (~5 m/min).

The waves are a result of the excitation of the natural resonant frequency of the test system. The limited number of resonant waves indicated that a dynamic equilibrium may not have been present before specimen failure. The resonant waves were not of high amplitude and useable data could be generated with curve fitting. However, this is not the optimum solution.

A specimen and/or fixture redesign would be needed to generate higher quality data at the upper rates. Some modifications of the fixture design would include minimizing the number of bolt holes, and reducing the fixture weight by removing material and/or changing material.

These changes would help improve the data quality at rates from 5 to 50 m/s. Generating useable data at even faster rates would require a specimen redesign. The major contributor to the current specimen design was the decision to include 2.5 unit cells within the test section. This choice dictated the overall specimen and fixture length.

As shown in Eq. 1 of Section 4.2, the specimen length affects both the distance between the grips and the fixture length. These factors directly affect the time for the stress wave to propagate in the system. Minimizing the specimen gage section would reduce the specimen failure loads, reduce the specimen length, reduce the fixture length, and reduce the resulting fixture weight. All of the factors would contribute to reducing the stress wave propagation speed and increasing the natural resonant frequency of the system. Increasing the natural frequency will result in minimizing the resonant wave amplitudes and maintaining a dynamic equilibrium at faster rates.

8.2 Rate Effect on 2D3A Strength

The 2D3A braid is designed to be in-plane quasi-isotropic. Additional layers introduce variations that are dependent on the braid stack-up, nesting of braid tows, mechanical bonding between layers, and resin content, amongst others. A fiber-dominated mechanical property should show little sensitivity to test rate since carbon fiber is relatively insensitive to strain rate over the tested rate regime [36]. A matrix-dominated property should exhibit some rate effect [37].

The peak tensile, compressive, and shear strengths of the 2D3A for the axial and transverse orientations are shown in Figures 31 and 32, respectively. The axial mechanical properties remain relatively unchanged through the tested rate regime. The slight decrease in the axial tensile strength

at the fastest rate is not statistically significant⁸. Five to seven resonant waves were present in the specimens before failure at the fastest rate and the specimens were probably not in dynamic equilibrium.

The transverse tensile strength does not change across the tested rates. There is a slight increase in the compression and shear strengths with increasing rate. Note the large difference between the transverse strength using the modified ASTM D 3039 and the bowtie configuration (Figure 32).

The following sections discuss each test type (tension, compression, shear, tube) in detail.

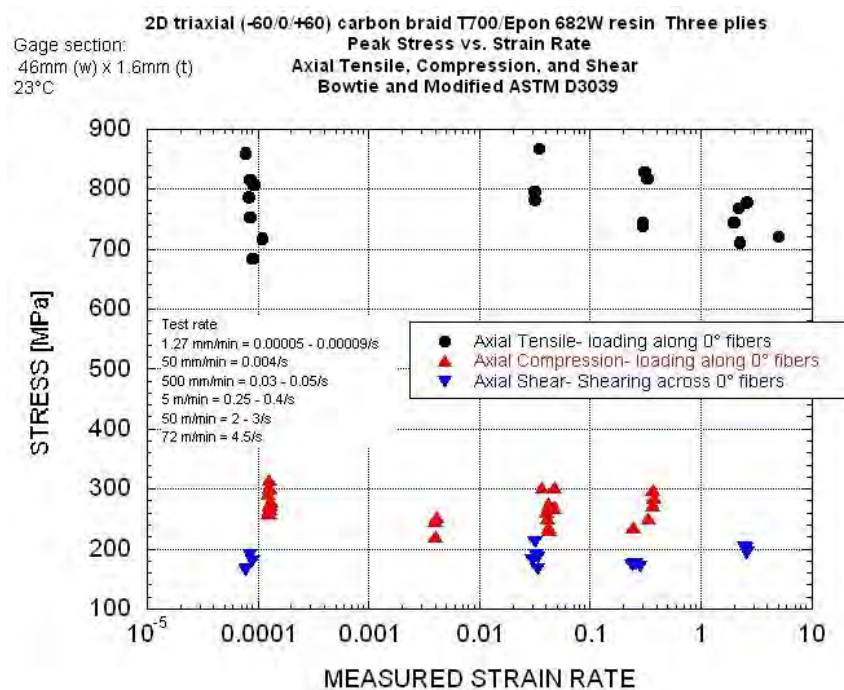


Figure 31. Peak Axial Strength of 2D3A at All Rates – Normalized to 56% Fiber Content

⁸ Two-tail Student's t-test assuming unequal variances and an alpha=0.05. All comments regarding statistical significance are based on this hypothesis.

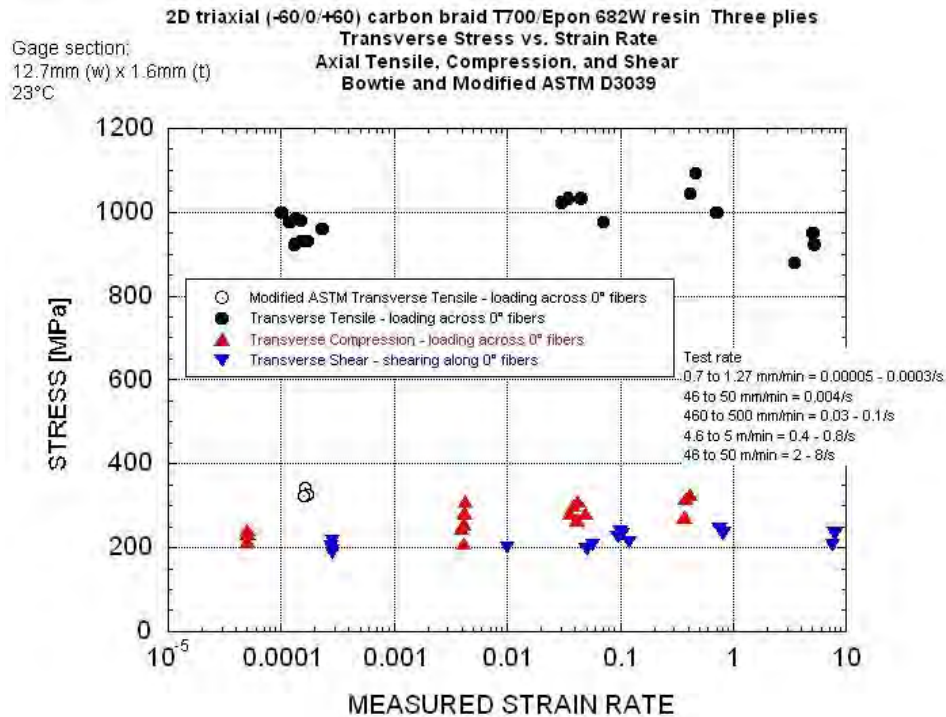


Figure 32. Peak Transverse Strength of 2D3A at All Rates Rates – Normalized to 56% Fiber Content

8.3. Tensile

8.3.1 Modified ASTM D 3039 Tensile

The tensile stress-strain curves for both the axial and transverse modified ASTM D 3039 are in Figure 33. The mechanical properties are summarized in Table 10 along with published results using a 6-layer laminate. Detailed summary tables and graphs are in Appendix J.

The UDRI results are similar to those of published data [11-14], except for the transverse tensile strength. The lower strength of the UDRI specimens was probably due to their smaller width (19.5 mm versus 35.8 mm) and greater sensitivity to edge cracks and early failure. The similarity in the other data indicated that the UDRI measured properties could be used for comparison to the published literature.

One of the axial specimens was strain gaged and the strain data were compared to DIC strain data taken over a similar region. Figure 34 shows the location of the strain gage and its relative size to the gage section. DIC data were in good agreement with the strain-gage data, as seen in Figure 35.

Axial failures were at both ends of the specimen and located close to the tab, as seen in Figure 36a. These failures were at the transition of the gripped and ungripped bias tows. One specimen (STL064-7) failed in the center gage. Its tensile strength was not significantly different from the ones that failed closer to the tab.

Half of the transverse specimens failed in the middle of the gage section (Figure 36b) and half towards the tab. The average strength of the two groups was significantly different. The average strength for the ones breaking in the center was 340 MPa versus 326 MPa for those that broke near to the tab.

The distinct variations in the surface contour can be seen in Figure 37a. The depth of the “ripple” increased with increasing alignment of the 0° tows through the thickness.

Table 10. Comparison of UDRI and Published Data for 2D3A with Epon 862W at Quasi-static Rates
Normalized to 56% Fiber Volume

		UDRI Modified ASTM D 3039 Test Rate of 1.27 mm/min Measured rate of 0.00007/s to 0.00016/s				Modified ASTM D 3039 from Littell PhD Thesis Test Rate of 0.635 mm/min			
		Engineering Breaking Stress [MPa]	Engineering Breaking Strain [%]	Elastic Modulus [GPa]	Poisson's Ratio	Engineering Breaking Stress [MPa]	Engineering Breaking Strain [%]	Elastic Modulus [GPa]	Poisson's Ratio
Axial	Average [DIC data]	857	1.95	43.3	0.31	800	1.78	46.9	0.30
	Std.Dev.	48.4	0.09	1.72	0.01	6	0.08	1.6	0.03
	Coeff. of Var. [%]	5.65	4.81	3.98	4.38	0.75	4.49	3.41	10.00
Transverse	Average [DIC data]	337	1.44	34.7	0.32	462	1.44	41.6	0.29
	Std.Dev.	8.08				36	0.09	1.3	0.02
	Coeff. of Var. [%]	2.40				7.79	6.25	3.13	6.90

Six layer laminate used by Littell versus 3-layer for UDRI

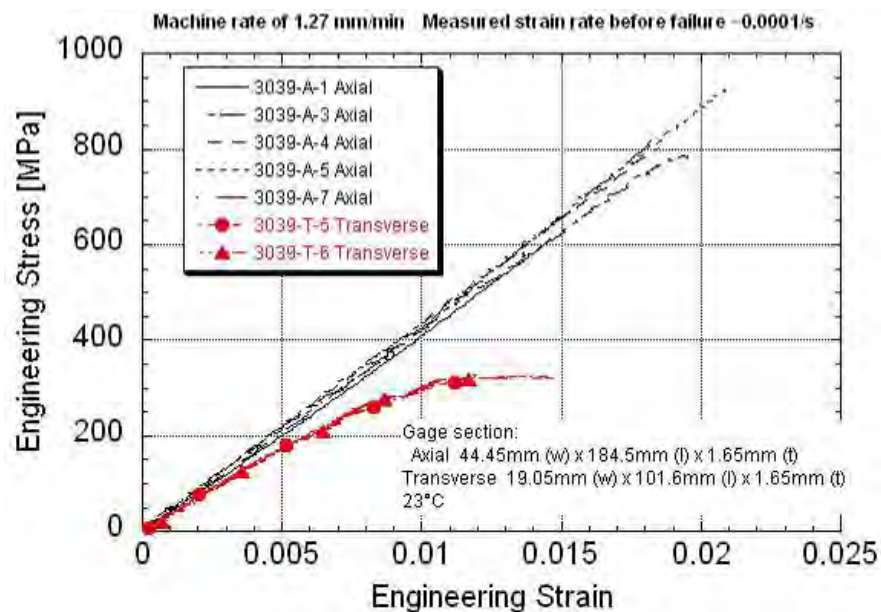


Figure 33. Tensile Stress-strain Curves for Modified ASTM D 3039 2D3A



Figure 34. Strain Gage Location for Axial Modified ASTM D 3039 2D3A

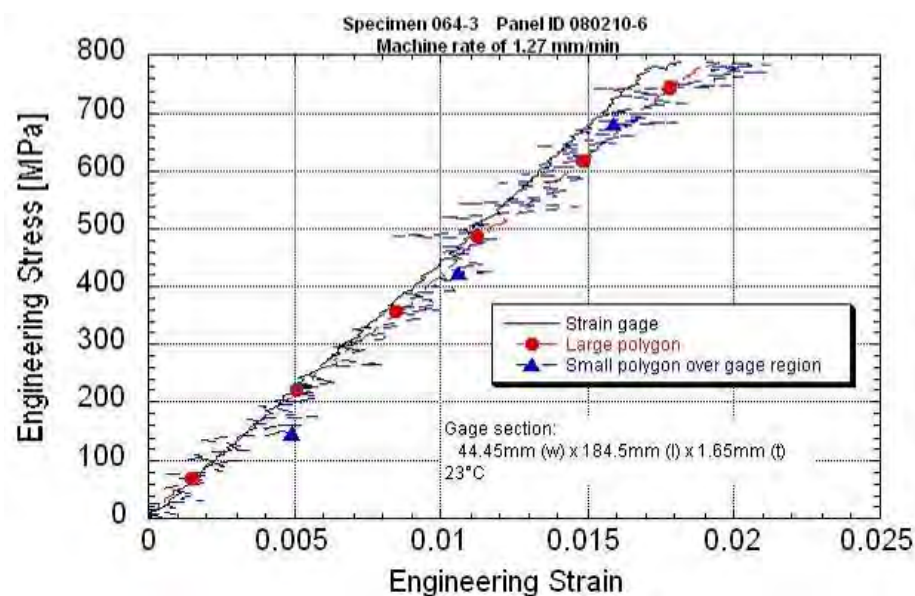
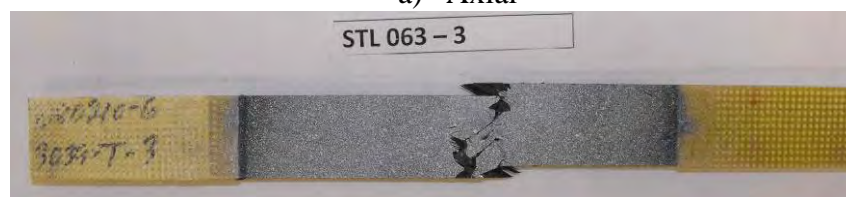


Figure 35. Comparison of Stress-strain Curves using Strain Gage and DIC Data



a) Axial



b) Transverse

Figure 36. Typical Failure Locations for Axial (a) and Tensile (b) Modified D 3039 Specimens

8.3.2 Bowtie Axial Tensile

Table 11 summarizes the axial mechanical property data. A summary stress-strain graph of the bowtie axial tests across all rates is given in Figure 37. Detailed data and summary graphs are in Appendix K.

Specimens which exhibited vertical cracking by the notch and towards the grip before final failure had a peak strength 30 to 50 MPa lower than those that did not. This contributed to the large standard deviation at certain rates.

The material response was similar within and amongst all rates. The strength and failure strain were insensitive to increasing strain rate. The stiffness at the two lower rates was equivalent. The modulus at the two upper rates was 25% higher. All specimens failed in the center section. A typical failure is shown in Figure 38.

Table 11. Bowtie Axial Tensile Data Summary for 2D3A

		Engineering Breaking Stress [MPa]	Normalized Peak Stress to 56 vol % Fiber [MPa]	Engineering Breaking Strain [%]	Elastic Modulus [GPa]	Poisson's Ratio
0.0001-0.0002/s 1.27 mm/min	Average	798	775	1.31	67.0	0.25
	Std.Dev.	56.7	60.1	0.06	2.47	
	Coeff. of Var. [%]	7.11	7.76	4.81	3.69	
0.03/s 0.5 m/min	Average	865	815	1.44	66.4	0.36
	Std.Dev.	48.9	46.1	0.07	4.18	
	Coeff. of Var. [%]	5.65	5.65	5.13	6.30	
0.3-0.45/s 5 m/min	Average	803	782	1.27	80.6	0.38
	Std.Dev.	60.4	47.7	0.21	5.36	0.01
	Coeff. of Var. [%]	7.53	6.09	16.2	6.66	2.33
2 to 5/s 36 to 45 m/min	Average	783	744	1.33	85.4	0.40
	Std.Dev.	19.2	29.4	0.13	6.62	0.06
	Coeff. of Var. [%]	2.46	3.96	10.0	7.76	15.2

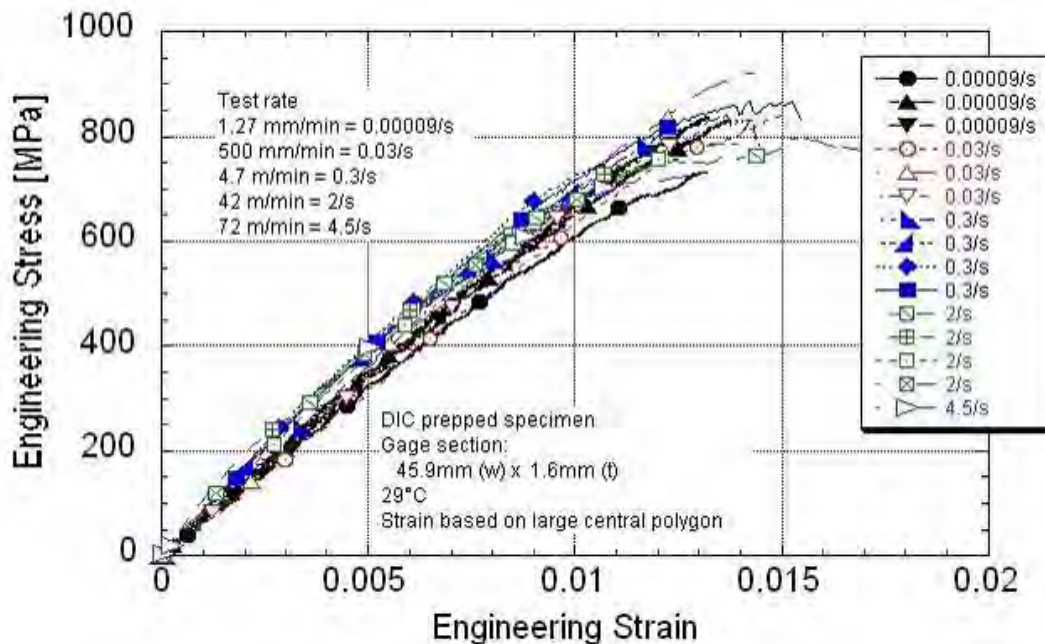


Figure 37. Representative Stress-strain Curves for 2D3A Bowtie Axial Specimens at All Rates

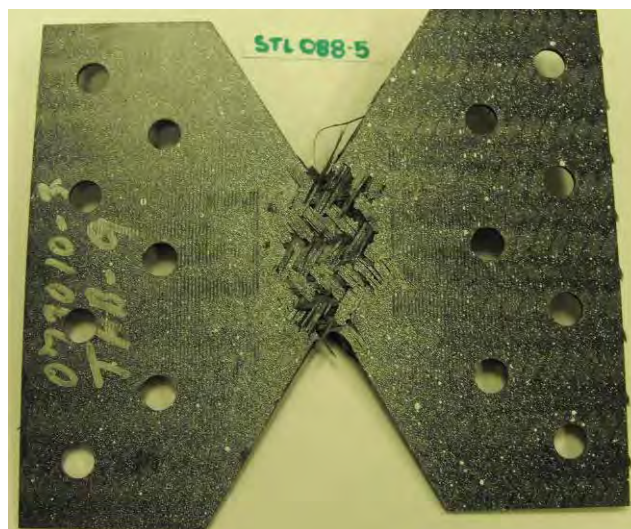


Figure 38. Typical Failure of Axial Bowtie Tensile Specimen

8.3.3 Bowtie Transverse Tensile

The initial bowtie specimens run at 1.27 mm/min showed extended tearing and cracking into the grip before final failure. Shortening the grip-to-grip distance by ~6mm increased the specimen area in the grip and resulted in less tearing before failure. All further tests were done with the shorter grip-to-grip distance.

Table 12 summarizes the transverse mechanical property data. A summary stress-strain graph of the transverse tensile stress-strain curves all rates is given in Figure 39. Detailed data and summary graphs are in Appendix L.

The peak strengths were rate insensitive and the coefficient of variability (COV) was low (3 to 4%). This suggests that all of the fiber tows were engaged and gripped in the fixture and the overall strength is a direct function of the contribution of both the axial and bias tows.

There was a wide disparity in the stress-strain response (Figure 39) compared to the axial tension (Figure 37). The stiffness and breaking strain had a very high COV (14 to 54%) and the material response appeared to fall into two groups.

Table 12. Bowtie Transverse Tensile Data Summary for 2D3A

		Egr Breaking Stress [MPa]	Normalized Peak Stress to 56 vol% Fiber [MPa]	Egr Breaking Strain [%]	Elastic Modulus [GPa]	Poisson's Ratio
0.00015/s 1.27 mm/min	Average	965	942	2.07	66.4	0.01-0.36
	Std.Dev.	30.1	29	0.50	9.6	
	Coeff. of Var. [%]	3.12	3.12	24.3	14.5	
0.045/s 0.5 m/min	Average	1017	992	1.72	116	0.25-0.6
	Std.Dev.	26.9	26	0.31	17.2	
	Coeff. of Var. [%]	2.65	2.65	18.1	14.8	
0.45/s 5 m/min	Average	1046	1026	2.02	81.9	0.03-0.47
	Std.Dev.	45.5	45	0.38	42.8	
	Coeff. of Var. [%]	4.35	4.40	18.6	52.2	
5/s 45 m/min	Average	918	950	2.34	57.9	.03-0.06
	Std.Dev.	34.6	36	0.74	7.1	
	Coeff. of Var. [%]	3.77	3.77	31.7	12.2	

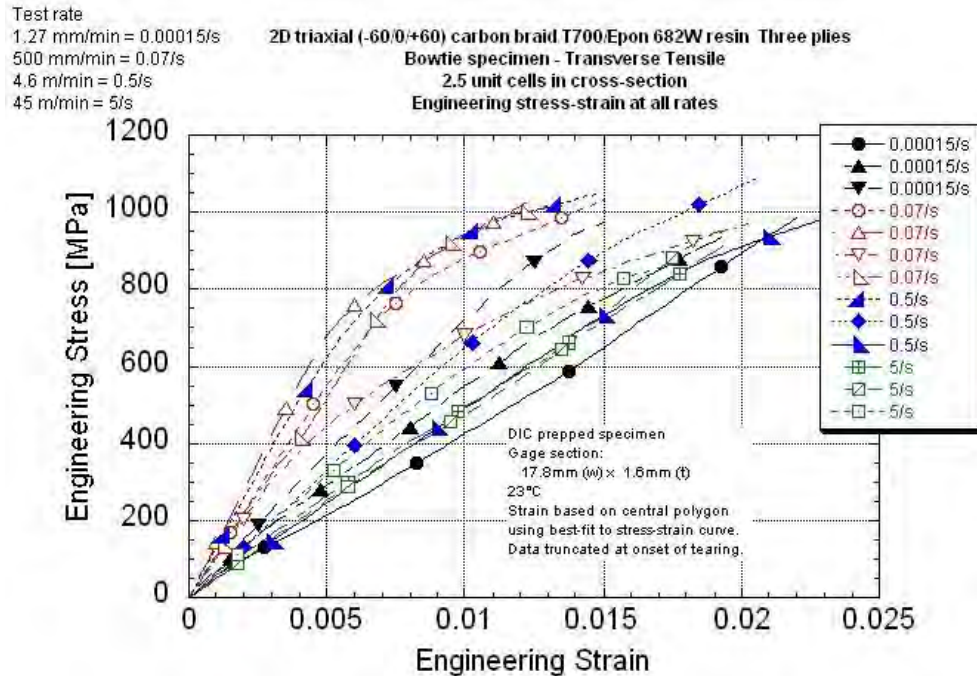


Figure 39. Representative Stress-strain Curves for 2D3A Bowtie Transverse Specimens at All Rates

The stiffness and failure strain reflects the ability of the fiber bundles in the center gage section to move in response to the applied load. The lower COV of the axial tension stiffness and strain (1 to 16%) compared to the transverse suggests that the material response is affected by the relative amount of axial and bias tows in the center gage.

The 2D3A panels consisted of three layers which were free to move and shift during processing. This resulted in panels with varying levels of alignment of the fibers through the thickness. Those with a high amount of alignment had higher variations in thickness in the center gage section. Each center gage width was equivalent to 2.5 unit cells in the corresponding direction. The beginning and end of a unit cell, as defined by the top layer, did not necessarily track through the thickness. Therefore, the amount of axial and bias tows in the tested center gage section could vary depending on the amount of alignment of the tows through the thickness.

Figure 40 illustrates the idealized locations of the 0° and bias tows for the axial and transverse cross-sections in a single layer. The ideal axial notch section (Figure 40a) should have five full tows of 0° fibers with the sixth tow just outside the notch (lightly shaded in Figure 40a). There are five full bias tows in both directions plus one partial tow in each direction. Small misalignment of the fiber bundles through the thickness would add some additional bias fibers. Larger misalignments would increase the number of axial fibers, which should raise the measured stiffness and modulus.

The similar behavior of the axial stiffness within a given rate suggests that the axial mechanical properties were dominated by the 0° fiber tows. Variations due to fiber misalignment through the thickness or along the 0° direction had minimal affects.

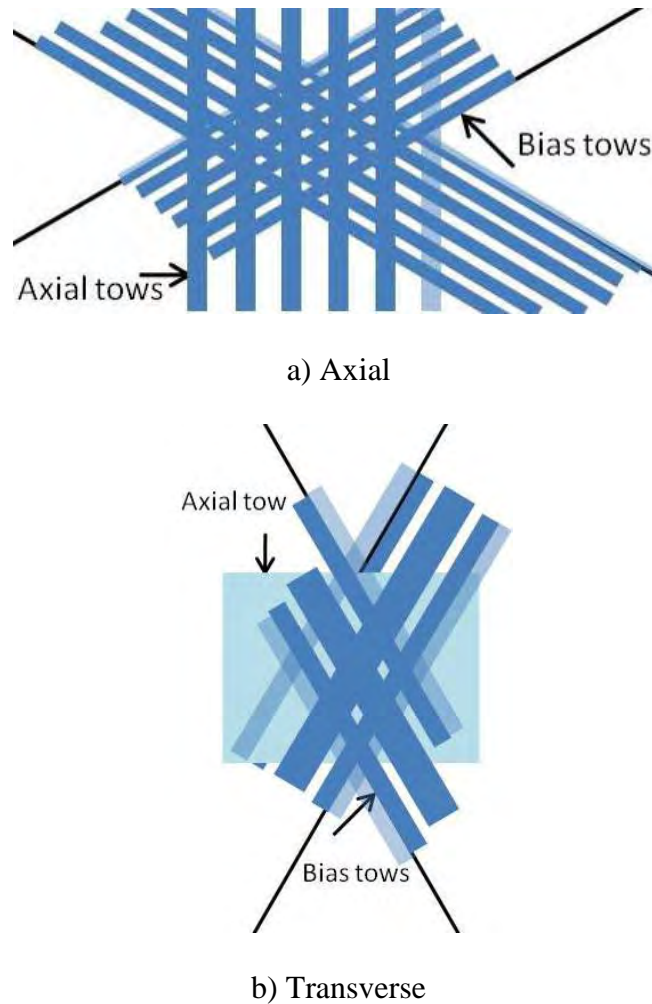


Figure 40. Schematic of Fiber Tow Location in Center Gage for Axial (a) and Transverse (b) Tensile Bowtie Specimen

The notch area of an idealized transverse gage (Figure 40b) will have one full bias tow in both directions and two partial tows (as represented by the lighter shaded rectangles). The axial tow width in the unmolded braid is over 6 mm with sections of bias tows ~ 4 mm wide in-between. The axial fiber tow width is of the same scale as the notch length. Therefore, the amount of axial fibers present in the center can vary depending on whether the notch is mainly in-between two axial tows or intersecting an axial tow; i.e., the center gage can contain anywhere from ~30% up to 100% of the axial fibers in a bundle. This assumes perfect alignment through the thickness. Misalignment of the bundles through the thickness would increase the likelihood of a larger percentage of axial fibers in the gage.

The variability in the transverse material stress-strain curves suggests that the stiffness (and corresponding failure strain) is highly sensitive to the fiber bundle distribution within the center gage. The amount of axial fibers in the notch is the probable cause for the range of values for the stiffness and strain.

8.3.4 Comparison of Bowtie Axial and Transverse Tensile Mechanical Properties

The 2D3A braid is designed to be in-plane quasi-isotropic. As such, one would expect similar properties testing in the axial or transverse direction. The tensile behavior across the rates is similar, as shown in Figure 41. The transverse strength is significantly higher than the axial.

The graph of the measured modulus and failure strain, Figures 42 and 43, reflect the variability in the transverse direction. It is difficult to identify a clear difference in the modulus between the axial and transverse. They are of similar magnitude. The transverse failure strain trends higher than the axial by 0.5 to 1.0 percentage points.

8.3.3 Comparison of Modified D 3039 and Bowtie Axial and Transverse

As mentioned in Section 4.5.1, the bowtie fixture grips 100% of the 0° and bias tows in the gage section under ideal conditions. A small number of fibers may not be gripped depending on the alignment of the tows through the thickness. Cracks initiated at the notch will be blunted by tows extending into the grips.

In contrast, the ASTM D 3039 straight-sided gage section allows for crack initiation along both sides of the straight edge. Only those bias tows close to the tab region are gripped. The axial and bias tows will also blunt the cracks, but the available surface for crack initiation and propagation is much higher than for the bowtie specimen.

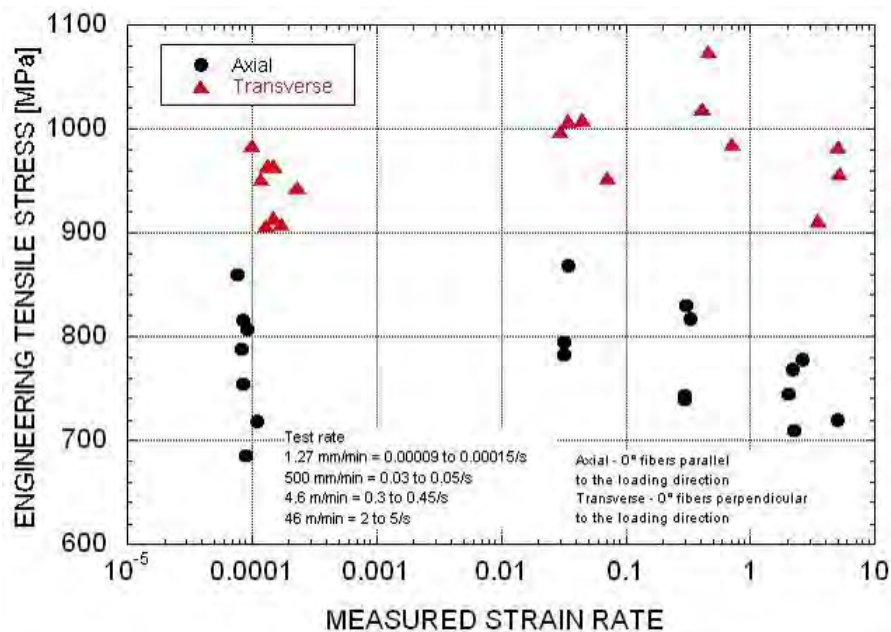


Figure 41. Measured Peak Tensile Stress of Axial and Transverse 2D3A Normalized to 56 vol% Fiber

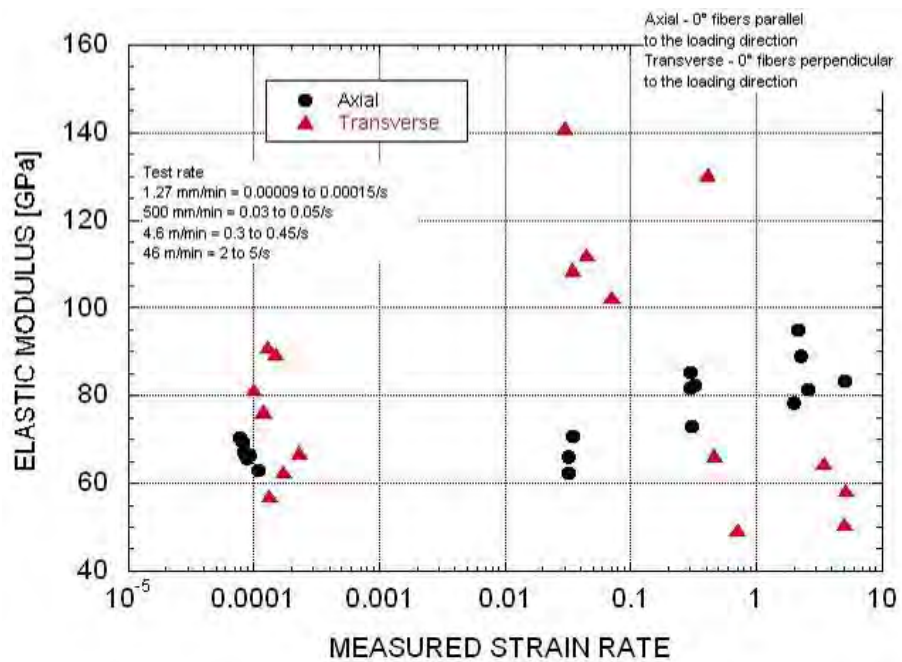


Figure 42. Measured Modulus of Axial and Transverse 2D3A

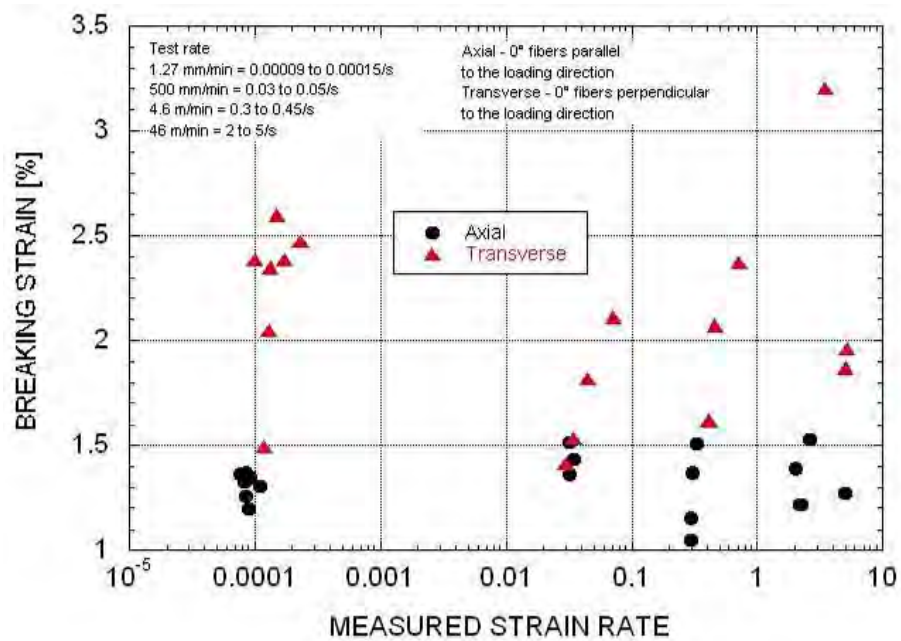


Figure 43. Failure Strain of Axial and Transverse 2D3A

Table 13 summarizes the tensile data for the bowtie and D 3039 configurations at an equivalent test rate. Additional details are given below.

Table 13. Comparison of Bowtie and Modified ASTM D 3039 Tensile Properties at 1.27 mm/min

		BOWTIE					MODIFIED ASTM D 3039				
		Egr Breaking Stress [MPa]	Normalized Peak Stress to 56 vol % Fiber [MPa]	Egr Breaking Strain [%]	Elastic Modulus [GPa]	Poisson's Ratio	Egr Breaking Stress [MPa]	Normalized Peak Stress to 56 vol % Fiber [MPa]	Egr Breaking Strain [%]	Elastic Modulus [GPa]	Poisson's Ratio
Axial	Average	841	817	1.35	68.4	0.25	846	857	1.95	43.3	0.31
	Std.Dev.	23.7	30.6	0.02	1.84		47.8	48.4	0.09	1.7	0.01
	Coeff. of Var. [%]	2.82	3.75	1.38	2.69		5.65	5.65	4.8	4.0	4.38
Transverse	Average	965	942	2.07	66.4	0.01-0.36	333	337	1.44	34.7	0.32
	Std.Dev.	30.1	29	0.50	9.6		8.0	8.1			
	Coeff. of Var. [%]	3.12	3.12	24.3	14.5		2.40	2.40			

8.3.3.1 Axial Tensile

The bowtie axial tensile strength at 1.27 mm/min was 40 MPa lower than the results using the modified ASTM D 3039 specimen. This was still within one standard deviation of the average. The equivalent axial tensile strength suggests that the contribution of the bias tows to the overall strength is minimal. However, the axial failure strain and stiffness were quite different, as seen in Figure 44. The bowtie failure strain was lower by a factor of 0.7 and the stiffness was 58% higher.

The difference in stiffness and failure strain is thought to be due to the restricted available movement of the fiber tows in the center gage section. The restriction is from both the specimen design, with a single region for the stress concentration and failure, and the engagement of the all of the tows in the grip. Cracks initiated in the longer length of the straight-sided D 3039 specimen allows for more movement of the tows to accommodate the increasing load. The resultant stiffness is lower and the total strain before failure is greater.

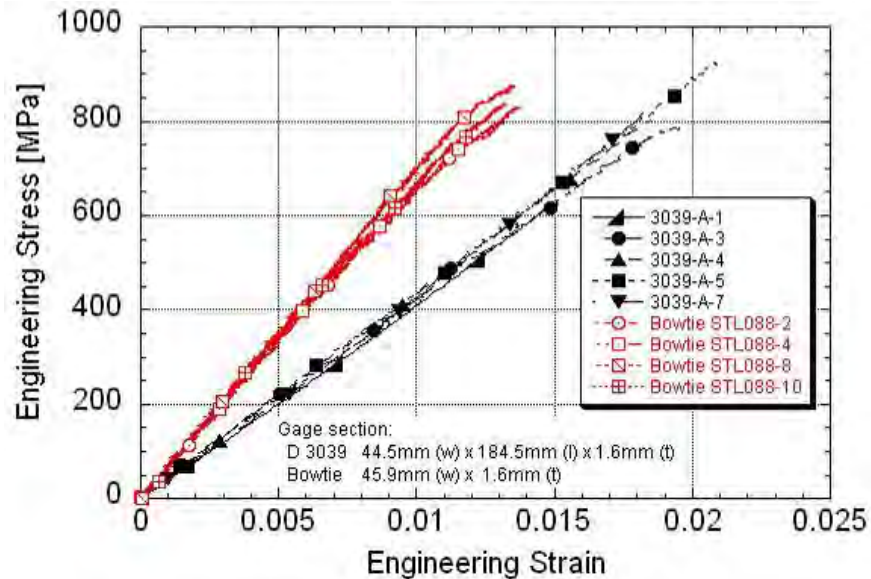


Figure 44. Comparison of Axial Tensile Stress-strain Response at 1.27 mm/min

8.3.3.2 Transverse Tensile

The bowtie transverse tensile properties are quite different. The tensile strength is 280% higher than for the ASTM D 3039. The failure strain is higher, probably because of limited crack propagation in the bowtie versus D 3039 specimen. The bowtie stiffness is higher because of the restricted movement of the gripped fiber tows and the varying amounts of axial fibers in the gage section. Figure 45 shows the stress-strain response for the two configurations.

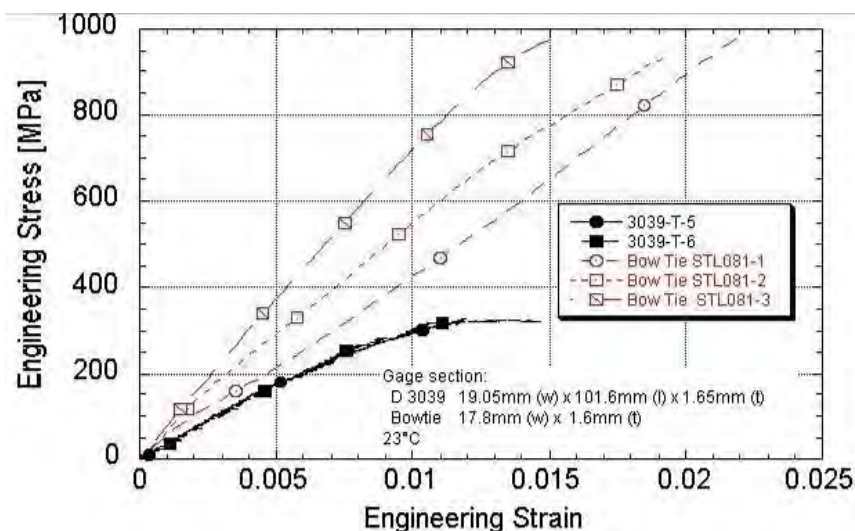


Figure 45. Comparison of Transverse Tensile Stress-strain Response at 0.6 to 1.27 mm/min for Modified ASTM D 3039 and Bowtie Specimens

8.4 Compression

As mentioned in Section 4.6.2, the tapered compression specimen had cracks initiating at the shoulder radius. Failure occurred at the shoulder radius and also in the unsupported section. Subsequent tests used a straight-sided specimen. The width of the specimen (66 to 71 mm) allowed for 4 unit cells in the axial direction and 14 unit cells in the transverse. The unsupported section was 3.2 mm long. The DIC window for the strain measurement covered at least 2.5 unit cells in the loading direction.

Specimens were tested at 1.27 mm/min using a solid backing plate and one with the DIC window to check to see whether the DIC window caused premature buckling or failure in the window. The results did not show a difference in the peak stress or failure location.

Detailed data and summary graphs are in Appendix M for the axial compression and Appendix N for the transverse compression.

8.4.1 Axial Compression

Table 14 summarizes the low rate data using the UDRI specimen configuration and results from Littell. The strength and modulus numbers are within one standard deviation. The failure strain is lower. However, variability data were not given by Littell and the difference may not be significant.

The mechanical properties for the test rates from 0.0004/s to 0.4/s are in Table 15. Figure 46 shows the axial compression stress-strain curves for the straight-sided specimens and Figure 47 includes the dogbone specimens. Figure 46 shows two individual specimens which appear to be outliers. However, two distinct groups are represented when the dogbone specimens are also plotted on the same curve (Figure 47).

The peak compressive strength of the dogbone specimen is not statistically different from the straight-sided specimen (Figure 48). They do have a higher measured modulus and lower failure strain (Figures 49 and 50). One would suspect that the differences are strictly due to the specimen shape. However, two of the straight-sided specimens had a similar response as the dogbone. The difference may be due to the onset of buckling of the axial tows. The modulus and failure strain were insensitive to the increasing strain rate.

The strength at 0.004/s is lower by 50 MPa than at the other rates. The strength data at the other rates are equivalent. There is no assignable cause for the lower strength at 0.004/s.

Figure 51 shows a typical failure for the dogbone and straight-sided axial specimen. Failure in the dogbone was initiated at the shoulder radius and propagated along the DIC window. The straight-sided specimen failed at the unsupported section.

Table 14. Comparison of Axial Compression UDRI and Published Data [13]

		Straight-sided UDRI Test Rate of 1.27 mm/min Measured rate of 0.00012/s			From Littell PhD Thesis [13] Test Rate of 0.635 mm/min		
		Engineering Breaking Stress [MPa]	Engineering Breaking Strain [%]	Elastic* Modulus [GPa]	Engineering Breaking Stress [MPa]	Engineering Breaking Strain [%]	Elastic Modulus [GPa]
Axial	Average [DIC data]	285	0.64	36.0/49.3	327	1.01	41.4
	Std.Dev.	20.6	0.04	2.96/4.27	47		6.0
	Coeff. of Var. [%]	7.22	6.84	8.22/8.66	14.5		14.5

*Two groupings in the stress strain response. Each group had a similar behavior across the rates. The two moduli represent the average for each grouping.

Six layer laminate used by Littell versus 3-layer for UDRI. Littell tested two specimens.

Table 15. Axial Compression Data Summary for 2D3A

		Engineering Breaking Stress [MPa]	Normalized Peak Stress to 56 vol % Fiber [MPa]	Engineering Breaking Strain [%]	Elastic Modulus [GPa]
0.00012/s 1.27 mm/min	Average	283	282	0.64	51.7
	Std.Dev.	13.1	18.0	0.04	4.12
	Coeff. of Var. [%]	4.63	6.37	6.84	7.97
0.004/s 0.48 m/min	Average	252	237	0.73	34.5
	Std.Dev.	16.1	15.1	0.06	2.57
	Coeff. of Var. [%]	6.37	6.37	8.80	7.46
0.45/s 0.48 m/min	Average	284	271	0.71	40.7
	Std.Dev.	26.6	24.7	0.05	5.68
	Coeff. of Var. [%]	9.39	9.12	7.2	13.96
0.4/s 4.5 m/min	Average	280	269	0.76	37.7
	Std.Dev.	30.8	25.1	0.15	4.50
	Coeff. of Var. [%]	10.99	9.32	19.4	11.94

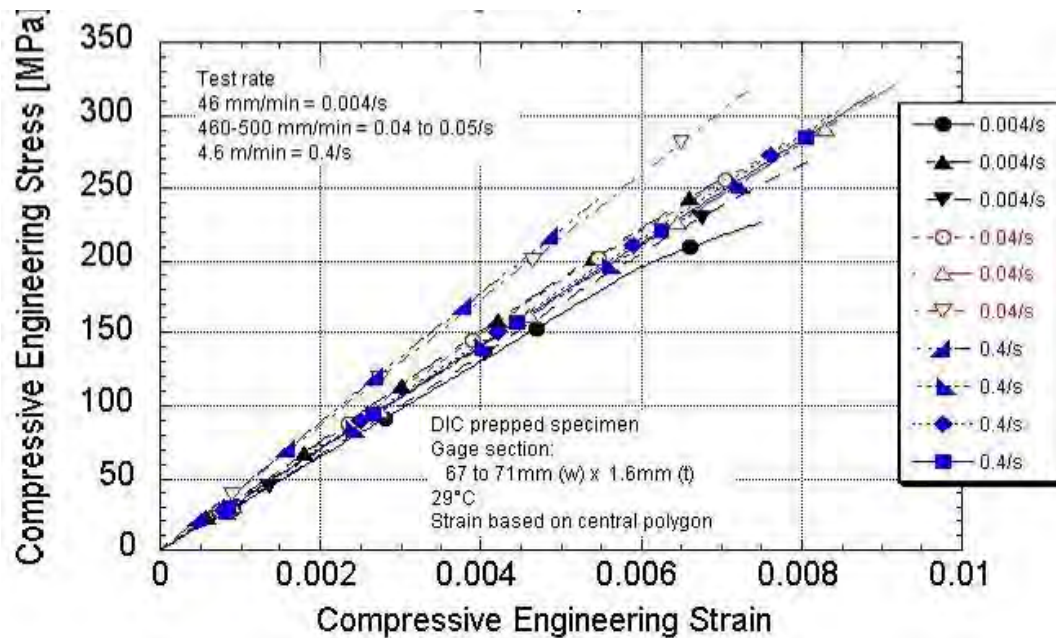


Figure 46. Axial Compressive Stress-strain Response at All Rates Using Straight-sided Specimens

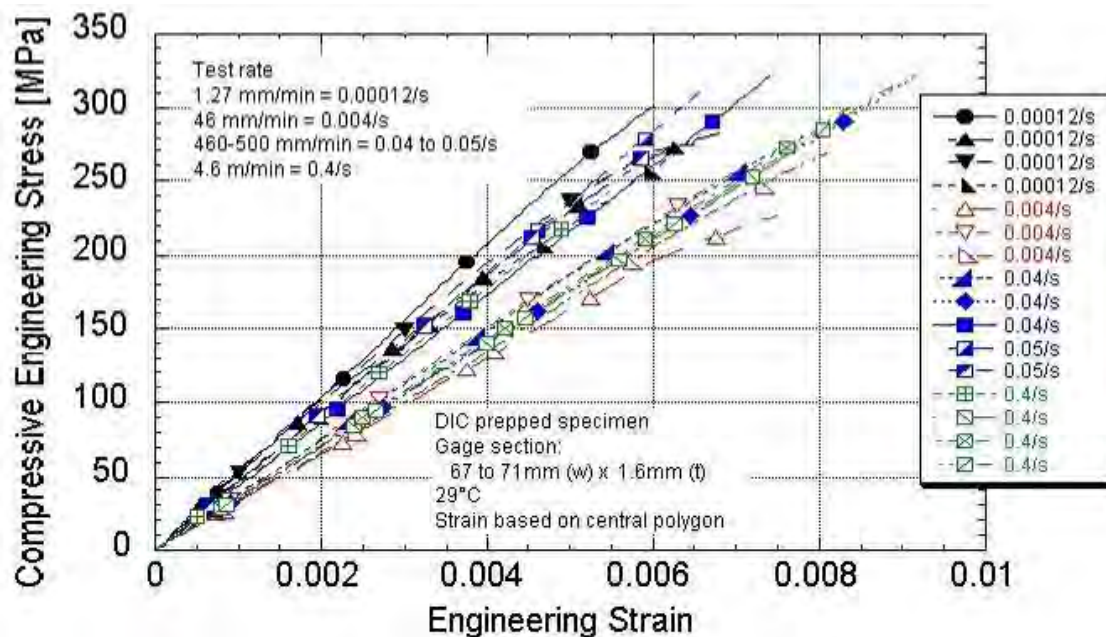


Figure 47. Axial Compressive Stress-strain Response at All Rates Using Dogbone and Straight-sided Specimens

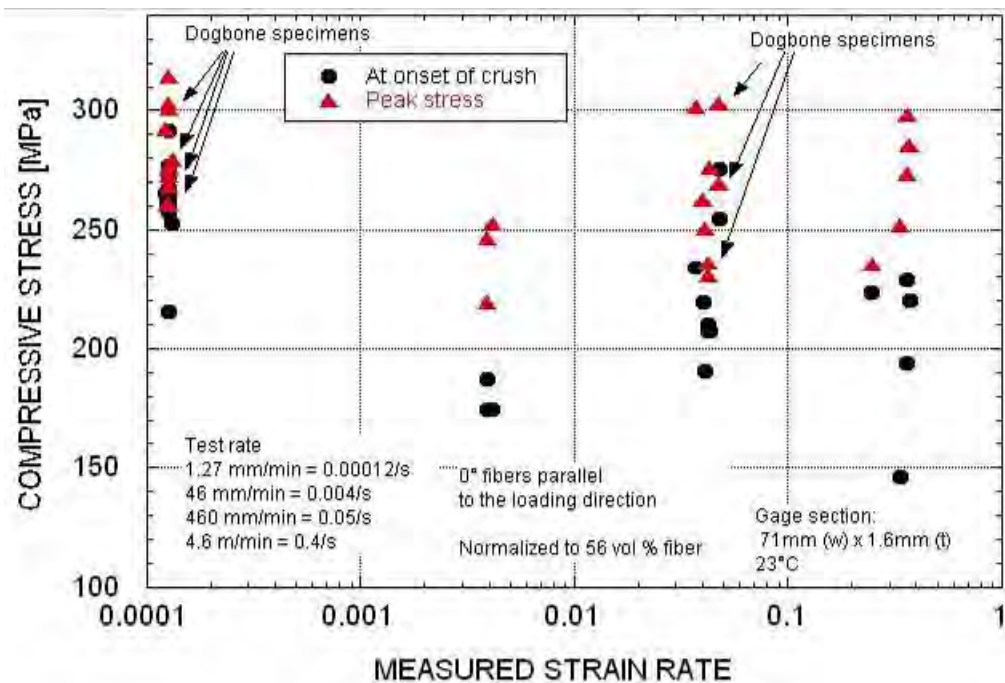


Figure 48. 2D3A Axial Compressive Strength as a Function of Strain Rate

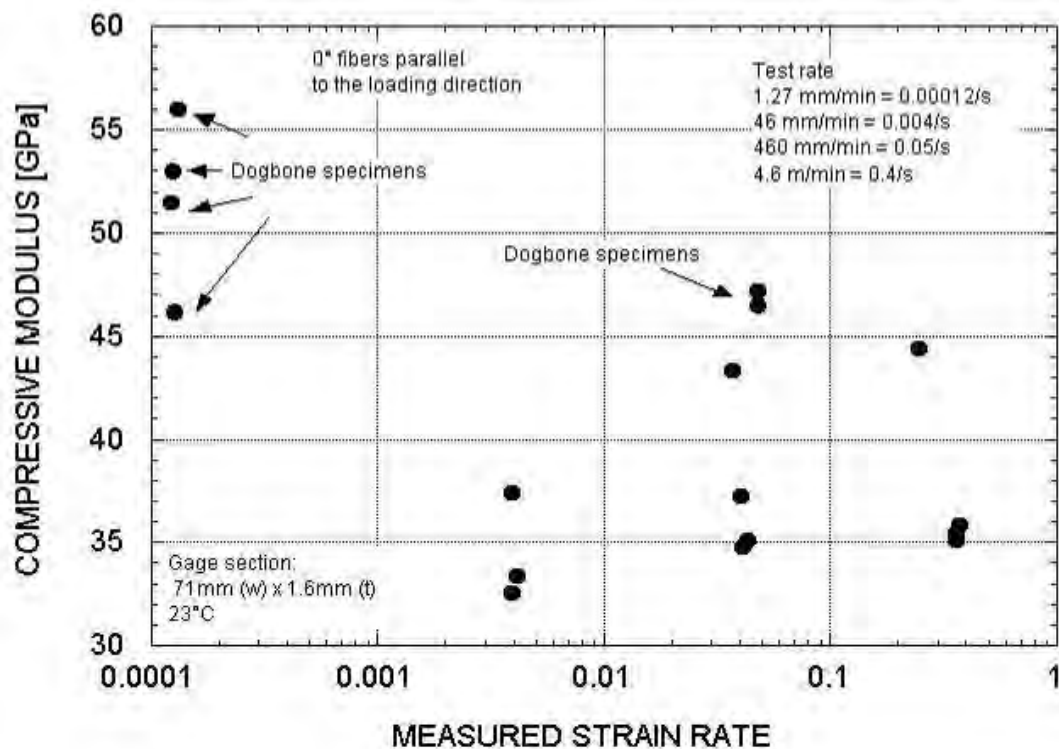


Figure 49. 2D3A Axial Compressive Modulus as a Function of Strain Rate

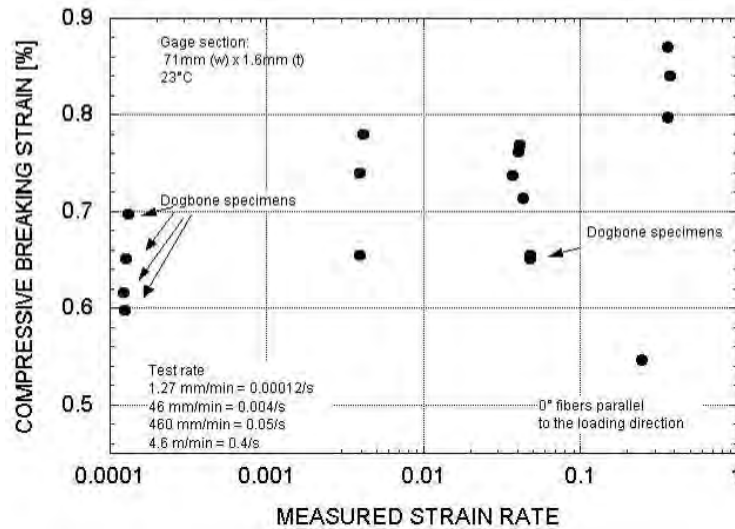
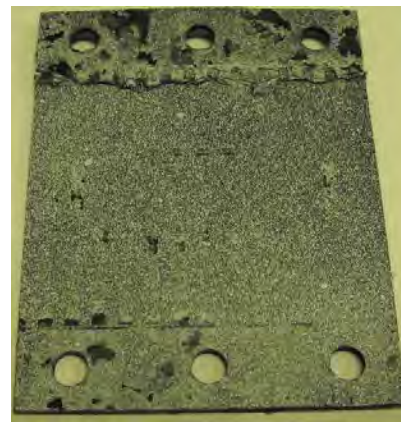


Figure 50. 2D3A Axial Compressive Failure Strain as a Function of Strain Rate



a) Dogbone



b) Straight-sided

Figure 51. Failure Location for Dogbone and Straight-sided Axial Compressive Specimens

8.4.2 Transverse Compression

Table 16 summarizes the low rate data using the UDRI specimen configuration and results from Littell [13]. The strength data are within one standard deviation. The UDRI data using the high rate specimen are summarized in Table 17.

Figure 52 shows the transverse compression stress-strain curves. All of these specimens were straight-sided. There is an increase of 18% in strength between 0.0004/s and 0.004/s if one excludes an outlier at 0.004/s (Figure 53). The strength across 0.004/s to 0.04/s remains the same. The modulus does not change between 0.004/s and 0.4/s (Figure 54). The modulus increased 13% between 0.04/s and 0.4/s. The failure strain was insensitive to the increasing strain rate from 0.004/s to 0.4/s (Figure 55). Typical failures are shown in Figure 56.

Table 16. Comparison of Transverse Compression UDRI and Published Data [13]

		Straight-sided UDRI Test Rate of 1.27 mm/min Measured rate of 0.00012/s			From Littell PhD Thesis [13] Test Rate of 0.635 mm/min		
		Engineering Breaking Stress [MPa]	Engineering Breaking Strain [%]	Elastic Modulus [GPa]	Engineering Breaking Stress [MPa]	Engineering Breaking Strain [%]	Elastic Modulus [GPa]
Transverse	Average [DIC data]	255	-	-	304	0.87	42.7
	Std.Dev.	32.2	-	-	44		6.2
	Coeff. of Var. [%]	12.6	-	-	14.5		14.5

Six layer laminate used by Littell versus 3-layer for UDRI. Littell tested two specimens.

Table 17. Transverse Compression Data Summary for 2D3A

		Engineering Breaking Stress [MPa]	Normalized Peak Stress to 56 vol % Fiber [MPa]	Engineering Breaking Strain [%]	Elastic Modulus [GPa]
0.00005/s 0.6 mm/min	Average	226	221	-	-
	Std.Dev.	15.2	15	-	-
	Coeff. of Var. [%]	6.73	6.73	-	-
0.004/s 0.48 m/min	Average	265	249	0.72	39.3
	Std.Dev.	34.0	32	0.12	2.8
	Coeff. of Var. [%]	12.8	12.8	17.2	7.25
0.4/s 0.48 m/min	Average	288	271	0.75	40.1
	Std.Dev.	18.2	17	0.08	1.7
	Coeff. of Var. [%]	6.33	6.33	10.0	4.1
0.4/s 4.7 m/min	Average	305	288	0.74	45.0
	Std.Dev.	27.8	26	0.04	2.3
	Coeff. of Var. [%]	9.11	9.11	5.8	5.2

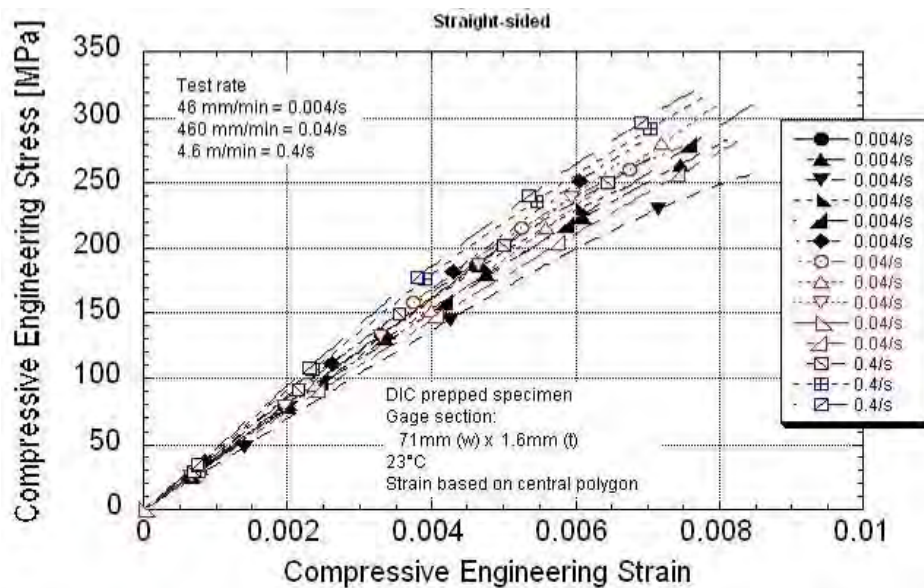


Figure 52. Transverse Compressive Stress-strain of 2D3A at All Rates

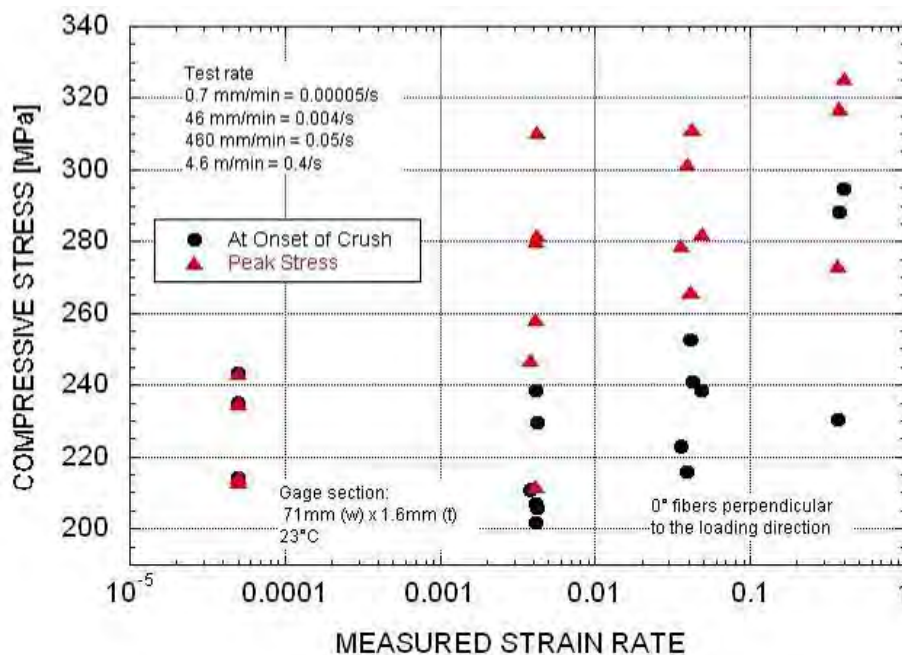


Figure 53. 2D3A Transverse Compressive Strength as a Function of Strain Rate

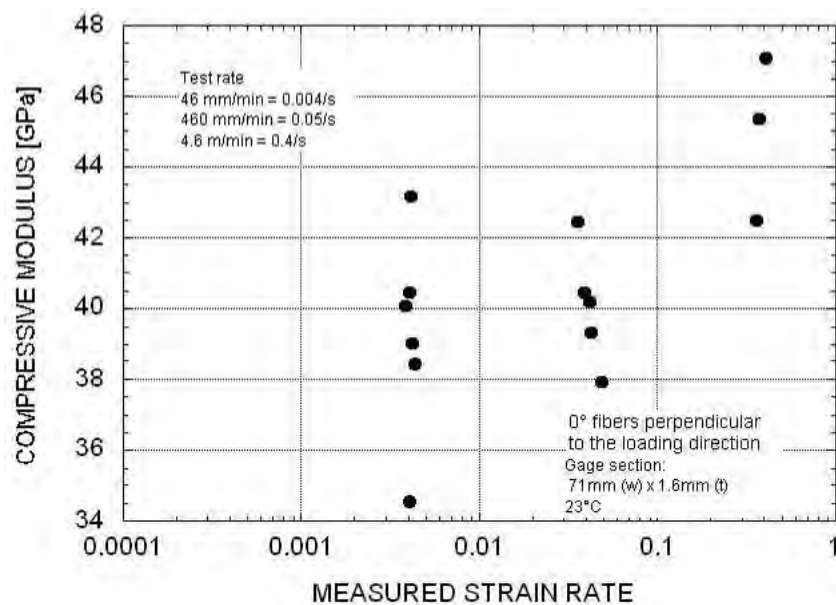


Figure 54. 2D3A Transverse Compressive Modulus as a Function of Strain Rate

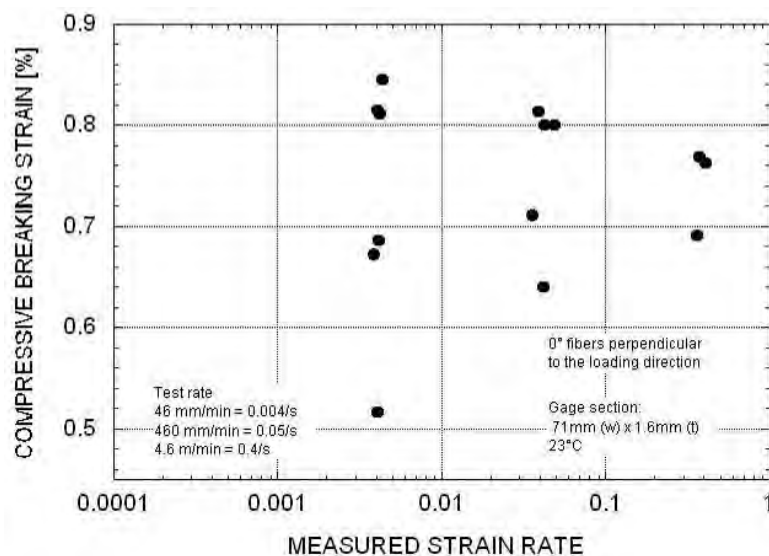


Figure 55. 2D3A Transverse Compressive Failure Strain as a Function of Strain Rate

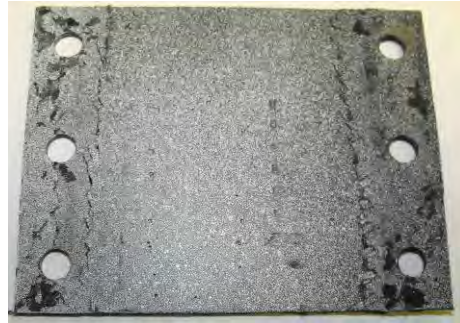


Figure 56. Typical Failure Location for Transverse Compressive Specimens

8.4.3 Comparison of Axial and Transverse Compression

The mechanical properties are shown in Figures 57 to 60. The axial and transverse peak strength data are equivalent across the tested rates. The exception is the transverse data at 0.00004/s, which had unusually low data as mentioned in Section 8.3.2. The data at this rate may not be an accurate representation of the strength, given the fact that both the axial and transverse strength data are equivalent and insensitive across the other tested rates.

The compressive modulus (Figure 58) is equivalent between the axial and transverse orientation. This is in part due to the two groupings of the axial stress-strain response. If one compares only the straight-sided specimens (Figure 59), then the transverse modulus appears to be slightly higher. However, the difference is not statistically significant because of the spread in the axial modulus data. The axial and transverse failure strains are equivalent (Figure 60).

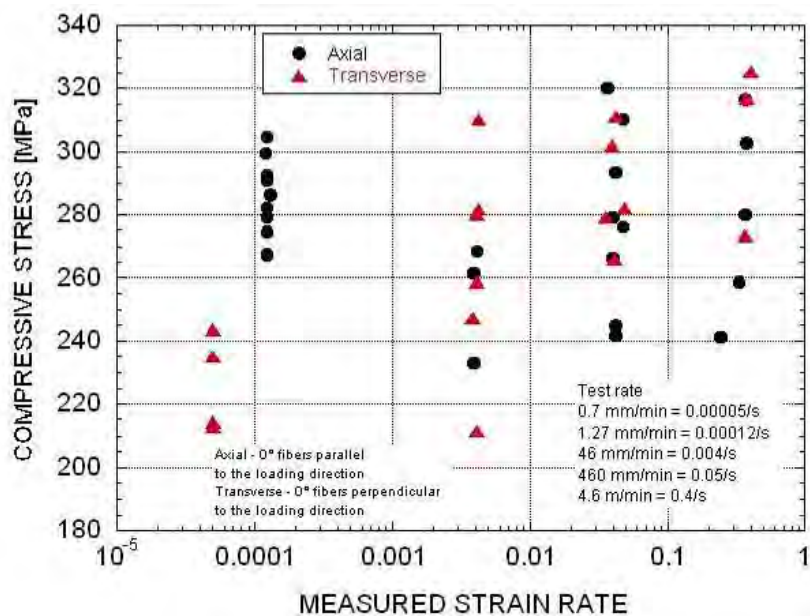


Figure 57. 2D3A Compressive Strength as a Function of Strain Rate

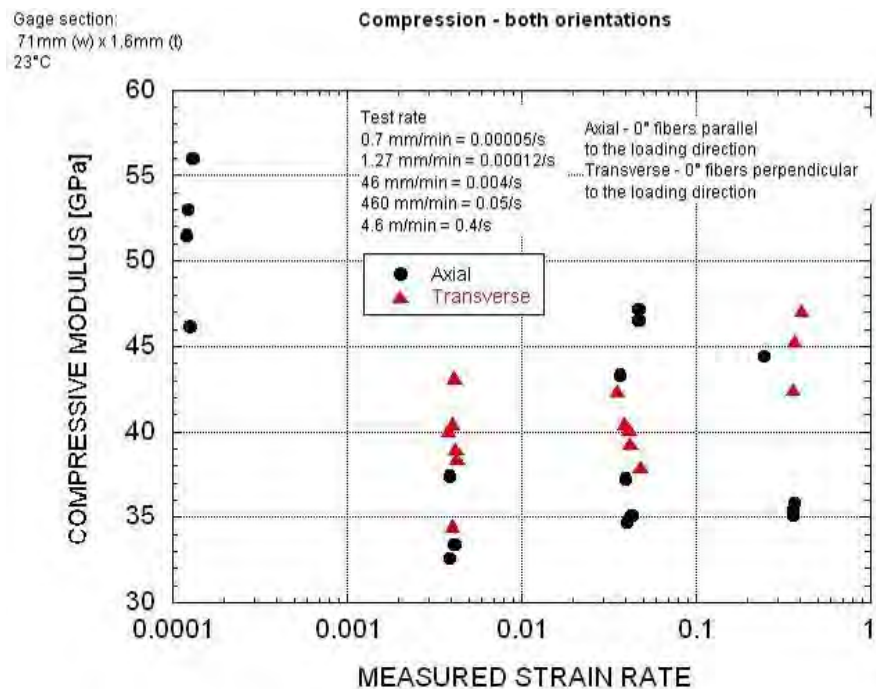


Figure 58. 2D3A Compressive Modulus as a Function of Strain Rate

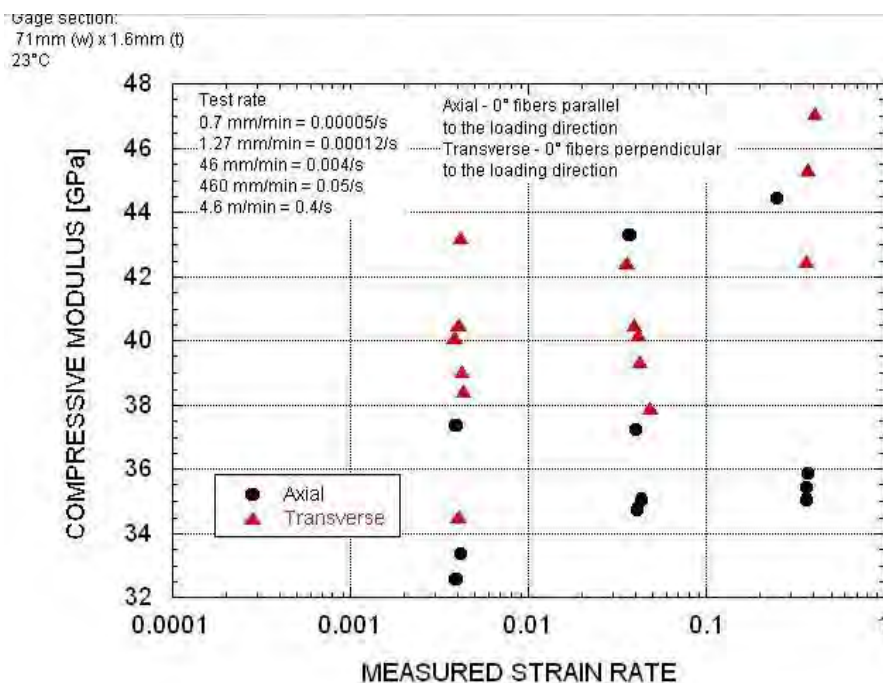


Figure 59. 2D3A Compressive Modulus as a Function of Strain Rate Using Straight-sided Specimens

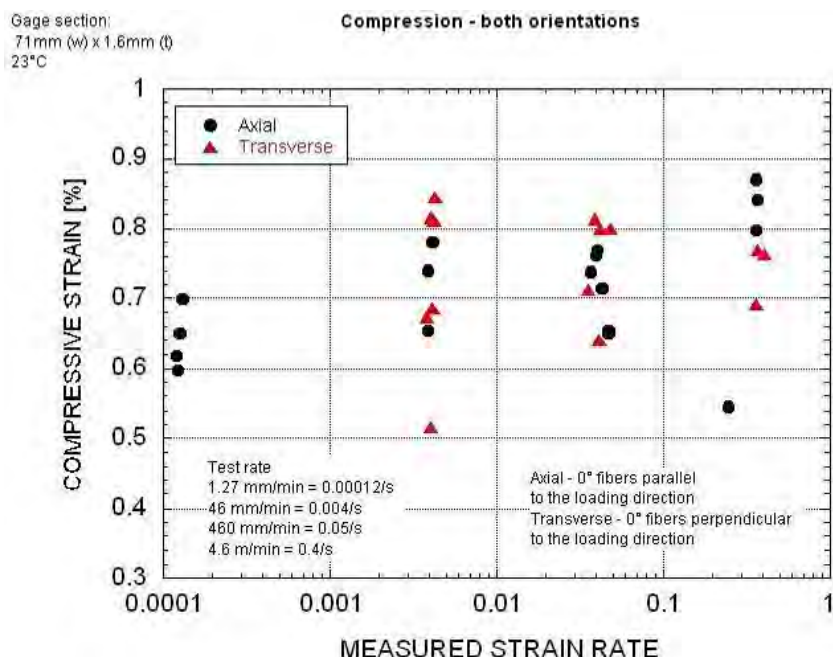


Figure 60. 2D3A Compressive Failure Strain as a Function of Strain Rate

8.5 Shear

The high rate fixture gripped the specimens out to the edge of the tab. Only the notch area was unsupported. About three to seven resonant waves were noticed at the maximum test rate of 45 m/s. The axial shear data package is in Appendix O and the transverse shear data are in Appendix P.

8.5.1 Comparison to Published Data

The data at the low rate are compared in Table 18. The UDRI shear data are lower by a factor of 0.72 than the data from Littell [13]. The shear modulus is equivalent.

8.5.2 Axial Shear (Shearing Across 0° Fiber Bundles)

The mechanical properties using the high rate shear specimen from 0.0008/s to 2.5/s are in Table 19. The axial stress-strain response across the tested rates is given in Figure 61. The peak strength, modulus, and strain as a function of the strain rate are graphed in Figures 62 to 64, respectively. Typical failures are shown in Figure 65.

About five to six low amplitude resonant waves were present before failure at the fastest rate of 49 m/min. This is below the desired 10 to 15 waves for dynamic equilibrium.

There is a positive trend in the strength as the rate increased. The average strength increased 10% between 0.0008/s and 2.5/s. However, there was no statistical significance in the

data amongst the three lower rates because of the variability. Therefore, the increase per decade was hard to measure.

Table 18. Comparison of UDRI Shear Data and Published Data [13]

		UDRI V-Notch Test Rate of 1.27 mm/min Measured rate of 0.00012/s			Littell V-notch [13] Test Rate of 0.635 mm/min		
		Engineering Breaking Stress [MPa]	Engineering Breaking Strain [%]	Elastic* Modulus [GPa]	Engineering Breaking Stress [MPa]	Engineering Breaking Strain [%]	Elastic Modulus [GPa]
Axial Shearing across 0° fibers	Average [DIC data]	177	0.75	32.9	257	-	32.0
	Std.Dev.	12.4	0.10	1.45	10	-	1.1
	Coeff. of Var. [%]	7.01	13.2	4.4	3.9	-	3.4
Transverse Shearing along 0° fibers	Average [DIC data]	195	0.75	29.2	Similar results for both orientations		
	Std.Dev.	17.1	0.04	3.47			
	Coeff. of Var. [%]	8.8	4.82	11.89			

Six layer laminate used by Littell versus 3-layer for UDRI. Littell tested two specimens.

Table 19. Axial Shear Data Summary for 2D3A
Shearing Across 0° Fiber Tows

		Engineering Breaking Stress [MPa]	Normalized Peak Stress to 56 vol % Fiber [MPa]	Engineering Breaking Strain [%]	Elastic Modulus [GPa]
0.00008/s 1.27 mm/min	Average	180	177	0.75	32.9
	Std.Dev.	11.3	12.4	0.10	1.45
	Coeff. of Var. [%]	6.30	7.01	13.24	4.40
0.03/s 0.5 m/min	Average	190	188	0.83	28.5
	Std.Dev.	15.9	16.0	0.11	1.24
	Coeff. of Var. [%]	8.40	8.54	13.13	4.35
0.25/s 5 m/min	Average	177	174	0.72	25.5
	Std.Dev.	2.6	2.3	0.11	2.91
	Coeff. of Var. [%]	1.48	1.29	14.7	11.4
2.5/s 49 m/min	Average	201	199	0.84	26.0
	Std.Dev.	5.2	5.1	0.03	0.84
	Coeff. of Var. [%]	2.58	2.58	3.6	3.24

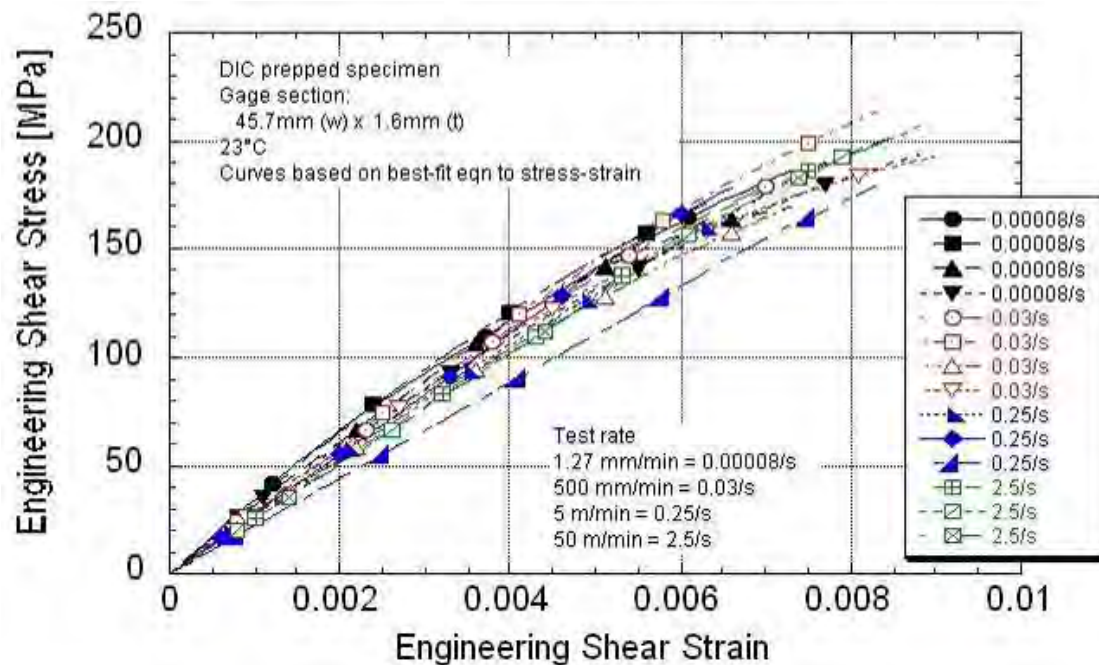


Figure 62. Axial Shear Stress-Strain Response of 2D3A Across Tested Rates

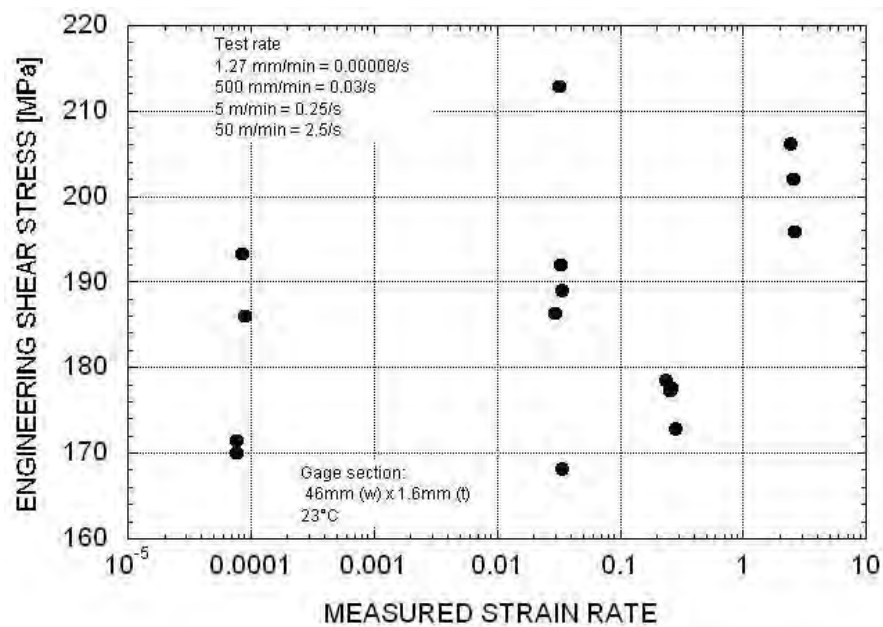


Figure 62. Axial Shear Strength of 2D3A Across Tested Rates

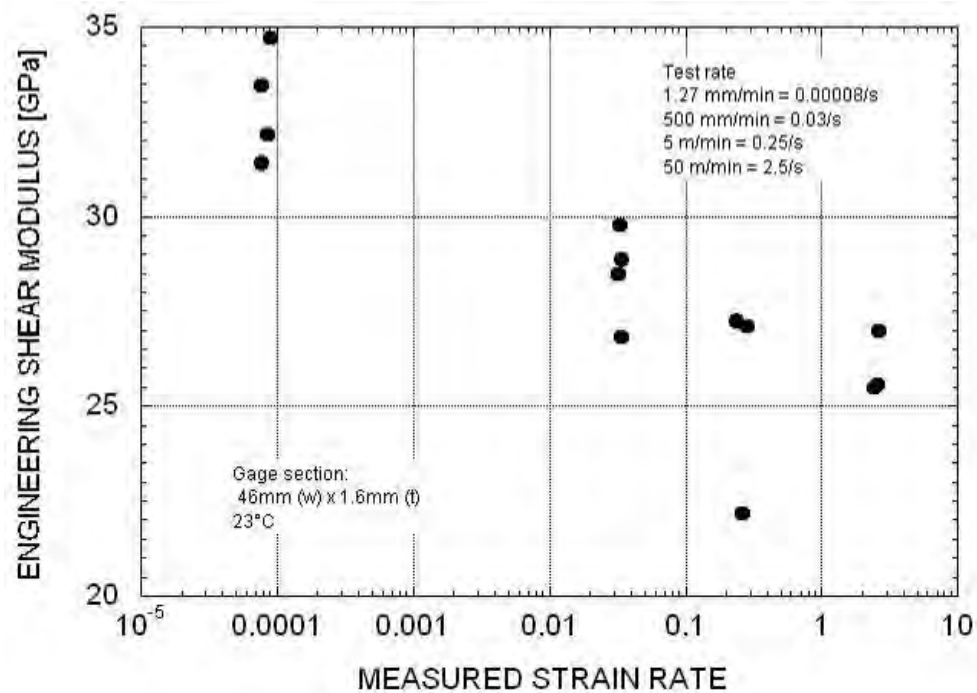


Figure 63. Axial Shear Modulus of 2D3A Across Tested Rates

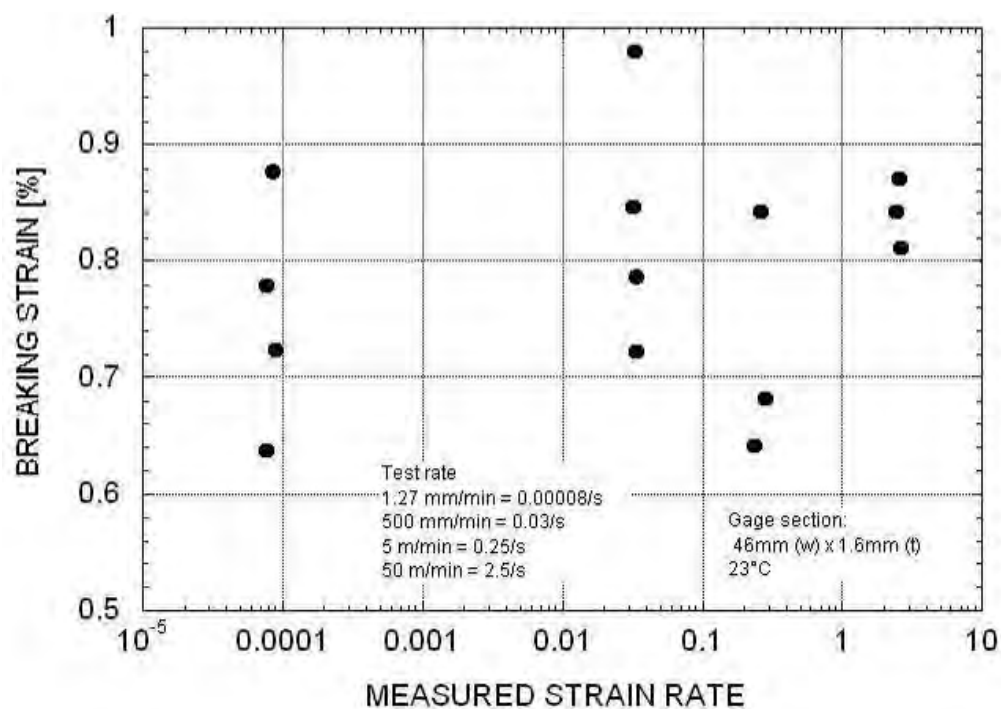


Figure 64. Axial Shear Failure Strain of 2D3A Across Tested Rates

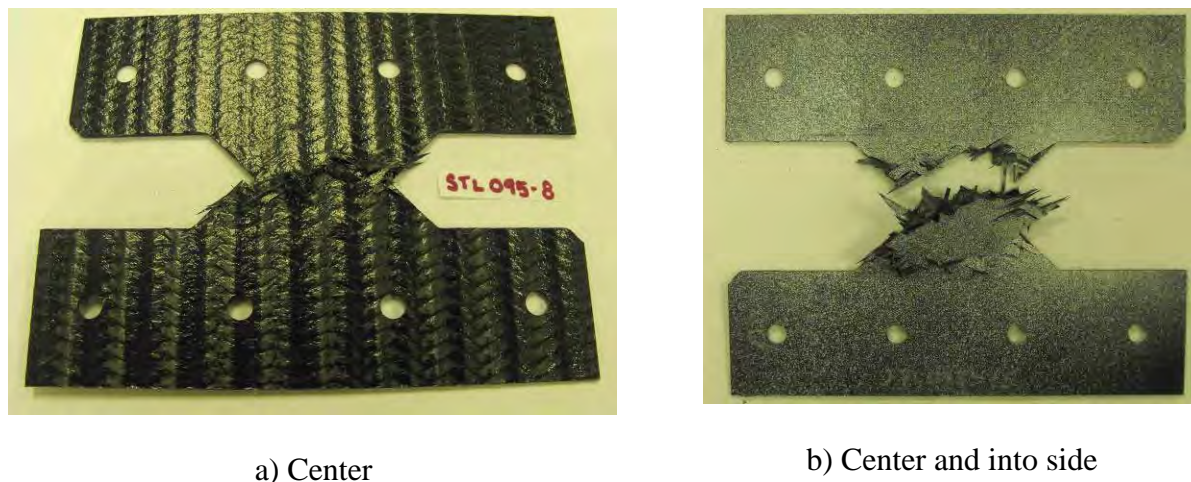


Figure 65. Typical Axial Shear Failure Locations

The stress-strain data were smoothed using a piecewise polynomial fit to the curve. The strain data at 0.25/s and 2.5/s [5 and 49 m/min] had a high amount of fluctuations, as seen in Figure 66. The elastic region for these curves was hard to define and the moduli for these rates are estimates. The apparent decrease in the modulus at rates above 0.025/s may be an artifact of the smoothing process.

The failure strain did not change across the tested rates.

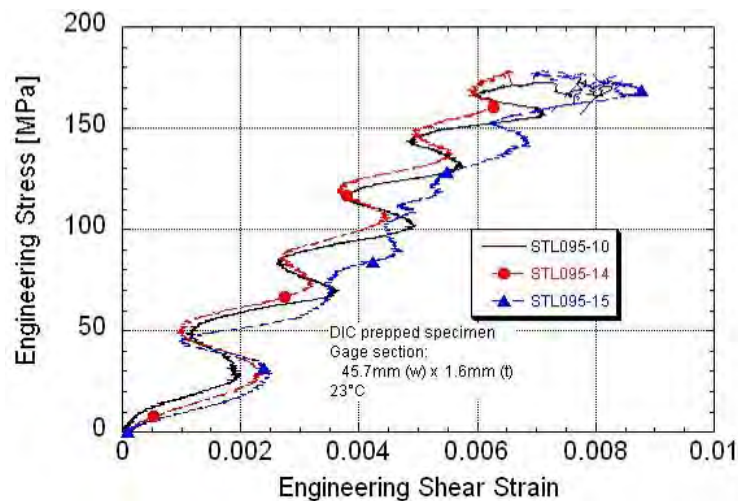


Figure 66. Unsmoothed Axial Shear Stress-Strain Response at 0.25/s

8.5.2 Transverse Shear (Shearing Along 0° Fiber bundles)

The mechanical properties using the high rate shear specimen from 0.0003/s to 8/s are in Table 20. The transverse shear stress-strain response across the tested rates is given in Figure 67. The peak strength, modulus, and strain as a function of the strain rate are graphed in Figures 68 to 70, respectively.

Typical failures are shown in Figure 71. Most of the specimen failed down the center or close to the center notch. It was noticed during testing that some of the initial failures occurred on the back face of the specimen, away from the DIC cameras (Figure 71b). The final surface crack was not necessarily indicative of where the crack initiated.

The strain oscillations were not as great as for the axial shear data and so it was easier to apply a polynomial fit to the data. The shear remained the same between 0.0003/s and 0.05/s. It increased about 10% with each decade up to 8/s. There was a large amount of variability at most rates. The modulus appears to increase slightly with rate, but the large spread in the data at 0.8/s makes it difficult to quantify the increase across each decade. The failure strain was insensitive to the increasing rate.

The transverse shear response was not sensitive to the number of unit cells in the center gage section. Increasing the specimen gage width by 250% did not change the stress-strain response.

The transverse shear fixture was slightly longer than the axial shear fixture and the natural resonance frequency was longer. Only three to five stress waves were present at the upper test rate of 49 m/min.

Table 20. Transverse Shear Summary Table of 2D3A
Shearing Along 0° Fibers

		Engineering Breaking Stress [MPa]	Normalized Peak Stress to 56 vol % Fiber [MPa]	Engineering Breaking Strain [%]	Elastic Modulus [GPa]
0.0003/s 1.27 mm/min	Average	200	195	0.75	29.2
	Std.Dev.	14.0	17.1	0.04	3.47
	Coeff. of Var. [%]	7.02	8.76	4.82	11.9
0.05/s to 0.1/s 0.5 m/min	Average	218	212	0.86	28.5
	Std.Dev.	17.1	18.8	0.12	2.08
	Coeff. of Var. [%]	7.86	8.87	13.5	7.28
0.8/s 5 m/min	Average	239	233	0.86	32.9
	Std.Dev.	6.4	6.1		
	Coeff. of Var. [%]	2.66	2.61		
8/s 49 m/min	Average	226	216	0.86	33.4
	Std.Dev.	15.9	10.9	0.09	1.59
	Coeff. of Var. [%]	7.02	5.08	10.9	4.76

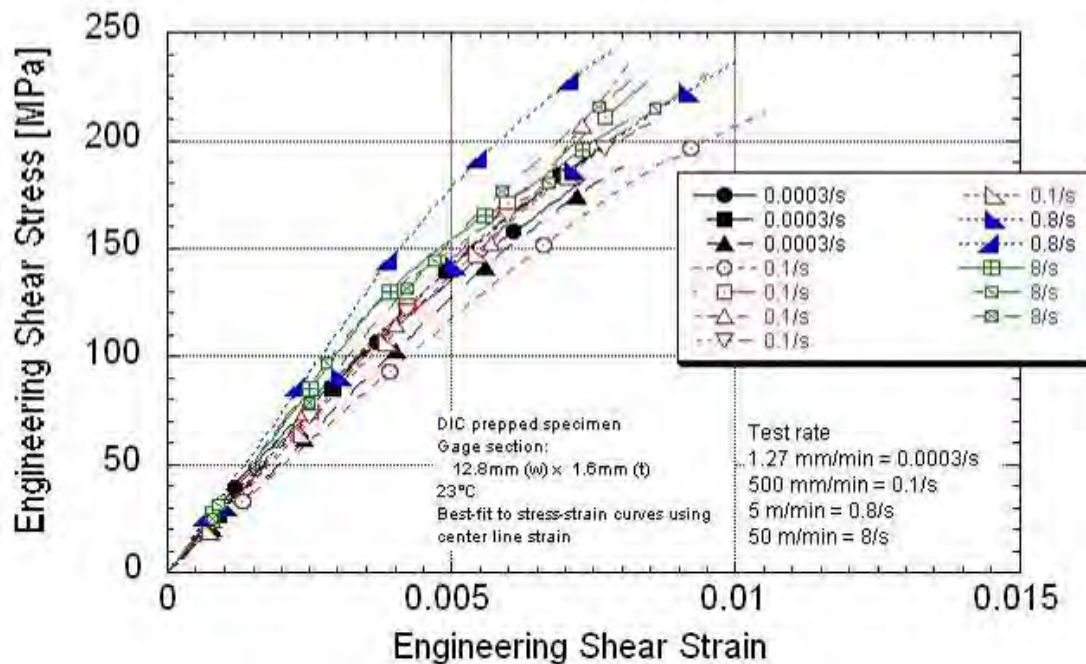


Figure 67. Transverse Shear Stress-Strain Response of 2D3A Across Tested Rates

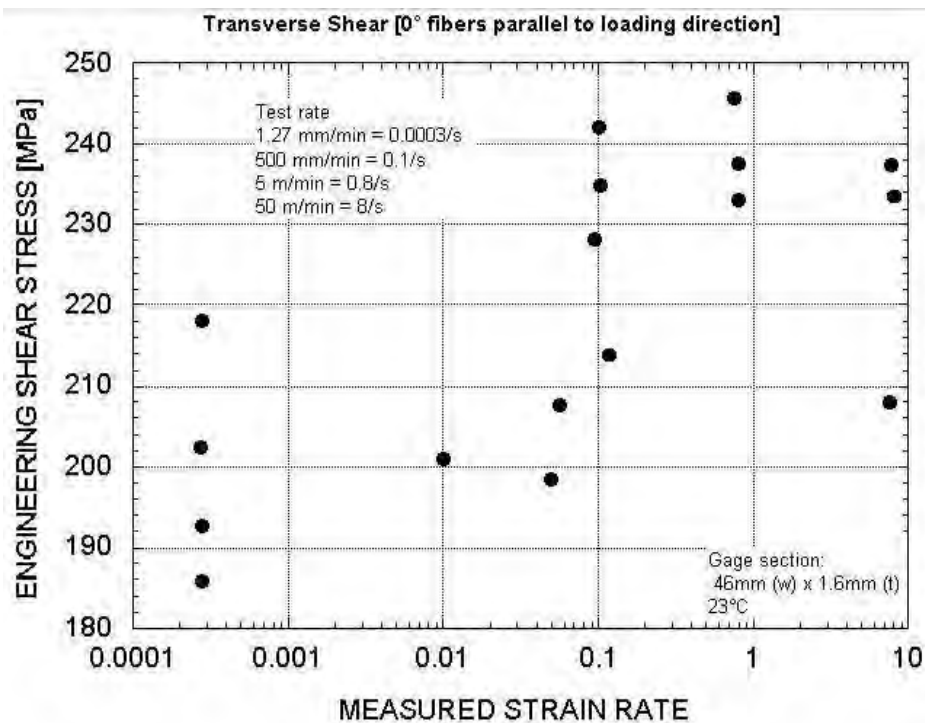


Figure 68. Transverse Shear Strength of 2D3A Across Tested Rates

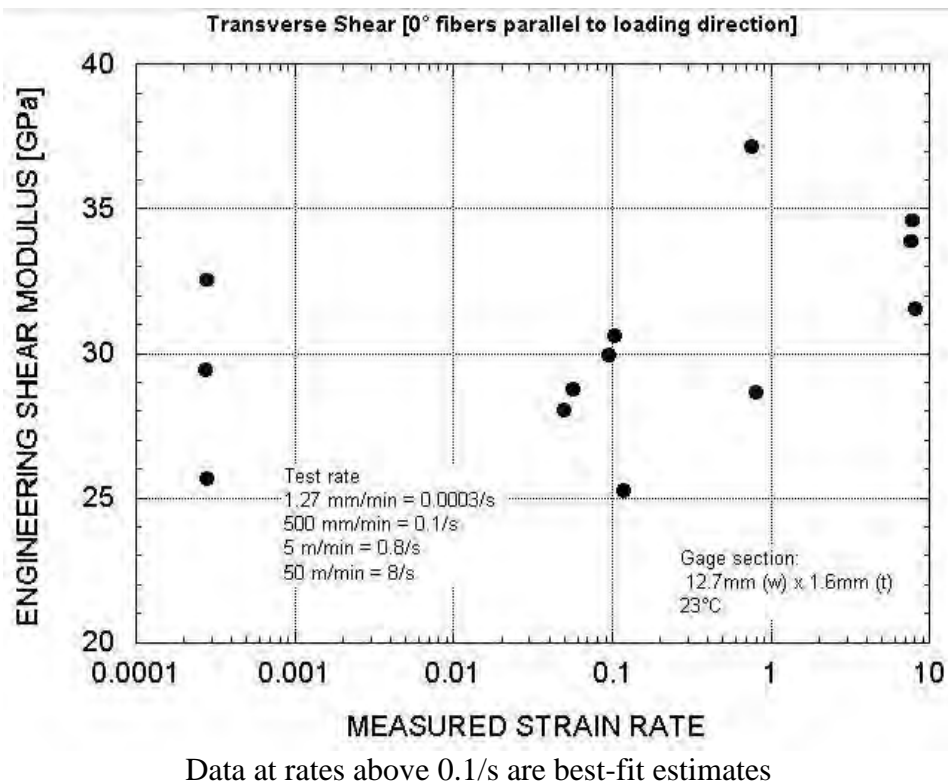


Figure 69. Transverse Shear Modulus of 2D3A Across Tested Rates

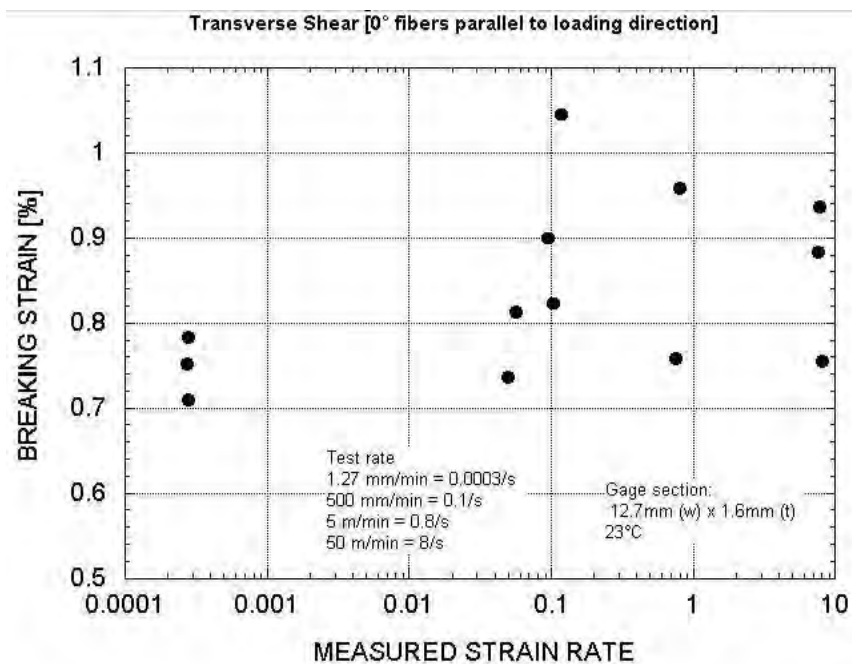


Figure 70. Transverse Shear Failure Strain of 2D3A Across Tested Rates

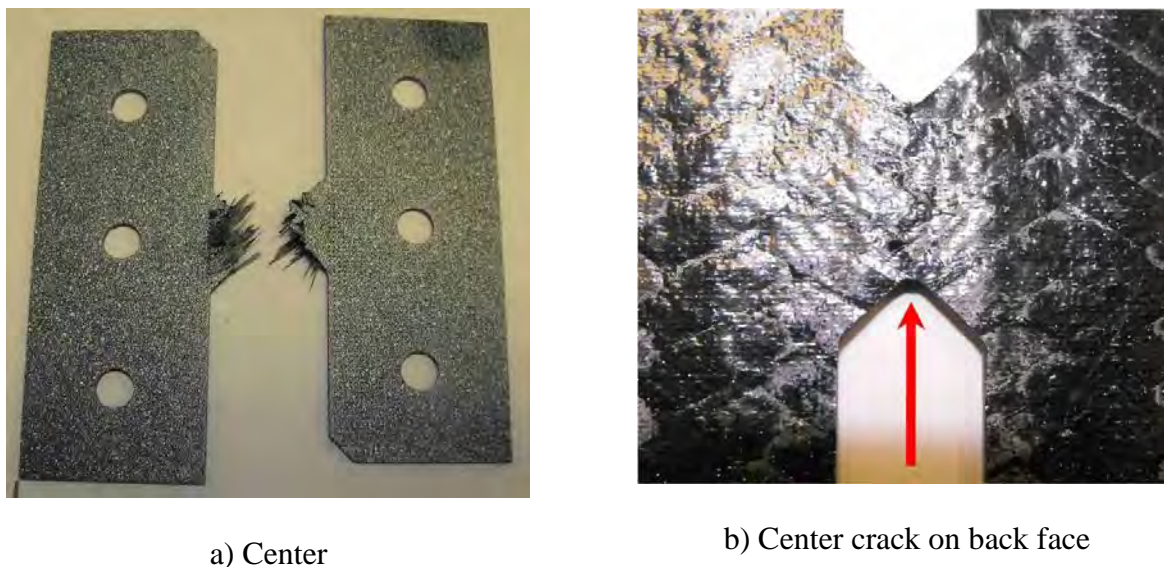


Figure 71. Typical Transverse Shear Failure Locations

8.5.3 Comparison of Axial and Transverse Shear

The mechanical properties are shown in Figures 72 to 74. The transverse shear strength is significantly higher than the axial shear strength (Figure 72). Differences in the modulus due to orientation are hard to identify (Figure 73). The axial and transverse failure strains are equivalent (Figure 74).

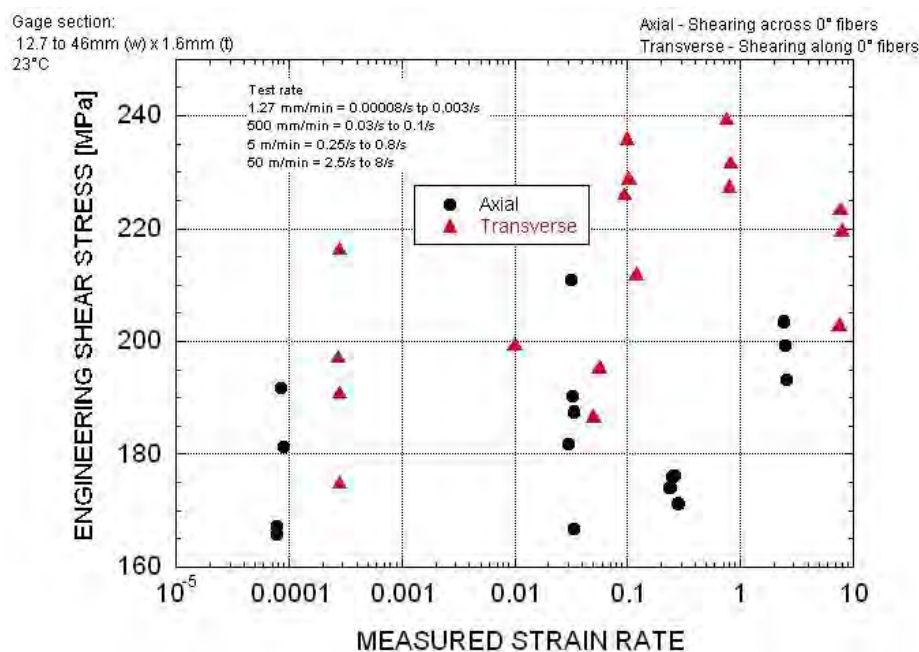


Figure 72. 2D3A Shear Strength as a Function of Strain Rate

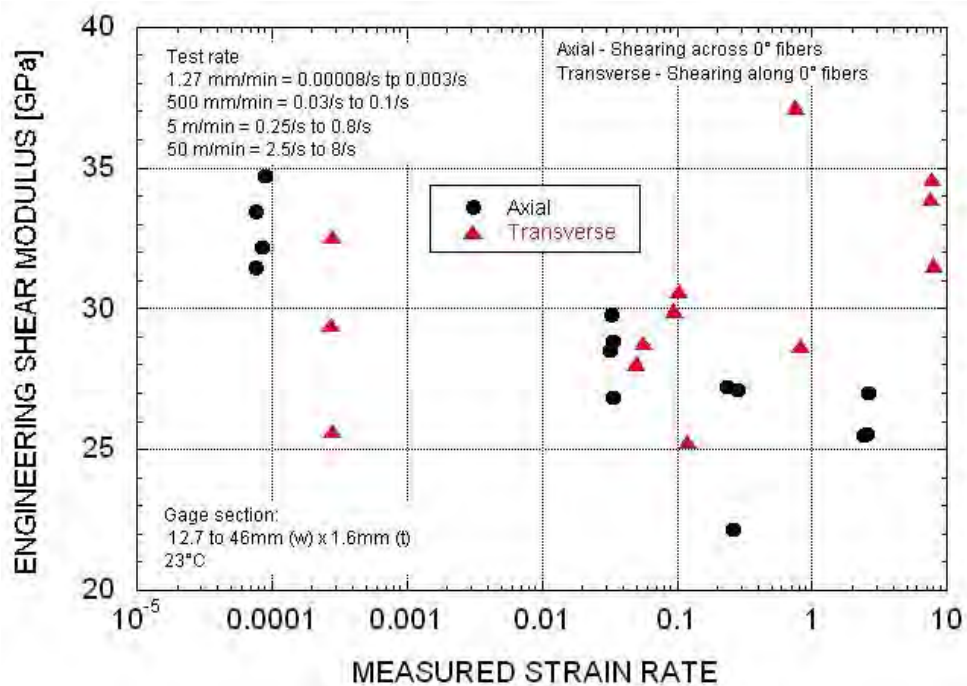


Figure 73. 2D3A Shear Modulus as a Function of Strain Rate

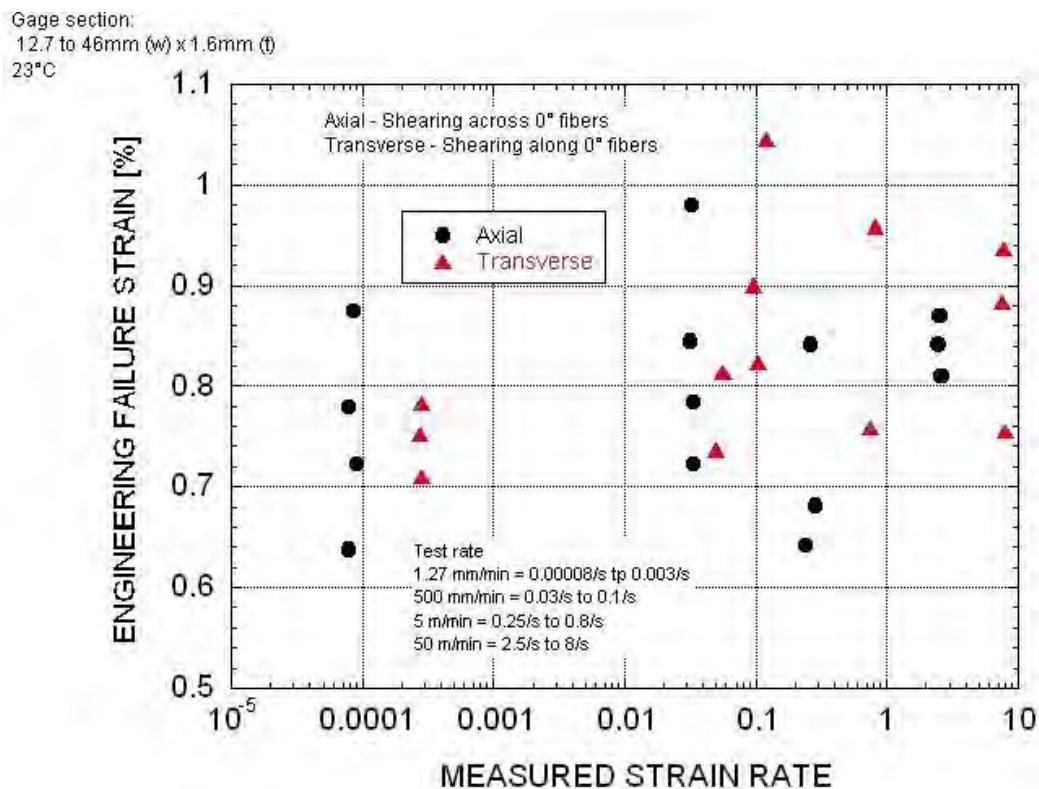


Figure 74. 2D3A Shear Failure Strain as a Function of Strain Rate

8.6 Compression Tube Tests

The flat ended tube exceeded the SME actuator capacity (98 kN). All subsequent tests were performed on tubes which had a single 45° angle cut on one end.

A typical low and high rate output curve is shown in Figure 75. The initial peak data can vary depending on the initial contact of the tube and the platen and the test speed. The slight variations can result in large differences in the measured peak. In addition, the initial load into the specimen is similar to an impulse load into the material and the first peak has a higher amplitude than all subsequent stress waves. The impulse load triggers resonant waves in the system and into the material. The high initial peaks are circled in Figure 75b. These waves cannot be avoided at the upper rates.

Figure 75b also shows the magnitude of the rebound of the platen at 440 m/min [7.4 m/s]. The load drops to zero after the initial impact. The platen is driven forward by the actuator and the platen continues to crush the tube.

All of the specimens exhibited a progressive crush. However, the failure modes varied. The low rate specimens failed in a combination of fan-folding and subsequent axial tearing of the sides with the torn sides (fronds) extending outward (Figure 76). The higher rate specimens had the outside layer folded over the outside of the tube. The next two layers were not able to fold over the first layer and tore along the axis in sections. The fronds either folded on the outside or into the middle of the tube (Figure 77).

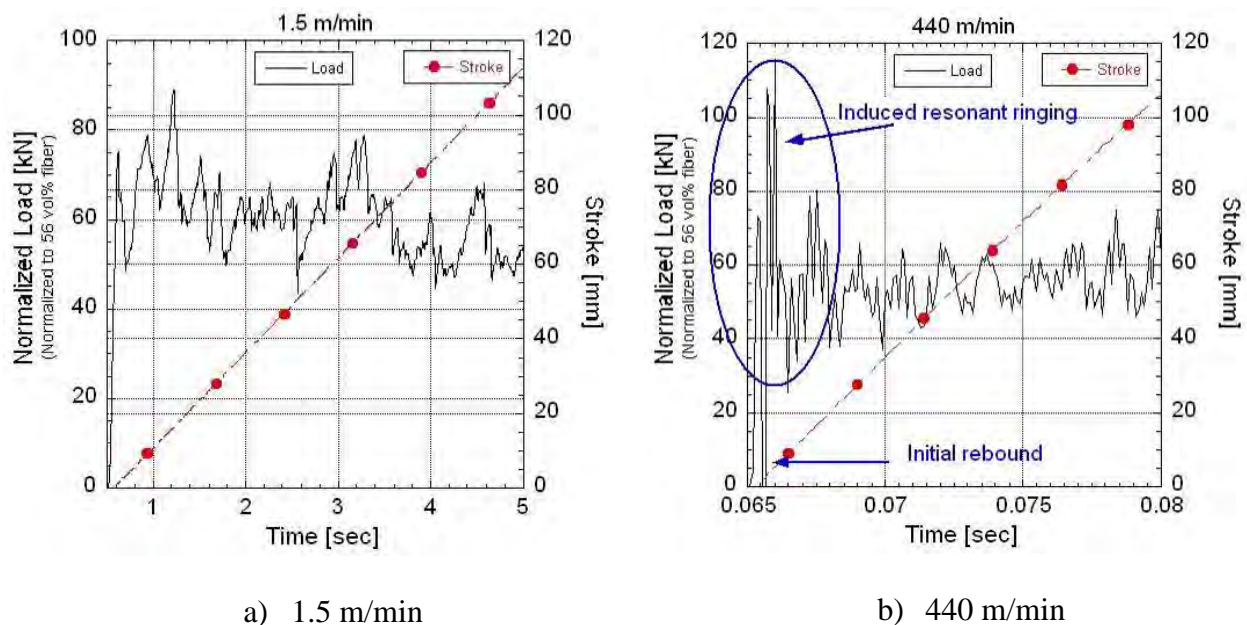


Figure 75. Typical Tube Crush Load-Displacement Curves at a Slow and Fast Rate



a) Fan folds



b) Fan folding and tearing

Figure 76. Low Rate Tube Failure



a) Side view with folded over braid

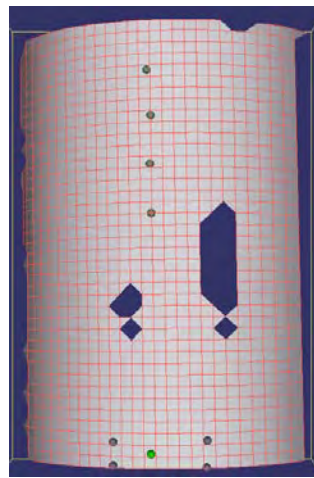


b) End view

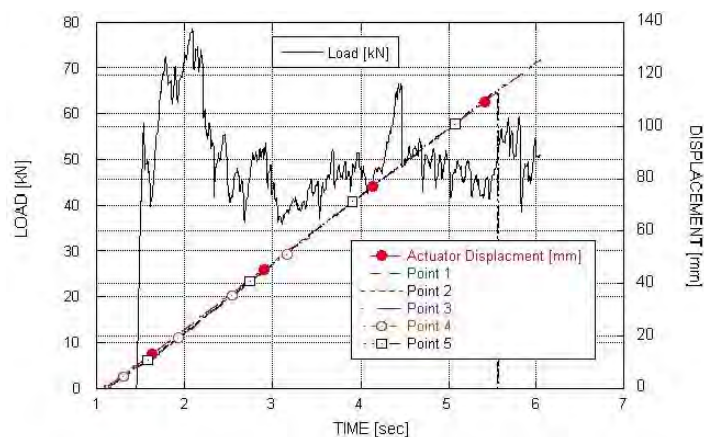
Figure 77. High Rate Tube Failure

Comparison of the data across the test rates had to consider the differences in the initial part of the curve and the failure mode. The displacements were zeroed at a load level of 40 kN for ease of comparison across the rates and the test systems.

The displacement of various sections along the tube was measured at 1.5 m/min using the SEM DIC. Oftentimes the DIC data were not valid because of material debris in the film image or the compressed tube material covering up the DIC markers. Figure 78 shows an example of the points tracked by the DIC and the comparison to the actuator stroke. The measured point displacements were equivalent to the actuator stroke after the initial ~15 mm of crush. This portion of the displacement was over the region of initial impact and induced resonant ringing at the higher rates. Any comparison of average crush data across the tested rates would have to exclude this section of the curve. Therefore, the actuator displacement was considered to be representative of the tube displacement.



a) DIC Tube Image



b) Comparison of Point and Actuator Displacement

Figure 78. Polygon Regions Tracked by the DIC and Comparison of the Measured Displacements to the Actuator Displacement

8.6.1 Tube Compression Strength

As mentioned in Section 7.4, the characteristics of the tube crush can be analyzed using various equations. The data for this program were compared using the SEA (Eq. 5), the SSCS (Eq. 6), and the CCR (Eq. 7). The median stress response was used for SSCS and CCR to minimize the resonant wave contribution. The CCR equation used the median stress normalized to 56% fiber volume for direct comparison to the normalized coupon compressive stress.

The crush behavior was well established within the first 20 to 30 mm of zeroed displacement at all of the rates, as seen in Figure 79. An arbitrary level of 25 mm was used as the start point for the median crush strength. A common endpoint of 115 mm of zeroed displacement was used for δ_2 because this value was reached at all of the rates.

Table 21 summarizes the results for the tube crush. A detailed summary table is in Appendix Q along with plots for each rate.

The SSCS and CCR were equivalent at 1.5 m/min and 140 m/min. The SSCS and CCR decreased by a factor of 0.88 to 0.91 between 140 and 440 m/min.

The SEA used for design purposes was equivalent at 1.5 m/min and 140 m/min. It was lower by a factor of 0.91 at 440 m/min (Figure 80). The SEA calculated under the assumption that the crush zone was equivalent to the actuator displacement (Eq. 5a) had similar results; i.e. equivalency at 1.5 and 140 m/min with a reduction by a factor of 0.93 by 440 m/min. However, the SEA at 1.5 m/min calculated via Eq 5b (considering the total deformation with the folds) is much lower than via Eq. 5a. This indicates that the fold length must be incorporated into the SEA calculation.

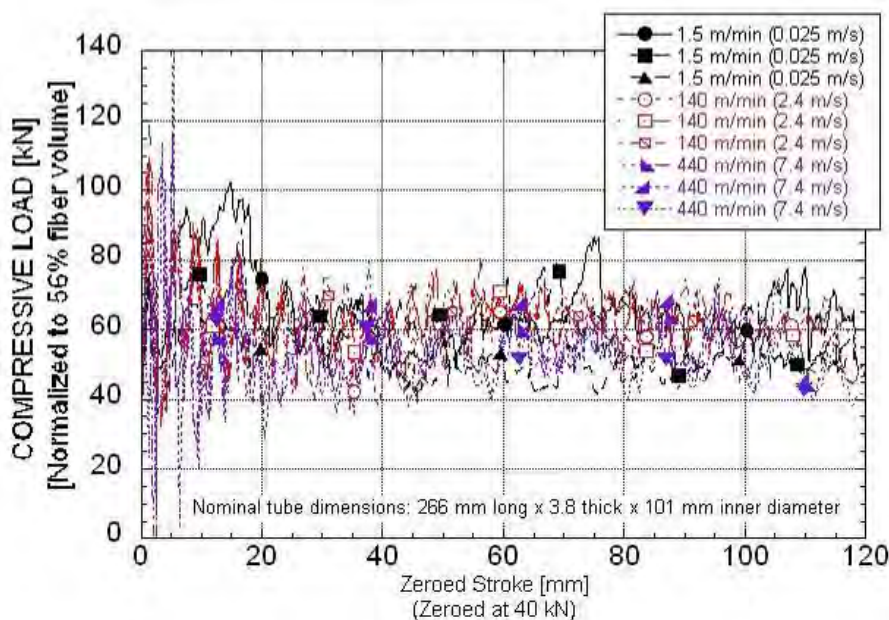


Figure 79. Load-Displacement Curves Across the Tested Rates

Table 21. Compression Tube Strength and Peak Temperatures

		Median Crush Load* [kN]	Median Crush Stress* [MPa]	Median Stress Normalized to 56% Fiber Volume [MPa]	Specific Sustained Crushing Stress [SSCS] [MPa]	Crush Compression Ratio**	Specific Energy Absorption ⁽¹⁾ with folding mode failure [SEA-FM] [kJ/kg]	Specific Energy Absorption ⁽²⁾ [SEA] [kJ/kg]	Specific Energy Absorption ⁽³⁾ [SEA] [kJ/kg ²]	Range of Peak Temperatures During Crush [°C]
1.5 m/min 0.0254 m/s	Average	47.0	74.9	95.8	51.5	0.35	43.3	53.3	19.9	-
	Std.Dev.	3.66	5.79	9.61	4.29	0.04	2.96	4.56	2.00	-
	Coeff. of Var. [%]	7.78	7.74	10.0	8.32	10.0	6.84	8.56	10.0	-
140 m/min 2.4 m/s	Average	47.8	77.1	97.4	53.2	0.36	-	52.5	20.9	173-362
	Std.Dev.	2.14	3.44	4.55	2.01	0.02	-	2.30	0.81	
	Coeff. of Var. [%]	4.48	4.46	4.67	3.77	4.67	-	4.37	3.89	
440 m/min 7.4 m/s	Average	43.3	69.2	85.8	47.8	0.32	-	48.9	19.0	254-308
	Std.Dev.	2.35	3.24	3.77	1.95	0.01	-	1.95	0.94	
	Coeff. of Var. [%]	5.43	4.69	4.39	4.08	4.39	-	3.98	4.96	

1) SEA calculated using $E_s = \text{Work}/(\text{area} \times \text{density})[\text{actuator displacement} + \text{displacement of folded length}]$

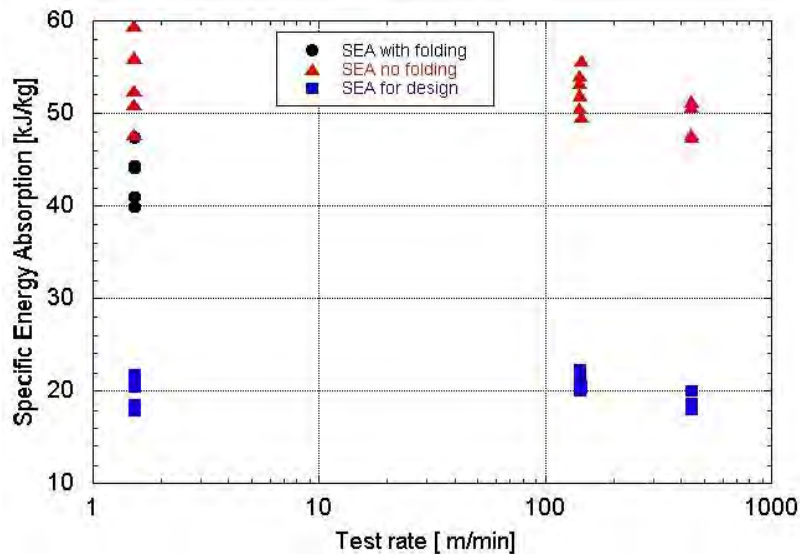
2) SEA calculated using $E_s = \text{Work}/(\text{area} \times \text{density})[\text{total actuator displacement}]$

3) SEA for design purposes $E_s = \text{Work}(\text{displacement at peak} - \text{displacement at end})/(\text{mass of tube} \times \text{displacement at end})$

The peak temperatures exceeded the calibration curve maximum of 200°C for all but one of the specimens.

A comparison of the SEA values using both Eq 5b at 1.5 m/min and Eq 5a at the two upper rates does not show a clear trend (Figure 80). The SEA for design purposes incorporated the fold length into the calculations and the trend tracks the trends seen in the SSCS and CCR. There is no clear consensus regarding the rate effects on carbon braid composites [35], although many report rate insensitivity at lower rates and a slight decrease with increasing rate. These tube results fall into this category.

A single tube with a flat end was tested at 2.4 m/s. The data were similar to the data for tubes which had the bevel crack initiator.

**Figure 80. SEA Across Tested Rates**

8.6.2 Tube Compression Strain

Strain data taken at discrete points along the length of the tube had a large amount of uncertainty. Strain data for a polygon taken ~130 mm from the top end of the tube is graphed in Figure 81. The peak of the stress-strain curve reflects the contribution of the high amplitude stress waves. The sustained crush strength was about one-quarter of that for the coupon data [~ 75 MPa vs 270 MPa] and the failure strain ranged from 0.4% to 0.8% compared to 0.9% for the coupons. The uncertainty level was fairly high (6 to 10%) but the shape of the tube compressive stress-strain curve was similar to the lower stiffness coupon data (Figure 82).

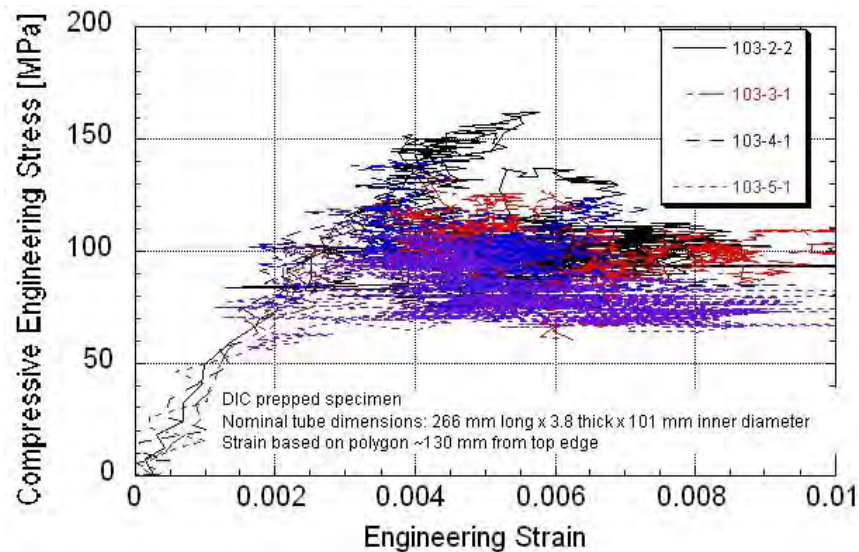


Figure 81. Tube Compressive Stress-Strain at 1.5 m/min

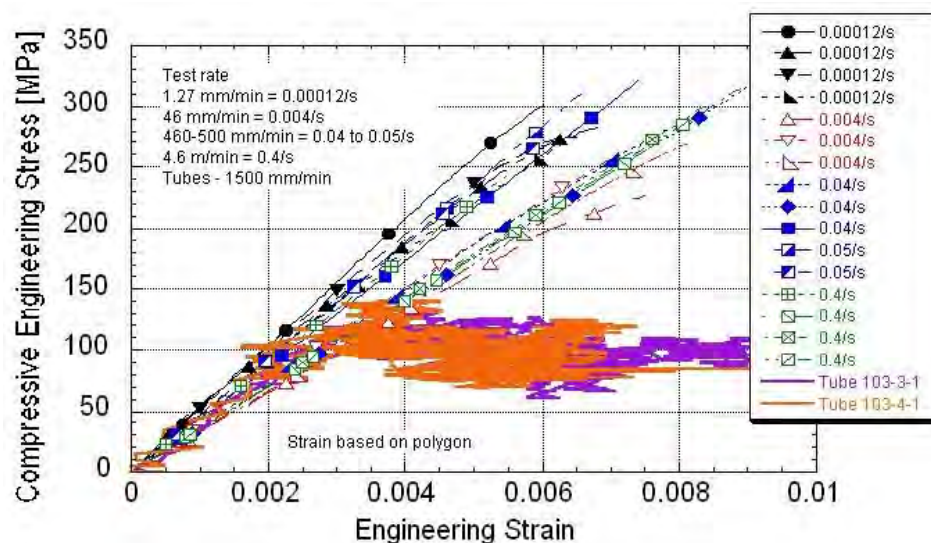


Figure 82. Comparison of Tube and Coupon Compressive Stress-Strain

8.6.3 Tube Temperatures

The peak temperatures exceeded the IR calibration curve maximum of 200°C for all but one of the specimens (STL103-7-2). Temperatures above 200°C were beyond the calibrated range. These data may be used for qualitative comparisons but should be used with extreme caution as absolute figures since they are extrapolated often well beyond the valid calibration range. The peak temperature given in Table 21 reflects the average peak temperature during the actual crush event.

Figure 83 shows the changing temperature as the test progressed in time over the region of the crush event. The actuator movement was complete within 0.05 seconds at 2.4 m/s and 0.02 seconds at 7.4 m/s, but the temperature continued to increase. The onset of the temperature rise was shifted to coincide with the load introduction as much as possible. The two data sets were not synchronized during the test.

The specimens run at 2.4 m/s showed a slower temperature rise than those at 7.4 m/s, as one would expect. The average peak temperature during the crush was ~270°C for both rates.

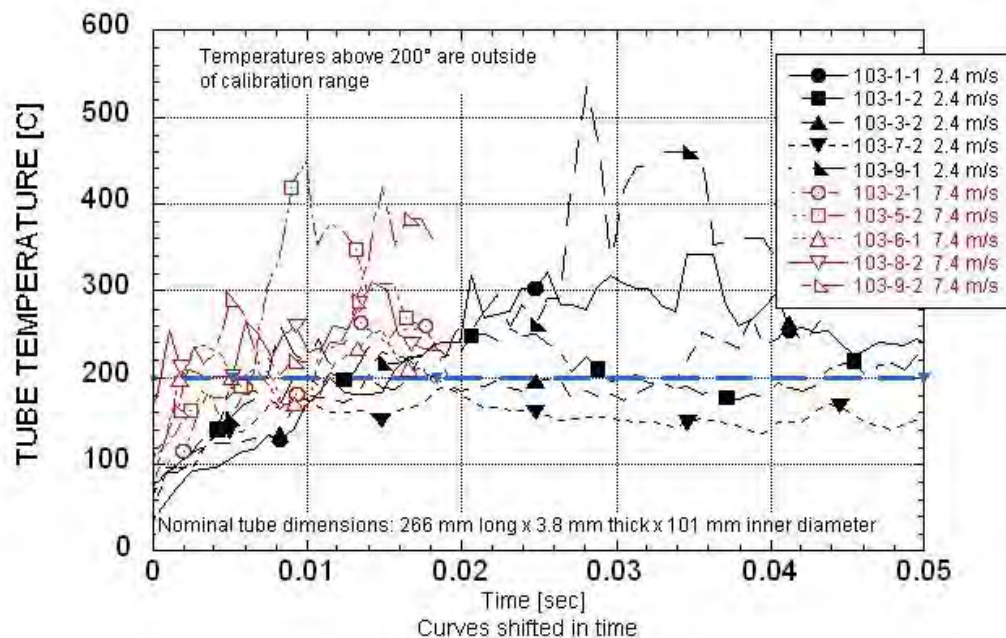


Figure 83. Composite Tube Temperatures During Crush

9.0 OVERALL SUMMARY

9.1 Material Selection and High Rate Specimen Designs

Two-dimensional triaxial carbon braid (2D3A) was selected for study after a review of the literature and consultation with technical experts. The $0^\circ/\pm 60^\circ$ braid was in-plane isotropic. The braid offered a method of providing off-axis strength and post-impact integrity in a form that would be suitable for an automotive structural component.

Composite panels and tubes were fabricated using Toray T700s C 12000 carbon fiber and Epon 862W epoxy resin. Each panel and tube contained three layers of the braid. The average fiber volume of the panels and braid were 57.2% and 44.4%, respectively.

Tension, compression, and shear mechanical properties were generated at test rates up to 50 m/min (0.8 m/sec). High rate specimens and fixtures were designed with the following requirements: a minimum of 2.5 unit cells in the test section, minimal specimen length, minimal fixture weight, and a failure load below 98 kN. The relevant quasi-static and high rate standards and recommended procedures were reviewed.

The final high rate specimens used the sizes in the standards as a guideline. The various fixture designs were able to transfer the loads into the specimens. Grip marks were evident in the tab region, which was indicative of shear loading through the tabs. The amount of load transferred through the bolts was not determined. No deformation was noted in the bolt holes.

Some resonant ringing was noted in the load response at the upper rates (~50 m/min). These data could be improved through fixture redesign, such as weight reduction and minimizing the number of bolts. Generating useable data at even faster rates would require a specimen redesign. The major contributor to the current specimen design was the decision to include 2.5 unit cells within the test section. Minimizing the test gage width would reduce the specimen length, failure loads, fixture length, and fixture weight. All of these factors combined would raise the natural system resonant frequency and improve the data quality at rates above 50 m/min.

The measured peak strengths had relatively low levels of variability (3 to 7%) compared to the modulus and failure strains (10% and higher). Future tests should include a minimum of five replicates per condition in order to identify statistically significant changes due to rate.

9.2 Comparison of Tensile Data Using the ASTM D 3039 and Bowtie Configuration

The high rate tensile specimen was a bowtie design. Data were generated at quasi-static rates for comparison to standard ASMT D 3039 tensile data. The bowtie axial tensile strength was similar to the data using the D 3039 specimen, but the stiffness was higher and the failure strain lower. The transverse tensile strength was almost three times higher than the D 3039 data. The D 3039 failure strain was lower, probably because of cracks initiated at the edge. The bowtie transverse stiffness varied, depending on the amount of axial fiber tows in the cross section.

The major difference between the specimen designs was the amount of fiber tows gripped in the fixture. The bowtie specimen gripped all of the axial and bias fiber tows which ran through the center gage section. The D 3039 gripped a limited number of bias and axial tows, especially in the transverse orientation. In addition, the D 3039 long gage section had many cut fiber tows along the edge which could act as crack initiation sites. The bow tie configuration had a central notch. Cracks initiated at this location, but they were blunted within 0.5 unit cells from the notch.

9.3 High Rate Coupon Mechanical Properties

9.3.1 Tensile

The bowtie axial tensile strength was 778 ± 50 MPa and the failure strain was $1.33 \pm 0.13\%$. The strength was rate insensitive. The failure strain had a negative trend with increasing rate, but it was not statistically significant due to the high variability. The stiffness increased with rate and was 25% higher at 2/s compared to 0.00009/s (82 GPa versus 67 GPa).

The bowtie transverse tensile strength and failure strain were significantly higher than the axial (979 ± 45 MPa and $2.01 \pm 0.49\%$). Both were rate insensitive. The modulus had a high amount of variability thought to be due to the relative amount of axial fibers in the center gage section. The transverse modulus was of similar magnitude as the axial modulus, but it ranged from 58 to 116 GPa.

9.3.2 Compression

The axial compression strength was 270 ± 25 MPa. It was rate insensitive. The stress-strain response exhibited two distinct groups in the behavior. The dogbone-shaped specimens tended to have a higher modulus and shorter failure strain. However, some of the straight-sided specimens also fell within this grouping. The difference may be due to the onset of buckling of the axial tows. The stiffness and failure strain were insensitive to rate within a given group.

The transverse compression strength exhibited a trend of increasing strength with rate but it was not statistically significant. A positive trend is expected since the compressive loads are loading bias fibers and resin rather than the axial fibers. The rate sensitivity of the epoxy should be reflected in the transverse compressive response. The overall strength was 259 ± 30 MPa, which was equivalent to the axial strength.

The transverse compressive modulus increased 13% between 0.04/s and 0.4/s (39.6 to 45 GPa). The failure strain had a large amount of variability. It had a decreasing trend with increasing rate but the trend was not statistically significant. The overall failure strain was $0.74 \pm 0.09\%$. The transverse modulus and failure strain were similar to the axial.

9.3.3 Shear

A discrete number of resonant stress waves (4 to 7) were present at the upper test rate of 50 m/min. Specimen and fixture redesign would improve the dynamic equilibrium and data quality at this rate.

The axial shear strength increased 13% between 0.0008/s to 2.5/s from 176 MPa to 198 MPa. The shear modulus was rate insensitive. The apparent decrease in axial modulus is thought

to be due to an artifact of the smoothing function used in the data analysis. The axial shear failure strain was $0.79 \pm 0.1\%$ and was rate insensitive.

The transverse shear strength increased 10% with each decade increase above 0.05/s. The shear modulus had a positive trend with rate. It increased 15% between the two bottom and two top rates, from 28.8 GPa at 0.0003/s to 33.1 GPa at 8/s. Once again, the variability within rates made it difficult to quantify the increase per decade. The transverse shear strain was $0.84 \pm 0.1\%$ and was rate insensitive.

The transverse shear strength was at least 13% higher than the axial shear strength at all rates. The failure strains were equivalent for both orientations.

9.4 Tube Compression

Carbon fiber 2D3A tubes were compressed at rates up to 440 m/min (7.4 m/s). The crush behavior was well established within 25 mm of the zeroed displacement. There was rate insensitivity between 1.5 m/min and 140 m/min. There was a slight decrease in the specific sustained crushing stress (SSCS), crush compression ratio (CCR), and the specific energy absorption (SEA) by a factor of 0.9 between 140 m/min and 440 m/min.

The sustained crush strength was about one-quarter of that for the coupon data [~ 75 MPa vs 270 MPa] and the failure strain ranged from 0.4% to 0.8% compared to 0.9% for the coupons. The uncertainty level was fairly high (6 to 10%) but the shape of the tube compressive stress-strain curve was similar to the lower stiffness coupon data. The average peak tube temperature during the crush was $\sim 270^\circ\text{C}$ at both rates.

10.0 RECOMMENDATIONS

The overall specimen size and thickness was dictated by the requirements for generating valid data at higher rates. The optimum gage width, determined through sensitivity studies, would help to optimize the fixture design. The combination of proper specimen size and fixture design will help to generate valid data at higher rates.

A minimum of five replicates per test condition is recommended to identify significant variations due to rate. In addition, the contribution of panel-to-panel variations and fiber tow alignment through the thickness were confounded in the data. A sensitivity study would be needed to establish these effects on the measured properties using the various specimen configurations.

The fiber tow locations through the thickness may have contributed to the variations in the measured material stiffness using the bowtie and V-notch design. Use of additional layers would help to homogenize the response. However, additional layers would increase the peak loads, which may limit the maximum test speeds. An optimized specimen width may reduce the peak loads. One could also use a different number of layers for the different orientations and tests. A&P Technologies has developed a tacking agent which helps to maintain fiber tow

alignment during processing. This would help to identify the contribution of tow location to the measured material response using the bowtie or V-notched specimens.

11.0 REFERENCES

1. Handbook of Composites, Lubin, G., editor, Society of Plastics Engineers Technical Monograph, Van Nostrand Reinhold Co., Inc., New York, 1982.
2. ASM Handbook Volume 21 Composites, ASM International, Material Park, OH, 2001.
3. Ganster, J., Fink, H. and Pinnow, M., “High-Tenacity Man-made Cellulose Fibre Reinforced Thermoplastics – Injection Moulding Compounds with Polypropylene and Alternative Matrices,” *Composites Part A*, **37**, 2006, 1796-1804.
4. Lee, B., Kim, H. and Yu, W., “Fabrication of Long and Discontinuous Natural Fiber Reinforced Polypropylene Biocomposites and their Mechanical Properties,” *Fibers and Polymers*, **10**, 2009, 83-90.
5. Ashori, A. and Nourbakhsh, A., “Mechanical Behavior of Agro-Residue-Reinforced Polypropylene Composites,” *J. of Applied Polymer Science*, **111**, 2009, 2616-2620.
6. Torayca® T700S Technical Data Sheet No. CFA-005, Toray Carbon Fibers America, Inc.
7. <http://www.matbase.com/material/fibres/glass/e-glass-fibre/properties>.
8. Materials, Design and Manufacturing for Lightweight Vehicles, Mallick, P. K., Editor, Woodhead Publishing in Materials Series, Woodhead Publishing Limited, 2010.
9. Thomason, J.L., “The Influence of Fibre Length and Concentration on the Properties of Glass Fibre Reinforced Polypropylene. 6. The Properties of Injection Moulded Long Fibre PP at High Fibre Content,” *Composites Part A*, **36**, 2005, 995-1003.
10. Short, W. T. and E. J. Wenzel, “Effects of Molding Process on Residual Fiber Length of Long Fiber Polypropylene Composites,” Paper 0082, Society of Plastics Engineers - 65th Annual Technical Conference of the Society of Plastics Engineers, Plastics Encounter at ANTEC 2007, Mar 6-11, 2007, Cincinnati, OH.
11. Bowman, C. L., Roberts, G. D., Braley, M. S., Xie, M., and Booker, M. J., “Mechanical Properties of Triaxial Braided Carbon/Epoxy Composites,” NASA TM—2002-211702, June 2002.
12. Littell, J. D., Binienda, W. K., Roberts, G. D. and Goldberg, R., “Characterization of Damage in Triaxial Braided Composites Under Tensile Loading,” *Journal of Aerospace Engineering*, **22**, 2009, 270-279.

13. Littell, J. D., "The Experimental and Analytical Characterization of the Macromechanical Response for Triaxial Braided Composite Materials," Ph.D Dissertation, U of Akron, 2008.
14. Roberts, G. D., et. al, "Characterization of Triaxial Braided Composite Material Properties for Impact Simulation" NASA TM-2009-215660, 2009.
15. Chiu, C. H., Tsai, K.-H., Huang, W. J., "Crush Failure Modes of 2D Triaxially Braided Hybrid Composite Tubes," *Composites Science and Technology*, **59**, 1999, 1713-1723.
16. Beard, S., and Chang, F-K., "Design of Braided Composites for Energy Absorption," *J. of Thermoplastic Composite Materials*, **15**, 2002, 3-10.
17. McGregor, C., Vaziri, R., and Xiao, X., "Finite Element Modeling of the Progressive Crushing of Braided Composite Tubes Under Axial Impact," *International Journal of Impact Engineering*, **37**, 2010, 662-672.
18. ASTM International, 100 Bar Harbor Drive, West Conshohocken, PA, www.astm.org.
19. SAE J2749, "Surface Vehicle Recommended Practice - High Strain Rate Tensile Testing of Polymers," SAE International, 400 Commonwealth Drive, Warrendale, PA 15096, www.sae.org.
20. SEP 1230, "The Determination of the Mechanical Properties of Sheet Metal at High Strain Rates in High-Speed Tensile Tests," STAHL-EISEN-Prüfblätter (SEP) des Stahlinstituts VDEh, Verlag Stahleisen GmbH, Postfach 10 51 64, 40042 Düsseldorf, Germany.
21. Pinnell, M., Hill, S. and Minch, A., "Special Concerns in High Strain Rate Tensile Testing of Polymers," SAE 2006 Transactions Journal of Materials and Manufacturing V115-5, April 3-6, 2006, Detroit, Michigan.
22. Eskandari, H., and J. A. Nemes, "Dynamic Testing of Composite Laminates with a Tensile Split Hopkinson Bar," *J. Composite Mater.*, **34**, 2000, 260-73.
23. Fitoussi, J., *et al.*, "Experimental Methodology for High Strain-Rates Tensile Behaviour Analysis of Polymer Matrix Composites," *Composites Science and Technology*, **65**, 2005, 2174-88.
24. Harding, J., and L. M. Welsh, "A Tensile Testing Technique for Fibre-Reinforced Composites at Impact Rates of Strain," *Journal of Materials Science*, **18**, 1983, 1810-26.
25. Rong, Jian, et al., "Tensile Impact Behavior of Multiaxial Multilayer Warp Knitted (MMWK) Fabric Reinforced Composites," *Journal of Reinforced Plastics and Composites*, **25**, 2006, 1305-15.
26. Zairi, F., et al., "Micromechanical Modelling and Simulation of Chopped Random Fiber Reinforced Polymer Composites with Progressive Debonding Damage," *International Journal of Solids and Structures*, **45**, 2008, 5220-36.

27. Kim, R. Y., Crasto, A. S., “Longitudinal Compression Strength of Glass Fiber-Reinforced Composites,” *J. of Reinforced Plastics and Composites*, **12**, 1994, 326-338.
28. Kim, R. Y., Crasto, A. S., “A Longitudinal Compression Test for Composites Using a Sandwich Specimen,” *J. of Composite Materials*, **26**, 1915-1929.
29. Masters, J. E., “Compression Testing of Textile Composite Materials,” NASA Contractor Report 198285, 1996.
30. Adams, D., O., Moriarty, J. M., Gallegos, A. M., and Adams, D. F., “Development and Evaluation of the V-Notched Rail Shear Test for Composite laminates,” Report No. DOT/FAA/AR-03/62, U. S. Department of Transportation, Federal Aviation Administration, September 2003.
31. Wang, Y. H., Jiang, J. H., Wanintrudal, C., et. al., “Whole Field Sheet-metal Tensile Test Using Digital Image Correlation,” *Experimental Techniques*, March/April 2000, 54-62.
32. Sutton, M., Orteu, J-J., Schreirr, H., Image Correlation for Shape, Motion and Deformation Measurements, Springer Publishing, 2009.
33. Sutton, M., et al., “Advances in Two-dimensional and Three-Dimensional Computer Vision,” *Photomechanics, Topics Applied Physics*, **77**, 2000, 323-372.
34. “Basics of 3D Digital Image Correlation,” Dantec Dynamics Application Note – T-Q-400-Basics 3DCORR-002a-EN.”
35. M. A. Courteau, Adams, D. O., “Composite Tube Testing for Crashworthiness Applications: A Review,” *J. of Advanced Materials*, **43**, 2011, 13 – 34.
36. Zhou, Y., Wang, Y., Jeelani, S., and Xia, Y., “Tensile Behavior of Carbon Fiber Bundles at Different Strain Rates,” *Materials Letters*, **64**, 2010, 246-248.
37. Chen, W. and Zhou, B., “Constitutive Behavior of Epon 828/T-403 at Various Strain Rates,” *Mechanics of Time-Dependent Materials*, **2**, 1998, 103-111.

APPENDIX A
MATERIAL PRODUCT SHEETS

CARBON FIBER

**TECHNICAL
DATA SHEET**
No. CFA-005

TORAYCA® T700S DATA SHEET

Highest strength, standard modulus fiber available with excellent processing characteristics for filament winding and prepreg. This never twisted fiber is used in high tensile applications like pressure vessels, recreational, and industrial.

FIBER PROPERTIES

	<i>English</i>	<i>Metric</i>	<i>Test Method</i>
Tensile Strength	711 ksi	4,900 MPa	TY-030B-01
Tensile Modulus	33.4 Msi	230 GPa	TY-030B-01
Strain	2.1 %	2.1 %	TY-030B-01
Density	0.065 lbs/in ³	1.80 g/cm ³	TY-030B-02
Filament Diameter	2.8E-04 in.	7 µm	
Yield			
6K	3,724 ft/lbs	400 g/1000m	TY-030B-03
12K	1,862 ft/lbs	800 g/1000m	TY-030B-03
24K	903 ft/lbs	1,650 g/1000m	TY-030B-03
Sizing Type	50C	1.0 %	TY-030B-05
& Amount	60E	0.3 %	TY-030B-05
	FOE	0.7 %	TY-030B-05
Twist	Never twisted		

FUNCTIONAL PROPERTIES

CTE	-0.38 $\alpha \cdot 10^{-6}/^{\circ}\text{C}$
Specific Heat	0.18 Cal/g $\cdot^{\circ}\text{C}$
Thermal Conductivity	0.0224 Cal/cm $\cdot\text{s}\cdot^{\circ}\text{C}$
Electric Resistivity	1.6 $\times 10^{-3} \Omega\cdot\text{cm}$
Chemical Composition: Carbon	93 %
Na + K	<50 ppm

COMPOSITE PROPERTIES *

Tensile Strength	370 ksi	2,550 MPa	ASTM D-3039
Tensile Modulus	20.0 Msi	135 GPa	ASTM D-3039
Tensile Strain	1.7 %	1.7 %	ASTM D-3039
Compressive Strength	215 ksi	1,470 MPa	ASTM D-695
Flexural Strength	245 ksi	1,670 MPa	ASTM D-790
Flexural Modulus	17.5 Msi	120 GPa	ASTM D-790
ILSS	13 ksi	9 kgf/mm ²	ASTM D-2344
90° Tensile Strength	10.0 ksi	69 MPa	ASTM D-3039

* Toray 250°F Epoxy Resin. Normalized to 60% fiber volume.

TORAY CARBON FIBERS AMERICA, INC.

T700S

COMPOSITE PROPERTIES**

Tensile Strength	355 ksi	2,450 MPa	ASTM D-3039
Tensile Modulus	18.0 Msi	125 GPa	ASTM D-3039
Tensile Strain	1.7 %	1.7 %	ASTM D-3039
Compressive Strength	230 ksi	1,570 MPa	ASTM D-695
Compressive Modulus	--- Msi	--- GPa	ASTM D-695
In-Plane Shear Strength	14 ksi	98 MPa	ASTM D-3518
ILSS	15.5 ksi	11 kgf/mm ²	ASTM D-2344
90° Tensile Strength	10.0 ksi	70 MPa	ASTM D-3039

** Toray Semi-Toughened 350°F Epoxy Resin. Normalized to 60% fiber volume.

See Section 4 for Safety & Handling information. The above properties do not constitute any warranty or guarantee of values.

These values are for material selection purposes only. For applications requiring guaranteed values, contact our sales and technical team to establish a material specification document.

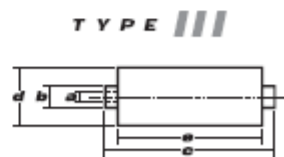
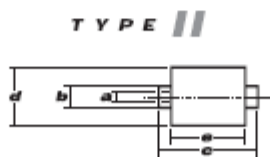
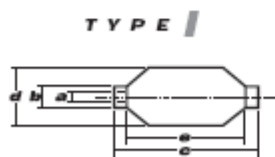
PACKAGING

The table below summarizes the tow sizes, twists, sizing types, and packaging available for standard material. Other bobbin sizes may be available on a limited basis.

Tow Sizes	Twist ¹	Sizing	Bobbin Net Weight (kg)	Bobbin Type ²	Bobbin Size (mm)					Spools per Case	Case Net Weight (kg)
					a	b	c	d	e		
6K	C	50C	2.0	III	76.5	82.5	280	140	252	12	24
	C	50C	6.0	III	76.5	82.5	280	200	252	4	24
12K	C	60E	6.0	III	76.5	82.5	280	200	252	4	24
	C	FoE	6.0	III	76.5	82.5	280	200	252	4	24
24K	C	50C	6.0	III	76.5	82.5	280	200	252	4	24
	C	60E	6.0	III	76.5	82.5	280	200	252	4	24
24K	C	60E	6.0	III	76.5	82.5	280	200	252	4	24
	C	FoE	6.0	III	76.5	82.5	280	200	252	4	24

¹ Twist A: Twisted yarn B: Untwisted yarn made from a twisted yarn through an untwisting process C: Never twisted yarn

² Bobbin Type See Diagram below



TORAY CARBON FIBERS AMERICA, INC.

6 Hutton Centre Drive, Suite #1270, Santa Ana, CA 92707 TEL: (714) 431-2320 FAX: (714) 424-0750
Sales@Toraycfa.com Technical@Toraycfa.com www.torayusa.com

RESIN EPON™ 862**Technical Data Sheet**

Re-issued March 2005

EPON™ Resin 862

Product Description

EPON™ Resin 862 (Diglycidyl Ether of Bisphenol F) is a low viscosity, liquid epoxy resin manufactured from epichlorohydrin and Bisphenol-F. This resin contains no diluents or modifiers. EPON Resin 862 may be used as the sole epoxy resin or combined with other resins such as EPON Resin 828. When blended with EPON Resin 828, EPON Resin 862 provides a technique to reduce viscosity with no sacrifice in chemical and solvent resistance properties, and the blended resin will exhibit improved crystallization resistance properties when compared to the neat, liquid, Bisphenol-A or Bisphenol-F type resins. When EPON Resin 862 is cross-linked with appropriate curing agents, superior mechanical, adhesive, electrical and chemical resistance properties can be obtained.

Application Areas/Suggested Uses

- Solventless or high solids/low VOC maintenance and marine coatings
- Chemical resistant tank linings, floorings, and grouts
- Fiber reinforced pipes, tanks, and composites
- Tooling, casting, and molding compounds
- Construction, electrical, and aerospace adhesives

Benefits

- Low viscosity
- Low color
- Reacts with a full range of epoxy curatives
- Good balance of mechanical, adhesive, and electrical properties
- Good chemical resistance
- Superior physical properties vs. diluted (6 Poise) resins

Sales Specification

Property	Units	Value	Test Method/Standard
Weight per Epoxide	g/eq	165 – 173	ASTM D1652
Viscosity at 25°C	P	25 – 45	ASTM D445
Color	Pt-Co	200 max.	ASTM D1209

Typical Properties

Property	Units	Value	Test Method/Standard
Density at 25°C	lb/gal	9.8	ASTM D1475

RESIN CURING AGENT EPIKURE™ W

Table 9 / Typical Properties of EPIKURE™ – 9000 Series & Composites

Product	Chemical Type	Gel Time @ 25°C ¹ (hours)	Viscosity @ 25°C (cP)	Color ⁷	Density (lb/gal)	Eq. Wt. ⁵	PHR ²	Comments
EPIKURE 9270	Polyamine	2.3 ³	500-1000	8	8.1	103	50 ⁴	For use in CIPP (Cured In Place Pipe) systems with EPON 9215. Offers good wetting characteristics and maintains optimal physical properties.
EPIKURE 9551	Polyamine	6	30-70	2	8.0	57-67	33	Provides excellent toughness and elongation.
EPIKURE 9553	Polyamine	0.5	<10	<1	7.2	29	15	Aliphatic amine, low viscosity, room temperature curing agent. Provides increased toughness characteristics.
EPIKURE 9554	Polyamine	~4	15-24	5	7.9	35-41	20	Provides good balance of processing and performance. Designed for use in SCRIMP-type processes.
EPIKURE W	Non-MDA Aromatic Amine	1.5 ⁴	100-350	7	8.5	42-48	24	Non-MDA aromatic amine, provides low viscosity and very long working times, with high performance properties after an elevated temperature cure.

¹ 100 gram mass² Parts by weight of curing agent per 100 parts of epoxy (EEW 190)³ 200 gram mass⁴ 3 gram mass @ 121°C⁵ Pot-life of 1 gallon mass with EPON 9215⁶ Parts by weight of curing agent per 100 parts of EPON 9215⁷ Gardner Color Scale⁸ Equivalent Weight Amount in grams required to react with one equivalent of epoxide

APPENDIX B
LAMINATE AND TUBE PHYSICAL PROPERTIES

Panel 072910-1 Laminate Physical Properties								
Submitted By:	Susan Hill		Date Submitted: 1/21/2011					
Program:	George Washington University		IFAS No. : 4238020003					
Material:	2D carbon 0/+/-60 / Epon 862 W		Panel I.D.: 072910-1					
Job No:			PI Request No:					
Fiber Density (g/cc) =	1.77	Resin Density (g/cc) =	1.2					
		No. of Plies:						
<u>Specimen Thicknesses</u>								
Spec. Number	thickness (in)							
A								
B								
C								
Avg:	#DIV/0!							
<u>Specific Gravity Determination</u>								
Tested By:								
Spec. Number	Wc (wt. in air) (x.xxxx g)	W (wt. in water) (x.xxxx g)	Md Spec. Grav. (x.xxx)					
A	1.8014	0.6296	1.532					
B	1.4928	0.5193	1.529					
C	1.3754	0.4750	1.523					
		Avg:	1.528					
<u>Laminate Physical Properties Determinations</u>								
Tested By:								
Spec. Number	Wc (spec. wt.) (x.xxxx g)	Wf (Fiber wt.) (x.xxxx g)	F.C. (Fiber cont.) (x.xx Wt.%)	R.C. (Resin Cont.) (x.xx Wt.%)	Vf (Vol. of Fibers) (x.xxxx cm3)	Vc (Vol. of Comp.) (x.xxxx cm3)	Fiber Volume (x.xx Vol.%)	Void Volume (x.xx Vol.%)
A	1.8014	1.1978	66.4927	33.51	0.6767	1.1758	57.55	-0.33
B	1.4928	0.9840	65.9164	34.08	0.5559	0.9763	56.94	-0.37
C	1.3754	0.8912	64.7957	35.20	0.5035	0.9031	55.75	-0.43
			Avg. =	34.27		Avg. =	56.75	-0.38
Wf = (Crucible & Fiber wt.) - (Crucible wt.)				F.C. = (Wf / Wc) x 100				
R.C. = 100 - F.C.				Vf = Wf / Fiber Density				
Vc = Wc / Md				Fiber Volume = (Vf / Vc) x 100				
Void Volume = 100 - Md*[(R.C. / Resin Density) + (F.C. / Fiber Density)]								

Panel 072910-2 Laminate Physical Properties								
Submitted By:	Susan Hill		Date Submitted:	2/22/2011				
Program:	George Washington University		IFAS No. :	4238020003				
Material:	2D carbon 0/+/-60 / Epon 862 W		Panel I.D.:	072910-2				
Job No:			PI Request No:					
Fiber Density (g/cc) =	1.77	Resin Density (g/cc) =	1.2	No. of Plies:				
<u>Specimen Thicknesses</u>								
Spec. Number	thickness (in)							
A	0.0612							
B	0.0645							
C	0.0630							
Avg:	0.063							
<u>Specific Gravity Determination</u>								
Tested By:								
Spec. Number	Wc (wt. in air) (x.xxxx g)	W (wt. in water) (x.xxxx g)	Md	Spec. Grav. (x.xxx)				
A	1.4292	0.0139		1.545				
B	1.4022	0.0114		1.534				
C	1.3979	0.0128		1.536				
		Avg:		1.538				
<u>Laminate Physical Properties Determinations</u>								
Tested By:								
Spec. Number	Wc (spec. wt.) (x.xxxx g)	Wf (Fiber wt.) (x.xxxx g)	F.C. (Fiber cont.) (x.xx Wt.%)	R.C. (Resin Cont.) (x.xx Wt.%)	Vf (Vol. of Fibers) (x.xxxx cm3)	Vc (Vol. of Comp.) (x.xxxx cm3)	Fiber Volume (x.xx Vol.%)	Void Volume (x.xx Vol.%)
A	1.4292	0.9816	68.6818	31.32	0.5546	0.9250	59.95	-0.27
B	1.4022	0.9572	68.2642	31.74	0.5408	0.9141	59.16	0.27
C	1.3979	0.9542	68.2595	31.74	0.5391	0.9101	59.24	0.14
			Avg. =	31.60		Avg. =	59.45	0.04
Wf = (Crucible & Fiber wt.) - (Crucible wt.)					F.C. = (Wf / Wc) x 100			
R.C. = 100 - F.C.					Vf = Wf / Fiber Density			
Vc = Wc / Md					Fiber Volume = (Vf / Vc) x 100			
Void Volume = 100 - Md*[(R.C. / Resin Density) + (F.C. / Fiber Density)]								

Panel 073010-1 Laminate Physical Properties								
Submitted By:	Susan Hill			Date Submitted:	1/10/2011			
Program:	George Washington University			IFAS No. :	4238020003			
Material:	2D carbon 0/+/-60 / Epon 862 W			Panel I.D.:	073010-1 Sample 1			
Job No:				PI Request No:				
Fiber Density (g/cc) =	1.77		Resin Density (g/cc) =	1.2		No. of Plies:		
<u>Specimen Thicknesses</u>								
Spec. Number	thickness (in)							
A	0.0622							
B	0.0660							
C								
Avg:	0.064							
<u>Specific Gravity Determination</u>								
Tested By:								
Spec. Number	Wc (wt. in air) (x.xxxx g)	W (wt. in water) (x.xxxx g)	Md Spec. Grav. (x.xxx)					
A (1)	1.3059	0.4410	1.505					
B (2)	2.0164	0.6801	1.504					
	Avg:		1.505					
<u>Laminate Physical Properties Determinations</u>								
Tested By:								
Spec. Number	Wc (spec. wt.) (x.xxxx g)	Wf (Fiber wt.) (x.xxxx g)	F.C. (Fiber cont.) (x.xx Wt.%)	R.C. (Resin Cont.) (x.xx Wt.%)	Vf (Vol. of Fibers) (x.xxxx cm3)	Vc (Vol. of Comp.) (x.xxxx cm3)	Fiber Volume (x.xx Vol.%)	Void Volume (x.xx Vol.%)
A (1)	1.3059	0.8359	64.0095	35.99	0.4723	0.8677	54.43	0.44
B (2)	2.0164	1.2765	63.3059	36.69	0.7212	1.3407	53.79	0.22
			Avg. =	36.34		Avg. =	54.11	0.33
Wf = (Crucible & Fiber wt.) - (Crucible wt.)				F.C. = (Wf / Wc) x 100				
R.C. = 100 - F.C.				Vf = Wf / Fiber Density				
Vc = Wc / Md				Fiber Volume = (Vf / Vc) x 100				
Void Volume = 100 - Md*[(R.C. / Resin Density) + (F.C. / Fiber Density)]								

Panel 073010-2 Laminate Physical Properties								
Submitted By:	Susan Hill			Date Submitted:	12/1/2010			
Program:	George Washington University			IFAS No. :	4238020003			
Material:	2D carbon 0/+/-60 / Epon 862 W			Panel I.D.:	073010-2			
Job No:				PI Request No:				
Fiber Density (g/cc) =	1.77		Resin Density (g/cc) =	1.2		No. of Plies:		
<u>Specimen Thicknesses</u>								
Spec. Number	thickness (in)							
A	0.0590							
B	0.0669							
C	0.0668							
Avg:	0.064							
<u>Specific Gravity Determination</u>								
Tested By:								
Spec. Number	Wc (wt. in air) (x.xxxx g)	W (wt. in water) (x.xxxx g)	Md Spec. Grav. (x.xxx)					
A	1.8041	0.5853	1.484					
B	1.3503	0.4717	1.532					
C	1.4275	0.4987	1.532					
	Avg:		1.516					
<u>Laminate Physical Properties Determinations</u>								
Tested By:								
Spec. Number	Wc (spec. wt.) (x.xxxx g)	Wf (Fiber wt.) (x.xxxx g)	F.C. (Fiber cont.) (x.xx Wt.%)	R.C. (Resin Cont.) (x.xx Wt.%)	Vf (Vol. of Fibers) (x.xxxx cm3)	Vc (Vol. of Comp.) (x.xxxx cm3)	Fiber Volume (x.xx Vol.%)	Void Volume (x.xx Vol.%)
A	1.8041	1.1791	65.3567	34.64	0.6662	1.2157	54.80	2.36
B	1.3503	0.9043	66.9703	33.03	0.5109	0.8814	57.97	-0.13
C	1.4275	0.9598	67.2364	32.76	0.5423	0.9318	58.20	-0.02
			Avg. =	33.48		Avg. =	56.99	0.74
Wf = (Crucible & Fiber wt.) - (Crucible wt.)				F.C. = (Wf / Wc) x 100				
R.C. = 100 - F.C.				Vf = Wf / Fiber Density				
Vc = Wc / Md				Fiber Volume = (Vf / Vc) x 100				
Void Volume = 100 - Md*[(R.C. / Resin Density) + (F.C. / Fiber Density)]								

Panel 073010-3 Laminate Physical Properties							
Submitted By:	Susan Hill			Date Submitted:	10/27/2010		
Program:	George Washington University			IFAS No. :	4238020003		
Material:	2D carbon 0/+/-60 / Epon 862 W			Panel I.D.:	073010-3		
Job No:				PI Request No:			
Fiber Density (g/cc) =	1.77		Resin Density (g/cc) =	1.2		No. of Plies:	
<u>Specific Gravity Determination</u>							
Tested By:							
Spec.	Wc	W	Md				
Number	(wt. in air)	(wt. in water)	Spec. Grav.				
	(x.xxxx g)	(x.xxxx g)	(x.xxx)				
A	1.2070	0.4184	1.526				
B	1.3279	0.4553	1.517				
C	1.5762	0.5481	1.528				
		Avg:	1.524				
<u>Laminate Physical Properties Determinations</u>							
Tested By:							
Spec.	Wc	Wf	F.C.	R.C.	Vf	Vc	Fiber
Number	(spec. wt.)	(Fiber wt.)	(Fiber cont.)	(Resin Cont.)	(Vol. of Fibers)	(Vol. of Comp.)	Fiber
	(x.xxxx g)	(x.xxxx g)	(x.xx Wt.%)	(x.xx Wt.%)	(x.xxxx cm3)	(x.xxxx cm3)	Volume
A	1.2070	0.9147	75.7829	24.22	0.5168	0.7910	65.34
B	1.3279	0.8613	64.8618	35.14	0.4866	0.8753	55.59
C	1.5762	1.0482	66.5017	33.50	0.5922	1.0315	57.41
			Avg. =	30.95		Avg. =	59.45
							1.26
Wf = (Crucible & Fiber wt.) - (Crucible wt.)				F.C. = (Wf / Wc) x 100			
R.C. = 100 - F.C.				Vf = Wf / Fiber Density			
Vc = Wc / Md				Fiber Volume = (Vf / Vc) x 100			
Void Volume = 100 - Md*[(R.C. / Resin Density) + (F.C. / Fiber Density)]							

Investigation of Opportunities for Lightweight Vehicles Using Advanced Plastics and Composites

Panel 073010-4 Laminate Physical Properties									
Submitted By:	Susan Hill			Date Submitted:	10/27/2010				
Program:	George Washington University			IFAS No. :	4238020003				
Material:	2D carbon 0/+/-60 / Epon 862 W			Panel I.D.:	073010-4				
Job No:				PI Request No:					
Fiber Density (g/cc) =	1.77		Resin Density (g/cc) =	1.2		No. of Plies:			
Specimen Thicknesses									
Spec. Number	thickness (in)								
D (spec STL094-14)	0.0632								
Avg:	0.063								
Specific Gravity Determination									
Tested By:									
Spec. Number	Wc (wt. in air) (x.xxxx g)	W (wt. in water) (x.xxxx g)	Md (Spec. Grav. (x.xxx))						
A	1.1371	0.3991	1.537						
B	1.5400	0.5418	1.538						
C	1.5755	0.5542	1.538						
D (spec STL094-14)	1.0639	0.3710	1.531						
	Avg:		1.536						
Laminate Physical Properties Determinations									
Tested By:									
Spec. Number	Wc (spec. wt.) (x.xxxx g)	Wf (Fiber wt.) (x.xxxx g)	F.C. (Fiber cont.) (x.xx Wt.%)	R.C. (Resin Cont.) (x.xx Wt.%)	Vf (Vol. of Fibers) (x.xxxx cm3)	Vc (Vol. of Comp.) (x.xxxx cm3)	Fiber Volume (x.xx Vol.%)	Void Volume (x.xx Vol.%)	
A	1.1371	0.7604	66.8719	33.13	0.4296	0.7398	58.07	-0.50	
B	1.5400	0.7966	51.7273	48.27	0.4501	1.0013	44.95	-6.82	
C	1.5755	0.8524	54.1035	45.90	0.4816	1.0244	47.01	-5.84	
D (spec STL094-14)	1.0639	0.6988	65.6829	34.32	0.3948	0.6949	56.81	-0.60	
	Avg. =		40.40		Avg. =		51.71	-4.38	
<p>Wf = (Crucible & Fiber wt.) - (Crucible wt.)</p> <p>R.C. = 100 - F.C.</p> <p>Vc = Wc / Md</p> <p>Void Volume = 100 - Md*[(R.C. / Resin Density) + (F.C. / Fiber Density)]</p> <p>F.C. = (Wf / Wc) x 100</p> <p>Vf = Wf / Fiber Density</p> <p>Fiber Volume = (Vf / Vc) x 100</p>									

SG similar for all but fiber content is low. Disregard for calculating normalizing factor.

Panel 073010-5 Laminate Physical Properties								
Submitted By:	Susan Hill		Date Submitted:	1/10/2011				
Program:	George Washington University		IFAS No. :	4238020003				
Material:	2D carbon 0/+/-60 / Epon 862 W		Panel I.D.:	073010-5				
Job No:			PI Request No:					
Fiber Density (g/cc) =	1.77	Resin Density (g/cc) =	1.2	No. of Plies:				
<u>Specimen Thicknesses</u>								
Spec. Number	thickness (in)							
A	0.0579	SAB-6 STL095-11						
B								
C	0.0660	SAB-8 STL095-15						
Avg:	0.062							
<u>Specific Gravity Determination</u>								
Tested By:								
Spec. Number	<u>Wc</u> (wt. in air) (x.xxxx g)	<u>W</u> (wt. in water) (x.xxxx g)	<u>Md</u> Spec. Grav. (x.xxx)					
A	1.1110	0.3820	1.520					
B								
C	1.1132	0.3795	1.512					
		Avg:	1.516					
<u>Laminate Physical Properties Determinations</u>								
Tested By:								
Spec. Number	<u>Wc</u> (spec. wt.) (x.xxxx g)	<u>Wf</u> (Fiber wt.) (x.xxxx g)	<u>F.C.</u> (Fiber cont.) (x.xx Wt.%)	<u>R.C.</u> (Resin Cont.) (x.xx Wt.%)	<u>Vf</u> (Vol. of Fibers) (x.xxxx cm3)	<u>Vc</u> (Vol. of Comp.) (x.xxxx cm3)	<u>Fiber Volume</u> (x.xx Vol.%)	<u>Void Volume</u> (x.xx Vol.%)
A	1.1110	0.7448	67.0387	32.96	0.4208	0.7309	57.57	0.68
C	1.1132	0.7214	64.8042	35.20	0.4076	0.7362	55.36	0.30
			Avg. =	34.08		Avg. =	56.46	0.49
Wf = (Crucible & Fiber wt.) - (Crucible wt.)					F.C. = (Wf / Wc) x 100			
R.C. = 100 - F.C.					Vf = Wf / Fiber Density			
Vc = Wc / Md					Fiber Volume = (Vf / Vc) x 100			

Panel 073010-5 Laminate Physical Properties								
Submitted By:	Susan Hill		Date Submitted:	12/1/2010				
Program:	George Washington University		IFAS No. :	4238020003				
Material:	2D carbon 0/+/-60 / Epon 862 W		Panel I.D.:	073010-6				
Job No:			PI Request No:					
Fiber Density (g/cc) =	1.77	Resin Density (g/cc) =	1.2	No. of Plies:				
<u>Specimen Thicknesses</u>								
Spec. Number	thickness (in)							
A	0.0580							
B	0.0652							
C	0.0636							
Avg:	0.062							
<u>Specific Gravity Determination</u>								
Tested By:								
Spec. Number	Wc (wt. in air) (x.xxxx g)	W (wt. in water) (x.xxxx g)	Md (Spec. Grav.) (x.xxx)					
A	1.2645	0.4433	1.535					
B	1.5085	0.5207	1.522					
C	1.2674	0.4387	1.525					
		Avg:	1.527					
<u>Laminate Physical Properties Determinations</u>								
Tested By:								
Spec. Number	Wc (spec. wt.) (x.xxxx g)	Wf (Fiber wt.) (x.xxxx g)	F.C. (Fiber cont.) (x.xx Wt.%)	R.C. (Resin Cont.) (x.xx Wt.%)	Vf (Vol. of Fibers) (x.xxxx cm3)	Vc (Vol. of Comp.) (x.xxxx cm3)	Fiber Volume (x.xx Vol.%)	Void Volume (x.xx Vol.%)
A	1.2645	0.8356	66.0815	33.92	0.4721	0.8238	57.31	-0.70
B	1.5085	1.0094	66.9142	33.09	0.5703	0.9911	57.54	0.50
C	1.2674	0.8415	66.3958	33.60	0.4754	0.8311	57.21	0.09
			Avg. =	33.54		Avg. =	57.35	-0.04
Wf = (Crucible & Fiber wt.) - (Crucible wt.)					F.C. = (Wf / Wc) x 100			
R.C. = 100 - F.C.					Vf = Wf / Fiber Density			
Vc = Wc / Md					Fiber Volume = (Vf / Vc) x 100			
Void Volume = 100 - Md*[(R.C. / Resin Density) + (F.C. / Fiber Density)]								

		Panel 080210-6 Laminate Physical Properties						
Submitted By:		Stonecash		Date Submitted:		9/2/2010		
Program:		GWU(Susan Hill)		IFAS No. :		4238020003		
Material:		2Dcarbon braid/862W		Panel I.D.:		080210-6		
Job No:		CKX		PI Request No:		CKX-JS-10-161		
Fiber Density (g/cc) =		1.77		Resin Density (g/cc) =		1.2		No. of Plies:
Specimen Thicknesses								
Spec. Number	thickness (in)							
1	0.0635							
2	0.0641							
3	0.0618							
Avg:	0.0631							
Specific Gravity Determination								
Tested By:		Andrews						
Spec. Number	Wc (wt. in air)	W (wt. in water)	Md Spec. Grav.					
	(x.xxxx g)	(x.xxxx g)	(x.xxx)					
1	0.6705	0.2348	1.534					
2	1.0695	0.3653	1.514					
3	1.1525	0.3357	1.394					
	Avg:		1.481					
Laminate Physical Properties Determinations								
Tested By:		Andrews						
Spec. Number	Wc (spec. wt.)	Wf (Fiber wt.)	F.C. (Fiber cont.)	R.C. (Resin Cont.)	Vf (Vol. of Fibers)	Vc (Vol. of Comp.)	Fiber Volume	Void Volume
	(x.xxxx g)	(x.xxxx g)	(x.xx Wt.%)	(x.xx Wt.%)	(x.xxxx cm3)	(x.xxxx cm3)	(x.xx Vol.%)	(x.xx Vol.%)
1	0.6705	0.4437	66.17	33.83	0.2507	0.4371	57.35	-0.59
2	1.0695	0.7228	67.58	32.42	0.4084	0.7064	57.81	1.29
3	1.1525	0.7424	64.42	35.58	0.4194	0.8268	50.73	7.93
	Avg. =		66.06	33.94	Avg. =		55.30	2.88
Wf = (Crucible & Fiber wt.) - (Crucible wt.)					F.C. = (Wf / Wc) x 100			
R.C. = 100 - F.C.					Vf = Wf / Fiber Density			
Vc = Wc / Md					Fiber Volume = (Vf / Vc) x 100			
Void Volume = 100 - Md*[(R.C. / Resin Density) + (F.C. / Fiber Density)]								

Tube Physical Properties			
Submitted By:	Susan Hill	Date Submitted:	3/28/2011
Program:	George Washington University	IFAS No. :	4238020003
Material:	2D carbon 0/+/-60 / Epon 862 W	Panel I.D.:	STL 103-1
Job No:		PI Request No:	
Fiber Density (g/cc) =	1.77	Resin Density (g/cc) =	1.2
		No. of Plies:	
Specimen Thicknesses			
Spec. Number	thickness (in)		
1	0.0785		
2	0.0789		
3	0.0790		
Avg:	0.0788		
Specific Gravity Determination			
Tested By:	Andrews		
Spec. Number	Wc (wt. in air) (x.xxxx g)	W (wt. in water) (x.xxxx g)	Md Spec. Grav. (x.xxx)
1	0.8892	0.2819	1.460
2	0.9653	0.3034	1.454
3	0.7928	0.2641	1.495
		Avg:	1.470
Laminate Physical Properties Determinations			
Tested By:	Andrews		
Spec. Number	Wc (spec. wt.) (x.xxxx g)	Wf (Fiber wt.) (x.xxxx g)	F.C. (Fiber cont.) (x.xx Wt.%)
			R.C. (Resin Cont.) (x.xx Wt.%)
			Vf (Vol. of Fibers) (x.xxxx cm3)
			Vc (Vol. of Comp.) (x.xxxx cm3)
			Fiber Volume (x.xx Vol.%)
			Void Volume (x.xx Vol.%)
1	0.8892	0.4809	54.08
2	0.9653	0.5147	53.32
3	0.7928	0.4819	60.78
		Avg. =	43.94
Wf = (Crucible & Fiber wt.) - (Crucible wt.)		F.C. = (Wf / Wc) x 100	
R.C. = 100 - F.C.		Vf = Wf / Fiber Density	
Vc = Wc / Md		Fiber Volume = (Vf / Vc) x 100	
Void Volume = 100 - Md*[(R.C. / Resin Density) + (F.C. / Fiber Density)]			

Tube Physical Properties			
Submitted By:	Susan Hill	Date Submitted:	3/28/2011
Program:	George Washington University	IFAS No. :	4238020003
Material:	2D carbon 0/+/-60 / Epon 862 W	Panel I.D.:	STL 103-2
Job No:		PI Request No:	
Fiber Density (g/cc) =	1.77	Resin Density (g/cc) =	1.2
		No. of Plies:	
Specimen Thicknesses			
Spec. Number	thickness (in)		
1	0.8040		
2	0.0765		
3	0.7920		
Avg:	0.5575		
Specific Gravity Determination			
Tested By:	Andrews		
Spec. Number	Wc (wt. in air) (x.xxxx g)	W (wt. in water) (x.xxxx g)	Md Spec. Grav. (x.xxx)
1	0.8742	0.2647	1.430
2	0.7638	0.2401	1.455
3	1.0881	0.3414	1.453
		Avg:	1.446
Laminate Physical Properties Determinations			
Tested By:	Andrews		
Spec. Number	Wc (spec. wt.) (x.xxxx g)	Wf (Fiber wt.) (x.xxxx g)	F.C. (Fiber cont.) (x.xx Wt.%)
			R.C. (Resin Cont.) (x.xx Wt.%)
			Vf (Vol. of Fibers) (x.xxxx cm3)
			Vc (Vol. of Comp.) (x.xxxx cm3)
			Fiber Volume (x.xx Vol.%)
			Void Volume (x.xx Vol.%)
1	0.8742	0.4469	51.12
2	0.7638	0.4121	53.95
3	1.0881	0.5815	53.44
		Avg. =	47.16
Wf = (Crucible & Fiber wt.) - (Crucible wt.)		F.C. = (Wf / Wc) x 100	
R.C. = 100 - F.C.		Vf = Wf / Fiber Density	
Vc = Wc / Md		Fiber Volume = (Vf / Vc) x 100	
Void Volume = 100 - Md*[(R.C. / Resin Density) + (F.C. / Fiber Density)]			

Tube Physical Properties			
Submitted By:	Susan Hill	Date Submitted:	3/28/2011
Program:	George Washington University	IFAS No. :	4238020003
Material:	2D carbon 0/+/-60 / Epon 862 W	Panel I.D.:	STL 103-3
Job No:		PI Request No:	
Fiber Density (g/cc) =	1.77	Resin Density (g/cc) =	1.2
		No. of Plies:	
Specimen Thicknesses			
Spec. Number	thickness (in)		
1	0.0813		
2	0.0791		
3	0.0821		
Avg:	0.081		
Specific Gravity Determination			
Tested By:	Andrews		
Spec. Number	Wc (wt. in air) (x.xxxx g)	W (wt. in water) (x.xxxx g)	Md Spec. Grav. (x.xxx)
1	0.8869	0.2736	1.442
2	0.9052	0.2839	1.452
3	1.0175	0.3150	1.444
		Avg:	1.446
Laminate Physical Properties Determinations			
Tested By:	Andrews		
Spec. Number	Wc (spec. wt.) (x.xxxx g)	Wf (Fiber wt.) (x.xxxx g)	F.C. (Fiber cont.) (x.xx Wt.%)
			R.C. (Resin Cont.) (x.xx Wt.%)
			Vf (Vol. of Fibers) (x.xxxx cm3)
			Vc (Vol. of Comp.) (x.xxxx cm3)
			Fiber Volume (x.xx Vol.%)
			Void Volume (x.xx Vol.%)
1	0.8869	0.4536	51.14
2	0.9052	0.4822	53.27
3	1.0175	0.5289	51.98
		Avg. =	47.87
Wf = (Crucible & Fiber wt.) - (Crucible wt.)		F.C. = (Wf / Wc) x 100	
R.C. = 100 - F.C.		Vf = Wf / Fiber Density	
Vc = Wc / Md		Fiber Volume = (Vf / Vc) x 100	
Void Volume = 100 - Md*[(R.C. / Resin Density) + (F.C. / Fiber Density)]			

Tube Physical Properties			
Submitted By:	Susan Hill	Date Submitted:	3/28/2011
Program:	George Washington University	IFAS No. :	4238020003
Material:	2D carbon 0/+/-60 / Epon 862 W	Panel I.D.:	STL 103-4
Job No:		PI Request No:	
Fiber Density (g/cc) =	1.77	Resin Density (g/cc) =	1.2
		No. of Plies:	
Specimen Thicknesses			
Spec. Number	thickness (in)		
1	0.0790		
2	0.0803		
3	0.0850		
Avg:	0.0814		
Specific Gravity Determination			
Tested By:	Andrews		
Spec. Number	Wc (wt. in air) (x.xxxx g)	W (wt. in water) (x.xxxx g)	Md Spec. Grav. (x.xxx)
1	0.8974	0.2532	1.456
2	0.9443	0.2947	1.449
3	1.3158	0.4001	1.433
		Avg:	1.446
Laminate Physical Properties Determinations			
Tested By:	Andrews		
Spec. Number	Wc (spec. wt.) (x.xxxx g)	Wf (Fiber wt.) (x.xxxx g)	F.C. (Fiber cont.) (x.xx Wt.%)
			R.C. (Resin Cont.) (x.xx Wt.%)
			Vf (Vol. of Fibers) (x.xxxx cm3)
			Vc (Vol. of Comp.) (x.xxxx cm3)
			Fiber Volume (x.xx Vol.%)
			Void Volume (x.xx Vol.%)
1	0.8974	0.4840	53.93
2	0.9443	0.5029	53.26
3	1.3158	0.6620	50.31
		Avg. =	47.50
Wf = (Crucible & Fiber wt.) - (Crucible wt.)		F.C. = (Wf / Wc) x 100	
R.C. = 100 - F.C.		Vf = Wf / Fiber Density	
Vc = Wc / Md		Fiber Volume = (Vf / Vc) x 100	
Void Volume = 100 - Md*[(R.C. / Resin Density) + (F.C. / Fiber Density)]			

Tube Physical Properties			
Submitted By:	Susan Hill	Date Submitted:	3/28/2011
Program:	George Washington University	IFAS No. :	4238020003
Material:	2D carbon 0/+/-60 / Epon 862 W	Panel I.D.:	STL 103-5
Job No:		PI Request No:	
Fiber Density (g/cc) =	1.77	Resin Density (g/cc) =	1.2
		No. of Plies:	
Specimen Thicknesses			
Spec. Number	thickness (in)		
1	0.0751		
2	0.0684		
3	0.0764		
Avg:	0.0733		
Specific Gravity Determination			
Tested By:	Andrews		
Spec. Number	Wc (wt. in air) (x.xxxx g)	W (wt. in water) (x.xxxx g)	Md Spec. Grav. (x.xxx)
1	0.8513	0.2691	1.457
2	0.6940	0.2307	1.493
3	0.7724	0.2452	1.461
		Avg:	1.470
Laminate Physical Properties Determinations			
Tested By:	Andrews		
Spec. Number	Wc (spec. wt.) (x.xxxx g)	Wf (Fiber wt.) (x.xxxx g)	F.C. (Fiber cont.) (x.xx Wt.%)
			R.C. (Resin Cont.) (x.xx Wt.%)
			Vf (Vol. of Fibers) (x.xxxx cm3)
			Vc (Vol. of Comp.) (x.xxxx cm3)
			Fiber Volume (x.xx Vol.%)
			Void Volume (x.xx Vol.%)
1	0.8513	0.4639	54.49
2	0.6940	0.4173	60.13
3	0.7724	0.4221	54.65
		Avg. =	43.58
Wf = (Crucible & Fiber wt.) - (Crucible wt.)		F.C. = (Wf / Wc) x 100	
R.C. = 100 - F.C.		Vf = Wf / Fiber Density	
Vc = Wc / Md		Fiber Volume = (Vf / Vc) x 100	
Void Volume = 100 - Md*[(R.C. / Resin Density) + (F.C. / Fiber Density)]			

Tube Physical Properties			
Submitted By:	Susan Hill	Date Submitted:	4/19/2011
Program:	George Washington University	IFAS No. :	4238020003
Material:	2D carbon 0/+/-60 / Epon 862 W	Panel I.D.:	STL 103-6
Job No:		PI Request No:	
Fiber Density (g/cc) =	1.77	Resin Density (g/cc) =	1.2
		No. of Plies:	
Specimen Thicknesses			
Spec. Number	thickness (in)		
1	0.0825		
2	0.0782		
3	770.0000		
Avg:	256.7202		
Specific Gravity Determination			
Tested By:	Andrews		
Spec. Number	Wc (wt. in air) (x.xxxx g)	W (wt. in water) (x.xxxx g)	Md Spec. Grav. (x.xxx)
1	1.3754	0.4232	1.440
2	0.9175	0.2783	1.432
3	1.0152	0.3182	1.452
	Avg:		1.441
Laminate Physical Properties Determinations			
Tested By:	Andrews		
Spec. Number	Wc (spec. wt.) (x.xxxx g)	Wf (Fiber wt.) (x.xxxx g)	F.C. (Fiber cont.) (x.xx Wt.%)
			R.C. (Resin Cont.) (x.xx Wt.%)
			Vf (Vol. of Fibers) (x.xxxx cm3)
			Vc (Vol. of Comp.) (x.xxxx cm3)
			Fiber Volume (x.xx Vol.%)
			Void Volume (x.xx Vol.%)
1	1.3754	0.7442	54.11
2	0.9175	0.4986	54.34
3	1.0152	0.6080	59.89
	Avg. =		43.89
Wf = (Crucible & Fiber wt.) - (Crucible wt.) R.C. = 100 - F.C. Vc = Wc / Md Void Volume = 100 - Md*[(R.C. / Resin Density) + (F.C. / Fiber Density)]			
F.C. = (Wf / Wc) x 100 Vf = Wf / Fiber Density Fiber Volume = (Vf / Vc) x 100			

Tube Physical Properties			
Submitted By:	Susan Hill	Date Submitted:	4/19/2011
Program:	George Washington University	IFAS No. :	4238020003
Material:	2D carbon 0/+/-60 / Epon 862 W	Panel I.D.:	STL 103-7
Job No:		PI Request No:	
Fiber Density (g/cc) =	1.77	Resin Density (g/cc) =	1.2
		No. of Plies:	
Specimen Thicknesses			
Spec. Number	thickness (in)		
1	0.0820		
2	0.0778		
3	0.0754		
Avg:	0.0784		
Specific Gravity Determination			
Tested By:	Andrews		
Spec. Number	Wc (wt. in air) (x.xxxx g)	W (wt. in water) (x.xxxx g)	Md Spec. Grav. (x.xxx)
1	1.2711	0.3909	1.440
2	1.0283	0.2935	1.395
3	0.9334	0.2873	1.440
		Avg:	1.425
Laminate Physical Properties Determinations			
Tested By:	Andrews		
Spec. Number	Wc (spec. wt.) (x.xxxx g)	Wf (Fiber wt.) (x.xxxx g)	F.C. (Fiber cont.) (x.xx Wt.%)
			R.C. (Resin Cont.) (x.xx Wt.%)
			Vf (Vol. of Fibers) (x.xxxx cm3)
			Vc (Vol. of Comp.) (x.xxxx cm3)
			Fiber Volume (x.xx Vol.%)
			Void Volume (x.xx Vol.%)
1	1.2711	0.6914	54.39
2	1.0283	0.4940	48.04
3	0.9334	0.5225	55.98
		Avg. =	47.20
Wf = (Crucible & Fiber wt.) - (Crucible wt.)		F.C. = (Wf / Wc) x 100	
R.C. = 100 - F.C.		Vf = Wf / Fiber Density	
Vc = Wc / Md		Fiber Volume = (Vf / Vc) x 100	
Void Volume = 100 - Md*[(R.C. / Resin Density) + (F.C. / Fiber Density)]			

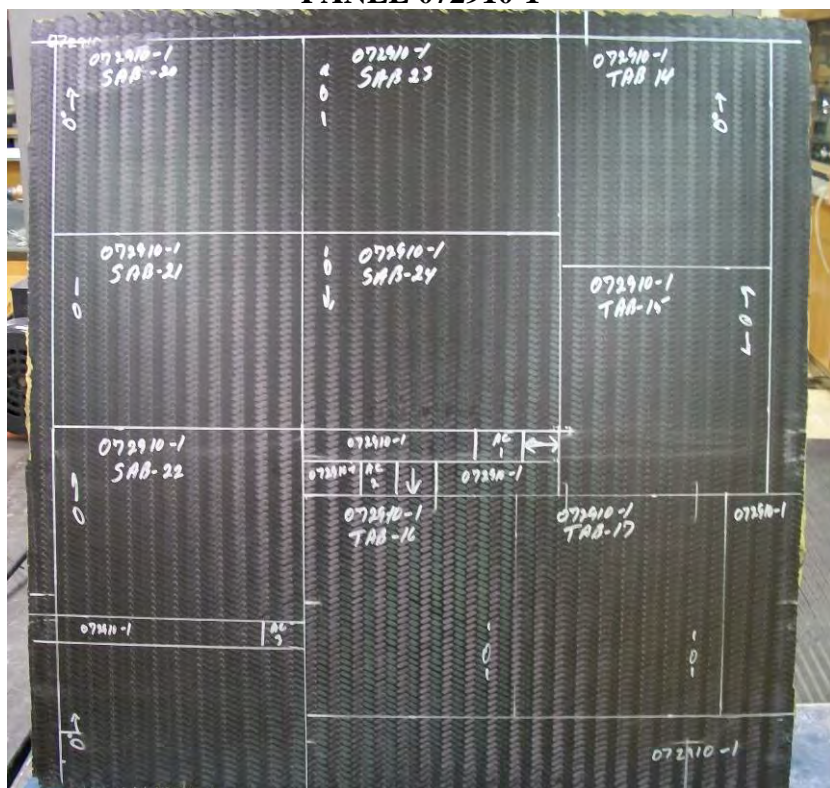
Tube Physical Properties								
Submitted By:	Susan Hill	Date Submitted:	4/19/2011					
Program:	George Washington University	IFAS No. :	4238020003					
Material:	2D carbon 0/+/-60 / Epon 862 W	Panel I.D.:	STL 103-8					
Job No:		PI Request No:						
Fiber Density (g/cc) =	1.77	Resin Density (g/cc) =	1.2					
		No. of Plies:						
Specimen Thicknesses								
Spec. Number	thickness (in)							
1	0.0810							
2	0.0802							
3	0.7790							
Avg:	0.3134							
Specific Gravity Determination								
Tested By:	Andrews							
Spec. Number	Wc (wt. in air) (x.xxxx g)	W (wt. in water) (x.xxxx g)	Md Spec. Grav. (x.xxx)					
1	1.4385	0.4406	1.437					
2	0.9300	0.2889	1.447					
3	1.0813	0.3335	1.442					
		0.3335	1.442					
Laminate Physical Properties Determinations								
Tested By:	Andrews							
Spec. Number	Wc (spec. wt.) (x.xxxx g)	Wf (Fiber wt.) (x.xxxx g)	F.C. (Fiber cont.) (x.xx Wt.%)	R.C. (Resin Cont.) (x.xx Wt.%)	Vf (Vol. of Fibers) (x.xxxx cm3)	Vc (Vol. of Comp.) (x.xxxx cm3)	Fiber Volume (x.xx Vol.%)	Void Volume (x.xx Vol.%)
1	1.4385	0.7850	54.57	45.43	0.4435	1.0010	44.30	1.29
2	0.9300	0.5115	55.00	45.00	0.2890	0.6427	44.96	0.77
3	1.0813	0.5907	54.63	45.37	0.3337	0.7499	44.51	0.97
			Avg. =	45.27		Avg. =	44.59	1.01
Wf = (Crucible & Fiber wt.) - (Crucible wt.) R.C. = 100 - F.C. Vc = Wc / Md					F.C. = (Wf / Wc) x 100 Vf = Wf / Fiber Density Fiber Volume = (Vf / Vc) x 100			
Void Volume = 100 - Md*[(R.C. / Resin Density) + (F.C. / Fiber Density)]								

Tube Physical Properties			
Submitted By:	Susan Hill	Date Submitted:	4/19/2011
Program:	George Washington University	IFAS No. :	4238020003
Material:	2D carbon 0/+/-60 / Epon 862 W	Panel I.D.:	STL 103-9
Job No:		PI Request No:	
Fiber Density (g/cc) =	1.77	Resin Density (g/cc) =	1.2
		No. of Plies:	
Specimen Thicknesses			
Spec. Number	thickness (in)		
1	0.0800		
2	0.0801		
3	0.0788		
Avg:	0.0796		
Specific Gravity Determination			
Tested By:	Andrews		
Spec. Number	Wc (wt. in air) (x.xxxx g)	W (wt. in water) (x.xxxx g)	Md Spec. Grav. (x.xxx)
1	1.3359	0.4175	1.450
2	0.9374	0.2871	1.437
3	0.9454	0.2893	1.437
		Avg:	1.441
Laminate Physical Properties Determinations			
Tested By:	Andrews		
Spec. Number	Wc (spec. wt.) (x.xxxx g)	Wf (Fiber wt.) (x.xxxx g)	F.C. (Fiber cont.) (x.xx Wt.%)
			R.C. (Resin Cont.) (x.xx Wt.%)
			Vf (Vol. of Fibers) (x.xxxx cm3)
			Vc (Vol. of Comp.) (x.xxxx cm3)
			Fiber Volume (x.xx Vol.%)
			Void Volume (x.xx Vol.%)
1	1.3359	0.7676	57.46
2	0.9374	0.5105	54.46
3	0.9454	0.5082	53.76
		Avg. =	44.78
Wf = (Crucible & Fiber wt.) - (Crucible wt.)		F.C. = (Wf / Wc) x 100	
R.C. = 100 - F.C.		Vf = Wf / Fiber Density	
Vc = Wc / Md		Fiber Volume = (Vf / Vc) x 100	
Void Volume = 100 - Md*[(R.C. / Resin Density) + (F.C. / Fiber Density)]			

APPENDIX C
SELECTED PANEL LAYOUTS

Sections used for fiber content analyses are labeled AD
Sections for photomicrographs are identified with a number and a directional arrow
indicating the mount surface

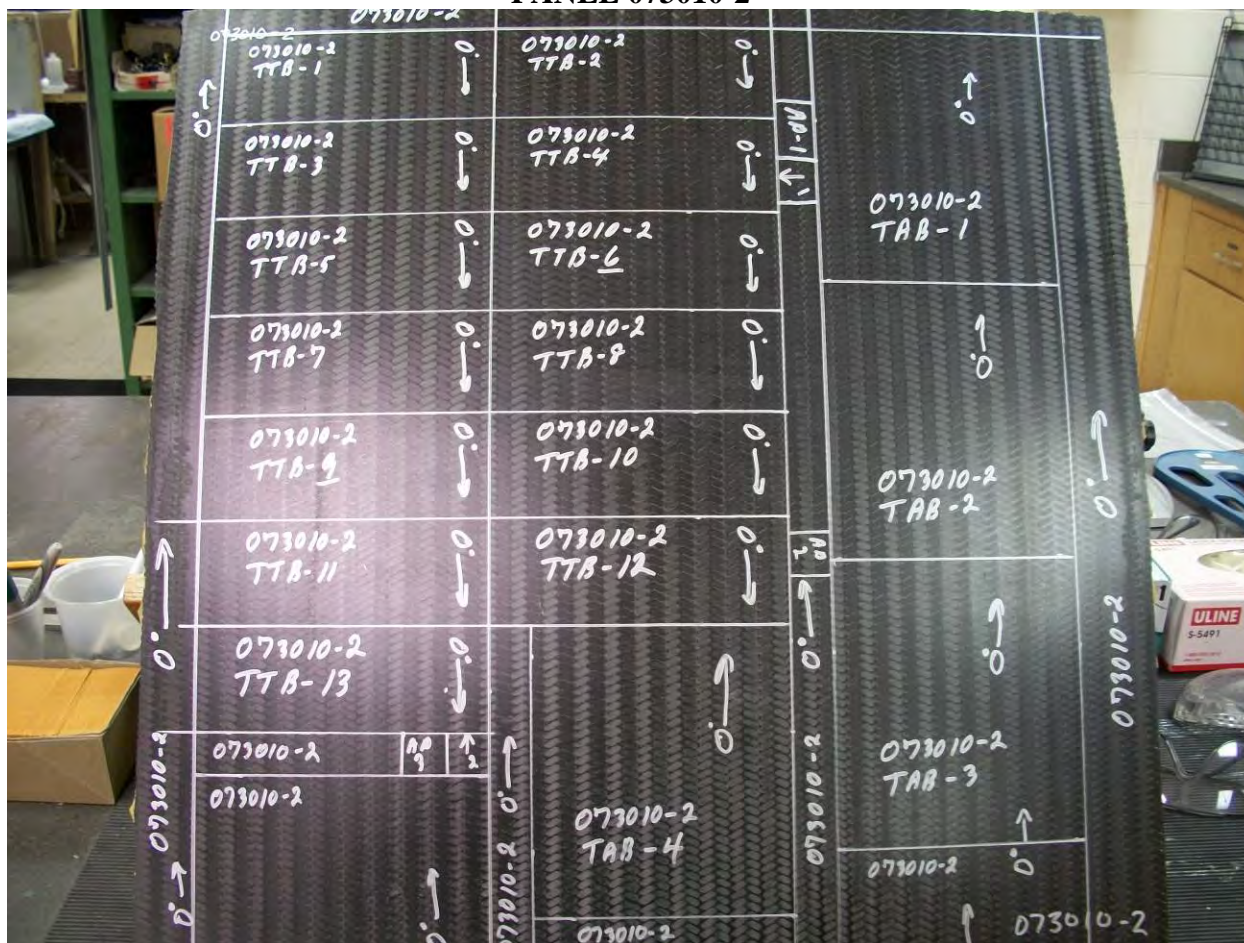
PANEL 072910-1



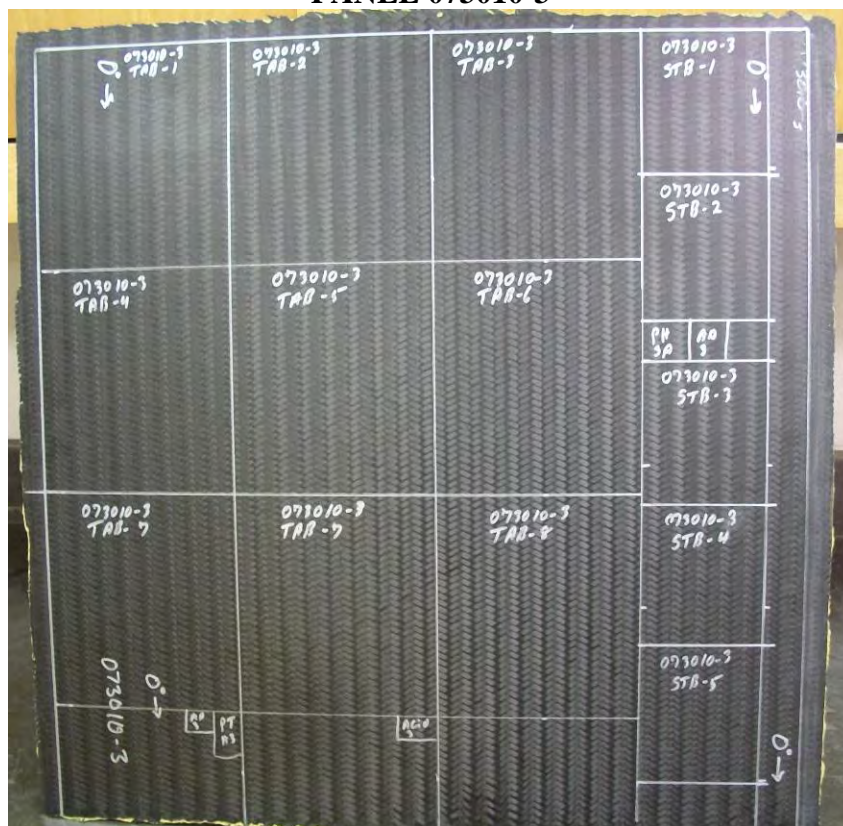
PANEL 072910-2



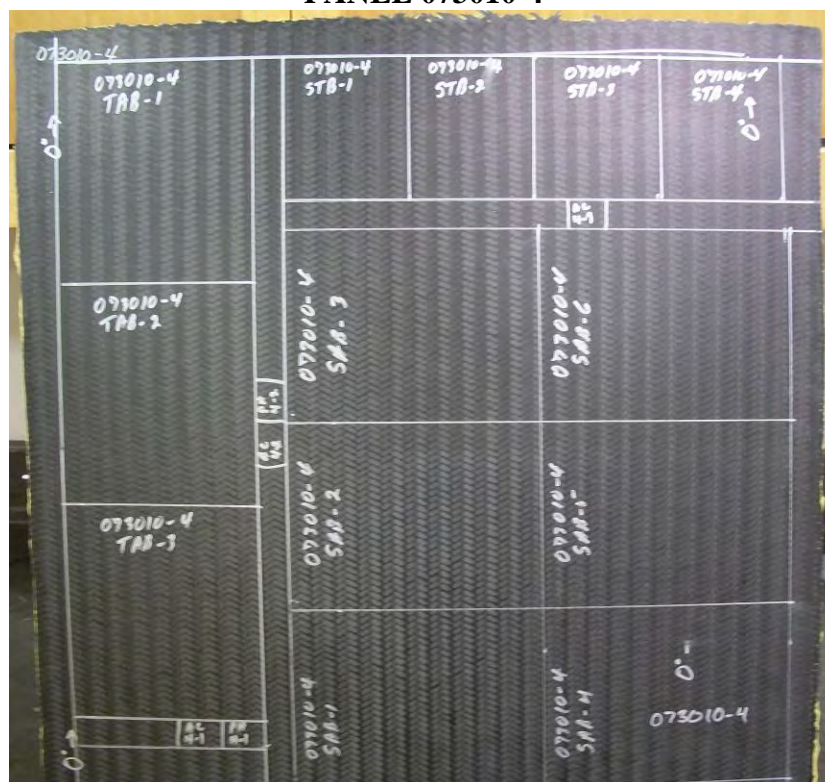
PANEL 073010-2



PANEL 073010-3



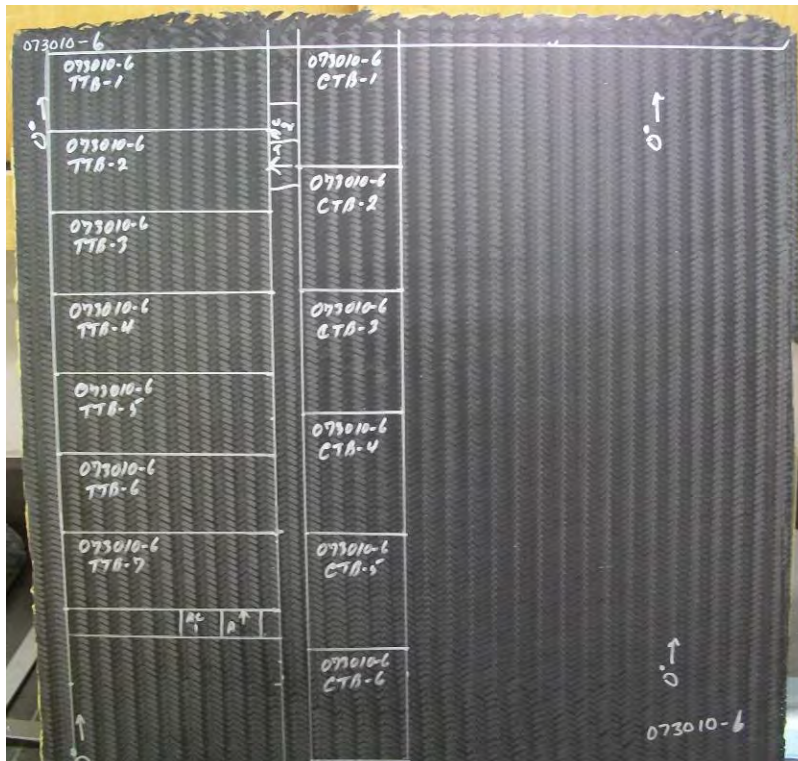
PANEL 073010-4



PANEL 073010-5



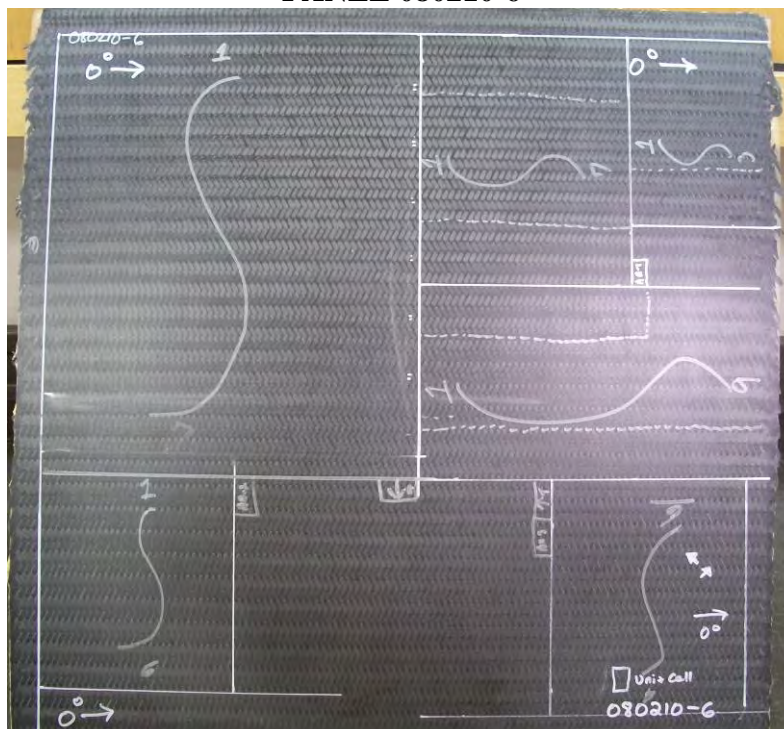
PANEL 073010-6 Initial



PANEL 073010-6 Balance

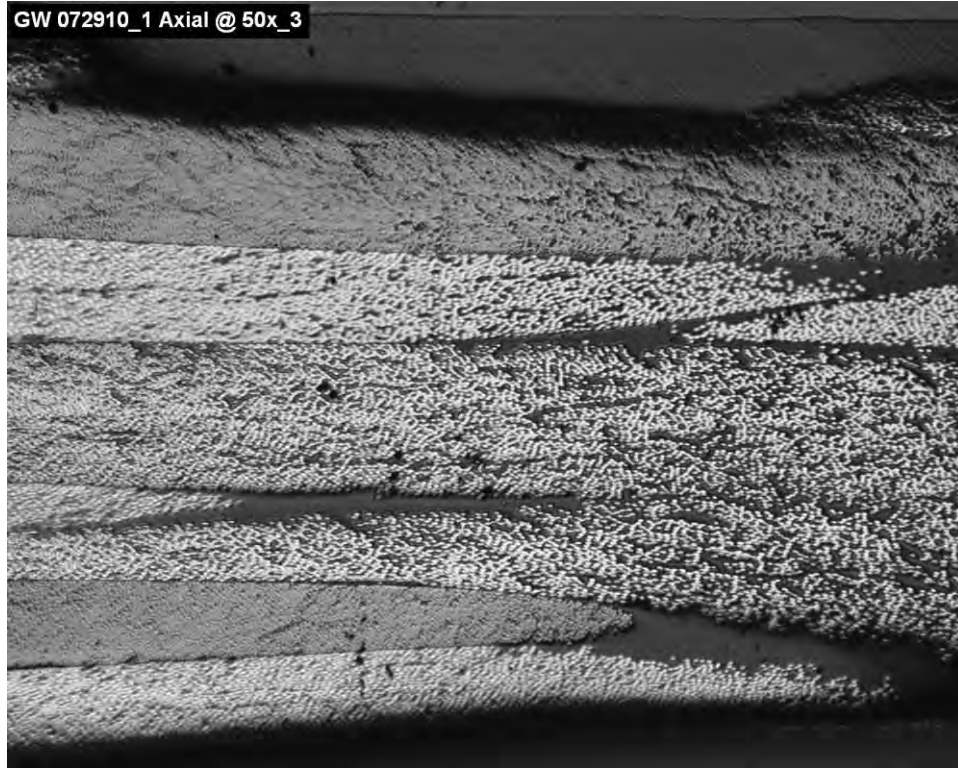


PANEL 080210-6

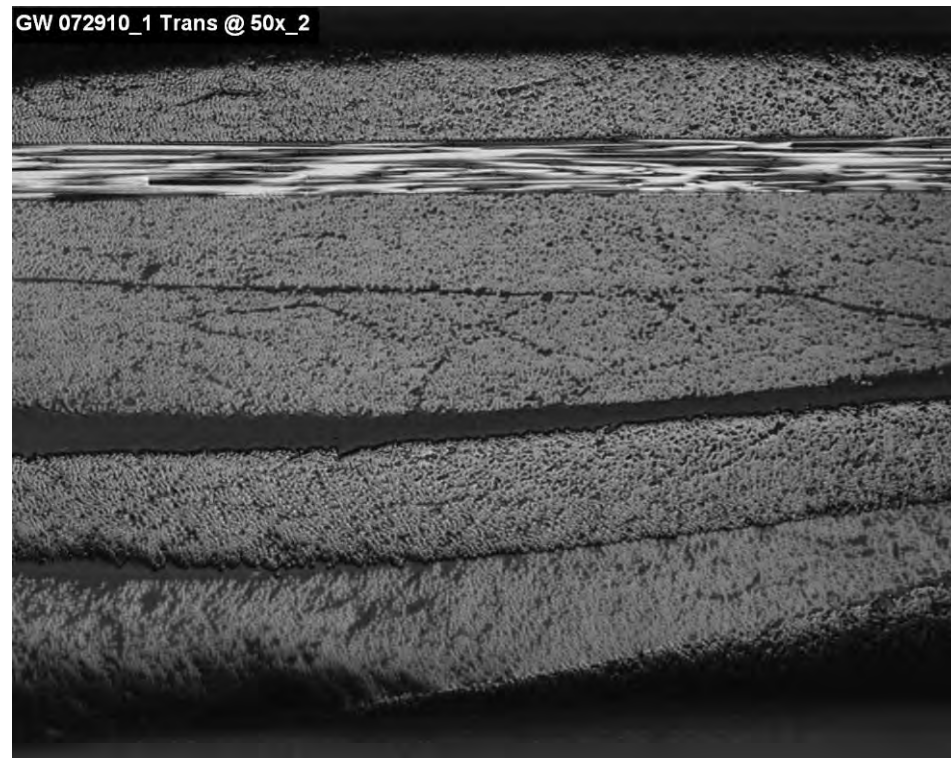


APPENDIX D
SAMPLE PHOTOMICROGRAPHS OF PANEL CROSS-SECTIONS AT 50X
PHOTOMICROGRAPHS OF TUBE CROSS-SECTIONS AT 25X

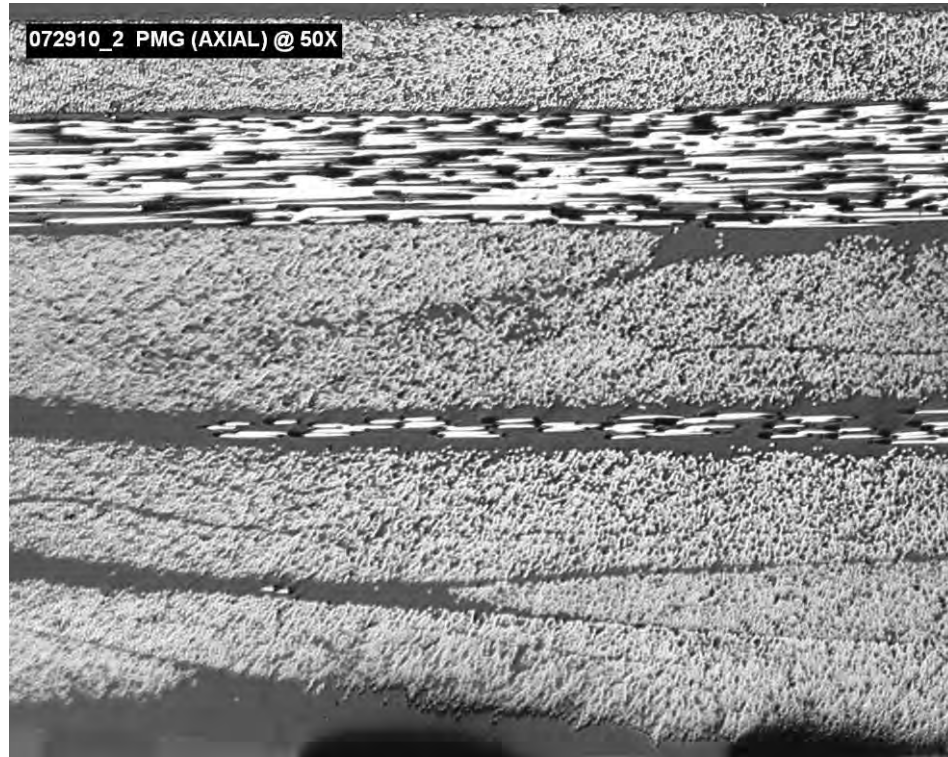
PANEL 072910-1 AXIAL



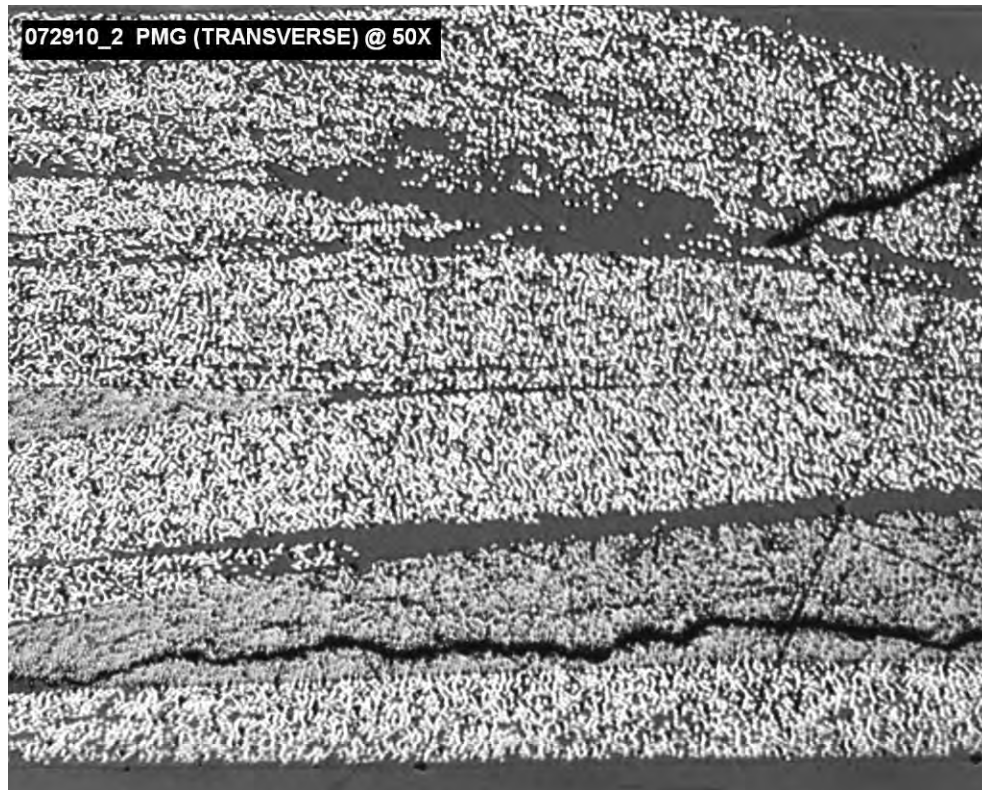
PANEL 072910-1 TRANSVERSE



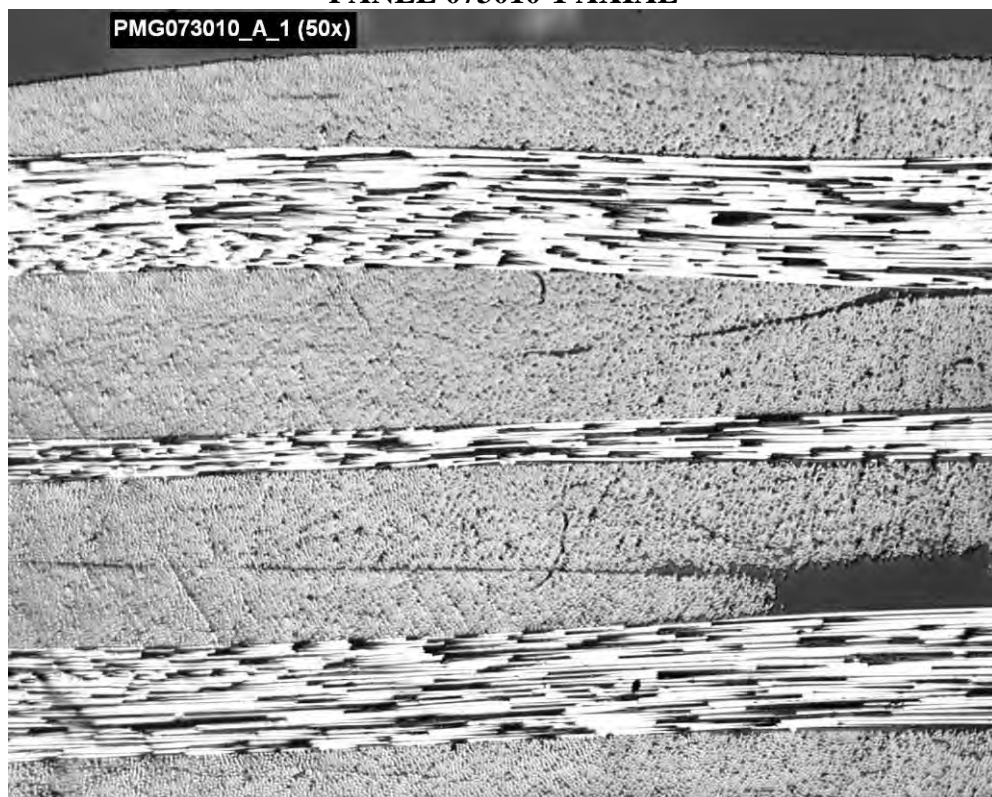
PANEL 072910-2 AXIAL



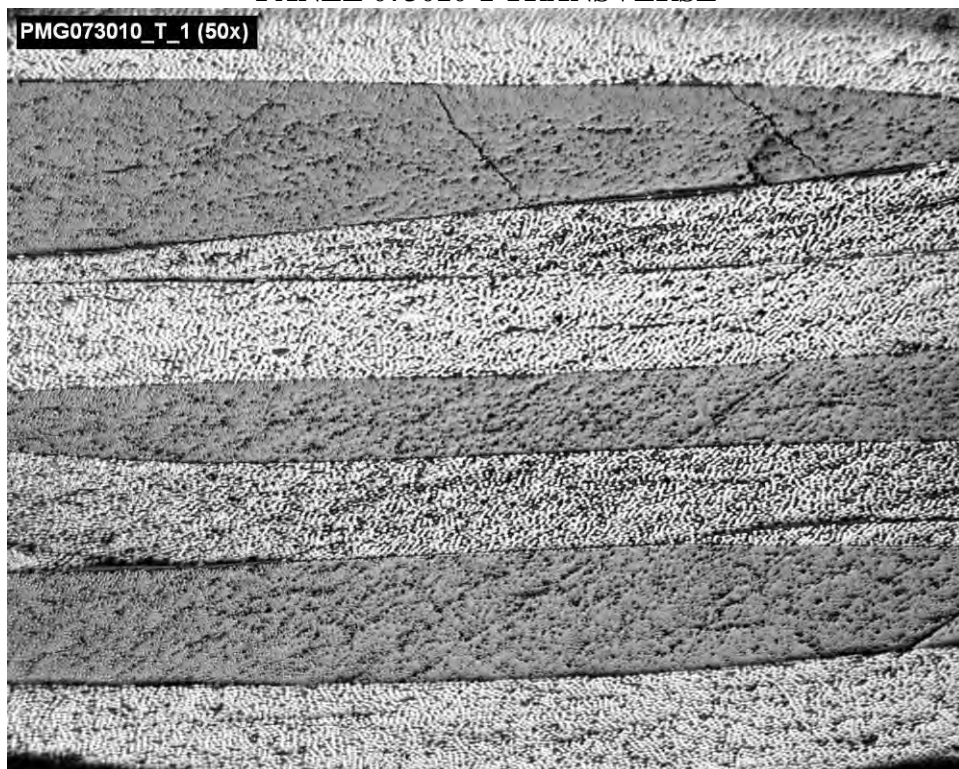
PANEL 072910-2 TRANSVERSE



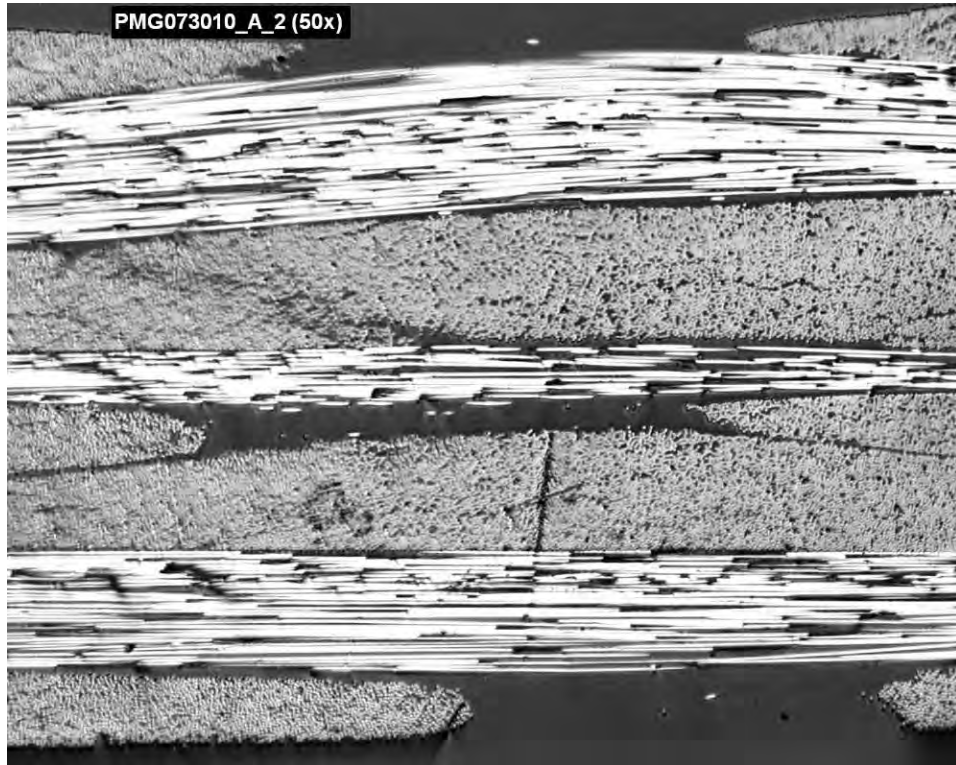
PANEL 073010-1 AXIAL



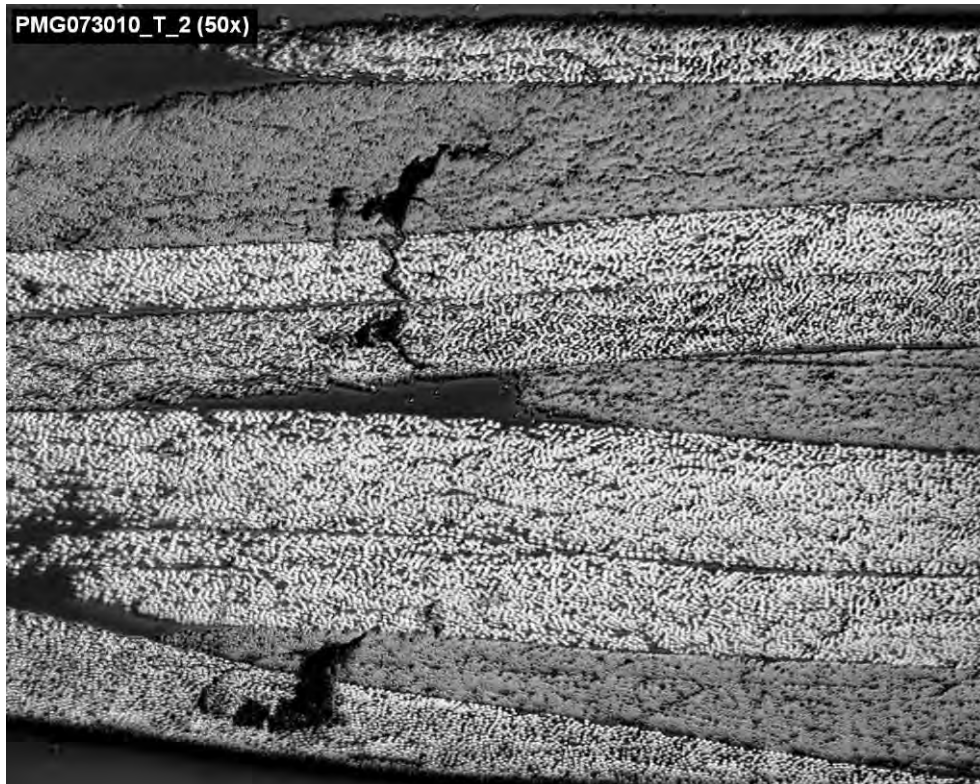
PANEL 073010-1 TRANSVERSE



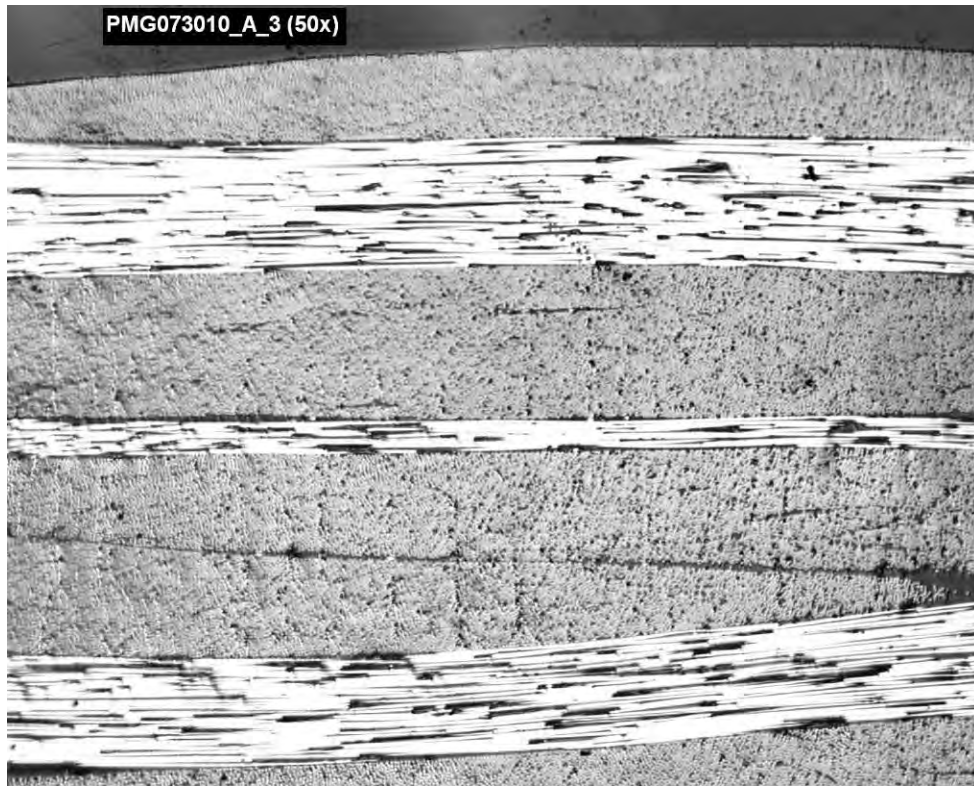
PANEL 073010-2 AXIAL



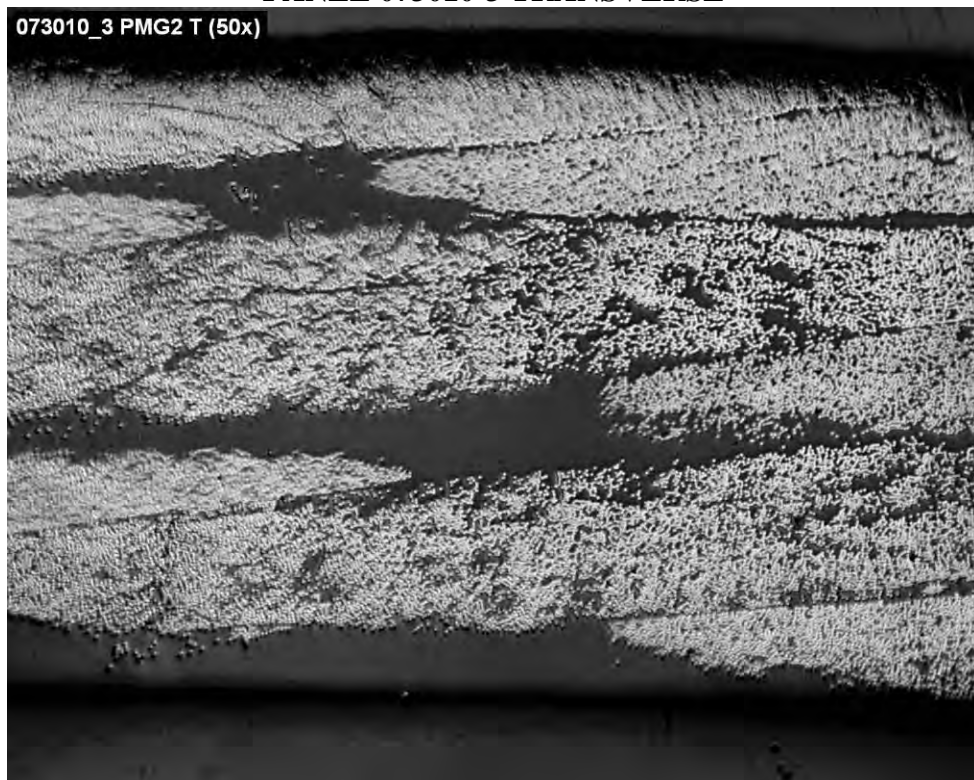
PANEL 073010-2 TRANSVERSE



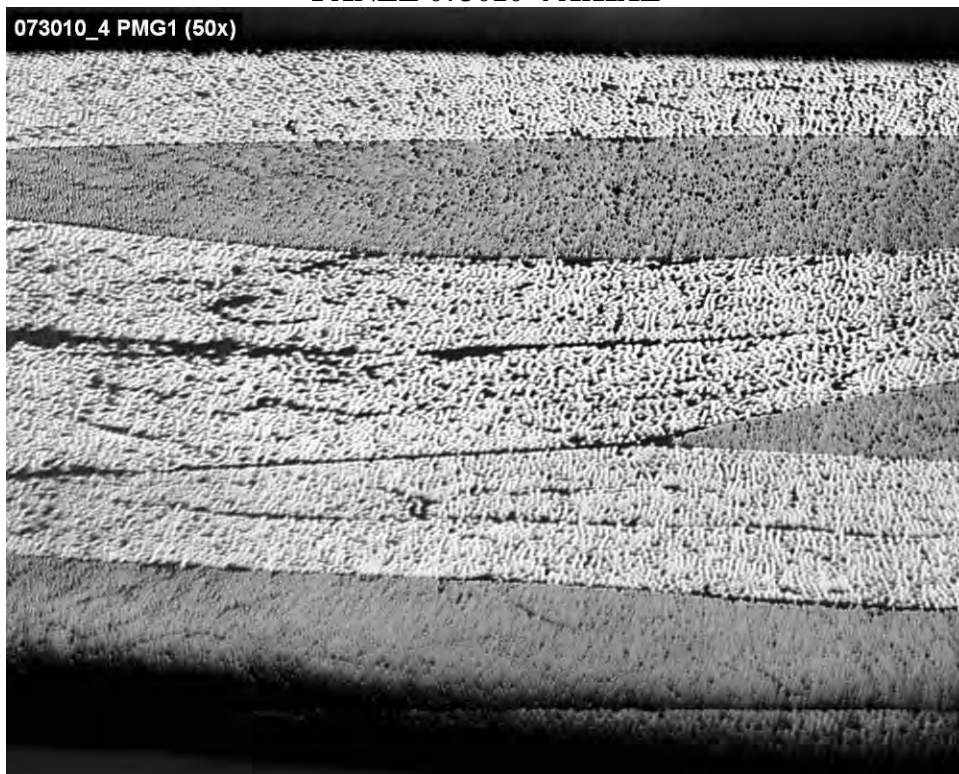
PANEL 073010-3 AXIAL



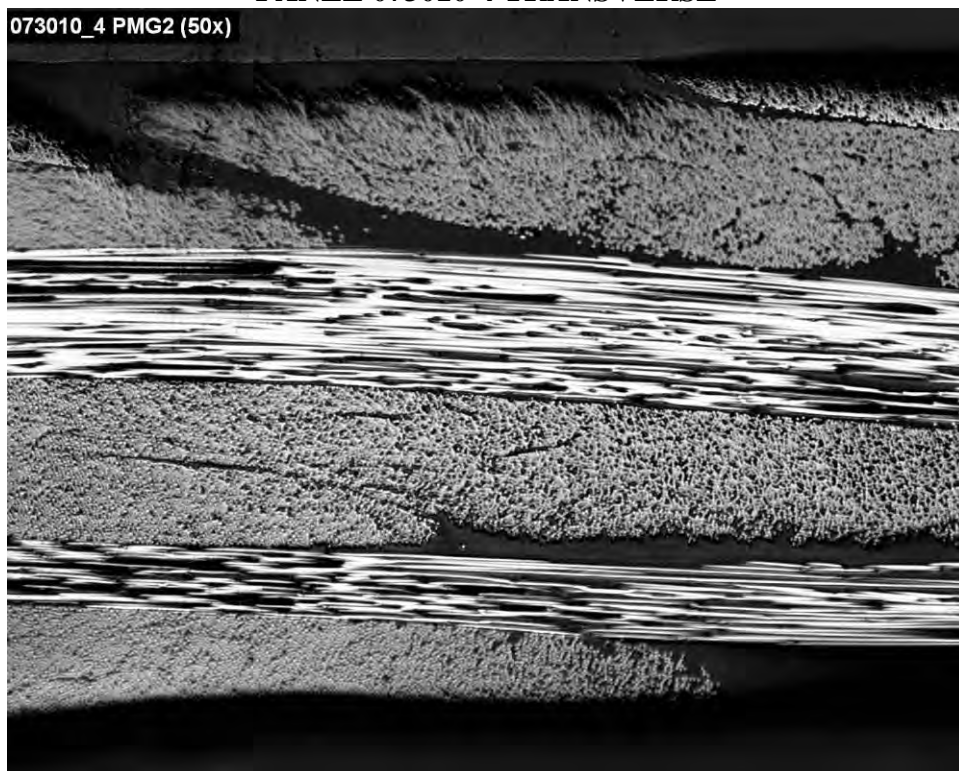
PANEL 073010-3 TRANSVERSE



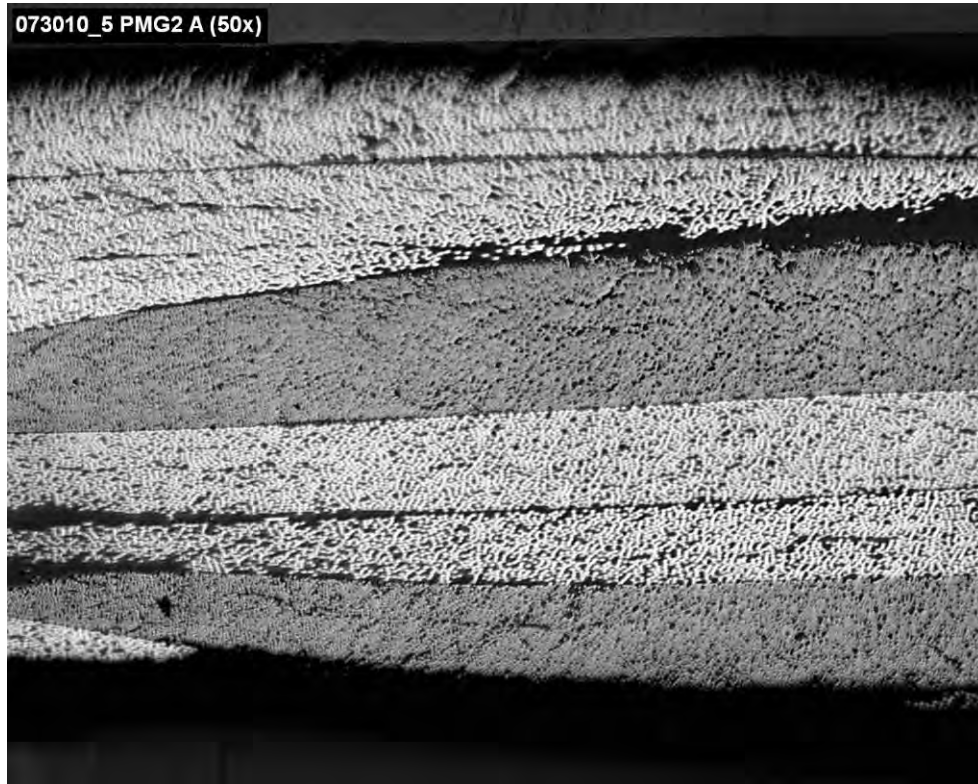
PANEL 073010-4 AXIAL



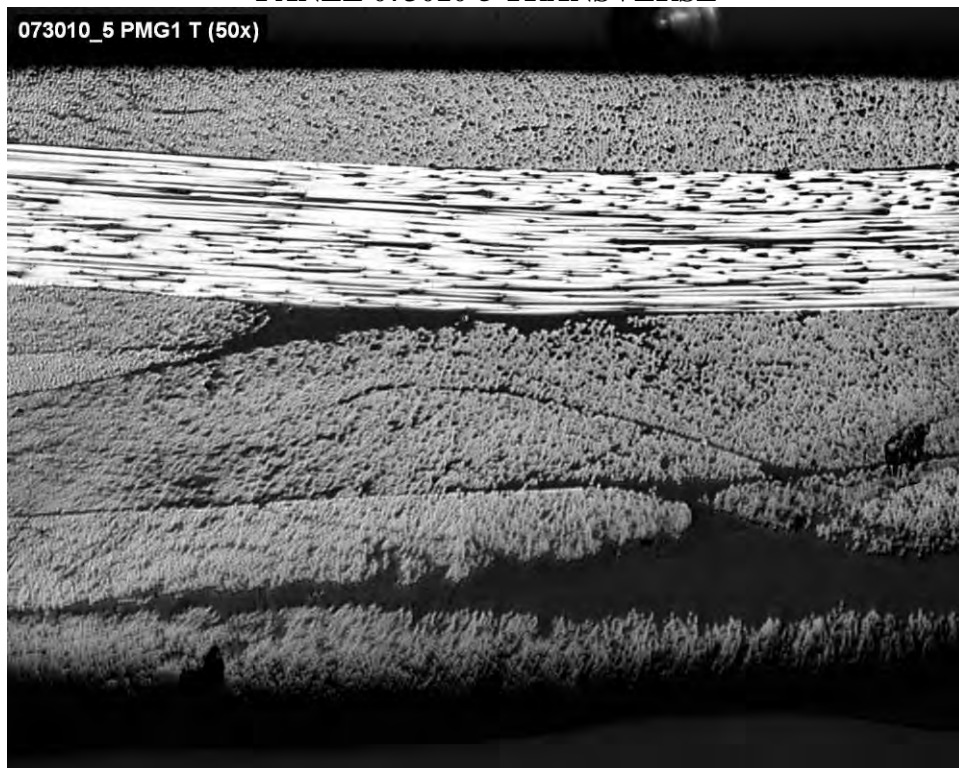
PANEL 073010-4 TRANSVERSE



PANEL 073010-5 AXIAL



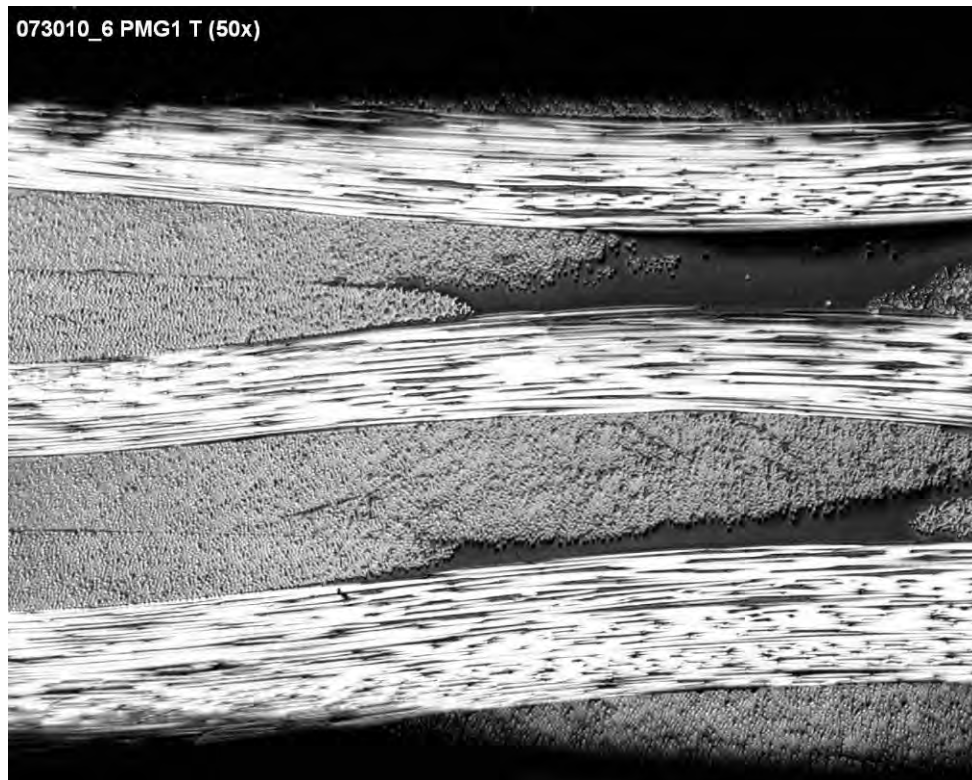
PANEL 073010-5 TRANSVERSE



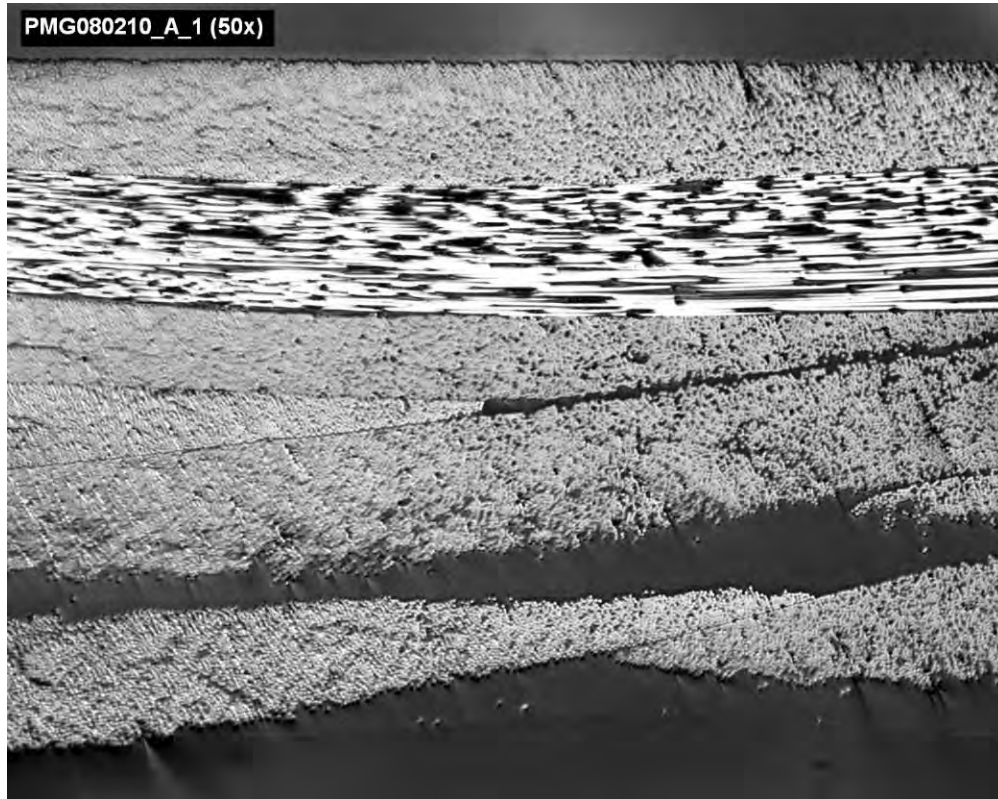
PANEL 073010-6 AXIAL



PANEL 073010-6 TRANSVERSE



PANEL 080210-6 AXIAL

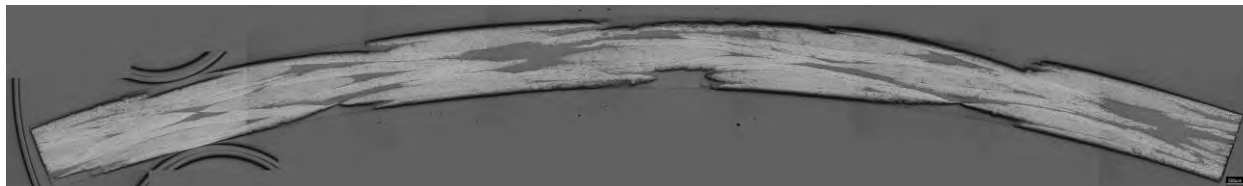


PANEL 080210-6 TRANSVERSE

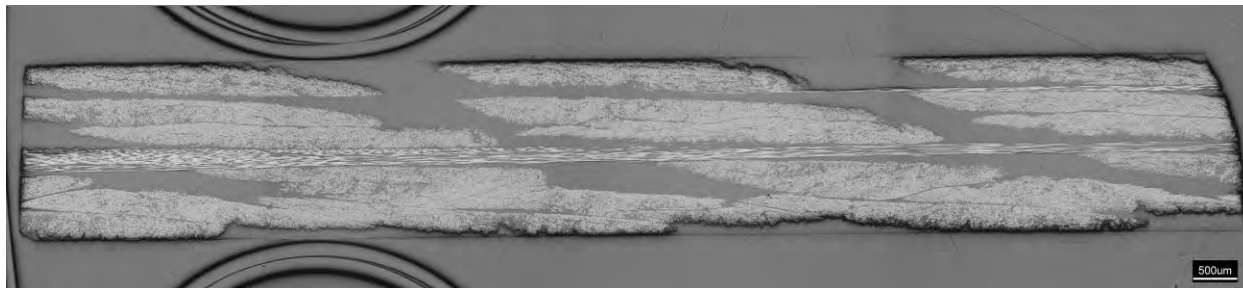


TUBE CROSS-SECTIONS AT 25X

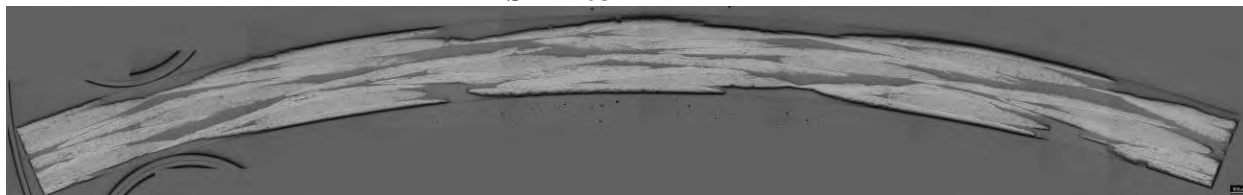
STL103-1 AXIAL



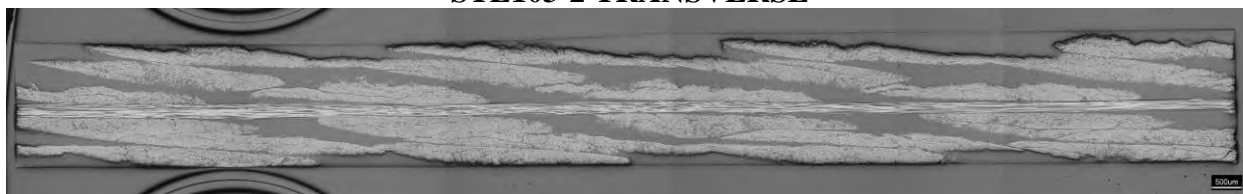
STL103-1 TRANSVERSE



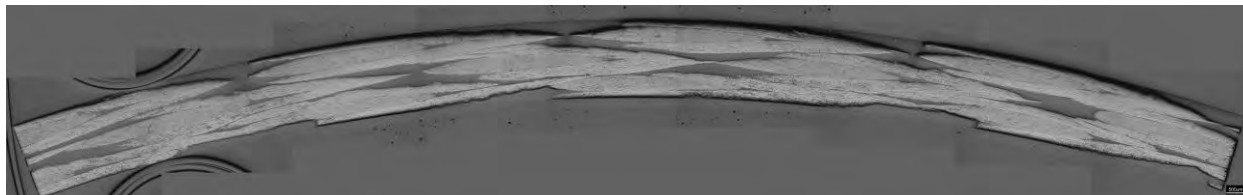
STL103-2 AXIAL



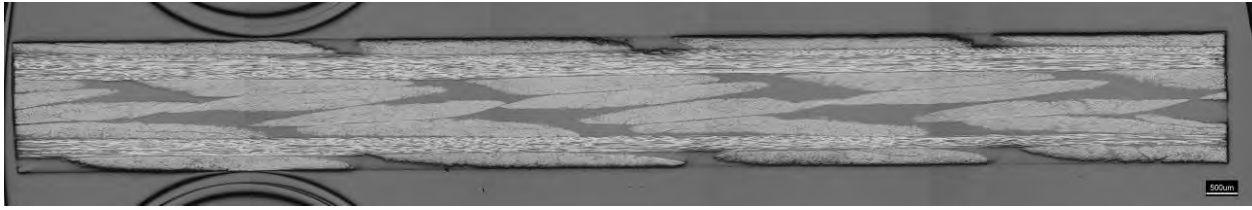
STL103-2 TRANSVERSE



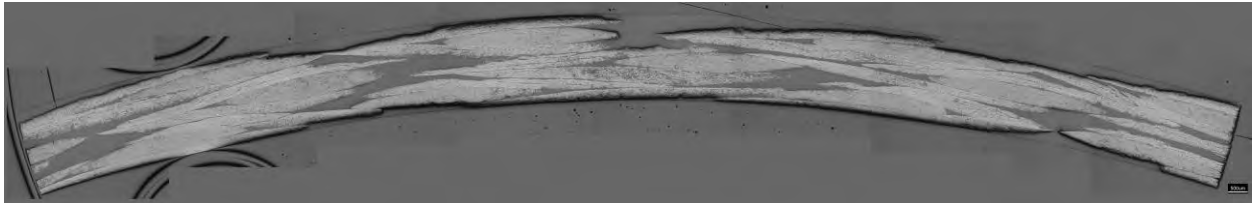
STL103-3 AXIAL



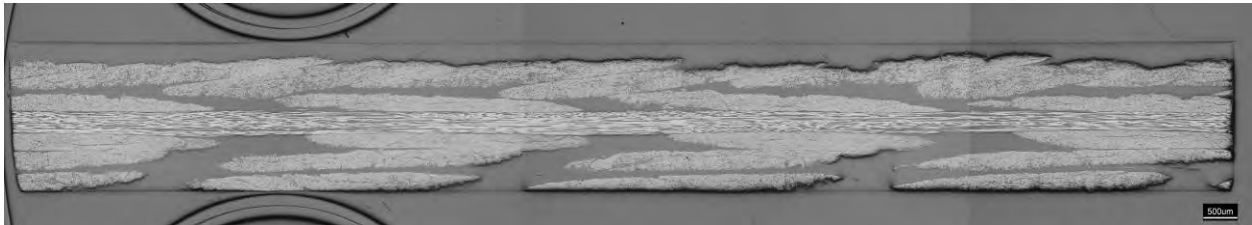
STL103-3 TRANSVERSE



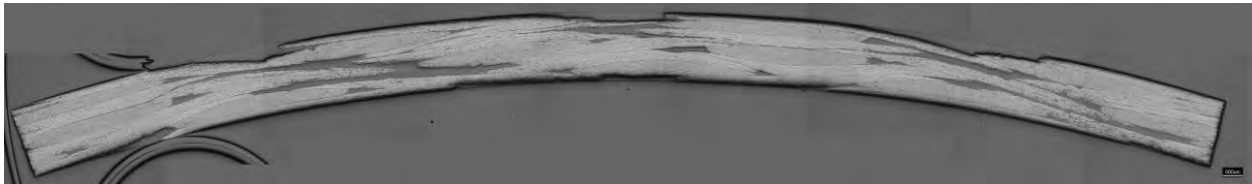
STL103-4 AXIAL



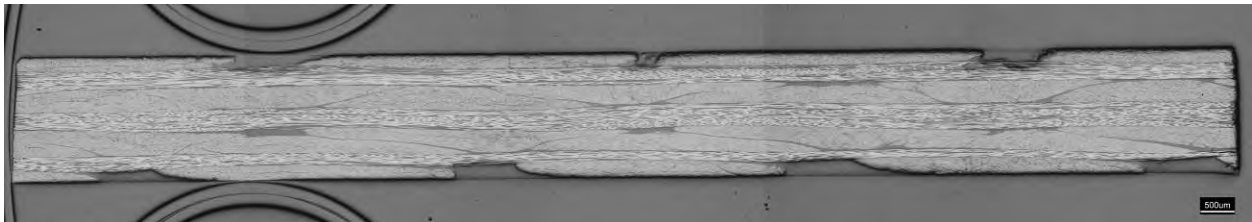
STL103-4 TRANSVERSE



STL103-5 AXIAL



STL103-5 TRANSVERSE



APPENDIX E
UNIT CELL MEASUREMENTS AND LOCATIONS

Notes: All measurements in units of millimeters; sub 1 is left most or top most as image is oriented, sub 2 is right most or lowest measurement as image is oriented.

Sub panel # is completely arbitrary and relates to separate pieces from same panel ID; number corresponds to sequence in which it was imaged.

Panel ID

072910-1 Sub panel#

N/A

1				2				3			
H ₁	H ₂	W ₁	W ₂	H ₁	H ₂	W ₁	W ₂	H ₁	H ₂	W ₁	W ₂
5.4	5.1	18.1	18.2	5.1	5.2	17.9	18.4	5.4	5.5	18.3	18.7

073010-1 Sub panel#

1

1				2				3			
H ₁	H ₂	W ₁	W ₂	H ₁	H ₂	W ₁	W ₂	H ₁	H ₂	W ₁	W ₂
5.3	5.0	17.0	17.7	5.3	5.4	18.4	18.0	4.9	5.5	16.6	16.7

073010-1 Sub panel#

2

1				2			
H ₁	H ₂	W ₁	W ₂	H ₁	H ₂	W ₁	W ₂
5.3	5.3	17.1	17.5	5.4	5.3	18.4	18.5

073010-2 Sub panel#

1

1			
H ₁	H ₂	W ₁	W ₂
5.3	5.5	18.3	18.2

073010-2 Sub panel#

2

1			
H ₁	H ₂	W ₁	W ₂
5.0	5.1	18.0	18.2

073010-2 Sub panel#

3

1			
H ₁	H ₂	W ₁	W ₂
4.9	5.6	17.1	17.6

073010-3 Sub panel#

1

1				2			
H ₁	H ₂	W ₁	W ₂	H ₁	H ₂	W ₁	W ₂
5.0	5.3	17.3	17.4	5.3	5.2	18.4	18.5

073010-3 Sub panel#

2

1				2			
H ₁	H ₂	W ₁	W ₂	H ₁	H ₂	W ₁	W ₂
5.3	6.0	18.2	18.1	5.1	5.6	17.9	17.9

073010-4 Sub panel#

1

1				2			
H ₁	H ₂	W ₁	W ₂	H ₁	H ₂	W ₁	W ₂
5.3	5.0	18.3	18.3	5.2	5.4	17.5	17.6

073010-4 Sub panel#

2

1				2			
H ₁	H ₂	W ₁	W ₂	H ₁	H ₂	W ₁	W ₂
5.1	5.2	18.2	17.7	4.9	5.1	17.5	17.3

073010-5 Sub panel#

1

1				2			
H ₁	H ₂	W ₁	W ₂	H ₁	H ₂	W ₁	W ₂
4.8	5.3	17.7	18.3	5.4	5.1	18.2	18.8

073010-5 Sub panel#

2

3				4			
H ₁	H ₂	W ₁	W ₂	H ₁	H ₂	W ₁	W ₂
5.0	5.3	18.6	18.4	5.0	5.3	18.4	17.4

073010-6 Sub panel#

1

1				2				3			
H ₁	H ₂	W ₁	W ₂	H ₁	H ₂	W ₁	W ₂	H ₁	H ₂	W ₁	W ₂
5.5	5.4	16.9	17.5	5.5	5.4	18.4	18.7	5.4	5.5	18.5	17.9

073010-6 Sub panel#

2

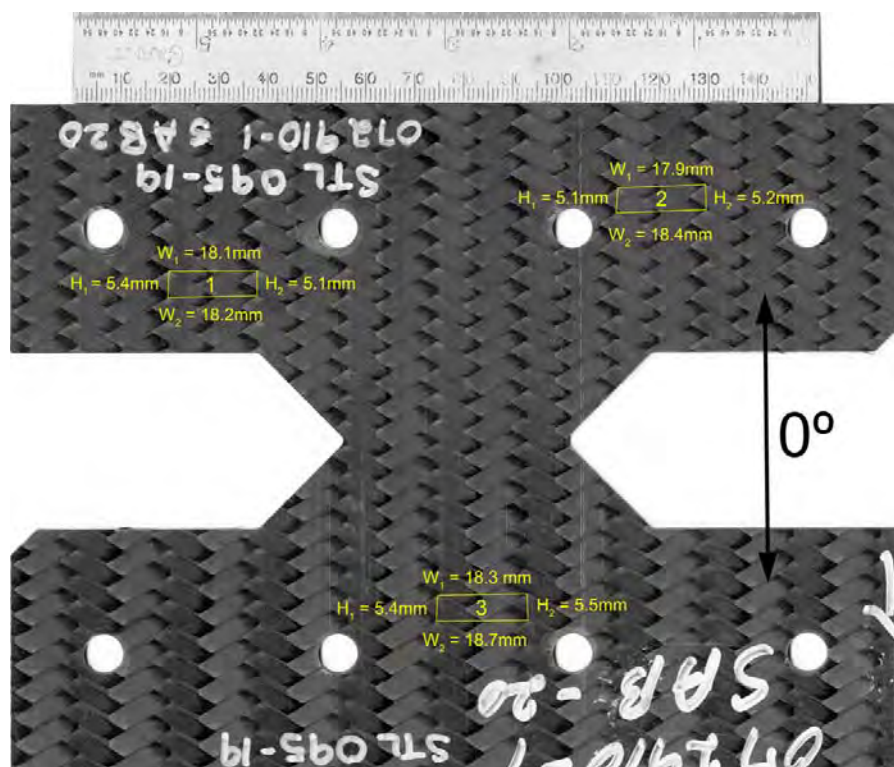
1				2			
H ₁	H ₂	W ₁	W ₂	H ₁	H ₂	W ₁	W ₂
5.1	5.3	17.7	17.6	5.4	5.3	17.2	17.3

080210-6 Sub panel#

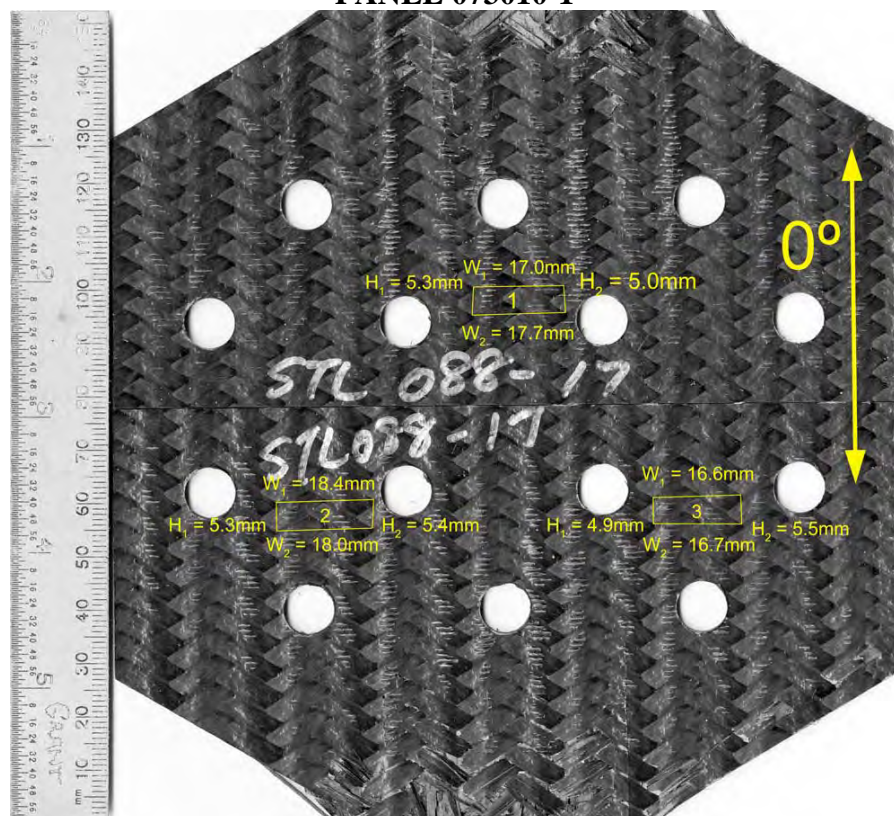
N/A

1				2				3			
H ₁	H ₂	W ₁	W ₂	H ₁	H ₂	W ₁	W ₂	H ₁	H ₂	W ₁	W ₂
4.9	5.0	17.5	18.4	4.8	5.0	18.2	18.2	5.4	5.3	18.0	18.3

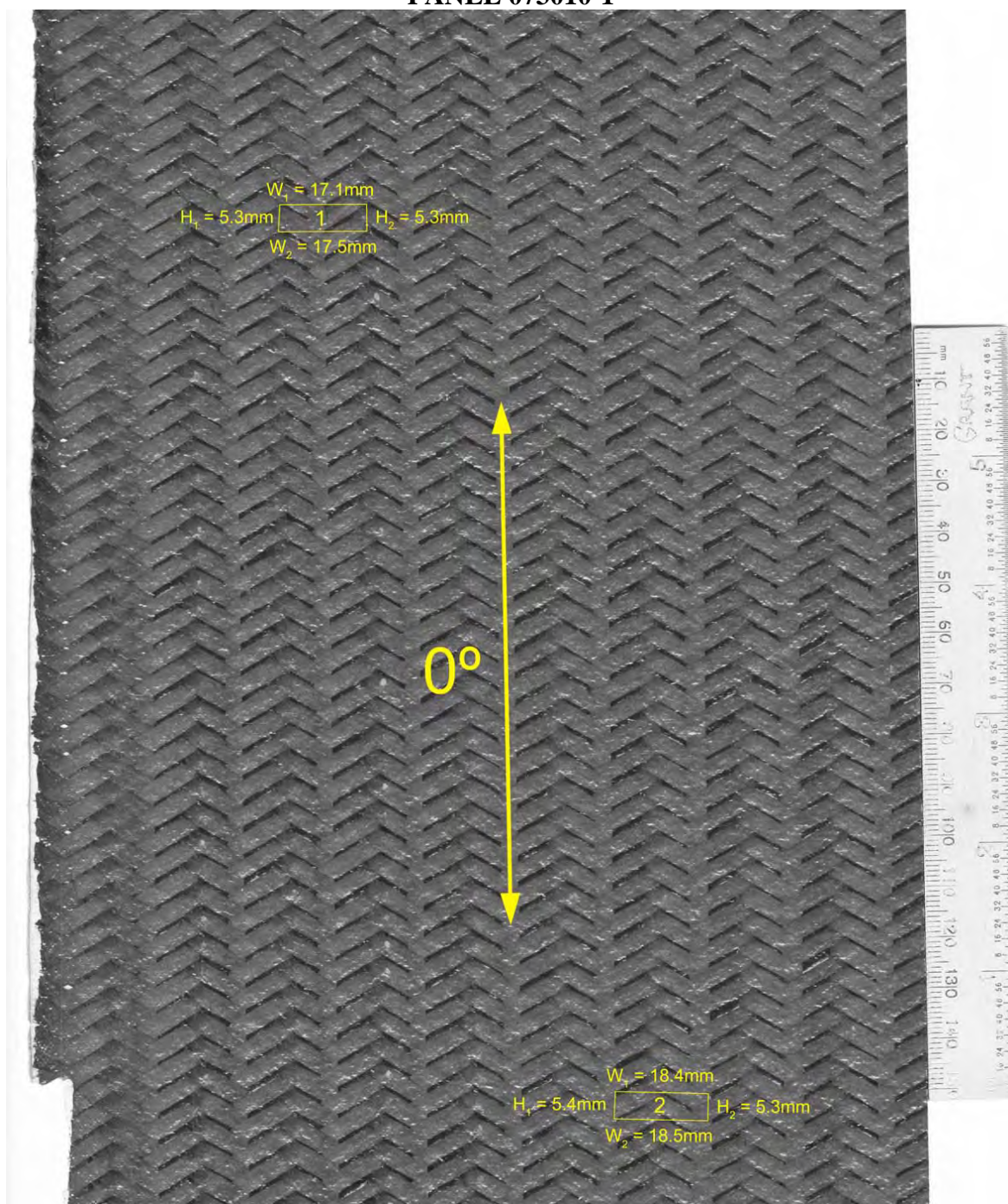
PANEL 072910-1



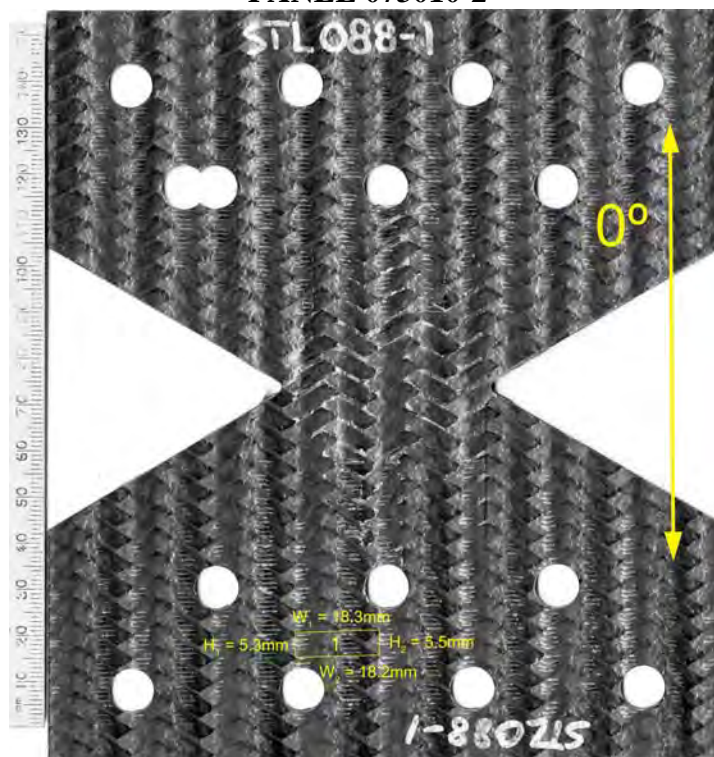
PANEL 073010-1



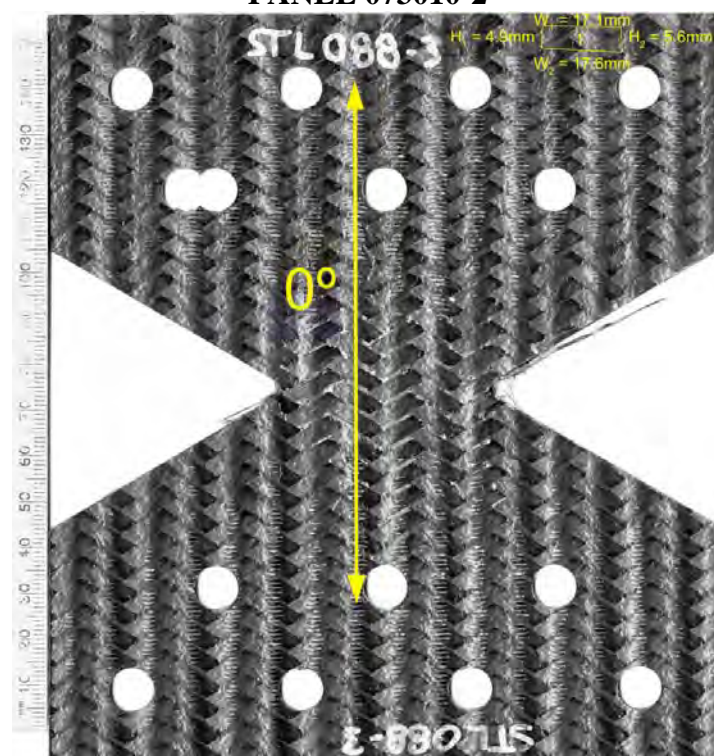
PANEL 073010-1



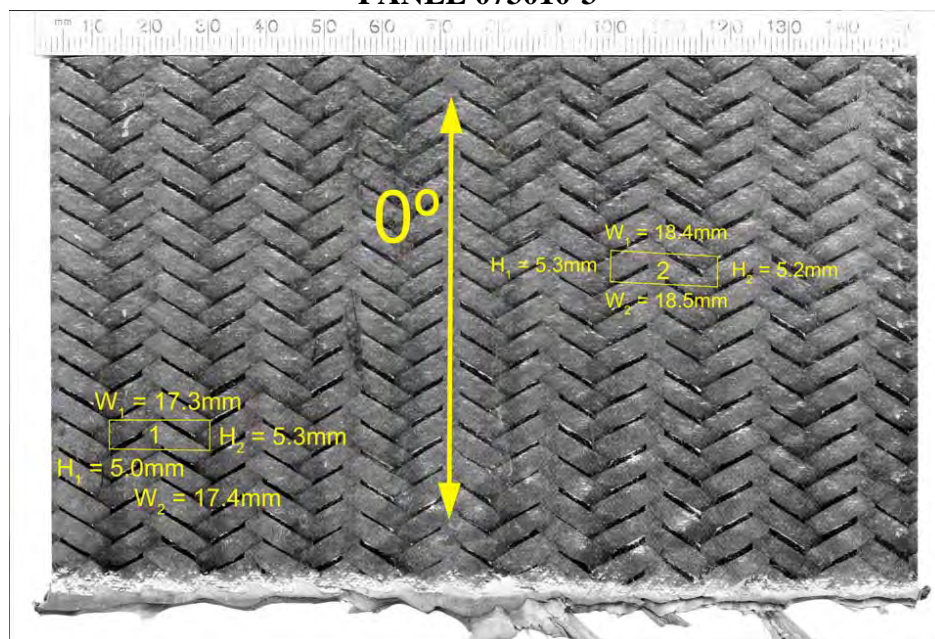
PANEL 073010-2



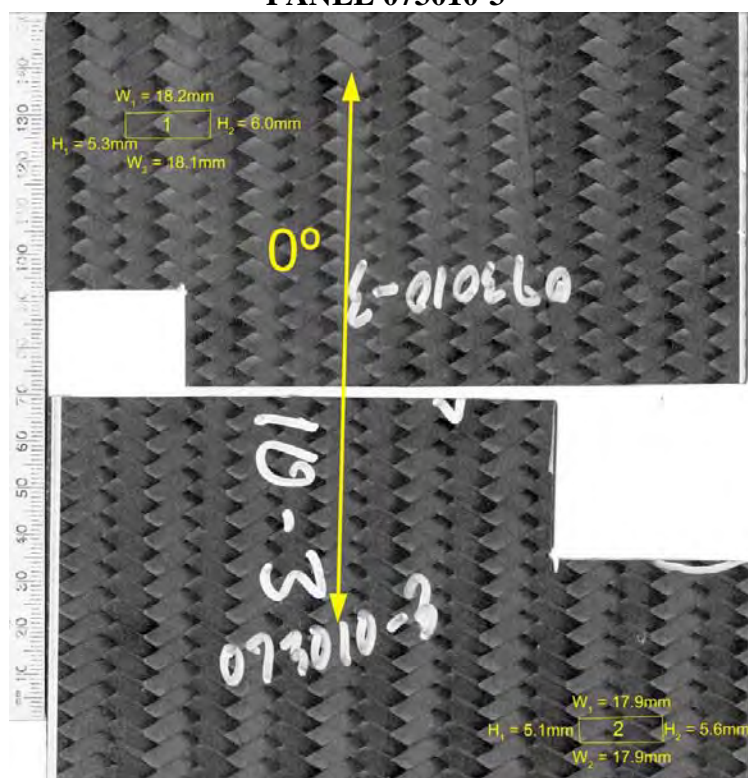
PANEL 073010-2



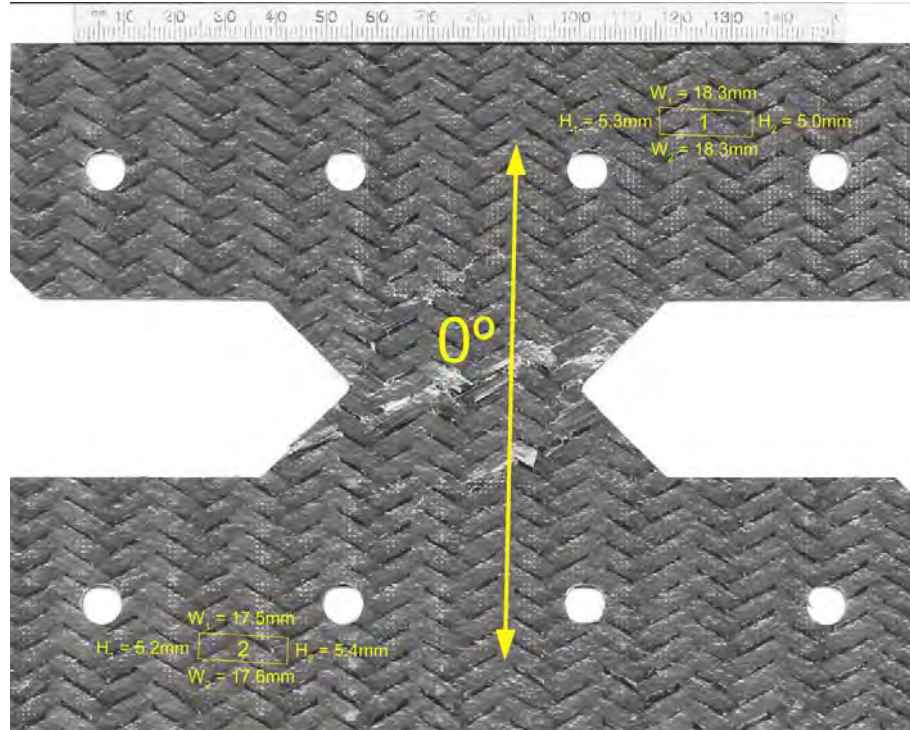
PANEL 073010-3



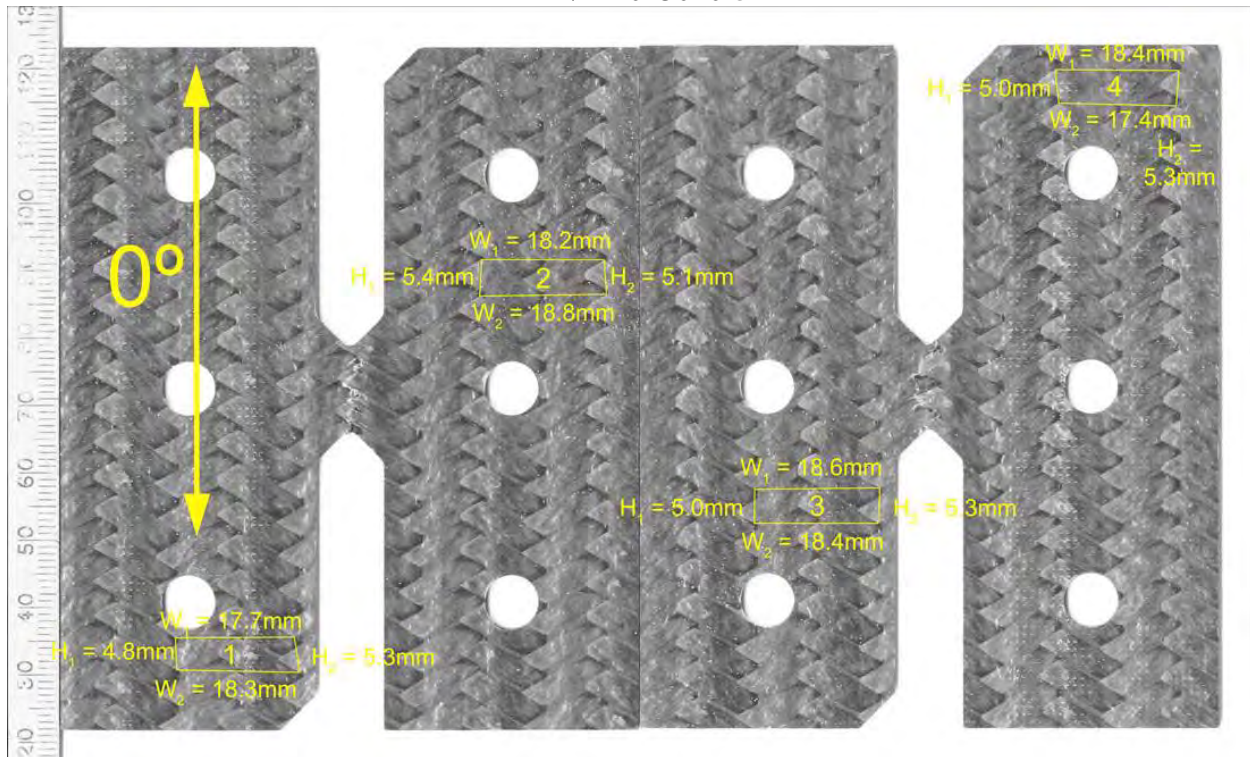
PANEL 073010-3



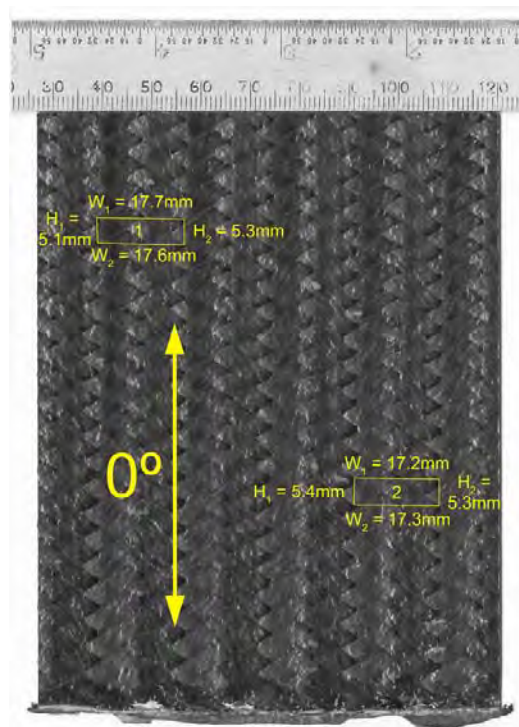
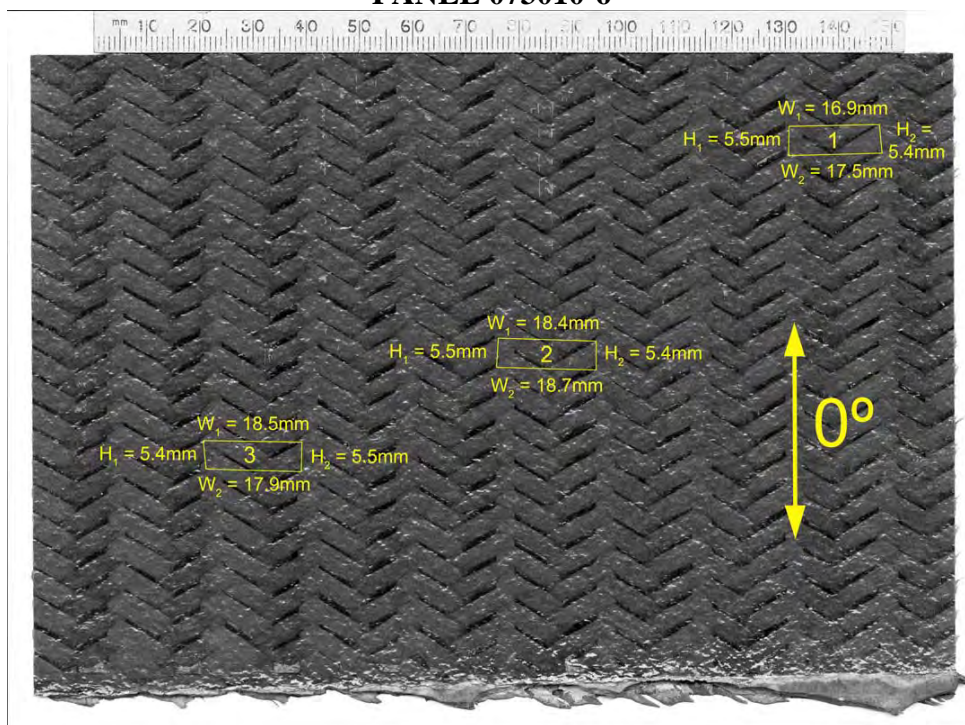
PANEL 073010-4



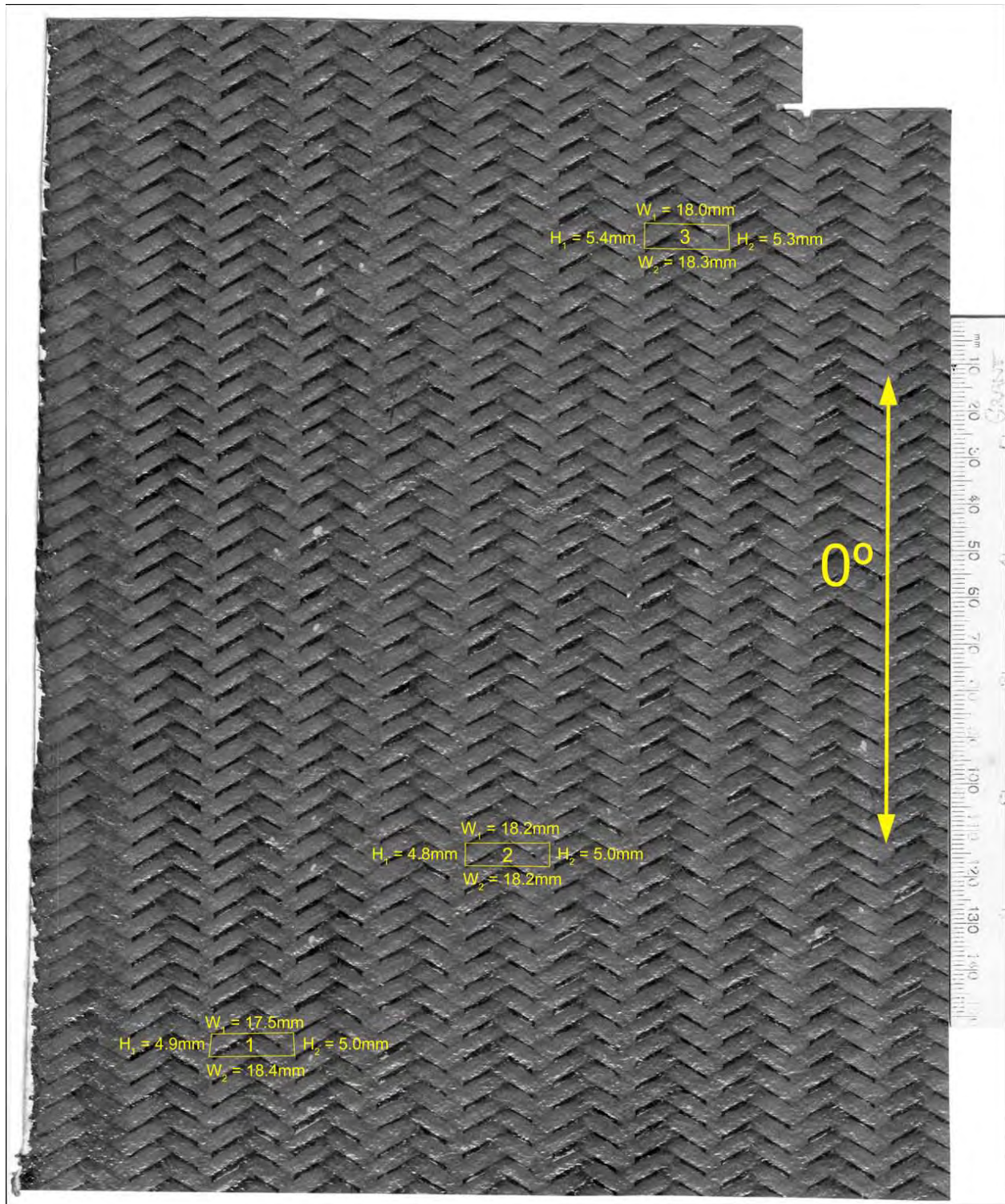
PANEL 073010-5



PANEL 073010-6



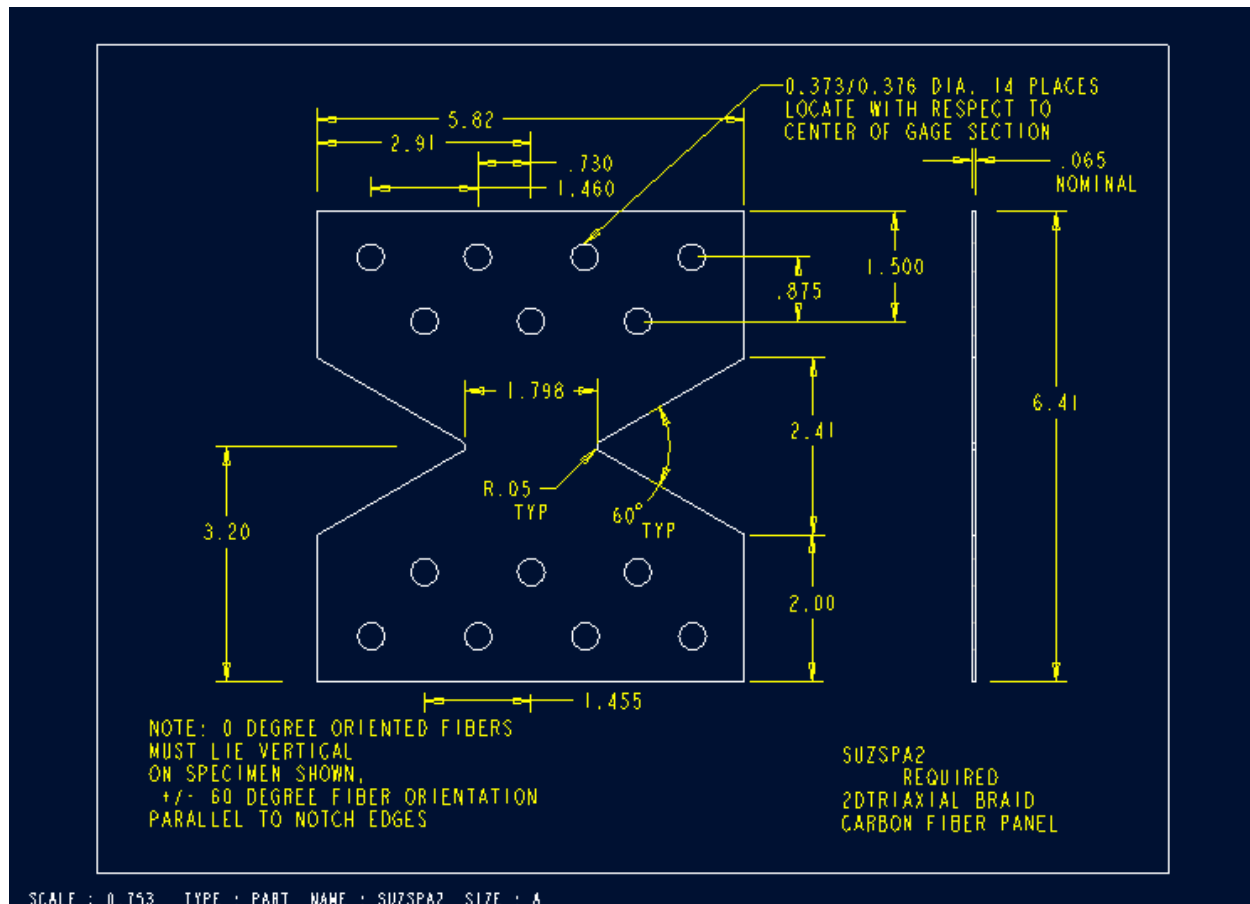
PANEL 080210-6



APPENDIX F
BOWTIE TENSILE SPECIMENS AND FIXTURE DRAWINGS

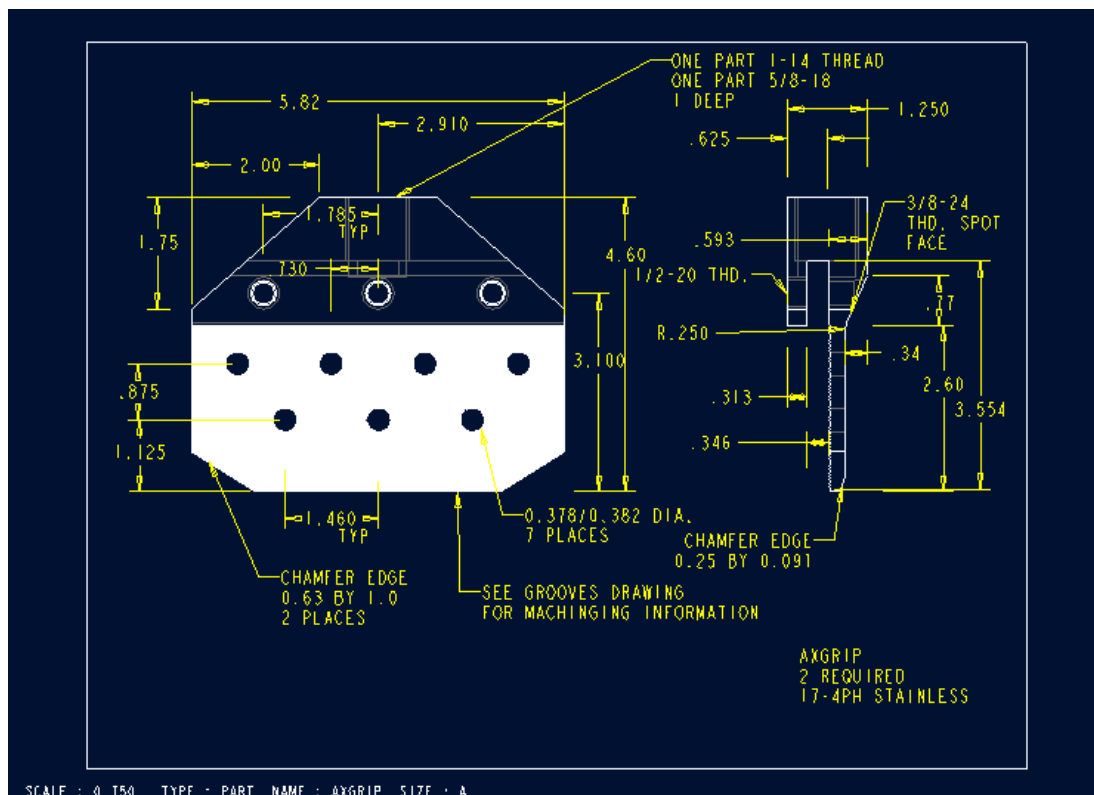
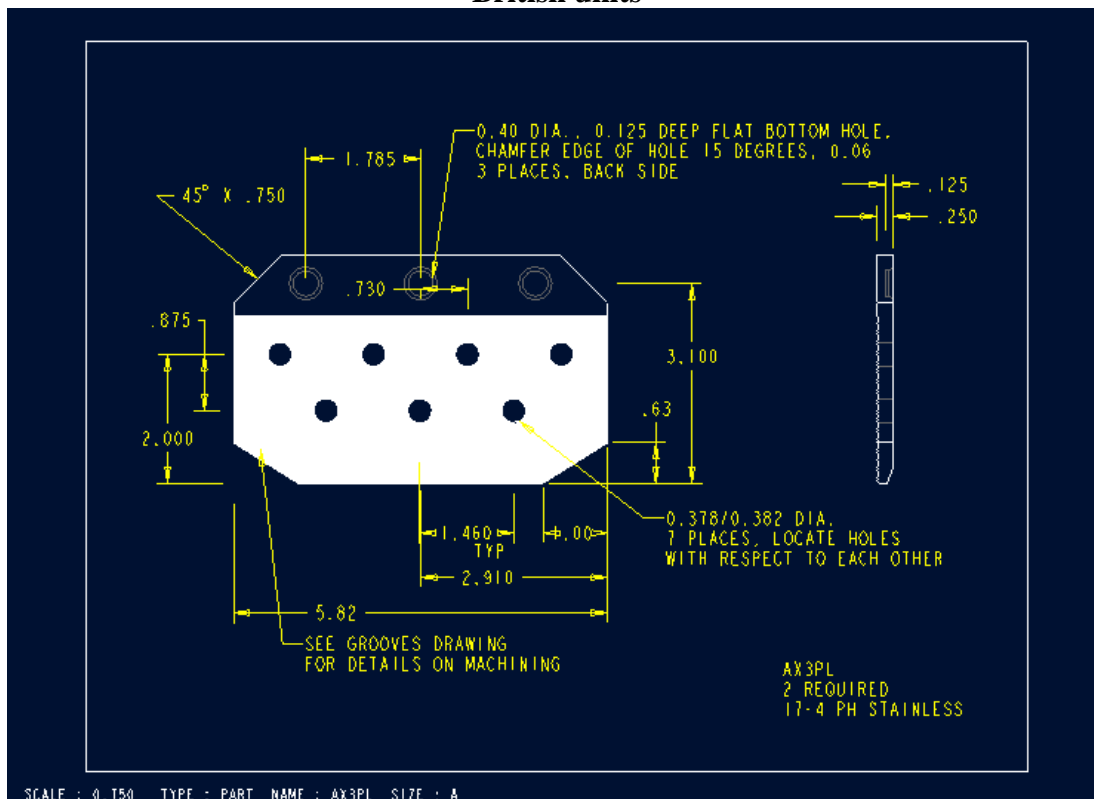
BOWTIE AXIAL TENSION SPECIMEN

British units



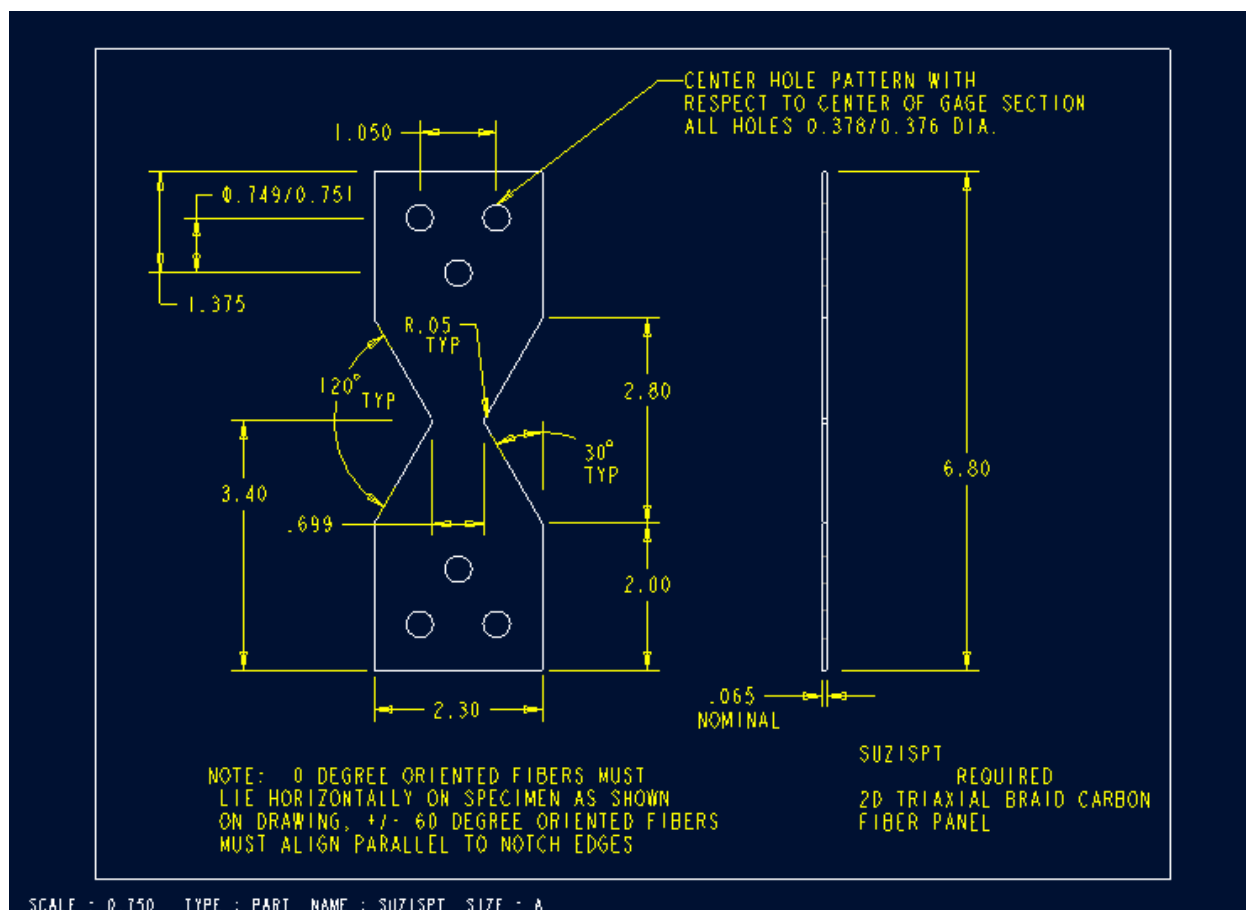
BOWTIE AXIAL TENSILE FIXTURE

British units



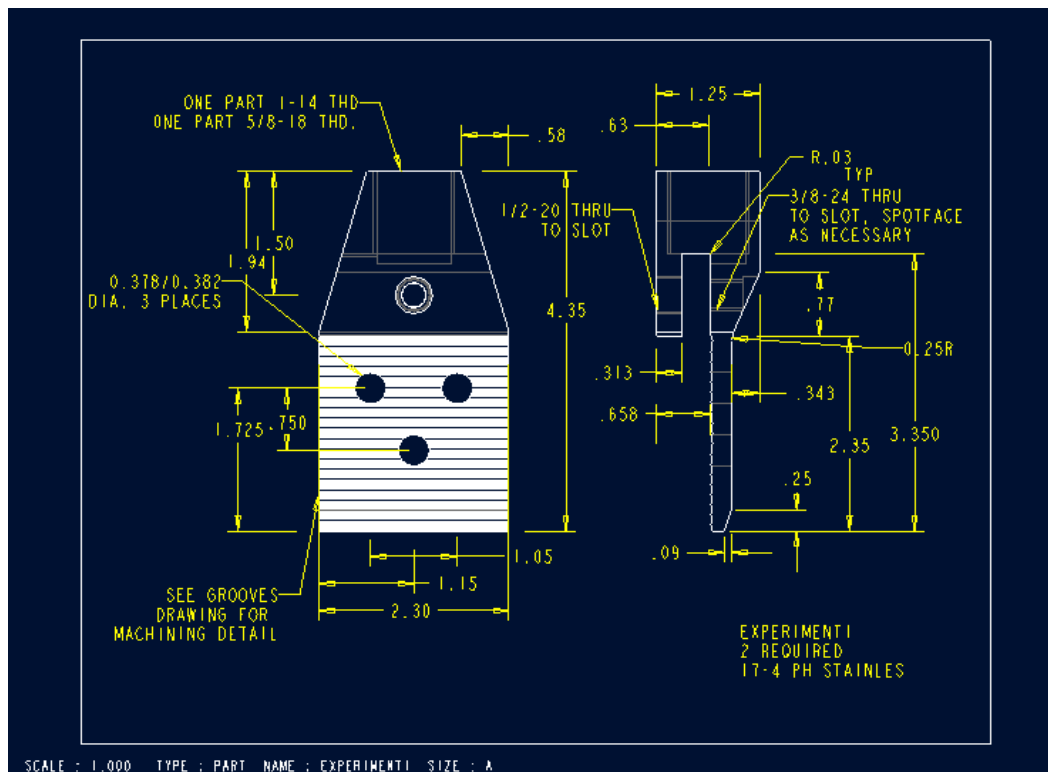
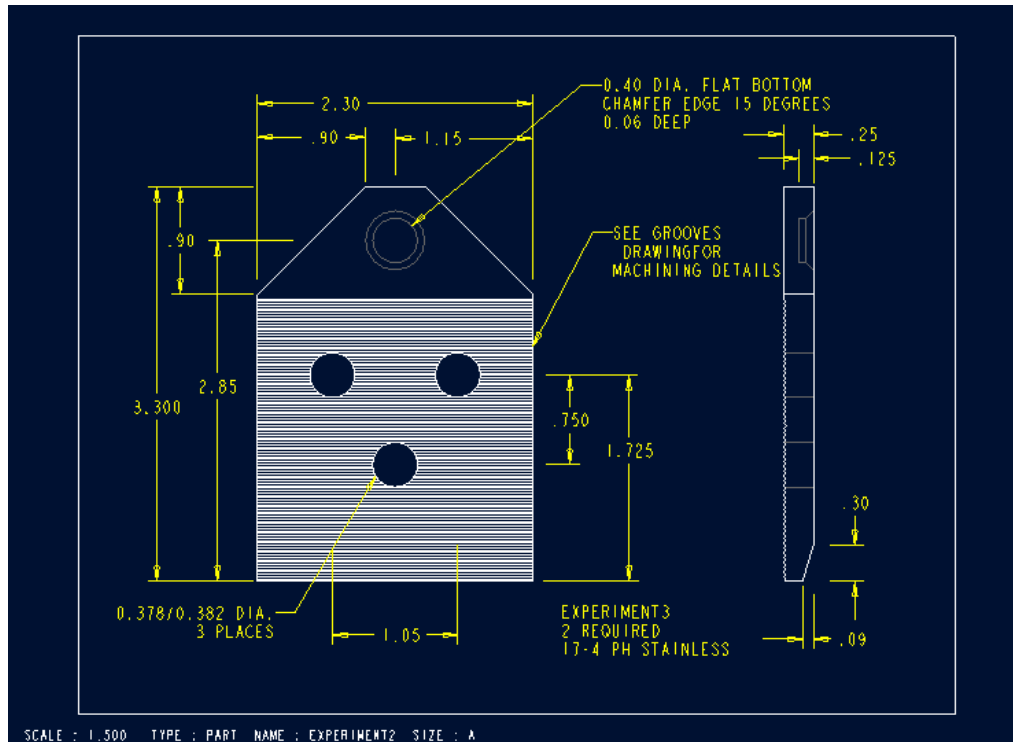
TRANSVERSE TENSILE BOWTIE SPECIMEN

British units



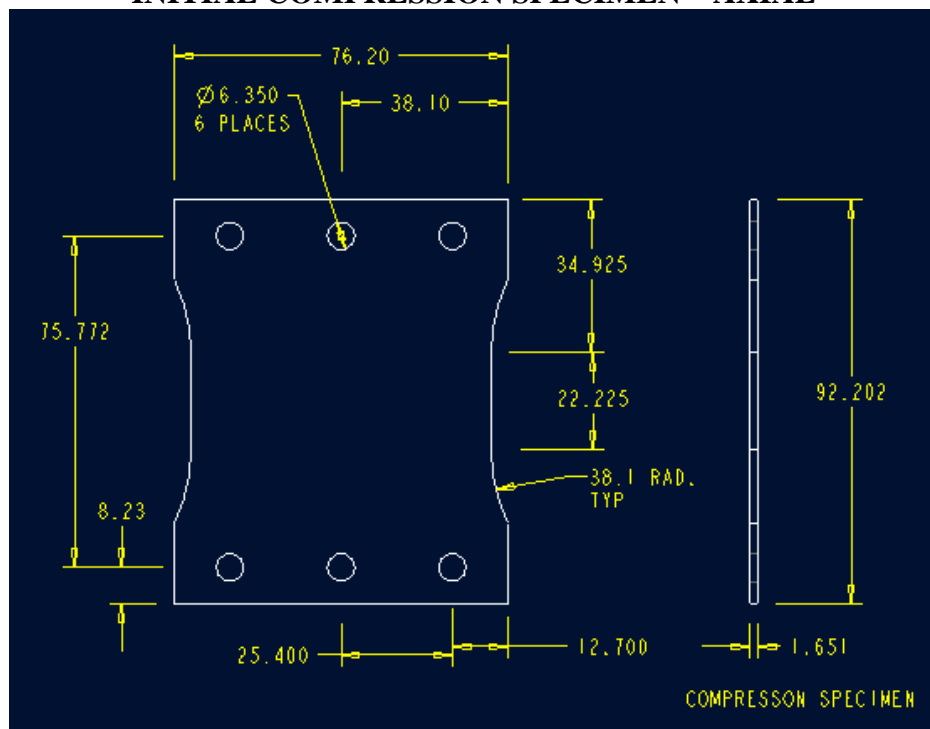
BOWTIE TRANSVERSE TENSILE FIXTURE

British units

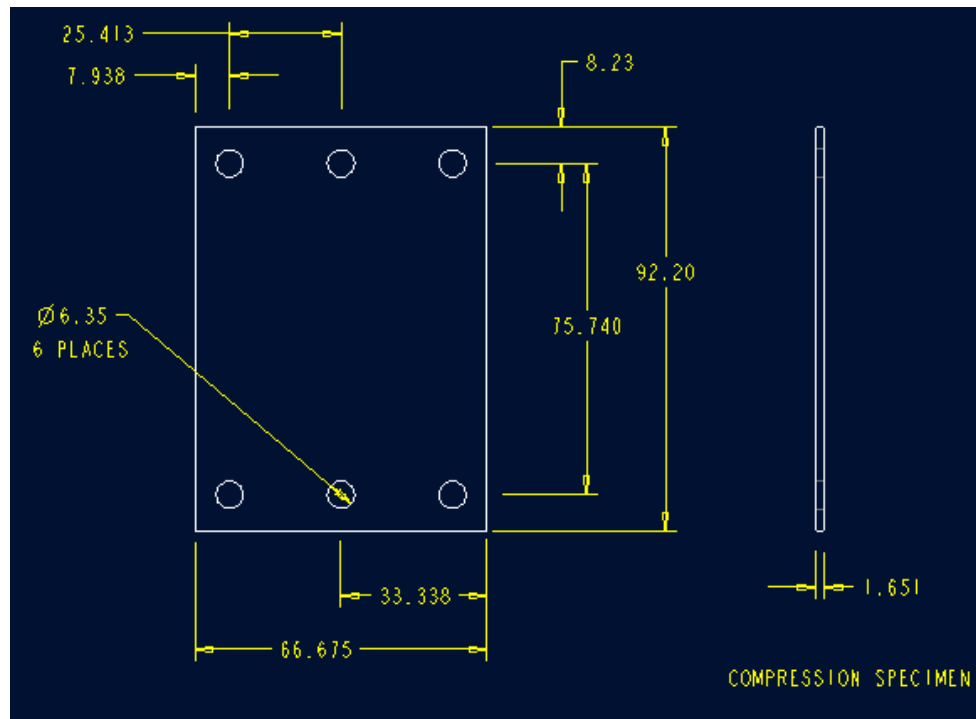


APPENDIX G
COMPRESSION SPECIMEN AND FIXTURE DRAWINGS

INITIAL COMPRESSION SPECIMEN – AXIAL

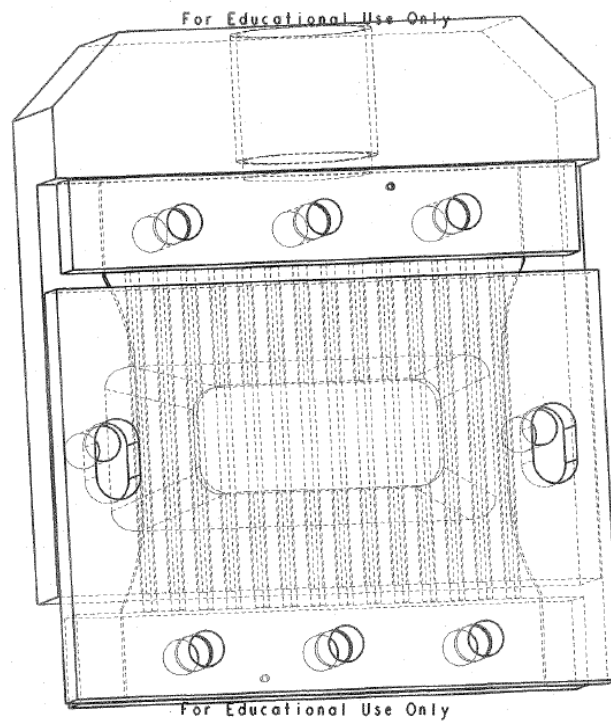
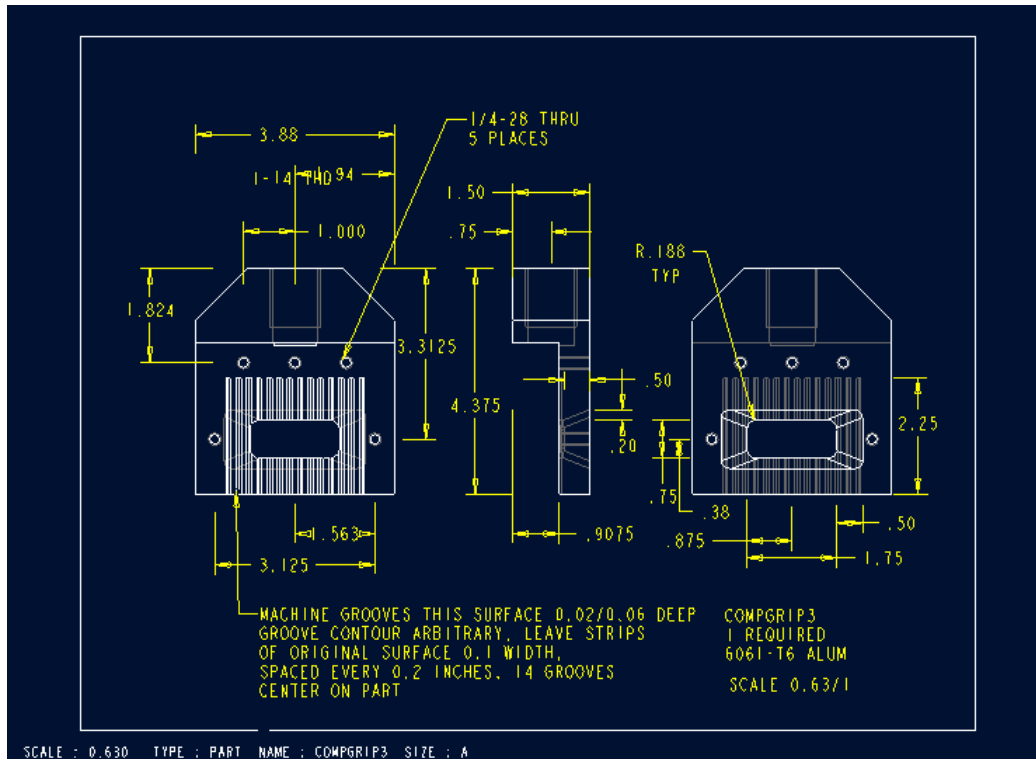


FINAL COMPRESSION SPECIMEN – BOTH ORIENTATIONS



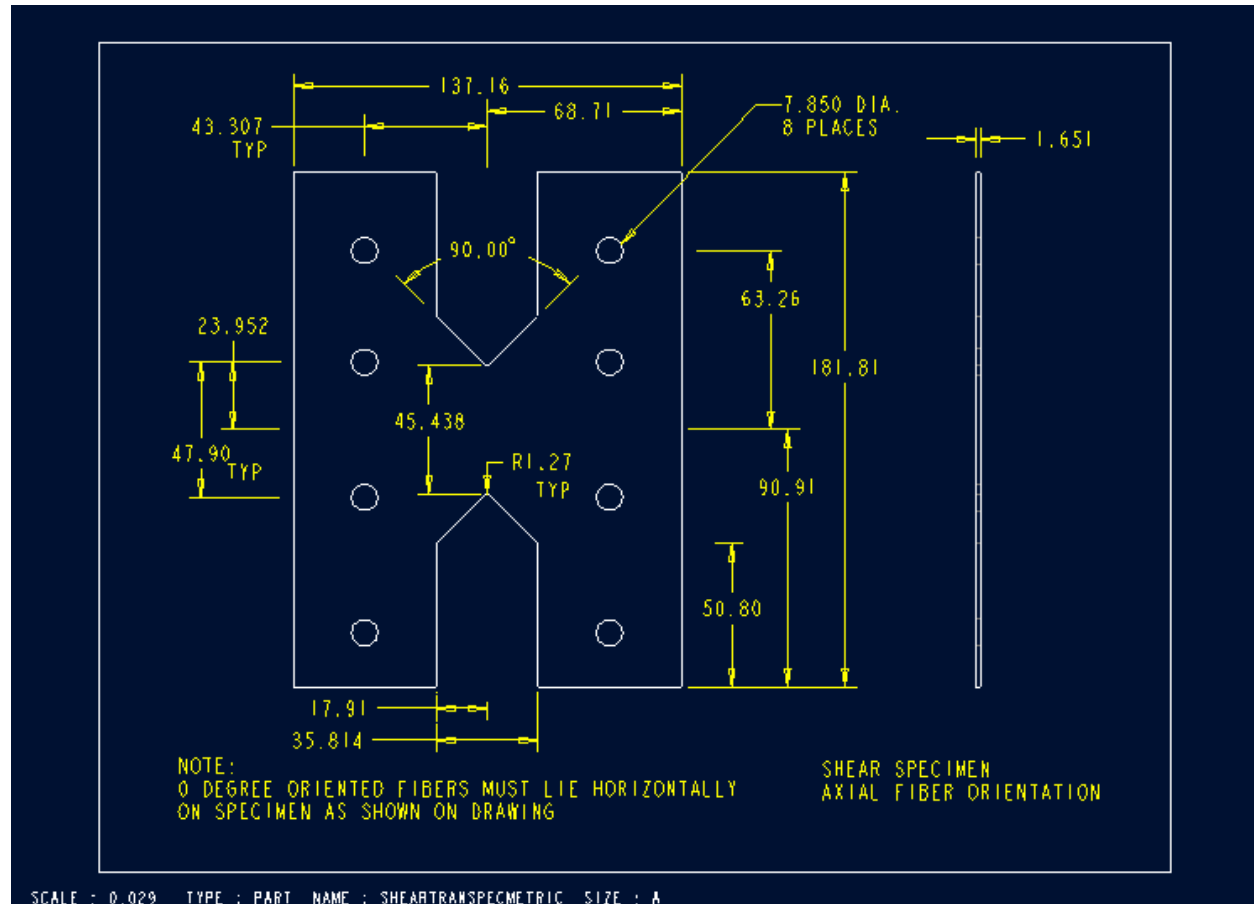
COMPRESSION FIXTURE – AXIAL ORIENTATION

British units

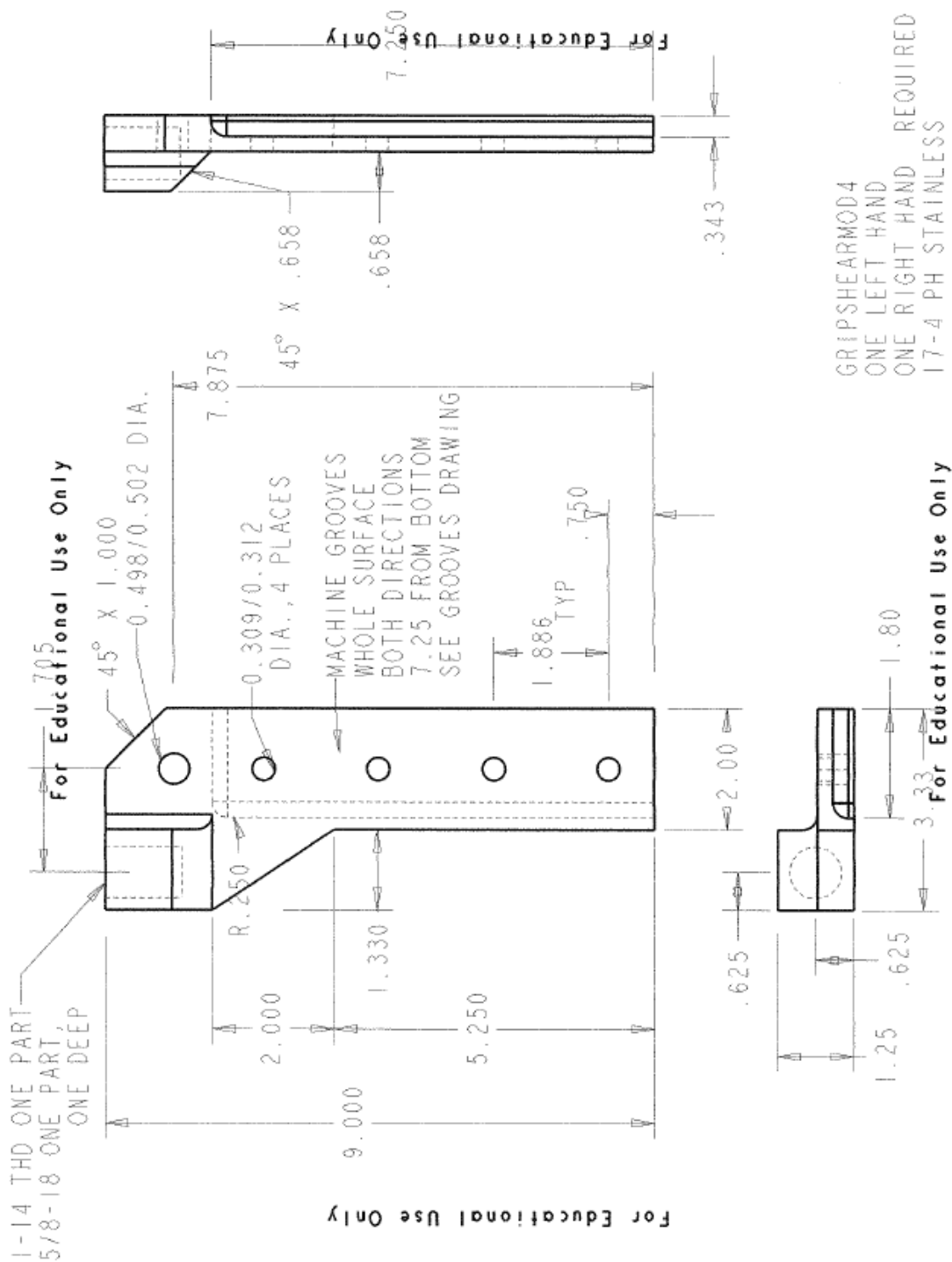


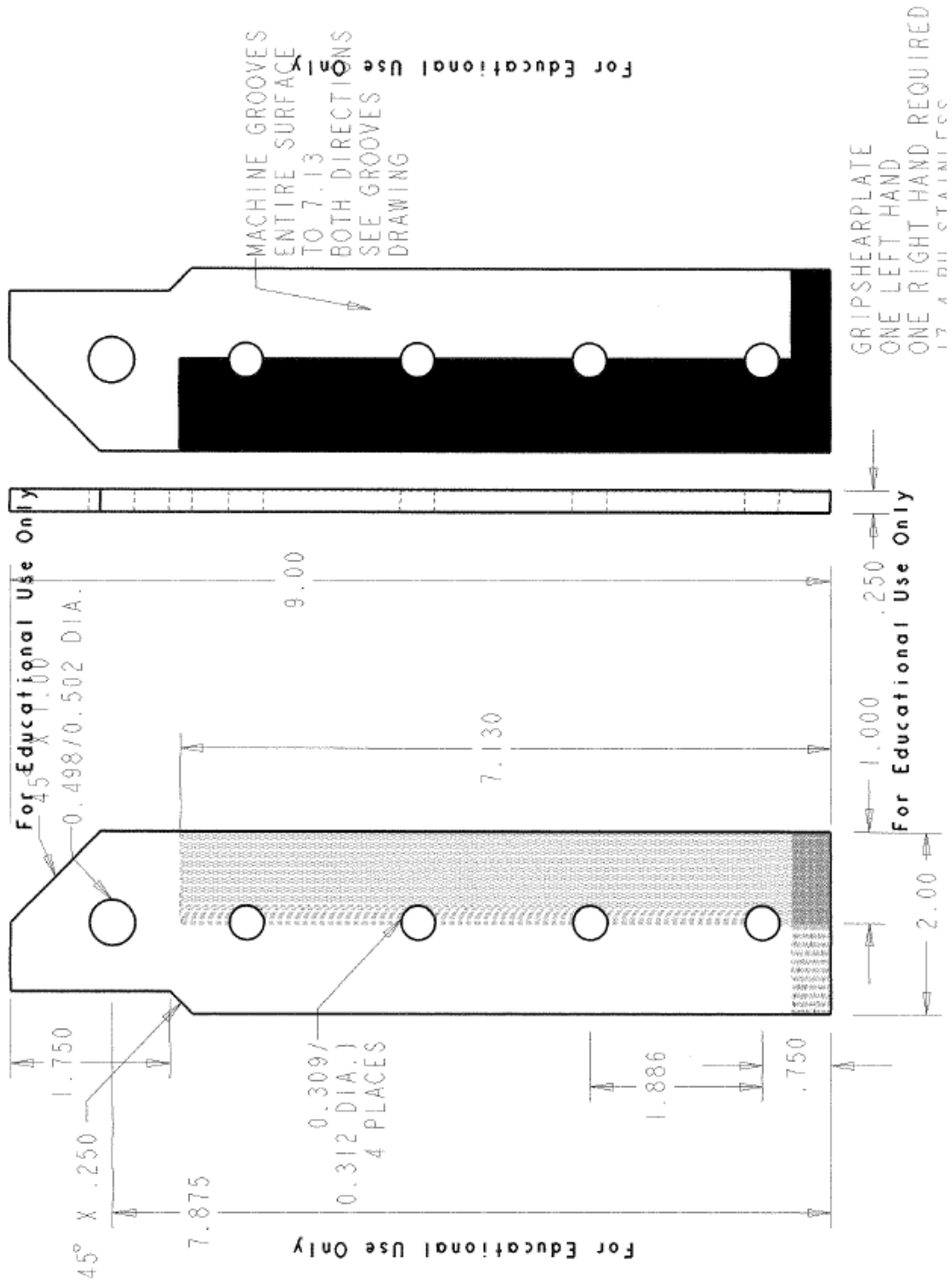
APPENDIX H
SHEAR SPECIMEN AND FIXTURE DRAWINGS

SHEAR SPECIMEN – AXIAL
Shearing across 0° fibers
Metric units



SHEAR FIXTURE – AXIAL ORIENTATION **British units**

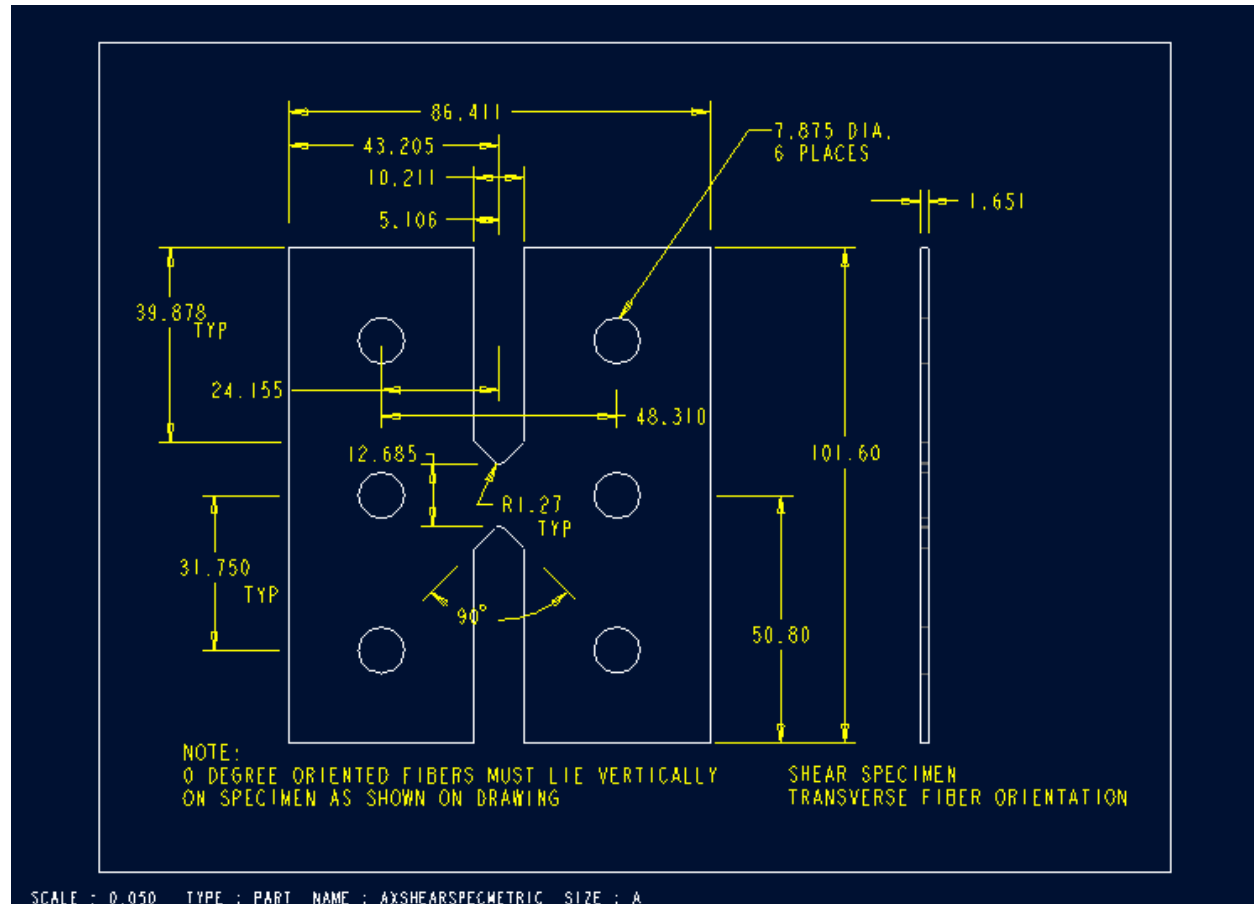




SHEAR SPECIMEN- TRANSVERSE ORIENTATION

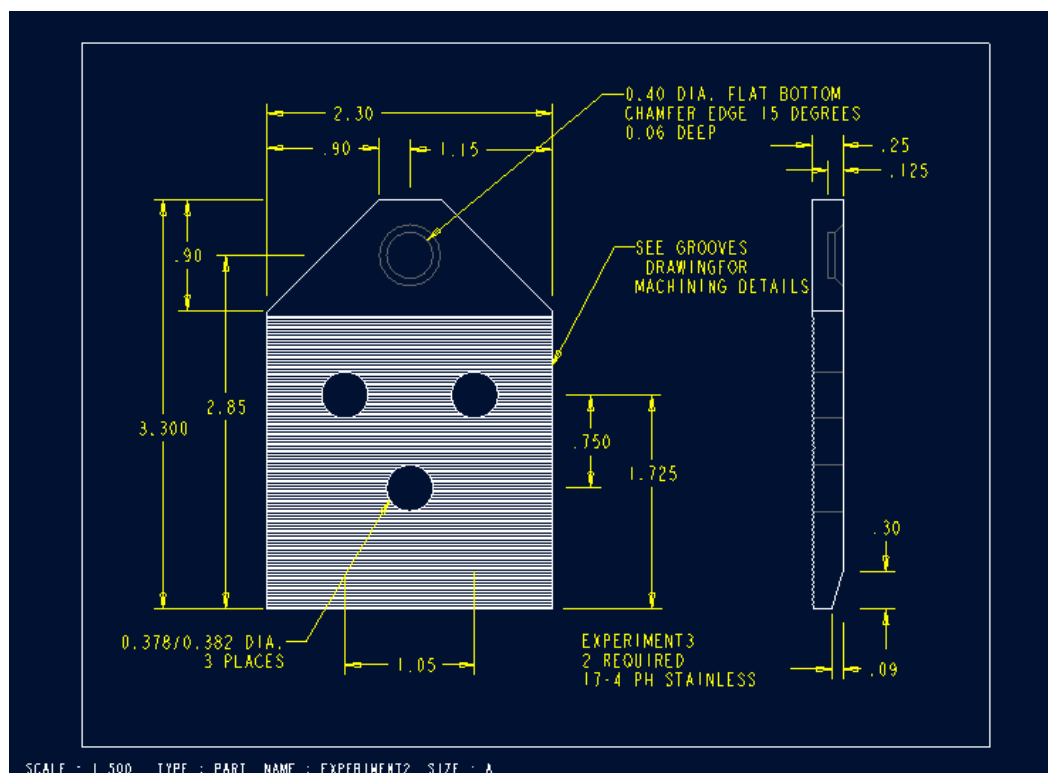
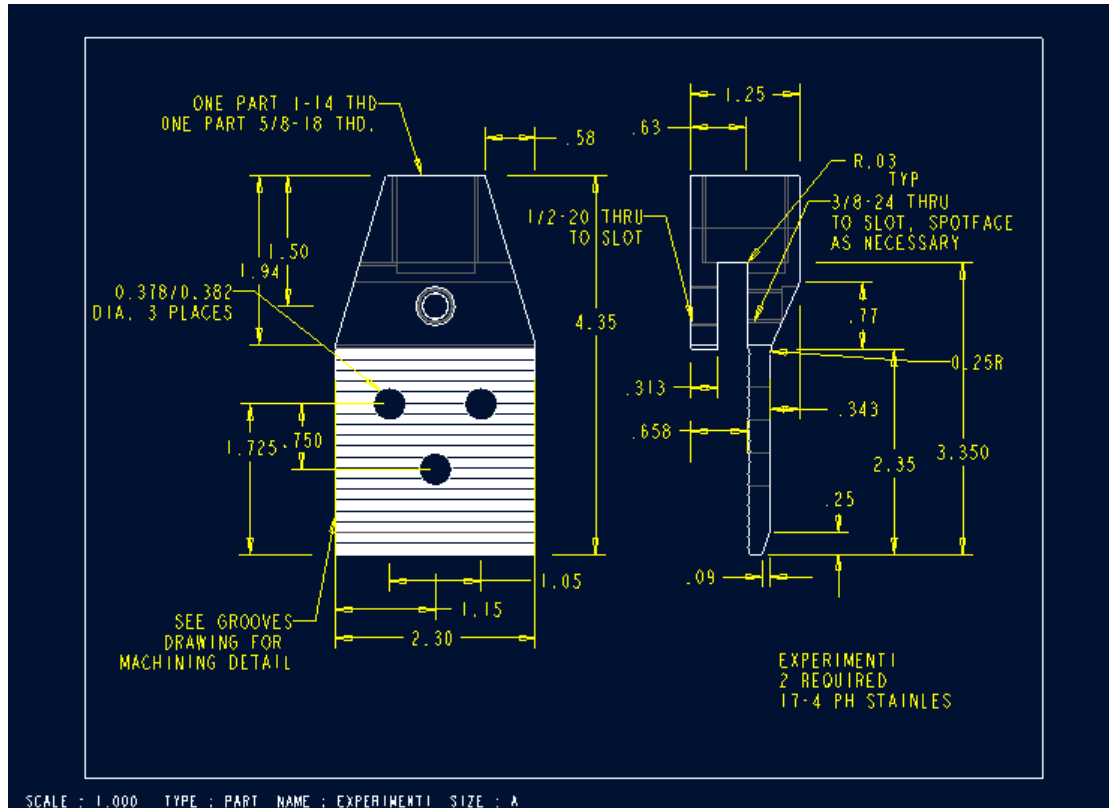
Shear across bias fibers

Metric Units



SHEAR FIXTURE- TRANSVERSE ORIENTATION

British Units



APPENDIX I
SME EQUIPMENT LIST AND CALIBRATIONS

LOW SPEED SYSTEM LVDT CALIBRATION

UDRI Structural Test Laboratory

443		Displacement Transducer Calibration Sheet		Cat./Item Number 02/59	
Machine Number	37	Calibration Date	12-Jan-10	Temp / Humidity	74F/39 %
Transducer Type/Capacity	LVDT/±2.5"		Transducer Conditioner	MTS 494.26 DUC 52-J1B AC	
Manufacturer	G.L. Collins	Serial Number	02050005	Readout	Station Manager
Model Number	A5453	p/n 390751-03L	Gage Factor	See range Mode: Gain/Delta K	Model # 494.04 Flextest 40
Serial Number	548262	Excitation Voltage	10	Serial #	02041419B
Allowable tolerance:	1.0% of Standard value	Condition Rec'd/Ret'd	Good/Good	Cal.Spec. #:	MTS494.26CalProc.
Comments: From CSC 140C Console Computer Dell 4FDZB1 RC10861					
Standard Data		lvdt1.scf		Range 1: 5 in. =V. full scale 10 Cal Value:	
				%Error	
				Pre-Cal Post-Cal	
Standard Used for This Range 17/24 Dial Indicator Std.		-6%		-3.2960	-3.285
Standard Type Starrett 25-5041		-60%		-3.0017	-3.000
Standard Capacity 0 - 5.000"		-50%		-2.4951	-2.500
Standard Serial Number 25-5041J		-40%		-1.9905	-2.000
Standard Calibration Data 23-Mar-09 wB&S Gage Blocks		-30%		-1.4918	-1.500
Standard Readout Meter Set F39		-20%		-.9944	-1.000
Standard Readout Meter S/N		-10%		-.4982	-.500
Comments Gain= .9025 x 1.27043 = 1.14656		0%		.0000	.000
DK= 1.0000 Phase= 60		10%		.4982	.500
Exc./AHz= 10.00/10kHz		20%		.9972	1.000
Polarity= normal ValvePol= invert.		30%		1.4964	1.500
ZF= 0.613		40%		1.9965	2.000
		50%		2.4992	2.500
		60%		2.9979	3.000
				3.3140	3.310
Standard Data		lvdt2.scf		Range 2: 2.5 in. =V. full scale 10 Cal Value:	
				%Error	
				Pre-Cal Post-Cal	
Standard Used for This Range 17/24		-100%		-2.50730	-2.50000
Standard Type Starrett 25-5041		-80%		-2.00090	-2.00000
Standard Capacity 0 - 5.000"		-60%		-1.49960	-1.50000
Standard Serial Number 25-5041J		-40%		-.99990	-1.00000
Standard Calibration Data 23-Mar-09 wB&S Gage Blocks		-20%		-.50090	-.50000
Standard Readout Meter Set F39		0%		.00000	.00000
Standard Readout Meter S/N		20%		.50010	.50000
Comments Gain= 1.7195 x 1.33114 = 2.28889		40%		.99990	1.00000
DK= 0.9966 Phase= 49		60%		1.49970	1.50000
Exc./AHz= 10.00/10kHz ZF= 0		80%		2.00020	2.00000
Polarity= normal ValvePol= invert.		100%		2.50330	2.50000
Standard Data		lvdt3.scf		Range 3: 1 in. =V. full scale 10 Cal Value:	
				%Error	
				Pre-Cal Post-Cal	
Standard Used for This Range 17/24		-100%		-1.0010	-1.000
Standard Type Starrett 25-5041		-80%		-.8012	-.800
Standard Capacity 0 - 5.000"		-60%		-.6017	-.600
Standard Serial Number 25-5041J		-40%		-.4016	-.400
Standard Calibration Data 23-Mar-09 wB&S Gage Blocks		-20%		-.2017	-.200
Standard Readout Meter Set F39		0%		.0000	.000
Standard Readout Meter S/N		20%		.2003	.200
Comments Gain= 3.249 x 1.76449 = 5.73281		40%		.4002	.400
DK= 0.9959 Phase= 49		60%		.6004	.600
Exc./AHz= 10.00/10kHz ZF= 0		80%		.8001	.800
Polarity= normal ValvePol= invert.		100%		1.0000	1.000
Standard Data		lvdt4.scf		Range 4: 0.5 in. =V. full scale 10 Cal Value: NA	
				%Error	
				Pre-Cal Post-Cal	
Standard Used for This Range 17/24 Dial Indicator Std.		-100%		-.49913	-.5000
Standard Type Starrett25-5041		-80%		-.39974	-.4000
Standard Capacity .000 - 5.000		-60%		-.30046	-.3000
Standard Serial Number 25-5041J		-40%		-.20055	-.2000
Standard Calibration Data 23-Mar-09 wB&S Gage Blocks		-20%		-.10016	-.1000
Standard Readout Meter Set F39		0%		.00000	.0000
Standard Readout Meter S/N		20%		.09978	.1000
Comments Gain= 6.2320 x 1.83981 = 11.4675		40%		.20023	.2000
DK= 0.9992 Phase= 49		60%		.30025	.3000
Exc./AHz= 10.00/10kHz ZF= 0		80%		.40015	.4000
Polarity= normal ValvePol= invert.		100%		.49987	.5000
Notes: Only range 1 was previously calibrated by MTS.					
Restrictions: For UDRI use only.					
Analysis: Range was within 1% required tolerance.					

LOW SPEED SYSTEM LOAD CELL CALIBRATION **UDRI Structural Test Laboratory**

444

Load Transducer Calibration Sheet

Cat./Item Number 03/53

Machine Number	37	Calibration Date	12-Jan-10	Temp / Humidity	74F/39%	Performed by	R.Glett
Transducer Type/Capacity	Load cell/+22000#		Transducer Conditioner	MTS494.26 DUC DC FlexTest 40		Readout	Flextest 40
Manufacturer	MTS		Serial Number	02050005		Mfg	MTS
Model Number	661.20E - 03		Gage Factor	See range Gain/Delta K Mode		Model #	494.04
Serial Number	V90922		Excitation Voltage	10.000 Vdc.		Serial #	02041419B
Allowable tolerance:	1% of Standard value		Condition Rec'd/Ret'd	good		Cal.Spec. #:	MTS494.26 dc cond.
Comments	FromCSC 140C	Console	Computer	Dell 4FDZ2B1	RC10861	Cal. Procedure	
Standard Data	Range: 20000 lbs. (1) =V. full scale 10 Cal Value:						
Std. Shunt 60kOhms	-60570	% of Full Scale		Transducer Readings		Standard Readings	
60270						%Error	
Standard Used for This Range	Load cell std. 17/06		Pre-Cal	Post-Cal	Applied	Reading	Pre-Cal Post-Cal
Standard Type	Eaton Lebow 3156-100k		-100%	-20028	-20028	-20000	-50082.3 0.14 0.14
Standard Capacity	+100000#		-80%	-16022	-16022	-16000	-40081.8 0.14 0.14
Standard Serial Number	2905		-60%	-12013	-12013	-12000	-30074.7 0.11 0.11
Standard Calibration Data	12-Jan-09 Morehouse Inst.		-40%	-8005	-8005	-8000	-20061.0 0.06 0.06
Standard Readout Meter	Eaton Lebow 7530		-20%	-3986	-3986	-4000	-10040.8 -0.35 -0.35
Standard Readout Meter S/N	1924		0%	0	0	0	0.0 #DIV/0! #DIV/0!
Comments	Gain= 285.98 x	1.75579 =	502.12205	20%	3990	3990	4000 9980.6 -0.25 -0.25
ValvePol= Invert	Polarity=	nomial		40%	7987	7987	8000 19971.5 -0.16 -0.16
Delta K= 0.9991	Zc=	-0.0061		60%	11991	11991	12000 29964.7 -0.08 -0.08
Excit.= 10.000	Zf=	0.000		80%	15990	15990	16000 39960.1 -0.06 -0.06
				100%	19990	19990	20000 49957.7 -0.05 -0.05
Standard Data	Range: 10000 lbs. (2) =V. full scale 10 Cal Value:						
		% of Full Scale		Transducer Readings		Standard Readings	
						%Error	
Standard Used for This Range	Load cell std. 17/01		Pre-Cal	Post-Cal	Applied	Reading	Pre-Cal Post-Cal
Standard Type	Lebow 3157		-100%	-10008	-10008	-10000	-10025.6 0.08 0.08
Standard Capacity	+10000Lb.		-80%	-8003	-8003	-8000	-8019.9 0.04 0.04
Standard Serial Number	696		-60%	-6000	-6000	-6000	-6014.4 0.00 0.00
Standard Calibration Data	21-Nov-07 Morehouse Inst.		-40%	-3998	-3998	-4000	-4009.0 -0.05 -0.05
Standard Readout Meter	Doric DS300-T2-07-08-21		-20%	-1999	-1999	-2000	-2003.8 -0.05 -0.05
Standard Readout Meter S/N	60407		0%	0	0	0	0.0 #DIV/0! #DIV/0!
Comments	Gain= 540.36 x	1.85918 =	1004.6267	20%	1996	1996	2000 1999.8 -0.20 -0.20
ValvePol= Invert	Polarity=	normal		40%	3994	3994	4000 4001.6 -0.15 -0.15
Delta K= 1.0010				60%	5996	5996	6000 6005.2 -0.07 -0.07
Excit.= 10	Zf=	0		80%	7999	7999	8000 8010.6 -0.01 -0.01
				100%	10001	10001	10000 10017.8 0.01 0.01
Standard Data	Range: 5000 lbs. (3) =V. full scale 10 Cal Value:						
		% of Full Scale		Transducer Readings		Standard Readings	
						%Error	
Standard Used for This Range	Load cell std. 17/01		Pre-Cal	Post-Cal	Applied	Reading	Pre-Cal Post-Cal
Standard Type	Lebow 3157		-100%	-5002	-5002	-5000	-5011.7 0.04 0.04
Standard Capacity	+10000Lb.		-80%	-4000	-4000	-4000	-4009.0 0.00 0.00
Standard Serial Number	696		-60%	-2999	-2999	-3000	-3006.4 -0.03 -0.03
Standard Calibration Data	21-Nov-07 Morehouse Inst.		-40%	-1998	-1998	-2000	-2003.8 -0.10 -0.10
Standard Readout Meter	Doric DS300-T2-07-08-21		-20%	-996	-996	-1000	-1001.2 -0.40 -0.40
Standard Readout Meter S/N	60407		0%	0	0	0	0.0 #DIV/0! #DIV/0!
Comments	Gain= 1036.48 x	1.93694 =	2007.6022	20%	997	997	1000 999.6 -0.30 -0.30
ValvePol= Invert	Polarity=	normal		40%	1997	1997	2000 1999.8 -0.15 -0.15
Delta K= 1.0027				60%	2997	2997	3000 3000.5 -0.10 -0.10
Excit.= 10	Zf=	0		80%	3999	3999	4000 4001.6 -0.02 -0.02
				100%	5001	5001	5000 5003.2 0.02 0.02
Standard Data	Range: 2500 lbs. (4) =V. full scale 10 Cal Value:						
		% of Full Scale		Transducer Readings		Standard Readings	
						%Error	
Standard Used for This Range	Load cell std. 17/26		Pre-Cal	Post-Cal	Applied	Reading	Pre-Cal Post-Cal
Standard Type	Sensotec 47/8587-07-01		-100%	-2511.3	-2511.3	-2500	-16.590 0.45 0.45
Standard Capacity	3000 #		-80%	-2009.3	-2009.3	-2000	-13.264 0.47 0.47
Standard Serial Number	747474		-60%	-1507.6	-1507.6	-1500	-9.942 0.51 0.51
Standard Calibration Data	11-Sep-08 Morehouse Inst.		-40%	-1004.3	-1004.3	-1000	-6.625 0.43 0.43
Standard Readout Meter	HP 34401A		-20%	-500.3	-500.3	-500	-3.311 0.06 0.06
Standard Readout Meter S/N	3146A33095		0%	0.0	0.0	0	0.000 #DIV/0! #DIV/0!
Comments	Gain= 1805.95 x	2.22901 =	4025.4896	20%	499.5	499.5	500 3.307 -0.10 -0.10
ValvePol= Invert	Polarity=	normal Filter		40%	1000.2	1000.2	1000 6.611 0.02 0.02
Delta K= 1.0024	Zc=			60%	1498.7	1498.7	1500 9.915 -0.09 -0.09
Excit.= 10	Zf=	0		80%	1999.9	1999.9	2000 13.220 0.00 0.00
				100%	2500.3	2500.3	2500 16.524 0.01 0.01

Notes: First Cal in our lab

Restrictions: Reproducible for UDRI use only.

Analysis: Within the 1% required tolerance.

LOW SPEED SYSTEM ALIGNMENT

Alignment for George Washington University

Gages Used : CEA-06-125UW-120

Gage Factor : 2.095

	Orientation 1 Front				Orientation 2 Back				Orientation 3 BFF				Orientation 4 BBF		
Load	G1	G2	G3		G1	G2	G3		G1	G2	G3		G1	G2	G3
0	0	0	0		0	0	0		0	0	0		0	0	0
500	425	420	473		409	429	470		415	399	466		432	401	465
1000	880	855	927		863	869	946		869	841	935		871	835	927
1500	1312	1301	1385		1328	1315	1401		1320	1290	1399		1337	1296	1409
2000	1755	1745	1805		1767	1750	1860		1770	1739	1853		1775	1750	1857
2500	2219	2166	2290		2210	2192	2309		2207	2176	2305		2227	2148	2297
3000	2670	2610	2728		2667	2626	2740		2647	2621	2750		2669	2607	2738
3500	3125	3015	3183		3119	3075	3196		3093	3063	3198		3106	3070	3190
4000	3566	3473	3638		3554	3508	3655		3540	3502	3635		3563	3506	3630
Sum	15952	15585	16429		15917	15764	16577		15861	15631	16541		15980	15613	16513
E _{ave}	16099				16209				16144				16155		
B _{y%}	-2.05				-2.27				-2.46				-2.22		
B _{z%}	-3.04				-1.26				-1.9				-3.03		

LOW SPEED SYSTEM EQUIPMENT LIST- SETUP 1

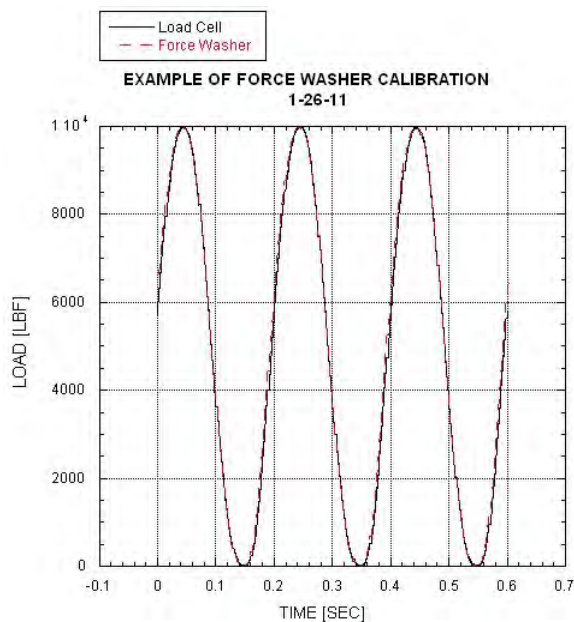
Testing Equipment Information	
GeorgeWashingtonUniv_ DIC	4238020003
Testing laboratory: KL-22	Point of contact: John Chumack
Telephone/Fax: 937-229-4426	Address:
Test machine information	
Manufacturer: MTS 810 2 Poster Frame #37	Manufacturer's reference number: Flex Test Station # 37
Maximum capacity (test machine): 20 Kip	Machine type (servo-hydraulic / servo-electric): S-H
Maximum capacity (load cell): 20K range	Method of data acquisition: Flex Test Peak Detectors_DIC
Range load cell used: LC #90922 = 22kip Range,	Filtering (if applicable):
Comments: Load Cell Sn#90922, Calibration date 14Jan10 - shunt cal check 03Sept10	
Flex Test Program Controller Software	
20kip 6" stroke LVDT sn#548262 Calibrated flex test Displacement .5 inch range	
Gripping information	
Type of grip: MTS Hydraulic Grip	Type of loading (tab, shoulder): Tab grip
Manufacturer: MTS 647	Method of specimen alignment in grip: MTS 609 Align cell
Manufacturer's reference number: 661.20E.03	Visual & Dial Indicator
Surface type/finish: Silver Anodized	Self aligning load train or grip (if applicable):
Wedge angle (if applicable):	Self aligning cell
Comments: 1500 PSI gripping force	
Instrumentation information	
Calibration/verification dates: 03Sept2010	Data disk/filename: see Cal sheet 03/09
Method of calibration: Static Standard Cell and Ga	Data sampling rate: see Cal sheet 03/53
Shunt Cal Check of Load Cell SN#90922 for use on 03Sept2010	
Comments: LVDT Cal date =12Jan10 6" stroke Actuator, see Cal sheet 02/59	
Frequency response	
Component 1: Dantec DIC 3D Imaging system	Frequency response:
Component 2: DVM Kiethely 175 SN#409294	Frequency response:
Component 3: Vishay 2311 Amplifiers SN#108523	Frequency response: DIC channel 3
Component 4: Vishay 2311 Amplifiers SN#108525	Frequency response: DIC channel 4
Component 5: Dantec TU-4XB Slow Speed Timing	Frequency response: 30-HZ
Overall frequency response:	
Ancillary equipment (please list and describe usage)	
Dantec DIC 3D Imaging system with Dantec Low Speed 5 Megapixel Cameras	
#3 Airbrush Spray Pattern 12 inches from subject	
Xenoplan 50mm lenses	
DIC 3D system with 2 Deedacool lights	
Vishay Strain Gages CEA-06-500UW-350 with cal resister 3.921K ohm	
Dantec TU-4XB Slow Speed Timing Box	

LOW SPEED SYSTEM – SETUP 2

Testing Equipment Information	
GeorgeWashingtonUniv_ DIC_phase2	4238030003
Testing laboratory: KL-22	Point of contact: John Chumack
Telephone/Fax: 937-229-4426	Address:
Test machine information	
Manufacturer: MTS 810 2 Poster Frame #37	Manufacturer's reference number: Flex Test Station # 37
Maximum capacity (test machine): 20 Kip	Machine type (servo-hydraulic / servo-electric): S-H
Maximum capacity (load cell): 20K range	Method of data acquisition: Flex Test Peak Detectors_DIC
Range load cell used: LC #90922 = 22kip Range,	Filtering (if applicable):
Comments: Load Cell Sn#90922, Calibration date 14Jan10 - shunt cal check 03Sept10	
Flex Test Program Controller Software	
20kip 6" stroke LVDT sn#548262 Calibrated flex test Displacement .5 inch range	
Gripping information	
Type of grip: UDRI Grips, Shear, Tensile, and Com	Type of loading (tab, shoulder): Tab grip
Manufacturer: MTS 647	Method of specimen alignment in grip: MTS 609 Align cell
Manufacturer's reference number: 661.20E.03	Visual & Dial Indicator
Surface type/finish: Black Painted	Self aligning load train or grip (if applicable):
Wedge angle (if applicable):	Self aligning cell
Comments:	
Instrumentation information	
Calibration/verification dates: 03Sept2010	Data disk/filename: see Cal sheet 03/09
Method of calibration: Static Standard Cell and G	Data sampling rate: see Cal sheet 03/53
Shunt Cal Check of Load Cell SN#90922 for use on 03Sept2010	
Comments: LVDT Cal date =12Jan10 6" stroke Actuator, see Cal sheet 02/59	
Frequency response	
Component 1: Dantec DIC 3D Imaging system	Frequency response: DIC Stroke channel 1
Component 2: DVM Kiethely 175 SN#409294	Frequency response: DIC Load channel 2
Component 3: Dantec TU-4XB Slow Speed Timing	Frequency response: 30-HZ
Component 4: Dantec TU-4XF High Speed Timing	Frequency response: 200K-HZ
Component 5:	
Component 6:	
Overall frequency response:	
Ancillary equipment (please list and describe usage)	
Dantec DIC 3D Imaging system with Dantec Low Speed 5 Megapixel Cameras	
#3 Airbrush Spray Pattern 12 inches from subject @ 15psi	
Slow Cam Xenoplan 50mm lenses or HS Cam 100mm High speed Lenses	
DIC 3D system with 2 Deedacool lights	
Dantec TU-4XB Slow Speed Timing Box	
Dantec TU-4XF High Speed Timing Box	

HIGH RATE SYSTEM LOAD WASHER CALIBRATION

Customer: GWU for High Rate		Date: 26 + 27 January 2011		Tech: John Chumack	
MTS #37 LC =SN#v90922		FW= Sn# 1416810 Kistler 9061A		45KIP - 1"-14	
PC = RC10096 card and BNC2110		FW Cal software V0_02b			
20k Range	Dynamic Tension 5hz	Gain sensitivity	Load Cell readin	FW reading lbf	
	0% - volts	0.777	0	0	
	20% - 2		4000	4000	
	40% - 4		8000	8000	
	60% - 6		12000	12000	
	80% - 8		16000	16000	
	100% - 10		20000	20000	
	0% -		0	0	
10k Range	Dynamic Tension 5hz	Gain sensitivity	Load Cell readin	FW reading lbf	
	0% - volts	0.858	0	0	
	20% - 2		2000	2000	
	40% - 4		4000	4000	
	60% - 6		6000	6000	
	80% - 8		8000	8000	
	100% - 10		10000	10000	
	0% -		0	0	
5k Range	Dynamic Tension 5hz	Gain sensitivity	Load Cell readin	FW reading lbf	
	0% - volts	0.897	0	0	
	20% - 2		1000	1000	
	40% - 4		2000	2000	
	60% - 6		3000	3000	
	80% - 8		4000	4000	
	100% - 10		5000	5000	
	0% -		0	0	



HIGH RATE SYSTEM LVDT CALIBRATION

UDRI Structural Test Laboratory										
Displacement Transducer Calibration Sheet										
								Cat./Item Number 02/35		
Machine Number	6		Calibration Date	26-Jan-11		Temp / Humidity	79F/7%		Performed by	R. Glett
Transducer Type/Capacity	LVDT/+2.5"		Transducer Conditioner	MTS458.13 ac		Readout	Console			
Manufacturer	G.L. Collins		Serial Number	410		Mfr	MTS			
Model Number	LMT711-P34		Gage Factor	see range below		Model #	458.10			
Serial Number	219172		Excitation Voltage	20.005 vp-p		Serial #	0125177-			
Allowable tolerance:	1.0% of Standard value		Condition Rec'd./Ret'd:	Fair/Fair used		Cal.Spec. #:	MTS407.14 LVDT			
Comments: in 22Kip actuator SN 466R										
Standard Data	Setup 1		Range 1 :	5 in.		=V. full scale	10		Cal Value:	NA
			% of	Transducer Readings		Standard Readings		%Error		
			Full Scale	Pre-Cal	Post-Cal	Applied	Reading	Pre-Cal	Post-Cal	
Standard Used for This Range	17/24 Dial Indicator		-65%	-3.2740	-3.2740	-3.237	-3.237	1.14	1.14	
Standard Type	Starrett 25-5041J		-60%	-3.0215	-3.0215	-3.000	-3.000	0.72	0.72	
Standard Capacity	0-5,000"		-50%	-2.5050	-2.5050	-2.500	-2.500	0.20	0.20	
Standard Serial Number	25-5041		-40%	-2.0015	-2.0015	-2.000	-2.000	0.08	0.08	
Standard Calibration Data	1-Jun-10 B&S Gage blks.F39		-30%	-1.5010	-1.5010	-1.500	-1.500	0.07	0.07	
Standard Readout Meter			-20%	-1.0000	-1.0000	-1.000	-1.000	0.00	0.00	
Standard Readout Meter S/N			-10%	-.4990	-.4990	-.500	-.500	-0.20	-0.20	
Comments			0%	.0000	.0000	.000	.000	0.00	0.00	
			10%	.5025	.5025	.500	.500	0.50	0.50	
			20%	1.0000	1.0000	1.000	1.000	0.00	0.00	
			30%	1.4990	1.4990	1.500	1.500	-0.07	-0.07	
			40%	1.9975	1.9975	2.000	2.000	-0.12	-0.12	
			50%	2.5000	2.5000	2.500	2.500	0.00	0.00	
			60%	3.0040	3.0040	3.000	3.000	0.13	0.13	
			67%	3.3555	3.3555	3.355	3.355	0.01	0.01	

HIGH RATE SYSTEM EQUIPMENT LIST

Testing Equipment Information	
GeorgeWashingtonUniv _ DIC_phase2	4238030003
Testing laboratory: KL-22	Point of contact: John Chumack
Telephone/Fax: 937-229-4426	Address:
Test machine information	
Manufacturer: MTS 4 Poster Frame #6	Manufacturer's reference number: MTS 458.10 on #6
Maximum capacity (test machine): 50 Kip	Machine type (servo-hydraulic / servo-electric): S-H
Maximum capacity (load cell): FW 45K range	Method of data acquisition: HSDAQ & GPTC v03b
FW range used: FW #1416810= 20kip , calibrated 5k, 10k, 19k range	Filtering (if applicable):
Comments: Force washer Sn#1416810, Calibration date 01Mar11 - shunt cal check 01Mar11	
HSDAQ 10 MHZ Pci card #6115	
22kip 6" stroke LVDT sn#219172 Calibrated Displacement 5 inch range	
MTS Micro Profiler 458.91	
Gripping information	
Type of grip: UDRI Grips, Shear, Tensile, and Compression	Type of loading (tab, shoulder): Tab grip
Manufacturer: UDRI Fixturing	Method of specimen alignment in grip: Dial indicator
Manufacturer's reference number: Compression, Axial, Transverse	Visual & Dial Indicator
Surface type/finish: Black Painted & white speckled	Self aligning load train or grip (if applicable):
Wedge angle (if applicable):	
Comments:	
Instrumentation information	
Calibration/verification dates: 01Mar2011	Data disk/filename: see Cal sheet 02/35
Method of calibration: Static Standard Cell and Gaged Blocks/dial indicator	Data sampling rate: see data run sheets
Shunt Cal Check of Load Cell #37 SN#90922 for use on 03Sept2010	
Comments: LVDT Cal date =26Jan11 6" stroke Actuator, see Cal sheet 02/35	
Frequency response	
Component 1: Dantec DIC 3D Imaging system	Frequency response: DIC Stroke channel 1
Component 2: DVM Kiethely 175 SN#409294	Frequency response: DIC Load channel 2
Component 3: Dantec TU-4XF High Speed Timing Box	Frequency response: 200KHZ
Component 4:	Frequency response:
Component 5:	
Component 6:	
Overall frequency response:	
Ancillary equipment (please list and describe usage)	
Dantec DIC 3D Imaging system with Dantec High Speed Cameras	
#3 Airbrush Spray Pattern & Spray can 12 inches from subject @ 15psi	
HS Cam 100mm High speed Lenses @ F11	
DIC 3D system with 2 Deedacool lights	
BNC-2110 NI A-D box	
Dantec TU-4XF High Speed Timing Box	
1 Jennings Fiber optics Bundle	

APPENDIX J
MODIFIED ASTM D3039 TENSILE DATA PACKAGE
Summary Tables
Summary Plots

Investigation of Opportunities for Lightweight Vehicles Using Advanced Plastics and Composites

Table J-1 Triaxial Braid T700 Carbon/Epon 862W Quasi-static Summary Table Using Modified ASTM D3039 Specimens - Axial Orientation

Digital Image Correlation (DIC) and Back-to-Back Gaged
 Nominal gage dimensions of 44.45 mm (w) X 1.65 mm (t) x 184.5 mm (l)
 Test speed of 1.275 mm/min (0.05 in/min) Minimum test system resonant frequency of 1 kHz
 Test conditions: 23°C RH: 50 +/-10%

	Test Date	UDRI Specimen ID	Panel ID	Engineering Peak* (Breaking) Stress [ksi]	Engineering Peak* (Breaking) Stress [MPa]	Engineering Breaking Strain [%]	Elastic Modulus [GPa]	Poisson's Ratio	Machine Rate [m/s]	Machine Rate [in/s]	Nominal Strain Rate [1/s]	Measured Strain Rate# [1/s]	Strain Range for Strain Rate Calc. [%]	Failure Location	Comments
Axial	9/20/2010	064-1	080210-6	117	808	1.91	42.2	0.289	0.000021	0.000834	0.000115	0.0000729	1.0-1.8	gage	Re-run. Increased grip pressure after slippage at 12786 lbf. Note 1
	9/20/2010	064-2	080210-6	131	903	-	-	-	0.000021	0.000834	0.000115	-	-	-	Note 1
	9/22/2010	064-3	080210-6	114	787	1.82 gaged 1.95 DIC	44.9 gaged 41.3 DIC	0.300 DIC	0.000021	0.000834	0.000115	0.0000720 gaged 0.0000708 DIC	1.0-1.8	gage	Gaged and DIC
	9/21/2010	064-4	080210-6	117	807	1.85	43.4	0.314	0.000021	0.000833	0.000115	0.0000737	1.0-1.8	gage	Broke both ends
	9/21/2010	064-5	080210-6	134	924	2.08	44.2	0.304	0.000021	0.000833	0.000115	0.0000715	1.0-1.8	gage	Broke both ends
	9/21/2010	064-6	080210-6	125	860	1.86	45.8	0.333	0.000021	0.000824	0.000113	0.0000722	1.0-1.8	gage	Note 1
	9/21/2010	064-7	080210-6	122	841	1.91	44.6	0.310	0.000021	0.000834	0.000115	0.0000753	0.8-1.9	gage	Re-run. Increased grip pressure after slippage
	9/21/2010	064-8	080210-6	122	842	2.07	41.3	0.307	0.000021	0.000833	0.000115	0.0000715	1.0-2.0	gage	Note 1
Average [DIC data]				123	846	1.95	43.3	0.308							
Std.Dev.				6.94	47.8	0.09	1.72	0.01							
Coeff. of Var. [%]				5.65	5.65	4.81	3.98	4.38							

Strain gage full scale was 2%. Strain data from back-to-back gages averaged to adjust for potential bending.

Note 1: Issues with DIC-recorded load. Full scale reached at 10,000 lbf [-620-640 Mpa]. Peak stress recorded by Test data acquisition.

Nominal rate based on gage length of 184.5mm.

1. Thickness was measured at two "peak" and two "valley" locations and averaged.

*DIC system 1-2 Hz sampling frequency was not always sufficient to capture peak. The sampling frequency was low in order to view most of the specimen within the region of interest for most tests. The peak stress was taken from the test machine output.

Investigation of Opportunities for Lightweight Vehicles Using Advanced Plastics and Composites

Table J-2 Triaxial Braid T700 Carbon/ Epon 862W Quasi-static Summary Table Using Modified ASTM D3039 Specimens - Transverse Orientation

Digital Image Correlation (DIC) and Back-to-Back Gaged
Nominal gage dimensions of 19.05 mm (w) X 1.65 mm (t) x 101.6 mm (l) for transverse
Test speed of 1.275 mm/min (0.05 in/min) Minimum test system resonant frequency of 1 kHz
Test conditions: 23°C RH: 50 +/-10%

	Test Date	UDRI Specimen ID	Panel ID	Engineering Peak* (Breaking) Stress [ksi]	Engineering Peak* (Breaking) Stress [MPa]	Onset of Engineering Failure Strain ** [%]	Final Engineering Breaking Strain ** [%]	Elastic Modulus [GPa]	Poisson's Ratio	Machine Rate [in/s]	Machine Rate [mm/s]	Nominal Strain Rate [1/s]	Measured Strain Rate# [1/s]	Strain Range for Strain Rate Calc. [%]	Failure Location	Comments
Transverse	9/16/2010	063-1	080210-6	49.0	338	-	-	-	-	0.000021	0.00083	0.000208	-	-	gage	No DIC data
	9/16/2010	063-2	080210-6	47.1	325	-	-	-	-	0.000021	0.00083	0.000208	-	-	gage	No DIC data
	9/16/2010	063-3	080210-6	49.7	343	-	-	-	-	0.000021	0.00083	0.000208	-	-	gage	No DIC data
	9/16/2010	063-4	080210-6	49.3	340	-	-	-	-	0.000021	0.00083	0.000208	-	-	gage	No DIC data
	9/27/2010	063-5	080210-6	47.7	329	1.36	1.44	34.7	0.32	0.000172	0.000832	0.000208	0.000172	0.6-1.1	gage	
	9/27/2010	063-6	080210-6	47.2	325	1.10 gaged 1.06 DIC	1.41 gaged 1.45 DIC	36.9 gaged 34.4 DIC	-	0.000157	0.000833	0.000208	0.000157	0.2-1.0	gage	Gaged and DIC. DIC modulus measured over a larger region.
Average of DIC specimens				48.3	333	1.36	1.44	34.70								
Std.Dev.				1.16	7.98											
Coeff. of Var. [%]				2.40	2.40											

Strain gage full scale was 5%. Strain data from back-to-back gages averaged to adjust for potential bending.

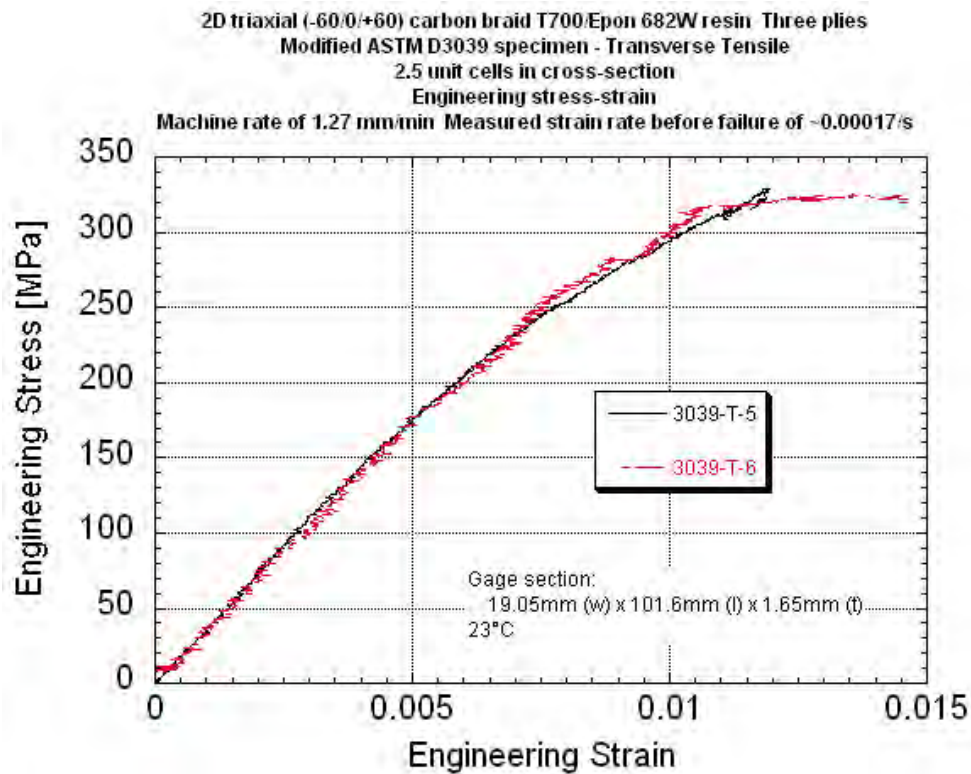
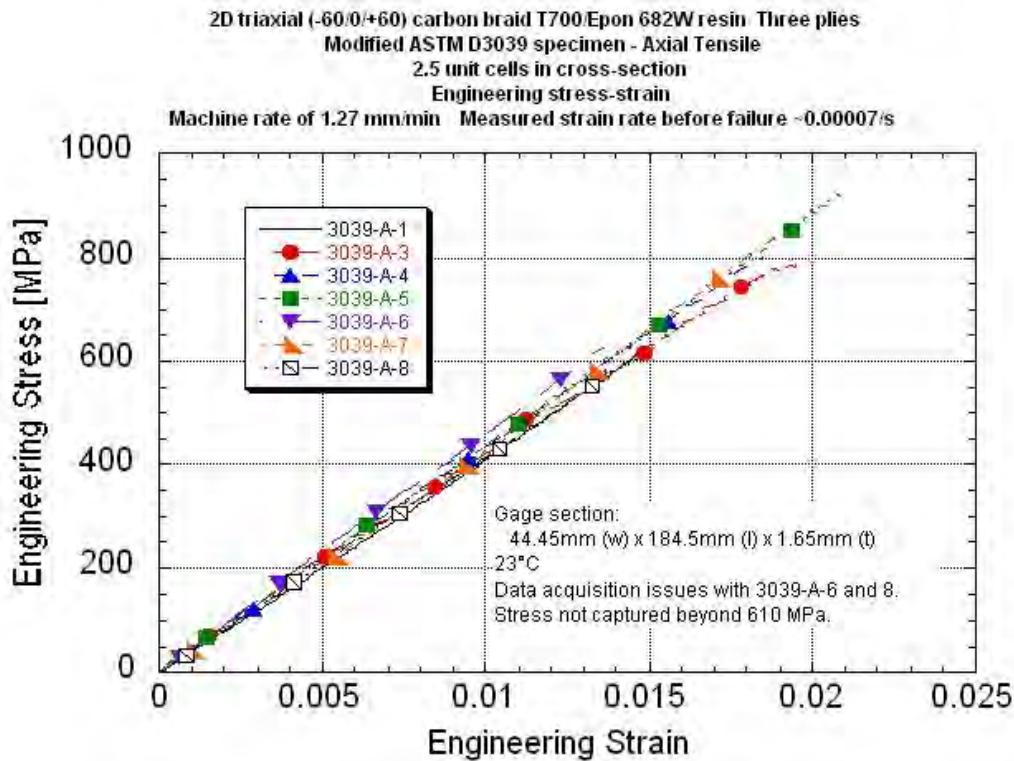
Note 1: Issues with DIC-recorded load. Full scale reached at 10,000 lbf [-620-640 MPa]. Peak stress recorded by Test data acquisition.

Nominal rate based on gage length of 101.6mm.

3. Thickness was measured at two "peak" and two "valley" locations and averaged.

*DIC system 1-2 Hz sampling frequency was not always sufficient to capture peak. The sampling frequency was low in order to view most of the specimen within the region of interest for most tests. The peak stress was taken from the test machine output.

**Transverse specimens - failure was taken at the point of maximum stress and strain before tearing.



APPENDIX K
BOWTIE AXIAL TENSILE DATA PACKAGE
Summary Table
Summary Stress-strain Plots With Rate
Summary Stress-time Plots With Rate

Investigation of Opportunities for Lightweight Vehicles Using Advanced Plastics and Composites

Axial Tensile Data Summary
2D Triaxial Carbon T700/ Epon862W Epoxy Braid
Bowtie Specimen Configuration - 2.5 unit cells in reduced cross section
Nominal center cross-section of 45.5mm wide x 1.65mm thick

	UDRI STL number	Peak Stress [MPa]	Normalized Peak Stress to 56% Fiber Volume [MPa]	Engineering Breaking Strain # [%]	Localized## Engineering Max Strain [%]	Localized## Engineering Min Strain [%]	Elastic Modulus Based on Center [GPa]	Elastic Modulus Based on High Strain Point [GPa]	Elastic Modulus Based on Low Strain Point [GPa]	Poisson's Ratio**	Measured Strain Rate Before Failure* [1/s]	Machine Rate [in/s]	Machine Rate [m/min]	Comments
0.00009/s	088-1	731	718	1.31	2.22	0.62	62.9	46.6	71.3	0.26	0.000109	0.00083	0.00126	Note 1
	088-2	829	815	1.37	2.06	0.88	67.3	43.2	77.8	-	0.000085	0.00083	0.00127	Note 1
	088-3	767	754	1.26	1.55	0.71	66.9	56.7	91.7	0.25	0.000083	0.00083	0.00127	
	088-4	822	808	1.35	1.88	0.60	66.5	-	94.5	-	0.000092	0.00083	0.00127	Note 1
	088-8	875	860	1.36	1.88	0.69	70.5	59.9	100	-	0.000077	0.00083	0.00127	Note 1
	088-9	728	686	1.20	2.00	0.44	65.8	41.5	92.7	-	0.000089	0.00083	0.00126	Note 1
	088-10	836	787	1.33	1.60	0.63	69.4	-	-	-	0.000083	0.00083	0.00127	Final failure at 1.72%.Note 1
	Average	798	775	1.31	1.88	0.65	67.0	49.6	88.0	0.25				
	Standard Deviation	57	60	0.06	0.24	0.13	2.5	8.3	11.0					
	COV [%]	7.11	7.76	4.81	12.7	20.5	3.69	16.7	12.5					
Excluding Specimens 088-1, 088-3, and 088-9 which had cracking into the grip before failure	Average	841	817	1.35	1.85	0.70	68.4	51.6	90.8					
	Standard Deviation	24	31	0.02	0.19	0.13	1.84	11.8	11.6					
	COV [%]	2.82	3.75	1.38	10.2	18.4	2.69	22.9	12.8					
0.03/s	088-5	844	795	1.51	2.44	0.94	62.5	46.1	62.7	-	0.0319	0.331	0.504	Final failure at 2.78%. Note 1
	088-6	921	868	1.43	1.50	0.48	70.8	52.7	101	-	0.0344	0.330	0.503	Note 1.
	088-7	831	782	1.37	1.83	0.55	65.9	50.7	94.5	0.36	0.0312	0.331	0.505	
	Average	865	815	1.44	1.92	0.65	66.4	49.8	85.9					
	Standard Deviation	49	46	0.07	0.48	0.25	4.2	3.4	20.4					
	COV [%]	5.65	5.65	5.13	24.8	37.8	6.30	6.75	23.74					
0.3/s	088-17	841	829	1.37	1.54	1.08	72.9	52.0	84.8	-	0.310	3.01	4.59	Note 1
	088-18	754	744	1.16	1.83	0.85	81.7	67.3	89.9	0.38	0.295	2.95	4.50	
	088-19	749	739	1.05	1.12	0.80	85.4	85.4	85.3	0.39	0.295	3.18	4.84	
	088-20	868	817	1.51	1.74	0.99	82.3	66.3	83.6	0.37	0.323	3.01	4.59	
	Average	803	782	1.27	1.56	0.93	80.6	67.7	85.9	0.38				
	Standard Deviation	60	48	0.21	0.32	0.13	5.4	13.7	2.8	0.01				
	COV [%]	7.53	6.09	16.2	20.3	14.0	6.66	20.2	3.23					
2/s Low amplitude resonant ringing -5 to 10 waves before failure	088-12	797	777	1.53	2.06	0.83	81.5	67.3	97.8	0.33	2.61	27.2	41.4	Note 2
	088-13	738	719	1.27	1.77	0.62	83.2	65.1	124	0.42	4.95	48.1	73.2	Notes 2 and 3
	088-14	789	769	1.22	1.49	0.55	95.0	85.1	118	0.47	2.19	23.7	36.0	Note 2
	088-15	790	744	1.39	1.59	0.86	78.2	58.9	79.2	-	1.97	24.8	37.8	Note 2
	088-16	754	711	1.22	1.99	0.88	88.9	70.6	97.8	0.38	2.23	25.0	38.0	Note 2
	Average [EXCLUDING 088-13]	783	744	1.33	1.78	0.75	85.4	69.4	103	0.40				
	Standard Deviation	19	29	0.13	0.25	0.15	6.6	9.7	18	0.06				
	COV [%]	2.46	3.96	10.0	13.8	20.5	7.76	14.0	17.4	15.2				

* Strain rate of central region ** Poisson's ratio taken at the first region of zero slope from the E11 vs Ratio curve.

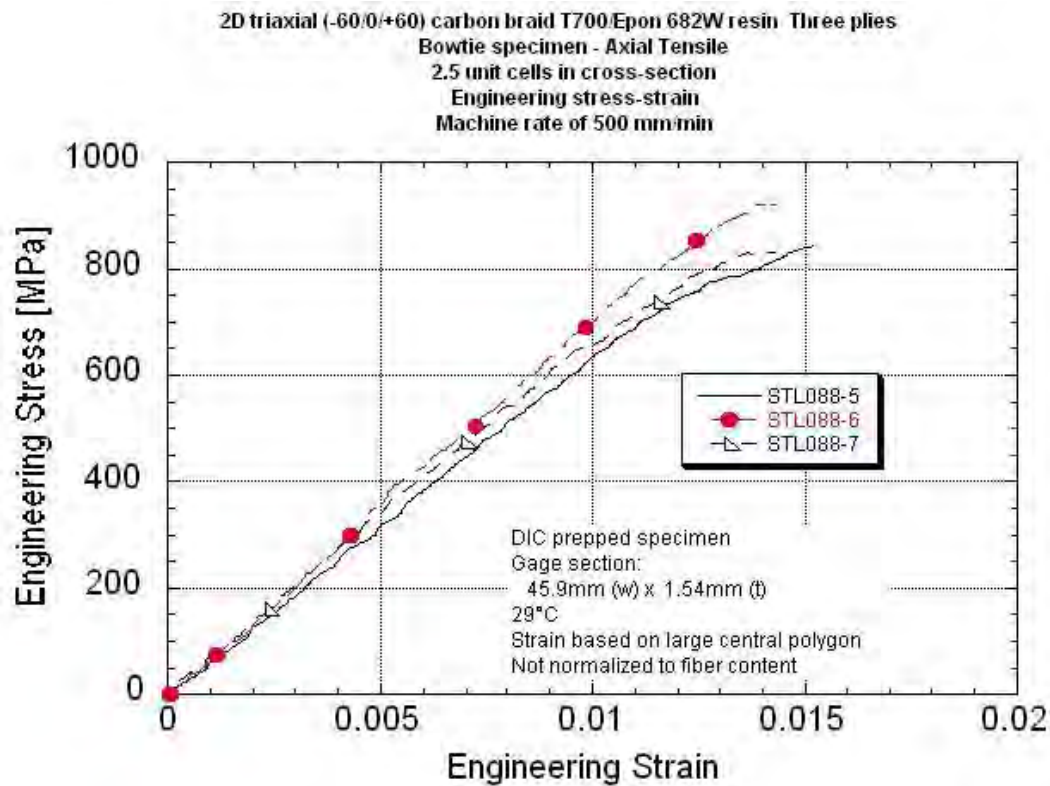
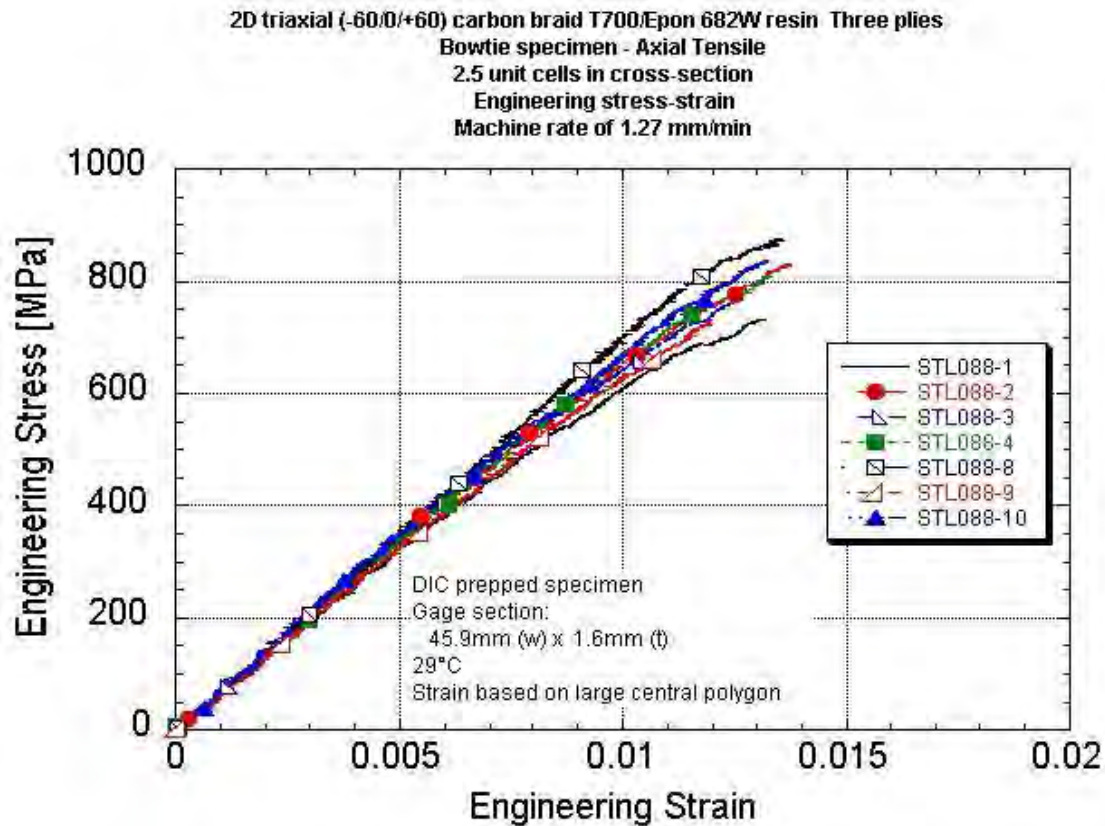
Strain as measured at a region of high strain on a fiber braid and a low strain region.

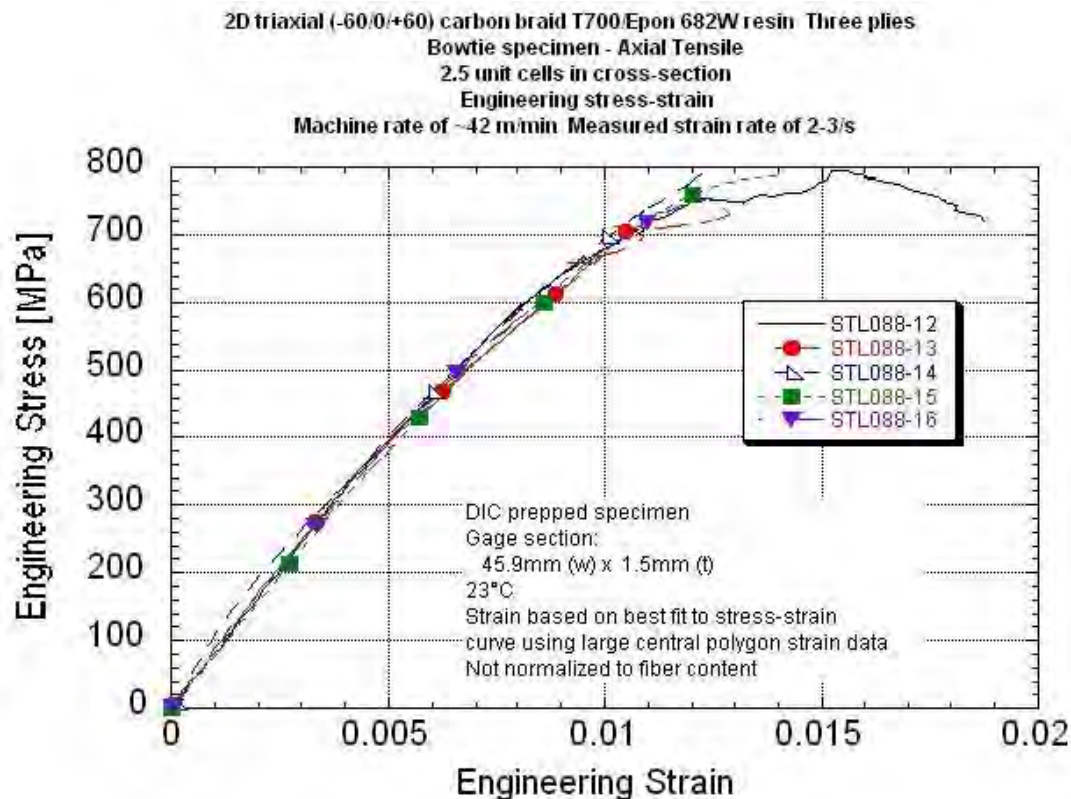
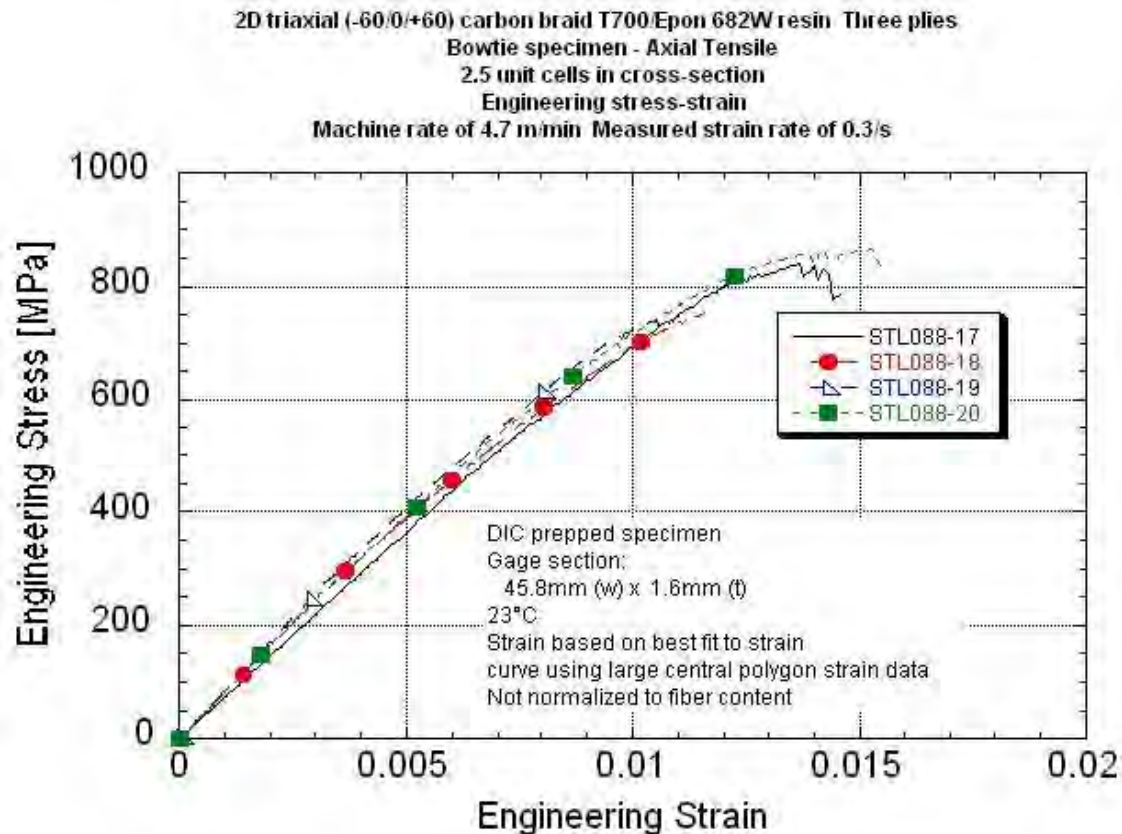
Specimen thickness varied due to the braid structure. Thickness was measured at two "peak" and two "valley" locations and averaged.

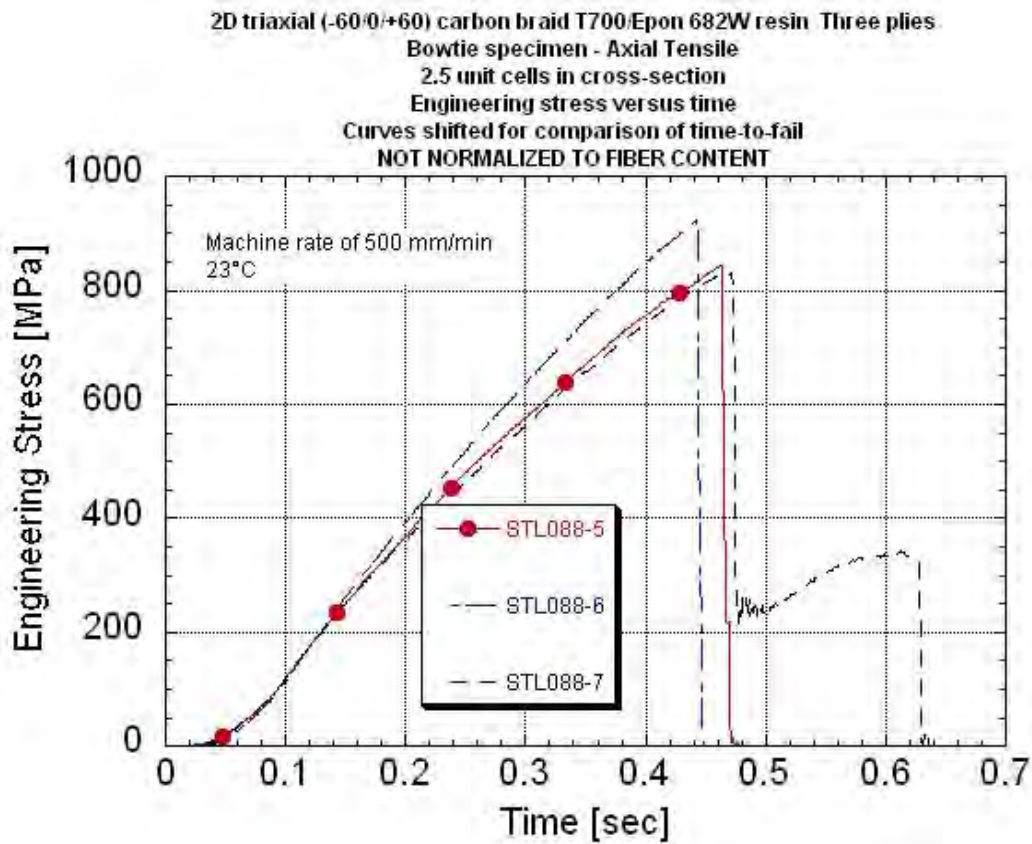
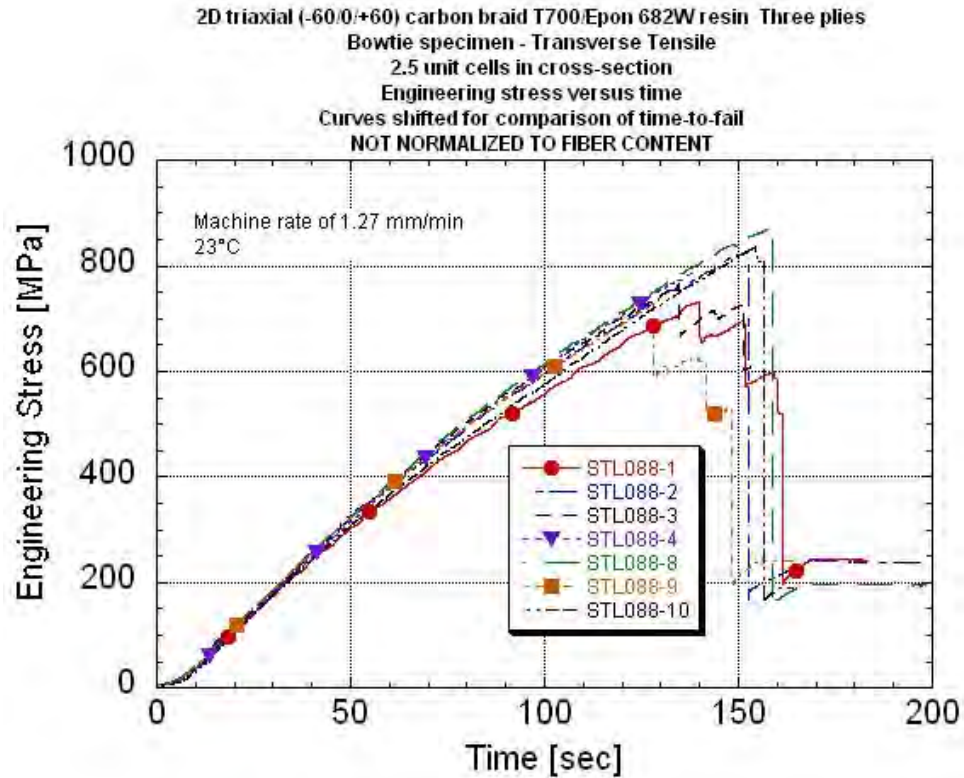
Note 1 Nonlinear increase of Poisson's ratio to end of test.

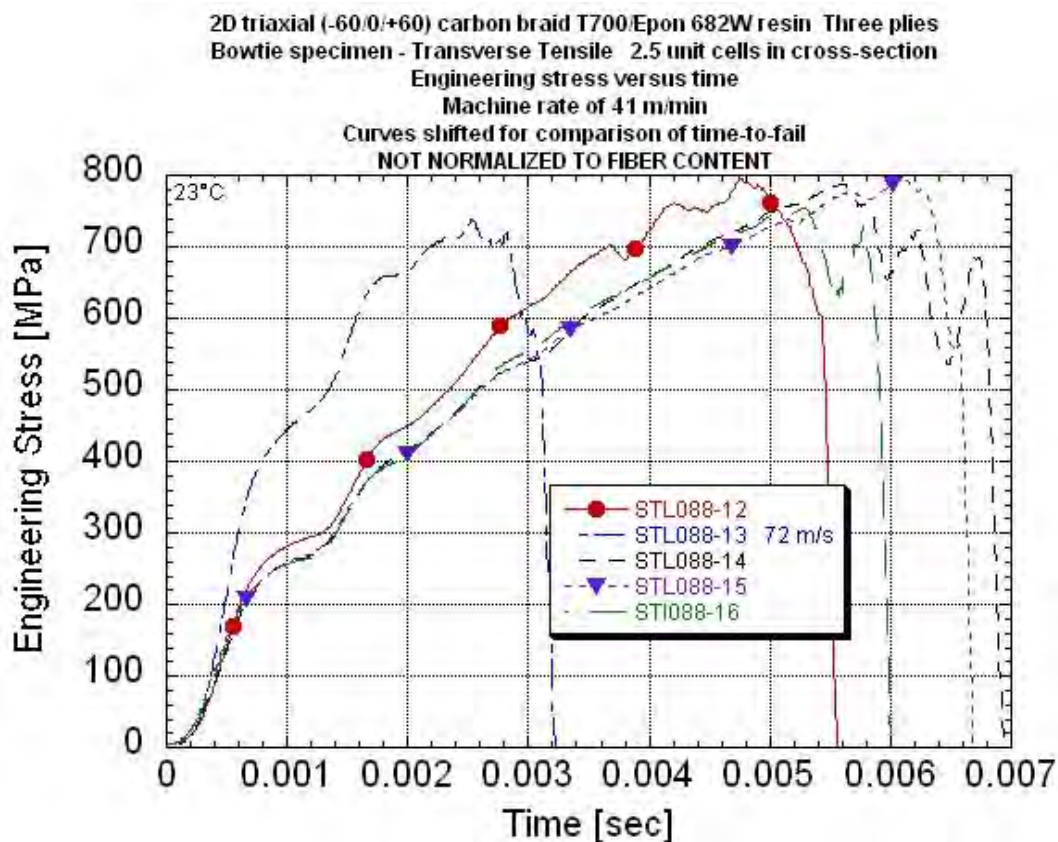
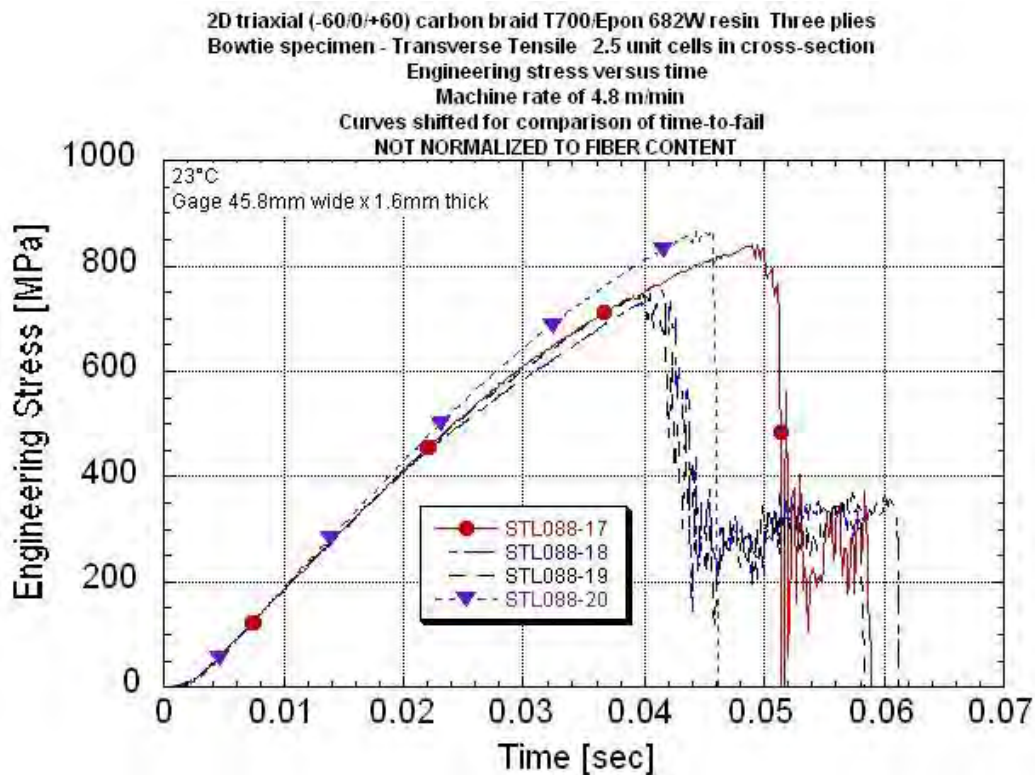
Note 2 Nonlinear stroke rate throughout loading cycle. Initial rate was 45.7 m/min through ~half of the loading. Had decreased to ~35 m/min by the end of the test. Reported machine rate is the average rate throughout the loading time.

Note 3 Resonant ringing superimpose onto material response. Limited number of stress waves before failure (~3 waves). Not included in average.









APPENDIX L
BOWTIE TRANSVERSE TENSILE DATA PACKAGE
Summary Table
Summary Stress-strain Plots With Rate
Summary Stress-time Plots With Rate

Investigation of Opportunities for Lightweight Vehicles Using Advanced Plastics and Composites

Transverse Tensile Data Summary
2D Triaxial Carbon T700/ Epon862W Epoxy Braid
Bowtie Specimen Configuration - Minimum of 2.5 unit cells in reduced cross-section
Nominal center cross-section of 17mm wide x 1.6mm thick

	Panel ID	UDRI STL number	Center polygon/line Gage Width [mm]	Peak Stress* [MPa]	Normalized Peak Stress to 56% Fiber Volume [MPa]	Engineering Breaking Strain # [%]	Localized## Engineering Max Strain [%]	Localized## Engineering Min Strain [%]	Elastic Modulus Based on Center [GPa]	Elastic Modulus Based on High Strain Point	Elastic Modulus Based on Low Strain Point	Poisson's Ratio Center line	Poisson's Ratio Center polygon	Measured Strain Rate*	Machine Rate [in/s]	Machine Rate [m/min]	Comments
0.00015/s Longer grip to grip distance	073010-2	074-1	-	931	914	-	-	-	-	-	-	-	-	-	0.00083	0.00126	No DIC data
	073010-2	074-3	6.88	923	907	2.05	3.76/4.99	0.93/1.55	91.1	-	-	-	0.47	0.00013	0.00083	0.00127	
	073010-2	074-5	12.69	960	944	2.47	3.80/3.84	1.59/1.82	67.0	-	-	-	0.51	0.00023	0.00083	0.00127	
	073010-2	074-7	7.49	982	964	1.52/2.60	2.02/4.01	1.32/1.70	89.4	-	-	-	0.22	0.00015	0.00083	0.00126	
	073010-2	074-9	9.59	1000	983	1.44/2.38	3.13/3.64	1.43/1.73	81.3	-	-	-	0.19	0.00010	0.00083	0.00127	
		Average		959	943	1.84/2.48	3.18/4.12	1.30/1.70	82.2				0.35				
		Standard Deviation		33	32	0.47/0.09	0.83/0.60	0.28/0.11	11.0				0.17				
		COV [%]		3.42	3.42	25.6/3.64	26.1/14.6	21.3/6.60	13.4				48.3				
0.00015/s Shorter grip to grip distance	073010-6	081-1	7.75	989	965	2.35	2.63	1.49	57.0	35.0	49.6	0.01	0.02	0.00020	0.00083	0.00127	
	073010-6	081-2	7.34	931	909	2.38	3.71	1.59	65.8	36.0	50.5	0.20	0.24	0.00017	0.00083	0.00127	
	073010-6	081-3	7.75	976	952	1.49	2.57	1.05	76.3	44.1	-	0.36	0.31	0.00014	0.00083	0.00127	
		Average		965	942	2.07	2.97	1.37	66.4	38.3	50.1		0.19				
		Standard Deviation		30	29	0.50	0.64	0.29	9.65	5.00	0.67		0.15				
		COV [%]		3.12	3.12	24.3	21.6	21.0	14.5	13.0	1.34		81.3				
0.045/s Shorter grip to grip distance	073010-6	081-4	7.49	1034	1009	1.82	2.87	0.68	112	48.9	-	0.60	0.54	0.0446	0.333	0.508	
	073010-6	081-5	7.82	1022	997	1.41	2.35	0.82	141	-	-	0.63	0.63	0.0298	0.334	0.509	
	073010-6	081-6	7.79	977	954	2.11	-	-	102	-	-	0.44	-	0.0706	0.334	0.509	center line strain only
	073010-6	081-7	7.87	1033	1008	1.54	-	-	109	-	-	0.238/0.408	0.238/0.408	0.0344	0.336	0.513	
		Average		1017	992	1.72	2.61	0.75	116				0.47/0.52				
		Standard Deviation		27	26	0.31	0.37	0.10	17.2				0.2-0.11				
		COV [%]		2.65	2.65	18.1	14.1	13.2	14.8				43.5/20.9				
0.45/s Shorter grip to grip distance	073010-6	081-8	7.87	1044	1019	1.62	-	-	130	-	-	0.47	0.50	0.412	3.08	4.70	
	073010-2	081-11	7.32	1093	1074	2.07	-	-	66.2	-	-	0.14	0.14	0.465	3.18	4.84	
	073010-2	081-13	8.05	1002	985	2.37	3.60	2.29	49.2	49.4	-	0.03	0.03	0.698	3.10	4.73	
		Average		1046	1026	2.02			81.9				0.22				
		Standard Deviation		46	45	0.38			42.8				0.24				
		COV [%]		4.35	4.40	18.6			52.2				109				
5/s Shorter grip to grip distance	073010-1	081-17	7.83	924	957	1.96	-	-	58.3	-	-	0.03	0.03	5.09	28.3	43.2	
	073010-1	081-18	7.75	949	982	1.87	2.28	-	50.6	45.1	-	0.06	0.09	5.05	29.7	45.3	
	073010-1	081-19	7.92	881	911	3.20	-	-	64.7	-	-	0.03	0.05	3.50	29.1	44.4	
		Average		918	950	2.34			57.9				0.06				
		Standard Deviation		35	36	0.74			7.1				0.03				
		COV [%]		3.77	3.77	31.7			12.2				50.2				

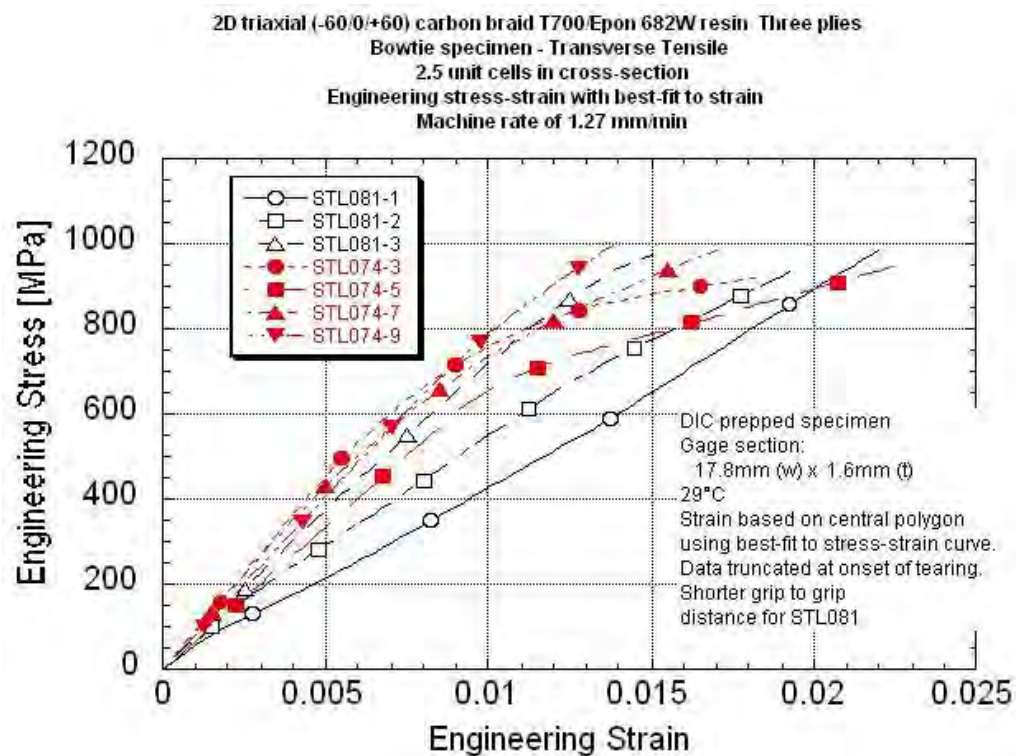
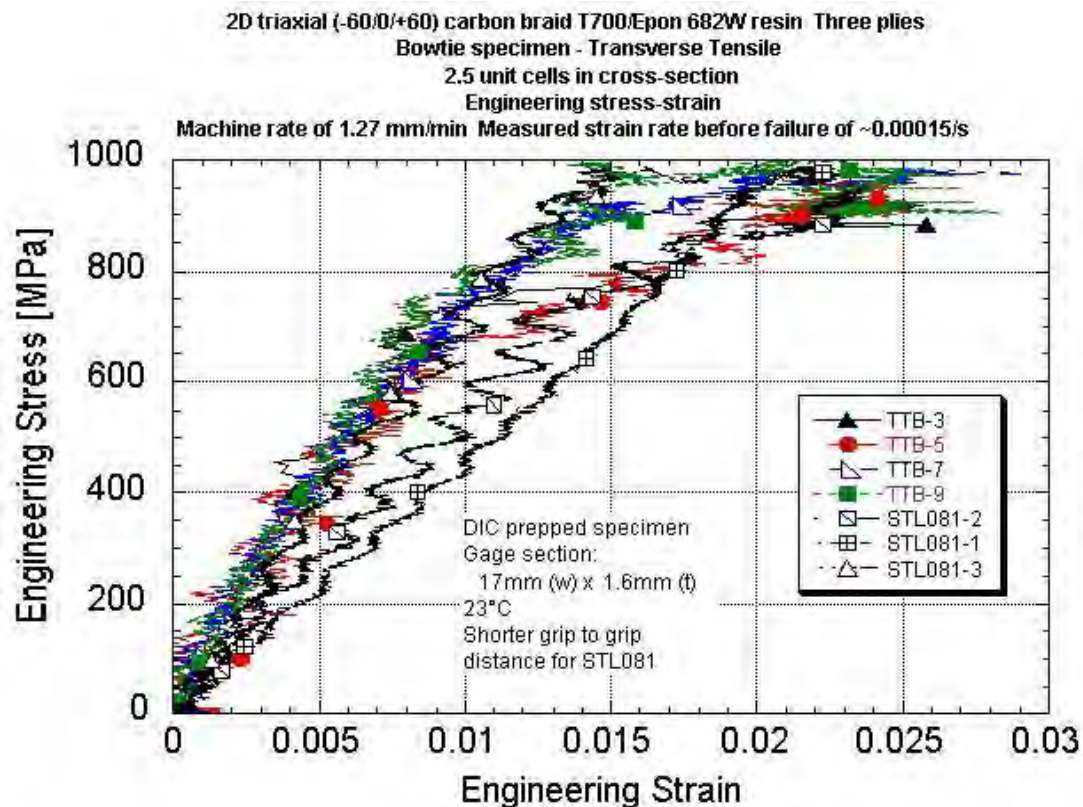
#Extended failure as cracking initiated along sides and traveled into center. Strain for central polygon at onset of cracking and final break.

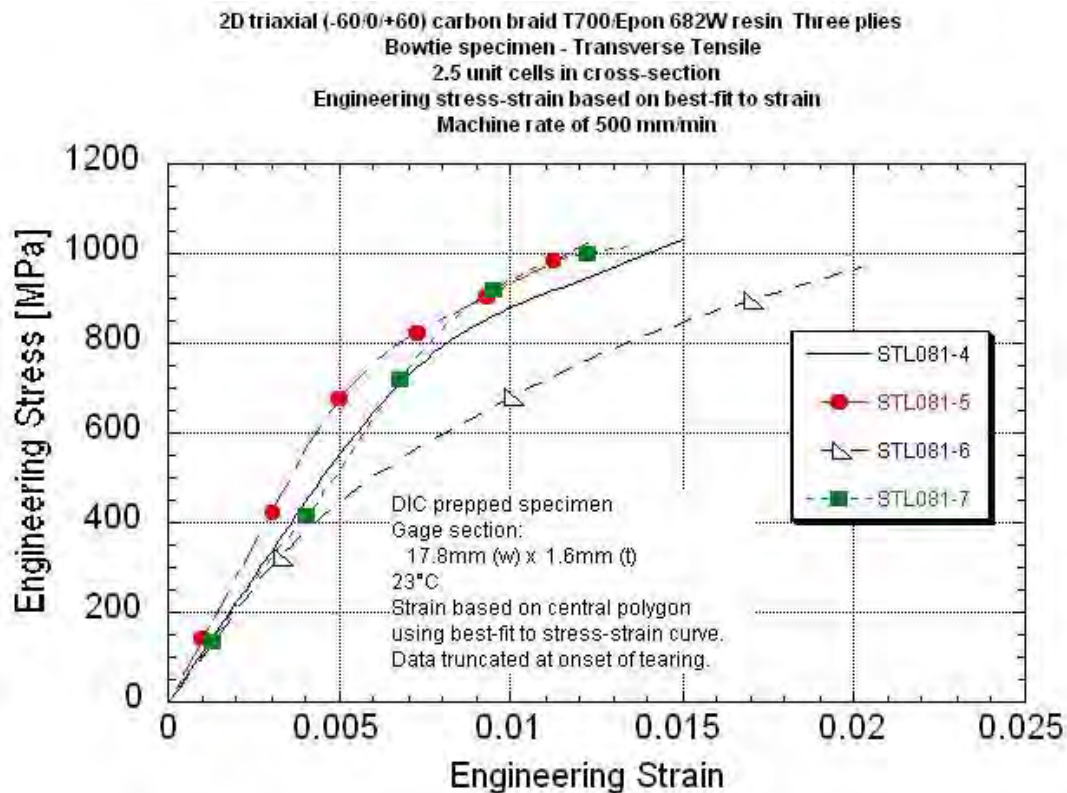
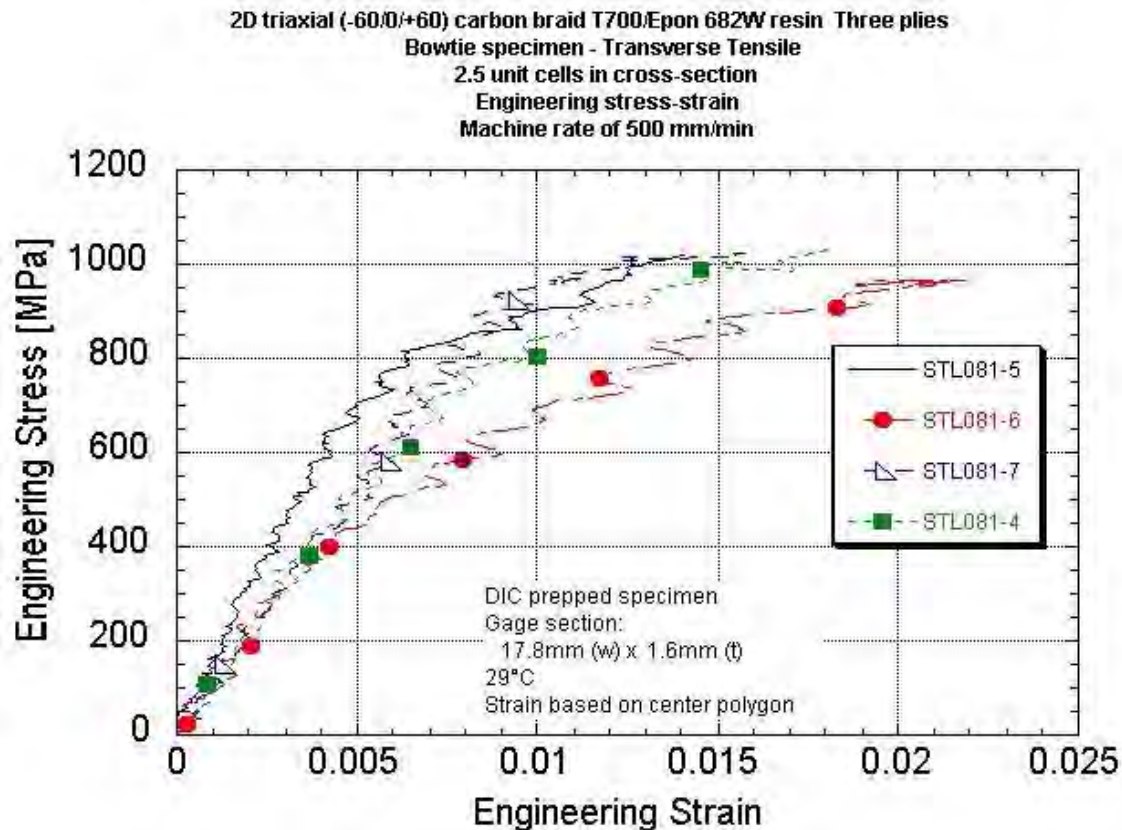
Strain as measured at a region of high strain on a fiber braid and low strain in center. Strain data from the onset of cracking and final break.

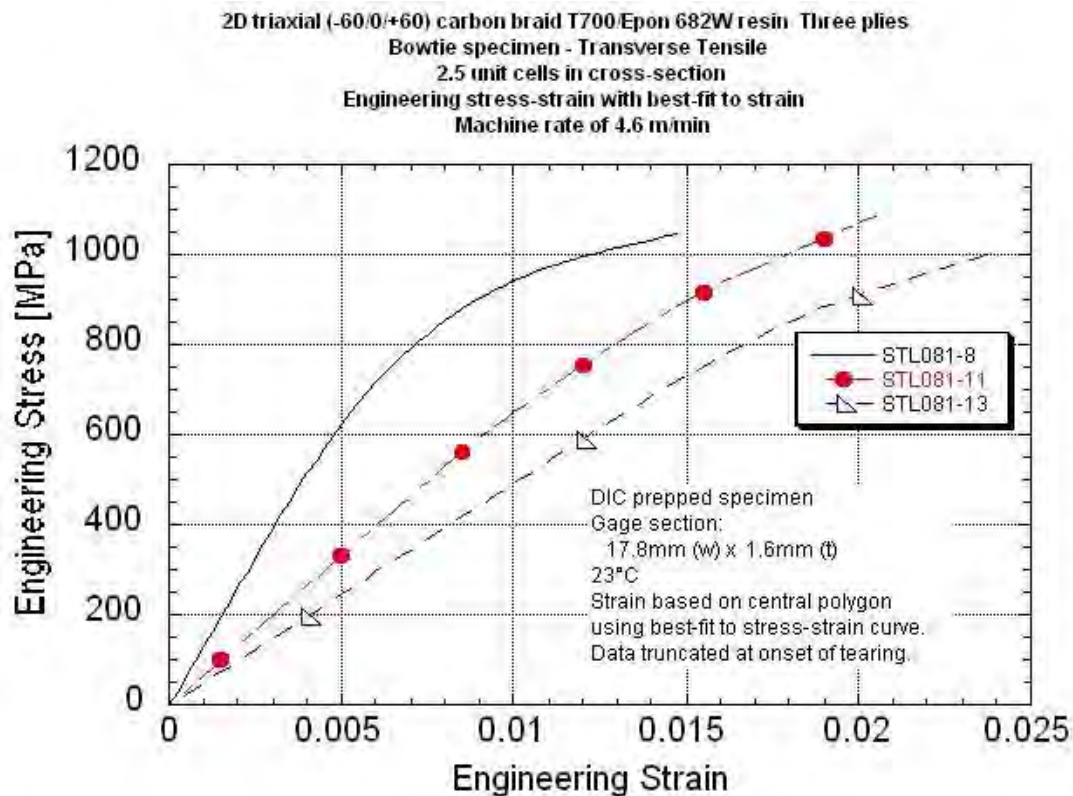
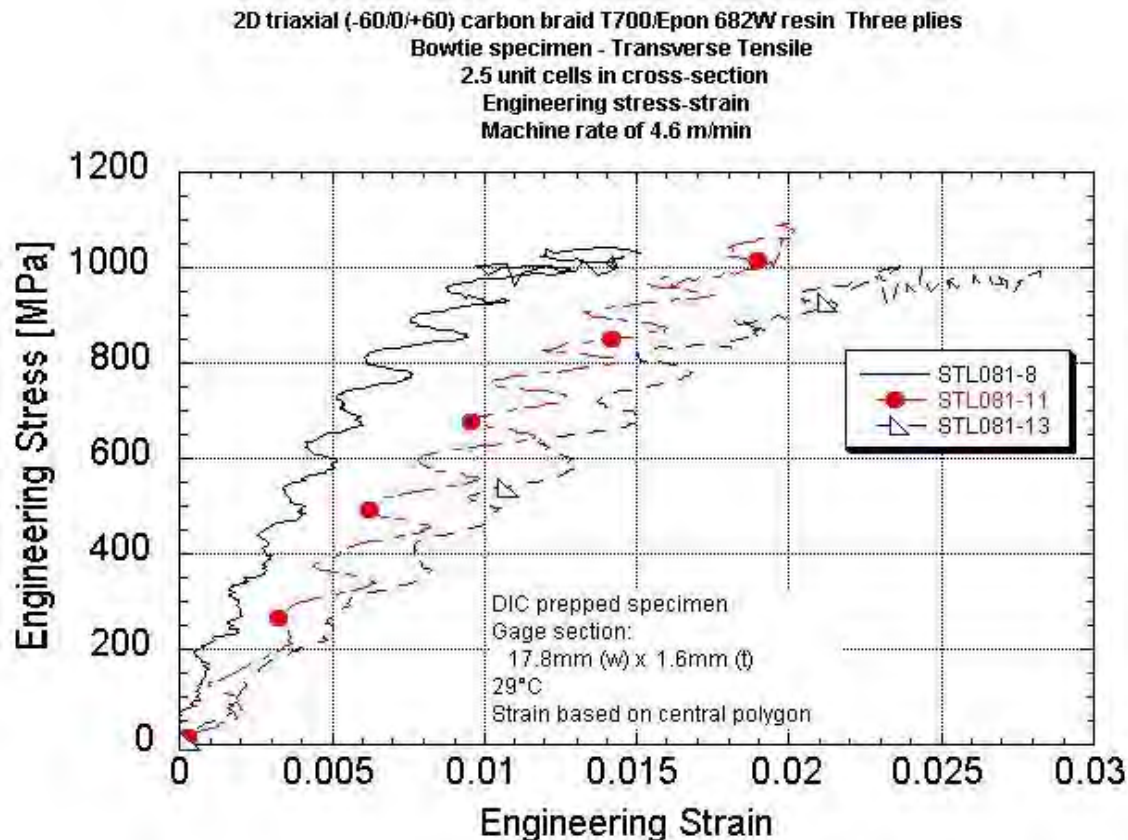
Specimen thickness varied due to the braid structure. Thickness was measured at two "peak" and two "valley" locations and averaged.

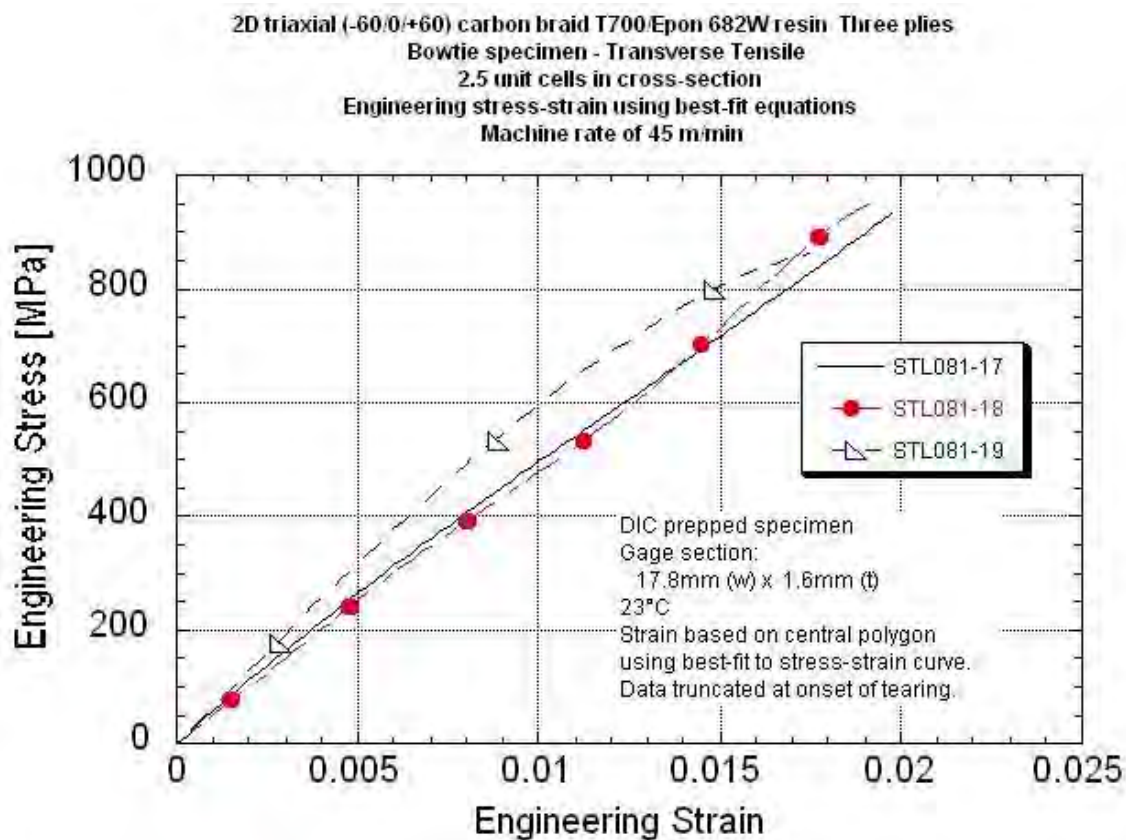
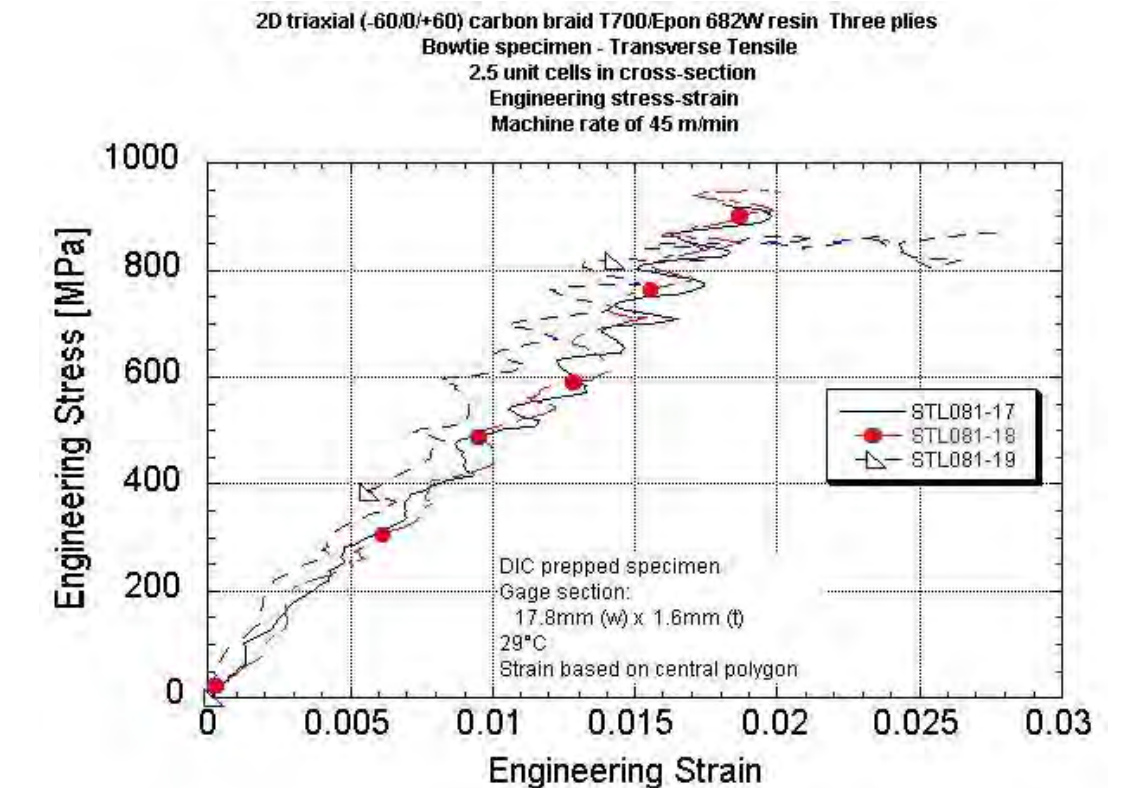
* The strain rate was measured over the strain experience over a stress range of 300 to 600 MPa.

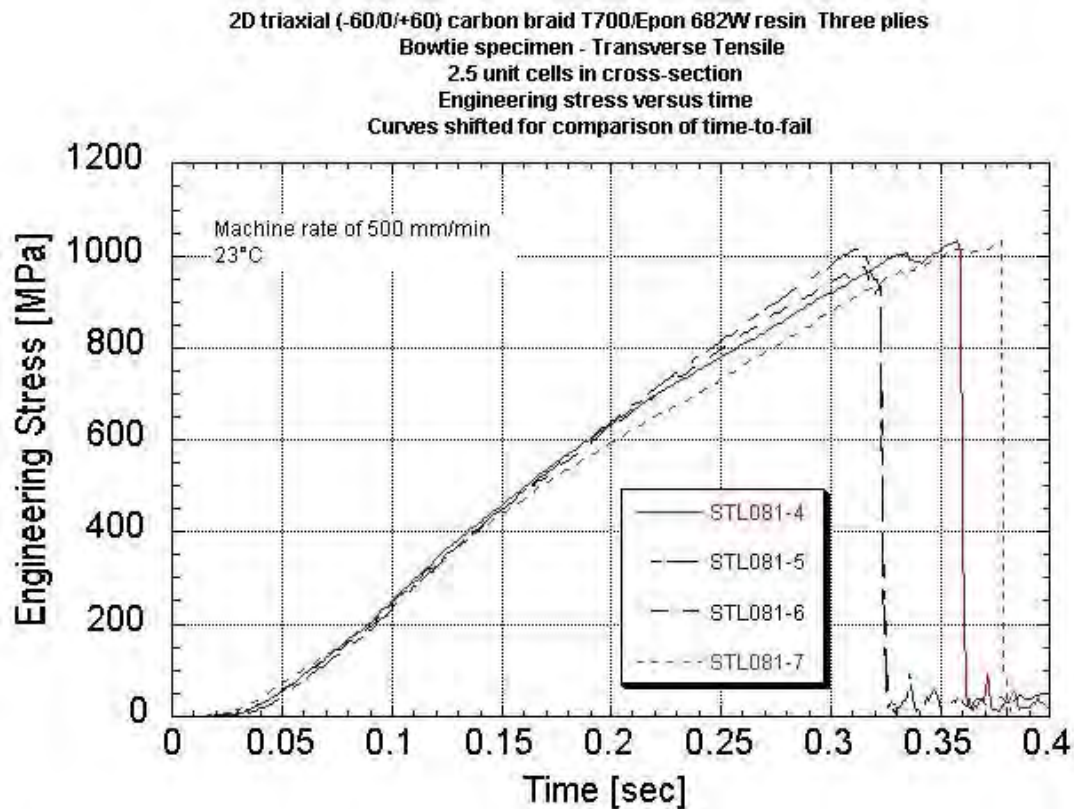
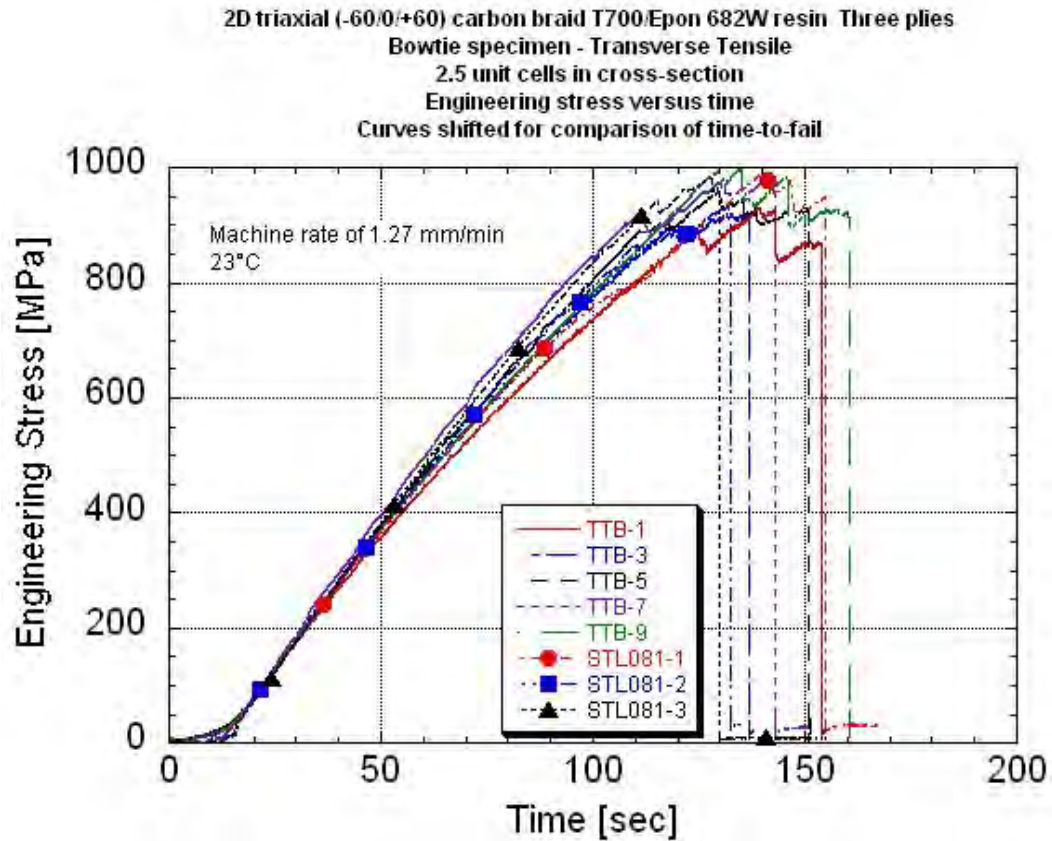
**The center line/polygon width traversed at least one unit cell (short side).

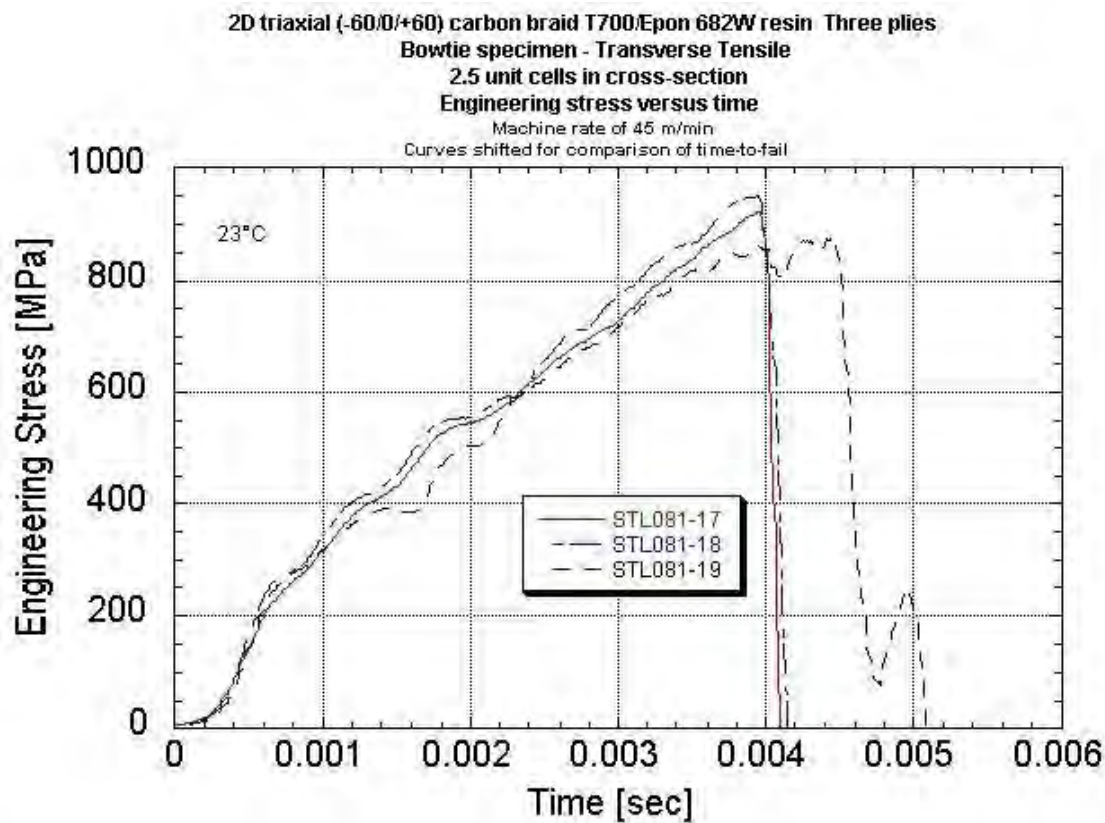
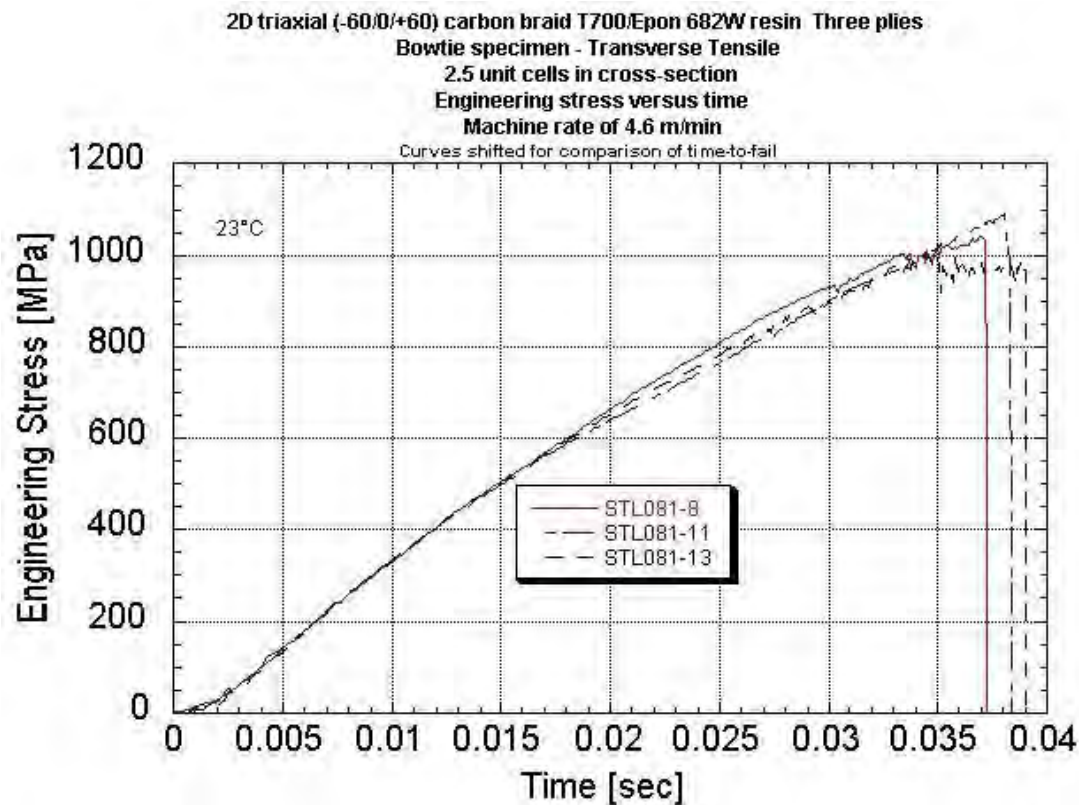












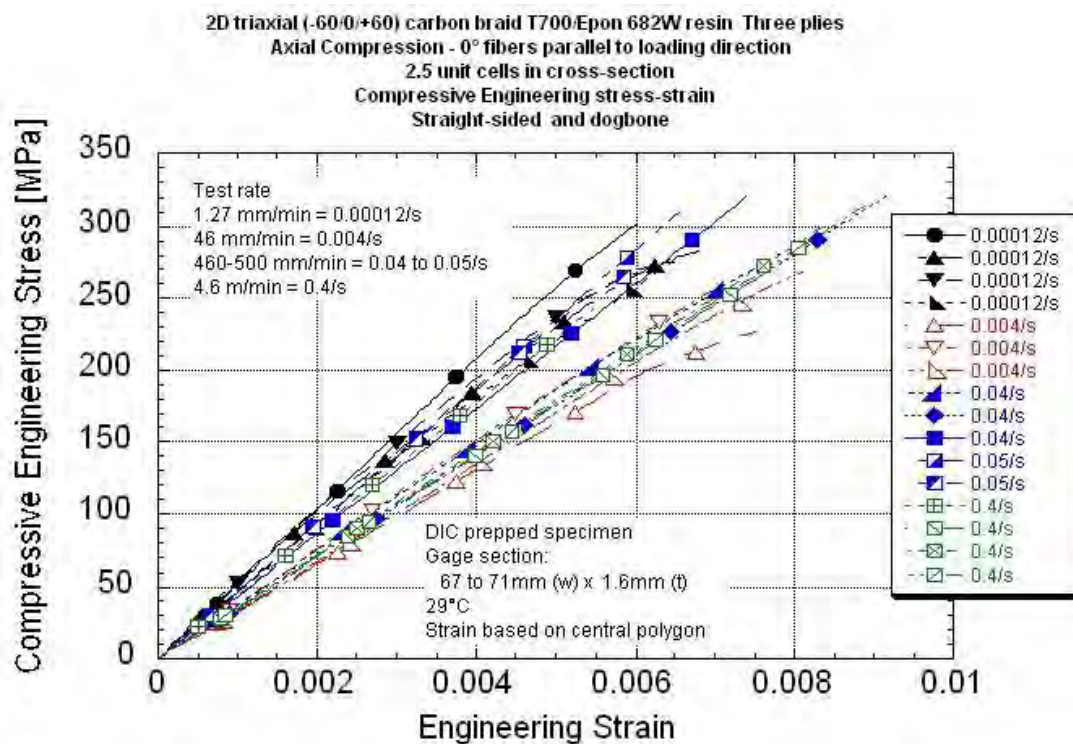
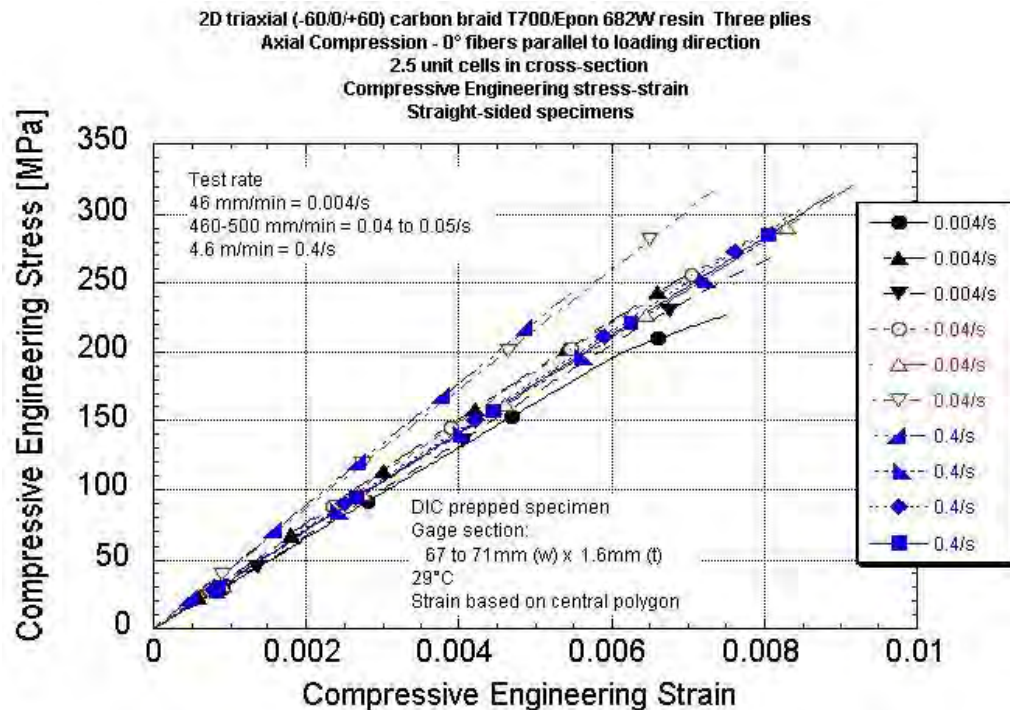
APPENDIX M
AXIAL COMPRESSION DATA PACKAGE
Summary Table
Summary Stress-strain Plots With Rate
Summary Stress-time Plots With Rate

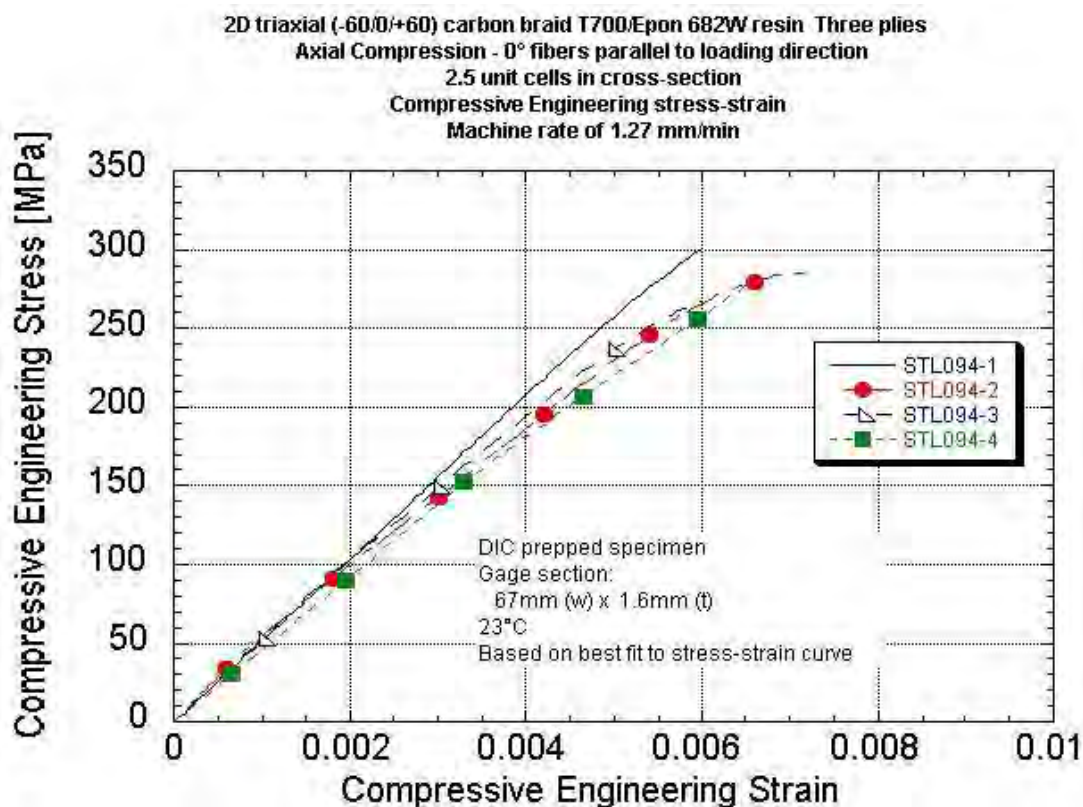
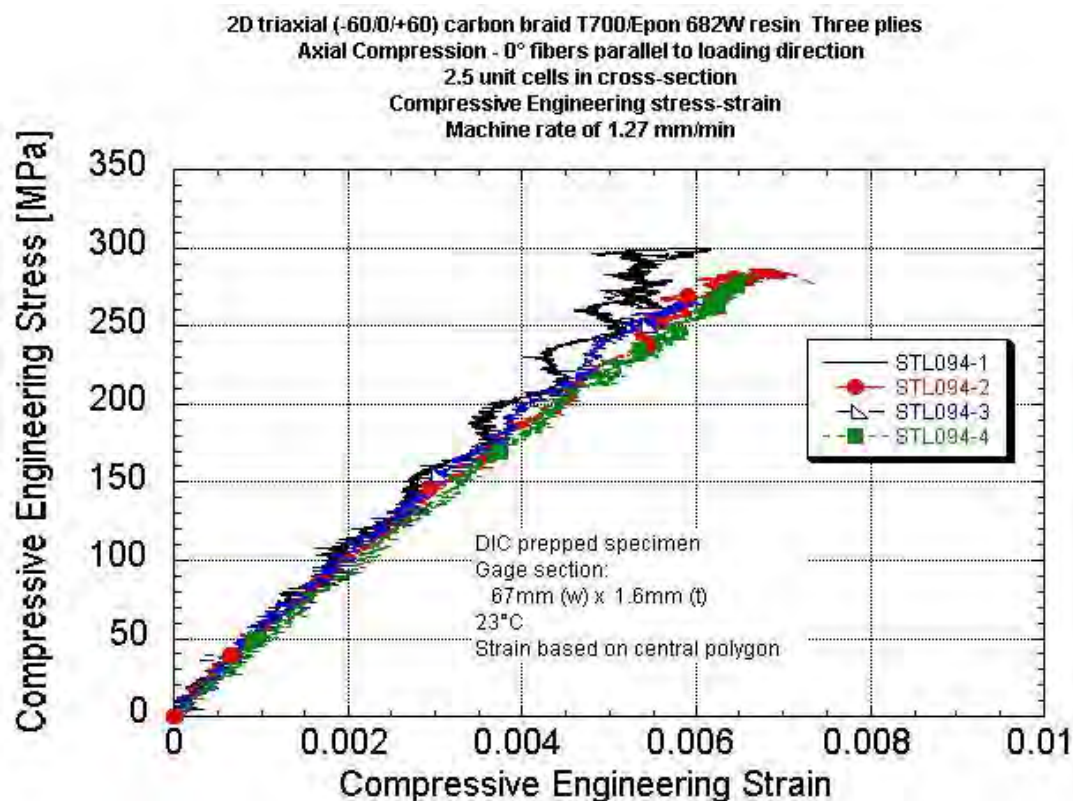
Investigation of Opportunities for Lightweight Vehicles Using Advanced Plastics and Composites

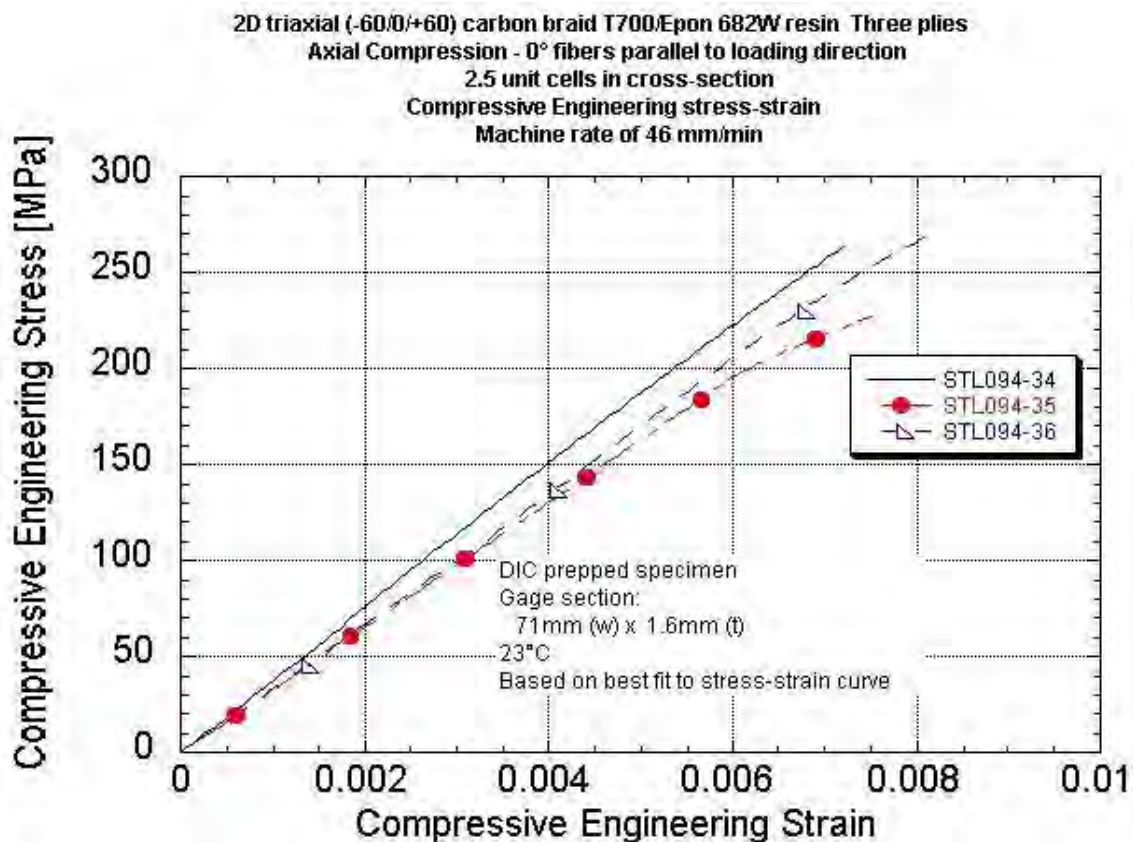
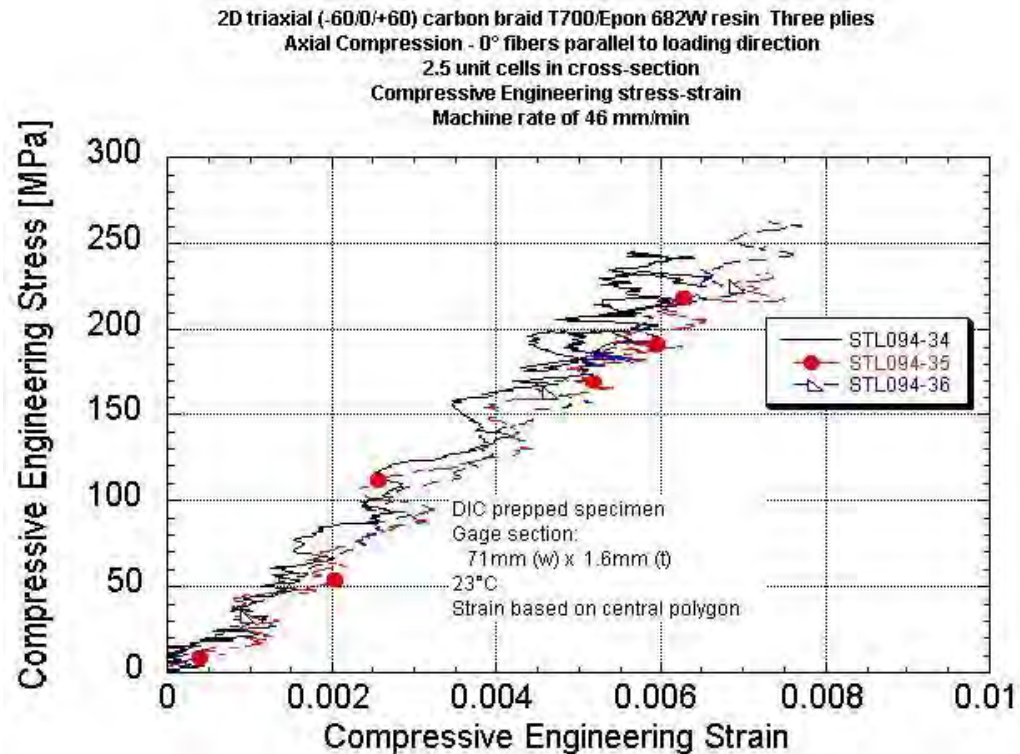
Axial Compression Data Summary - 0° fibers parallel to loading direction
2D Triaxial Carbon T700/ Epon862W Epoxy Braid
Minimum of 2.5 unit cells in cross section - Unit cell size (length x width) = 17.8mm x 5.5mm
Nominal center cross-section of 71mm wide x 1.65mm thick

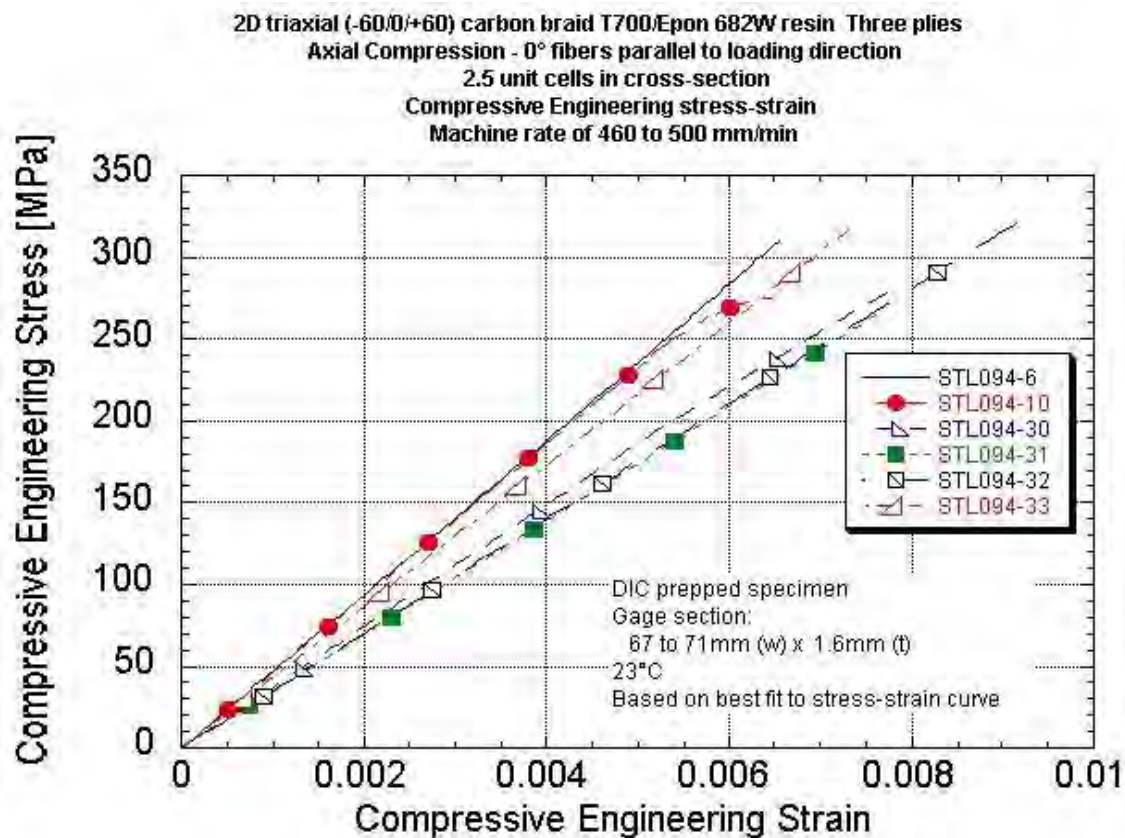
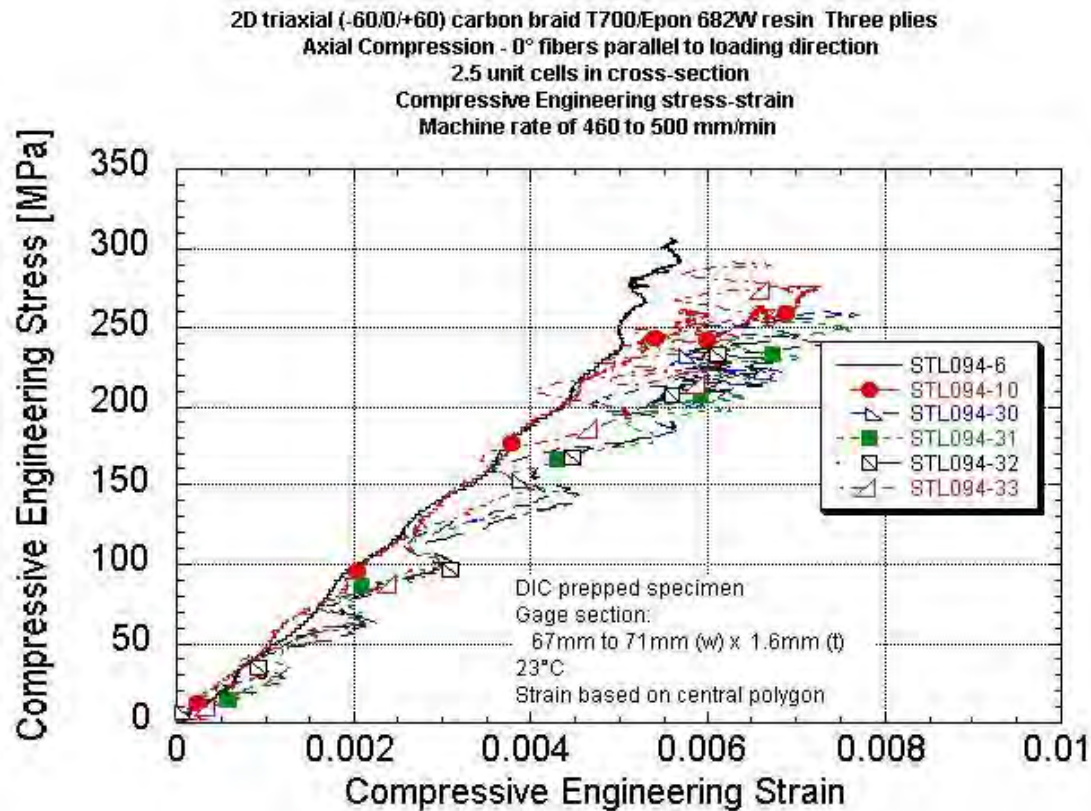
	Panel ID	UDRI STL number	Center polygon size length x width [mm]	Stress at Onset of Crush [MPa]	Onset of Crush Stress Normalized to 56% Fiber Volume [MPa]	Peak Stress [MPa]	Peak Stress Normalized to 56% Fiber Volume [MPa]	Engineering Breaking Strain # [%]	Localized## Engineering Max Strain [%]	Localized## Engineering Min Strain [%]	Elastic Modulus Based on Center [GPa]	Elastic Modulus Based on High Strain Point [GPa]	Measured Strain Rate* [1/s]	Machine Rate [in/s]	Machine Rate [m/min]	Comments
0.00012/s	073010-6 CAB-1	094-1	25.7x6.55	272	266	299	292	0.62	0.92	0.35	51.5	68.3	0.000121	0.00083	0.00127	Dogbone
	073010-6 CAB-2	094-2	-	259	253	286	279	0.70	-	-	56.0	-	0.000131	0.00083	0.00127	Dogbone
	073010-6 CAB-3	094-3	28.4x8.41	268	261	267	261	0.60	0.71	-	53.0	-	0.000124	0.00083	0.00127	Dogbone
	073010-6 CAB-4	094-4	27.0x8.28	221	215	282	275	0.65	-	-	46.2	-	0.000125	0.00083	0.00127	Dogbone
	073010-6 CAB-8	094-7	-	279	272	279	273	-	-	-	-	-	-	0.00083	0.00127	Straight. No DIC window
	073010-6 CAB-9	094-8	-	267	261	267	261	-	-	-	-	-	-	0.00084	0.00127	Straight. No DIC window
	073010-6 CAB-10	094-9	-	271	264	275	268	-	-	-	-	-	-	0.00084	0.00127	Straight. No DIC window
	073010-1 CAB-18	094-11	-	267	277	267	277	-	-	-	-	-	-	0.00083	0.00127	Straight. DIC window
	073010-1 CAB-21	094-12	-	282	292	304	315	-	-	-	-	-	-	0.00083	0.00127	Straight. DIC window
	073010-1 CAB-22	094-13	-	259	268	292	303	-	-	-	-	-	-	0.00083	0.00127	Straight. DIC window
073010-1 CAB-25	094-14	-	249	257	291	301	-	-	-	-	-	-	0.00083	0.00127	Straight. DIC window	
		Average		263	262	283	282	0.64	0.81		51.7					
	Standard Deviation			17	19	13	18	0.04	0.15		4.1					
	COV [%]			6.41	7.15	4.63	6.37	6.84	18.3		7.97					
0.004/s	072910-2 CAB-34	094-34	26.57x7.39	199	187	262	246	0.66	-	-	37.4	-	0.003942	0.0312	0.0475	
	072910-2 CAB-35	094-35	26.16x7.94	186	175	233	220	0.74	-	-	32.6	-	0.003932	0.0313	0.0476	
	072910-2 CAB-36	094-36	26.83x8.57	186	175	269	253	0.78	-	-	33.4	-	0.004134	0.0318	0.0485	
	072910-2 CAB-37	094-37	-	223	210	245	231	-	-	-	-	-	-	0.0311	0.0474	No Dic data
		Average			198	187	252	237	0.73			34.5				
	Standard Deviation			17	16	16	15	0.06			2.6					
	COV [%]			8.82	8.82	6.37	6.37	8.8			7.46					
0.04-0.05/s	073010-6 CAB-5	094-5	-	213	207	242	236	-	-	-	-	-	-	0.341	0.520	Dogbone. No DIC data
	073010-6 CAB-6	094-6	25.66x6.55	282	276	310	303	0.66	0.73	-	47.2	-	0.0477	0.335	0.510	Dogbone
	073010-6 CAB-13	094-10	30.05x9.07	261	255	276	269	0.65	-	-	46.5	-	0.0474	-	-	Dogbone. Issues with stroke data capture
	072910-2 CAB-30	094-30	26.99x7.62	233	219	279	263	0.76	-	-	37.3	-	0.0401	0.312	0.476	Straight
	072910-2 CAB-31	094-31	26.03x7.54	203	191	266	251	0.77	-	-	34.8	-	0.0406	0.318	0.485	Straight
	072910-2 CAB-32	094-32	26.60x7.04	220	207	293	276	0.71	-	-	35.1	-	0.0426	0.320	0.487	Straight
	072910-2 CAB-33	094-33	25.94x7.43	248	234	320	301	0.74	-	-	43.3	-	0.0366	0.315	0.480	Straight
		Average			237	227	284	271	0.71			40.7				
	Standard Deviation			28	30	27	25	0.05			5.7					
	COV [%]			12.0	13.1	9.39	9.12	7.2			14.0					
0.4/s	073010-6 CAB-11	094-23	-	150	146	259	252	-	-	-	-	-	-	3.15	4.80	Straight. No DIC
	073010-6 CAB-16	094-24	25.37x7.87	229	224	242	236	0.55	-	-	44.4	-	0.245	3.01	4.58	Straight
	073010-6 CAB-17	094-25	26.52x8.44	234	229	280	273	0.80	-	-	35.1	-	0.363	2.98	4.54	Straight
	072910-2 CAB-26	094-26	25.81x7.74	234	220	303	285	0.84	-	-	35.9	-	0.371	3.01	4.59	Straight
	072910-2 CAB-27	094-27	27.79x7.30	206	194	316	298	0.87	-	-	35.4	-	0.364	3.08	4.69	Straight
		Average			211	203	280	269	0.76			37.7				
	Standard Deviation			36	34	31	25	0.15			4.5					
	COV [%]			17.0	16.9	11.0	9.32	19.4			11.9					

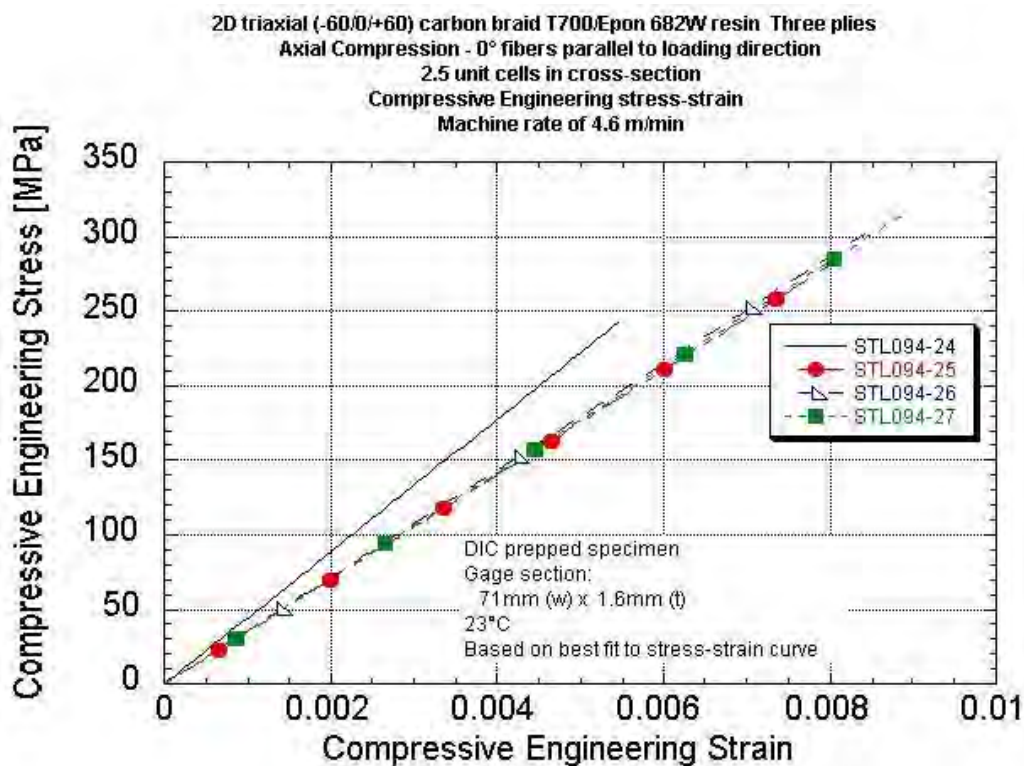
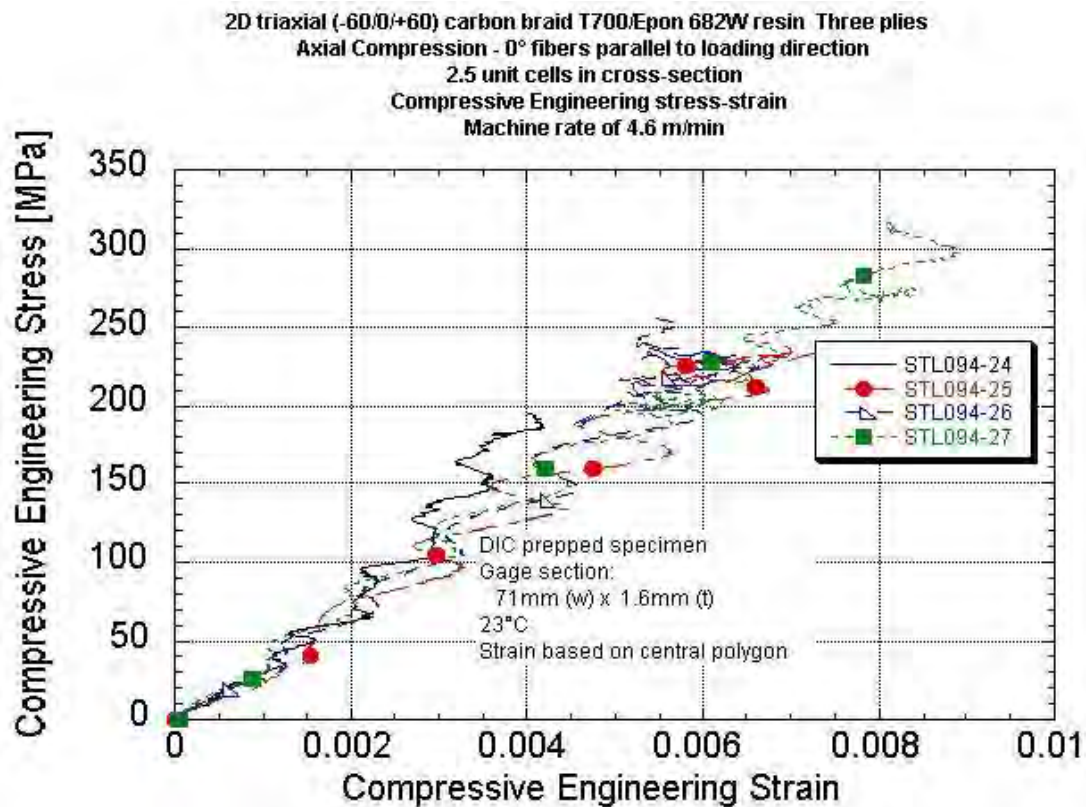
* Strain rate of central region ## Strain as measured at a region of high strain on a fiber braid and a low strain region.
Specimen thickness varied due to the braid structure. Thickness was measured at two "peak" and two "valley" locations and averaged.

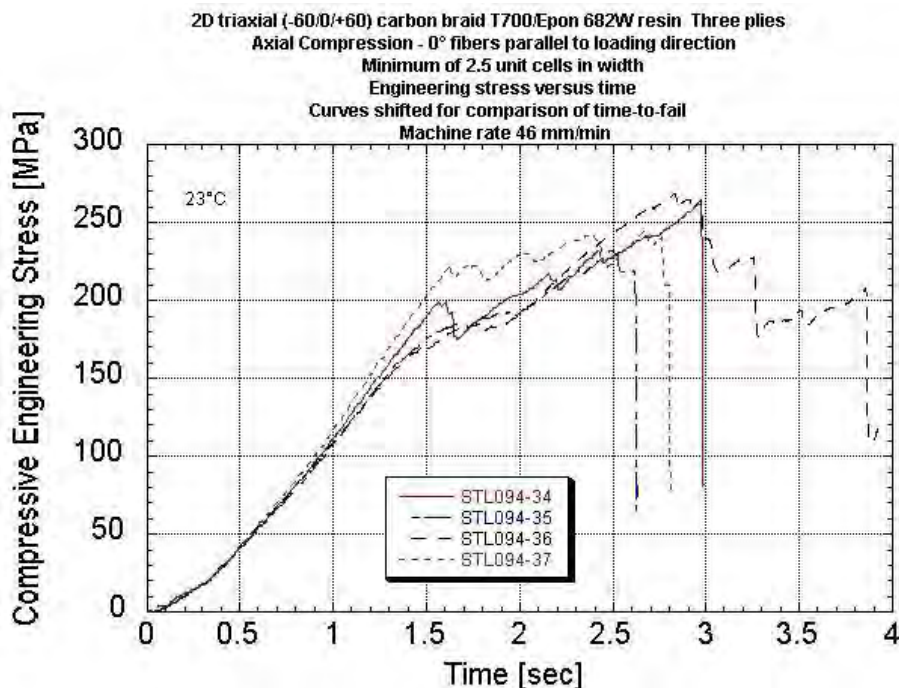
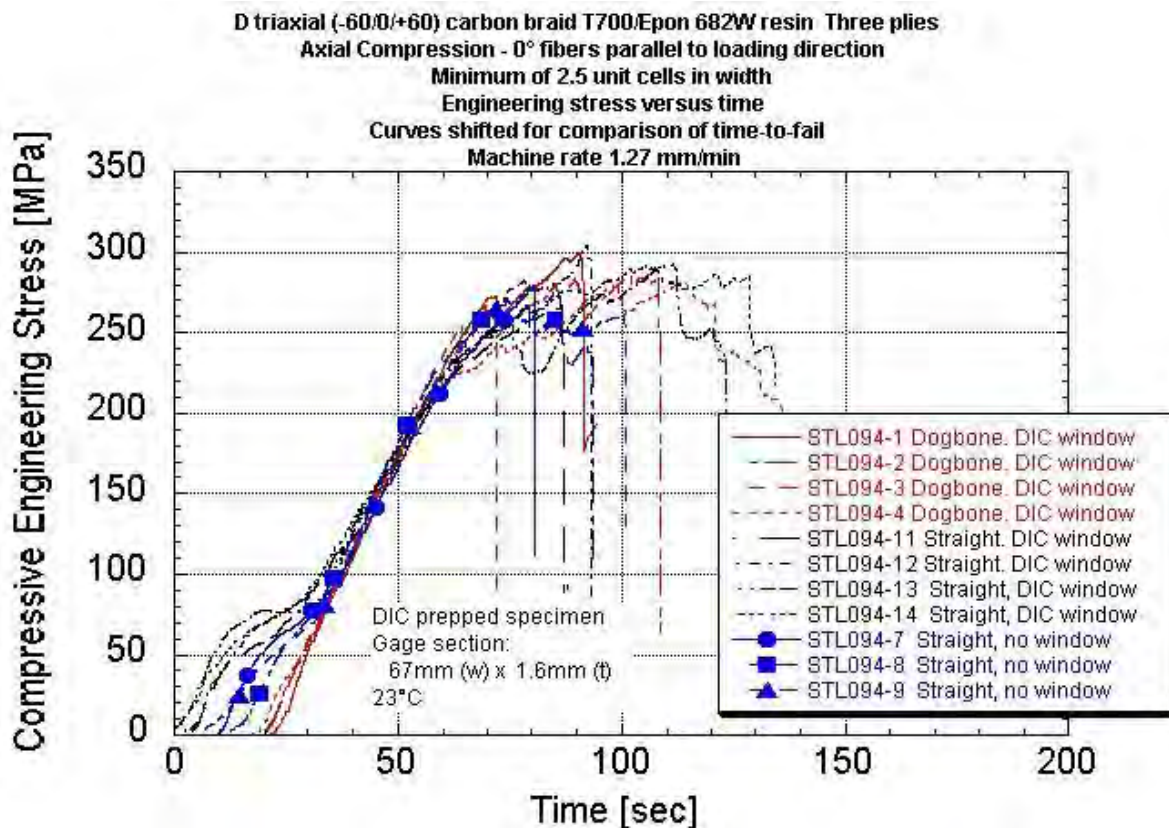


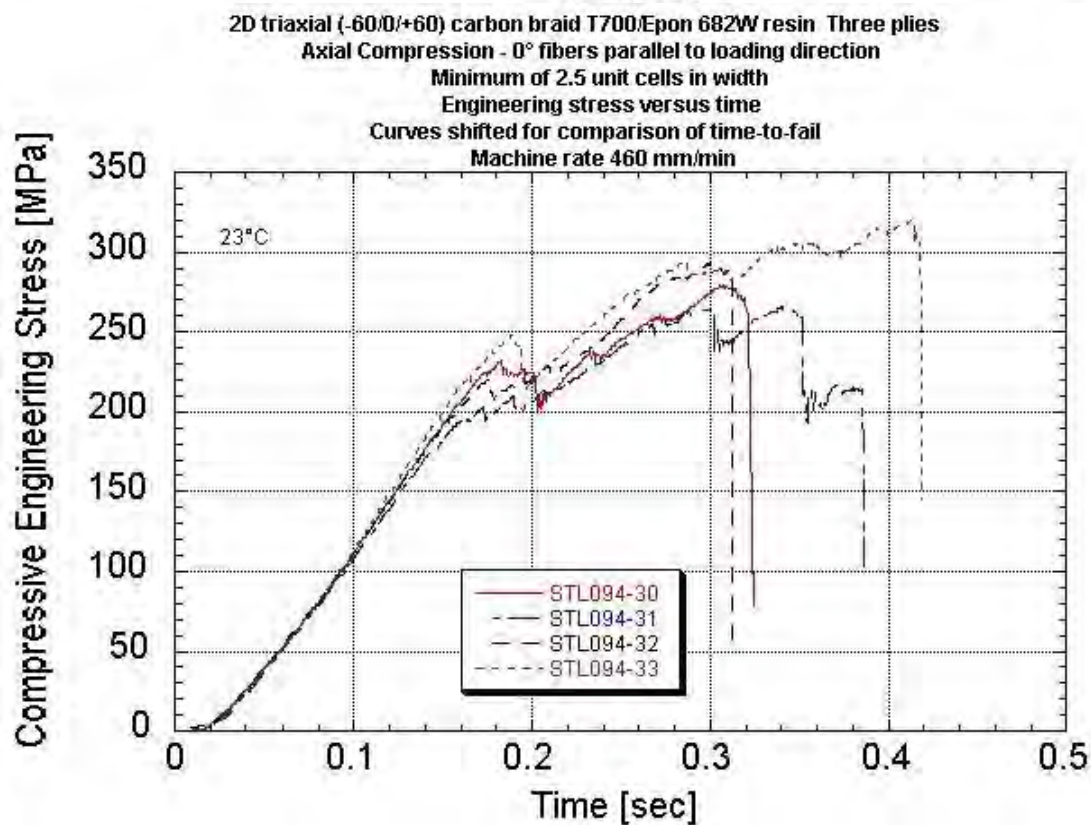
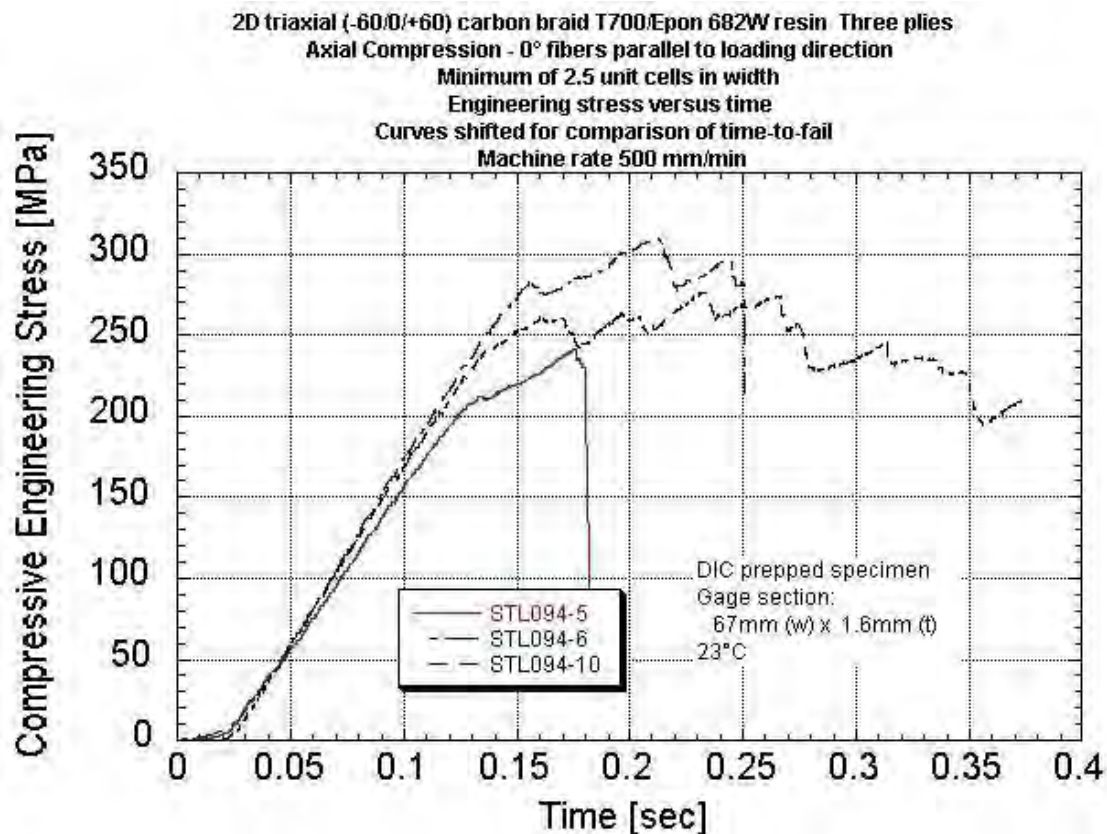


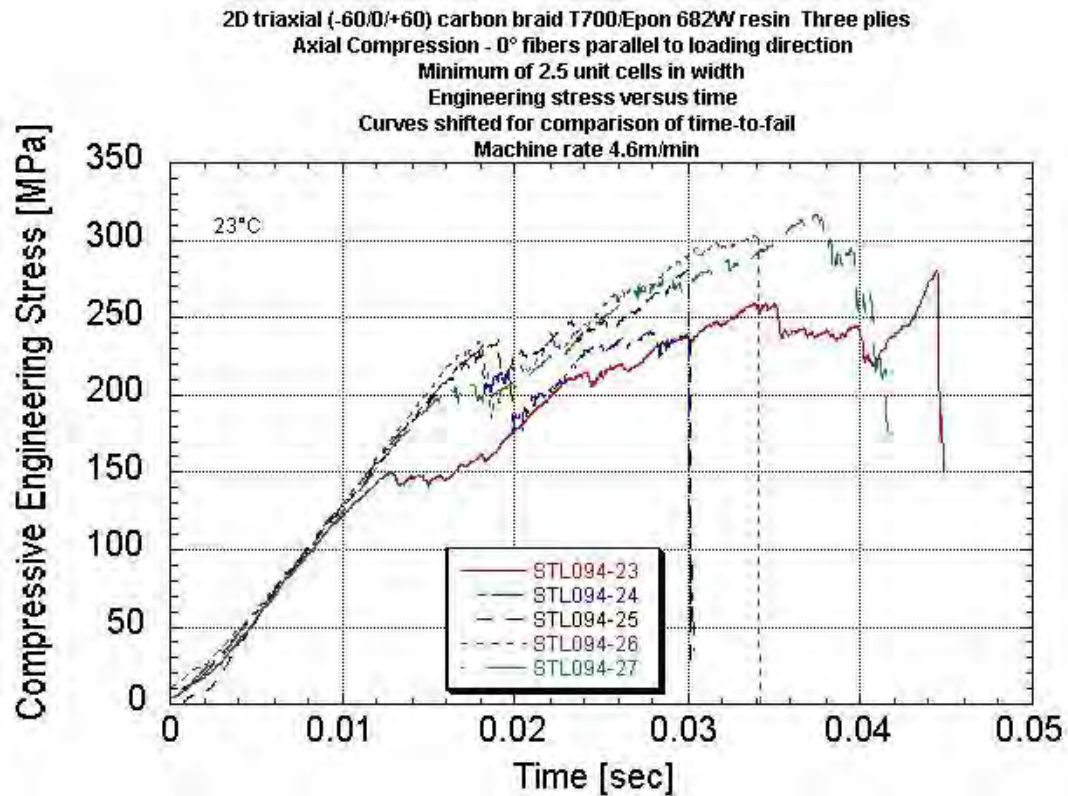












APPENDIX N
TRANSVERSE COMPRESSION DATA PACKAGE
Summary Table
Summary Stress-strain Plots With Rate
Summary Stress-time Plots With Rate

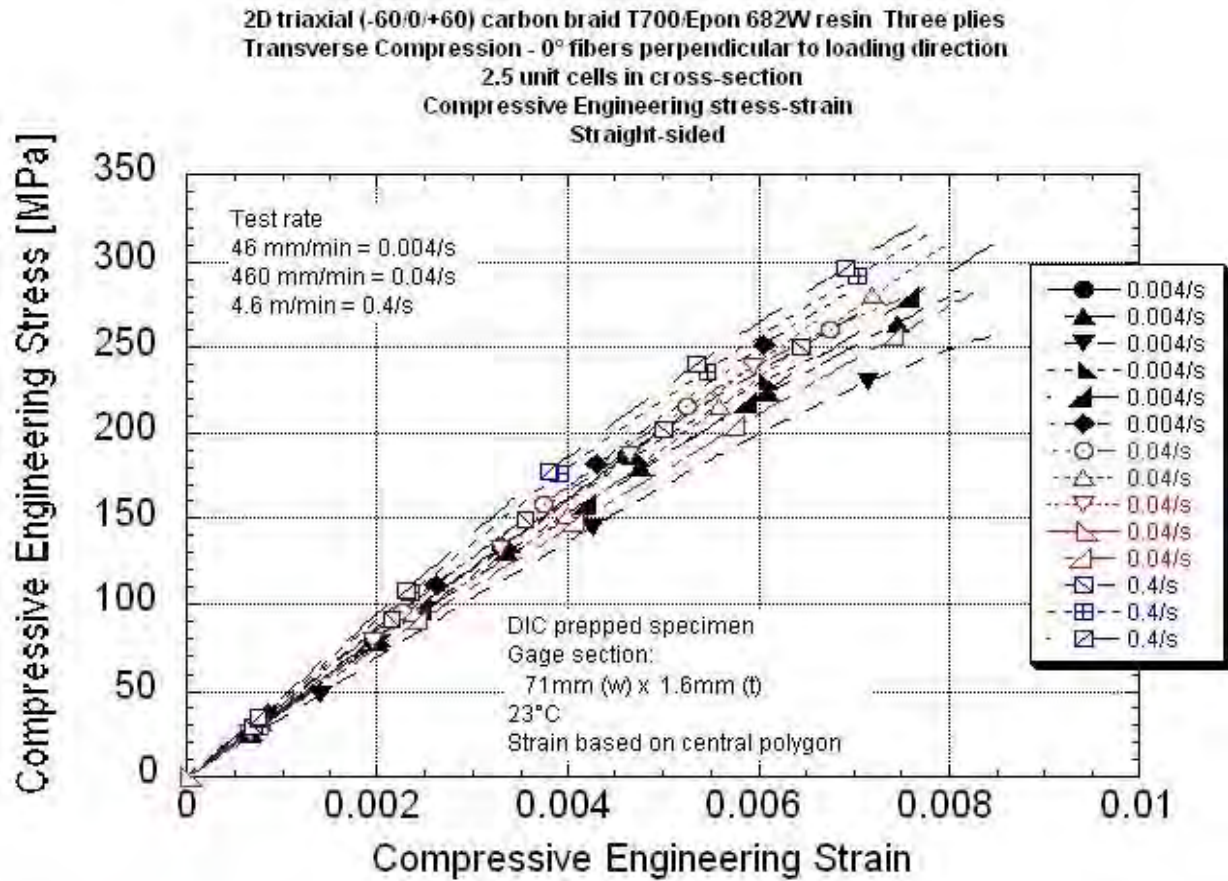
Investigation of Opportunities for Lightweight Vehicles Using Advanced Plastics and Composites

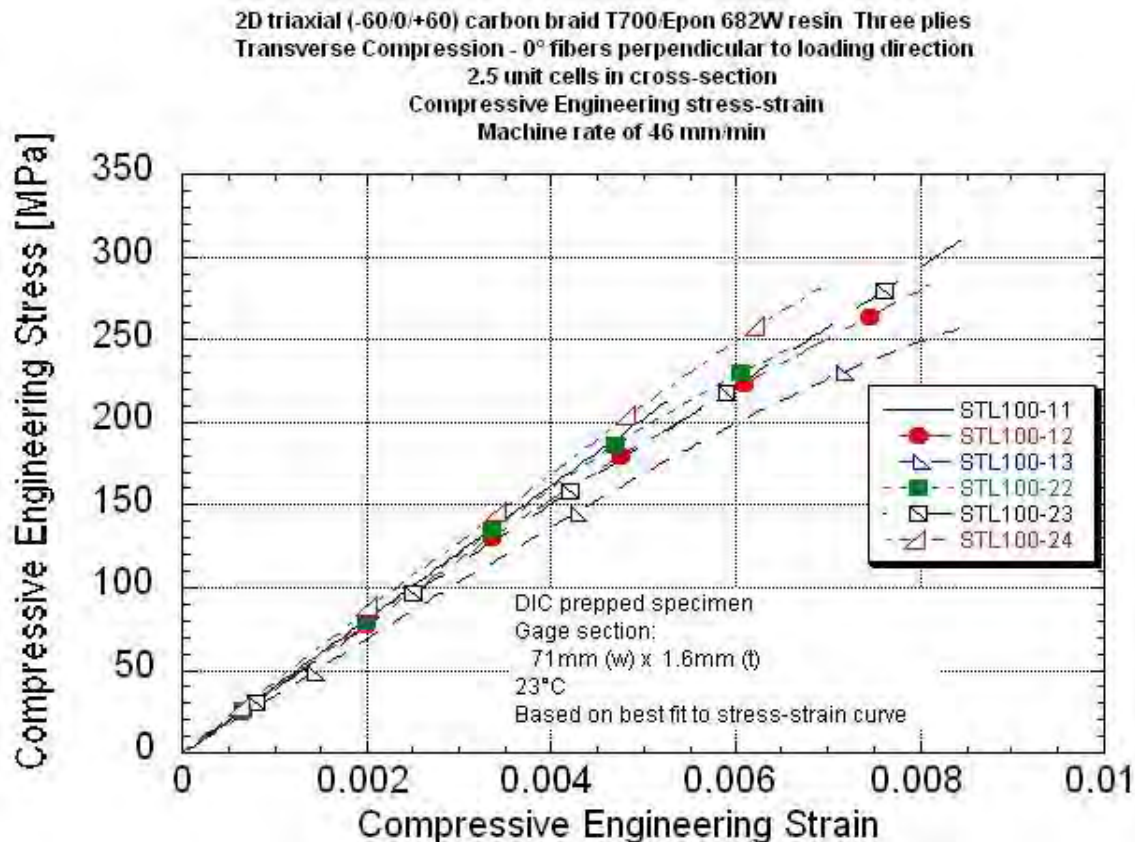
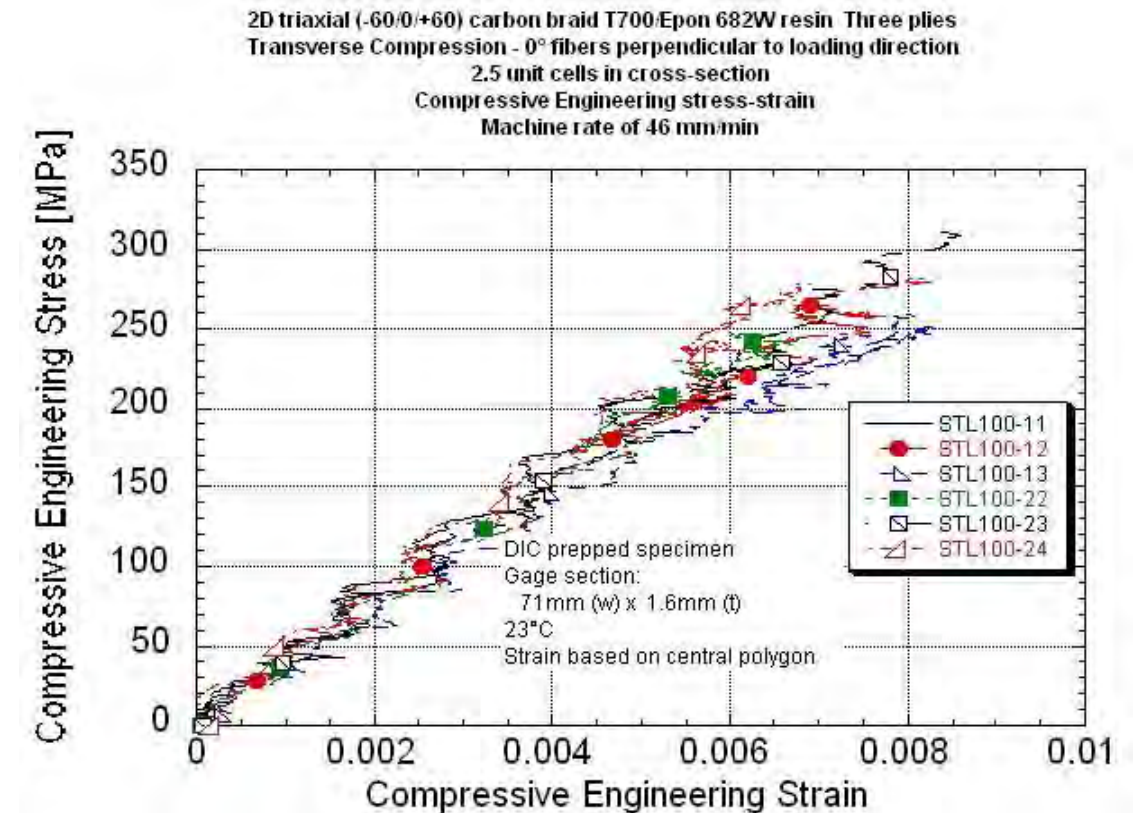
Transverse Compression Data Summary - 0° Fibers perpendicular to loading direction
2D Triaxial Carbon T700/ Epon862W Epoxy Braid
Minimum of 2.5 unit cells in cross section
Nominal center cross-section of 71mm wide x 1.65mm thick

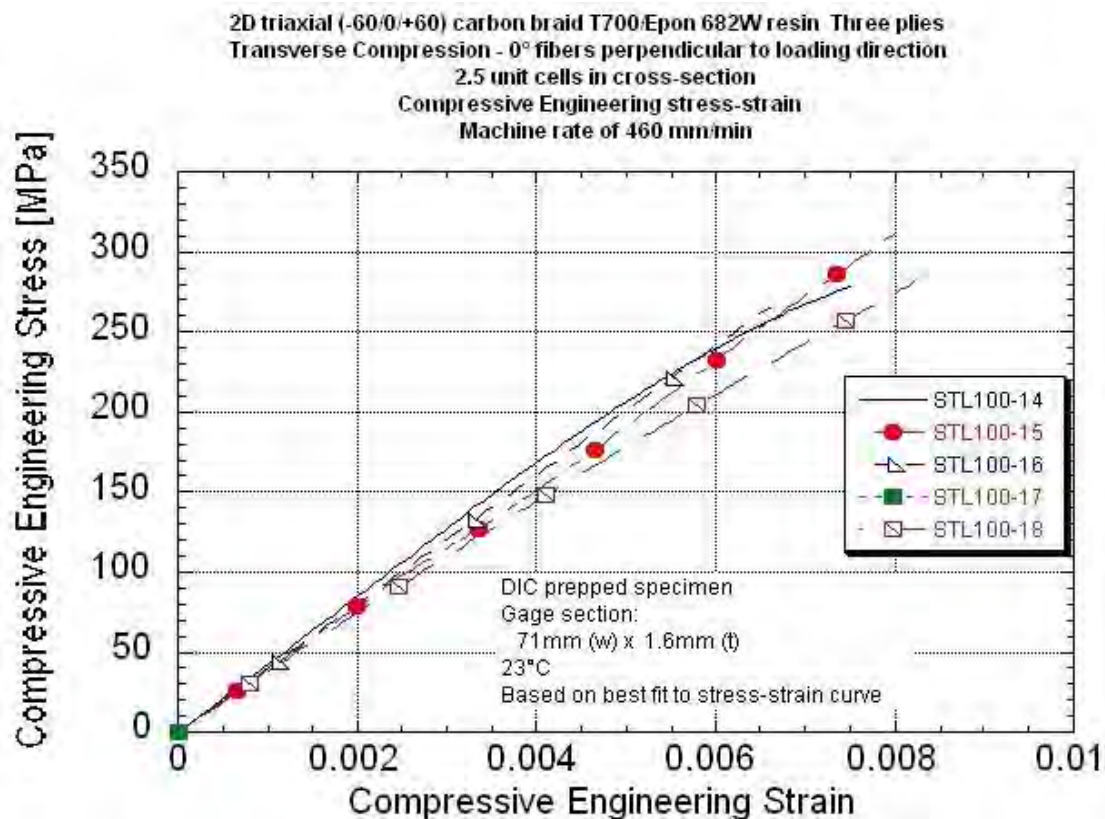
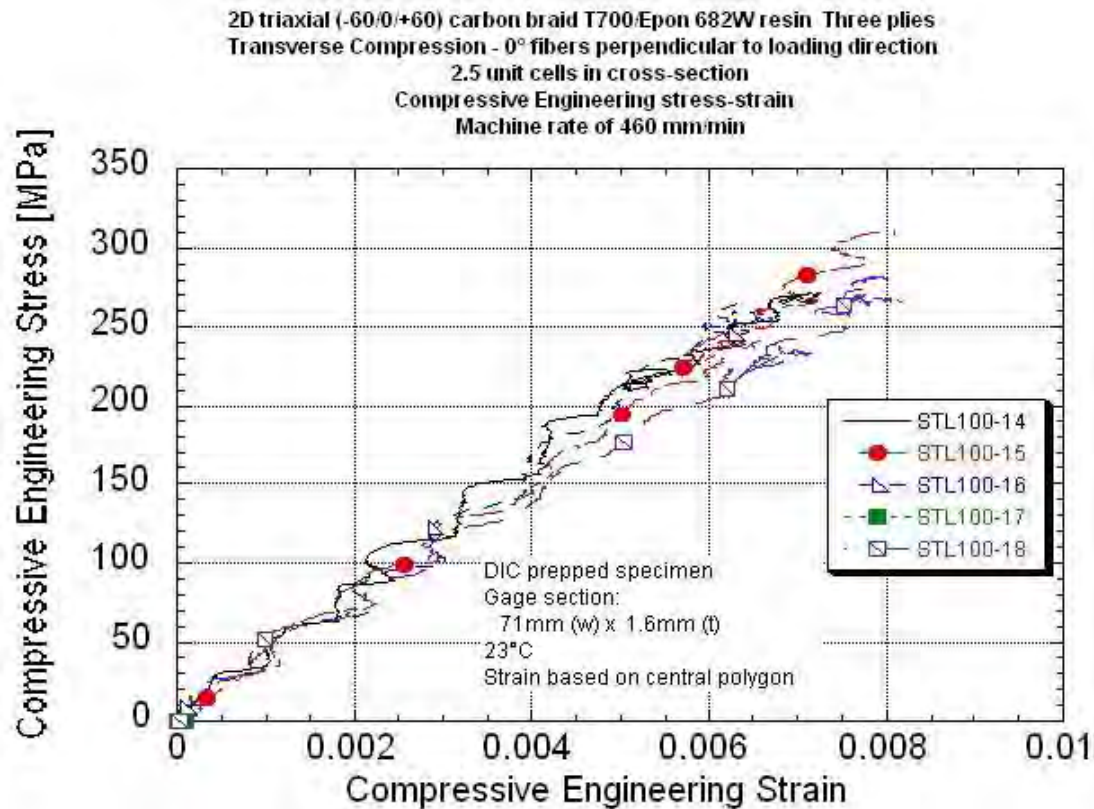
	Panel ID	UDRI STL number	Center polygon size length x width [mm]	Stress at Onset of Crush [MPa]	Normalized Stress at Onset of Crush to 56% Fiber Volume [MPa]	Peak Stress [MPa]	Normalized Peak Stress to 56% Fiber Volume [MPa]	Engineering Breaking Strain [%]	Elastic Modulus Based on Center [GPa]	Measured Strain Rate * [1/s]	Machine Rate [in/s]	Machine Rate [m/min]	Comments
~0.00005/s	073010-6 CTB-1	100-1	-	214	209	214	209	-	-	-	0.00041	0.00062	No DIC
	073010-6 CTB-2	100-2	-	235	229	235	229	-	-	-	0.00041	0.00063	No DIC
	073010-6 CTB-3	100-3	-	213	208	213	208	-	-	-	0.00041	0.00063	No DIC
	073010-6 CTB-4	100-4	-	244	238	244	238	-	-	-	0.00041	0.00063	No DIC
		Average		226	221	226	221						
		Standard Deviation		15	15	15	15						
		COV [%]		6.73	6.73	6.73	6.73						
0.004/s	072910-2 CTB-11	100-11	7.89x27.16	207	195	212	199	0.52	40.5	0.00410	0.031	0.047	
	072910-2 CTB-12	100-12	7.42x25.44	206	194	282	265	0.81	39.0	0.00422	0.032	0.048	
	072910-2 CTB-13	100-13	7.79x26.38	202	190	259	244	0.82	34.5	0.00407	0.032	0.048	
	072910-2 CTB-22	100-22	7.61x26.17	211	199	247	233	0.67	40.1	0.00385	0.032	0.049	bottom fixture paired
	072910-2 CTB-23	100-23	7.83x26.34	230	216	310	292	0.85	38.5	0.00427	0.032	0.049	bottom fixture paired
	072910-2 CTB-24	100-24	7.70x26.43	238	225	280	264	0.69	43.2	0.00414	0.032	0.049	bottom fixture paired
		Average		216	203	265	249	0.72	39.3				
		Standard Deviation		15	14	34	32	0.12	2.8				
		COV [%]		6.90	6.90	12.85	12.85	17.17	7.25				
0.04/s	072910-2 CTB-14	100-14	7.67x26.52	223	210	279	263	0.71	42.4	0.0356	0.32	0.48	
	072910-2 CTB-15	100-15	7.85x25.75	241	227	311	293	0.80	39.3	0.0421	0.31	0.48	
	072910-2 CTB-16	100-16	7.78x27.54	253	238	266	250	0.64	40.2	0.0410	0.31	0.47	
	072910-2 CTB-17	100-17	7.88x27.46	216	203	302	284	0.81	40.5	0.0392	0.32	0.48	
	072910-2 CTB-18	100-18	7.66x27.49	238	225	282	266	0.80	37.9	0.0486	0.32	0.48	
		Average		234	221	288	271	0.75	40.1				
	Standard Deviation		15	14	18	17	0.08	1.7					
		COV [%]		6.27	6.27	6.33	6.33	10.0	4.12				
0.4/s	072910-2 CTB-10	100-10	25.54x8.09	177	167	269	253	>.483	35.5	0.366	3.24	4.9	DIC window horizontal
	072910-2 CTB-19	100-19	7.84x26.04	230	217	274	258	0.69	42.5	0.361	3.09	4.7	
	072910-2 CTB-20	100-20	7.54x26.42	288	272	317	299	0.77	45.3	0.372	3.11	4.7	
	072910-2 CTB-21	100-21	7.79x27.72	295	277	325	307	0.76	47.1	0.406	3.00	4.6	
	Average [EXCLUDING 100-10]				271	255	305	288	0.74	45.0			
	Standard Deviation				35	33	28	26	0.04	2.3			
	COV [%]				13.0	13.0	9.11	9.11	5.8	5.17			

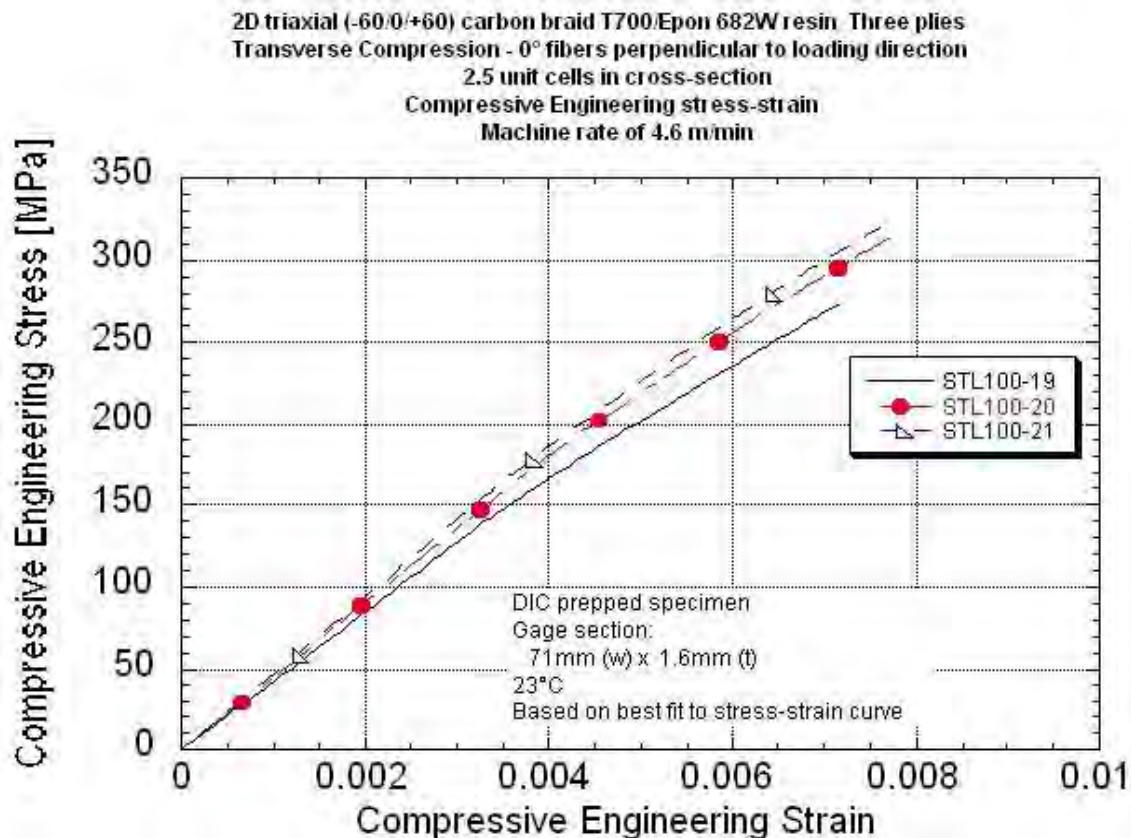
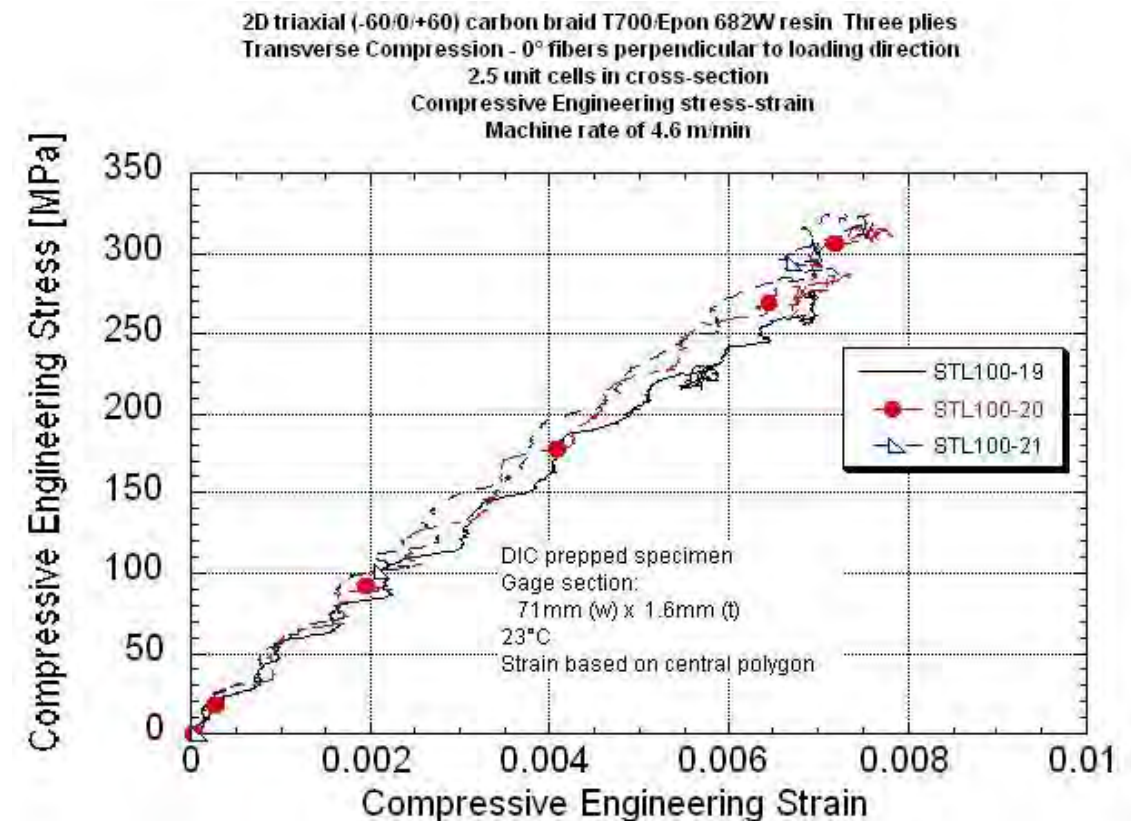
* Strain rate of central region

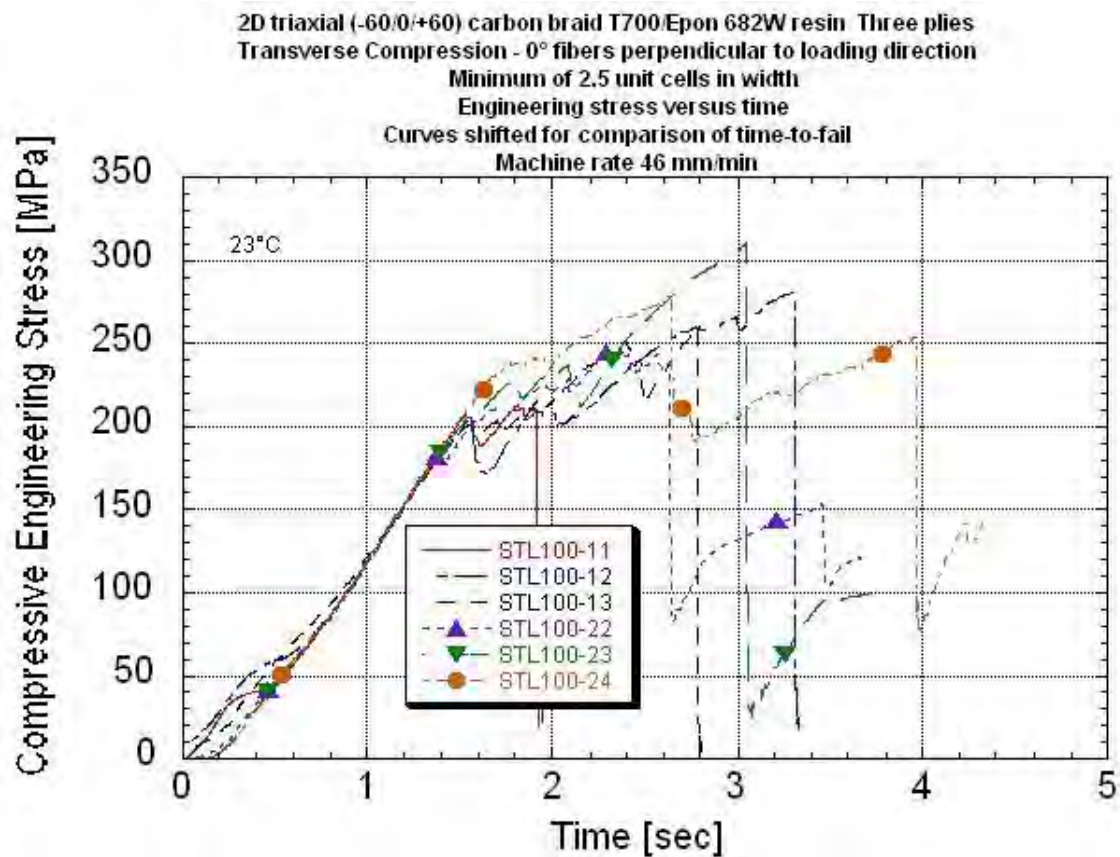
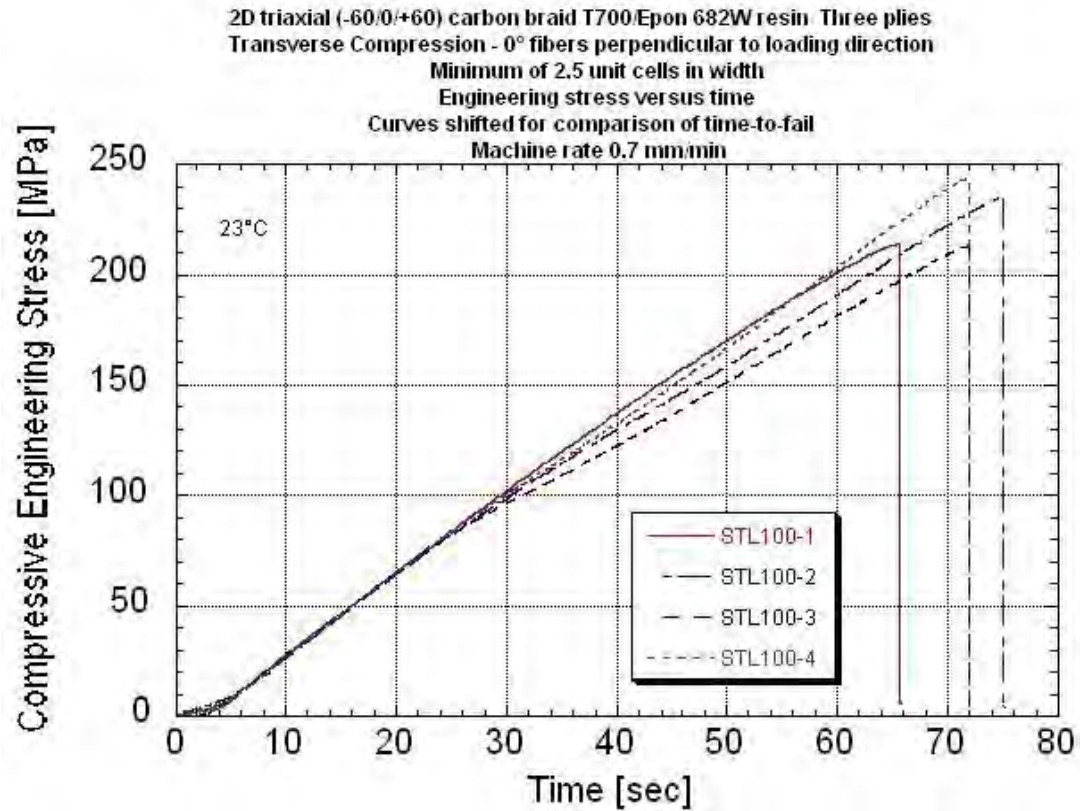
Specimen thickness varied due to the braid structure. Thickness was measured at two "peak" and two "valley" locations and averaged.

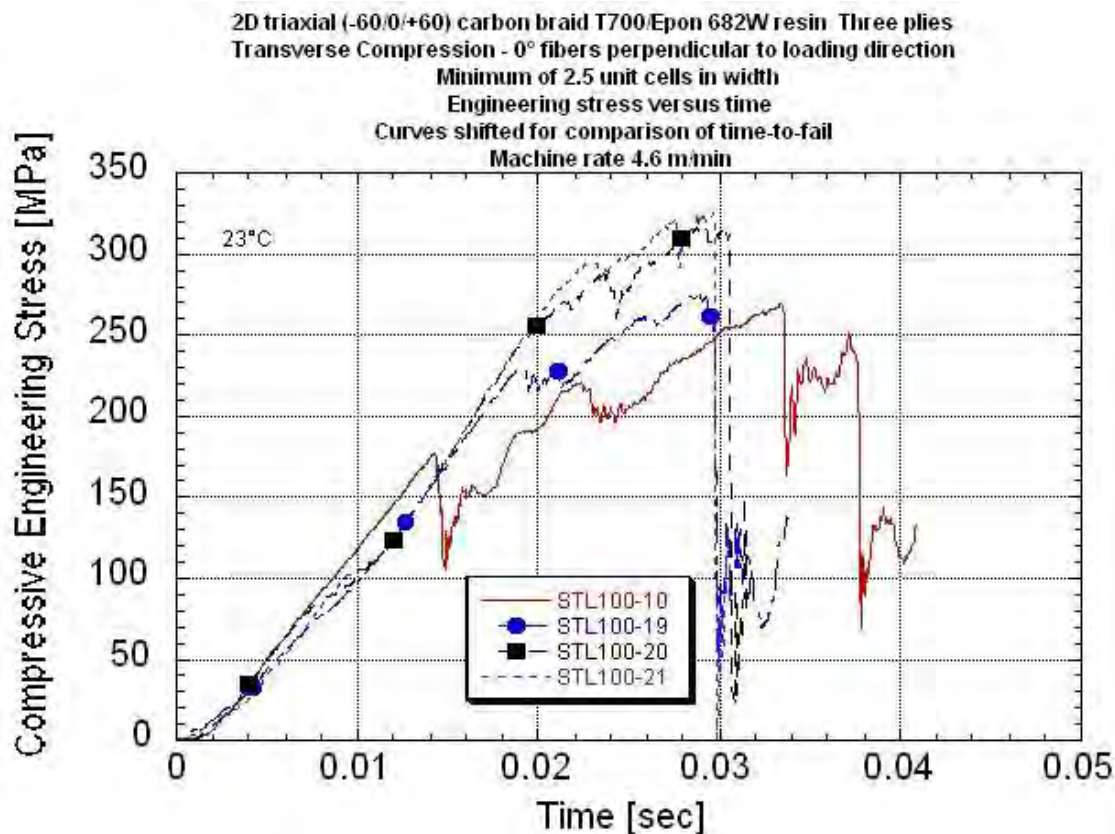
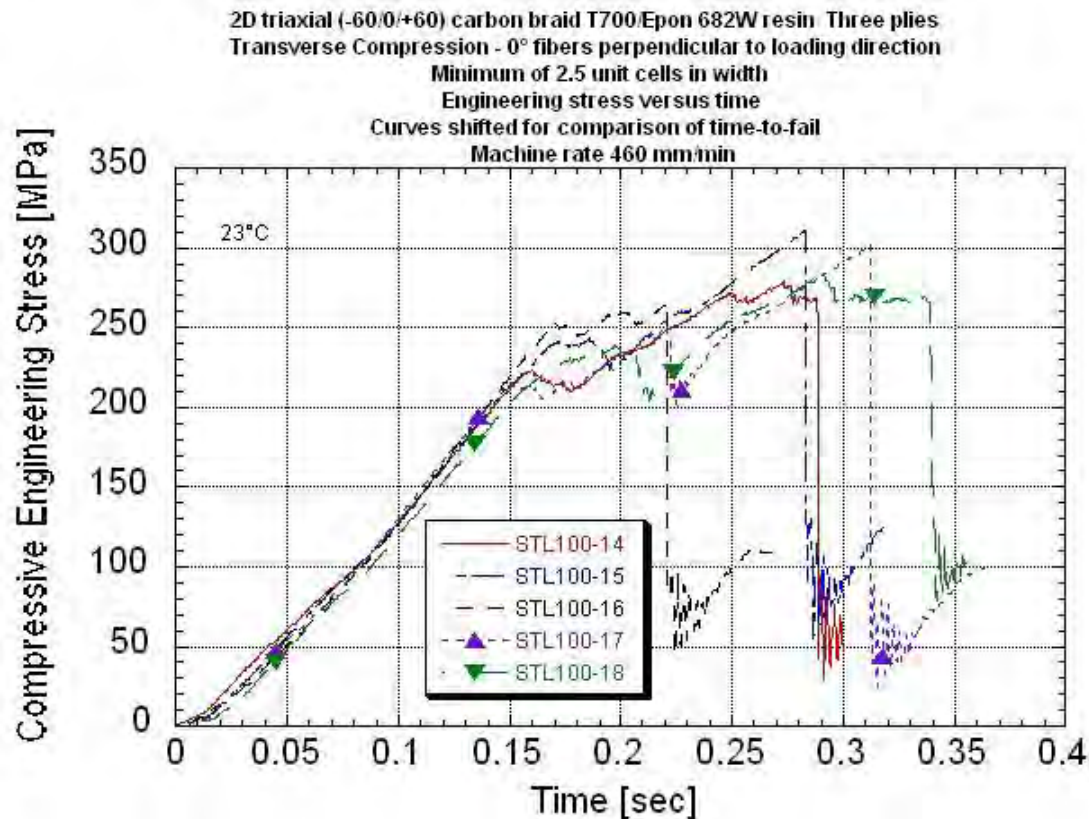












APPENDIX O
AXIAL SHEAR DATA PACKAGE
Shearing across 0° Fibers
Summary Table
Summary Stress-strain Plots With Rate
Summary Stress-time Plots With Rate

Investigation of Opportunities for Lightweight Vehicles Using Advanced Plastics and Composites

Axial Shear⁽¹⁾ Data Summary 2D Triaxial Carbon T700/ Epon862W Epoxy Braid Bowtie Specimen Configuration - 2.5 unit cells in reduced cross section Nominal center cross-section of 46mm wide x 1.65mm thick

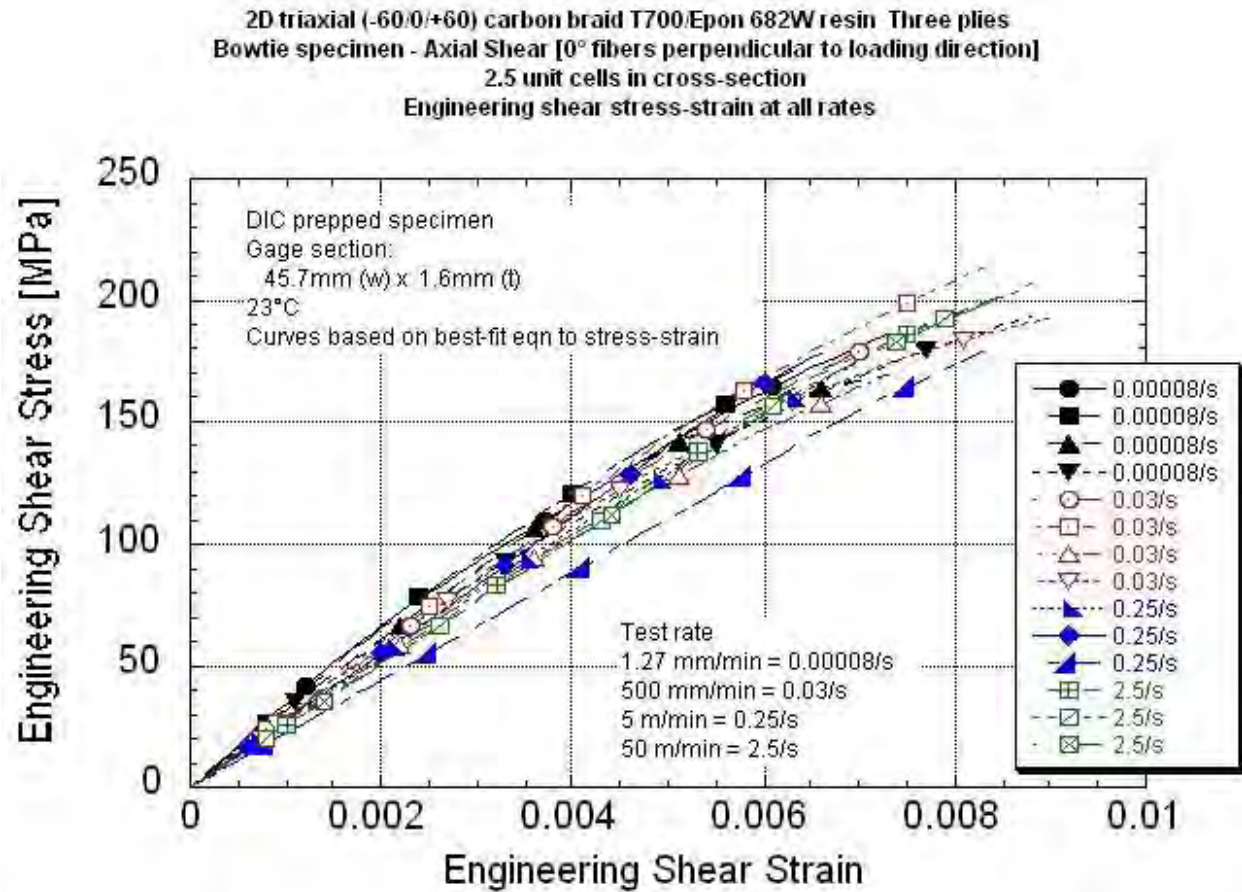
	Panel ID	UDRI STL number	Center line/polygon length [mm]	Peak Stress [MPa]	Normalized Peak Stress to 56% Fiber Volume [MPa]	Engineering Breaking Strain # [%]	Localized## Engineering Max Strain [%]	Localized## Engineering Min Strain [%]	Shear Modulus Based on Center Line [GPa]	Measured Strain Rate	Machine Rate [in/s]	Machine Rate [m/min]	
0.00008/s	073010-4 SAB-4	095-1	37.4	186	181	0.724	0.963	0.700	34.7	0.000089	0.00083	0.00127	
	073010-4 SAB-6	095-2	27.8	172	167	0.638	0.947	0.400	33.4	0.000077	0.00083	0.00127	
	073010-4 SAB-3	095-3	26.7x5.71	170	166	0.780	1.07	0.491	31.4	0.000076	0.00083	0.00127	Final failure at 1.22%
	073010-5 SAB-4	095-9	28.9	193	192	0.876	1.29	0.742	32.2	0.000085	0.00083	0.00127	
0.03/s	Average			180	177	0.755	1.07	0.583	32.9				
	Standard Deviation			11	12	0.100	0.16	0.164	1.45				
	COV [%]			6.30	7.01	13.2	14.6	28.2	4.40				
	073010-4 SAB-5	095-4	-	186	182	-	-	-	-	-	0.334	0.509	No DIC data
0.03/s	073010-5 SAB-9	095-5	23.1	189	188	0.786	-	-	28.9	0.0339	0.334	0.509	
	073010-5 SAB-1	095-6	29.6	213	211	0.846	1.02	0.726	28.5	0.0318	0.335	0.510	
	073010-5 SAB-2	095-7	30.4	168	167	0.723	0.934	0.608	26.8	0.0339	0.326	0.497	
	073010-5 SAB-3	095-8	30.7	192	190	0.980	1.11	-	29.8	0.0330	0.333	0.508	Final failure at 1.63%
0.25/s	Average			190	188	0.834	1.02	0.667	28.5				
	Standard Deviation			16	16	0.109	0.088		1.24				
	COV [%]			8.40	8.54	13.1	8.6		4.35				
	073010-5 SAB-5	095-10	27.4	173	171	0.682	-	-	27.1	0.279	3.26	4.96	
0.25/s	073010-5 SAB-7	095-12	-	177	176	-	-	-	-	-	3.26	4.96	No DIC data
	073010-4 SAB-1	095-14	27.0	179	174	0.642	0.960	-	27.3	0.240	3.26	4.97	
	073010-5 SAB-8	095-15	27.4	178	176	0.842	-	-	22.2	0.260	3.27	4.98	
	Average			177	174	0.722			25.5				
2.5/s	Standard Deviation			3	2	0.106			2.91				
	COV [%]			1.48	1.29	14.7			11.4				
	072910-01 SAB-21	095-16	27.8	196	193	0.811	-	-	27.0	2.60	32.3	49.3	Note 1
	072910-01 SAB-24	095-17	28.0	202	199	0.871	-	-	25.6	2.50	32.2	49.1	No DIC data. Note 1
2.5/s	072910-01 SAB-22	095-18	28.2	206	203	0.842	-	-	25.5	2.47	32.4	49.4	Note 1
	Average			201	199	0.841			26.0				
	Standard Deviation			5	5	0.03			0.84				
	COV [%]			2.58	2.58	3.57			3.24				

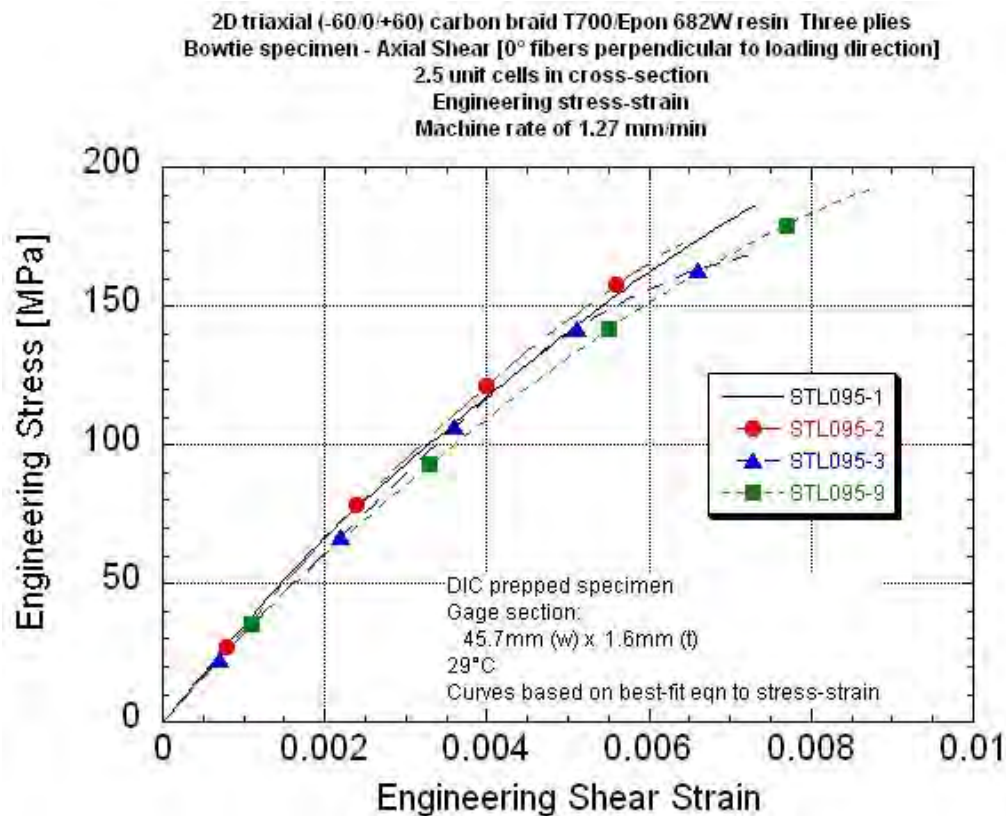
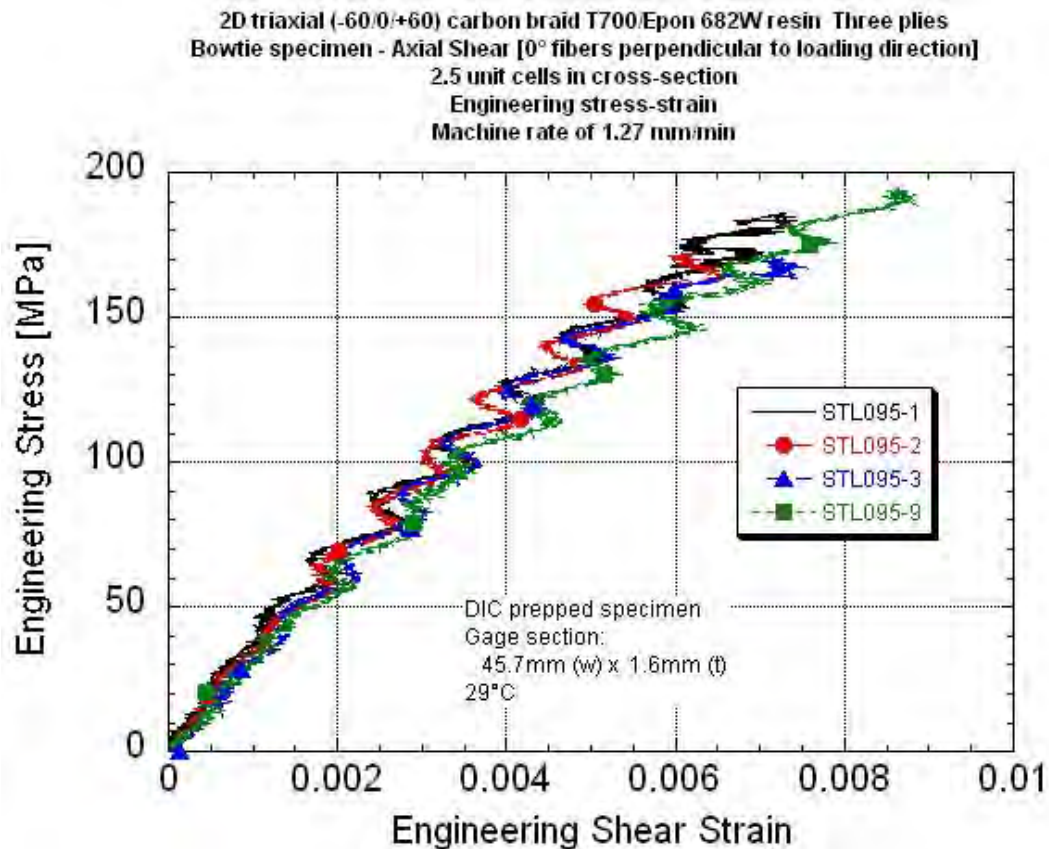
(1) Shear through the long side (18mm) of the unit cell. 0° fibers perpendicular to loading direction.

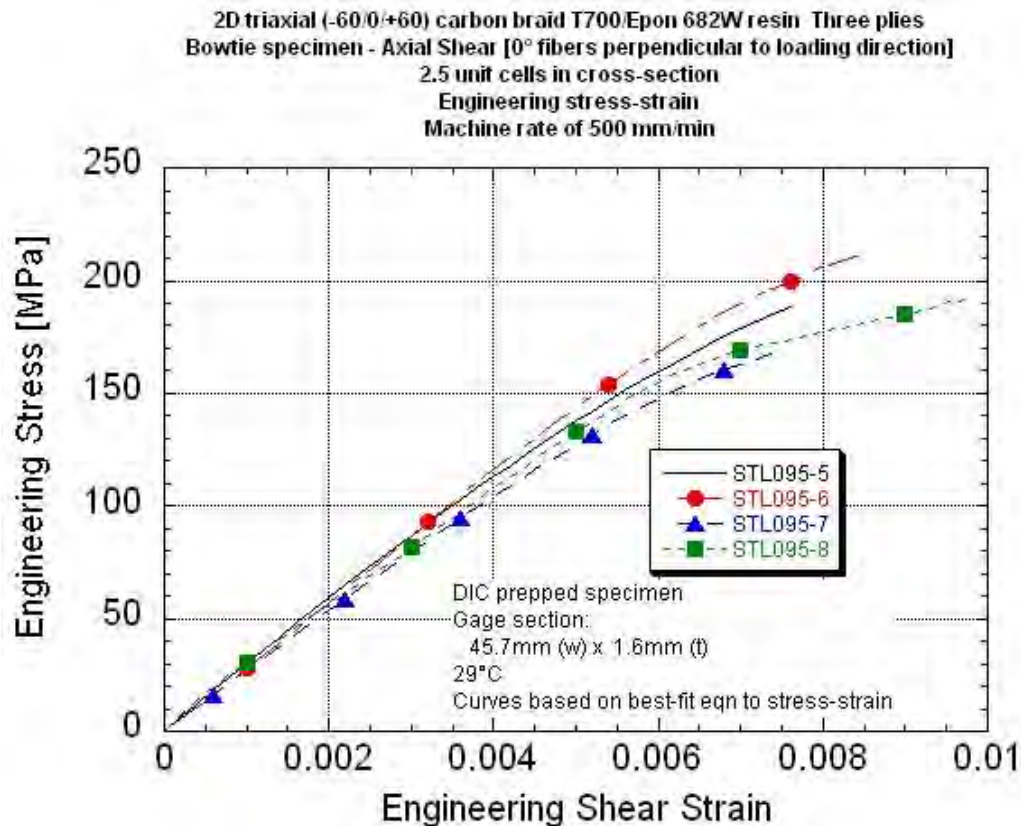
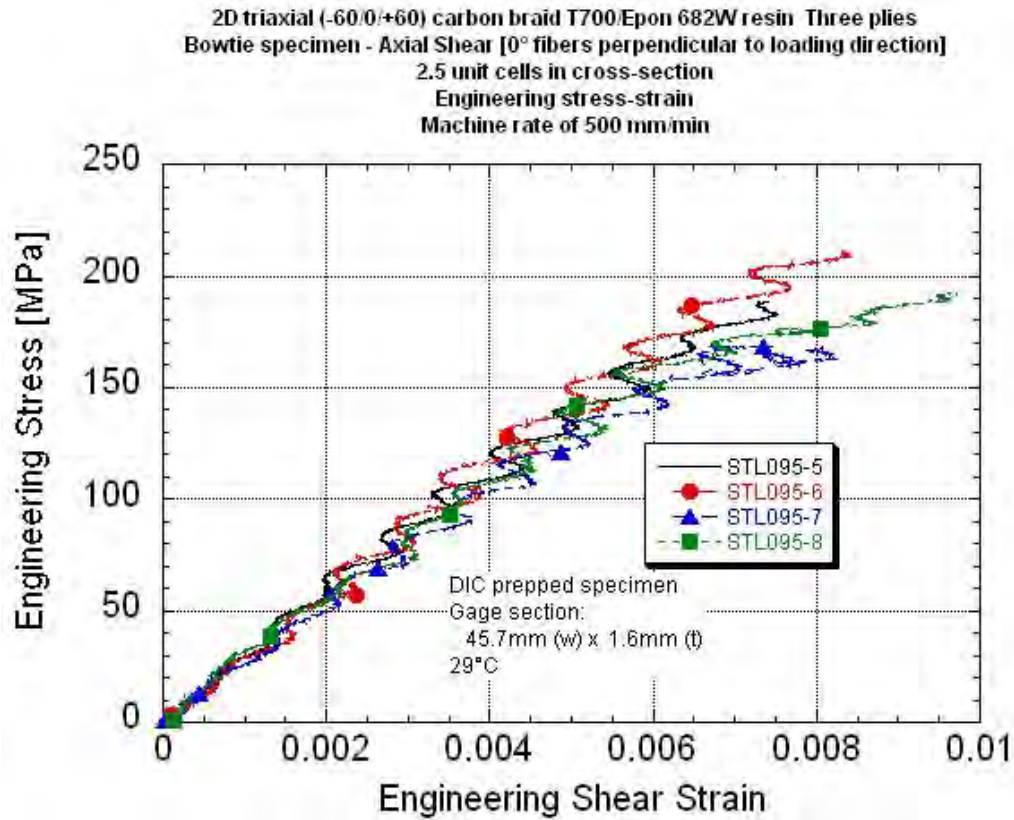
#Based on center line ## Strain as measured at a region of high strain on a fiber braid and low strain in center. Breaking strain taken at first large drop in stress.

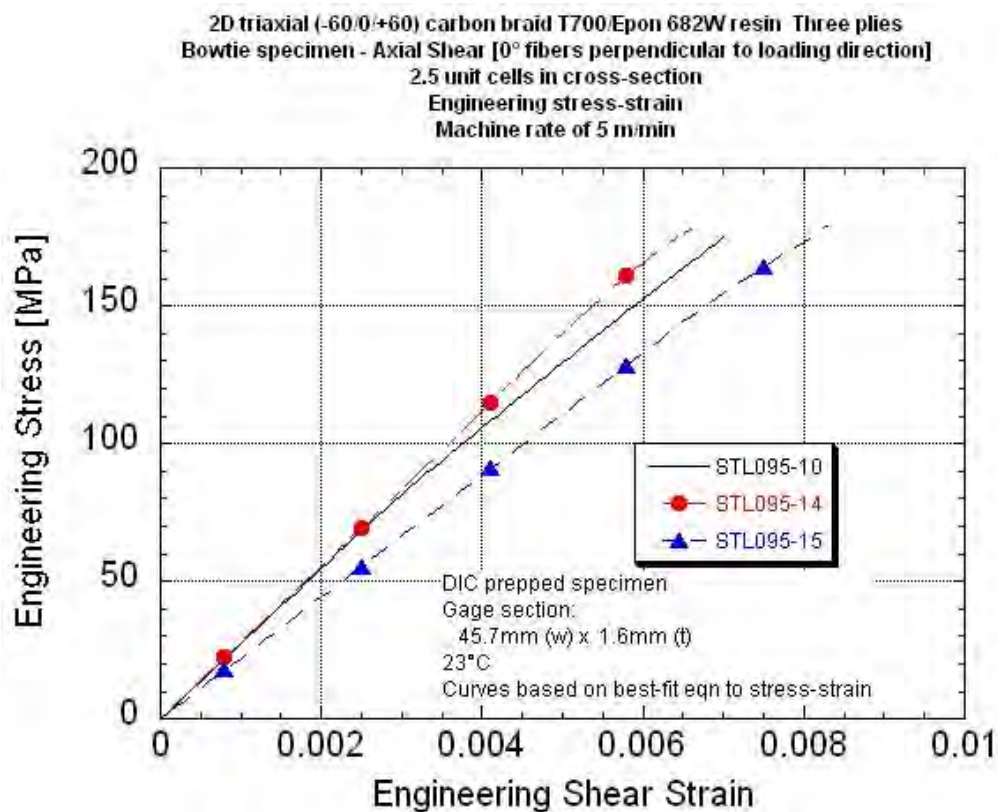
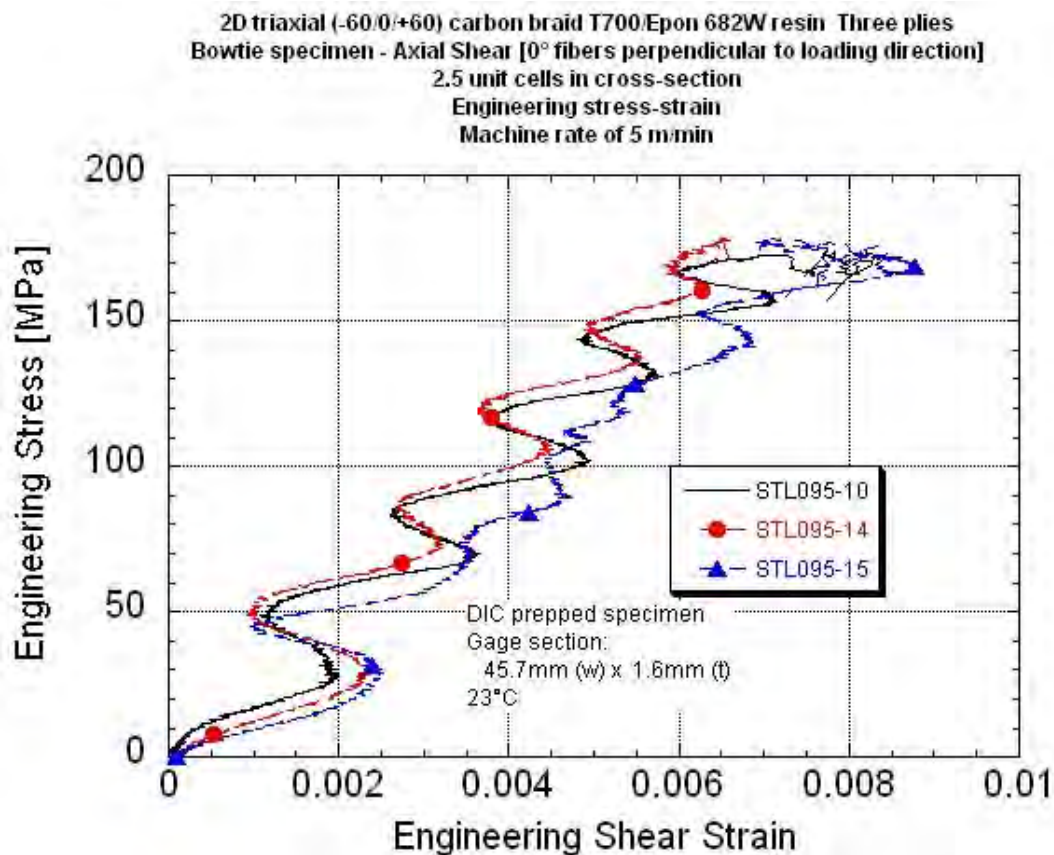
Specimen thickness varied due to the braid structure. Thickness was measured at two "peak" and two "valley" locations and averaged.

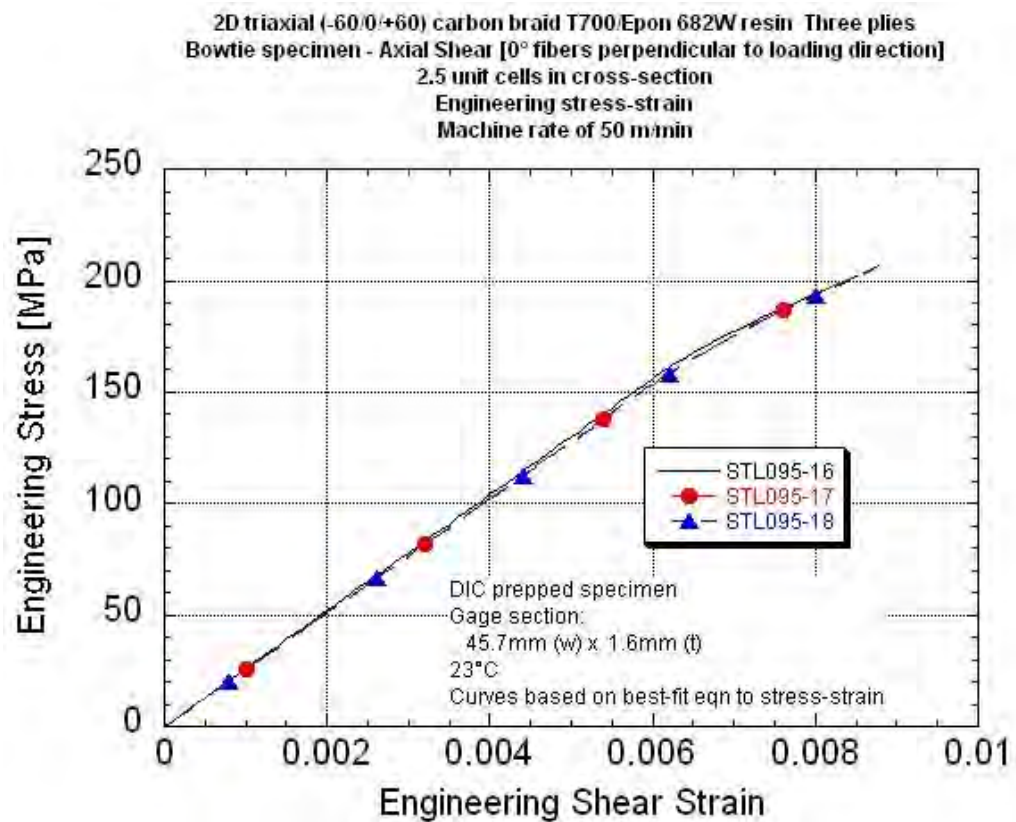
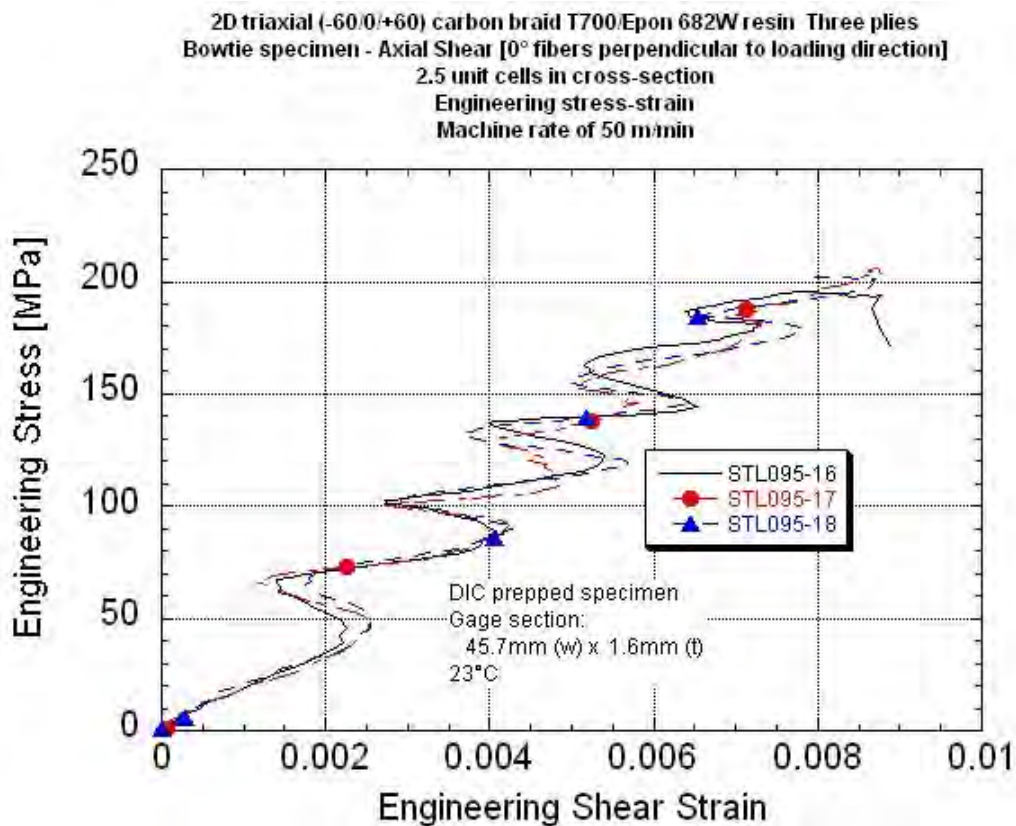
Note 1 Five to six low amplitude system resonant waves in stress response before failure.

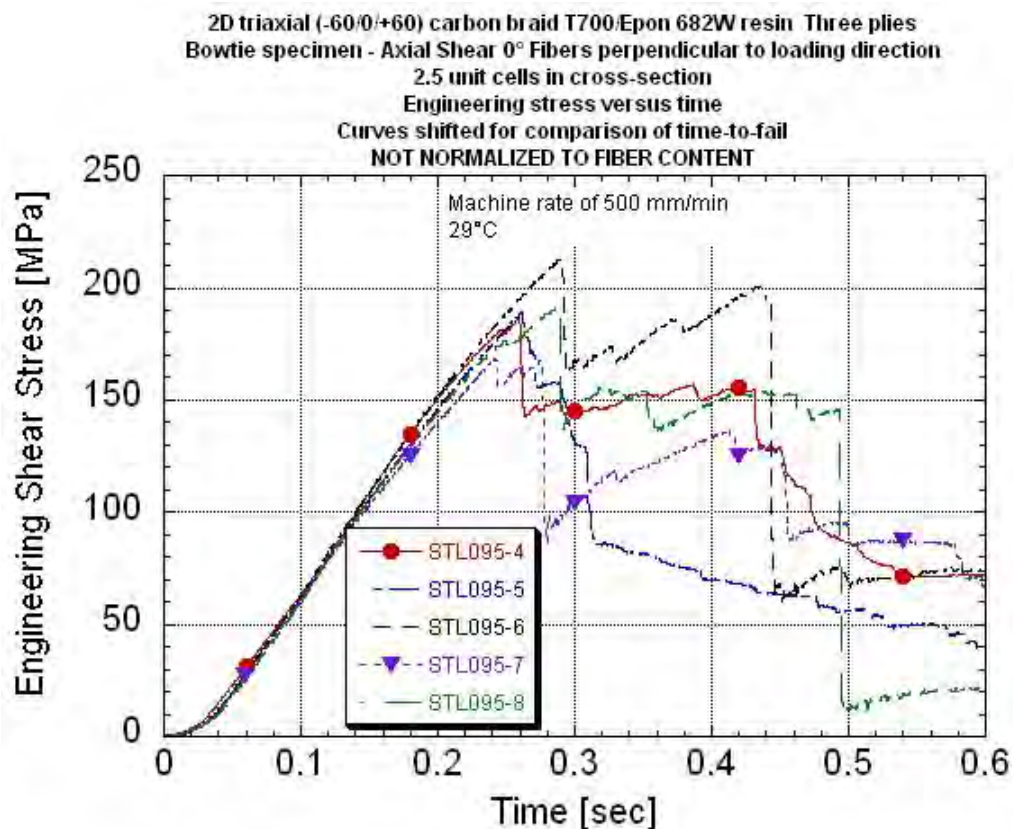
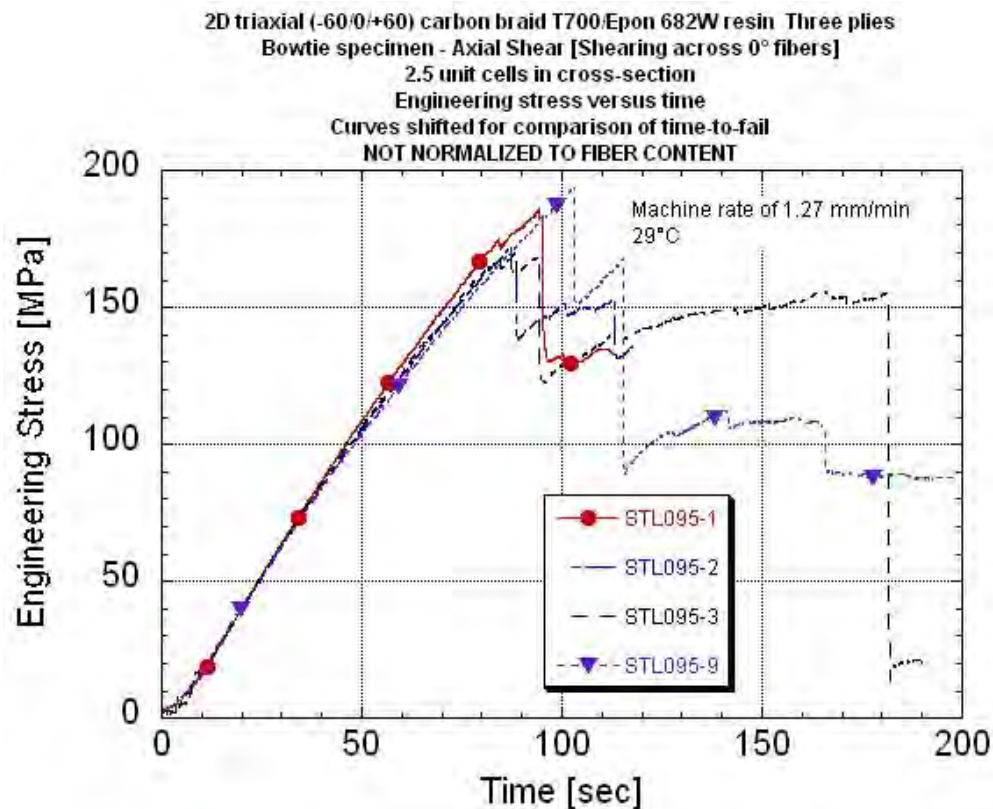


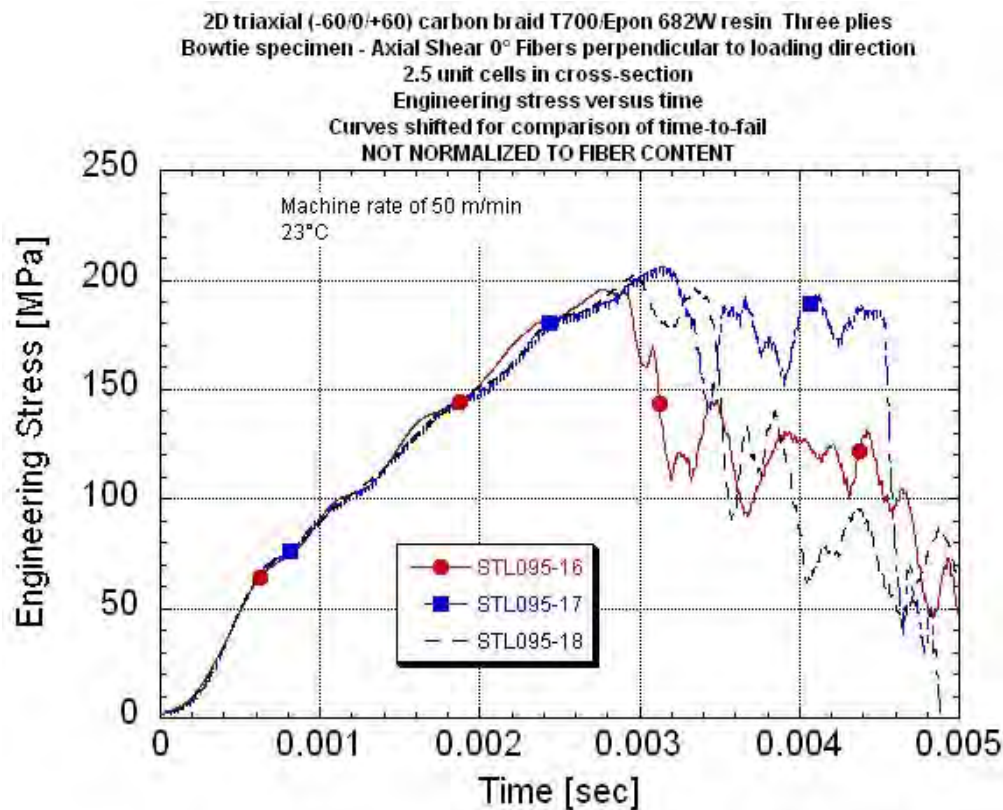
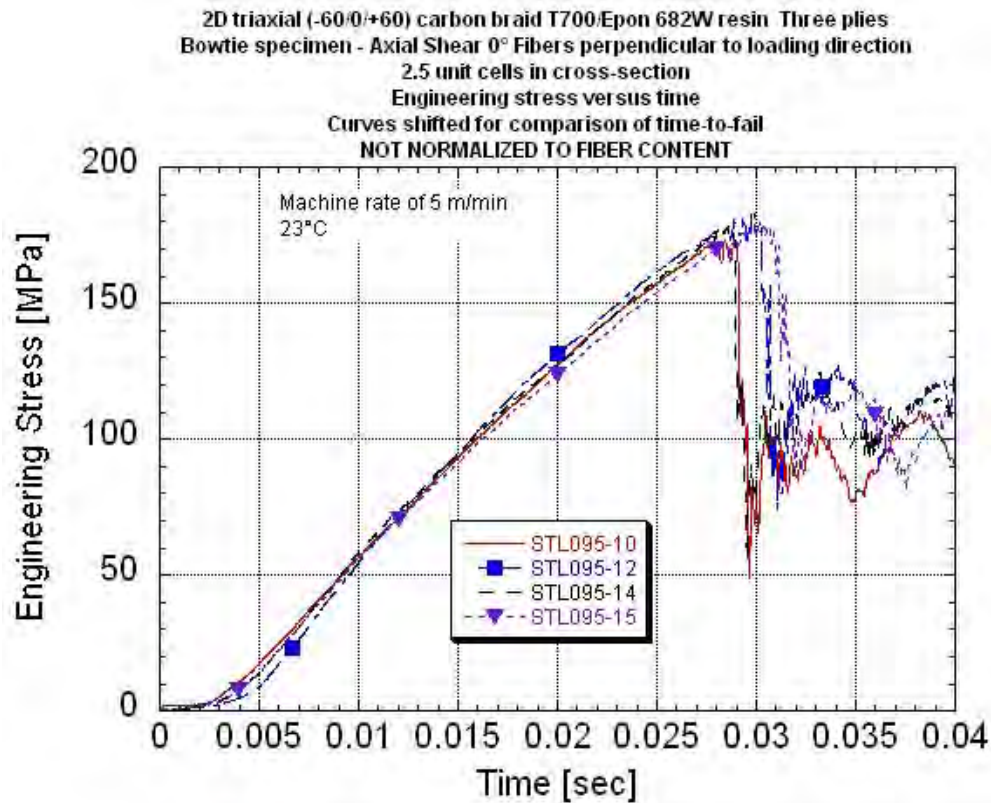












APPENDIX P
TRANSVERSE SHEAR DATA PACKAGE
Shearing along 0° Fibers
Summary Table
Summary Stress-strain Plots With Rate
Summary Stress-time Plots With Rate

Investigation of Opportunities for Lightweight Vehicles Using Advanced Plastics and Composites

Transverse Shear⁽¹⁾ Data Summary 2D Triaxial Carbon T700/ Epon862W Epoxy Braid Bowtie Specimen Configuration - 2.5 unit cells in reduced cross section Nominal center cross-section of 12.7mm wide x 1.65mm thick

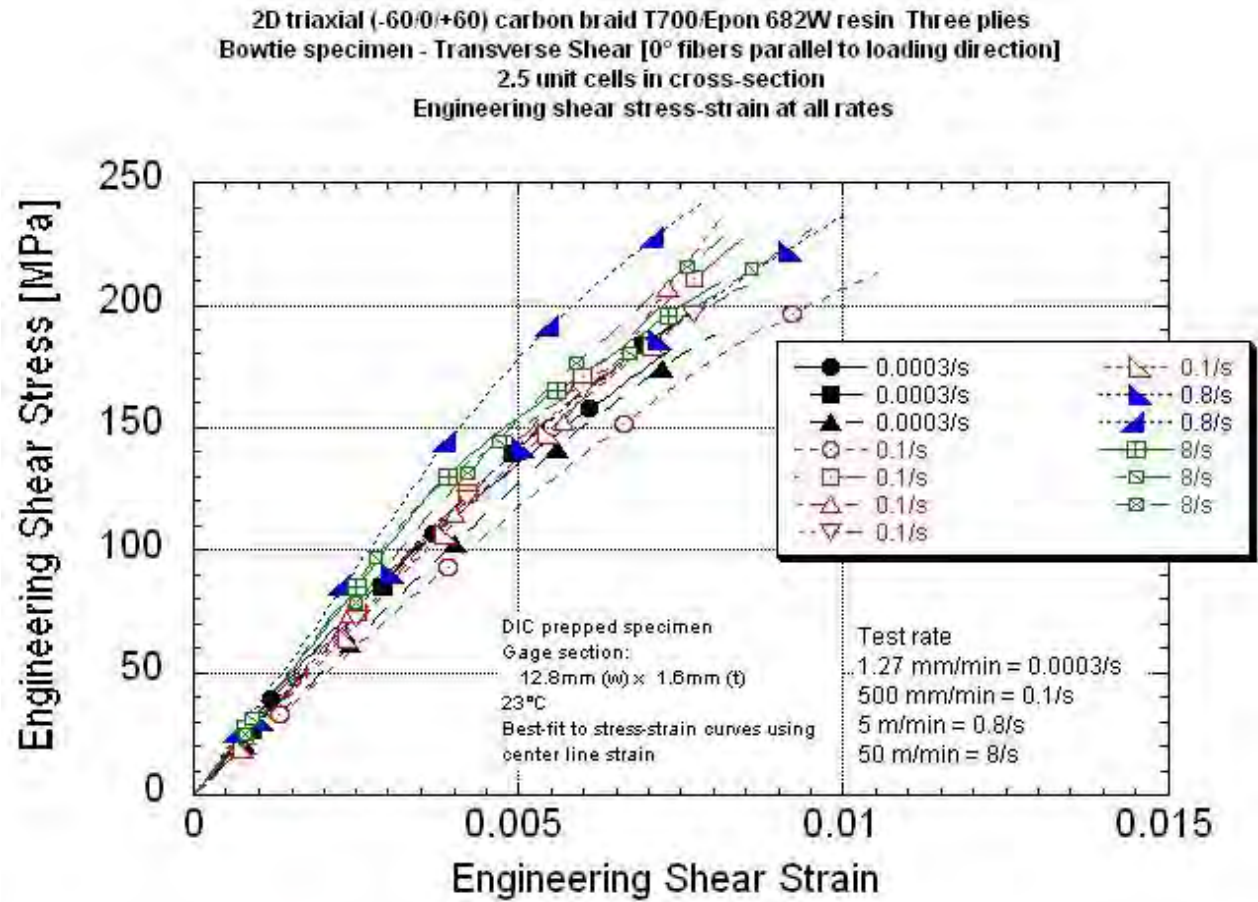
	Panel ID	UDRI STL number	Center line length [mm]	Peak Stress [MPa]	Normalized Peak Stress to 56% Fiber Volume [MPa]	Engineering Breaking Strain # [%]	Localized## Engineering Max Strain [%]	Localized## Engineering Min Strain [%]	Shear# Modulus [GPa]	Measured Strain Rate Before Failure [1/s]	Machine Rate [in/s]	Machine Rate [m/min]	
0.0003/s	073010-3 STB-5	093-6	9.32	186	175	0.711	-	-	32.6	0.000282	0.00084	0.00128	
	073010-4 STB-4	093-7	10.9	202	197	0.752	-	-	29.4	0.000276	0.00083	0.00127	
	073010-5 STB-4	093-8	-	218	216	-	-	-	-	-	0.00083	0.00127	No DIC data
	073010-5 STB-5	093-9	9.39	193	191	0.783	-	-	25.7	0.000283	0.00083	0.00127	
0.05 to 0.1/s	Average			200	195	0.749			29.2				
	Standard Deviation			14	17	0.036			3.5				
	COV [%]			7.02	8.76	4.82			11.9				
	073010-5 STB-6	093-1	8.51	214	212	1.05	-	-	25.3	0.118	0.320	0.487	
	073010-5 STB-3	093-2	-	201	199	-	-	-	-	-	0.335	0.510	No DIC data
	073010-5 STB-2	093-3	7.88	228	226	0.901	-	-	30.0	0.095	0.335	0.510	
	073010-4 STB-3	093-4	-	242	236	-	-	-	-	-	0.335	0.510	No DIC data
0.8/s	073010-4 STB-1	093-5	7.37	235	229	0.824	-	-	30.6	0.102	0.335	0.510	
	073010-3 STB-4	093-10	21.0	208	196	0.814	-	-	28.8	0.0559	0.341	0.520	Wider center section
	073010-3 STB-3	093-11	24.5	198	187	0.737	1.05	0.52	28.0	0.0496	0.336	0.511	Wider center section
	Average			218	212	0.864			28.5				
	Standard Deviation			17	19	0.117			2.1				
	COV [%]			7.86	8.87	13.5			7.28				
	073010-6 STB-Y-1	093-13	7.34	233	228	-	-	-	-	-	3.26	4.96	Issues with DIC
8/s	073010-6 STB-Y-2	093-14	7.31	238	232	0.958	1.33	0.93	28.7	0.812	3.26	4.96	
	073010-4 STB-2	093-18	7.62	246	240	0.759	0.80	0.63	37.2	0.753	3.26	4.97	
	Average			239	233	0.858			32.9				
8/s	Standard Deviation			6	6								
	COV [%]			2.66	2.61								
	073010-6 STB-Y-3	093-12	7.67	208	203	0.883	-	-	33.9	7.49	31.8	48.4	Note 1
8/s	073010-3 STB-3	093-16	8.20	237	224	0.937	0.96	-	34.6	7.73	31.9	48.6	Note 1
	073010-3 STB-1	093-17	7.62	233	220	0.755	-	-	31.6	7.97	32.4	49.3	Note 1
	Average			226	216	0.858			33.4				
	Standard Deviation			16	11	0.093			1.6				
	COV [%]			7.02	5.1	10.9			4.8				

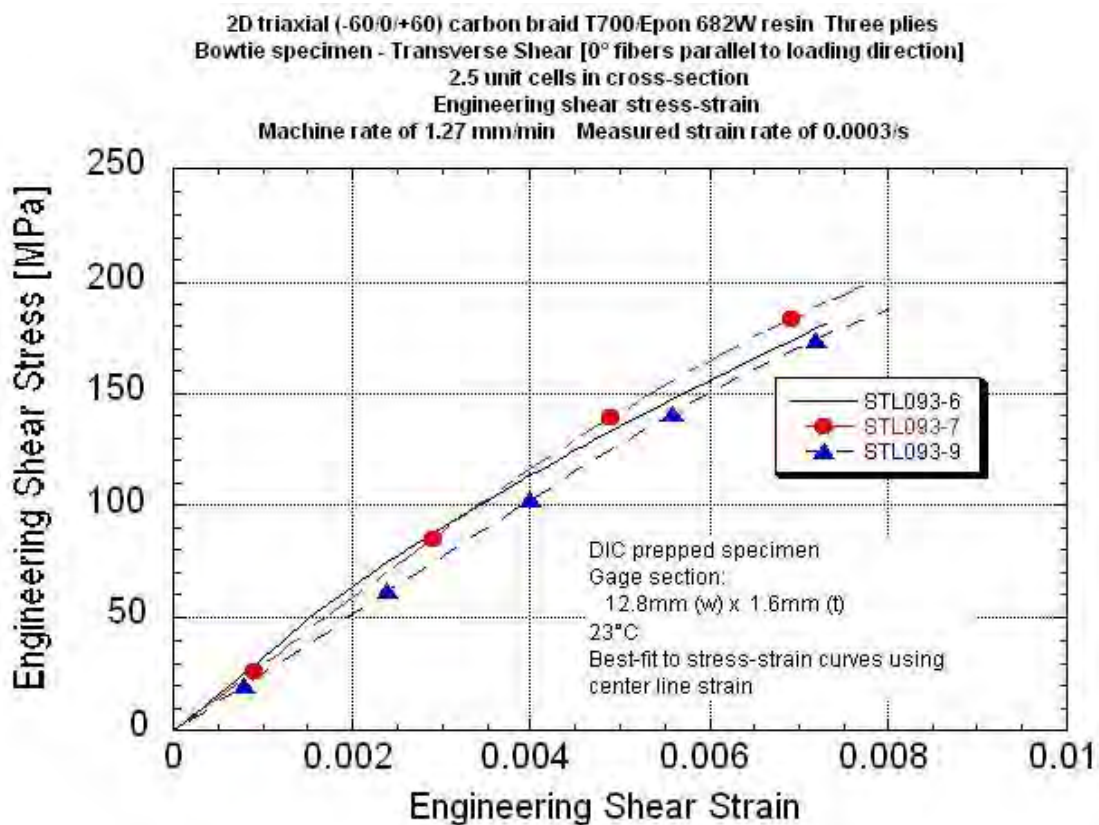
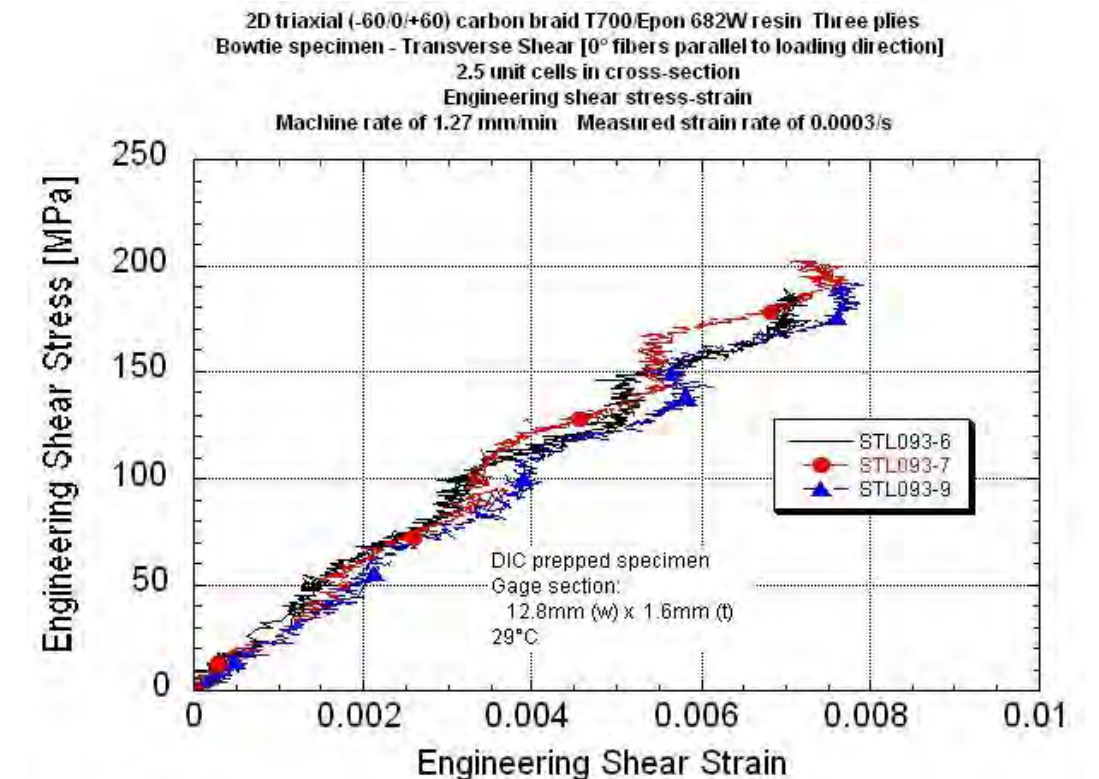
(1) Shear through the short side (5mm) of the unit cell. 0° fibers parallel to loading direction.

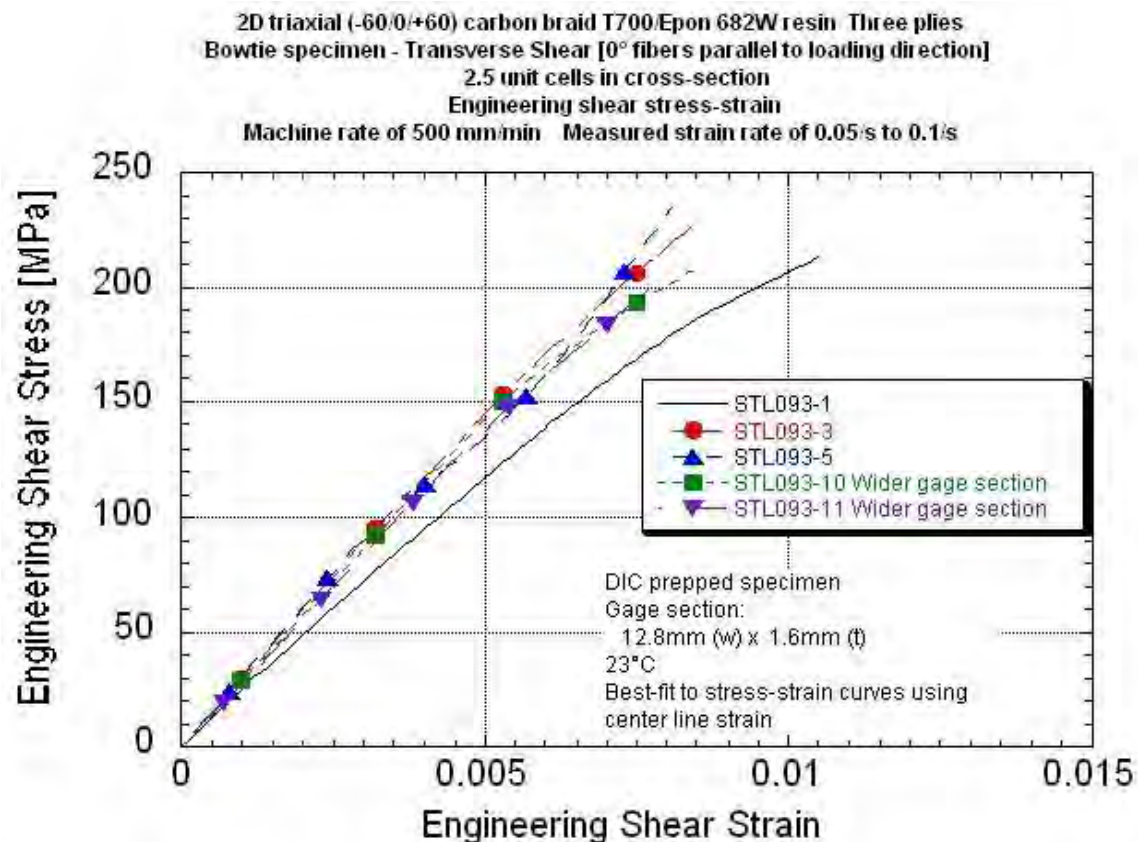
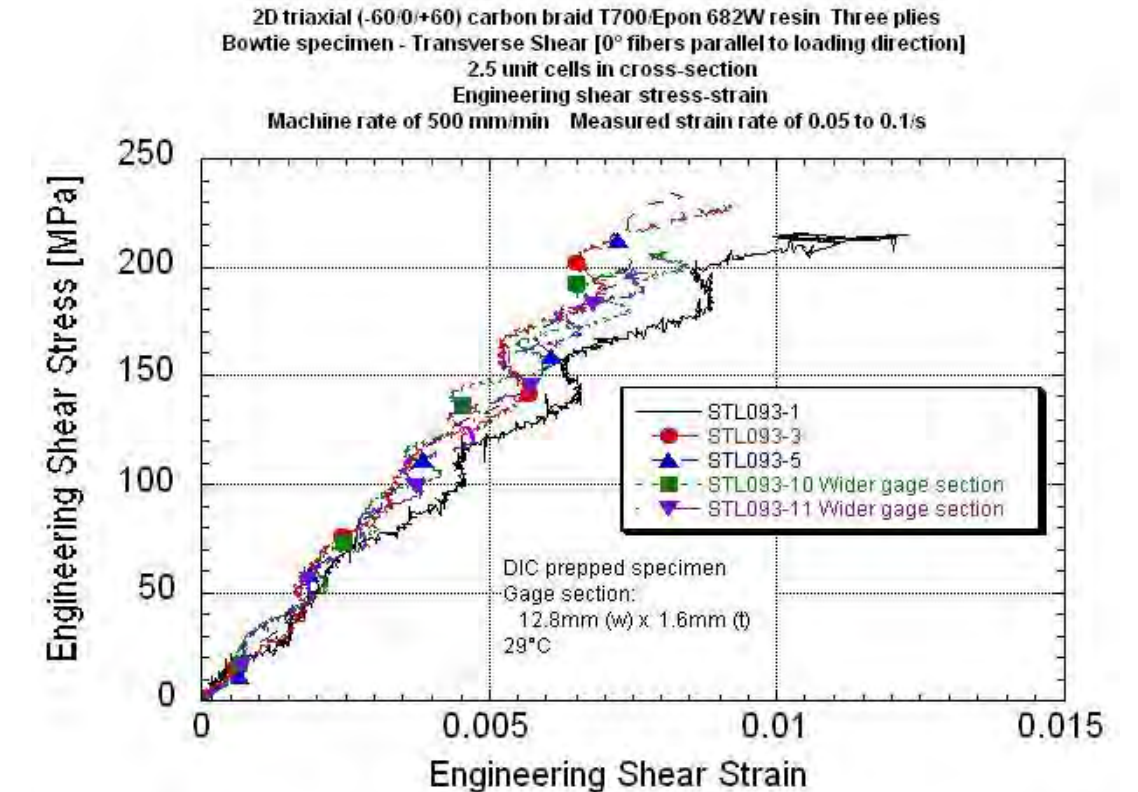
#Based on center line strain. ## Strain as measured at a region of high strain on a fiber braid and low strain in center. Strain data from the onset of cracking and final break.

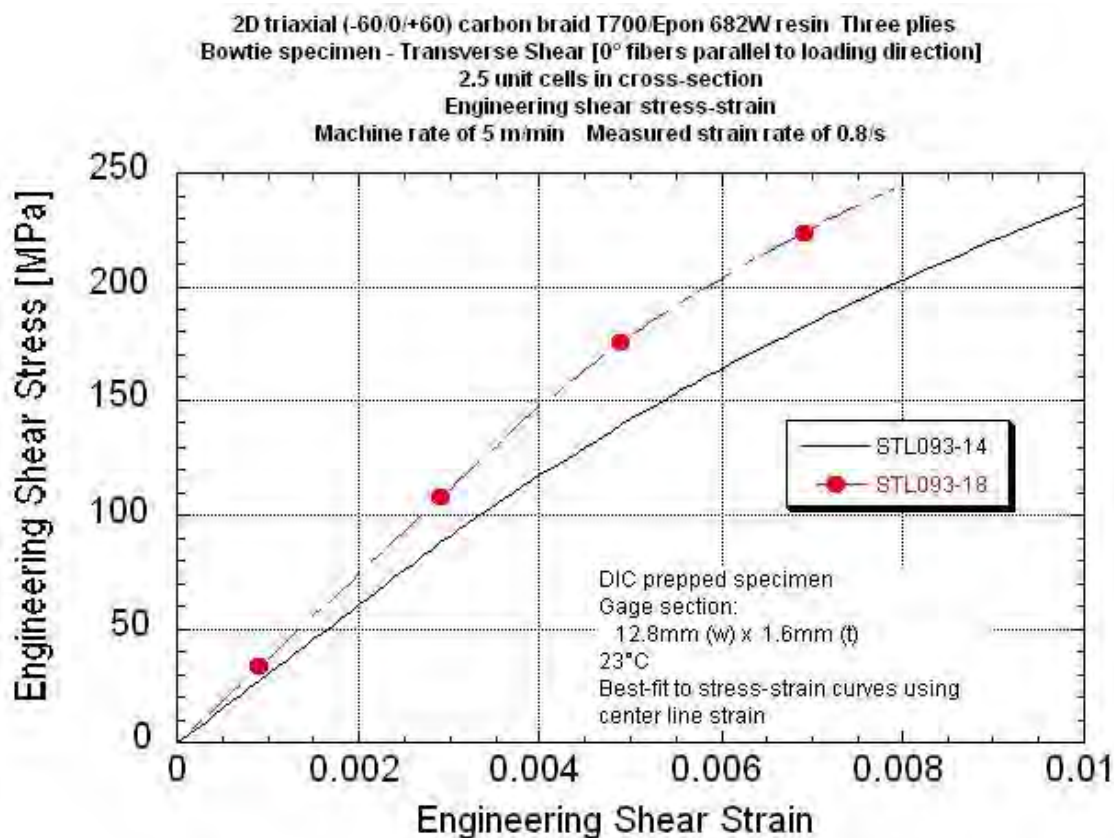
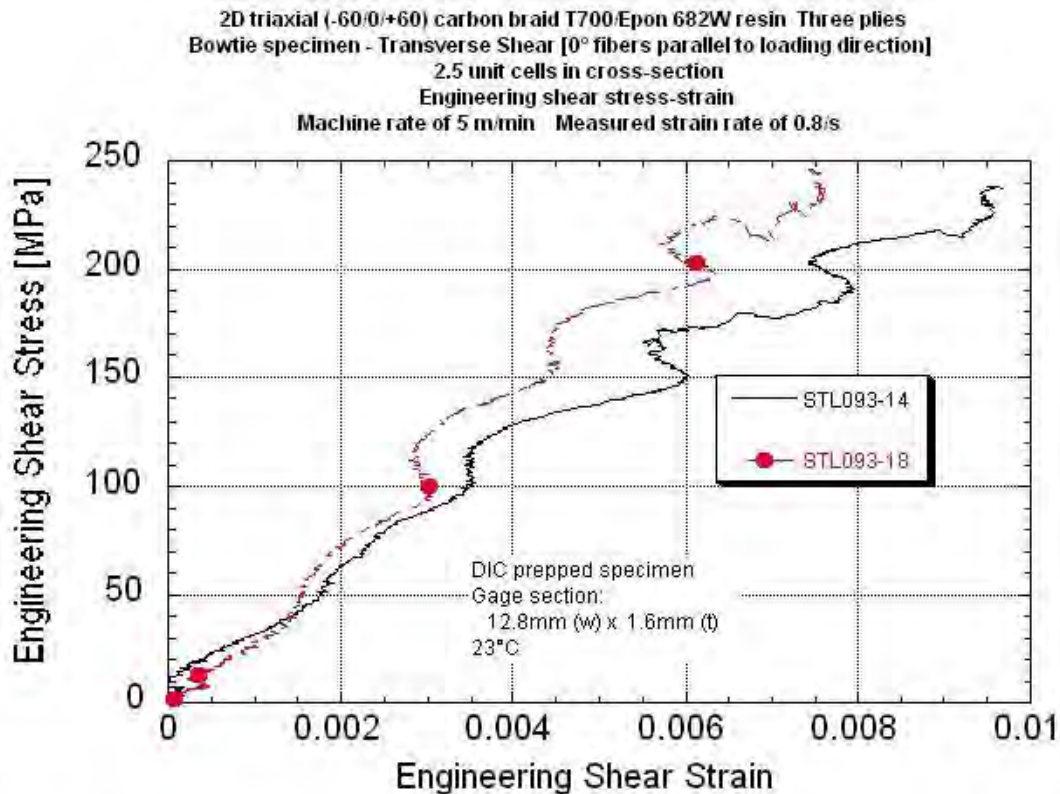
Specimen thickness varied due to the braid structure. Thickness was measured at two "peak" and two "valley" locations and averaged.

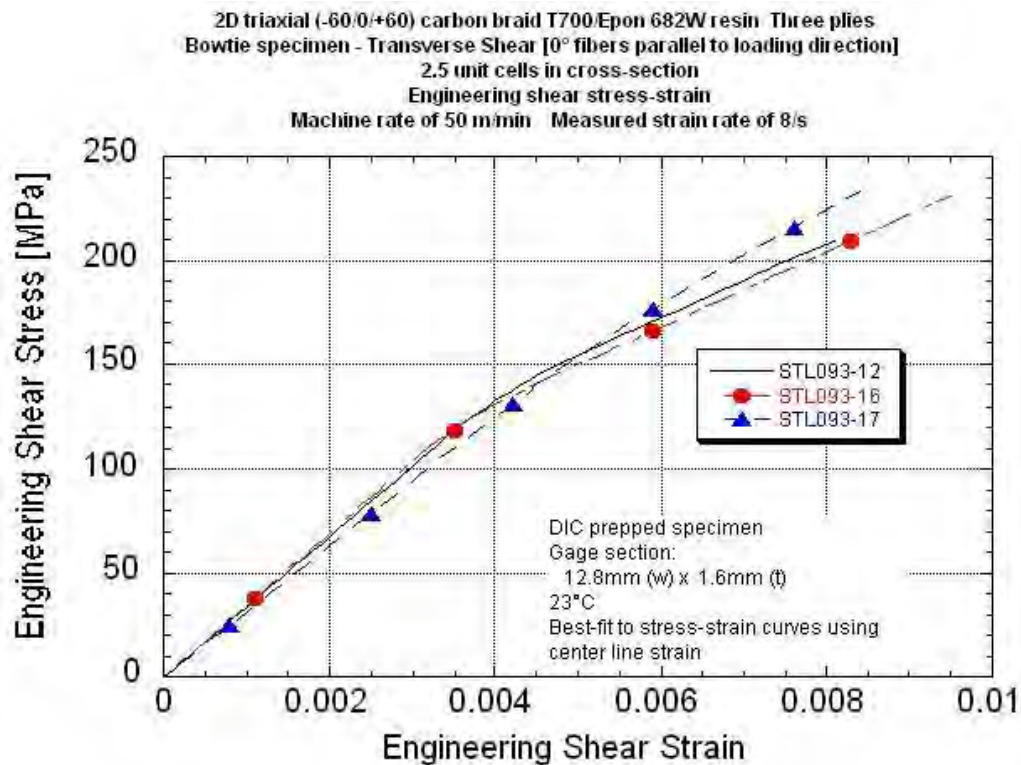
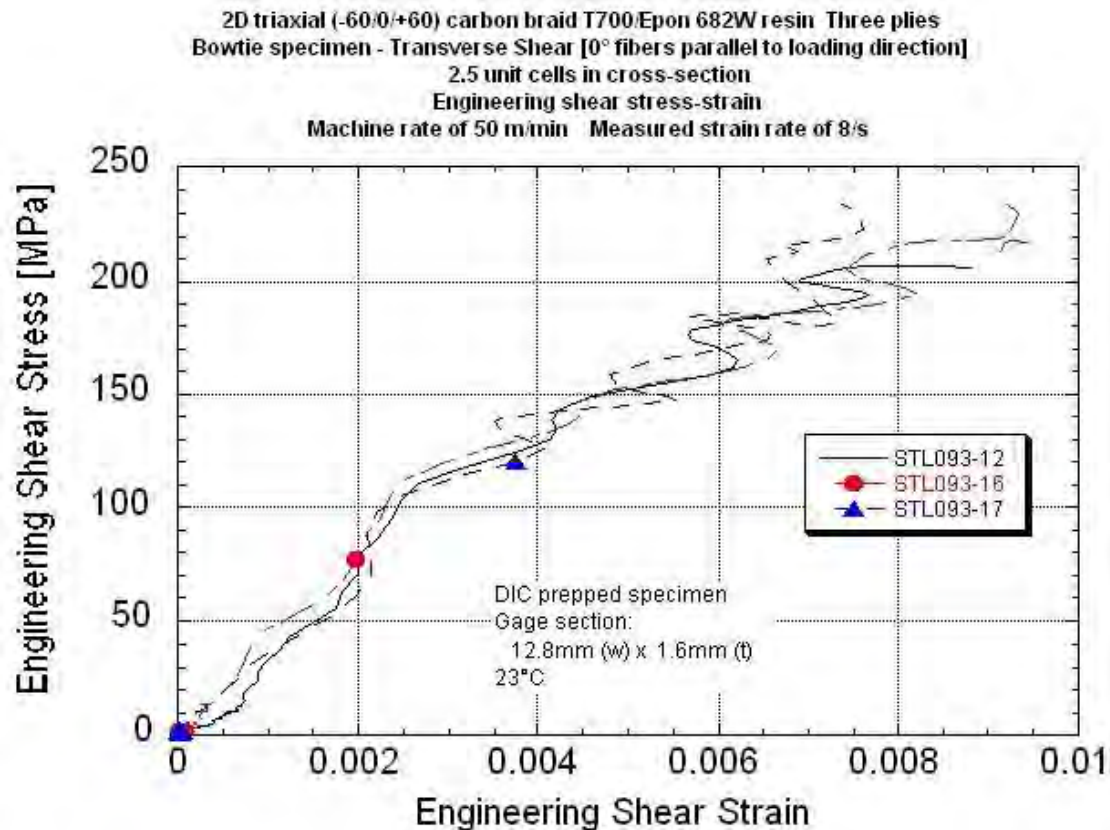
Note 1 Three to four low amplitude system resonant waves in stress response before failure. Failure stress at break depended on when failure occurred, i.e., in the peak or valley of a stress wave.

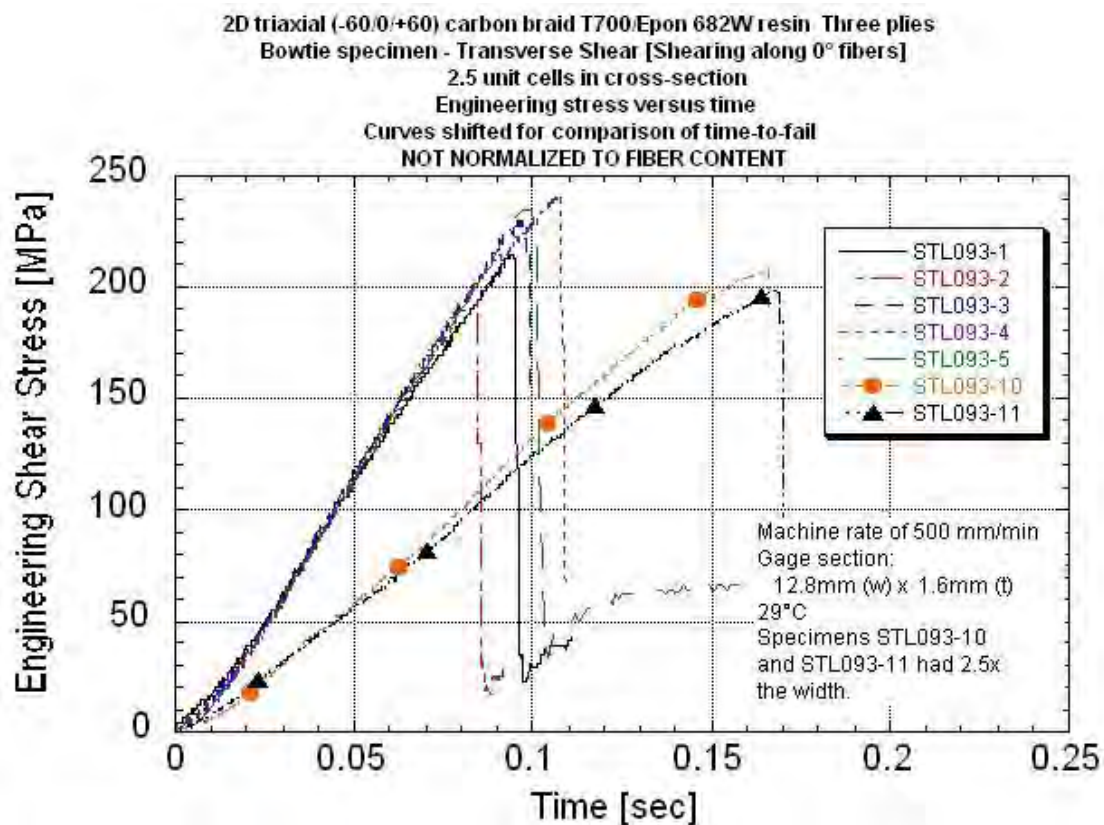
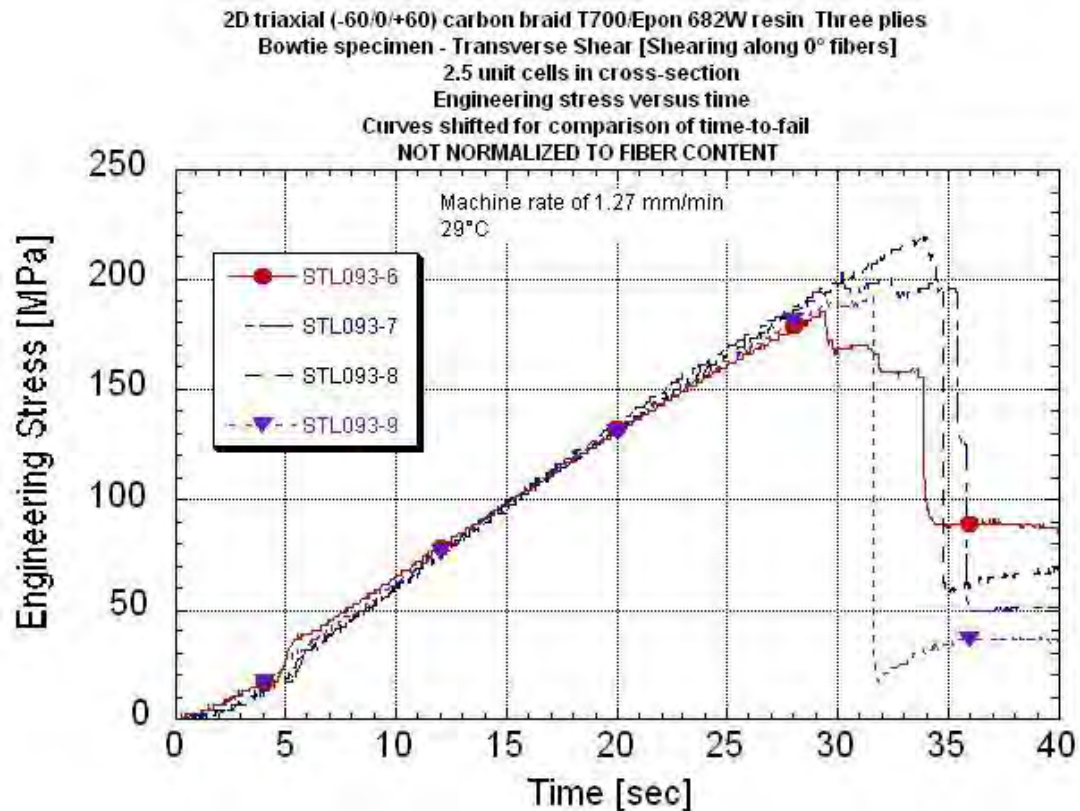


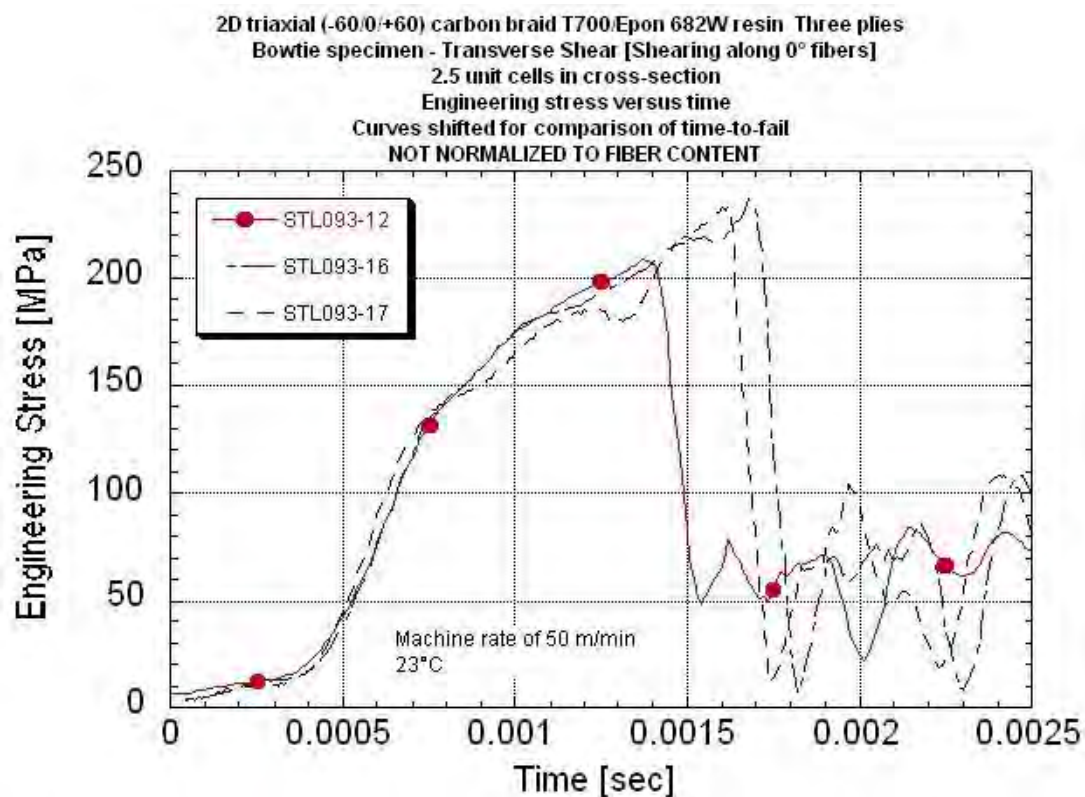
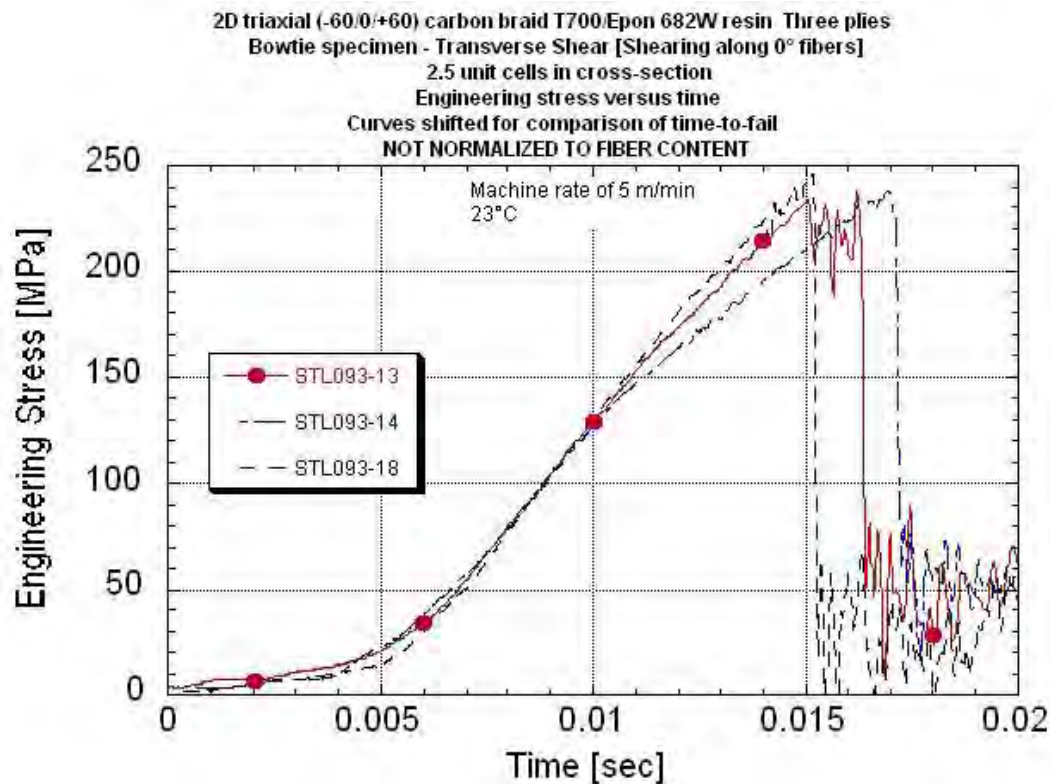












APPENDIX Q
TUBE COMPRESSION DATA PACKAGE
Summary Table
Summary Plots

Investigation of Opportunities for Lightweight Vehicles Using Advanced Plastics and Composites

Tube Compression Data Summary
2D Triaxial Carbon T700/ Epon862W Epoxy Braid
Average fiber content of 44.44 vol%. Nominal inner diameter of 101 mm and a wall thickness of 3.8 mm.

Speed on top edge of specimen	Starting Tube Serial ID	UDRI STL number	Tube Weight [gm]	Cross-sectional Area [sq. mm]	Density [gm/cc]	Work up to ≤ 115 mm [kJ]	Median Crush Load* [kN]	Median Crush Stress* [MPa]	Median Stress Normalized to 56% Fiber Volume [MPa]	Specific Sustained Crushing Stress [SSCS]	Crush Compression Ratio**	Specific Energy Absorption ⁽¹⁾ with folding mode failure [SEA-FM] [kJ/kg]	Specific Energy Absorption ⁽²⁾ [SEA] [kJ/kg]	Specific Energy Absorption ⁽³⁾ [SEA] [kJ/kg*2]	Average Peak ⁽⁴⁾ Temperature During Crush [°C]	Machine Rate [m/s]	Machine Rate [m/min]	Comments
1.5 m/min	1050	103-2-2	256	627	1.45	5.83	47.8	76.2	98.8	52.7	0.36	44.3	55.9	20.5	-	0.02548	1.53	
	1051	103-3-1	256	629	1.47	5.57	48.0	76.4	100	51.9	0.37	44.1	52.4	21.4	-	0.02546	1.53	
		103-4-1	258	629	1.45	5.34	45.1	71.7	93.6	49.6	0.35	41.0	51.0	18.5	-	0.02541	1.52	
	1053	103-5-1	253	626	1.47	5.04	42.2	67.3	80.4	45.8	0.30	39.9	47.6	17.9	-	0.02546	1.53	
	1054	103-6-2 Run 2	255	628	1.44	6.19	52.0	82.8	106	57.5	0.39	47.4	59.5	21.8	-	0.02542	1.53	Set-up Initial run with a flat end. Exceed actuator capacity. Rerun with angle cut
		Average				5.60	47.0	74.9	95.8	51.5	0.35	43.3	53.3	20.0				
		Standard Deviation				0.44	3.66	5.79	9.61	4.29	0.04	2.96	4.56	1.75				
		COV [%]				7.89	7.78	7.74	10.0	8.32	10.0	6.84	8.56	8.7				
140 m/min	1049	103-1-1	253	619	1.47	5.19	47.6	76.9	92.5	52.3	0.34	-	49.6	20.3	296	2.38	143	
	1049	103-1-2	253	623	1.47	5.70	50.6	81.2	97.7	55.3	0.36	-	54.1	22.3	252	2.36	142	
	1051	103-3-2	253	629	1.45	5.43	47.2	75.1	98.7	51.9	0.36	-	51.9	21.2	233	2.36	142	
		103-4-2	235	619	1.45	4.89#	50.1	80.9	106	55.9	0.39	-	55.7	20.6	-	2.38	143	Setup run. Length shorter by 25 mm
	1055	103-7-2	253	621	1.43	5.14	44.9	72.4	95.3	50.8	0.35	-	50.5	20.1	173	2.37	142	
		103-9-1	255	614	1.44	5.43	46.7	75.9	95.0	52.7	0.35	-	53.3	21.0	362	2.36	141	
		Average				5.37	47.8	77.1	97.4	53.2	0.36		52.5	20.9	263			
		Standard Deviation				0.22	2.14	3.44	4.55	2.01	0.02		2.30	0.81	71			
		COV [%]				4.15	4.5	4.5	4.67	3.77	4.67		4.37	3.89	27			
440 m/min	1050	103-2-1	255	631	1.45	4.97	43.0	68.1	84.2	47.1	0.31	-	47.3	18.6	254	7.35	441	
	1053	103-5-2	255	625	1.47	5.36	45.9	73.5	90.9	50.0	0.34	-	50.7	20.0	404 [excluded from avg]	7.36	441	
	1054	103-6-1	253	622	1.44	4.89	42.0	67.5	83.6	46.9	0.31	-	47.4	18.4	254	7.34	440	
	1057	103-8-2	256	633	1.44	5.39	45.3	71.5	88.5	49.6	0.33	-	51.3	20.0	308	7.34	440	
		103-9-2	254	615	1.44	4.85	40.2	65.4	81.8	45.4	0.30	-	47.7	18.1	289	7.35	441	
		Average					43.3	69.2	85.8	47.8	0.32		48.9	19.0	276			
		Standard Deviation					2.35	3.24	3.77	1.95	0.01		1.95	0.94	27			
		COV [%]					5.43	4.69	4.39	4.08	4.39		3.98	4.96	10			
150 m/min Flat end	1055	103-7-1	255	622	1.43	5.10	43.4	69.7	91.7	48.9	0.34	-	50.0	19.6	311	2.37	142	No crack initiator

*Load/Stress measured over a region from 25 mm net zeroed displacement up to stroke limit. #Out to 98mm. Not included in average.

** Normalized to 56% fiber volume. Ultimate strength of 271 MPa.

The displacement was zeroed at a value of 40 kN normalized load. All failures at 1.5 m/min were a combination of folding and tearing, with the exception of 103-6-2. Failure for 103-6-2 was all by folding.

The specimen thickness varied due to the braid structure. The measured thickness was an average of "peaks" and "valleys" from three locations along the length of the original tube.

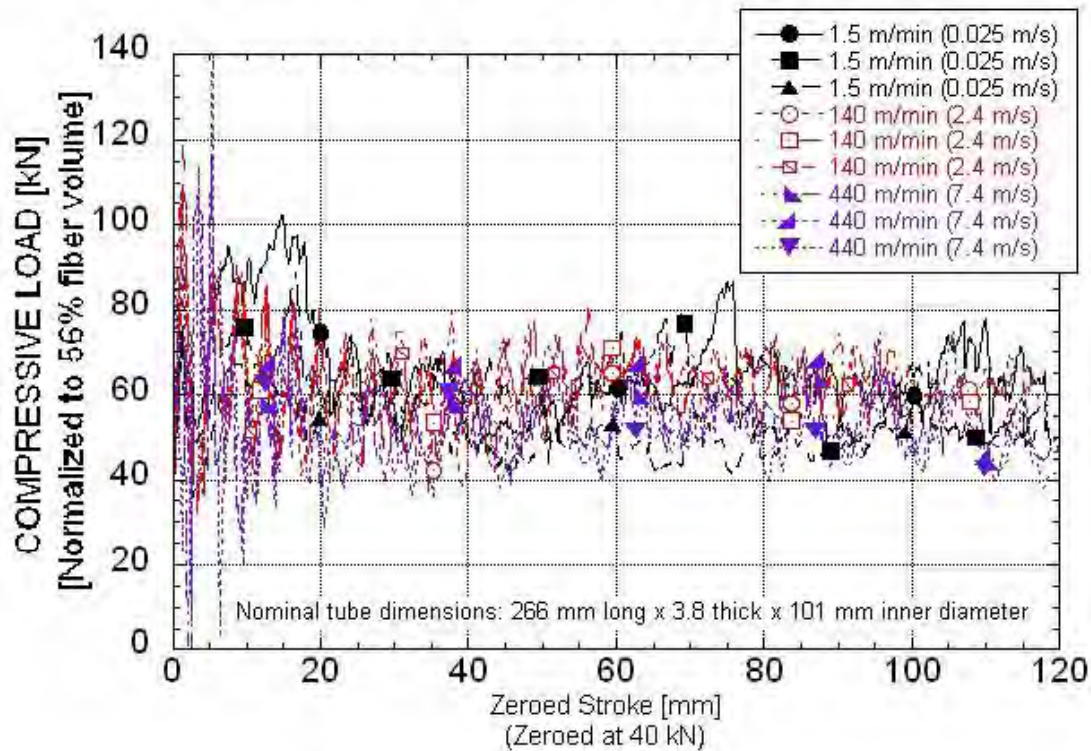
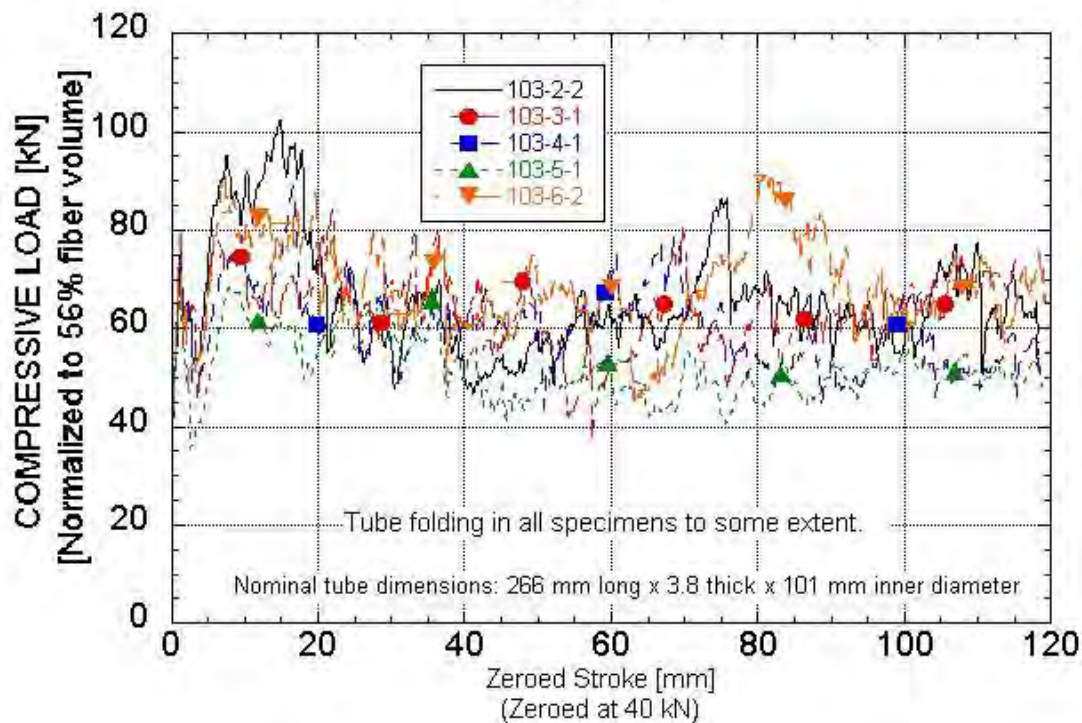
1) SEA calculated using $E_s = \text{Work}/(\text{area} \cdot \text{density} \cdot [\text{actuator displacement} + \text{displacement of folded length}])$

2) SEA calculated using $E_s = \text{Work}/(\text{area} \cdot \text{density} \cdot \text{total actuator displacement})$

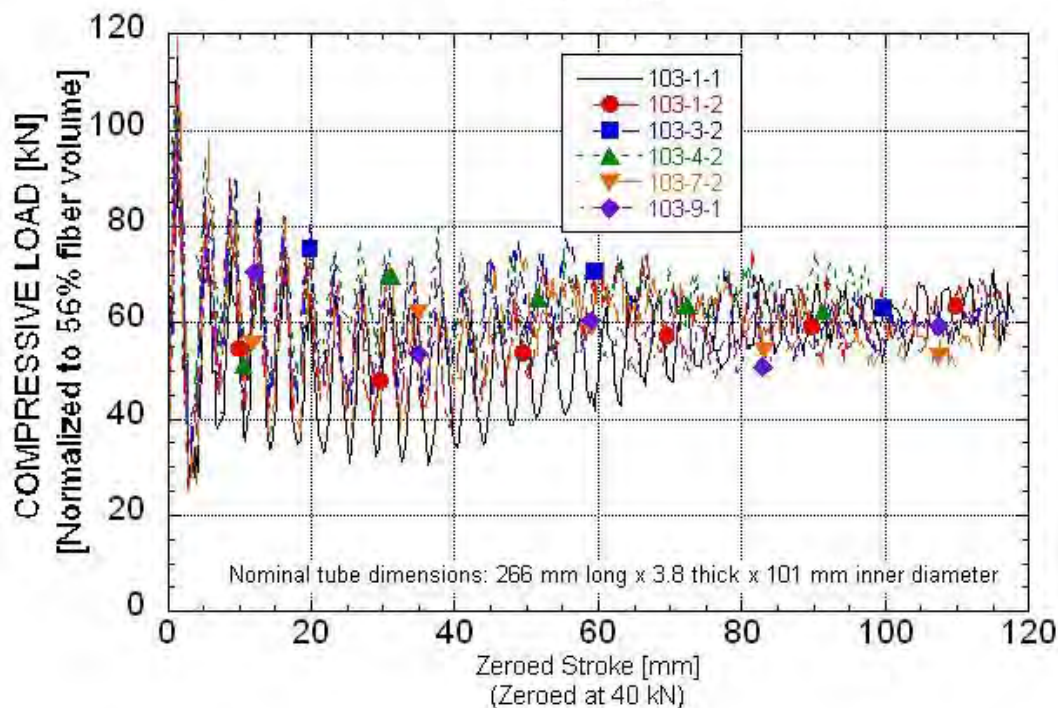
3) SEA for design purposes $E_s = \text{Work}(\text{displacement at peak} - \text{displacement at end})/(\text{mass of tube} \cdot \text{displacement at end})$ Adjusted for fan-fold length at 1.5 m/min.

4) All but one of the specimens had the peak temperature exceed the calibration curve limit of 200°C. Peak data are estimated using the calibration correlation equation.

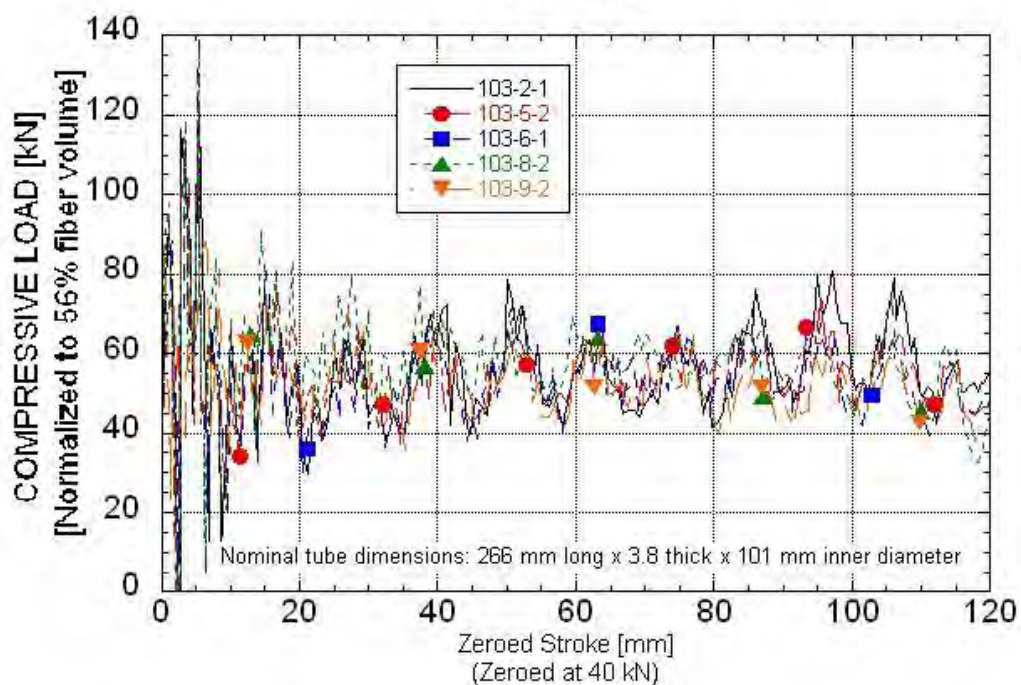
NORMALIZED LOAD vs. ACTUATOR DISPLACEMENT

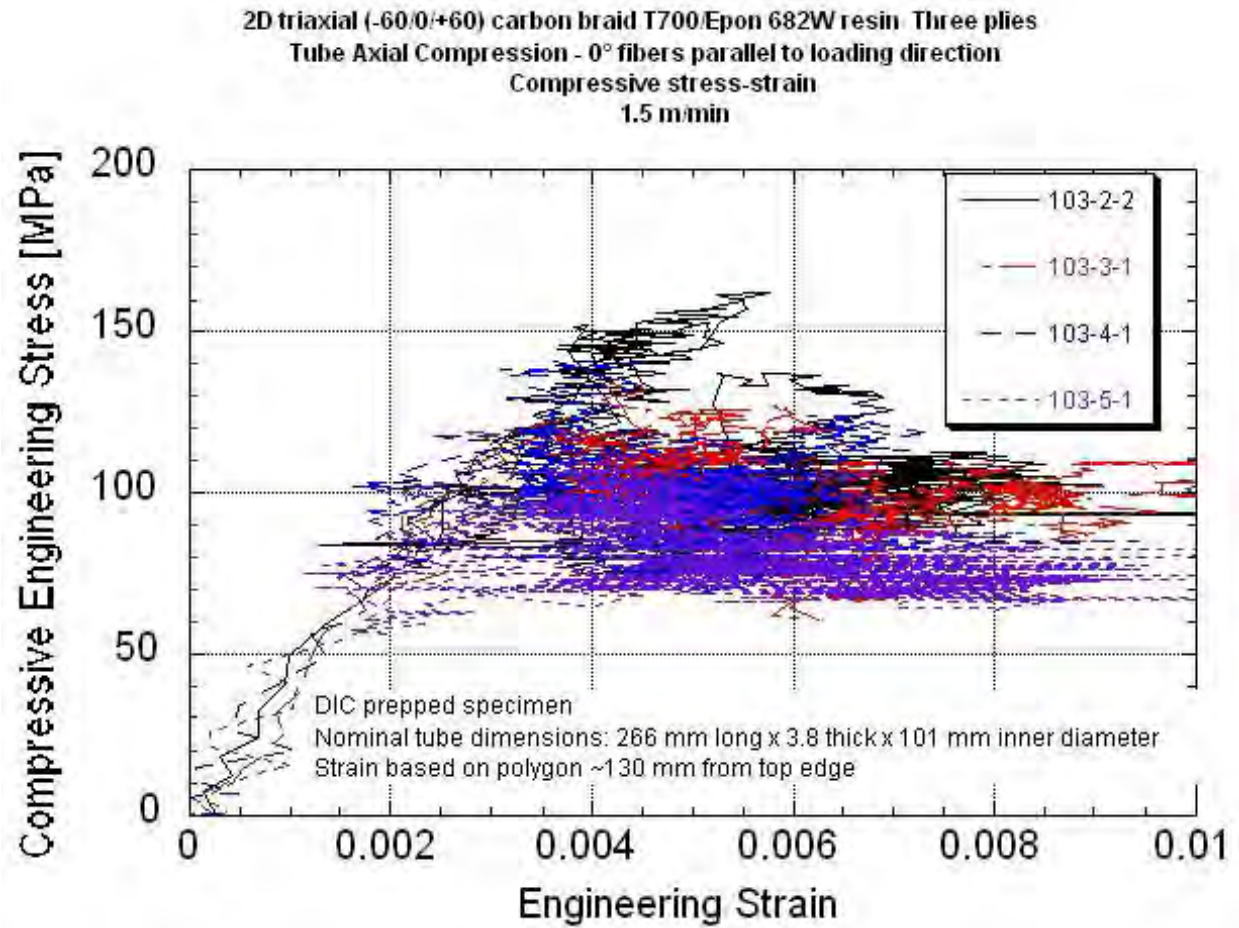
NORMALIZED LOAD vs. ACTUATOR DISPLACEMENT
1.52 m/min

NORMALIZED LOAD vs. ACTUATOR DISPLACEMENT
140 m/min



NORMALIZED LOAD vs. ACTUATOR DISPLACEMENT
440 m/min





DOT HS 811 692
December 2012



U.S. Department
of Transportation
**National Highway
Traffic Safety
Administration**



9111-120512-v2a